UNIVERSITÀ DI PARMA

UNIVERSITA' DEGLI STUDI DI PARMA

DOTTORATO DI RICERCA IN
" *Scienze Chimiche*"

CICLO XXXVII

Recovery and recycling of lanthanides from permanent magnets: Techniques for reuse in innovative applications

Coordinatori:

Chiar.ma Prof.ssa Alessia Bacchi
Chiar.mo Prof. Giovanni Maestri

Tutore:

Chiar.mo Prof. Matteo Tegoni

Dottorando: Alex Falco

Anni Accademici 2021/2022 – 2023/2024

Abstract

This PhD thesis explores novel approaches for the extraction, separation, and functional reuse of rare earth elements, focusing particularly on neodymium (Nd) and dysprosium (Dy) from end-of-life permanent magnets. These elements, crucial for various technological applications, present significant recovery challenges due to their chemical similarity. The work is divided into two principal sections, each addressing a different phase of recovery and functionalization.

In the first part, the research examines the design, synthesis, and characterization of specialized organic ligands capable of selectively complexing Nd and Dy. By utilizing a range of ligands with varied coordination environments, a selective precipitation method was developed, enhancing both the economic and environmental sustainability of the separation process. Ligands were synthesized through the condensation of tren or 1,3-diaminopropanol with functionalized salicylaldehyde derivatives, yielding heptadentate and pentadentate Schiff-base ligands. Subsequent reduction of these Schiff bases produced a more stable ligand structure suitable for harsher processing conditions. This part of the thesis provides a foundation for effective rare-earth separation by optimizing the solubility and stability of the metal-ligand complexes.

The second part develops lanthanide-based materials aimed at biomedical applications. Using recovered Nd and Dy ions, dimeric, trimeric, and tetrameric 12-metallacrown-4 (12-MC-4) complexes were synthesized for potential use in bio-imaging and/or targeted therapy. The assembly of these complexes involved linking monomeric 12-MC-4 units with dicarboxylic ligands with different angle bond to form structures suited for fluorescence and stability studies. Functionalization with NBD-based chromophores enabled luminescence at visible wavelengths, making

these materials suitable as fluorescent probes. Additionally, metallacrowns were modified with biotin to allow selective interaction with streptavidin, useful for targeted tumor imaging.

This thesis underscores the viability of a coordinated approach to rare-earth recovery and functionalization, advancing the field of sustainable recycling while expanding the scope of biomedical applications for recovered materials.

Abbreviations

δ	Chemical shift
DMF	Dimethylformamide
DMSO	Dimethylsolfoxide
NBD	Nitrobenzoxadiazole
ABD	Amminobenzoxadiazole
Ipa	Isopthalic acid
DiMe	Dimethyl
AcOEt	Ethyl acetate
DCM	Dichloromethane
MeCN / ACN	Acetonitrile
MeOH	Methanol
EtOH	Ethanol
THF	Tetrahydrofuran
MC	Metallacrown
SS	Solid state
PM	Permanent Magnet
REE	Rare-earth element
GFP	Green fluorescent protein
frn	fluorenone
bipy	bipyridile

Index

0. Premise

At the beginning of the 19th century, the chemist Jöns Jacob Berzelius and the geologist Wilhelm Hisinger discovered a new element called cerium, which was later identified as one of the rare earth metals. Initially, this element was used in the production of gas lamp mantles.[1] Today, there are 15 recognized rare earth elements, ranging from lanthanum to lutetium, although yttrium and scandium are considered in that group based on their electronic configuration.[2] Interestingly, the term "rare earth" does not refer to the scarcity of these metals in the Earth's crust, but rather to the difficulty in extracting and separating them from their ores. These metals are commonly referred to as lanthanides or lanthanoids today.

Due to their exceptional optical and magnetic properties, lanthanides are used in various technological fields, such as communication (fiber optics), glass and ceramics manufacturing, phosphor lamps, catalysts, metal alloys, and magnets, to name a few. Fe-Nd-B permanent magnets in particular, have attracted significant and ongoing interest since their discovery.[3,4] They were first applied in the production of hybrid motors in the early 2000s and have since been used in the development of wind energy technologies.[5–7] Today, their applications range from electric motors to batteries and hard drives. **Figure 0.1** illustrates the forecasted increase in demand for magnets for specific applications up to 2030.

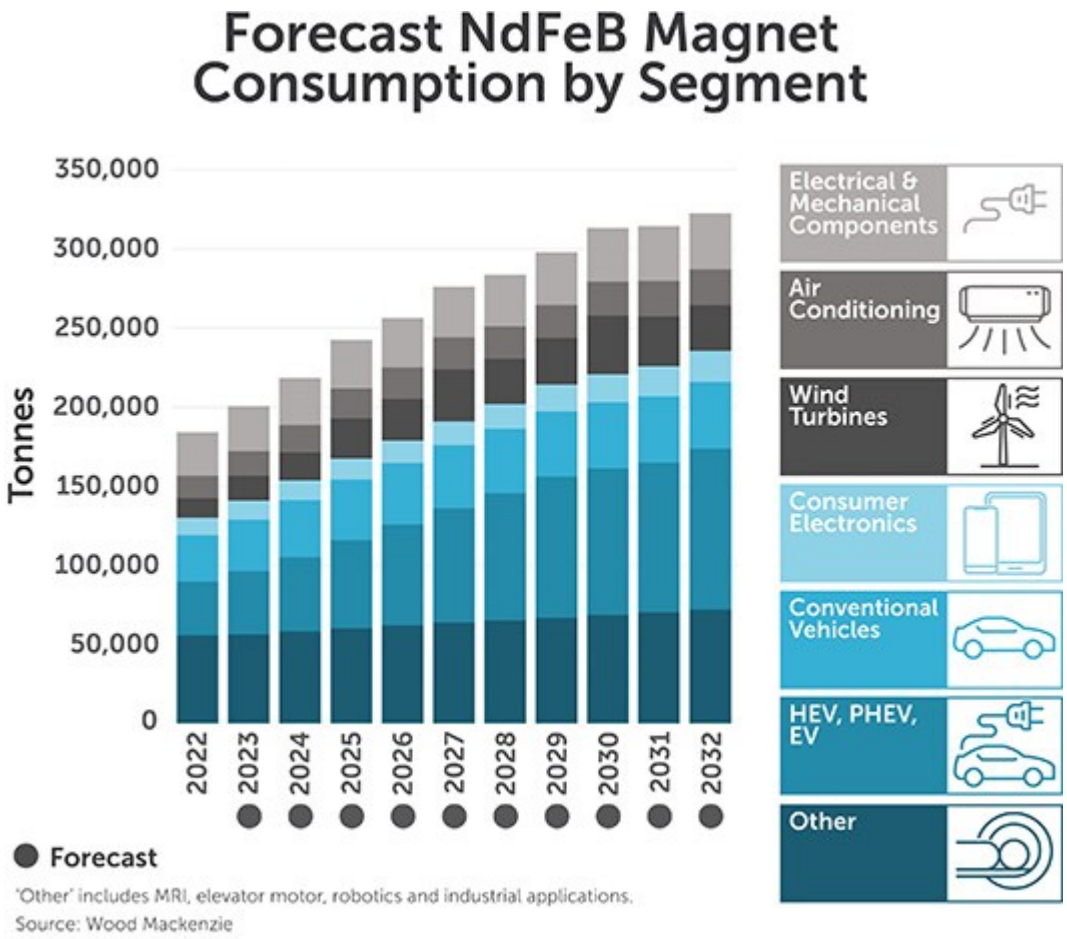

Figure 0.1. Forecast NdFeB magnet consumption divided by technological segment.

Depending on their size and application, magnets have a lifespan ranging from 2-3 years to up to 30 years. When these magnets reach the end of their life, various processes are currently employed to recycle them and recover high-value metals such as Nd, Dy, Tb, and Gd.[8–11] The need to recover these metals arises from several factors, including the location of rare earth deposits in geopolitically challenging areas, the low environmental sustainability of mineral extraction processes, and the growing quantities of end-of-life electronic materials. Perhaps most importantly, the desire of some regions, including Europe, to achieve economic independence

from the rare earth metals market has prompted governments and international agencies to invest significant funding into the recovery of these elements from exhausted materials. This effort is largely justified by the fact that underdeveloped technologies, high costs, and low environmental sustainability of the current processes keep the recovery rate of lanthanides from end-of-life devices below 2% of the total input.[9,12,13]

In this thesis, coordination chemistry, which has shown significant advancements in the separation of lanthanides in recent years, is explored as a tool for improving these processes.

This PhD thesis is structured into two parts. The first part focuses on the design, synthesis, and characterization of two organic ligands capable of forming distinct complexes with neodymium and dysprosium. Specifically, I have investigated the development of an alternative, cost-effective, and environmentally sustainable method to recover and separate neodymium and dysprosium by utilizing selective precipitation of the complexes formed by these two lanthanides in different organic solvents. The second part addresses the synthesis of dimeric, trimeric, and tetrameric metallamacrocyclic entities (Metallacrowns, MCs), highlighting the unique structure and optical properties of these supramolecules in light of their potential applications as contrast agents and in biological imaging.

Part 1: **Polydentate ligands for neodymium (Nd) and dysprosium (Dy) separation**

Chapter 1: **Rare earth elements: from discovery to application to recovery**

1.1 Introduction

1.1.1 The discovery of the rare earth elements

The study of lanthanide chemistry originated in Scandinavia. In 1794, Johann Gadolin successfully isolated an "earth" (oxide) from a black mineral that he named “Yttria”, later known as gadolinite. Shortly thereafter, M.H. Klaproth, J.J. Berzelius, and W. Hisinger obtained another earth, called "ceria," from the mineral cerite. However, it was not until the period between 1839 and 1843 that the Swedish chemist C.G. Mosander first succeeded in separating these earths into their constituent oxides. Specifically, ceria was resolved into the oxides of cerium and lanthanum, along with a mixed oxide called "didymia" (a mixture of the oxides of metals ranging from praseodymium to gadolinium). Similarly, the original yttria was separated into substances named erbia, terbia, and yttria. When Mendeleev first published his Periodic Table in 1869, he was only able to include lanthanum, cerium, didymium (now known to be a mixture of praseodymium and neodymium), another mixture in the form of erbia, and yttrium. Unreliable data on atomic mass made it difficult to correctly position these elements in the table. Furthermore, some of these elements had not yet been isolated in pure form. It was not until Henry Moseley (1887–1915), who analyzed the X-ray spectra of elements, that the concept of atomic number gained significance. Noteworthy, Moseley demonstrated that there are 15 elements from lanthanum to lutetium (with

lutetium only being identified in 1907). Finally, and perhaps interestingly, the discovery of the radioactive element promethium had to wait until after World War II.[14–16]

1.1.2 General aspects of the rare earth elements (REEs)

According to the International Union of Pure and Applied Chemistry (IUPAC) Recommendations Rare Earth Elements (REEs) or rare earth metals reported in **Figure 1.1**, are a group of seventeen chemical elements, including the fifteen lanthanides from Lanthanum (La, atomic number 57) to Lutetium (Lu, atomic number 71), along with Yttrium (Y, atomic number 39) and Scandium (Sc, atomic number 21).[2] Within this group of elements, promethium (Pm) is distinctive as the only predominantly artificial element (Pm occurs naturally only in in trace amounts in nature within uranium ores, and all its isotopes are radioactive).[17]

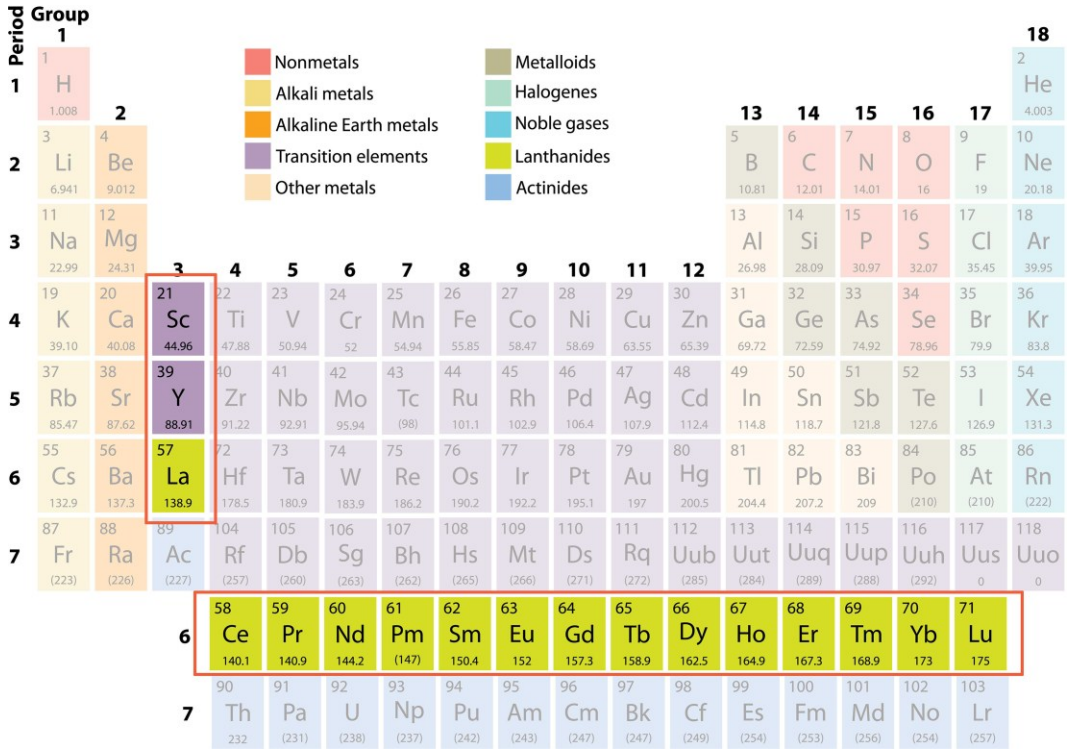

Figure 1.1. Rare Earth Elements (REEs) in the periodic table.

Originally, the name “rare earth” referred to nearly any unfamiliar oxides found in nature. However, in the 1920s, its usage evolved to denote the elements themselves rather than their oxides, highlighting a specific group of elements that were difficult to separate from each other. The elements were divided in two main groups: the “Cerium group” or “Light Rare Earth Elements” (LRREs), which typically ranged from lanthanum (La) to europium (Eu), and the “Yttrium group” or “Heavy Rare Earth Elements” (HREEs), which spanned from gadolinium (Gd) to lutetium (Lu), including yttrium (Y). Despite its lower atomic weight, yttrium was grouped with the HREEs due to its similar ionic radius and its presence in the same ores as the other HREEs. Due to the fact that many of the elements are not particularly rare, the term “lanthanide” has been introduced. As a matter of fact, **Figure 1.2**

illustrates the abundance of rare earth elements in the earth crust, highlighting two trends: lighter REEs are more abundant than the heavier ones, and even atomic numbered REEs are more abundant than odd numbered rare earth elements .

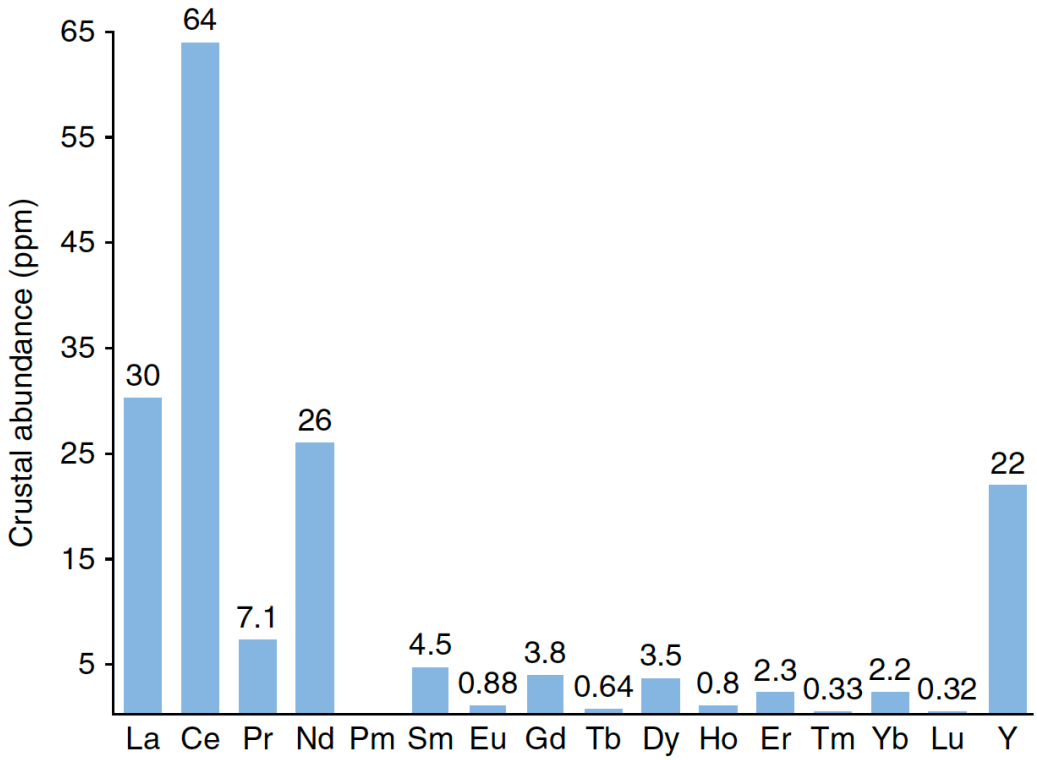

Figure 1.2. Crustal abundances of rare earth elements.

Overall, cerium (Ce), the most abundant lanthanide, shares a comparable crustal abundance with nickel and copper. However, thulium (Tm) and lutetium (Lu), the rarest lanthanides, are more abundant than precious metals like gold and the platinum group elements.[16] Rare earth elements (REEs) typically exist in the +3 oxidation state (Ln^{III}) within all known geochemical systems, except for europium,

which can also exist in the +2 oxidation state (Ln^{2+}), and cerium, which can also exist in the +4 state (Ln^{4+}).

1.1.3 Electronic configuration and lanthanide contraction

Lanthanides exhibit a distinctive feature in their electron configuration due to the gradual filling of the 4f orbitals. Starting with lanthanum (La) where the 5d shell as a lower energy than the 4f, so its electron configuration is [Xe] $6s^2$ $5d^1$. As more protons are added to the nucleus, as the 4f orbitals contract towards the core becoming more stable than the 5d orbitals. Consequently, the electronic configuration of cerium (Ce) becomes [Xe] $6s^2$ $5d^1$ $4f^1$. This pattern continues until europium (Eu), where the stability of the half-filled f shell results in the addition of the next electron to the 5d orbital, as observed in the configuration of gadolinium (Gd), which is [Xe] $6s^2$ $5d^1$ $4f^7$. The earlier pattern is resumed with terbium (Tb) until the end of the series.[16] **Figure 1.3** represents the radial distribution probability densities [D(r)] for 4f, 5s, 5d, 6s and 6p orbitals of Neodymium.[18] The electrons of the 4f orbitals are located closer to the nucleus, but, according to their D(r) they have a less shielding effect compared to the 5s and 5pelectrons.

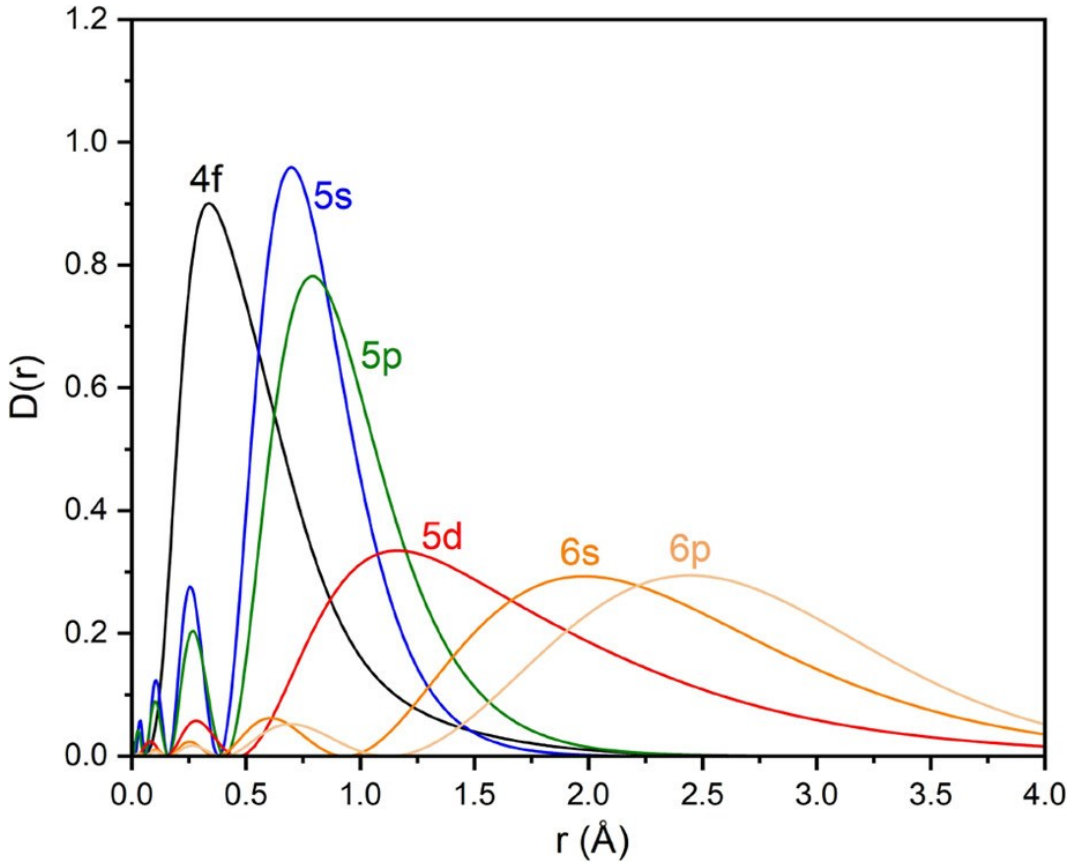

Figure 1.3. Radial distribution probability densities $D(r) = r^2R(r)^2$ for 4f, 5s, 5p, 6s and 6p orbitals of Nd. $R(r)$ is the radial wavefunction.

Lanthanide metals present a periodic property known as "lanthanide contraction". This feature consists into an observed decrease in both the atomic and ionic radii as the atomic number increases (see **Figure 1.4** and **Table 1.1**).[16] The decrease in radius relates to an increase in the nuclear charge, which is only partially compensated by the increase in electrostatic repulsion between the electrons. Due to the different radial probability density, the shielding efficiency decreases in the order $s > p > d > f$. Consequently, an increase in the nuclear charge (increasing Z)

results into a greater attraction of the electrons towards the nucleus, in turn determining the observed slight contraction of the atomic and ionic radii.[19]

Table 1.1. Atomic and ionic radii of Rare Earth Elements (pm)

La	**Ce**	**Pr**	**Nd**	**Pm**	**Sm**	**Eu**	**Gd**	**Tb**	**Dy**	**Ho**	**Er**	**Tm**	**Yb**	**Lu**
187.7	182.5	182.8	182.1	181.0	180.2	204.2	180.2	178.2	177.3	176.6	175.7	174.6	194.0	173.4
La^{III}	**Ce^{III}**	**Pr^{III}**	**Nd^{III}**	**Pm^{III}**	**Sm^{III}**	**Eu^{III}**	**Gd^{III}**	**Tb^{III}**	**Dy^{III}**	**Ho^{III}**	**Er^{III}**	**Tm^{III}**	**Yb^{III}**	**Lu^{III}**
103.2	101.0	99.0	98.3	97.0	95.8	94.7	93.8	92.3	91.2	90.1	89.0	88.0	86.8	86.1

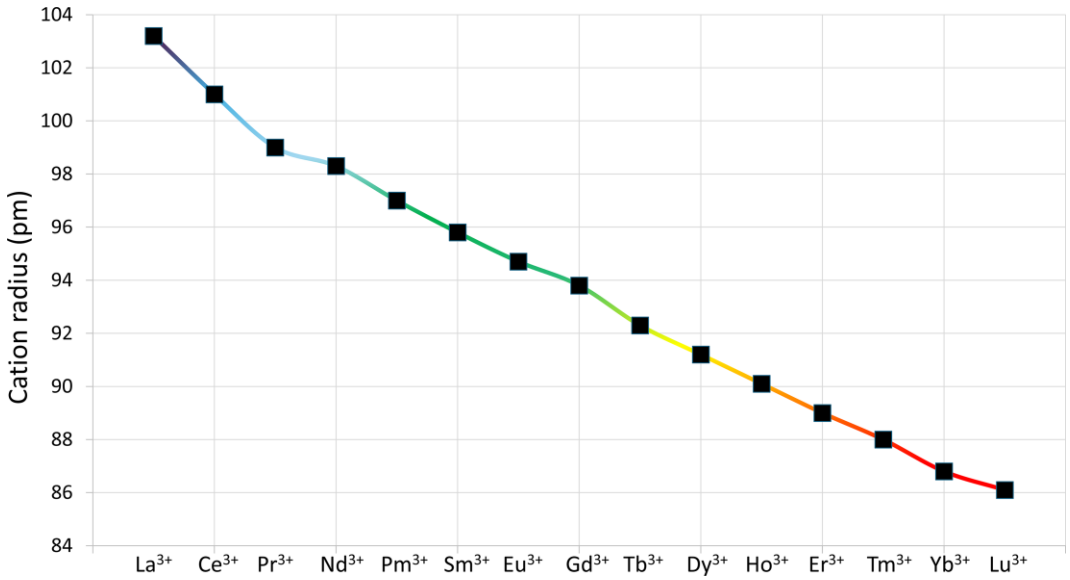

Figure 1.4. Graphic representation of the ionic radii of the most common oxidation states of REEs (pm).

Although the lanthanide contraction seems to have a minimal effect on the chemical properties of these elements, by contrast it is significant as it extends through fifteen elements within the same family of the periodic table.[20] This decrease in size indeed strongly impacts many chemical properties of their complexes, eventually allowing their separation on the basis of a difference in properties such as solubility or stability of formation.

1.1.4 Rare-Earth Elements applications

Due to their peculiar physical and chemical properties, such as unique magnetic and optical properties, Rare-Earth Elements (REEs) have found many technological applications, as graphically represented in **Figure 1.5**.

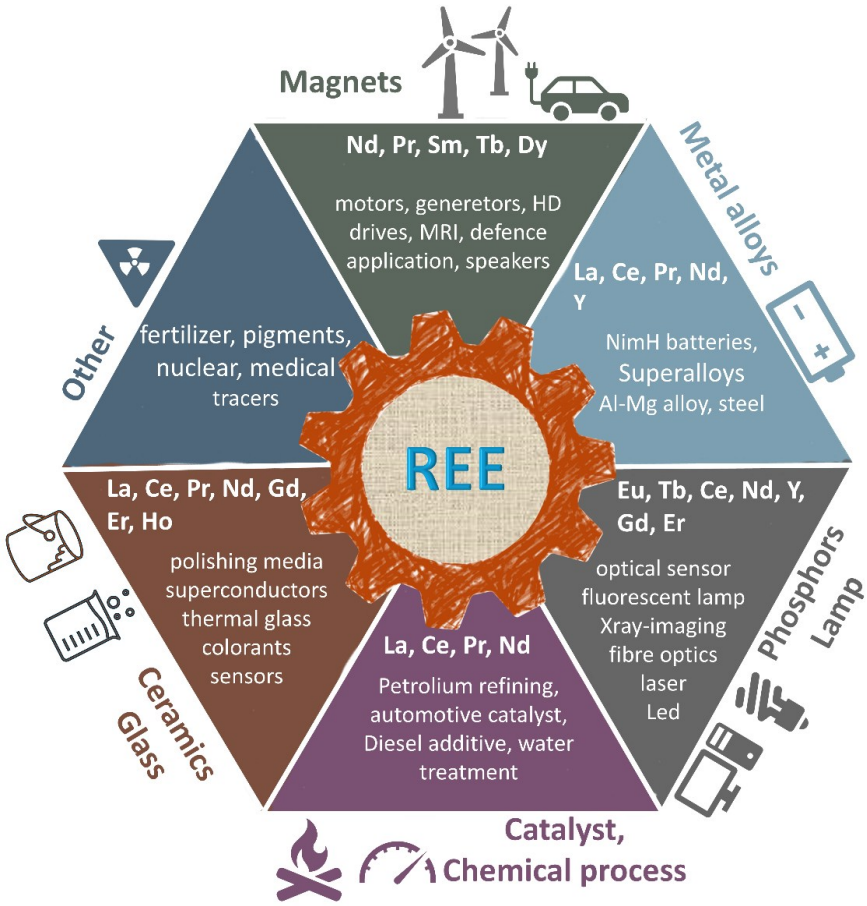

Figure 1.5. Uses of the rare-earth elements.

Below is a summary of the primary technological uses of lanthanides (**Figure 1.6** - **Figure 1.16**).[1]

Lanthanium is primarily used as a catalyst in fluid catalytic cracking (FCC), in nickel-metal hydride batteries, and in the production of glass and ceramics. It is a key component in mischmetal and pyrophoric flints, which contain 25-45% lanthanum by weight. In metallurgy, lanthanum acts as a reducing agent, improves the formation of spheroidal graphite in cast iron, and enhances oxidation resistance when alloyed. Lanthanum admixtures also reduce the hardness and temperature sensitivity of metallic molybdenum. High-quality cathodes made of lanthanum hexaboride are used to generate free electrons, replacing traditional tungsten wire. In the glass industry, high-purity lanthanum oxide is essential for producing high-refractive-index glasses, such as those used in camera lenses. Lanthanum-cobalt alloys (LaCo5) are employed as magnetic materials, while lanthanum-doped barium titanate is used in PTC thermistors. Lanthanum also plays a role in high-temperature solid oxide fuel cells (SOFCs) as a cathode material, when combined with cobalt, iron, manganese, and strontium. In the medical field, lanthanum-titanium alloys are used in the production of corrosion-resistant, easily sterilizable surgical instruments, which are particularly suitable due to their lower allergy potential compared to other metal alloys.

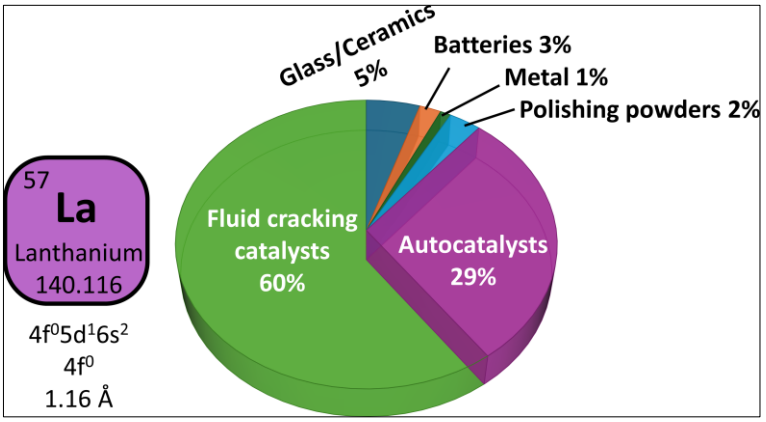

Figure 1.6. The pie chart illustrates the primary applications of lanthanum.

Cerium compounds have a wide range of practical applications, with primary uses in polishing, metallurgy, autocatalysts, and glass production. Cerium is also utilized in batteries, fluid cracking catalysts, ceramics, fertilizers, water treatment, paints, and coatings. Cerium dioxide, in particular, is used in the optical industry for fine glass polishing, as a decolorizer in glassmaking, in petroleum cracking catalysts, and in three-way auto-emission catalysts, due to its ability to switch between +3 and +4 oxidation states. In metallurgy, cerium is employed in iron and non-ferrous alloys to enhance high-temperature oxidation resistance, assist in the removal of sulfur and oxygen during melting, and as an additive in aluminum and iron-based alloys that resist high temperatures. Mischmetal, an alloy predominantly composed of cerium, is primarily used in lighter flints and as an alloying additive. Another alloy, Cerium-iron (Cereisen), consisting of 70% cerium and 30% iron, is used to produce sparks in lighters, roller coasters, and special effects in movies.

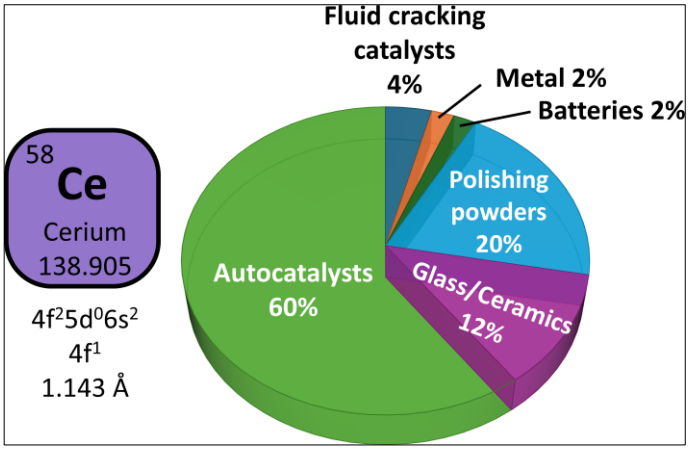

Figure 1.7. The pie chart illustrates the primary applications of cerium.

Praseodymium is primarily used as a substitute for neodymium in NdFeB magnets, especially within the EU. It is also utilized in magnesium alloys to produce high-strength metals for aircraft engines and in compounds that color glass and enamel, enhancing UV absorption for protective glasses used in welding. Additionally, praseodymium plays a significant role in magnet applications, contributing to the strength and durability of NdFeB magnets.

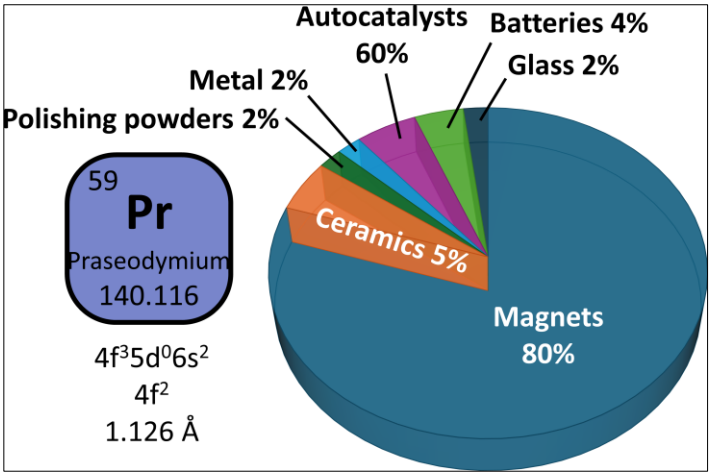

Figure 1.8. The pie chart illustrates the primary applications of praseodymium.

Neodymium-iron-boron (NdFeB) compounds are used to produce the strongest permanent magnets, which are essential for various applications, including magnetic resonance imaging (MRI), micromotors, hard disk drives, permanent magnet rotors in electric vehicles (EVs) and wind turbines, linear motors in CNC machines,

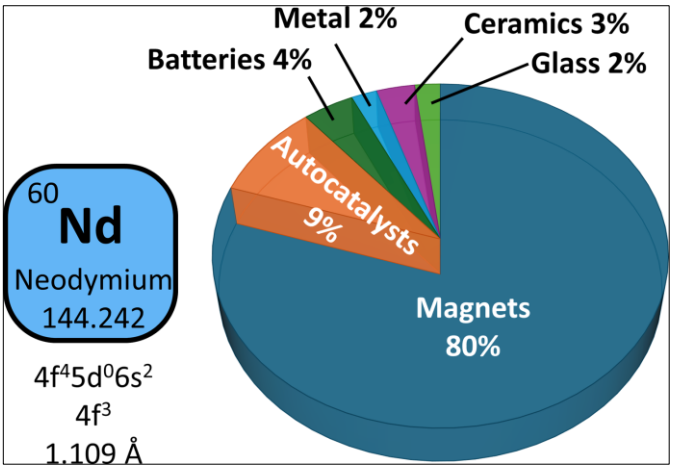

Figure 1.9. The pie chart illustrates the primary applications of neodymium.

and high-quality speakers and headphones. NdFeB magnets are stronger and cheaper than samarium-cobalt (SmCo) magnets but are more sensitive to heat. Additionally, neodymium is used for glass staining, producing violet to maroon tones, UV-absorbing glass, and in neodymium-YAG lasers. It is also used in capacitor dielectrics, flintstones, polybutadiene rubber production, and as an alloying element in various applications.

Samarium's main application is in SmCo permanent magnets, which, while having slightly lower magnetization than NdFeB magnets, are much more resistant to demagnetization and can withstand temperatures above 700 °C. These properties make SmCo magnets ideal for use in small motors, headphones, and high-end magnetic pickups for musical instruments. Samarium is also used in niche applications related to its optical properties, such as laser doping and radiography, as well as in the nuclear industry.

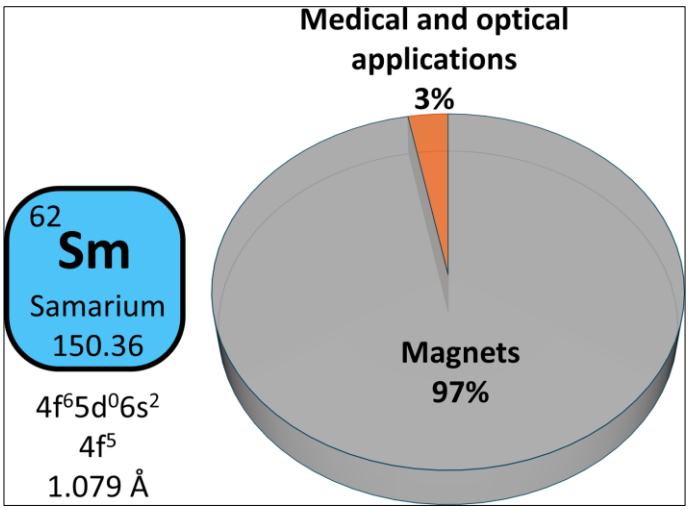

Figure 1.10. The pie chart illustrates the primary applications of samarium.

Europium is primarily utilized in lighting applications, constituting 5% of the phosphor composition used in various technologies, including cathode ray tube screens, compact fluorescent lamps, and plasma display screens. Europium-doped phosphors are essential for producing red and blue light, with Eu^{3+} typically used for red phosphors and Eu^{2+} for blue. Beyond lighting, europium's neutron absorption capabilities make it suitable for nuclear reactor control rods, and its fluorescence properties are employed in anti-counterfeiting measures for euro banknotes. Europium exists in both +2 and +3 oxidation states, with Eu^{2+} being unusually stable. The most significant europium compound is Europium (III) oxide, used as a dopant in fluorescent dyes, while Europium (II) oxide is a rare, stable, ferromagnetic compound under normal conditions.

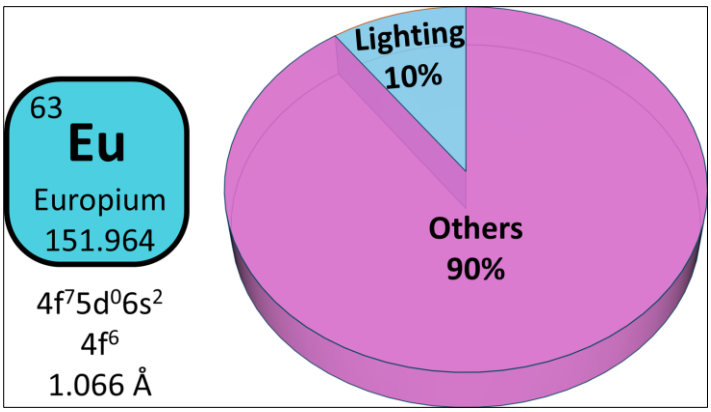

Figure 1.11. The pie chart illustrates the primary applications of europium.

Gadolinium is primarily utilized in NdFeB and SmCo alloys for temperature compensation and corrosion resistance. Its major applications include the production of gadolinium yttrium garnet for microwave applications, and gadolinium oxide as a luminophore for green phosphors in television tubes and

radar screens. In medicine, gadolinium is widely used as a contrast agent in magnetic resonance imaging (MRI) due to its high paramagnetism, enhancing contrast differences in MRI scans. Gadolinium also finds use in metallurgical applications, improving the workability, machinability, and high-temperature oxidation resistance of alloys, as well as in nuclear reactors as a burnable absorber material to manage reactivity. Additionally, gadolinium gallium garnet has been employed in magnetic bubble memory and optomagnetic data storage.

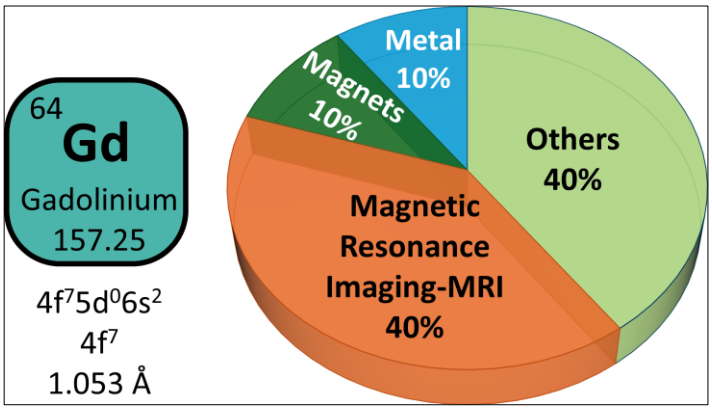

Figure 1.12. The pie chart illustrates the primary applications of gadolinium.

Terbium is primarily used in the EU to enhance the performance of NdFeB magnets by increasing their intrinsic coercivity and Curie temperature, allowing them to operate at elevated temperatures. Terbium is also used in lighting applications, contributing to the

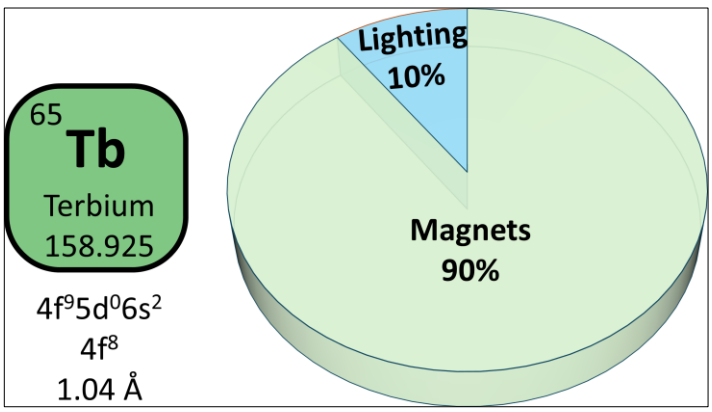

Figure 1.13. The pie chart illustrates the primary applications of terbium.

yellow or green color in neon and fluorescent lamps. Additionally, terbium-doped materials are used in semiconductors, high-temperature fuel cells, and laser materials. Terbium alloys, such as terbium-iron-cobalt, are used in rewritable magneto-optical discs, while terbium-dysprosium alloys are known for their magnetostriction properties, making them valuable in materials testing technology.

Dysprosium, though produced in limited quantities, is essential for enhancing the performance of various advanced materials and technologies. It is primarily used as an alloying element in NdFeB permanent magnets to improve high-temperature performance and resistance to demagnetization. Dysprosium also plays a role in nuclear reactor control rods, magnetostrictive materials like Terfenol-D, and certain lighting and laser applications. Its growing demand in magnets for wind turbines and electric vehicle powertrains has made it a critical, yet scarce, resource, particularly as China, the leading supplier, restricts exports to boost domestic value.

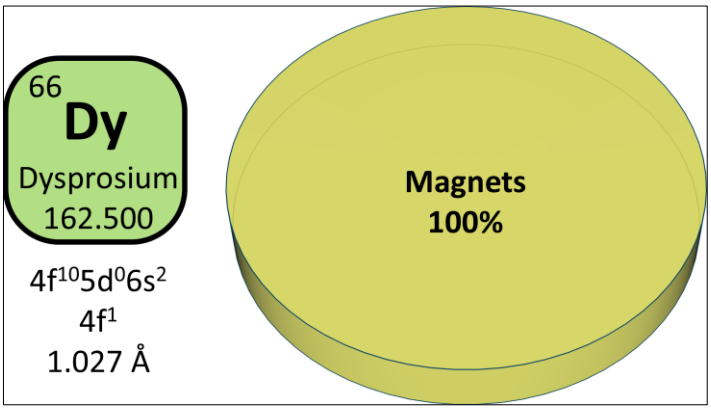

Figure 1.14. The pie chart illustrates the primary applications of dysprosium.

Erbium is predominantly used in optical applications, with 74% of its usage focused on glass. Its pink-colored ^{III} ions give erbium its optical fluorescent properties, making it valuable in various laser technologies, including erbium-doped fiber amplifiers (EDFAs) used in optical communications, and in medical and dental lasers Er:CrYSGG and Er:YAG. Additionally, erbium is employed in the nuclear industry for neutron-absorbing control rods and in metallurgy as an additive in alloys and cryocoolers. The unique optical properties of erbium also allow it to be used as a colorant for glass, ceramics, and zirconia, and its role in high-resolution particle detection further underscores its importance in advanced technologies.

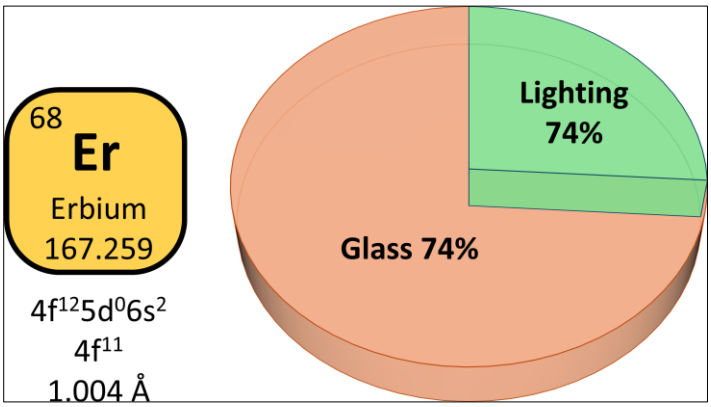

Figure 1.15. The pie chart illustrates the primary applications of erbium.

Holmium, thulium, ytterbium, and lutetium are primarily used in niche applications, largely due to their optical properties. Holmium is employed in high-performance magnets, nuclear reactor control rods, solid-state lasers, and in the production of yellow glass for calibration purposes. Lutetium finds use in positron

emission tomography (PET) detectors, particularly in scintillator crystals, and as a therapeutic agent for neuroendocrine tumors. Ytterbium is utilized in fiber optics, lasers, photovoltaics, and as a γ-radiation source in nuclear medicine. It also improves the mechanical properties of stainless steels and is used in high-quality permanent magnets. Thulium, though limited in commercial applications, serves as a source of X-rays in materials testing and as a scintillator in X-ray technology and dosimeters. Thulium-doped crystals are also active mediums in high-efficiency diode-pumped solid-state and fiber lasers.

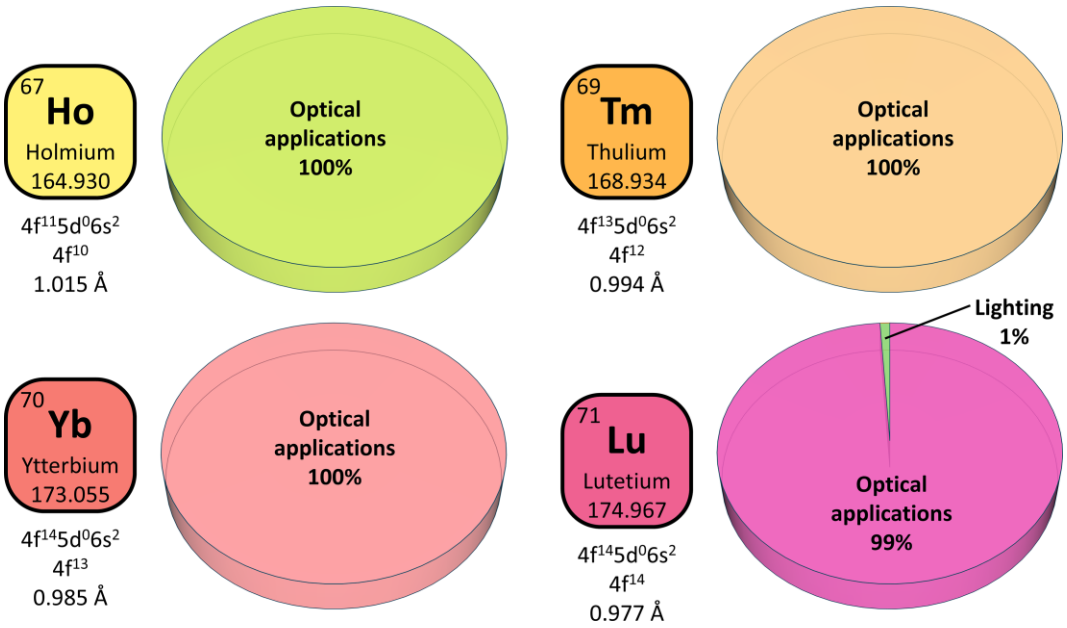

Figure 1.16. The pie chart illustrates the primary applications of holmium, thulium, ytterbium and lutetium.

1.1.5 Wordwide supply of Rare-earth elements

Established markets for rare-earth elements (REEs) include catalysts, glassmaking, lighting systems, and metallurgy, accounting for 38% of global REE

consumption. Conversely, newer markets such as battery alloys, ceramics and permanent magnets represent 49% of global REEs consumption. Lanthanum and cerium dominate the established markets, whereas dysprosium, neodymium and praseodymium are key in the newer markets, collectively contributing to ~29% of global rare-earth elements consumption .[21] Rare-earth elements (REEs), along with other strategic resources like cobalt (Co), lithium (Li) and nickel (Ni), are named "Critical Raw Materials" (CRMs) .[22] Since 2010, the European Commission has been focusing on assessing the availability, accessibility and critical importance of such raw materials, with REEs being included in this context .[23] However, this trend extends beyond Europe and now includes any other major economic powers, including the United States .[24] As reported by the European Commission, in 2023 China has been the world leading producer of light and heavy REEs (see **Figure 1.17**).

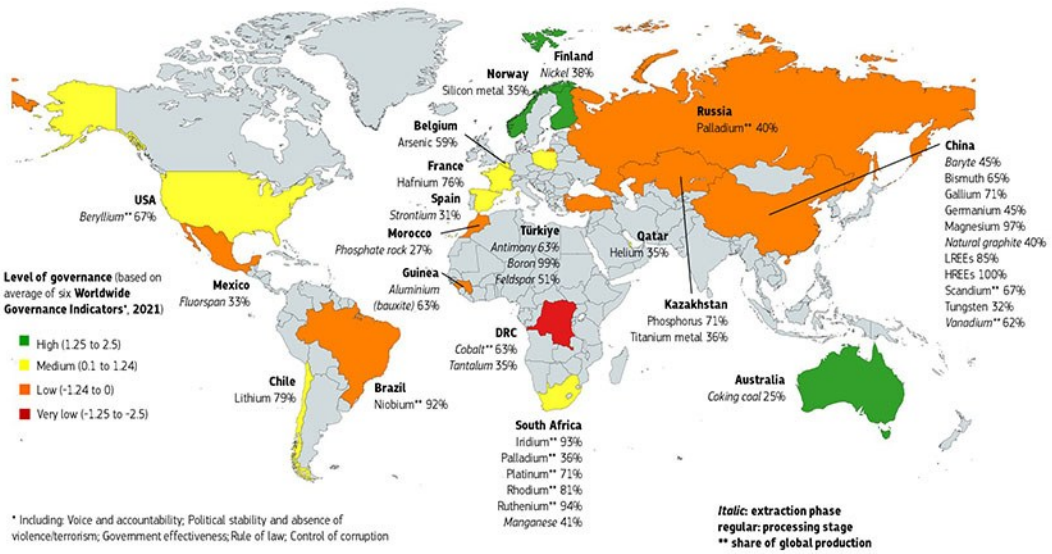

Figure 1.17. Countries accounting for largest share of global supply of Critical Raw Materials (CRM).

China's dominance in the REE market is also confirmed by a report made by the U.S Geological Survey (USGS). In 2024, the United Stated imported rare earth compounds and metals for a total of $190 million, with 72% directly sourced from China and 22% derived from mineral concentrates and chemical intermediates produced in Australia, China and other countries. In addition, in December 2023, China implemented export bans and restrictions on strategic materials and technologies listed in the "Catalogue of Technologies Prohibited and Restricted from Export in China", including a category called "Nonferrous Metal Smelting and Processing Industry. The escalating demand for REE metals, coupled with the increasing costs and the Chinese dominance in this market, have led to a supply deficit in the rest of the world. Moreover, the so-called "balance problem" arises from the need to maintain an equilibrium between the demand and supply of individual rare-earth elements, as imbalances can result in shortages or excesses of certain elements.[25] It is important to bear in mind that REEs occur in different ratios in minerals and ores, reflecting the natural abundance of each single element. For instance, neodymium is much less abundant than lanthanum or cerium, implying that mining REE ores for neodymium also produces significant amounts of lanthanum and cerium that must be managed. Consequently, recycling REEs from End-of-Life (EOL) products plays a significant and complementary role in the overall supply of REEs, reducing the need for additional mining of their ores to meet the global demand.[26] However, as long as the recycling rates and substitution of REEs remain low, it can be assumed that supply security will be crucial for producers and consumers around the world. Given these circumstances, western nations, especially Europe , are exploring new methods to recover these metals from waste materials.[27]

1.1.6 Permanent magnets as secondary source of REE

Neodymium–iron–boron (NdFeB) permanent magnets have been regarded as the most effective magnets available since their market debut in 1984, thanks to their outstanding energy density, which can theoretically reach up to 512 kJ/m³.[3,4] This efficiency makes them ideal for lightweight, mobile applications, leading to their widespread use in wind turbines, electric and hybrid vehicles (EVs and HEVs), household appliances, computer hard drives, and various small electronic devices.[5–7,28,29] The lifespan of NdFeB magnets varies depending on their application, ranging from 2–3 years in consumer electronics to 20–30 years in wind turbines. The size of these magnets also varies significantly, from less than 1 gram in small electronics to over 1 kilogram in EVs and HEVs, and up to 1000–2000 kilograms in the generators of modern wind turbines.[8] These magnets are composed of about 31–32% rare-earth elements (REEs), mainly neodymium (Nd) and praseodymium (Pr), along with smaller amounts of heavy rare-earth elements (HREEs) like dysprosium (Dy), terbium (Tb), and gadolinium (Gd), depending on the application (**Figure 1.18**).

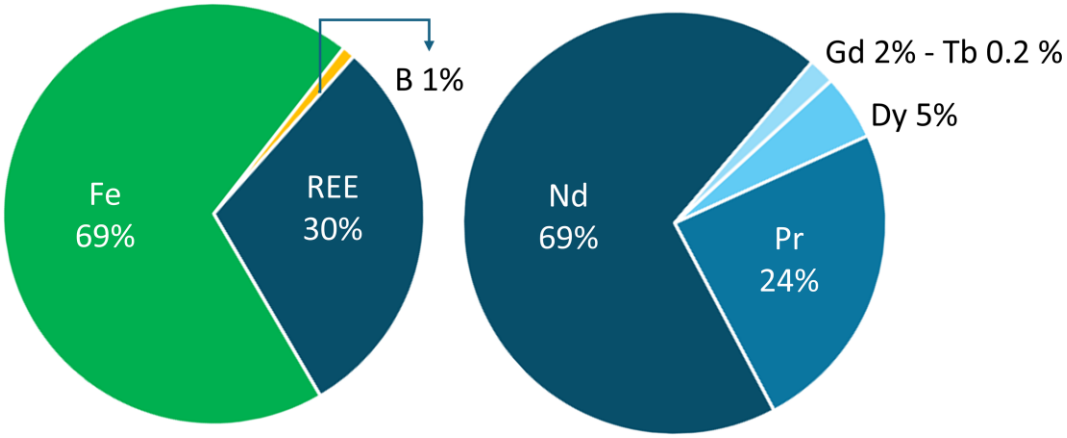

Figure 1.18. General composition of a Permanent Magnets (PM).

Recycling the REEs contained in NdFeB magnets from end-of-life (EOL) products is expected to play a crucial role in supplementing primary REE supplies in the future. However, the collection and recovery of these magnets, particularly from small consumer electronics, present significant challenges both socially and technologically. Currently, there are no mature or economically viable technologies for recycling EOL NdFeB magnets and recovering the associated REEs. Most methods are still in the research and development phase. It is anticipated that by 2030, recycled REEs from EOL magnets will make a meaningful contribution to the total REE supply in the magnet sector.[30] Moreover, recycling REEs is important for addressing the "balance problem," which involves the overproduction of elements like lanthanum (La) or cerium (Ce) when mining for Nd and Dy. **Figure 1.19** illustrates an estimation of the actual return flow by application in tons of NdFeB magnets and the overall recycling rate from 2018 to 2040, highlighting an exponential growth expected in the coming years.[25,31]

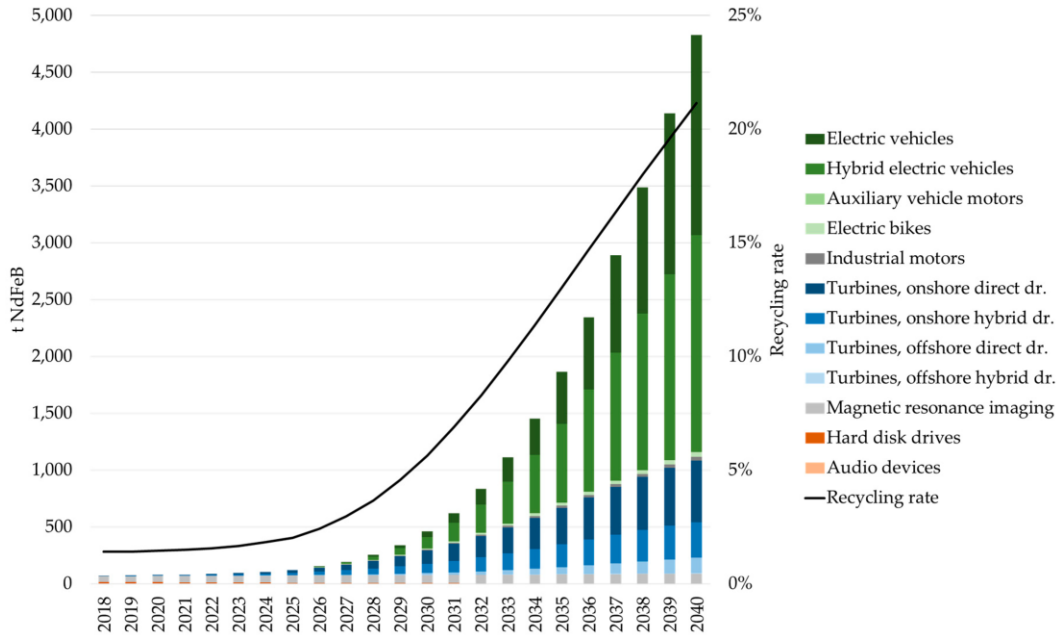

Figure 1.19. Estimation of the realistic return flows by application in tons of NdFeB permanent magnets and overall recycling rate.[31]

The degree of oxidation and contamination levels of the magnets is variable from material to material, leading to differences in the available recycling options depending on the application area. Large magnets, like those commonly found in wind turbines and hybrid electric vehicles typically exhibit reduced levels of oxidation and contamination. As a result, after a simple pretreatment they can be directly used in the production of new NeFeB permanent magnets.[8,9] This approach requires minimal environmental impact and yields magnets at a very low cost, avoiding the energy-intensive and agent-consuming procedures of traditional recycling techniques. On the other hands, this method is not suitable for recycling highly contaminated crushed materials since the performance of the obtained magnets tends to be invariably low.[32]

Hydrometallurgy stands out as the main method for recovering REEs from NdFeB scraps, offering an easily controlled process for metal extraction. The general process is represented in **Figure 1.20**.[33] Typically, pretreating the magnet through crushing and demagnetization is known to enhance the recovery efficiency. Subsequently, either complete or selective leaching of the magnet is performed. Both caustic soda and inorganic acids (H_3PO_4, H_2SO_4, HNO_3 and HCl) have been used , as well as organic acids such as acetic acid (CH_3COOH), citric acid ($C_6H_8O_7$) and maleic acid ($C_4H_4O_4$).[34–36] The latter ligands were used to form complexes which exhibit different solubility and/or distribution in non-miscible solvents, eventually allowing the separation of different lanthanides.

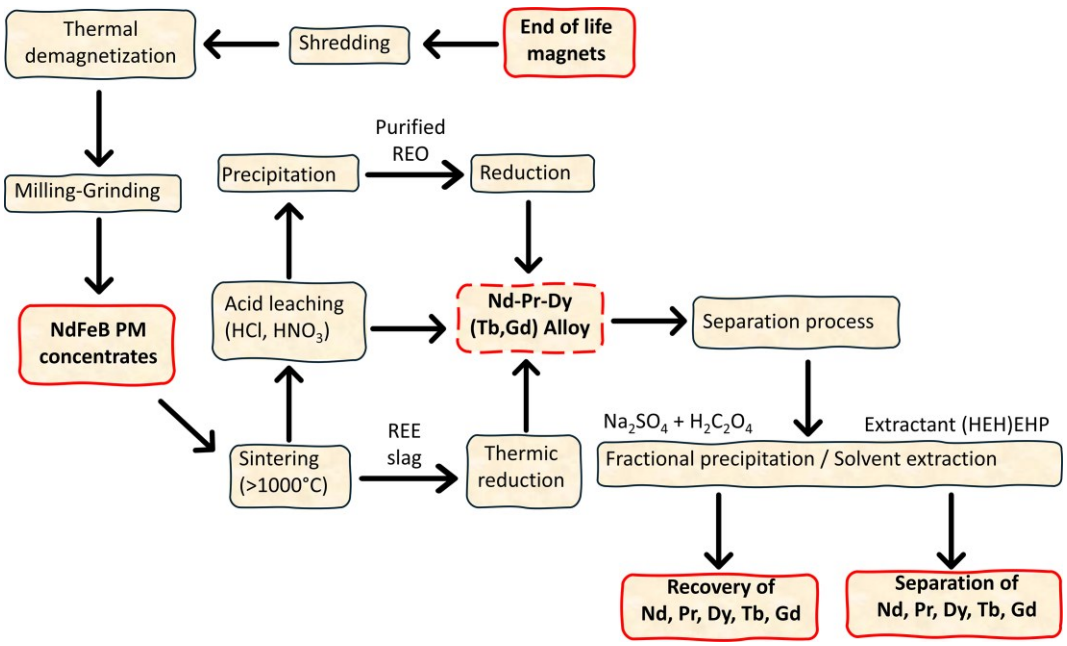

Figure 1.20. General flow diagram developed for hydrometallurgical extraction and recovery of REEs from end-of-life magnets.

Pyrometallurgical techniques have been employed as alternative strategies for extracting valuable metals from electronic waste. These methods typically involve a combination of processes such as combustion, drossing, sintering, melting, and smelting in a plasma arc furnace at high temperatures.[37] **Figure 1.21** describes the process in which permanent magnet waste is demagnetized, grinded and milled to form a single slag phase. In the subsequent reductive step, iron (Fe), as well as some more noble metals (such as boron and metals from the permanent magnet coating), are separated into an iron phase. The resulting REE oxide-rich slag is further concentrated via flotation or segregation, or it is used directly in a hydrometallurgical purification step followed by a calcination step to produce REE_2O_3. These processes operate at high temperatures and offer alternative methods to hydrometallurgical approaches, which aim to reduce high water consumption, the use of large amounts of chemicals, and the generation of hazardous waste during the recovery process .[32] In hydrometallurgical processes, acidic solutions dissolve not only rare-earth metals but also iron and boron, leading to significant wastewater production. Iron and boron residues are considered industrial waste because the cost of recycling iron is not economically viable, and boron is a toxic element that requires environmentally controlled disposal .[38] Pyrometallurgy, therefore, provides an alternative recovery route, especially in regions where water scarcity is a concern, and waste generation needs to be minimized.

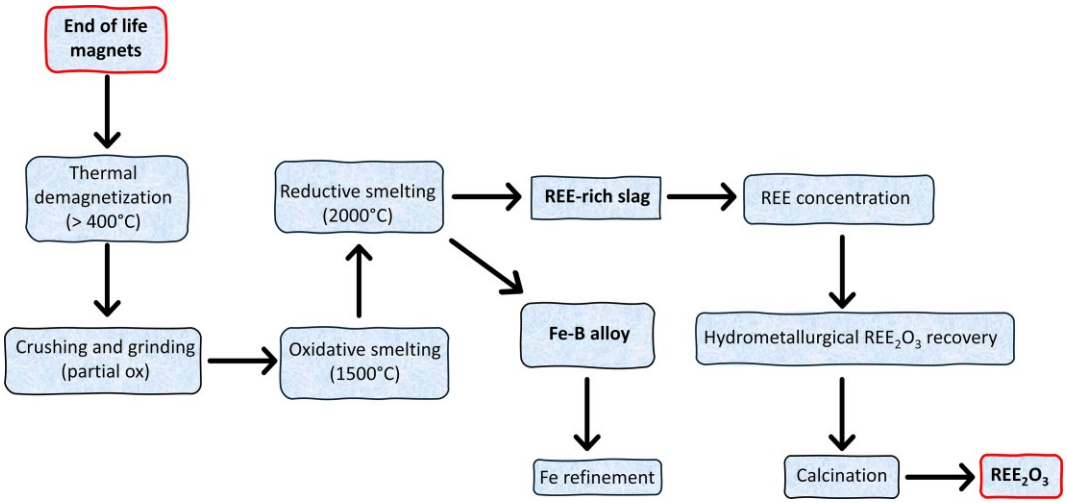

Figure 1.21. General flow diagram developed for pyrometallurgical extraction and recovery of REEs from end-of-life magnets.

Finally, solvometallurgical approaches are rapidly emerging as alternative or complementary routes in relation to hydrometallurgical and pyrometallurgical processes .[39] Solvometallurgy use non aqueous media or less conventional organic solvents, and it was found as a suitable strategy when water could interfere with materials and phases during the recycling process. Indeed, most of the processes in solvometallurgy are conceptually very similar to those used in hydrometallurgy, although water is substituted by non-aqueous solvents or ionic liquids.[11]

1.1.7 Rare-earth elements (REEs) separation

After the extraction of rare-earth elements from NdFeB permanent magnets, the subsequent challenge lies in their separation from each other. As previously noted, the similarity in chemical properties among lanthanides complicates this task significantly. In the past, the only methods available for rare-earths separation were sequences of recrystallization, used until the first half of the 20th century .[40] However, these methods yielded limited quantities of products with low purity levels. Over time, these earlier methods have been surpassed and various alternative and more sophisticated techniques have been introduced to tackle this challenge.[41–43] Among these techniques, the most used ones include fractional precipitation , solvent extraction or ion exchange.[44–48]

Fractional precipitation (**Figure 1.22**) is a technique used to separate ions in the form of salts or complexes with different (although similar) solubilities by inducing their gradual precipitation from a solution. This method involves a series of precipitation steps, each designed to enrich the separating phase (precipitate) with one element, possibly the desired one. The effectiveness of quantitative separation depends on several variables, possibly the most important the initial concentration of the ions/ligands and the solubility of the metal complexes formed in solution.

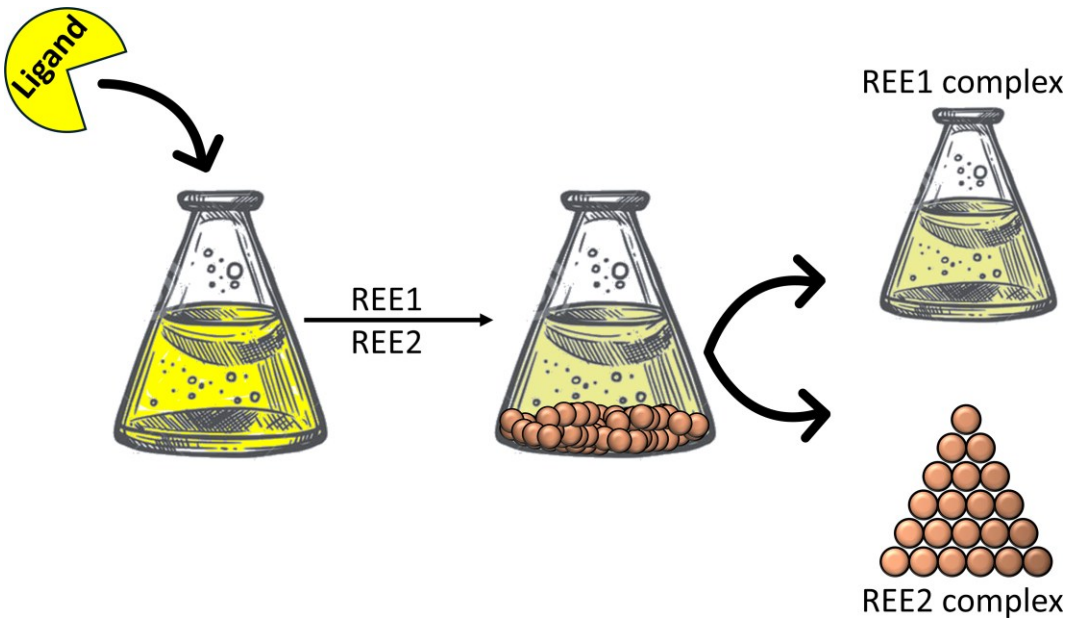

Figure 1.22. general scheme of fractional precipitation process.

Separation by solvent extraction (**Figure 1.23**) is an alternative route to fractional precipitation. Conceptually this strategy relies on a simple setup, namely that a ligand is dissolved in a water-immiscible organic solvent which forms a heterogeneous mixture with an aqueous solution containing rare-earth elements (REEs). During the mixing process, the REEs are transferred from the aqueous medium to the organic phase because of the formation of complexes with the ligand. In this way, one phase can be enriched of one or more REEs and separation may be obtained by sequences of extraction steps or by subsequent fractional precipitation.[49] Although the strategy is conceptually simple, the yield of separation is a function several parameters that may be difficult to be optimized or of several chemical features that are difficult to predict. These include the stability of the metal complexes formed or the different affinity to the aqueous/organic phases of the ligand when present free or in the form of the metal complex.

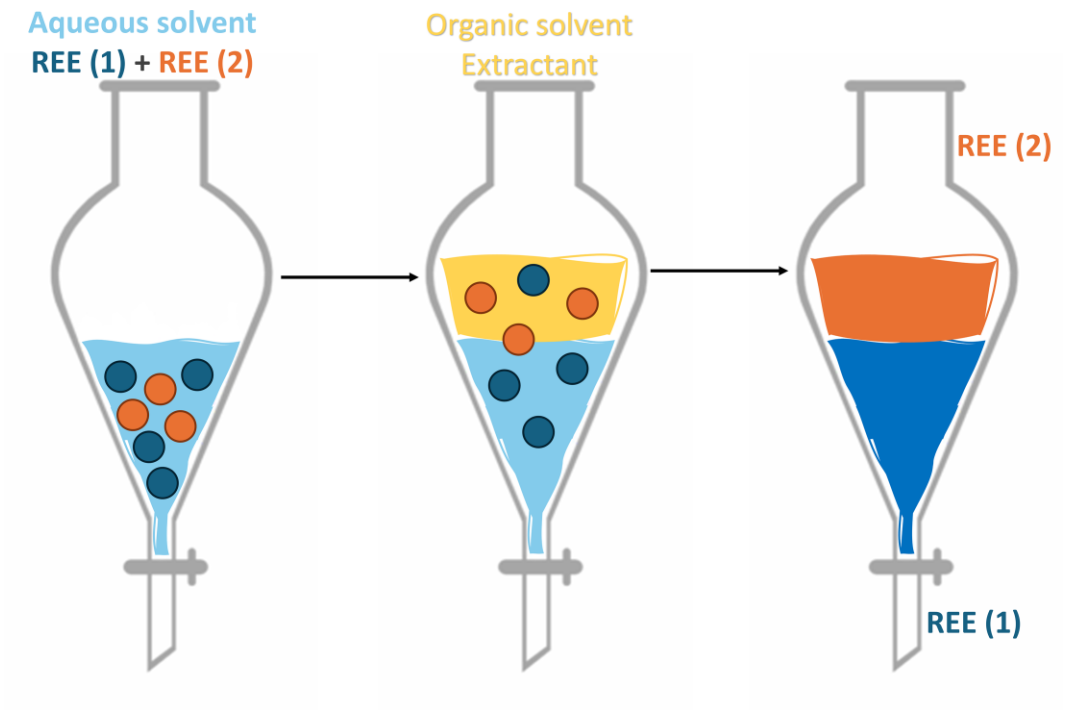

Figure 1.23. General Scheme of a solvent-solvent extraction process.

The ion exchange (**Figure 1.24**) method is a widely used technique for separating lanthanides due to its efficiency into discriminating chemically similar elements. The process starts by converting lanthanide compounds into inorganic salts, usually with chlorides or nitrates as counterions. This decomposition of the starting compounds is often obtained by dissolving them in strong acids. The resulting solution is then passed through an ion exchange resin. Although lanthanides have similar chemical properties, Slight differences in the ionic radii and charge densities of lanthanides lead to differences in their chemical properties that, although small, are large enough to allow different extents of interaction of the ions with the resin. The metal ions are then eluted by introducing a complexing agent, such as EDTA or

ammonium nitrate, to the mobile phase enabling the release of the cations from the resin which are eluted with different retention times. Eventually, the lanthanides can be further purified and converted into their desired forms, such as oxides or metals, through solvent removal and calcination.

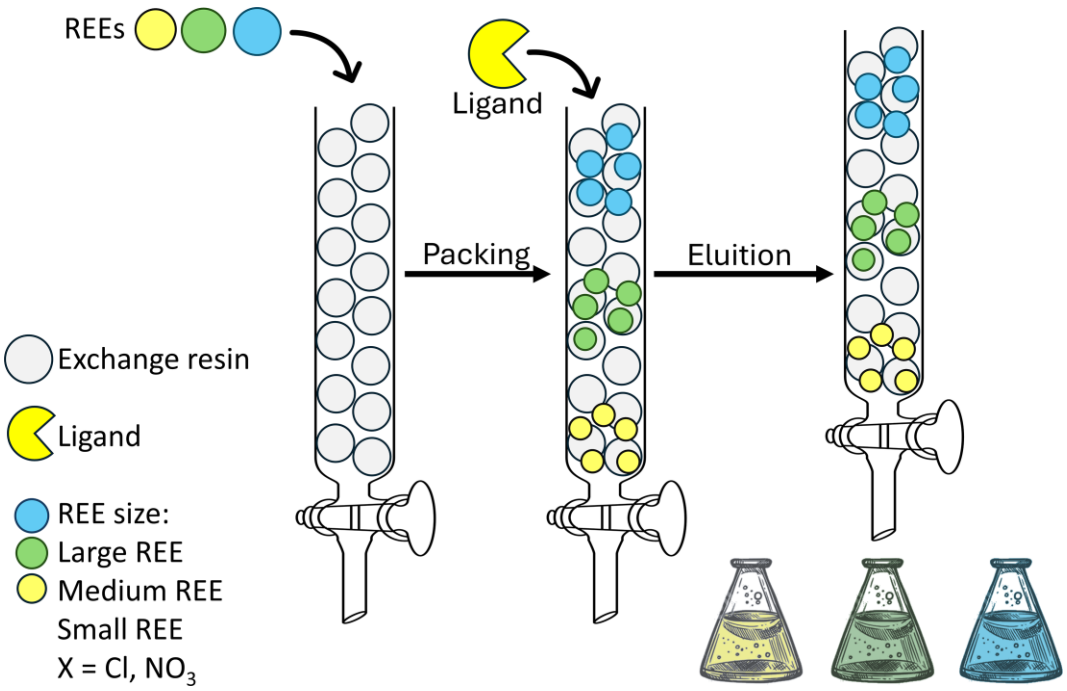

Figure 1.24. Generic scheme of an ion exchange process.

Overall, technical, economic and environmental sustainability of conventional separation methods such as the ones mentioned above is often limited by the use of a large amount of costly reagents and solvents.[50] Also, these drawbacks are often not compensated by selectivity and efficiency in the separation of the elements which remain low. Novel chemical approaches proposed in the literature focus therefore on discriminating between rare-earth element (REE) cations using

relatively inexpensive ligands that form polymetallic complexes or complexes where the different lanthanides have different coordination numbers (**Figure 1.25**). This method leverages therefore variations in cation size within the REE series taking advantage from the formation of complexes with different nuclearities, hydration numbers, or affinities for supramolecular entities, which in turn results in differences in solubility.[51–55] While this strategy is generally more effective for separating light REE (LREE) cations compared to heavy REE (HREE) cations, it offers simplicity and efficiency, often achieving high separation factors in a single step, typically in the range of 100–1000 for LREE-HREE separation, with cheap ligands that do not require costly processes for their synthesis and purification.

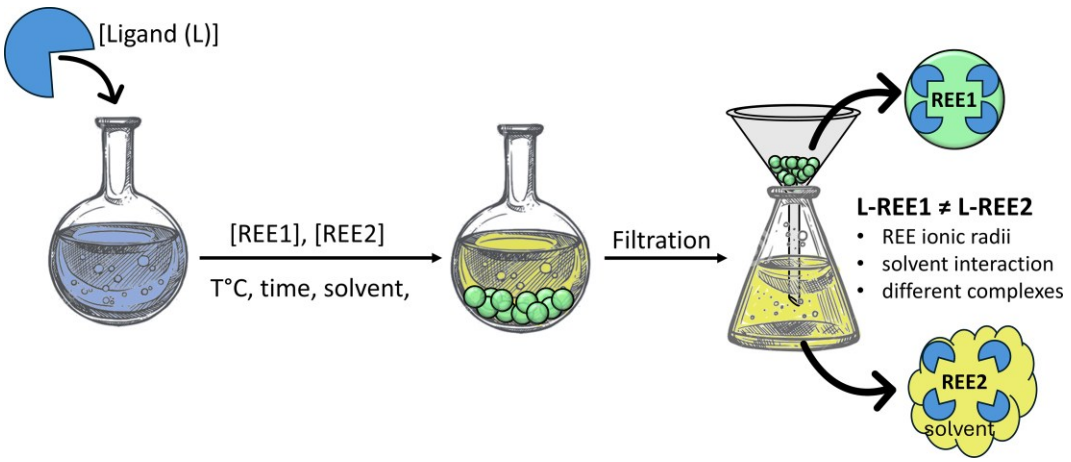

Figure 1.25. General scheme of separation by selective precipitation driven by formation of different complexes.

In developing these processes, it is essential to optimize conditions such as metal concentration, additives, pH, solvents, and crystallization parameters to enhance complexation-driven metal separation and recovery.[56] However, this latter

approach can be ultimately described as taking advantage of the preference of different lanthanides for different coordination numbers (CNs) which is a well-recognized phenomenon.[57] Indeed, light REE cations tend to favor higher CNs than heavy REE cations, due to differences in ionic radius. As shown in this thesis, this rather simple chemical behavior is crucial in the crystallization of REE inorganic compounds and plays a key role in effective REE separation.[56,58]

Chapter 2: **Trensal-type ligand for selective recovery and separation of Nd and Dy**

2.1 Introduction

In the field of the recovery of rare-earth element (REE), it is predicted that an effective approach can be designed by employing multifunctional ligands specifically designed to selectively interact with lanthanide or actinide cations, allowing their separation.[51,55,59–63] These ligands are engineered to display precise metal-to-ligand interaction geometries and strengths, tailored to individual metal ions. For example, studies have shown that dysprosium and neodymium tend to form distinct monomeric and dimeric complexes, respectively, when coordinated with a polydentate $N'N_3O_3$ donor ligand, resulting in different solubilities that may be used in their separation.[51,64]

Literature data highlight that the differences in the preferred coordination numbers (c.n.) and geometries of different lanthanides lead to different physical properties, and that the latter can be leveraged for their separation. The Trensal tripodal ligand (H_3trensal = 2,2',2"-tris(salicylideneimino)triethylamine) is known for its ability to bind trivalent lanthanide ions and is particularly significant in this context.[65] This ligand typically fulfills a coordination number of seven, with an arrangement that favors the stability of the formed lanthanide complexes. The Trensal ligand can be synthesised straightforwardly, and the introduction of different functionalization on the parent molecule has led to the creation of the Trensal family, characterized by a rigid, pre-organized donor atom structure and a flexible ethylene linker. These

structural features allow the ligand to adapt to the specific size and geometry needs of the lanthanides while preserving its capacity to form stable complexes.

The results reported in this section emphasize the design and synthesis of functionalized Trensal ligands and examine their coordination with Nd^{III} and Dy^{III} ions in organic solutions. A thorough structural analysis of the resulting complexes indicates that Nd tends to form complexes with a coordination number greater than seven by incorporating solvent molecules, whereas Dy consistently forms seven-coordinated complexes. These distinct coordination patterns produce different solubility profiles, which can be strategically exploited to optimize the separation of Nd and Dy, particularly in acetone, by fine-tuning the ligand-to-metal stoichiometric ratio.

2.2 Aim of the project

The objective of this work was to synthesize and study a series of functionalized Trensal ligands, and to employ these compounds for the selective separation of neodymium (Nd) and dysprosium (Dy), two critical rare-earth elements (REEs). Through a comprehensive analysis of the structural and thermodynamic properties of Nd and Dy complexes formed with these ligands in organic solvents, we attempted to elucidate the nature of metal-ligand interactions and the properties of the metal species. The final aim is to optimize separation processes of the two lanthanides by exploiting differences in solubility and coordination of the related complexes.

2.3 Results and discussions

2.3.1 Synthesis and characterization of Trensal^R ligand (Trensal=2,2',2''-tris(salicylideneimino)triethylamine)

Tris-(2-aminoethyl)amine (1 eq.) and different functionalized salicylaldehyde (3 eq.) were reacted in absolute ethanol/chloroform at reflux for three hours, **Scheme 1.** The resulting yellow solutions were left to evaporate overnight obtaining crystalline needles. The solids were isolated by filtration and washed with cold ethanol and hexane obtaining Trensal^R in high yield. To promote the formation of the three iminic functions, a solvent with low water content (chloroform or absolute ethanol) and a small excess of aldehyde (0.05 eq.) were used.

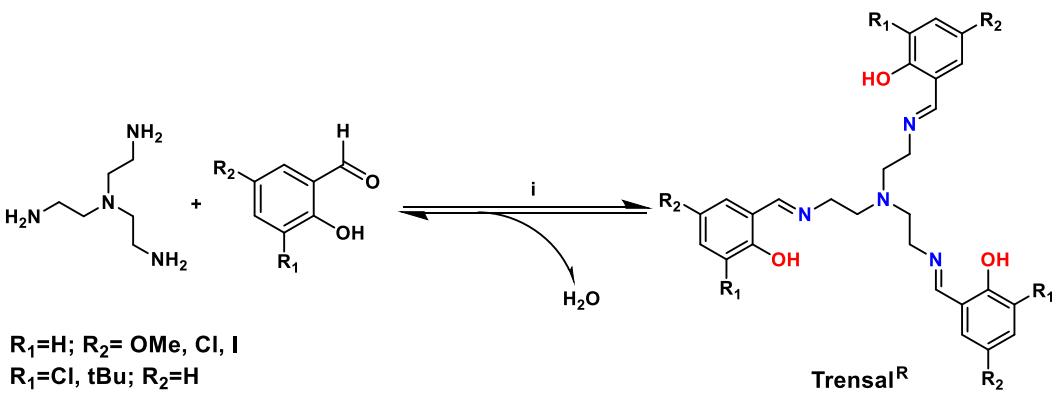

Scheme 1.1. Scheme of the synthesis of the Trensal ligands. i) Tris(2-aminoethyl)amine (1 eq), salicylic aldehyde^R (3 eq), EtOH or $CHCl_3$, reflux, 3 h.

Trensal is a heptadentate ligand featuring hard donor atoms, specifically three phenolic oxygens, along with intermediate donors, namely the central amino

nitrogen and three iminic nitrogen atoms. Its high denticity makes it highly effective for complexing with lanthanide ions which in general present high coordination numbers.

These ligands can be synthesized with ease using aldehydes that carry various functional groups in the ortho and para positions, many of which are readily available at relatively low cost. The substituents are selected to impart different lipophilic properties (as shown in **Table 2.1**) to the resulting ligand, allowing to obtain libraries of ligands and complexes with different solubilities in different non-aqueous solvents. Additionally, bulky substituents may exert a subtle yet important influence on the stability of [Ln(Trensal^{R})] complexes, particularly when comparing lanthanides with slightly varying ionic radii, such as Nd^{III} (0.98 Å) and Dy^{III} (0.91 Å) Å).[66]

Table 2.1. The theoretical partition coefficients of the ligands are shown in increasing order of lipophilicity.[67]

Ligand Trensal^{R}	**logP**
Trensal (H_3L_1)	4.54
Trensal$^{p\text{-}OMe}$ (H_3L_2)	4.64
Trensal$^{o\text{-}Cl}$ (H_3L_3)	5.81
Trensal$^{p\text{-}Cl}$ (H_3L_4)	6.51
Trensal$^{p\text{-}I}$ (H_3L_5)	7.72
Trensal$^{o\text{-}tBu}$ (H_3L_6)	8.64

All the ligands were characterized by ^{1}H NMR spectroscopy and ESI-MS. The ^{1}H NMR spectrum in DMSO-d_6 confirmed the formation of the desired product (signals associated to the presence of iminic proton (-N-C**H**-Ph) at ≈ 8.23 ppm and of N_{amine}-CH_2-CH_2-N_{imine} at ≈ 6.18 and 6.20 ppm respectively). The purity of the compound is also assessed by the aldehydic peak absence around 10 ppm (**Figure 2.1 – Figure 2.6).**

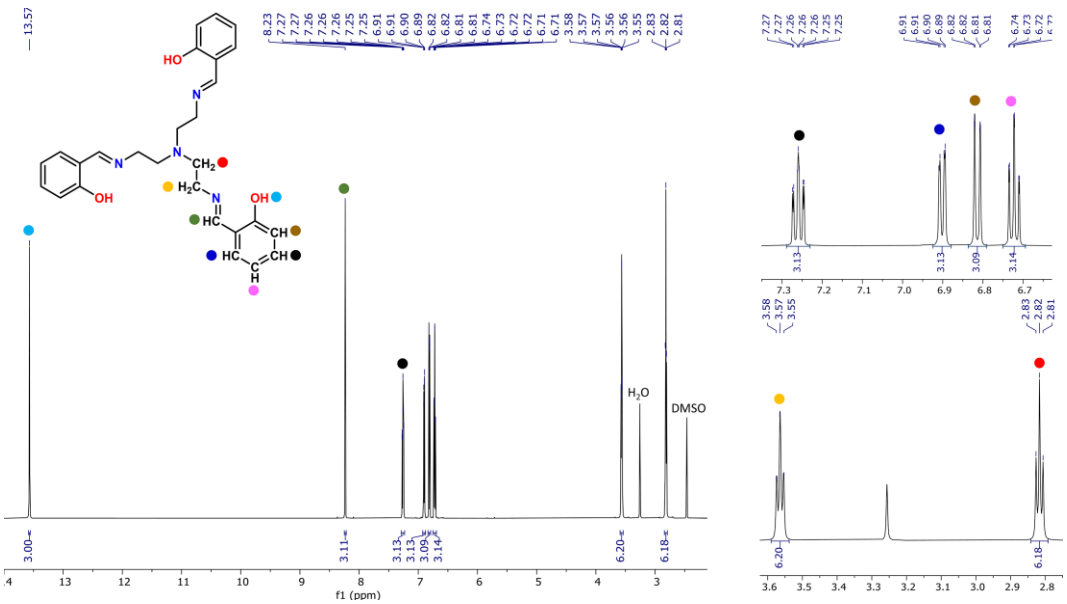

Figure 2.1. ^{1}H-NMR (600 MHz, DMSO) spectrum of H_3L_1.

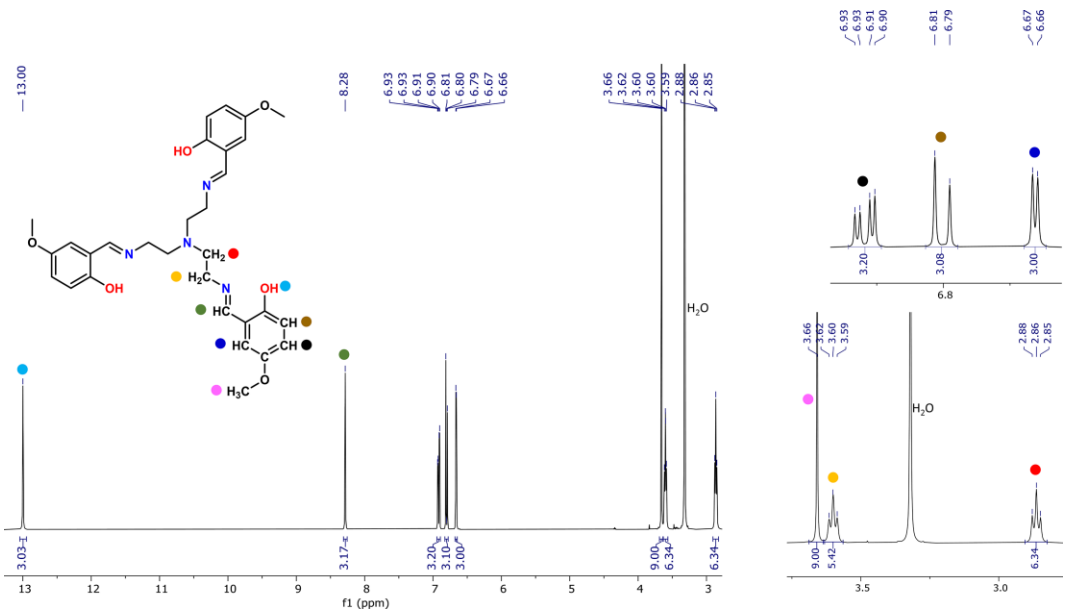

Figure 2.2. ^{1}H-NMR (400 MHz, DMSO) spectrum of H_3L_2.

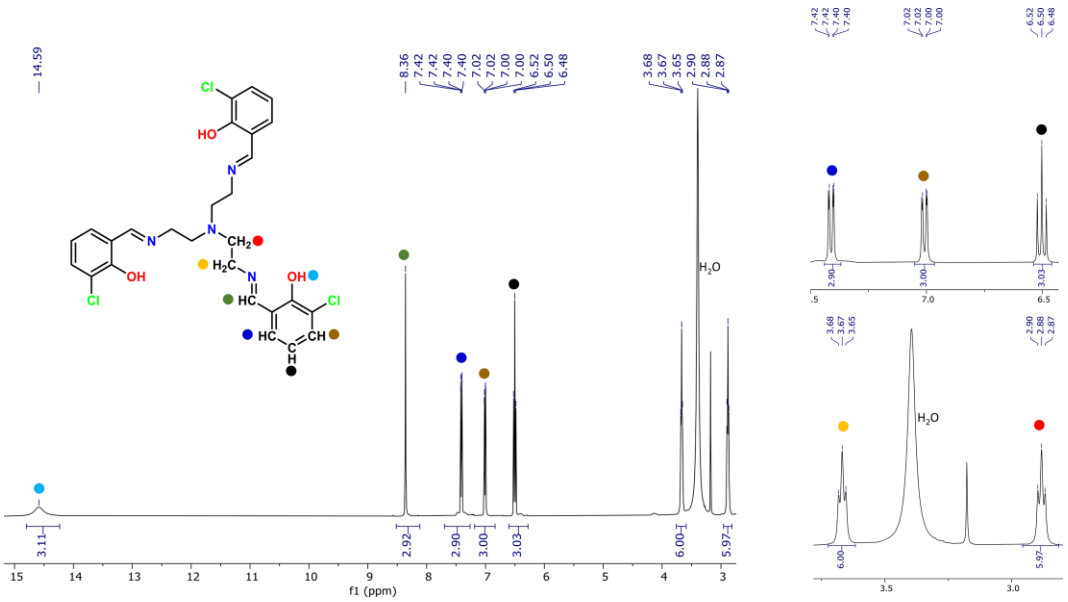

Figure 2.3. ^{1}H-NMR (400 MHz, DMSO) spectrum of H_3L_3.

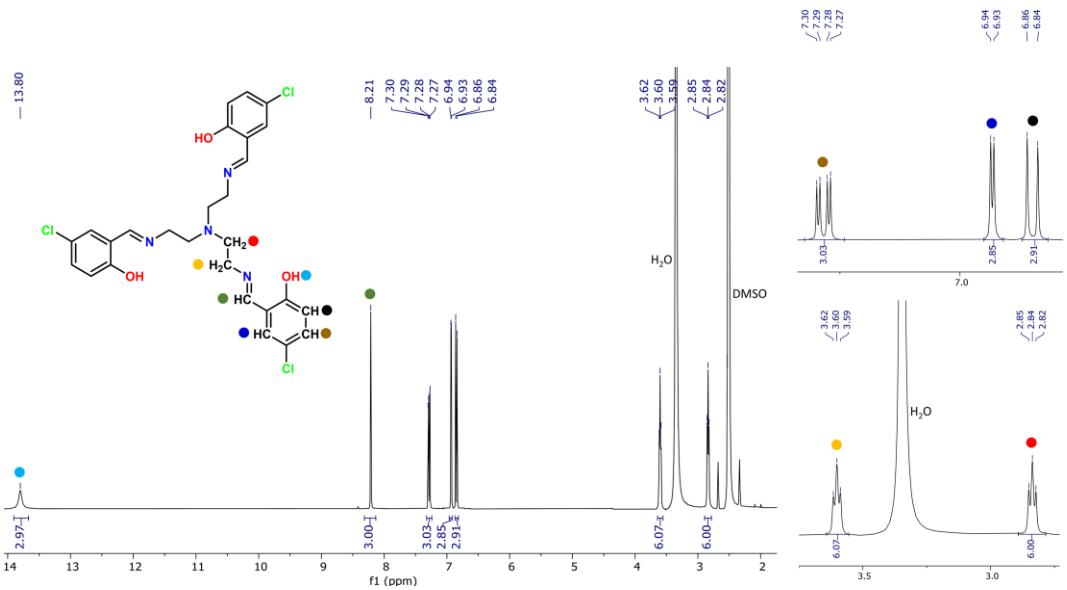

Figure 2.4. ^{1}H-NMR (400 MHz, DMSO) spectrum of H_3L_4.

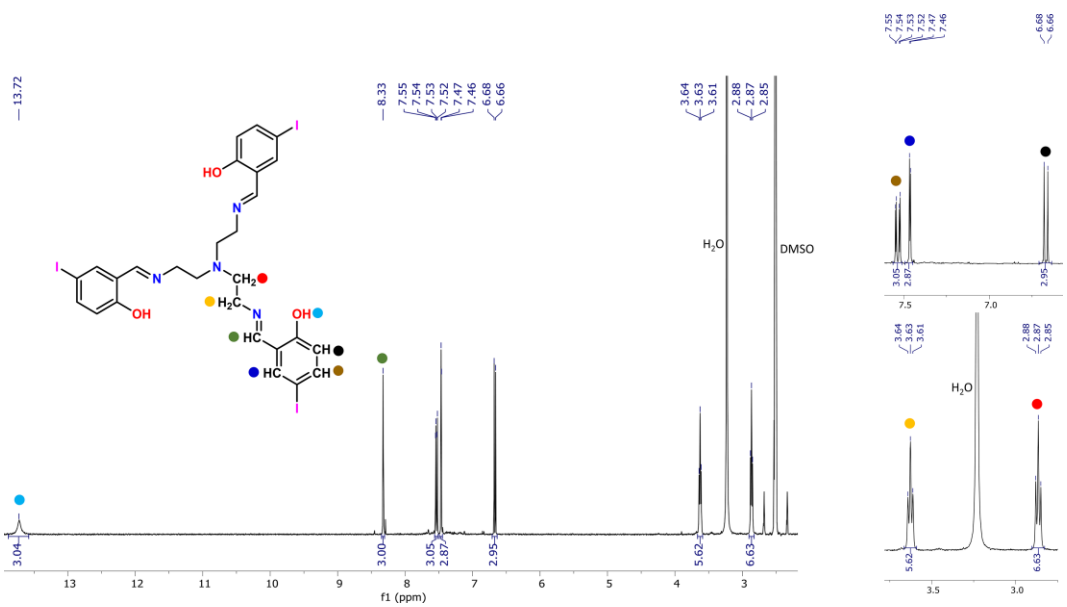

Figure 2.5. ^{1}H-NMR (400 MHz, DMSO) spectrum of H_3L_5.

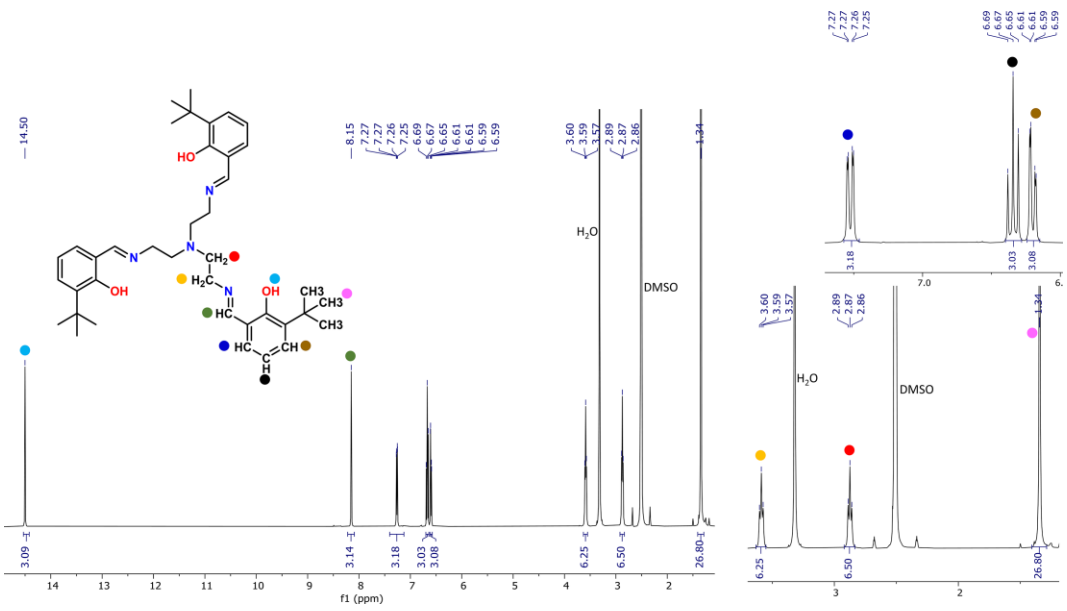

Figure 2.6. ^{1}H-NMR (400 MHz, DMSO) spectrum of H_3L_6.

The identity of the desired ligand molecules was also confirmed by ESI-MS spectra in which the ion signal is visible in negative mode (**Figure 2.7 – Figure 2.12).**

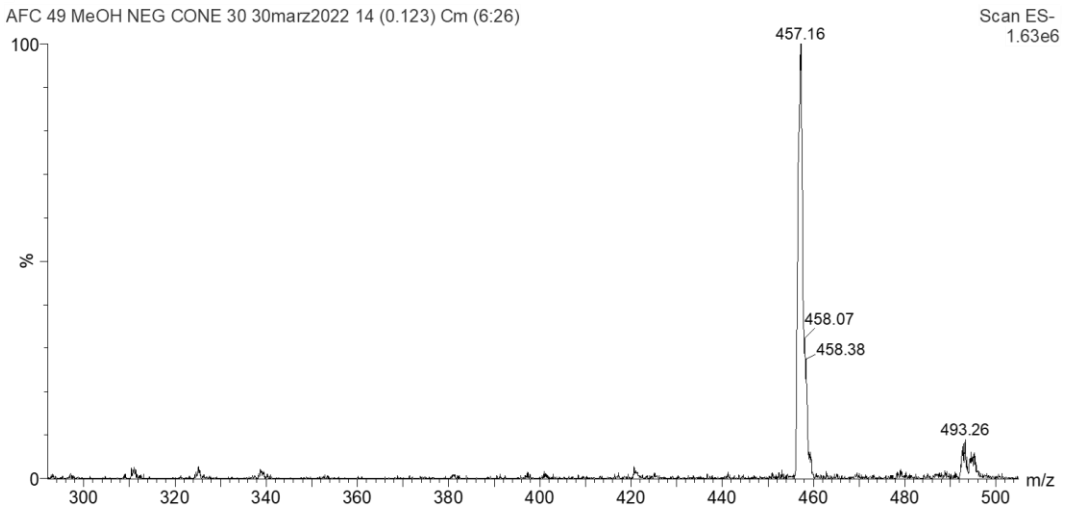

Figure 2.7. UPLC-ESI (-) mass spectrum of H_3L_1 (CH_3OH); *m/z* $[L_1]^-$= 457.16.

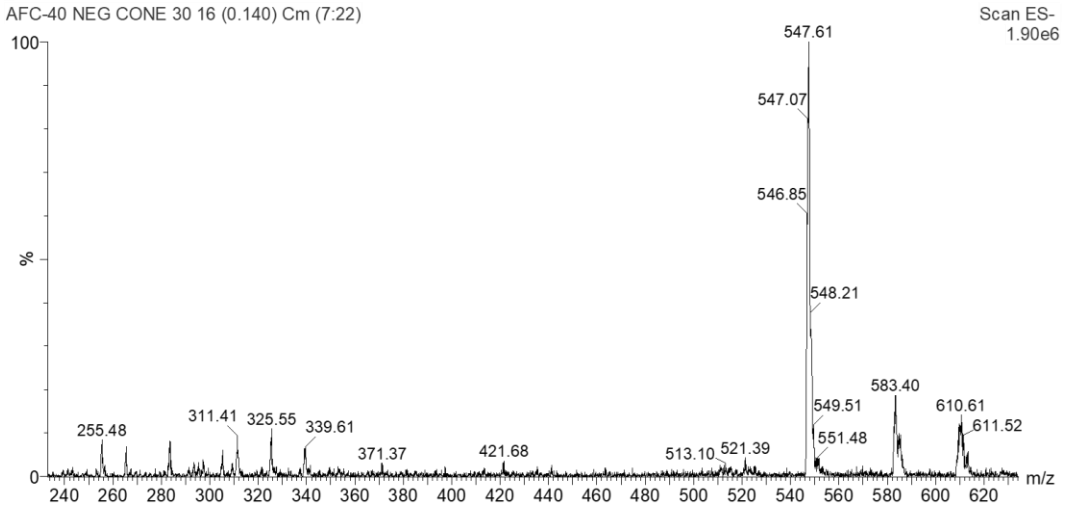

Figure 2.8. UPLC-ESI (-) mass spectrum of H_3L_2 (CH_3OH); *m/z* $[L_2]^-$= 547.61.

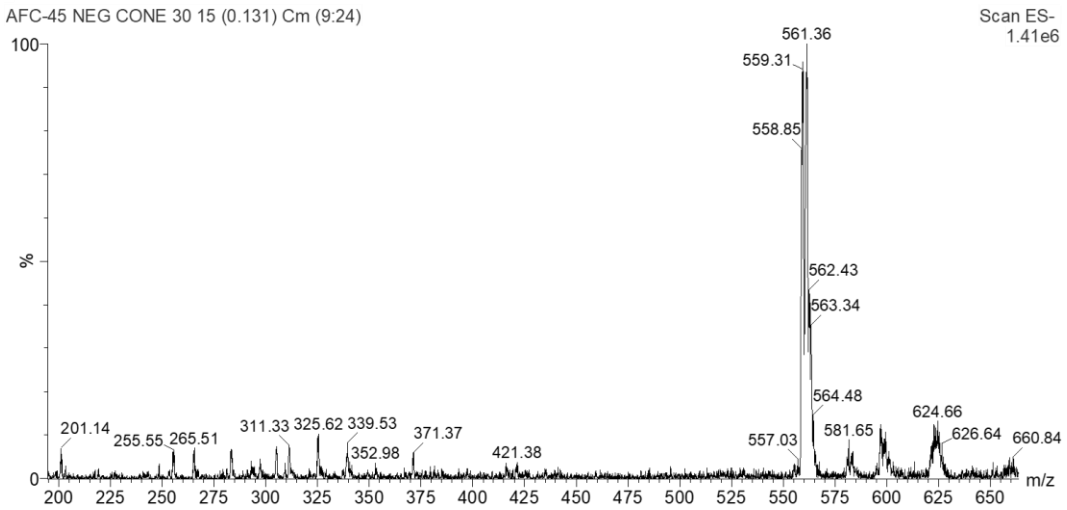

Figure 2.9. UPLC-ESI (-) mass spectrum of H_3L_3 (CH_3OH); *m/z* $[L_3]^-$= 561.36.

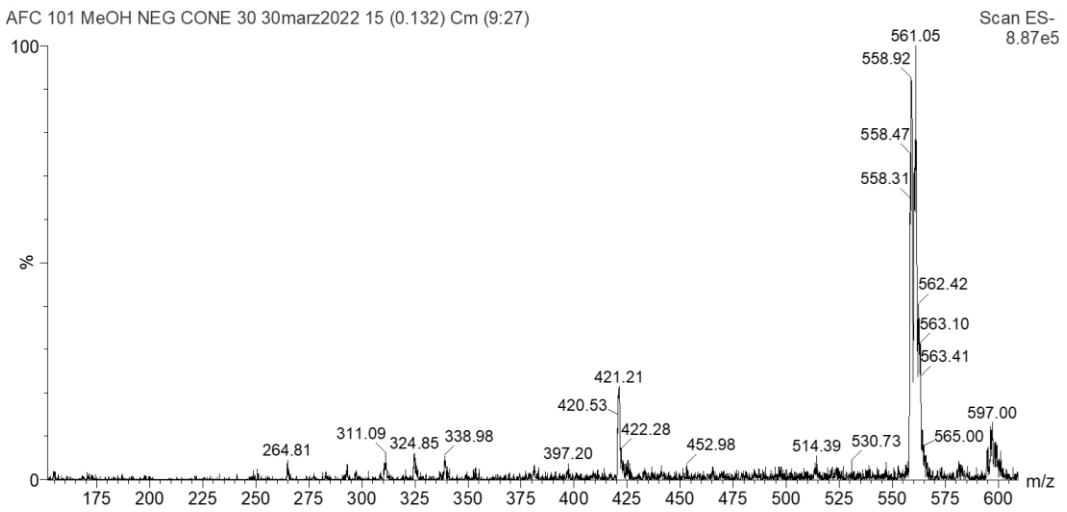

Figure 2.10. UPLC-ESI (-) mass spectrum of H_3L_4 (CH_3OH); *m/z* $[L_4]^-$= 561.05.

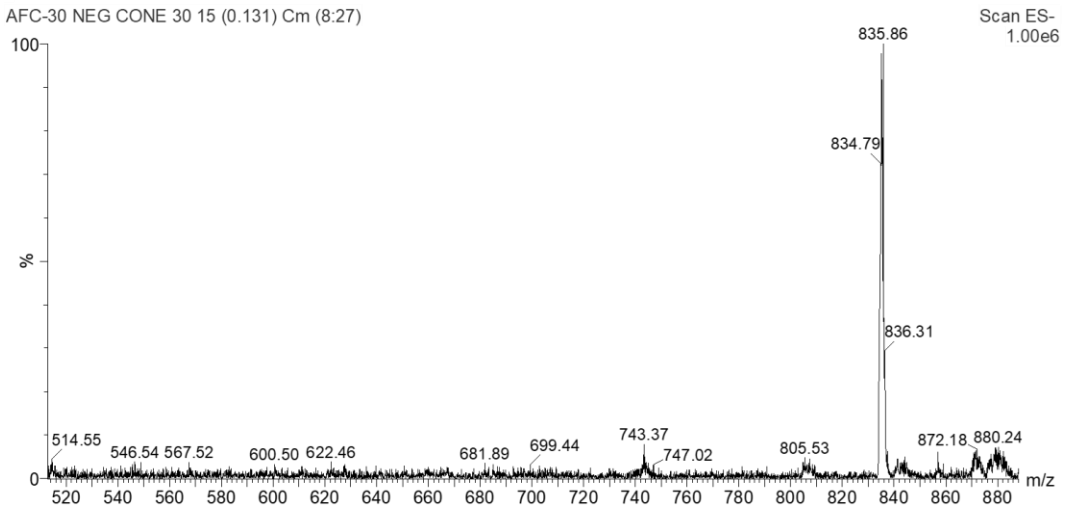

Figure 2.11. UPLC-ESI (-) mass spectrum of H_3L_5 (CH_3OH); *m/z* $[L_5]^-$= 835.86.

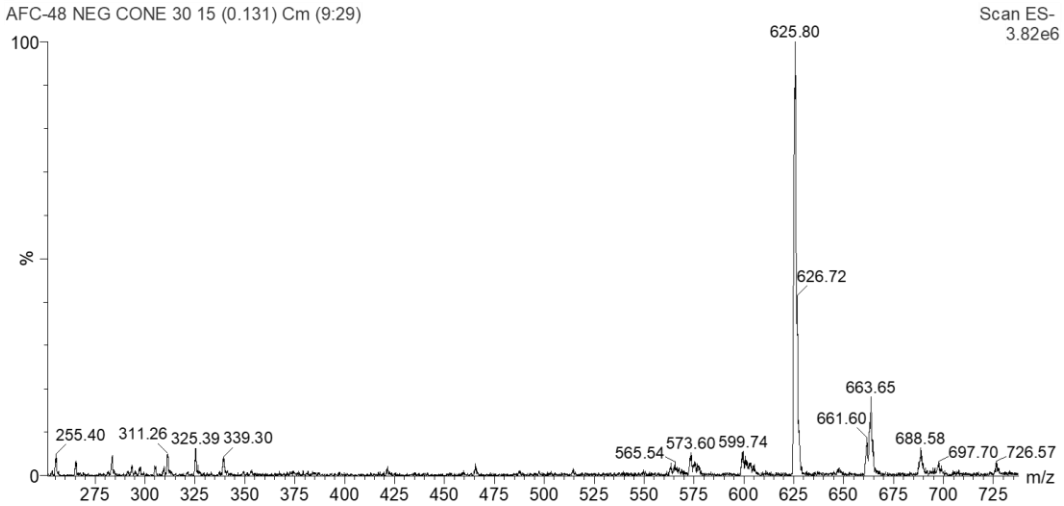

Figure 2.12. UPLC-ESI (-) mass spectrum of H_3L_6 (CH_3OH); *m/z* $[L_6]^-$= 625.80.

2.3.2 Synthesis and characterization of Nd^{III} and Dy^{III} complexes

The Trensal ligands were used in the synthesis of the Nd^{III} and Dy^{III} complexes as here described. A solution of Trensal^{R} ligand (1 mmol) and triethylamine (3 mmol) was prepared in acetone or acetonitrile (10 mL). $Ln(NO_3)_3 \cdot 6H_2O$ (1 mmol) was dissolved in the same reaction solvent (5 mL) and added to the ligand solution. The resulting mixture was stirred and refluxed for 1 h. The precipitate obtained was filtered off, washed and dried under vacuum (**Scheme 2.2**).

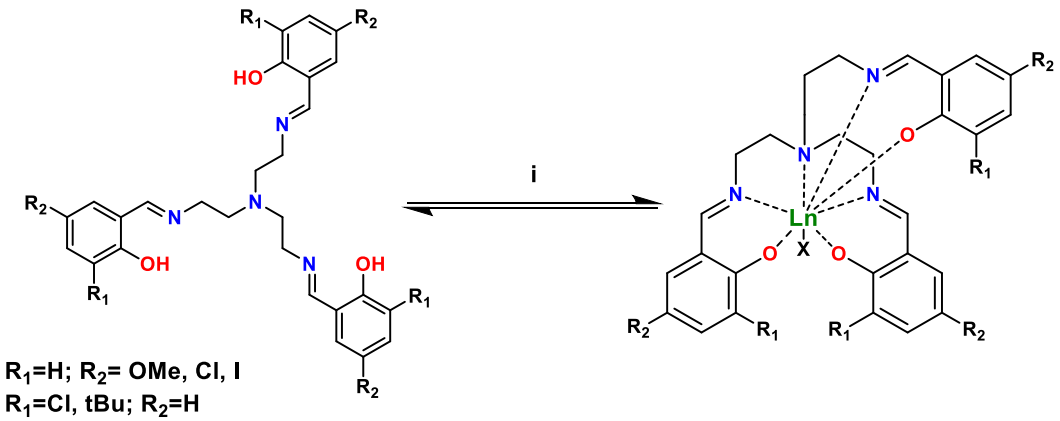

Scheme 2.2. Scheme of the synthesis of Nd and Dy complexes. ii) Trensal^{R} (1 eq), Et_3N (3 eq), $Ln(NO_3)_3 \cdot 6H_2O$ (1 eq) (Ln= Dy, Nd), acetone or CH_3CN, reflux, 1 h.

Lanthanide nitrate salts ($Ln(NO_3)_3$) were selected as the inorganic precursors to replicate the leaching solutions typically generated by common hydrometallurgical processes, which often involve dissolving lanthanide-containing materials using nitric acid. For instance, NdFeB waste magnets and mixtures of Ln_2O_3 from initial separation treatments can be dissolved in HNO_3 solutions prior to further concentration and separation steps. As a result, a mixture of lanthanide nitrates was used as the feed solution for these experiments. **Table 2.2** reports the list of the lanthanide complexes of which the crystal structure has been determined by X ray crystallography. All complexes were characterized using single-crystal X-ray diffraction (SC-XRD). The purity of the bulk material from which the crystals were obtained was confirmed through elemental analysis. Due to the limited solubility of the complexes in numerous common solvents, their spectroscopic characterization in solution was not possible. Suitable crystals for XRD analysis were obtained by slow evaporation of hot DMF solutions in which the complex powders were dissolved. Crystals of $[Nd(Trensal^{p\text{-}OMe})(H_2O)]$ and [Nd(Trensal)]·ACN were successfully grown within one week directly from the reaction bulk by gradually reducing the temperature by 5 °C per day, using acetone and acetonitrile as solvents, respectively. **Table 2.2** summarizes all crystal structures obtained from SC-XRD analysis.

Table 2.2. Summary of the Ln(Trensal^{R}) complexes

Ligand	Complex	
Trensal	[Dy(Trensal)]	(**1**)[c]
	[Nd(Trensal)(H_2O)]	(**7**)[c]
	[Nd(Trensal)]·ACN	(**8**·ACN)[b]
Trensal$^{o\text{-}Cl}$	[Dy(Trensal$^{o\text{-}Cl}$)]	(**2**)[c]
	[Nd(Trensal$^{o\text{-}Cl}$)(DMF)]·DMF	(**11**·DMF)[c]
Trensal$^{o\text{-}tBu}$	[Dy(Trensal$^{o\text{-}tBu}$)]·Acetone	(**3**·Acetone)[a]
	[Nd(Trensal$^{o\text{-}tBu}$)]·DMF	(**10**·DMF)[c]
Trensal$^{p\text{-}I}$	[Dy(Trensal$^{p\text{-}I}$)]·3DMF	(**4**·3DMF)[c]
	[Nd(Trensal$^{p\text{-}I}$)(DMF)(H_2O)]·DMF	(**9**·DMF)[c]
Trensal$^{p\text{-}OMe}$	[Dy(Trensal$^{p\text{-}OMe}$)]	(**5**)[c]
	[Nd(Trensal$^{p\text{-}OMe}$)(H_2O)]	(**13**)[c]
Trensal$^{p\text{-}Cl}$	[Dy(Trensal$^{p\text{-}Cl}$)]	(**6**)[c]
	[Nd(Trensal$^{p\text{-}Cl}$)(DMF)(H_2O)]	(**12**)[c]

[a] The synthesis was performed in acetone. Crystals were obtained by slow evaporation of acetone.

[b] The synthesis was performed in acetonitrile. Crystals were obtained by slow evaporation of CH_3CN.

[c] Recrystallized by slow evaporation of DMF.

2.3.3 Description of [Ln(Trensal^{R})] crystal structures

The structural characterization of the complexes was an essential step into the interpretation of the different properties of the compounds, and into the rational design of next generations of ligands, (**Figures 2.13** and **Figure 2.14)**. Details of the structural investigation for [Dy(Trensal)] (**1**), [Dy(Trensal$^{o\text{-}Cl}$)] (**2**), [Dy(Trensal$^{o\text{-}tBu}$)]·Acetone (**3**·Acetone), [Dy(Trensal$^{p\text{-}I}$)]·3DMF (**4**·3DMF), [Dy(Trensal$^{p\text{-}OMe}$)] (**5**) and [Dy(Trensal$^{p\text{-}Cl}$)] (**6**), [Nd(Trensal)(H_2O)] (**7**), [Nd(Trensal)]·ACN (**8**·ACN), [Nd(Trensal$^{p\text{-}I}$)(DMF)(H_2O)]·DMF (**9**·DMF), [Nd(Trensal$^{o\text{-}tBu}$)]·DMF (**10**·DMF),

[Nd(Trensal$^{o\text{-}Cl}$)(DMF)]·DMF (**11**·DMF), [Nd(Trensal$^{p\text{-}Cl}$)(DMF)(H_2O)] (**12**) and [Nd(Trensal$^{p\text{-}OMe}$(H_2O)] (**13**) are reported in the Supporting Information (**Tables S2.1-S2.9)**. Dy complexes exhibit an invariant molecular structure with respect to the metal environment. Hence, compounds **1**-**6** will be described together. The metal coordination geometry is capped octahedral, with the three phenoxy oxygen atoms and three imine nitrogen atoms that occupies the vertices of the octahedron, and the tertiary aminic nitrogen atom comprising the seventh coordination site (**Figure 2.13a, S2.1-S2.12**). Consistently, the Dy-$N_{capping}$ distance (2.674(3)-2.766(7) Å) is significantly longer than the other Dy-N bond distances (2.460(2)-2.503(4) Å). The Dy-O bond distance (2.187(3)-2.223(2) Å) is the shortest among the coordination environment, in agreement with the presence of the negative charge on the oxygen atom. On the contrary, when the coordinated metal is Nd, the complexes show different molecular structures, and they usually show the presence of solvent molecules of crystallization interacting with the metal center. In more detail, only in **8**·ACN and **10**·DMF the metal coordination is capped octahedral and similar to that of the Dy complexes (**Figure S2.15-S2.16** and **S2.19-S2.20**). However, the coordination bond distances are longer in the Nd complexes, in agreement with the larger size of the Nd^{III} with respect to Dy^{III}. A direct comparison is possible since **8**·ACN, **10**·DMF, and the Dy complexes have the same c.n. of 7, see **Figure 2.13a**. The Nd-$N_{capping}$ distance (2.798(2)-2.821(4) Å) is significantly longer than the other Nd-N bond distances (2.596(1)-2.601(4) Å) with the Nd-O bond distances being the shortest (2.248(3)-2.273(1) Å). The metal coordination in **11**·DMF is capped octahedral, obtained by interaction with three phenoxy oxygen atoms and three imine nitrogen atoms that defines the octahedron, with the oxygen of the coordinated DMF that represents the capped position (**Figure 2.13b**, **S2.21-S2.22**). The Nd-$N_{central}$ distance is too long (3.012(2) Å) to contribute to the metal coordination irrespective of the proper orientation of the

lone pair. In addition, the DMF coordinated at the metal is disordered over to sites with equivalent occupancy, which does not alter the overall complex geometry. The Nd-$O_{capping}$ distance (2.522(4) Å) is shorter than the Nd-N bond distances (2.595(2)-2.622(2) Å), but it is longer than the other Nd-O bond distances from the phenoxy groups (2.303(1)-2.337(1) Å), which remain the shortest in this the coordination environment. The metal coordination in **7** and **13** is antiprismatic, achieved by three phenoxy oxygen atoms, three imine nitrogen atoms, the central N of the ligand and one molecule of water (**Figure 2.13c**, **S2.13**-**S2.14** and **S2.25-S2.26**). The Nd-$N_{central}$ distance (2.776(2) Å for **7** and 2.82(2) Å for **13** is the longest, followed by the other Nd-N bond distances (2.583(2)-2.677(2) Å for **7** and 2.58(3)-2.72(2) Å for **13** and by the Nd-O_{water} one (2.523(2) Å for **7** and 2.49(2)-2.53(2) Å for **13**). The shortest distances are those involving the phenoxy groups (2.299(2)-2.410(2) Å for **7** and 2.24(2)-2.38(2) Å for **13**). Compounds **9**·DMF and **12** exhibit a capped antiprismatic metal coordination, where the seven coordination sites provided by the ligand are complemented by water and a DMF molecules. The central N atom of the ligand occupies the capping position (**Figure 2.13d**, **S2.17-S2.18** and **S2.23-S2.24**). In both complexes, the Nd-$N_{central}$ distance (2.841(3) Å for **9**·DMF and 2.846(2) Å for **12**) is significantly longer than the other Nd-N bond distances (2.647(3)-2.708(3) Å for **9**·DMF and 2.626(2)-2.733(2) Å for **12**), followed by the Nd-O_{Water} (2.531(3) Å for **9**·DMF and 2.525(1) for **12** and Nd-O_{DMF} 2.588(3) Å for **9**·DMF and 2.535(1) Å for **12**). As expected, the shortest distances are those involving the phenoxy groups (2.352(3)-2.397(2) Å for **9**·DMF and 2.349(1)-2.410(1) Å for **12**).

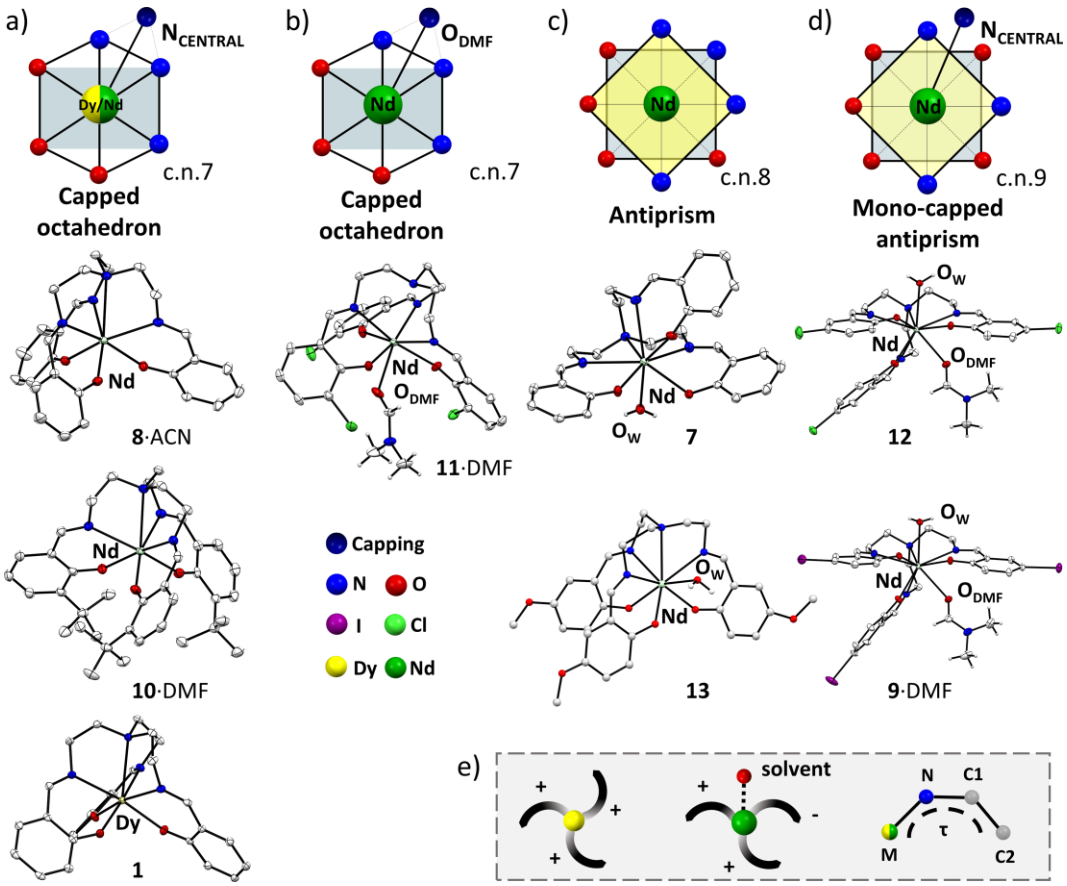

Figure 2.13. Molecular structures of selected complexes, together with a schematic representation of the metal geometry. a) [Nd(Trensal)]·ACN (**8**·ACN), [Nd(Trensal$^{o\text{-}tBu}$)]·DMF (**10**·DMF) and [Dy(Trensal)] (**1**) as representatives of the c.n. 7; b) [Nd(Trensal$^{o\text{-}Cl}$)(DMF)]·DMF (**11**·DMF); c) [Nd(Trensal)(H_2O)] (**7**) and [Nd(Trensal$^{p\text{-}OMe}$(H_2O)] (**13**); d) [Nd(Trensal$^{p\text{-}Cl}$)(DMF)(H_2O)] (**12**) and [Nd(Trensal$^{p\text{-}I}$)(DMF)(H_2O)]·DMF (**9**·DMF). Solvent of crystallization and most of the H atoms were removed from clarity. e) Different orientations of the three arms of the ligands as a function of the sign of the τ angle (M-$N_{central}$-C1-C2). Image reprinted from https://pubs.acs.org/doi/full/10.1021/acs.inorgchem.2c02619.

From the structural analysis it is evident that two general features can be derived by the comparison of the Dy and Nd systems. The larger size of Nd leads to an increase of the bond distances pertaining to the coordination environment with respect to the Dy cases. As a result, the Nd atom is generally more exposed to the solvent and can therefore expand the c.n. from 7 to 9. The presence of the solvent (water or DMF) bound to Nd is particularly interesting since it offers additional interaction sites towards the bulk of the solvent, thus altering the solubility properties of the compounds. The ligands under investigation are characterized by a three-fold symmetry and they exhibit conformationally rigid coordination moieties (functionalized phenyl rings) connected to the central atom through the more flexible ethylene linkers.

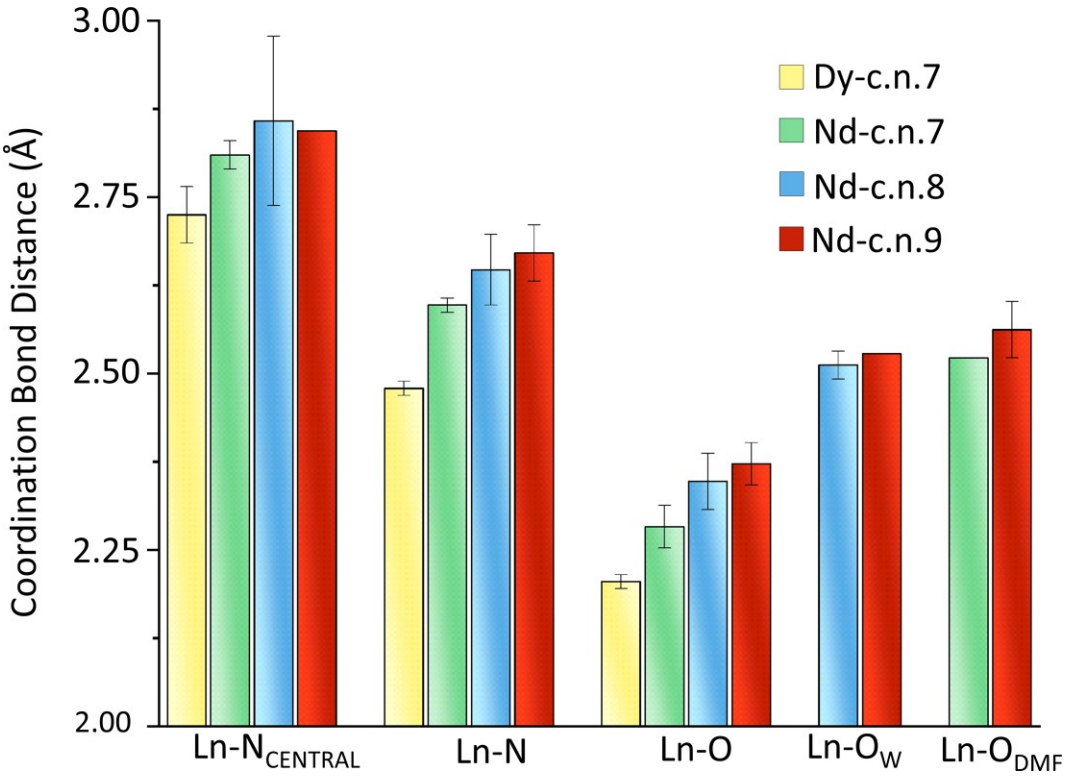

Figure 2.14. Mean values of the coordination bond distances as a function of the c.n., lanthanide and donor atoms observed in the crystal structures of the complexes listed in **Table 2.2**. Image reprinted from https://pubs.acs.org/doi/full/10.1021/acs.inorgchem.2c02619.

Another interesting feature worth of note is the different peripheral functionalization of the phenoxy groups of the ligands, and its influence in the interactions that are exchanged within the lattice. Indeed, the presence of iodine atoms, chlorine atoms, or methoxy groups, in some of the ligands promote the formation of weak interactions between the complex molecules and adjacent molecules or solvent of crystallization, **Figure 2.15** and **Figures S2.8, S2.18, S2.24**. More specifically, iodine atoms can act as halogen bond donors toward a nucleophile system such as the oxygen atom of DMF, whereas the methoxy group

can exchange weak hydrogen bonds with aromatic or aliphatic CH moieties. These observations are suggestive of a potential different solubility of Nd complexes *vs* Dy complexes, according to the different interaction that a single molecular entity can exchange with a bulk solvent such as acetone, which is endowed with, though weak, coordination ability, as well as potentially acting as halogen and hydrogen bond acceptor.

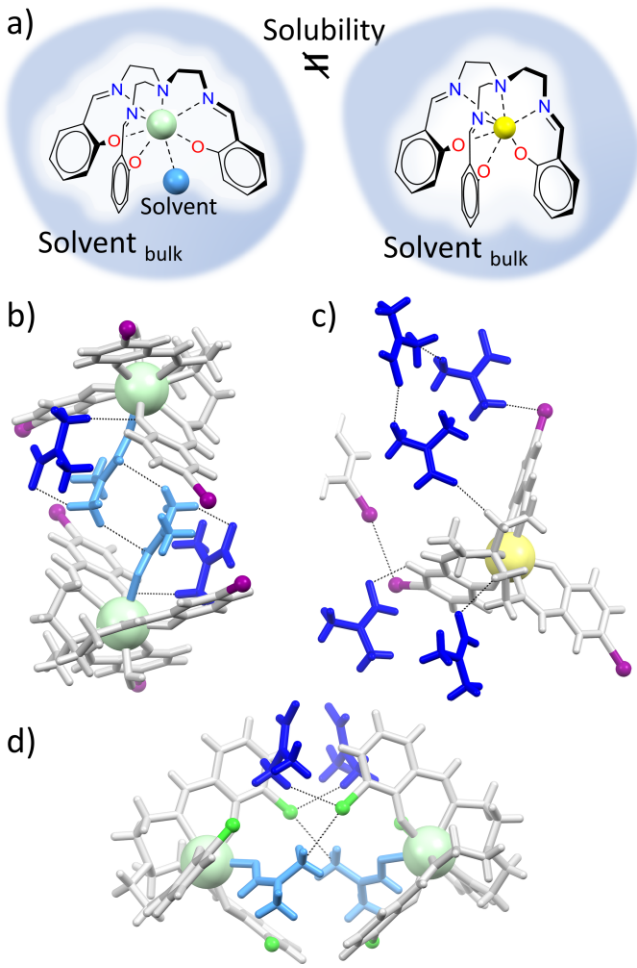

Figure 2.15. a) Description of the potential influence of the coordinated solvent molecules on the Nd and Dy complexes on the solubility; b-d) interactions

exchanged by the coordinated solvent (light blue) and by solvent of crystallization (blue) with the complex molecules in **9**·DMF, **4**·3DMF and **12**. Nd in light green, Dy in yellow. Image reprinted from https://pubs.acs.org/doi/full/10.1021/acs.inorgchem.2c02619.

2.3.4 Solubility test of [Ln(Trensal^{R})] complexes

Since the complexes of Nd^{III} and Dy^{III} present significant structural differences, we carried out the synthesis of the complexes in different solvents in order to evaluate if these complexes remain in solution or rather separate as solids when formed in solution. The different behavior of the complexes were analyzed in terms of differences in their solubility, possibly as the result of the role of solvent molecules where coordinated to the lanthanide ions.

Among the solvents tested, acetone proved to be the most effective in highlighting the differences in solubility between Nd and Dy complexes when the same ligand was used. **Figure 2.16** shows that the complexes formed in acetone with the Trensal$^{p\text{-}OMe}$ ligand exhibit contrasting solubility behaviors, indicating that Trensal$^{p\text{-}OMe}$ is a promising candidate for the selective separation of these two metals in this solvent.

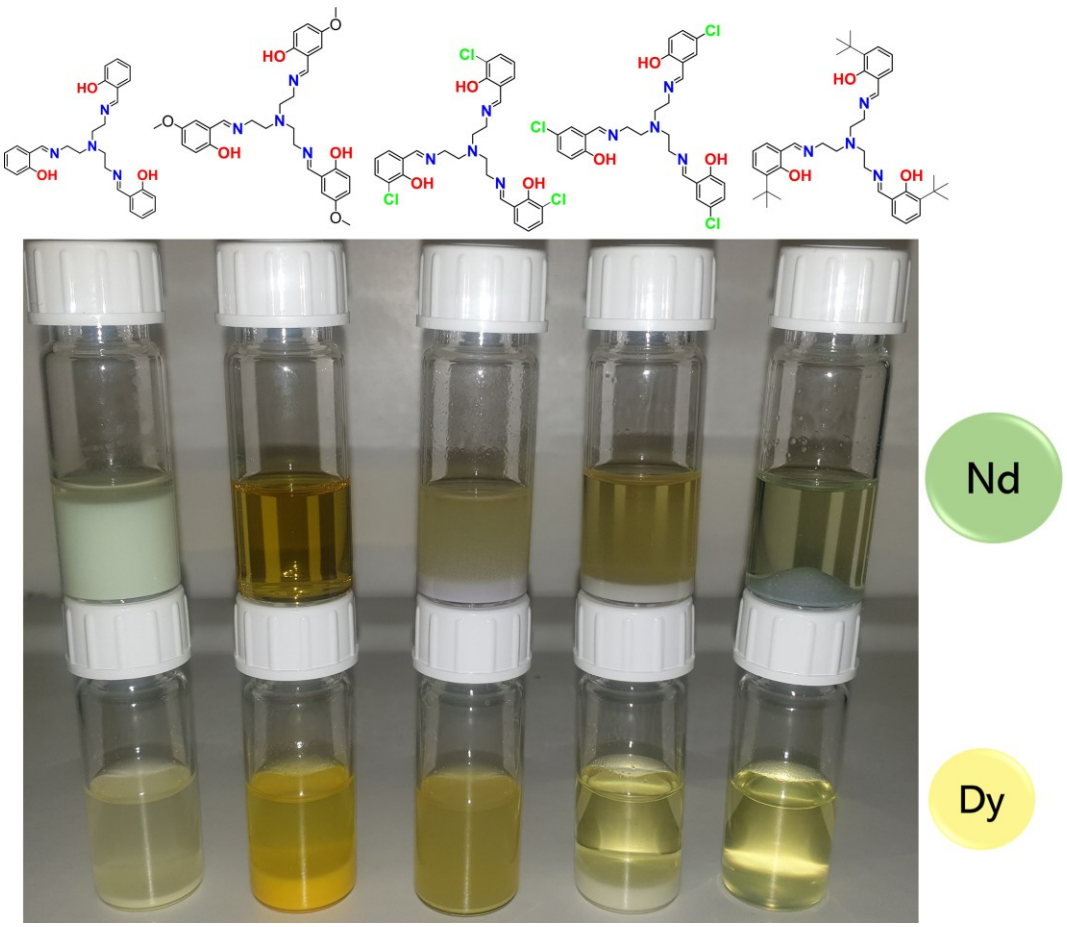

Figure 2.16. Vials containing Trensal^{R} complexes of Nd and Dy prepared by mixing equimolar amount of ligand and metal (C_{Metals} = 4 mM) at 25 °C. Image reprinted from https://pubs.acs.org/doi/full/10.1021/acs.inorgchem.2c02619.

2.3.5 Stability in solution of Trensal$^{p\text{-}OMe}$ ligand in various conditions

The ligand Transal$^{p\text{-}OMe}$ was used as a reference compound for attempting to shed light on the stability of the ligand itself under various medium/solvent conditions.

Initially, a solution of Trensal$^{p\text{-}OMe}$ ($6x10^{-5}$ M in acetone) was prepared, and the UV-Vis spectrum collected immediately after sample preparation. A spectrum was collected on the same solution, the latter kept at room temperature for one month. The spectra, reported in **Figure 2.17**, show a quite perfect overlap, indeed suggesting that the ligand is stable in non-anhydrous solvents and that decomposition of the imine group did not occur.

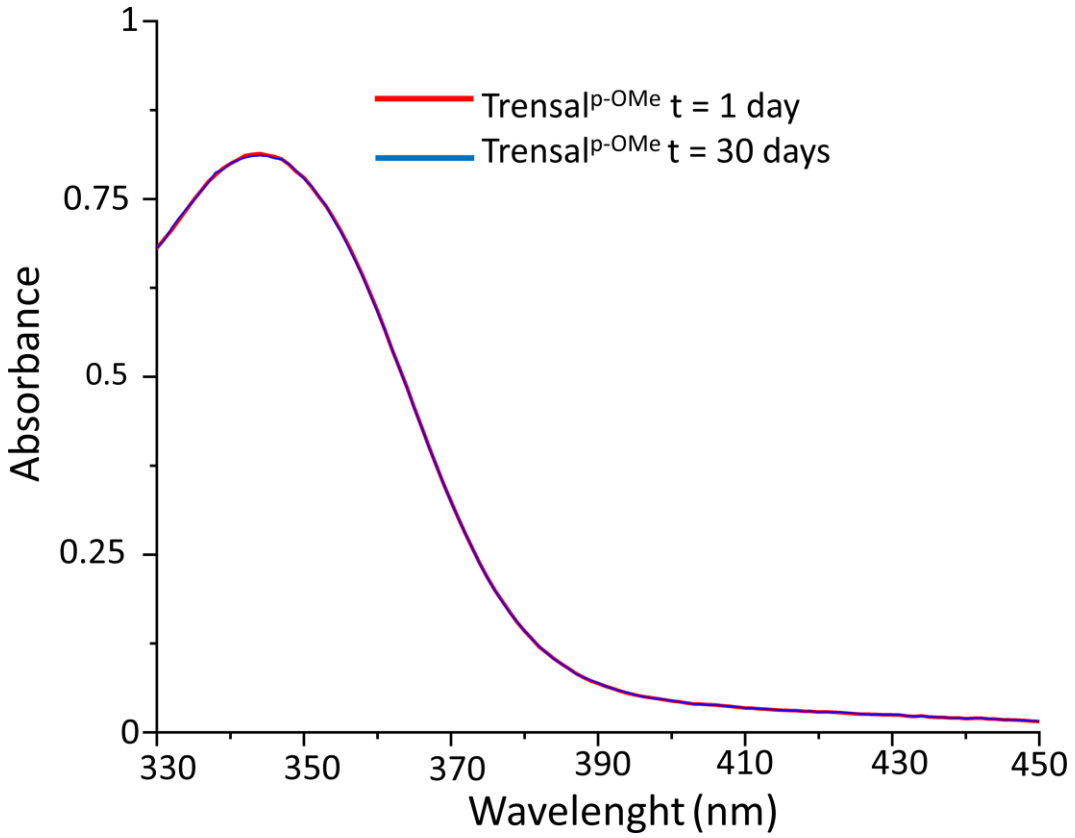

Figure 2.17. UV-visible spectra of Trensal$^{p\text{-}OMe}$. Uv-Visible spectra were collected under stirring at 25 °C in acetone. Spectra were collected immediately after dissolution and 1 month after dissolution using the same solution C_{Ligand} = 6x10^{-5} M, solution kept at 25 °C.

For a better understanding of the stability of these ligands, and to provide a more accurate description of their chemical reactivity, the UV-Vis absorption spectra of the Trensal$^{p\text{-}OMe}$ ligand dissolved in aqueous media were collected. The ligand was dissolved in aqueous buffered solutions with pH values ranging from 4.4 to 10.1. The spectra were recorded over time with a 30-second interval between consecutive scans. **Figures 2.18** present the results of these analyses. The spectra

change over time at all pH values examined, suggesting that the tris-imino functional groups of the Trensal-type ligands are the source of the chemical instability in aqueous media. Indeed, the ligands are not stable in water and, as expected, undergo hydrolysis in a very short time across different pH values.

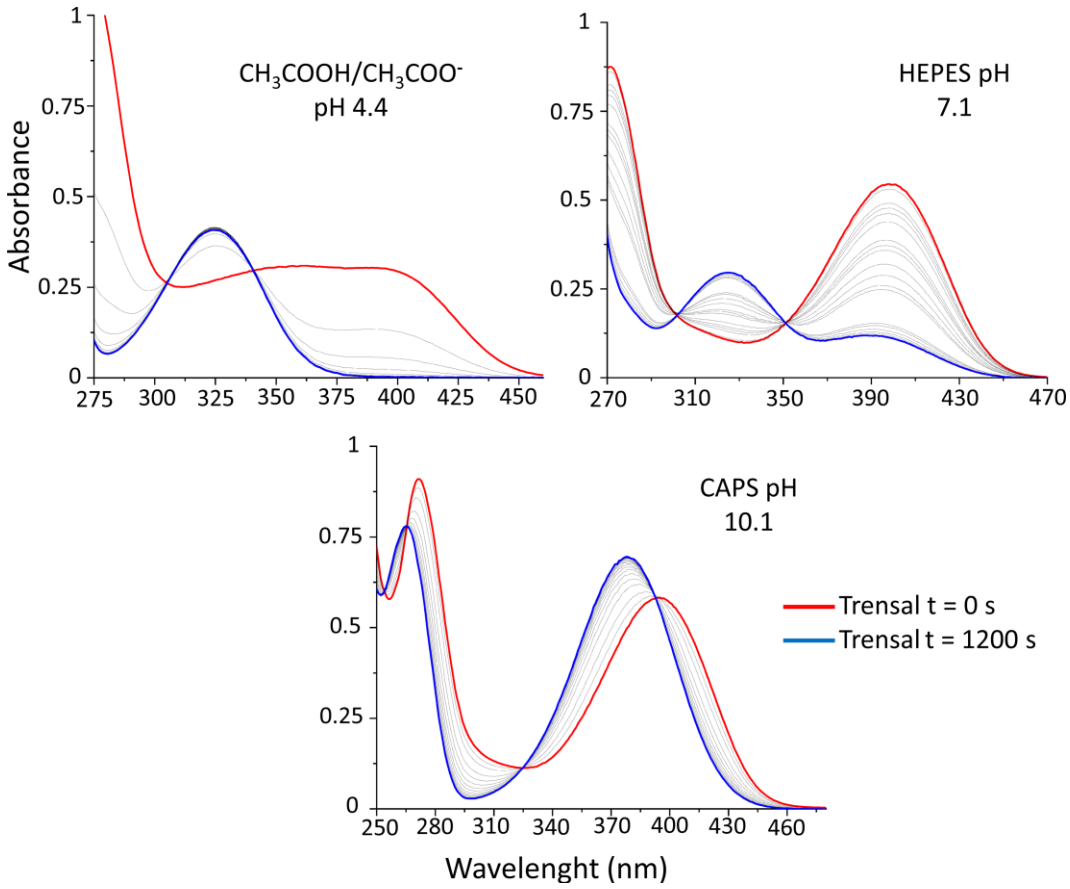

Figure 2.18. UV vis spectra collected over time of Trensal$^{p\text{-}OMe}$ dissolved in aqueous buffer solutions at different pH. Uv-Visible spectra were collected under stirring at 25 °C in 50 mM aqueous acetate buffer at pH 4.4 (left), in 50 mM aqueous HEPES buffer at pH 7.1 (right) and in 50 mM aqueous CAPS buffer at pH 10.1 (bottom). UV-Visible spectra were collected every 60 s for 1200 s. Image reprinted from https://pubs.acs.org/doi/full/10.1021/acs.inorgchem.2c02619.

2.3.6 Study of the equilibria of formation of [Dy/Nd(Trensal$^{p\text{-}OMe}$)] complexes

We attempted the study of the formation equilibria of the complexes of Trensal$^{p\text{-}OMe}$ with Nd and Dy in acetone by UV spectrophotometric titrations of a $6x10^{-5}$ M ligand solution. Titrations of the ligand were carried out in the presence of a base, by adding aliquots of metal until reaching the 1:1 metal-to-ligand equivalence point. The UV-Vis spectra of samples containing Trensal$^{p\text{-}OMe}$ with increasing amounts of Nd and Dy are shown in **Figure 2.19**. For both metals, the ligand band at around 340 nm decreases in absorbance in favor of an increase in the band at 390 nm (which appears as a shoulder or broad band for Nd). The presence of an isosbestic point at 360 nm in these spectra supports the hypothesis that the 1:1 lanthanide-ligand complexes are the only species formed in solution, even in the presence of excess ligand.

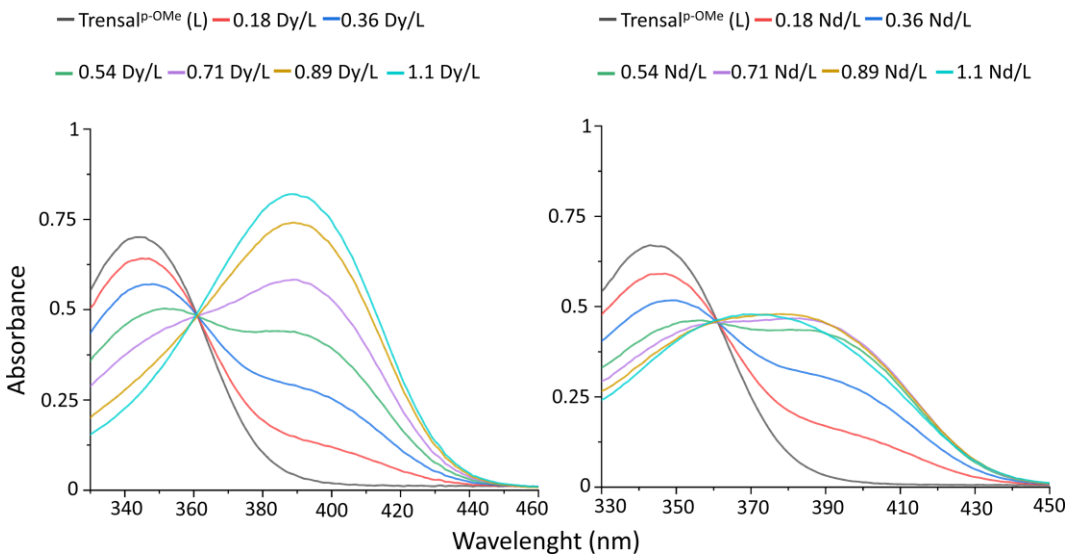

Figure 2.19. Spectral dataset for the titration of solutions of Trensal$^{p\text{-}OMe}$ with $Dy(NO_3)_3 \cdot 6H_2O$ (left) and $Nd(NO_3)_3 \cdot 6H_2O$ (right). Spectra were collected under stirring at 25 °C in acetone. The Trensal$^{p\text{-}OMe}$ solution ($6.46 \cdot 10^{-5}$ M) was titrated with ten aliquots of $Dy(NO_3)_3 \cdot 6H_2O$ and $Nd(NO_3)_3 \cdot 6H_2O$ stock solutions ($2 \cdot 10^{-3}$ M), ranging from a metal-to-ligand ratio (M/L) of 0.1 eq up to 1 eq. Image reprinted from https://pubs.acs.org/doi/full/10.1021/acs.inorgchem.2c02619.

The results reported in the previous sections, and in particular the molecular structures and the titration experiments, demonstrate that the Trensal ligands form, with Nd and Dy, 1:1 complex species which are stable in organic solvents. Differences in the structure, especially due to the presence of solvent molecules incorporated into the coordination sphere of Nd, does not seem to influence the stability in solution of the complexes of this metal compared to that of the Dy species.

2.3.7 Nd and Dy separation

The separation of Nd from Dy using the Trensal$^{p\text{-}OMe}$ ligand was attempted by exploiting the different solubility of the complexes in acetone. The amount of metal present in the solution and solid phase (after separating any precipitate, if present) by mixing the ligand with the metal salts was determined by ICP-AES.

We predicted that where the ligand is in excess relative to the metals, the separation efficiency may be influenced primarily by the different solubility of the two Nd and Dy complexes, assuming similar thermodynamic stabilities. Conversely, where the metal is present in excess, we predicted that the efficiency of separation may also be affected by differences in the stability of the complexes. With a reduced ligand concentration, differing stabilities can lead to different concentrations of the complexes in solution, which in turn may affect the overall solubility. For these reasons, the separation efficiency related to Nd vs. Dy using Trensal$^{p\text{-}OMe}$ was evaluated by mixing 1:1 solutions of Nd and Dy ($C_{Nd} = C_{Dy} = 3.87 \cdot 10^{-3}$ M) with ligand solutions in various ratios ranging from sub-stoichiometric to excess ligand concentrations: Nd:Dy ratios of 1:1:3, 1:1:2, 1:1:1, and 1:1:0.5 (see **Figures 2.20** and **S2.29**). Where present, the solid phase was separated by filtration on a ceramic septum.

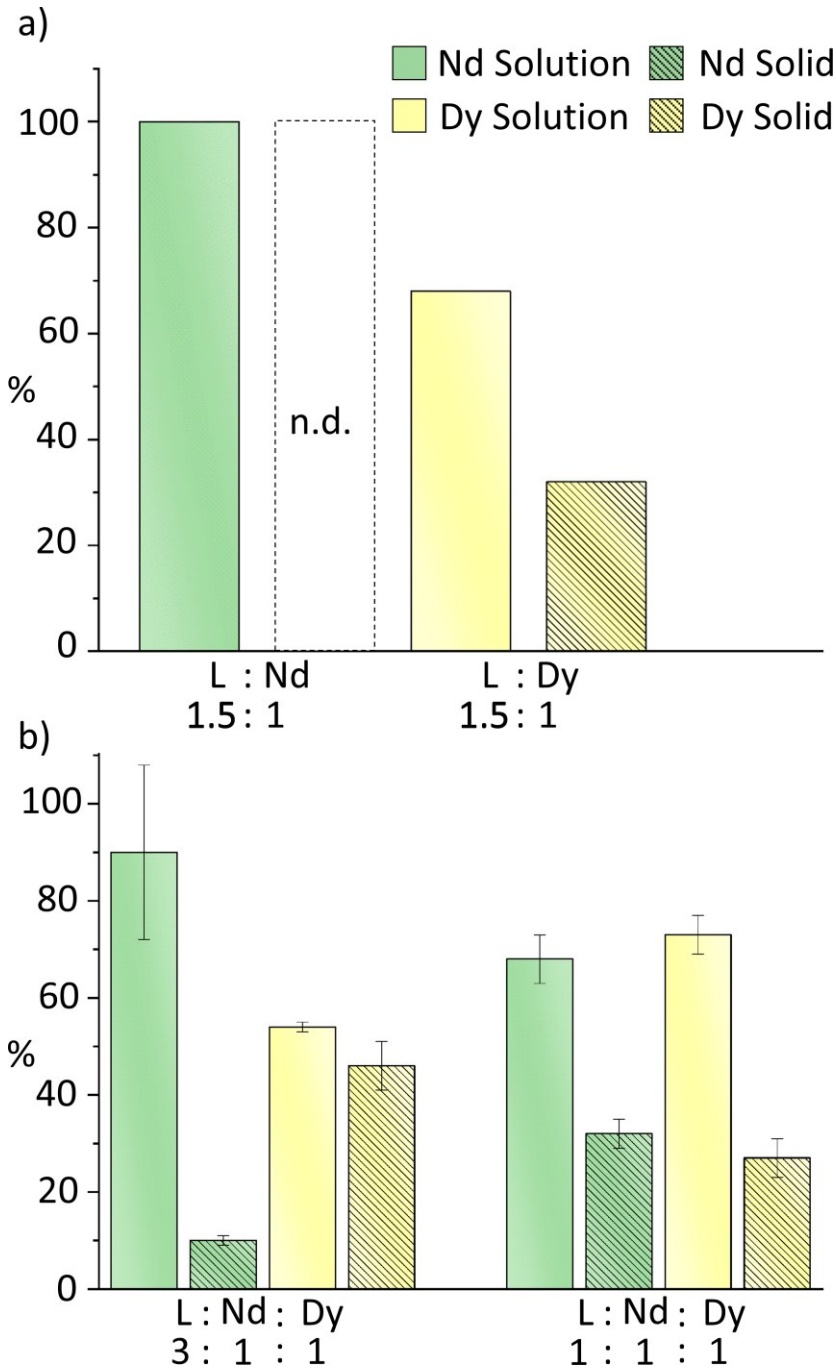

Figure 2.20. Amount of Nd or Dy (reported as % of the initial reactant quantity) determined by ICP-AES analyses. a) Nd and Dy recovered in solution and solid phases when present individually in acetone after 3 h. b) Amount of Nd and Dy recovered from the solution and solid phases for two different stoichiometric ratios

in acetone after 3 h after mixing Nd^{III}, Dy^{III}, and $Trensal^{p\text{-}OMe}$ (L) in the 1:1:3 and 1:1:1 stoichiometric ratio. The metal cations were added as nitrate salts. Image reprinted from https://pubs.acs.org/doi/full/10.1021/acs.inorgchem.2c02619.

In the reacting systems where an excess of ligand is present (C_{Ln} = 7.73 × 10^{-3} M; $C_{Trensalp\text{-}OMe}$ = 1.16 × 10^{-2} M; M ratio of 1:1.5) the Nd complex was found to be completely soluble in acetone, whereas the Dy complex exhibited the formation of a precipitate (refer to **Figure 2.16** for solubility data). Specifically, for the Dy complex, at least 40% of the total mass of metal was recovered in the solid phase. This difference in solubility indeed puts on the basis for the potential separation of the two metals. That maximum separation of the two metals (obtained as an enrichment of one of the two lanthanides of either or both the solution or solid phases) could be achieved using a 0.5-fold excess of ligand relative to each metal ion (Nd:Dy = 1:1:3). More in detail, for the Nd:Dy ratio of 1:1:3 the amounts of Nd and Dy complexes in the solid phase were quantified at 10% and 46%, while in the solution phase Nd and Dy were quantified at 90% and 54%, respectively. This indicates an enrichment of Nd in the solution phase and a significant enrichment of Dy in the solid phase. Indeed, when reducing the ligand concentration from stoichiometric (Nd:Dy = 1:1:2) to sub-stoichiometric ratios (Nd:Dy = 1:1:1), the discrimination between the two metals diminishes, as both the solution and the recovered solid phases contained roughly equal amounts of Nd and Dy in each phase, as illustrated in **Figures 2.20b** and **S2.29**. Finally, results reported in **Figure 2.20** predicted that, for the concentration used, the Nd complex should be completely soluble. However, perhaps interestingly when both metals are present together with the ligand an unexpected co-precipitation of the Nd complex as a minor component with the Dy complex was observed.

We put forward here the hypothesis that the observed differences in solubility are principally associated with variations in the molecular structures. In particular, we believe that the expansion of the coordination number in the Nd complex, which facilitates additional interactions with the surrounding solvent, plays a pivotal role in this scenario. To further substantiate this hypothesis, we assessed our findings against the stability constants reported for the Dy/Trensal$^{p\text{-}Me}$ (K_f = 5.78(4)) and Nd/Trensal$^{p\text{-}Me}$ (K_f = 5.35(1)) complexes.[68] **Figure 2.21** presents a plot of the percentages of metal complexes and the total complexed metal calculated from these formation constants for concentrations of 3.5 and 0.35 mM and Nd:Dy ratios of 1:1:1-3. Interestingly, based on the formation constants reported above only when the total metal is in excess with respect of the ligand (i.e. Nd:Dy:L = 1:1:1 stoichiometry) the concentration of [Dy(Trensal^{R})] is greater than that of [Nd(Trensal^{R})]. Conversely, in the excess of ligand the two metals are fully complexed as expected for two values of formation constants that are similar.

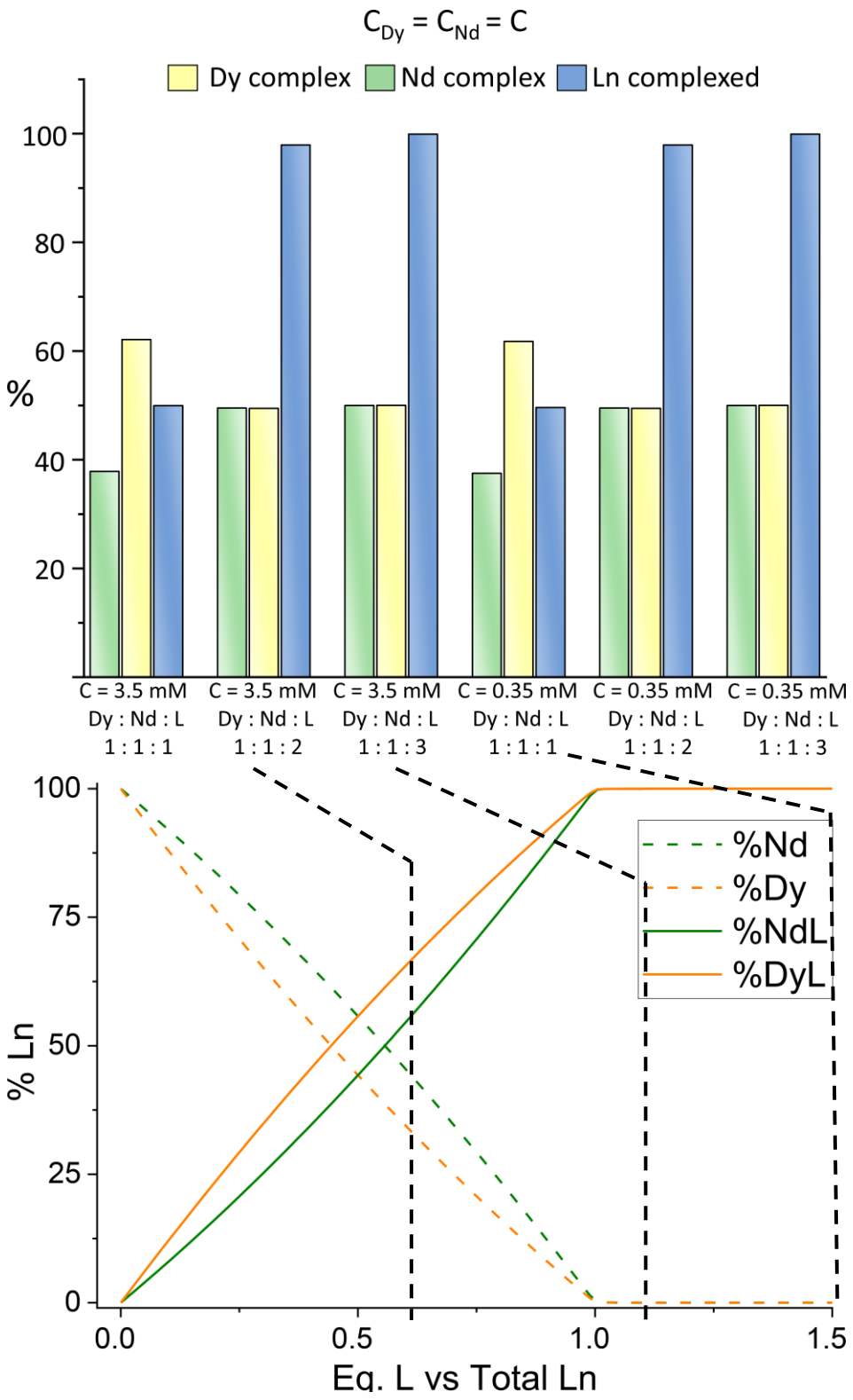
$C_{Dy} = C_{Nd} = C$
Dy complex
Nd complex
Ln complexed
%
100
80
60
40
20
C = 3.5 mM
Dy : Nd : L
1 : 1 : 1
C = 3.5 mM
Dy : Nd : L
1 : 1 : 2
C = 3.5 mM
Dy : Nd : L
1 : 1 : 3
C = 0.35 mM
Dy : Nd : L
1 : 1 : 1
C = 0.35 mM
Dy : Nd : L
1 : 1 : 2
C = 0.35 mM
Dy : Nd : L
1 : 1 : 3
%Nd
%Dy
%NdL
%DyL
% Ln
100
75
50
25
0
0.0
0.5
1.0
1.5
Eq. L vs Total Ln

Figure 2.21. Above: Speciation of the [Nd(Trensal^{R})] and [Dy(Trensal^{R})] systems (% Ln) as a function of the different stochiometric ratio Ln:Trensal^{R}. The green and yellow bars represent the percentage of the [Nd(Trensal^{R})] and [Dy(Trensal^{R})] complexes (over total Ln), respectively, for the specified Nd:Dy:L stoichiometry; The blue bar represents the % of total Ln present in solution in the form of [Ln(Trensal^{R})] complexes. Below: representative distribution diagram of a system Nd:Dy:L = 1:1:3 (Total Ln:L = 1:0-1.5; C_L = 3.5 10^{-3} M). The reported values are based on the previously reported formation constant ([Nd(Trensal$^{p\text{-}Me}$)]. Image reprinted from https://pubs.acs.org/doi/full/10.1021/acs.inorgchem.2c02619.

The data presented in this plot is worthy of note, as the ligand Trensal$^{p\text{-}OMe}$ belongs to the same ligand class as those reported in this study, differing only in its peripheral functionalization. **Figure 2.21** shows that at both concentrations with 2 equivalents of total lanthanide versus ligand, 50% of the Ln ions are coordinated, indicating ligand saturation. Under stoichiometric conditions (Dy:Nd = 1:1:2, i.e., Ln = 1:1) or with excess ligand, all metal content is complexed, with no observed preference or selectivity for either metal. The data suggest a very slight preference for Dy over Nd, but this preference only becomes apparent in the presence of excess metal and does not account for the significant differences in solubility between the two complex species. Therefore, it is clear that the different thermodynamic stabilities of the complexes are not the primary factor influencing their solubility. Specifically, in cases with Nd:Dy ratios of 1:1:3 and 1:1:2, where both Dy and Nd are fully complexed, the differing solubilities of the complexes should be attributed to the distinct nature of the molecular entities in solution.

2.4 Conclusions

In this study, we aimed to tackle the fundamental challenge of recovering critical metals, particularly those in the REE family, which are extensively used in the production of Nd(Dy)FeB permanent magnets. The proportion of Dy used in these magnets has varied over time, depending on the manufacturer and application, decreasing from approximately 5 wt.% in early magnets to about 1 wt.% in current standards.[69] In contrast, Nd constitutes the second largest component, accounting for around 26-30 wt.% of these devices. The most critical aspect of recovering and reusing these metal components lies in the separation of Dy from Nd. Due to their similar chemical properties and reactivity, this process poses significant challenges and increases purification costs. Many recently proposed processes for recycling REE-based permanent magnets aim to bypass this step, instead focusing on producing REE oxide mixtures of sufficient quality for low-profile applications. However, insights from coordination chemistry can offer straightforward strategies for their separation. A review of the CCDC database reveals that Dy and Nd can adopt coordination numbers (c.n.) ranging from 6 to 11, with Nd showing a preference for c.n. 9 (43% of structures) and Dy for c.n. 8 (55%), as shown in **Figure S2.30**. These differences can be leveraged to identify ligands that selectively meet the geometric preferences of one metal over the other. Ligands in the Trensal family exhibit some flexibility in the ethylene branches connecting to the central nitrogen atom but are characterized by a heptadentate N_4O_3 donor set. This semi-rigid ligand nature of the ligands is sufficient for sequestering lanthanide ions, meeting the requirements of Dy, as all reported structures display the same structural motif. In contrast, Nd requires additional ancillary ligands in its coordination sphere, such as solvent molecules. This seemingly minor structural difference between Nd and Dy complexes results in a significant difference in

solubility between [Nd(Trensal$^{p\text{-}OMe}$(H_2O)] and [Dy(Trensal$^{p\text{-}OMe}$] in acetone. The separation efficiency achieved using the Trensal$^{p\text{-}OMe}$ ligand in a one-pot reaction under very mild conditions compares favorably with cascade processes that typically require extensive use of extractants. Although not yet perfect, the application of this class of ligands provides a strong foundation for designing ligands capable of Nd/Dy separation by considering the metals' preferences.[68] Another potential strategy involves using suitable ancillary ligands for Nd to further enhance the solubility difference between Nd and Dy species. This approach opens the door to employing various ligand classes designed to minimize costs and environmental impact, allowing for the implementation of separation techniques that use green, non-aqueous media to produce refined REEs for high-value applications. Non-aqueous solvents can enhance selective metal complexation/precipitation and facilitate solvent and complex recycling from the solution, thereby reducing wastewater production.

2.5 Experimental section

2.5.1 Materials and methods

All chemicals were purchased from Merck and Alfa Aesar and were used without further purification. Anhydrous solvents were dried and stored over molecular sieves (3 Å). NMR experiments were performed on either a Brüker Avance 400 MHz instrument and JEOL 600 MHz ECZ600R instrument at 298 K and chemical shifts (ppm) are referenced to tetramethylsilane. Infrared (IR) spectra were obtained with a Thermo Scientific Nicolet 5PCFT-IR-ATR (diamond) spectrometer in the 4000-400 cm^{-1} interval. ESI-MS analyses were carried out using a Waters Acquity Ultra Performance LC with Waters Acquity SQ Detector and with ESI interface. The mixtures were analyzed in negative ionization mode by direct perfusion in ESI-MS interface with an injection flow of 20 ml/min. Elemental analyses (CHN) were performed on Thermo Fischer Scientific FlashSmart CHNS analyzer.

2.5.2 X-ray diffraction data collection and treatment

Single crystal diffraction data were collected with a Bruker D8 PhotonII area detector diffractometer (Mo Kα: λ = 0.71073 Å). Complete datasets were obtained by merging several series of exposure frames collected at 200 K. An absorption correction was applied with the program SADABS.[70] The structures were solved with ShelxT[71] and refined on F^2 with full-matrix least squares (ShelxL)[72], using the Olex2 software package.[73] Non hydrogen atoms were refined with anisotropic thermal parameters for all compounds except for **13**, which, apart from the metal,

was refined with isotropic thermal parameters due to the poor data quality. In **11**·DMF the coordinated solvent molecule was found disordered over two sites. In **8**·ACN the solvent laid on a three-fold symmetry axis and was refined with an overall occupancy of 0.5. In **4**·3DMF one of the solvent molecules was found disordered over two sites. In the structure of the complexes, the hydrogen atoms were placed at their calculated positions, whereas for Trensal$^{p\text{-}I}$ and Trensal$^{p\text{-}OMe}$ the hydrogen atoms of the OH groups were found by the residual electron density map and refined. The crystal structures of **1**[74] and **8**·ACN[75] were previously reported and are here commented for comparison purposes.

2.5.3 ICP-AES analysis

The metal content of the sample was determined via Inductively Coupled Plasma Atomic Emission Spectroscopy (ICP-AES). Samples for analysis were prepared as follows: solid samples of 5 to 15 mg of the compounds were suspended in 5 mL of HNO_3 65% and 1 mL of H_2O_2 30%, then digested in a Milestone microwave MLS-1200 MEGA (digestion sequence: 1 min at 250-Watt, 1 min at 0-Watt, 5 min at 250-Watt, 5 min at 400-Watt, 5 min at 650-Watt, 5 min of cooling). The solutions were diluted to 50 mL with bi-distilled water and analyzed using an emission spectrometer JY 2501 with coupled plasma induction in radial configuration HORIBA Jobin Yvon (Kyoto, Japan), ULTIMA2 model. Instrumental features: monochromator Model JY 2501; focal length 1 m; resolution 5 pm; nitrogen flow 2 L/min. ICP source: nebulizer Meinhard, cyclonic spraying chamber; argon flow 12 L/min; wavelengths range 160-785 nm; optical bench temperature 32 °C. The wavelength used for quantitative analysis was chosen by examining the emission line with greater relative intensity, ensuring that there was no spectral interference

with the Argon emission lines. Acquisition parameters: wavelength Nd: 410.946 nm, Dy: 394.469 nm. Voltage: 580 V; gain: 100. The quantitative analysis was performed after the acquisition of a calibration line using standard solutions in HNO_3 10% to simulate the final acidity of the samples. The concentration range of the standards varied from 0.1 mg/L to 50 mg/L of Dy and Nd. Data acquisitions and processing were performed using the ICP JY v 5.2 software (Jobin Yvon). Measurements were performed in triplicate and the syntheses performed in duplicates.

2.5.4 UV−Vis Spectroscopy and Treatment of Data.

The UV−vis spectra were recorded on a Perkin Elmer Photodiode Array Lambda 465 spectrophotometer provided with a Peltier thermostat, using 1 cm path length quartz cuvettes. Spectra of the ligand/metal systems were recorded in the spectral range of 250−500 nm. Titrations of the ligand with Nd or Dy in acetone or acetonitrile were carried out by adding aliquots (∼15 μL) of a 2×10^{-3} M solution of the metal in a 6.3×10^{-5} M solution of the ligand (initial volume of 2.6 mL, ligand:triethylamine = 1:3, L:Ln = 1:0−1.1). The calculations of the logarithms of the formation constants of the Ln/L species were carried out using HypSpec2014 software.[76] Species distribution diagrams were obtained using the Hyss 2009 software.[76]

2.6 Chemistry

2.6.1 Synthesis of ligands and complexes

General procedure for synthesis of ligands H_3L_1-H_3L_6. To a solution of salicylaldehyde (3 mmol) in solvent (20 mL), tris-(2-aminoethyl)amine (1 mmol) was added. The resulting yellow solution was stirred and refluxed for at least 3 h**.** The solution was cooled to room temperature obtaining a precipitate, which was filtered off. The precipitate was washed with cold solvent and dried under vacuum.

Trensal (H_3L_1). Yellow solid, yield 86%. ^{1}H-NMR (600 MHz, DMSO-d6) δ, ppm: 13.57 (s, 3H, OH), 8.23 (s, 3H, CH-N_{imine}), 7.30 (dt, 3H, Ar), 6.93 (dd, j = 7.7 Hz, j = 1.7 Hz, 3H, Ar), 6.87 (dd, j = 8.3 Hz, j = 1.1 Hz, 3H, Ar), 6.76 (dt, j = 7.4 Hz, j=1.1 Hz, 3H, Ar), 3.57 (t, j = 6.1 Hz, 6H, N_{imine}-CH_2), 2.80 (t, j = 6.1 Hz, 6H, N-CH_2). ^{13}C NMR (101 MHz, DMSO-d_6) δ, ppm: 166.65, 161.38, 132.59, 131.97, 119.01, 118.73, 116.98, 57.40, 55.41. ESI-MS (MeOH) m/z= 457.16 $[L_1]^-$. Elemental Analysis [Calc. for $C_{27}H_{30}N_4O_3$, %] C, 70.72; H, 6.59; N, 12.21; [Found %] C 70.7; H, 6.7; N, 12.3.

Trensal$^{p\text{-}OMe}$ (H_3L_2). Yellow solid, yield 81%. ^{1}H-NMR (400 MHz, DMSO-d_6) δ, ppm: 12.99 (s, 3H, OH), 8.28 (s, 3H, CH-N_{imine}), 6.92 (dd, j = 8.9 Hz, j = 3.1 Hz, 3H, Ar), 6.80 (d, j = 8.9 Hz, 3H, Ar), 6.66 (d, j = 3.1 Hz, 3H, Ar), 3.63 (t, j = 6, Hz, 6H, N_{imine}-CH_2), 2.86 (t, j = 6.0 Hz, 6H, N-CH_2). ^{13}C NMR (101 MHz, DMSO-d_6) δ, ppm: 166.86, 153.18, 148.68, 123.64, 118.41, 117.57, 115.02, 56.63, 55.33, 56.15. ESI-MS (MeOH) m/z= 547.61 $[L_2]^-$. Elemental Analysis [Calc. for $C_{30}H_{36}N_4O_6$, %] C, 65.67; H, 6.61; N, 10.21; [Found %] C, 65.77; H, 6.75; N, 10.23.

Trensal$^{o\text{-}Cl}$ (H_3L_3). Brown solid, yield 52%. ^{1}H-NMR (400 MHz, DMSO-d_6) δ, ppm: 14.59 (s, 3H, OH), 8.36 (s, 3H, CH-N_{imine}), 7,41 (dd, j = 7.7 Hz, j = 1.7 Hz, 3H, Ar), 7.01

(dd, j = 7.9 Hz, j = 1.7 Hz, 3H, Ar), 6.50 (t, j = 7.7 Hz, Hz, 3H, Ar), 3.67 (t, j = 5.8 Hz, 6H, N_{imine}-CH_2), 2.88 (t, j = 5.8 Hz, 6H, N-CH_2). ^{13}C NMR (101 MHz, DMSO-d_6) δ, ppm: 166.73, 163.13, 133.58, 131.80, 122.90, 117.83, 115.97, 54.52, 53.46. ESI-MS (MeOH) m/z= 561.36 $[L_3]^-$. Elemental Analysis [Calc. for $C_{27}H_{27}N_4O_3Cl_3$, %] C, 57.71; H, 4.84; N, 9.97; [Found %] C, 55.48; H, 5.07; N, 8.74.

Trensal$^{p\text{-}Cl}$ (H_3L_4). Yellow solid, yield 78%. ^{1}H-NMR (400 MHz, DMSO-d_6) δ, ppm: 13.80 (s, 3H, OH), 8.21 (s, 3H, CH-N_{imine}), 7.28 (dd, j = 8.8 Hz, j = 2.7 Hz, 3H, Ar), 6.93 (d, j = 2.7 Hz, 3H, Ar), 6.85 (d, j = 8.8 Hz, 3H, Ar), 3.60 (t, j = 5.7 Hz, 6H, N_{imine}-CH_2), 2.84 (t, j = 5.7 Hz, 6H, N-CH_2). ^{13}C NMR (101 MHz, DMSO-d_6) δ, ppm: 165.51, 160.66, 132.49, 130.66, 122.02, 119.52, 119.13, 56.73, 54.91. ESI-MS (MeOH) m/z= 561.05 $[L_4]^-$. Elemental Analysis [Calc. for $C_{27}H_{27}N_4O_3Cl_3$, %] C, 57.71; H, 4.84; N, 9.97; [Found %] C, 57.98; H, 4.93; N, 9.94.

Trensal$^{p\text{-}I}$ (H_3L_5). Yellow solid, yield 78%. ^{1}H-NMR (400 MHz, DMSO-d_6) δ, ppm: 13.72 (s, 3H, OH), 8.32 (s, 3H, CH-N_{imine}), 7.53 (dd, j = 8.7 Hz, j = 2.3 Hz, 3H, Ar), 7.46 (d, j = 2.3 Hz, 3H, Ar), 6.67 (d, j = 8.7 Hz, Hz, 3H, Ar), 3.63 (t, j = 5.9 Hz, 6H, N_{imine}-CH_2), 2.86 (t, j = 6.0 Hz, 6H, N-CH_2). ^{13}C NMR (101 MHz, DMSO-d_6) δ, ppm: 165.55, 161.89, 140.88, 139.70, 120.97, 120.11, 79.65, 56.58, 54.97. ESI-MS (MeOH) m/z= 835.86 $[L_5]^-$ Elemental Analysis [Calc. for $C_{27}H_{27}N_4O_3I_3$, %] C, 38.77; H, 3.25; N, 6.69; [Found %] C, 39.19; H, 3.34; N, 6.77.

Trensal$^{o\text{-}tBu}$ (H_3L_6). Yellow solid, yield 74%. ^{1}H-NMR (400 MHz, DMSO-d_6) δ, ppm: 14.50 (s, 3H, OH), 8.15 (s, 3H, CH-N_{imine}), 7.26 (dd, j = 7.7 Hz, j = 1.8 Hz, 3H, Ar), 6.67 (t, j = 7.6 Hz, 3H, Ar), 6.60 (dd, j = 7.7 Hz, j = 1.7 Hz, 3H, Ar), 3.59 (t, j = 5.9 Hz, 6H, N_{imine}-CH_2), 2.87 (t, j = 6.0 Hz, 6H, N-CH_2), 1.34 (s, 27H, tBu). ^{13}C NMR (101 MHz, DMSO-d_6) δ, ppm: 167.14, 160.90, 132.89, 130.34, 129.41, 118.58, 117.95, 57.42,

55.66, 34.83, 29.57. ESI-MS (MeOH) m/z= 626 $[L_6]^-$. Elemental Analysis [Calc. for $C_{39}H_{54}N_4O_3$, %] C, 74.71; H, 8.68; N, 8.94; [Found %] C, 74.83; H, 8.83; N, 9.00.

General procedure for synthesis of complexes. To a solution of Trensal^R ligand (1 mmol) and triethylamine (3 mmol) in acetone or acetonitrile (**1**,**7** and **8**) (10 mL), $Ln(NO_3)_3 \cdot 6H_2O$ (1 mmol) previously dissolved in the same reaction solvent (5 mL) was added. The resulting mixture was stirred and refluxed for 1 h. The precipitate obtained was filtered off, washed and dried under vacuum.

[Dy(Trensal)]. Pale-yellow solid, yield 67%. Elemental Analysis [Calc. for $DyC_{27}H_{24}N_4O_3$, %] C, 52.47; H, 4.40; N, 9.07; [Found %] C, 52.26; H, 4.43; N, 9.07. The compound can be recrystallized in DMF yielding colorless crystals of [Dy(Trensal)] (**1**).

[Dy(Trensal$^{o\text{-}Cl}$)]. Pale-yellow solid, yield 65%. Elemental Analysis [Calc. for $DyC_{27}H_{24}N_4O_3Cl_3$, %] C, 44.95; H, 3.35; N, 7.77; [Found %] C, 44.79; H, 3.44; N, 8.09. The compound can be recrystallized in DMF yielding colorless crystals of [Dy(Trensal$^{o\text{-}Cl}$)] (**2**).

[Dy(Trensal$^{o\text{-}tBu}$)]. Pale-yellow solid, yield 58%. Elemental Analysis [Calc. for $DyC_{39}H_{51}N_4O_3$, %] C, 59.57; H, 6.54; N, 7.12; [Found %] C, 59.73; H, 6.86; N, 6.90. Colorless crystals of [Dy(Trensal$^{o\text{-}tBu}$)]·Acetone (**3**·Acetone) were obtained by cooling to room temperature the acetone solution of the compound.

[Dy(Trensal$^{p\text{-}I}$)]. Pale-yellow solid, yield 67.8%. Elemental Analysis [Calc. for $DyC_{27}H_{24}N_4O_3I_3$, %] C, 32.57; H, 2.43; N, 5.63; [Found %] C, 32.28; H, 2.38; N, 5.73.

The compound can be recrystallized in DMF yielding colorless crystals of [Dy(Trensal$^{p\text{-}I}$)]·3DMF (**4**·3DMF).

[Dy(Trensal$^{p\text{-}OMe}$)]. Pale-yellow solid, yield 44%. Elemental Analysis [Calc. for $DyC_{30}H_{33}N_4O_6$, %] C, 50.89; H, 4.70; N, 7.91; [Found %] C, 50.92; H, 4.67; N, 7.69. The compound can be recrystallized in DMF yielding colorless crystals of [Dy(Trensal$^{p\text{-}OMe}$)] (**5**).

[Dy(Trensal$^{p\text{-}Cl}$)]. Pale-yellow solid, yield 65%. Elemental Analysis [Calc. for $DyC_{27}H_{24}N_4O_3Cl_3$, %] C, 44.95; H, 3.35; N, 7.77; [Found %] C, 44.84; H, 3.35; N, 7.95. The compound can be recrystallized in DMF yielding colorless crystals of [Dy(Trensal$^{p\text{-}Cl}$)] (**6**).

[Nd(Trensal)(H_2O)]0.5ACN. Light-blue solid, yield 87%. Elemental Analysis [Calc. for $C_{27}H_{24}N_4O_3Nd(C_2H_3N)_{0.5}H_2O$, %] C, 52.68; H, 4.81; N, 9.87; [Found %] C, 53.04; H, 4.61; N, 9.84. The compound can be recrystallized in DMF yielding colorless crystals of [Nd(Trensal)(H_2O)] (**7**).

[Nd(Trensal)]. In a test tube, a solution of $Nd(NO_3)_3{\cdot}6H_2O$ (0.057 mmol, 25 mg) in ACN was stratified over a solution of Trensal (0.085 mmol, 39.22 mg) and triethylamine (0.25 mmol, 0.035 mL) in DMF. The reaction was carried out at 60°C overnight without stirring, yielding purple crystals of [Nd(Trensal)]·ACN (**8**·ACN).

[Nd(Trensal$^{p\text{-}I}$)(H_2O)]. Light-blue solid, yield 61%. Elemental Analysis [Calc. for $NdC_{27}H_{24}N_4O_3I_3H_2O$, %] C, 32.58; H, 2.63; N, 5.63; [Found %] C, 32.67; H, 2.95; N, 5.57. The compound can be recrystallized in DMF yielding light-blue crystals of [Nd(Trensal$^{p\text{-}I}$)(DMF)(H_2O)]·DMF (**9**·DMF).

[Nd(Trensal$^{o\text{-}tBu}$)]. Green solid, yield 68%. Elemental Analysis [Calc. for $NdC_{39}H_{51}N_4O_3$, %] C, 60.98; H, 6.69; N, 7.29; [Found %] C, 60.59; H, 6.80; N, 7.07. The compound can be recrystallized in DMF yielding colorless crystals of [Nd(Trensal$^{o\text{-}tBu}$)]·DMF (**10**·DMF).

[Nd(Trensal$^{o\text{-}Cl}$)]. Light-blue solid, yield 77%. Elemental Analysis [Calc. for $NdC_{27}H_{24}N_4O_3Cl_3$, %] C, 46.12; H, 3.44; N, 7.97; [Found %] C, 45.76; H, 3.44; N, 8.12. The compound can be recrystallized in DMF yielding light-blue crystals of [Nd(Trensal$^{o\text{-}Cl}$)(DMF)]·DMF (**11**·DMF).

[Nd(Trensal$^{p\text{-}Cl}$)(H_2O)]. Light-blue solid, yield 73%. Elemental Analysis [Calc. for $NdC_{27}H_{24}N_4O_3Cl_3H_2O$, %] C, 44.97; H, 3.63; N, 7.77; [Found %] C, 45.24; H, 4.03; N, 7.48. The compound can be recrystallized in DMF yielding light-blue crystals of [Nd(Trensal$^{p\text{-}Cl}$)(DMF)(H_2O)] (**12**).

[Nd(Trensal$^{p\text{-}OMe}$)(H_2O)]. Yellow solid, yield 42%. Elemental analysis [Calc. for $NdC_{30}H_{33}N_4O_6H_2O$, %] C, 50.90; H, 4.98; N, 7.91; [Found %] C, 50.50; H, 4.94; N, 7.61. Yellow crystals of [Nd(Trensal$^{p\text{-}OMe}$(H_2O)] **(13)** were obtained by cooling to room temperature the ACN solution of the compound.

Chapter 3: **Salpen-type ligand for selective recovery and separation of Nd and Dy**

3.1 Introduction

As shown in the previous sections, the flexibility of a polydentate ligand or the tendency of a lanthanide ion to expand its coordination number compared to a different one are key aspects for determining the solubility of a REE complex. In this work, we intended to explore a different type of ligand which, instead of forming solely mononuclear species, may form also di- or polynuclear ones. The rationale under this design is that the impact of the different ionic radii or of the coordination numbers among lanthanides may experience an amplification if more than one lanthanide is present in solution. We therefore decided to use a potentially pentadentate ligand called Salpen, with an N_2O_3 donor atom set.

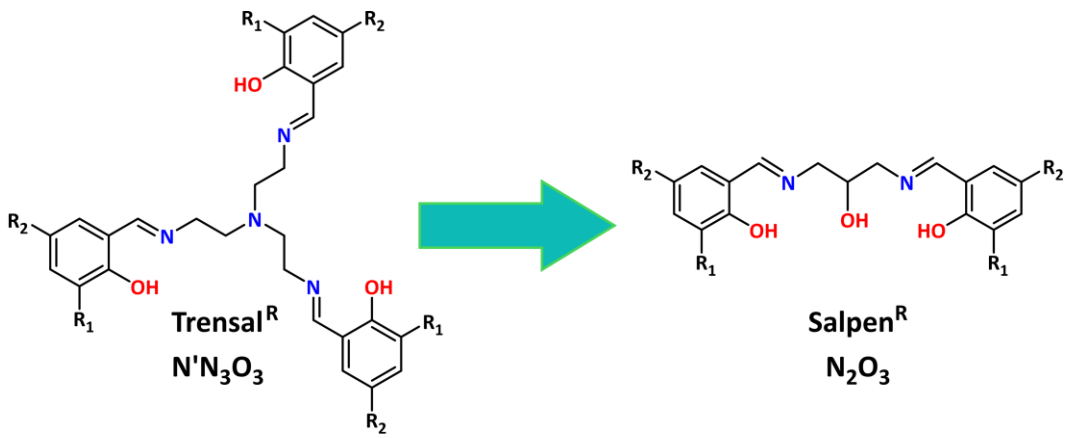

R_1= -H; R_2= -OMe, -Cl, -I
R_1= -Cl, -tBu; R_2= -H

R_1 = -H, R_2 = -H, -Cl, -OMe
R_2 = -H, R_1 = -tBut

Scheme 3.1. Scheme representing the Trensal^R and the Salpen^R ligands along with their set of donor atoms.

Compared to Trensal (see **scheme 3.1** and **Chapter 2**), Salpen has a lower denticity (from heptadentate to pentadentate), which does not allow it to fully satisfy the coordination geometry requirements of lanthanides without the assistance of another ligand or additional molecules coordinated to the metal centers. Various aldehyde functionalizations were selected to alter the lipophilicity of the system and the steric bulk of the ligands around the metal, allowing us to study how these two factors affect the type of complexes formed in terms of nuclearity and solubility. Similarly, we investigated the possibility of reducing the imine functions, which are unstable and prone to hydrolysis, to obtain amine ligands that are more stable under strong acidic/basic conditions and could potentially be recovered and reused for separation tests. The Nd and Dy complexes with Salpen^R ligands (R = -H, -OMe, -tBut) and H_2Salpen exhibited different solubility in ethanol, and the separation tests revealed a different distribution of metals between the solid phase and solution, which were analyzed by ICP-OES.

3.2 Aim of the project

The goal of this project is to explore the use of Salpen-type ligands, which possess an N_2O_3 donor set, for the selective separation of neodymium (Nd) and dysprosium (Dy) based on solubility differences of their metal complexes. By varying the functional groups on these ligands, we aim to modulate their lipophilicity and steric bulk around the metal centers, studying how these factors influence complex nuclearity and solubility. Additionally, this work seeks to evaluate the potential for imine-to-amine ligand reduction to improve stability, enabling possible ligand recycling for sustainable separation applications.

3.3 Results and discussions

3.3.1 Synthesis and characterization of Salpen^R ligand (N,N'-(2-hydroxypropane-1,3-diyl)bis(salicylaldimine)

1,3-Diamino-2-hydroxypropane (1 eq.) was reacted with various functionalized salicylaldehydes (3 eq.) in absolute ethanol at reflux for three hours, as shown in **Scheme 3.2**. The resulting yellow solutions were concentrated under vacuum. Subsequently, approximately double the volume of hexane was added to the solution, and it was left at -4 °C overnight, resulting in yellow crystals. The solids were isolated by filtration, yielding Salpen^R in high yield. To promote the formation of the two iminic functions, a solvent with low water content (absolute ethanol) and a slight excess of aldehyde (0.05 eq.) were used.

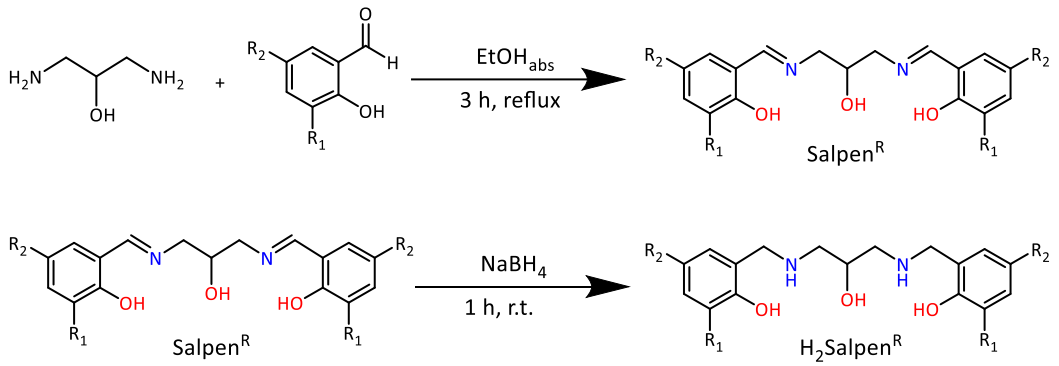

R_1 = H, R_2 = H, Cl, OMe
R_2 = H, R_1 = tBut

Scheme 3.2. Scheme of the synthesis of the Salpen^R ligands.

To obtain the reduced analogues of these compounds, to a yellow solution of the Salpen ligands (1 eq.) in methanol, $NaBH_4$ (3 eq.) was added to reduce the imino group to an amino group. Stirring continued until the solution changed color from yellow to colorless. Methanol was then evaporated, and the product was purified by liquid-liquid extraction.

The Salpen^R and H_2Salpen^R ligands (see **Figure 3.1**) are a library of potentially pentadentate compounds characterized by a number of hard and intermediate-hard donor atoms, such as phenolic oxygens, alcohol, and two imine/amine nitrogens. This characteristic, together with the medium-high denticity, makes it a suitable ligand for lanthanide coordination. These ligands can be synthesized with ease using aldehydes that carry various functional groups in the *ortho* and *para* positions, many of which are readily available at relatively low cost. The presence of an imine group in Salpen^R is a source of instability towards hydrolysis, therefore

to overcome this problem, the ligands were reduced to $H_2Salpen^R$, turning the imine group into an amino group. This conversion modifies the conformational flexibility as well as of the donor ability of the ligand (imminic versus secondary ammine nitrogen atoms), while maintaining a similar type of donor atoms. The ligands were specifically design to alter the steric hindrance around specific residues, such as the *t*-butyl groups adjacent to the phenolic OH, as well as modifying the overall lipophilicity of the ligand.

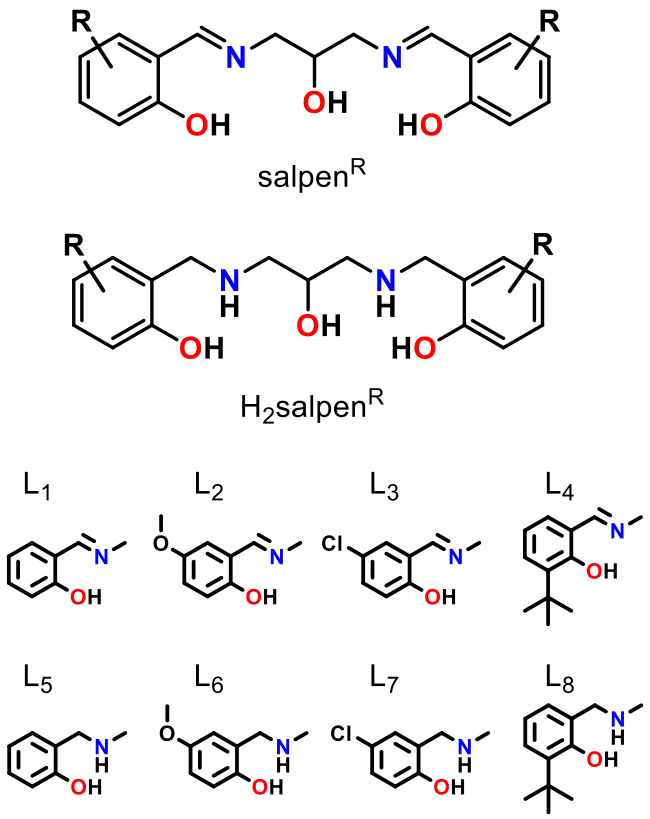

Figure 3.1. Molecular structures of the $Salpen^R$ and $H_2Salpen^R$ ligands.

All ligands were characterized by ^{1}H NMR spectroscopy and ESI-MS. The ^{1}H NMR spectrum of the Salpen^{R}-type ligand confirmed the formation of the desired product, with signals associated with the iminic proton (-N=CH-Ph) observed at approximately 8.55 ppm (orange dot). The multiplet at ≈ 5.22 ppm is assigned to the hydroxyl proton, indicated in red, while the multiplet at ≈ 3.80 ppm, marked in purple, corresponds to the tertiary carbon proton (-CH-OH) attached to the alcohol group. Finally, the two signals indicated by the yellow dot are assigned to the protons of the secondary carbons. The purity of the compounds is further assessed by the absence of the aldehydic peak around 10 ppm (**Figure 3.2-3.5**), except for Salpen$^{o\text{-}tBut}$.

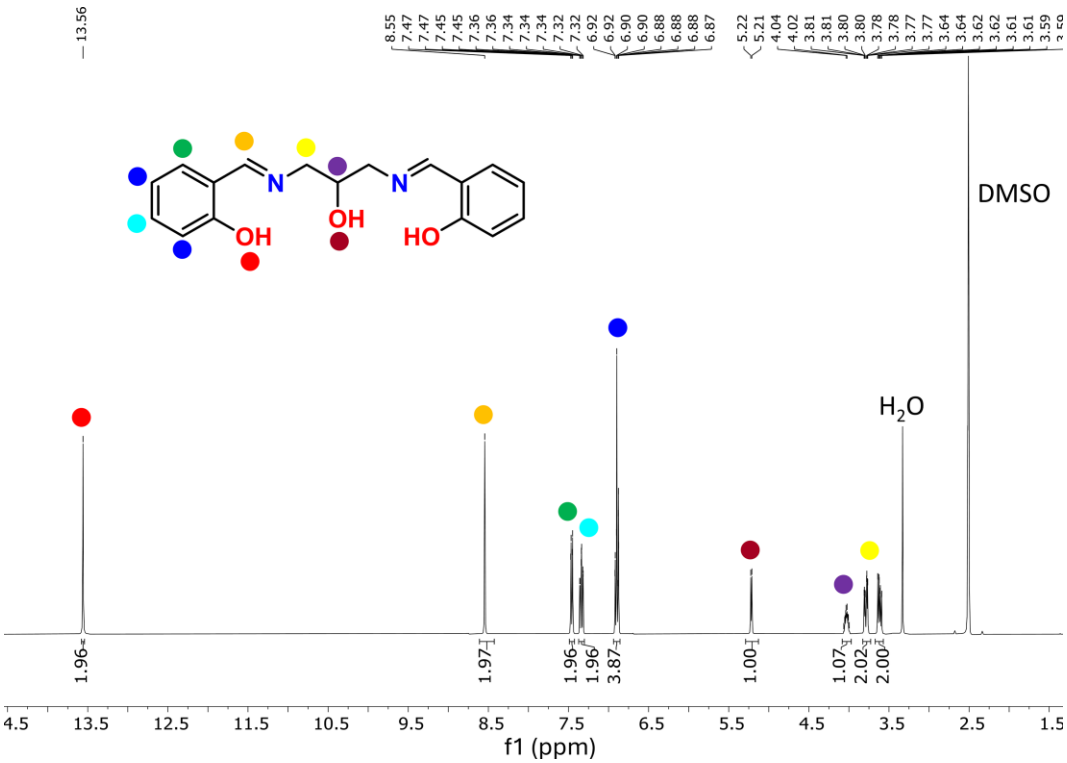

Figure 3.2. ^{1}H-NMR (400 MHz, DMSO) spectrum of Salpen.

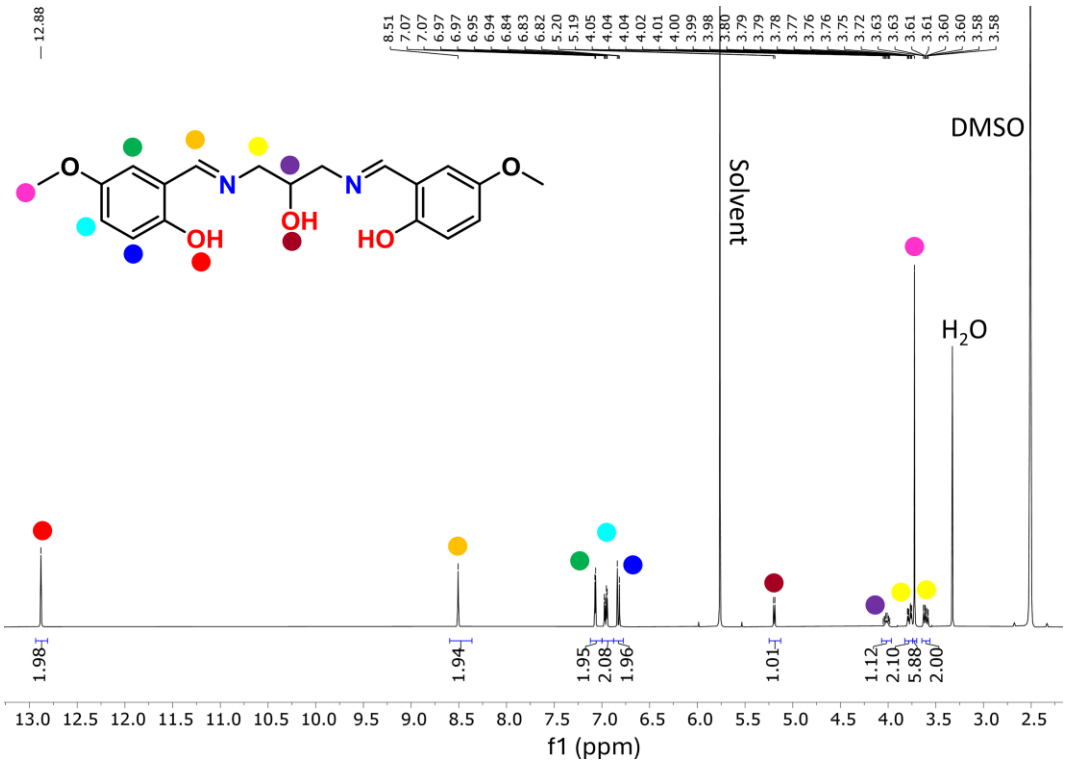

Figure 3.3. ^{1}H-NMR (400 MHz, DMSO) spectrum of Salpen$^{p\text{-}OMe}$.

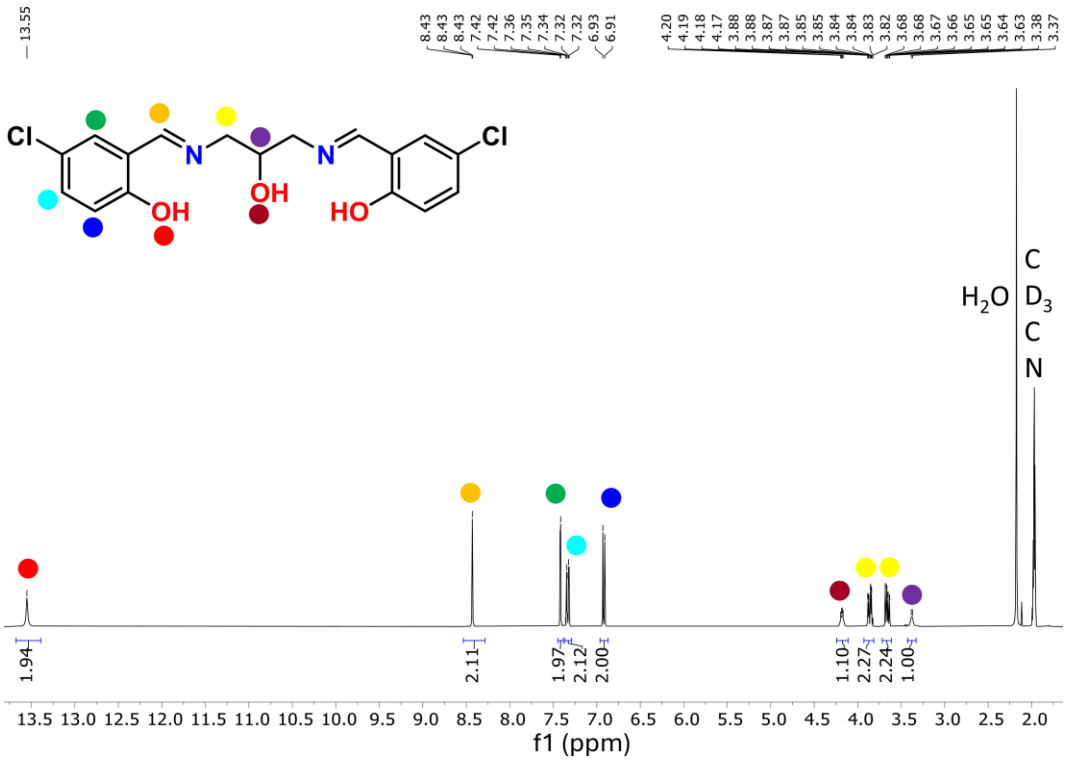

Figure 3.4. ^{1}H-NMR (400 MHz, CD_3CN) spectrum of Salpen$^{p\text{-}Cl}$.

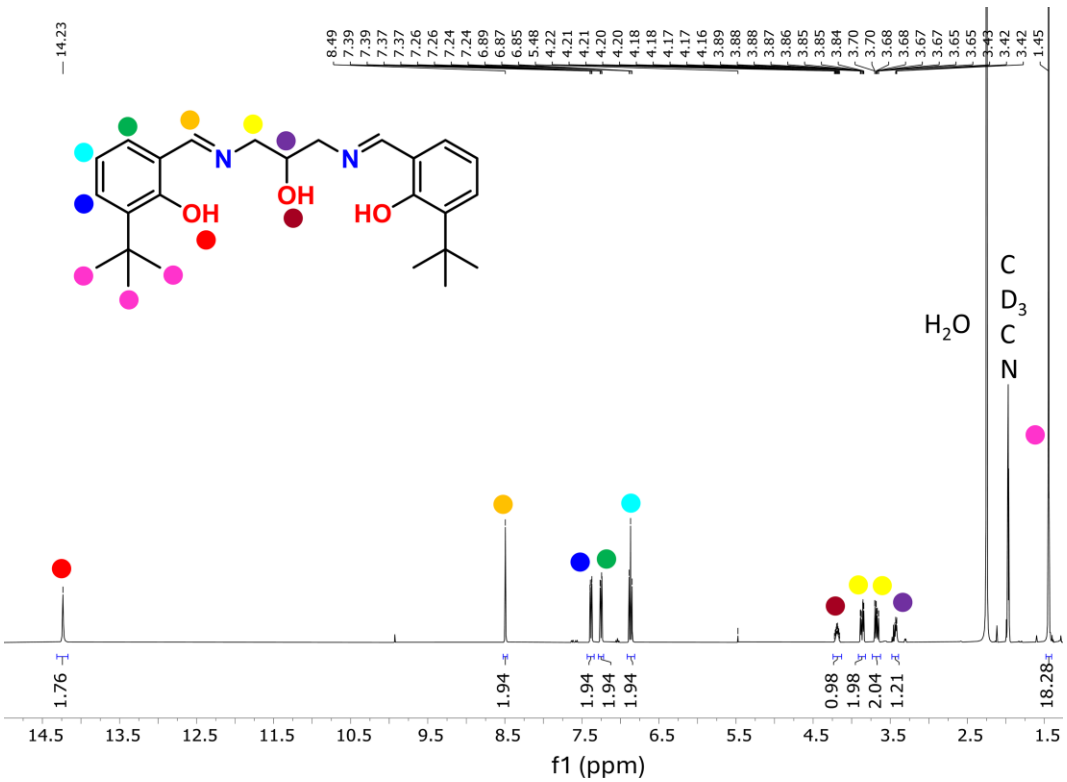

Figure 3.5. ^{1}H-NMR (400 MHz, CD_3CN) spectrum of Salpen$^{o\text{-}tBut}$.

For ligand Salpen$^{o\text{-}tBut}$, a small impurity (1%) attributed to the presence of excess aldehyde (≈ 10 ppm) was found. Purification was attempted using column chromatography; however, the aldehyde coelutes with the product. Consequently, the ligand was used without further purification.

The reduction of Salpen^{R} ligands to H_2Salpen^{R} is confirmed by the disappearance of the iminic proton peak (-N=CH-Ph) at ≈ 8.55 ppm and the appearance of an integrable peak for 4 protons, located between 4.3 ppm and 3.5 ppm, attributable to the benzyl carbon protons, indicated by the orange dot. The ^{1}H NMR spectrum of H_2Salpen^{R} is shown below (**Figure 3.6-3.9**).

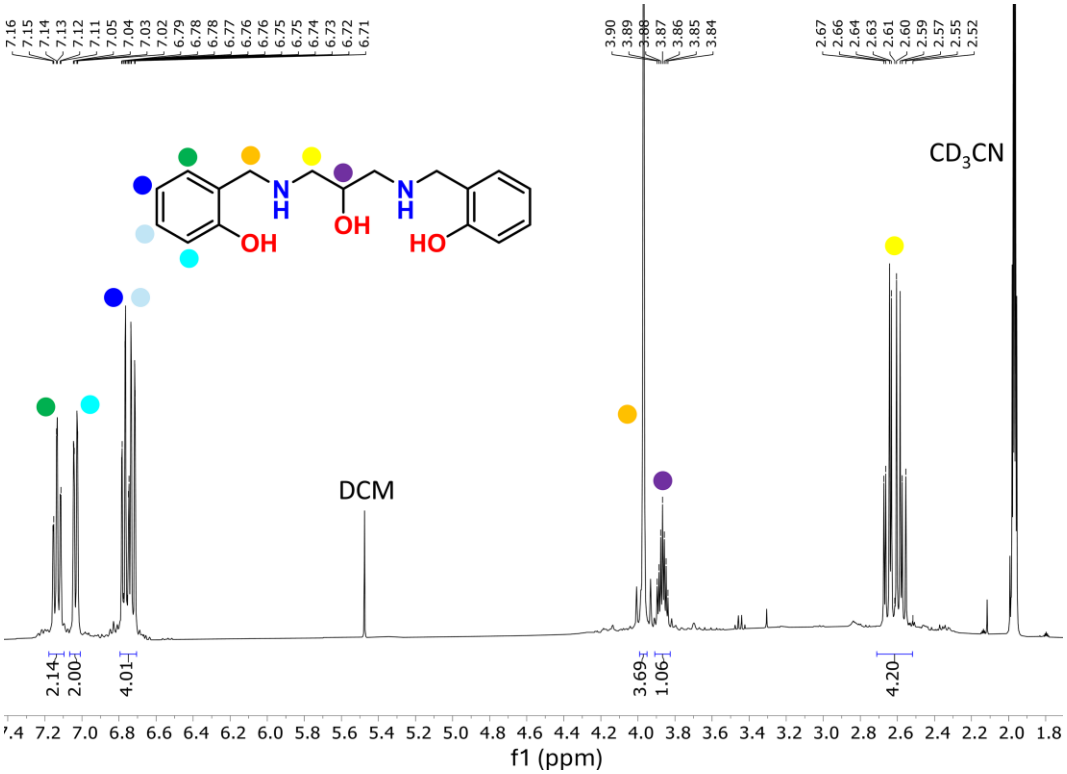

Figure 3.6. ^{1}H-NMR (400 MHz, CD_3CN) spectrum of H_2Salpen.

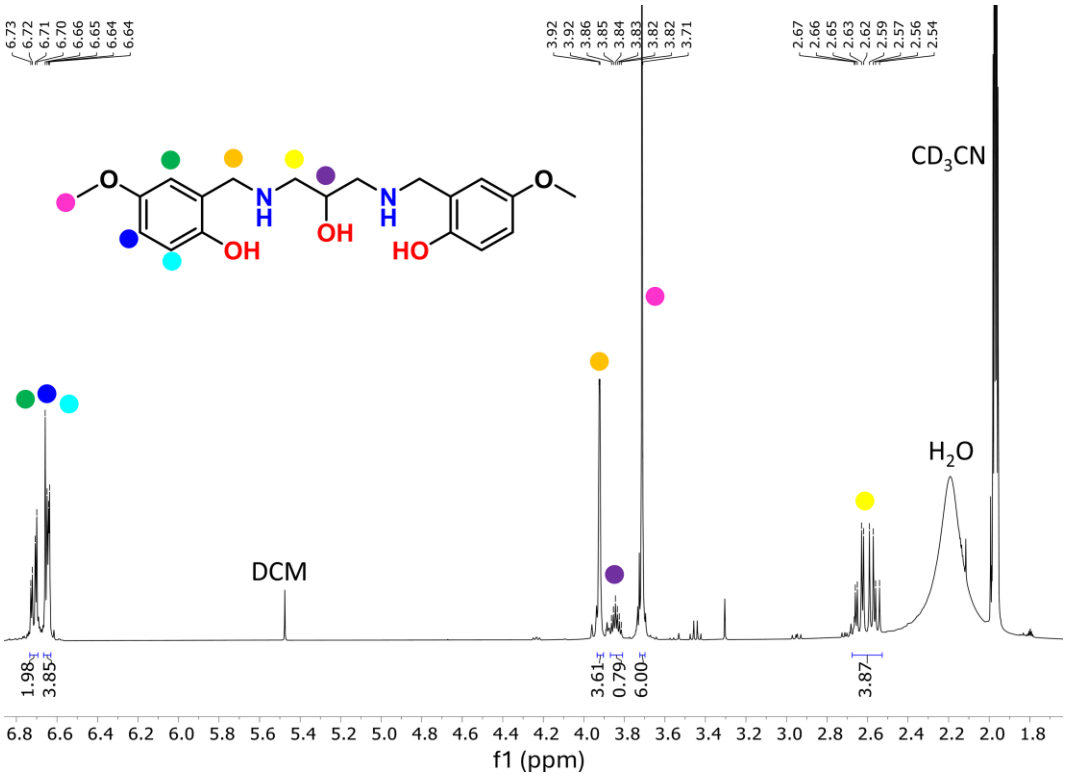

Figure 3.7. ^{1}H-NMR (400 MHz, CD_3CN) spectrum of $H_2Salpen^{p\text{-}OMe}$.

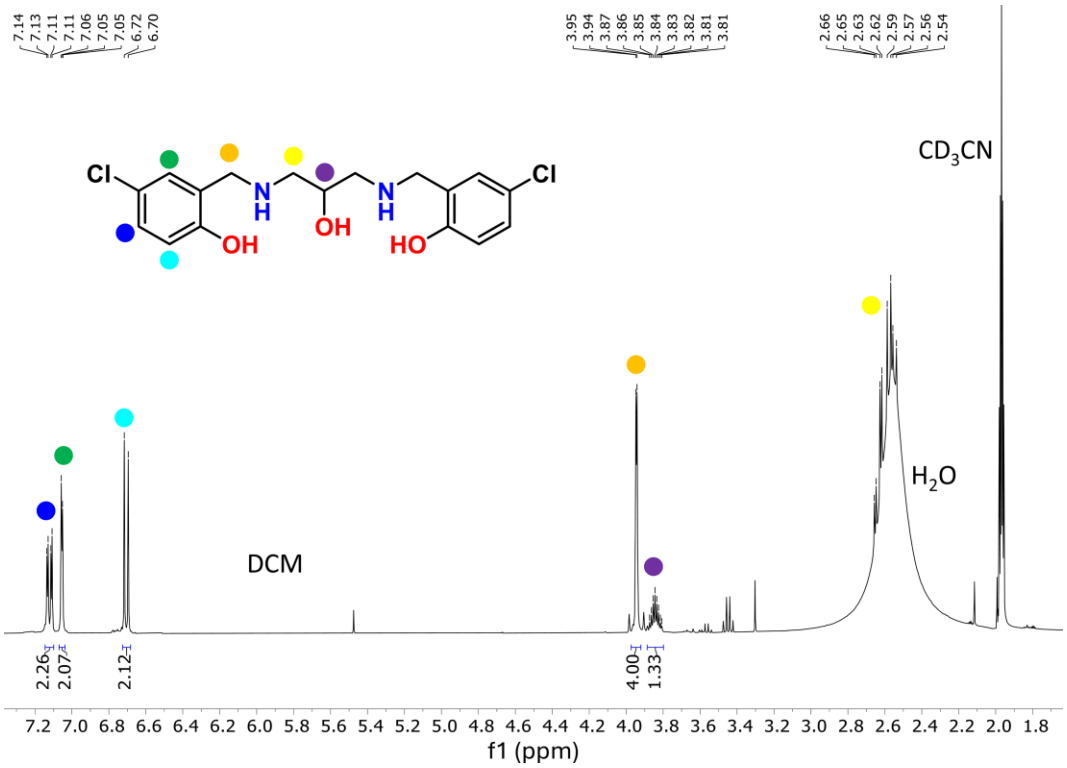

Figure 3.8. ^{1}H-NMR (400 MHz, CD_3CN) spectrum of $H_2Salpen^{p\text{-}Cl}$.

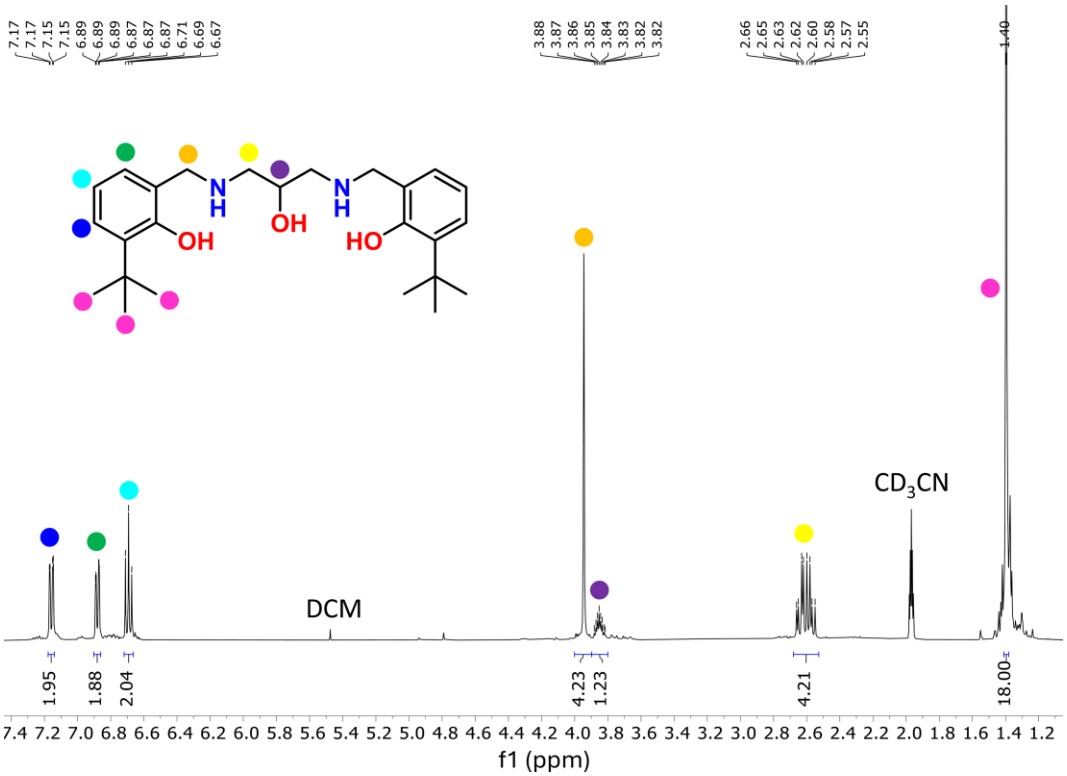

Figure 3.9. ^{1}H-NMR (400 MHz, CD_3CN) spectrum of $H_2Salpen^{o\text{-}tBut}$.

The identity of the Salpen^{R} and H_2Salpen^{R} molecules was also confirmed by ESI-MS spectra in which the ion signal is visible in negative mode (**Figure 3.10-3.17**).

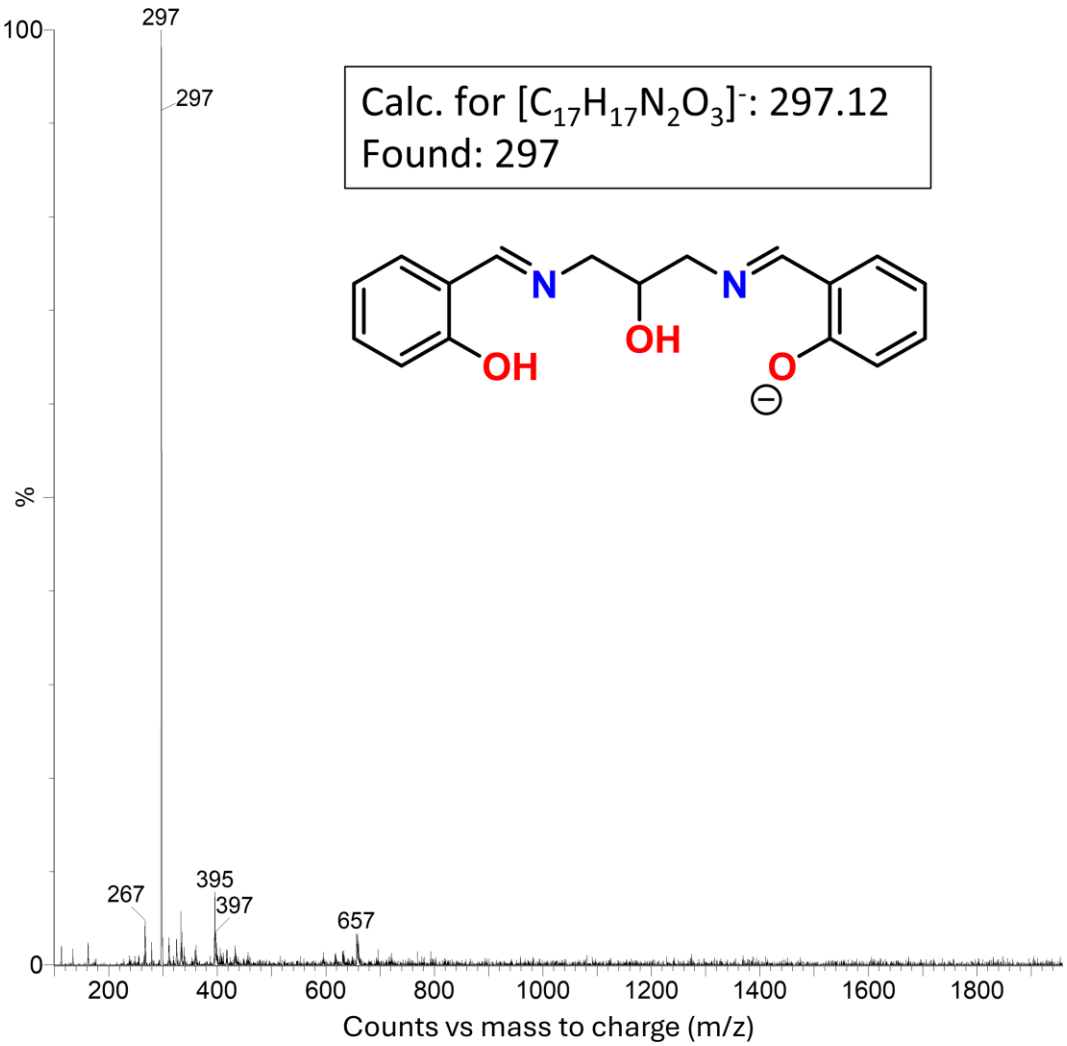

Figure 3.10. UPLC-ESI (-) mass spectrum of Salpen (ACN); *m/z* $[L_1]^-$= 297.12.

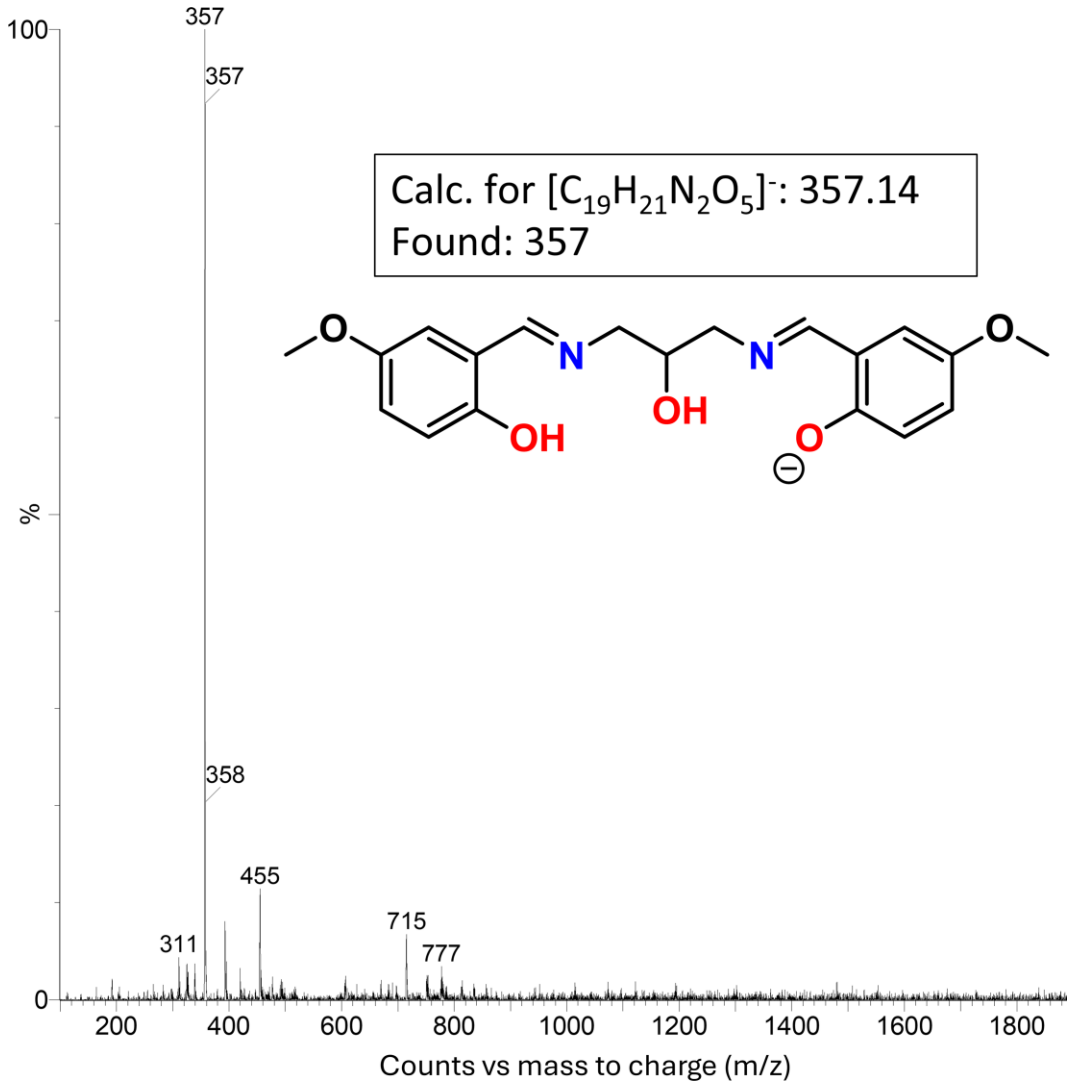

Figure 3.11. UPLC-ESI (-) mass spectrum of Salpen$^{p\text{-}OMe}$ (ACN); *m/z* $[L_1]^-$= 357.14.

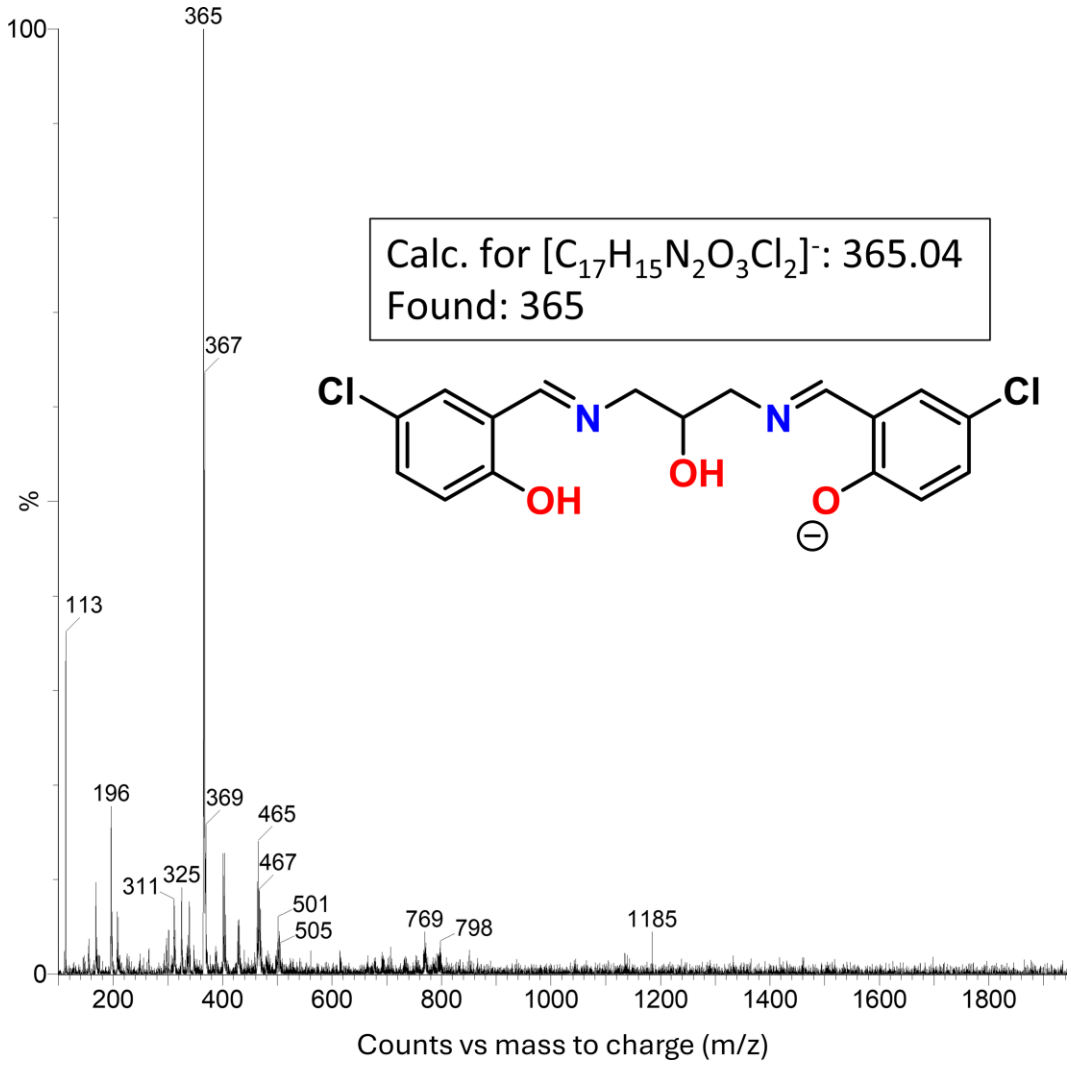

Figure 3.12. UPLC-ESI (-) mass spectrum of Salpen$^{p\text{-}Cl}$ (ACN); *m/z* $[L_1]^-$= 365.04.

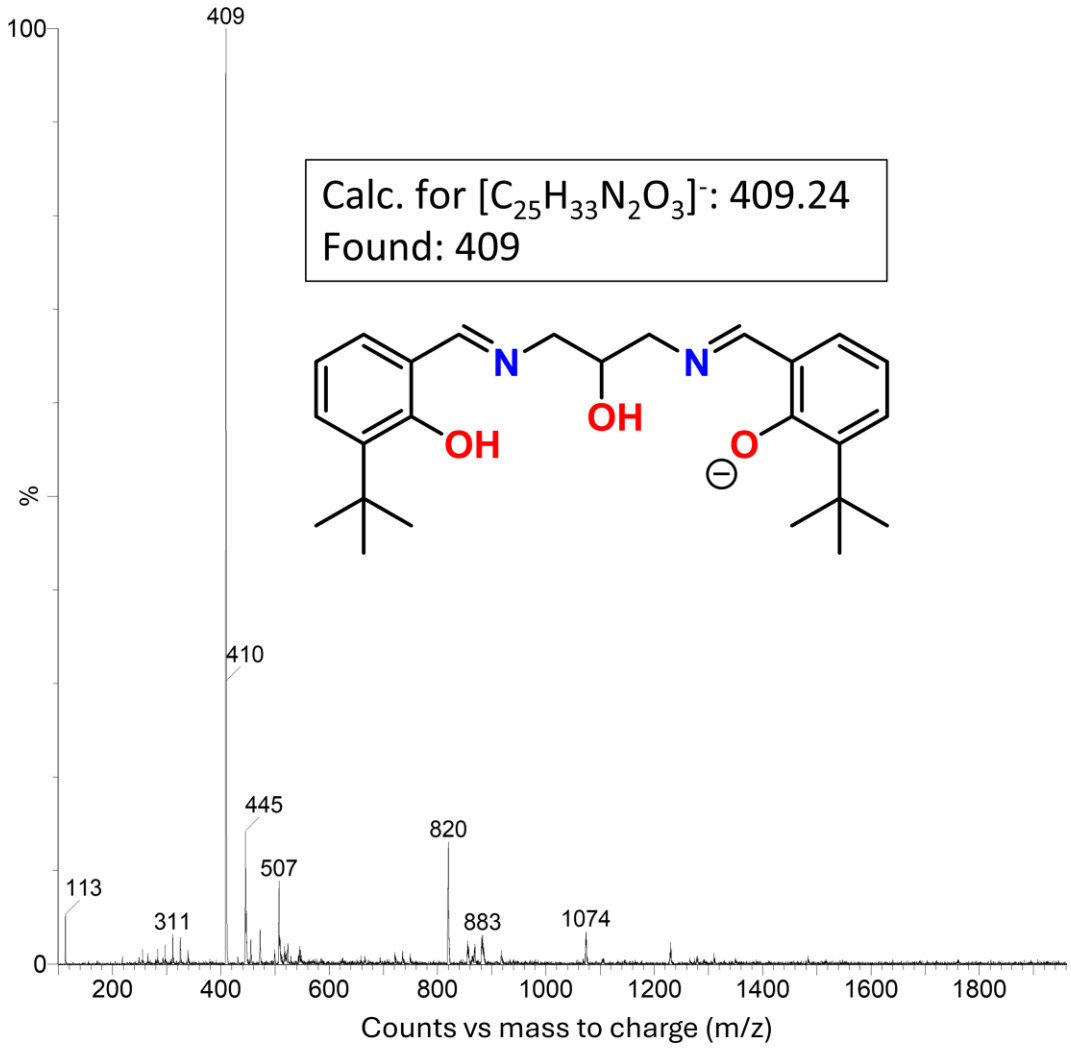

Figure 3.13. UPLC-ESI (-) mass spectrum of Salpen$^{o\text{-}tBut}$ (ACN); *m/z* $[L_1]^-$= 409.24.

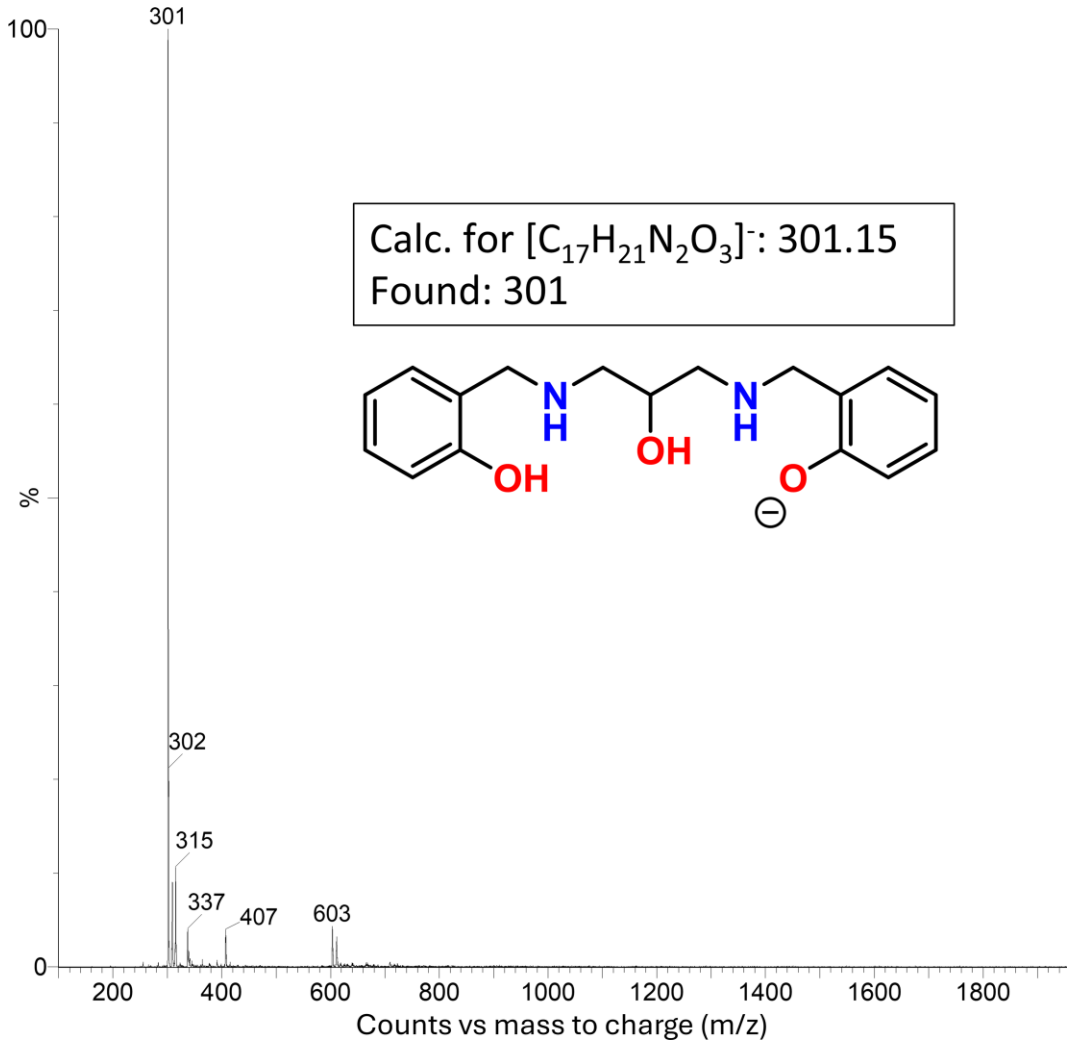

Figure 3.14. UPLC-ESI (-) mass spectrum of H_2Salpen (ACN); *m/z* $[L_1]^-$= 297.12.

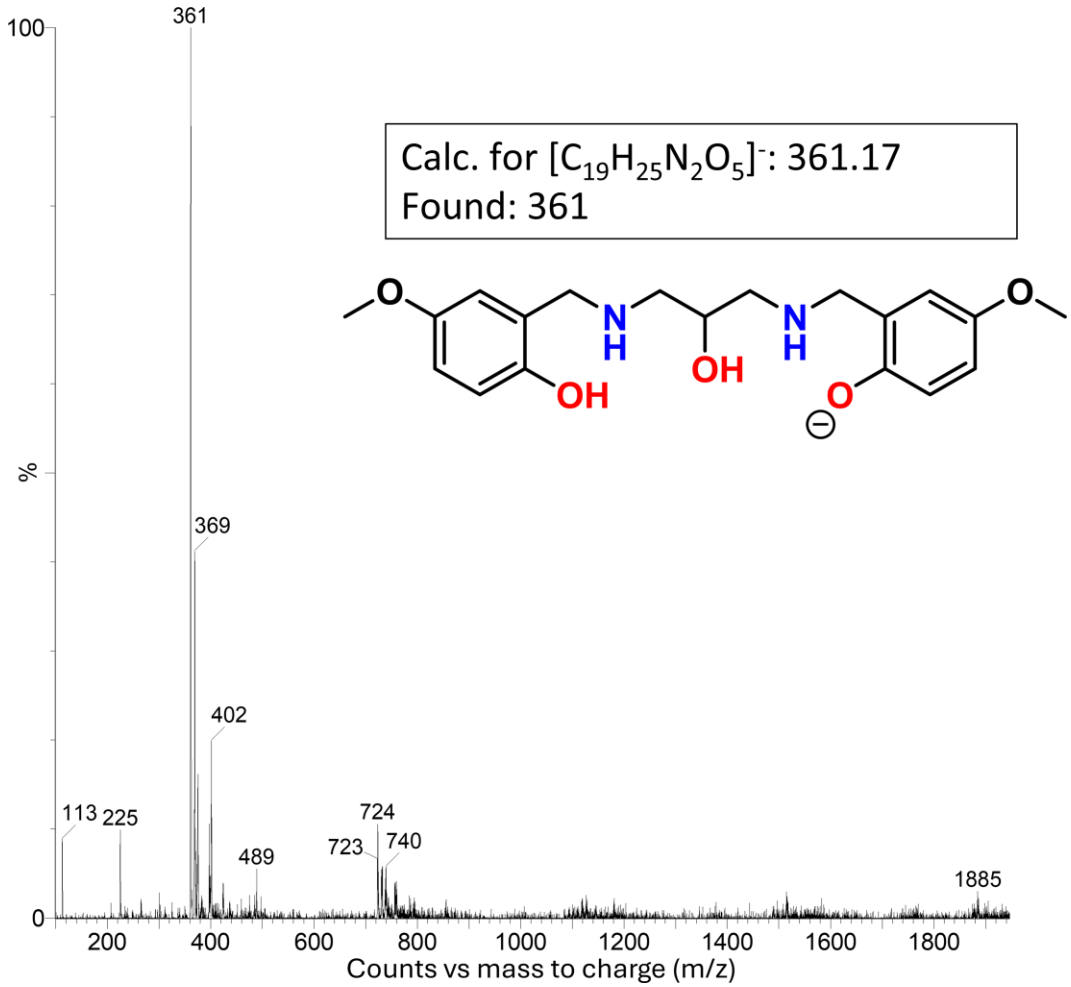

Figure 3.15. UPLC-ESI (-) mass spectrum of H_2Salpen $^{p\text{-}OMe}$ (ACN); *m/z* $[L_1]^-$= 357.14.

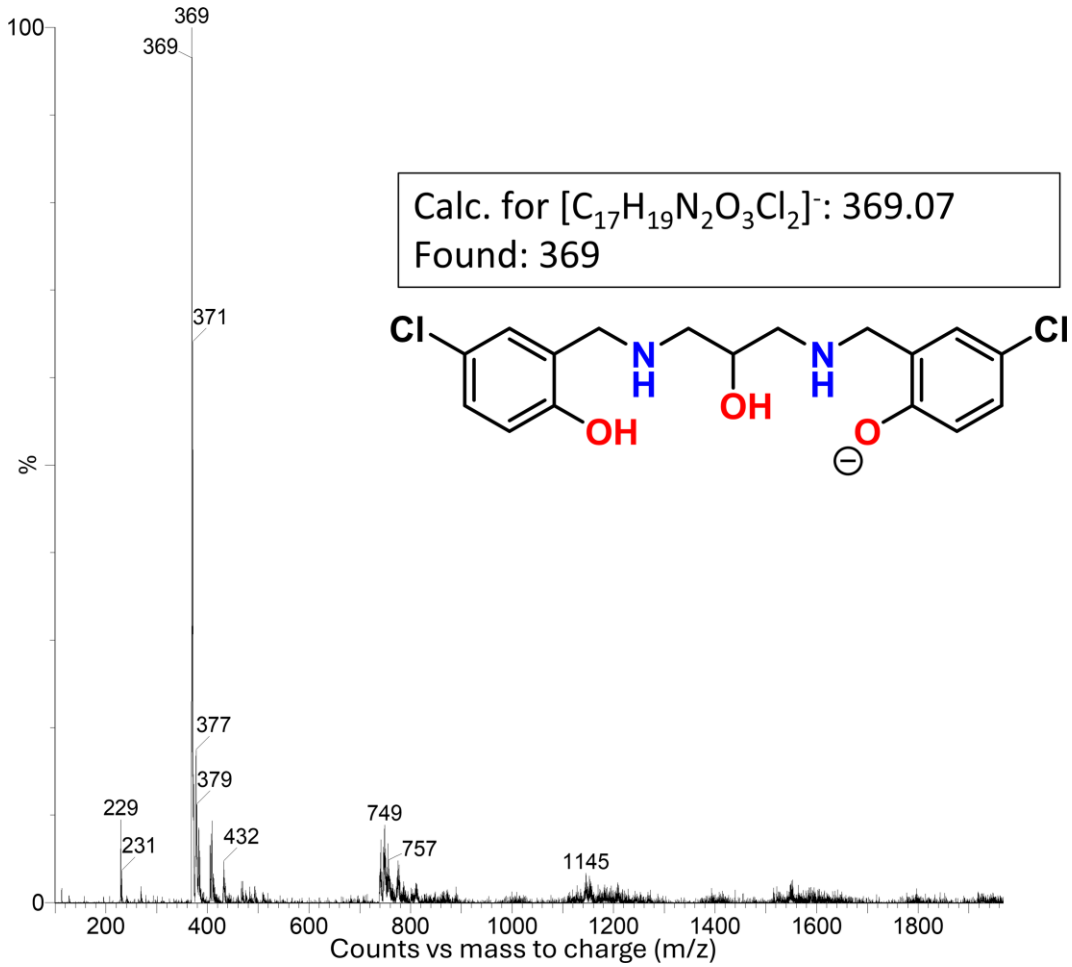

Figure 3.16. UPLC-ESI (-) mass spectrum of $H_2Salpen^{p\text{-}Cl}$ (ACN); *m/z* $[L_1]^-$= 365.04.

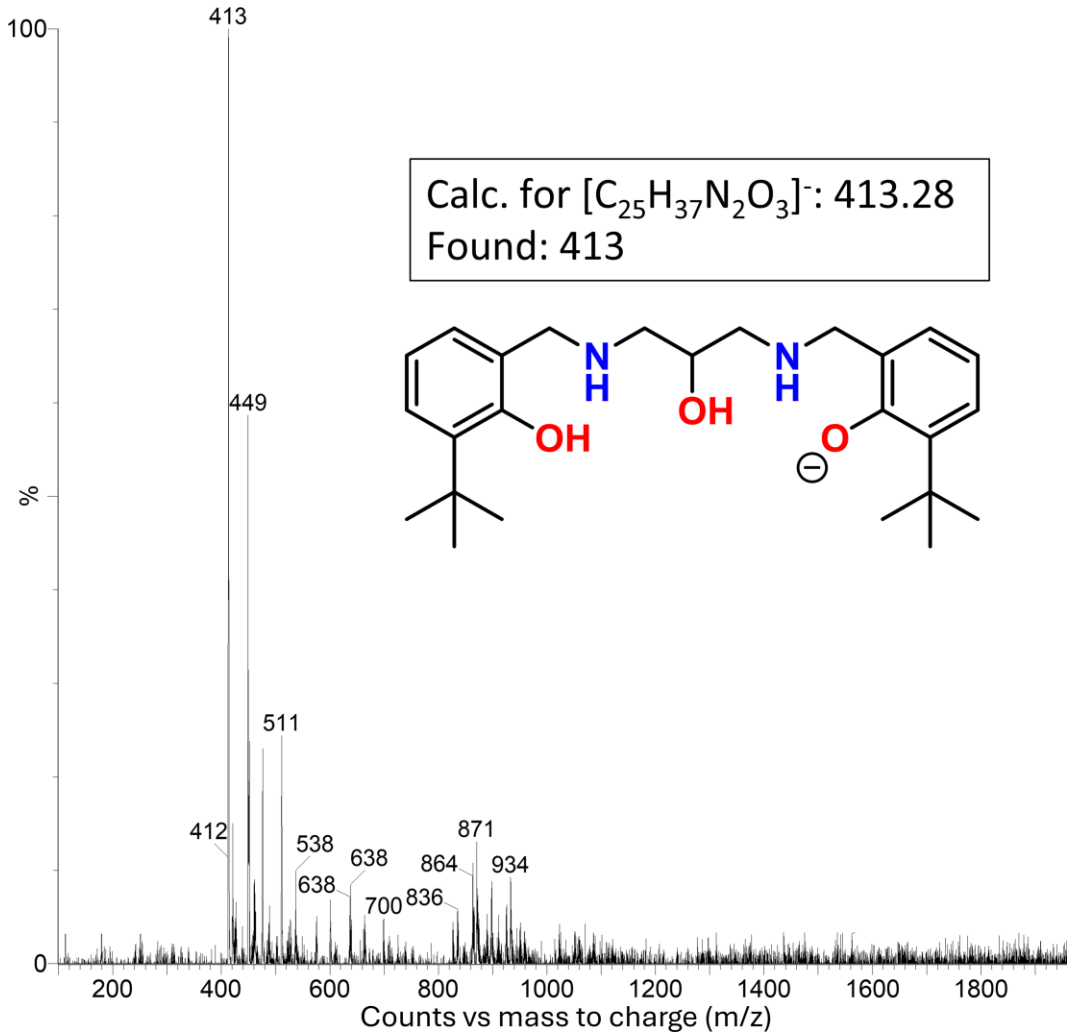

Figure 3.17. UPLC-ESI (-) mass spectrum of H_2Salpen $^{o\text{-}tBut}$ (ACN); *m/z* $[L_1]^-$= 409.24.

3.3.2 Synthesis and characterization of Nd and Dy complexes

The Salpen ligands were used in the synthesis of the Nd^{III} and Dy^{III} complexes as here described. A solution of Salpen^R ligand (1 mmol) and triethylamine (3 mmol) was prepared in ethanol 96% (10 mL). $Ln(NO_3)_3{\cdot}6H_2O$ (1 mmol) was dissolved in the same reaction solvent (5 mL) and added to the ligand solution. The resulting

mixture was stirred and refluxed for 1 h. The precipitate obtained was filtered off, washed and dried under vacuum (**Scheme 3.3**).

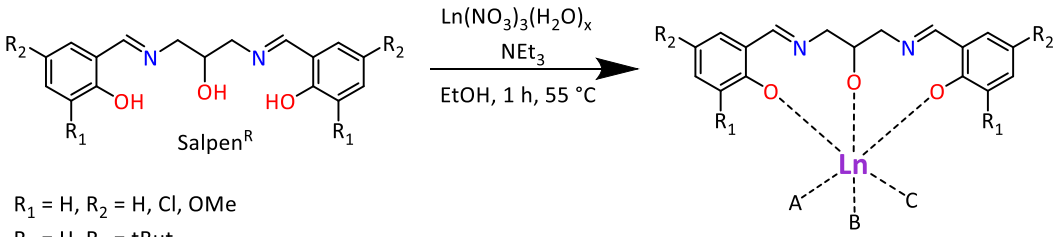

R_1 = H, R_2 = H, Cl, OMe
R_2 = H, R_1 = tBut
Ln = Dy, Nd
A, B or C = Salpen^R and/or solvent

Scheme 3.3: Scheme of the synthesis of Nd and Dy complexes.

Figure 3.18 shows the different solubilities of the Nd and Dy complexes formed with the various Salpen-type ligands in 96% ethanol. The reactions were conducted in 96% ethanol by mixing a 10 mM ligand solution with a 10 mM solution of $Ln(NO_3)_3 \cdot 6H_2O$, resulting in a total volume of 6 mL. Triethylamine (3 eq.) was added to the resulting solution and stirred for 1 hour at 55 °C. In the image, the compounds were allowed to cool to room temperature, and it can be observed that under these conditions, there is a significant difference in solubility between the Nd and Dy complexes with the Salpen (a) and Salpen$^{p\text{-}OMe}$ (b) ligands. The Salpen$^{o\text{-}tBut}$ (d) ligand shows an inversion of solubility, while the complexes obtained using Salpen$^{p\text{-}Cl}$ (c) are both insoluble in ethanol.

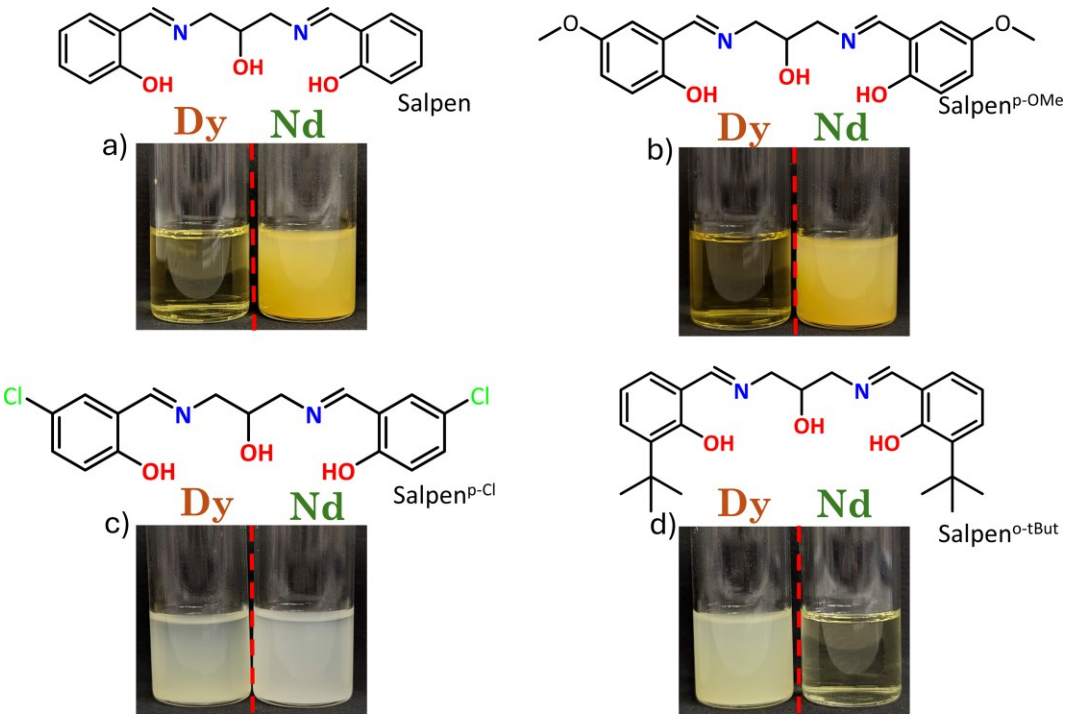

Figure 3.18. Vials containing Salpen^{R} complexes of Nd and Dy prepared by mixing equimolar amount of ligand and metal in 96% ethanol (C_{Metals} = 10 mM) at 25 °C.

The H_2Salpen ligands were also used in the synthesis of the Nd^{III} and Dy^{III} complexes. A solution of Salpen^{R} ligand (1 mmol) and piperidine (3 mmol) was prepared in 96% ethanol (10 mL). $Ln(NO_3)_3 \cdot 6H_2O$ (1 mmol) was dissolved in the same reaction solvent (5 mL) and added to the ligand solution. The resulting mixture was stirred and refluxed for 1 hour. The precipitate obtained was filtered off, washed, and dried under vacuum (**Scheme 3.4**). Triethylamine was replaced with piperidine (pK_b = 2.9) as it is stronger than triethylamine (pK_b = 4.22) in competing with the ligand's secondary amine in the acid-base equilibrium with phenolic protons. In this case, Y complexes were also prepared for the purpose of NMR characterization rather than separation from other metals.

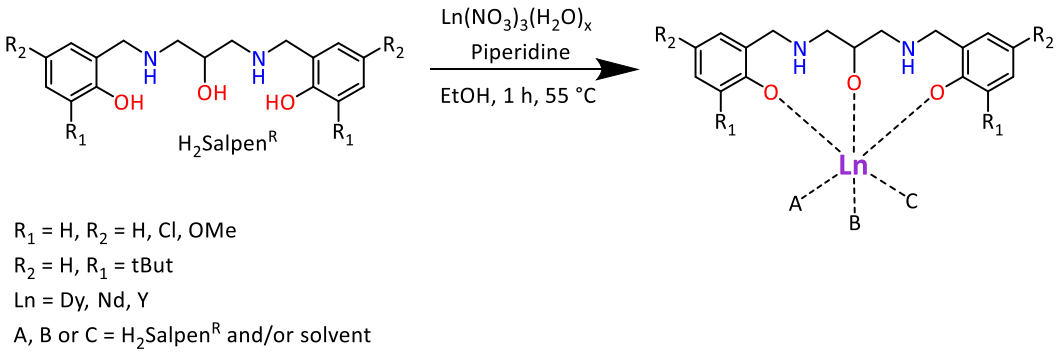

Scheme 3.4: Scheme of the synthesis of Nd and Dy complexes.

The same solubility tests for the Nd and Dy complexes were performed with the reduced ligands, using exactly the same conditions as described above for the Salpen ligands. **Figure 3.19** shows the vials containing the Nd and Dy complexes obtained with the various ligands in ethanol.

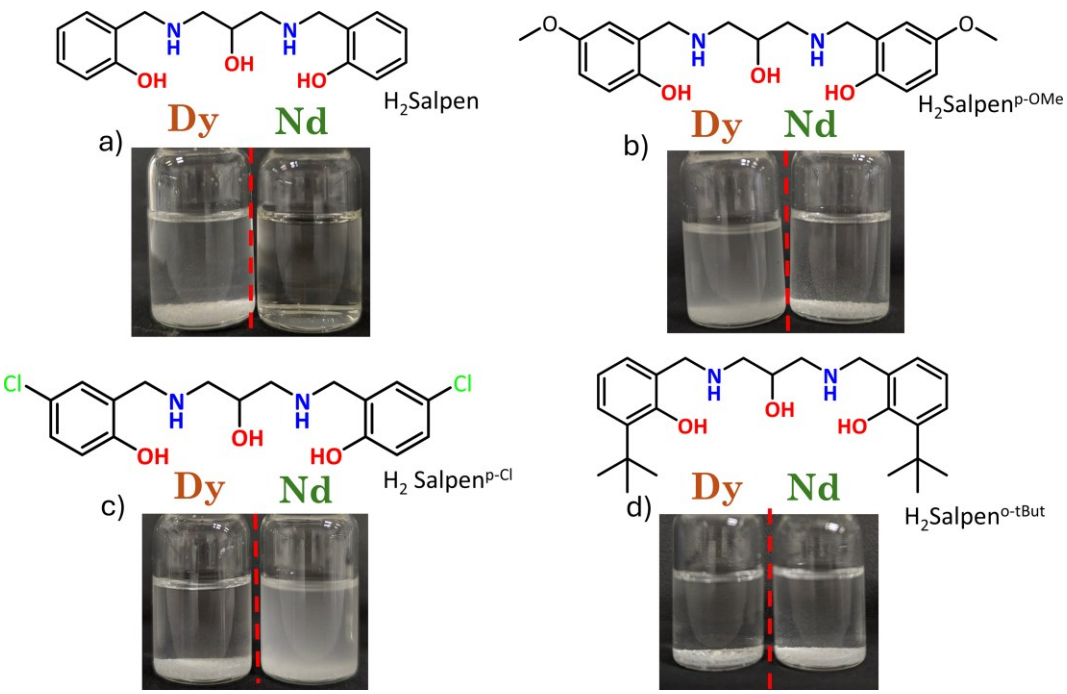

Figure 3.19. Vials containing $H_2Salpen^R$ complexes of Nd and Dy prepared by mixing equimolar amount of ligand and metal in 96% ethanol (C_{Metals} = 10 mM) at 25 °C.

With this series of ligands, only the complexes obtained with the non-functionalized ligand (H_2Salpen, (a)) form species with different solubility for Nd and Dy. Indeed, as in the previous case with the Salpen ligand, the Nd complexes are insoluble in this solvent, while the Dy complexes are soluble.

Lanthanide nitrate salts ($Ln(NO_3)_3$) were selected as the inorganic precursors to replicate the leaching solutions typically generated by common hydrometallurgical processes, which often involve dissolving lanthanide-containing materials using nitric acid. For instance, NdFeB waste magnets and mixtures of Ln_2O_3 from initial separation treatments can be dissolved in HNO_3 solutions prior to further

concentration and separation steps. As a result, a mixture of lanthanide nitrates was used as the feed solution for these experiments.

Table 3.1 reports the list of the lanthanide complexes of which the crystal structure has been determined by X ray crystallography. All complexes were characterized using single-crystal X-ray diffraction (SC-XRD). Suitable crystals for XRD analysis were obtained by slow evaporation of various organic solvent solutions in which the complex powders were dissolved or directly from the bulk reaction. Crystals of $[Dy(Salpen^{o\text{-}tBut})THF]_2 \cdot THF$, $[Dy_3(Salpen^{p\text{-}OMe})_3(OH)(DMF)_2(NO_3)] \cdot 2DMF$, $[Dy_4(Salpen)_3(H_2O)_2(OH)_2(HCOO)(DMF)]$ $[Dy_4(Salpen)_3(H_2O)(OH)_2(HCOO)(DMF)_2](NO_3)_2(H_2O)_{0.2} \cdot 2.75DMF$ and $[Y_2(H_2Salpen^{o\text{-}tBut})(EtOH)(NO_3)(Et_3NH)] \cdot EtOH$ were successfully grown within three week directly from the reaction bulk by gradually reducing the temperature by 5 °C per day, using DMF or EtOH as solvents. Crystals of $[Dy(Salpen^{o\text{-}tBut})THF]_2 \cdot THF$ and $[Dy_6(Salpen)_4(H_2O)_2(OH)_4(NO_3)_2] \cdot Acetone$ were obtained by dissolving the powder of the compounds in THF and acetone, respectively. Table X summarizes all crystal structures obtained from SC-XRD analysis.

Table 3.1. Summary of the $Ln(Salpen^R)$ crystal structure determined by X ray diffraction.

Ligand	Complex	Ann.
$Salpen^{o\text{-}tBut}$	$[Dy(Salpen^{o\text{-}tBut})THF]_2 \cdot THF$	**(1)**
$Salpen^{p\text{-}OMe}$	$[Dy_3(Salpen^{p\text{-}OMe})_3(OH)(DMF)_2(NO_3)] \cdot 2DMF$	**(2)**
Salpen	$[Dy_4(Salpen)_3(H_2O)_2(OH)_2(HCOO)(DMF)(NO_3)]$ $[Dy_4(Salpen)_3(H_2O)(OH)_2(HCOO)(DMF)_2(NO_3)]$ $(H_2O)_{0.2} \cdot 2.75DMF$	**(3)**
Salpen	$[Dy_6(Salpen)_4(H_2O)_2(OH)_4(NO_3)_2] \cdot Acetone$	**(4)**
$H_2Salpen^{o\text{-}tBut}$	$[Y_2(H_2Salpen^{o\text{-}tBut})(EtOH)(NO_3)(Et_3NH)] \cdot EtOH$	**(5)**

All complexes were obtained as powders in milligram yields and characterized by elemental analysis, except for [Nd(Salpen$^{o\text{-}tBut}$)], for which only the yield is reported.

3.3.3 Description of [Ln(Salpen^{R})] crystal structures

Details of the structural investigation for [Dy(Salpen$^{o\text{-}tBut}$)THF]$_2$·THF **(1)**, [Dy$_3$(Salpen$^{p\text{-}OMe}$)$_3$(OH)(DMF)$_2$(NO$_3$)]·2DMF **(2)**, [Dy$_4$(Salpen)$_3$(H$_2$O)$_2$(OH)$_2$(HCOO)(DMF)(NO$_3$)][Dy$_4$(Salpen)$_3$(H$_2$O)(OH)$_2$(HCOO)(DMF)$_2$(NO$_3$)]·(H$_2$O)$_{0.2}$·2.75DMF **(3)**, [Dy$_6$(Salpen)$_4$(H$_2$O)$_2$(OH)$_4$(NO$_3$)$_2$]·Acetone **(4)** and [Y$_2$(H$_2$Salpen$^{o\text{-}tBut}$)(EtOH)(NO$_3$)(Et$_3$NH)]·EtOH **(5)** are reported in the Supporting Information (**Tables S3.1-S3.10)**.

[Dy(Salpen$^{o\text{-}tBut}$)THF]$_2$·THF crystalizes in monoclinic crystal system and space group P2$_1$/c. The dimeric complex consists of two metal centers coordinated by two equivalent Salpen-type ligands. The lanthanides are epta-coordinated in a distorted capped octhaedral geometry in which the donor set comprises two phenolic oxygen atoms (O12 and O11), one THF oxygen (O1S), one bridging oxygen atoms (O1) of the ligand, and the imine nitrogen atoms (N11 and N12). The bridging oxygen (O1) represent the capped position (**Figure 3.20**). The Dy–O$_{hydroxyl}$ [2.192(2) – 2.321(2) Å] bond distances are shorter than the Dy-O$_{THF}$ bond distance [2.488(2) Å], according with the negative charge on the oxygen atoms of the ligand. The Dy–N bond distances varies in the range 2.474(2) – 2.457(2) Å. The THF molecule bound to the metal center is disordered over sites with equivalent occupancy, which does not alter the overall complex geometry. Each of the two symmetry related ligands adopts a semi-bent conformation with the two peripheral phenyl rings that form an angle of approximately 115 deg (**Figure S3.1**).

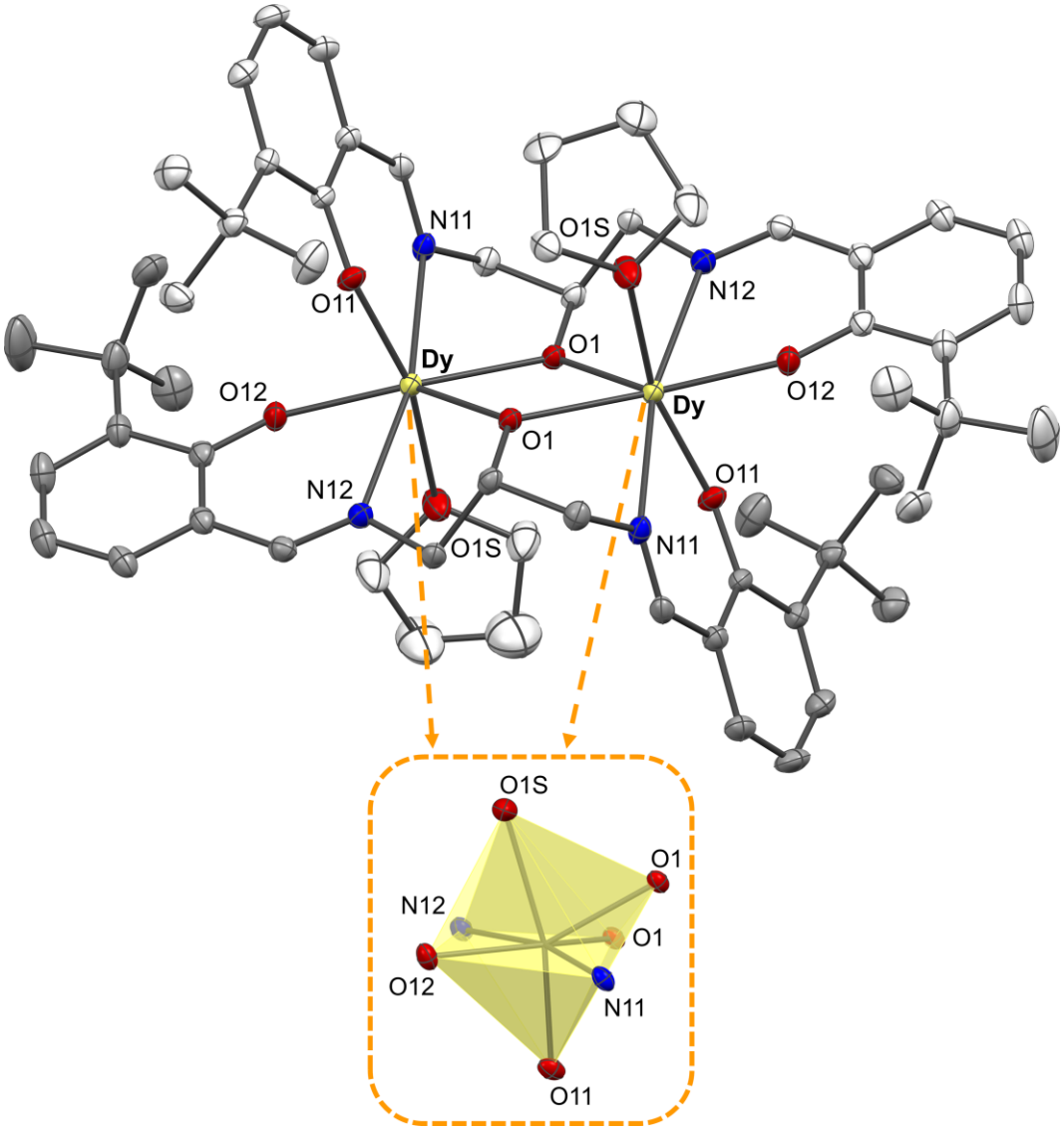

Figure 3.20. Molecular structure of the dimeric complex [Dy(Salpen$^{o\text{-}tBut}$)THF]$_2$·THF. Solvent of crystallization and the hydrogen atoms were omitted for clarity. Thermal ellipsoids were depicted at the 30% probability level. The capped octahedral geometry of Dy is highlighted. Dy (pale-yellow), N (blue), O (red), C (grey and light grey).

The compound $[Dy_3(Salpen^{p\text{-}OMe})_3(OH)(DMF)_2(NO_3)]\cdot 2DMF$ crystalizes in the monoclinic crystal system and space group $P2_1/c$. The trimeric complex consists of three Dy atoms coordinated by three $Salpen^{p\text{-}OMe}$ ligands, two DMF molecules (O1T and O1V) and one hydroxyl group (O1H). The dysprosium atoms are octa-coordinated, with Dy1 and Dy3 exhibiting a distorted dodecahedral geometry, while Dy2 displays a distorted antiprismatic geometry. The three ligands, represented in dark grey, medium grey and off-white in **Figure 3.21**, are differently distributed in the metal coordination sphere as they exhibit three distinct conformations. The first ligand (having C1 as the central carbon atom) interacts with two metal centers (Dy2 and Dy3) and it is predominantly folded around one metal (Dy3) adopting a bent conformation, with the dihedral angle between the planes of the aromatic rings of approximately 88 deg (**Figure S3.2**). The ligand is doubly deprotonated and it employs two iminic nitrogen atoms (N11 and N12), one phenolate oxygen atom (O11) and the non-deprotonated central oxygen atom (O1) to interact with Dy3. The other phenolate oxygen atom (O12) is bridging between Dy3 (2.312(3) Å) and Dy2 (2.411(10) Å). The second ligand (with C2) is fully deprotonated and it adopts a semi-bent conformation with the dihedral angles between the aromatic rings of approximately 118 deg (**Figure S3.2**). For this ligand, the central hydroxylic oxygen atom (O2) is bridging all three metal centres with bond distances in the range [2.355(1)- 2.411(9) Å]. One iminic nitrogen atom (N13) and one phenolic oxygen atom (O13) interact with Dy1 (2.509(4) Å and 2.220(10) Å, respectively), while the other iminic nitrogen atom (N14) and phenolic oxygen atom (O14) are coordinated to Dy2 with bond distances of 2.550(8) Å and 2.200(6) Å, respectively. The third ligand (with C3) adopts an elongated conformation with the dihedral angles between the aromatic rings of approximately 148 deg (**Figure S3.2**). The ligand behaves as tetradentate as it is not deprotonated on the central hydroxyl group

(disordered over two sites O3/O3A). In this ligand, two iminic nitrogen atoms (N15 and N16) are coordinated to Dy1 with distances of 2.550(4) Å and 2.533(8) Å, respectively. One phenolate oxygen atom (O15) is bridging between Dy1 (2.346(2) Å) and Dy2 (2.391(10) Å), while the other phenolate oxygen (O16) is bridging between Dy1 (2.331(3) Å) and Dy3 (2.334(1) Å). Given the fact that two ligands exhibit a -2 charge and one ligand a -3 charge, an additional nitrate anion and an hydroxyl group are present to balance the positive charges of the three cations (+3). The hydroxyl group O1H resides over the three independent metal centers with bond distances ranging from 2.328(4) Å to 2.449(9) Å. The nitrate anion is disordered in two positions, which are close to the central hydroxyl oxygen O1 of one ligand and the hydroxyl residue O1H, respectively, forming hydrogen bonds (O1-O3N, 2.750(3) Å and O1H-O4N, 2.920(3) Å). The coordination environment of Dy2 is completed by two DMF molecules O1T (2.416(10) Å) and O1V (2.395(10) Å).

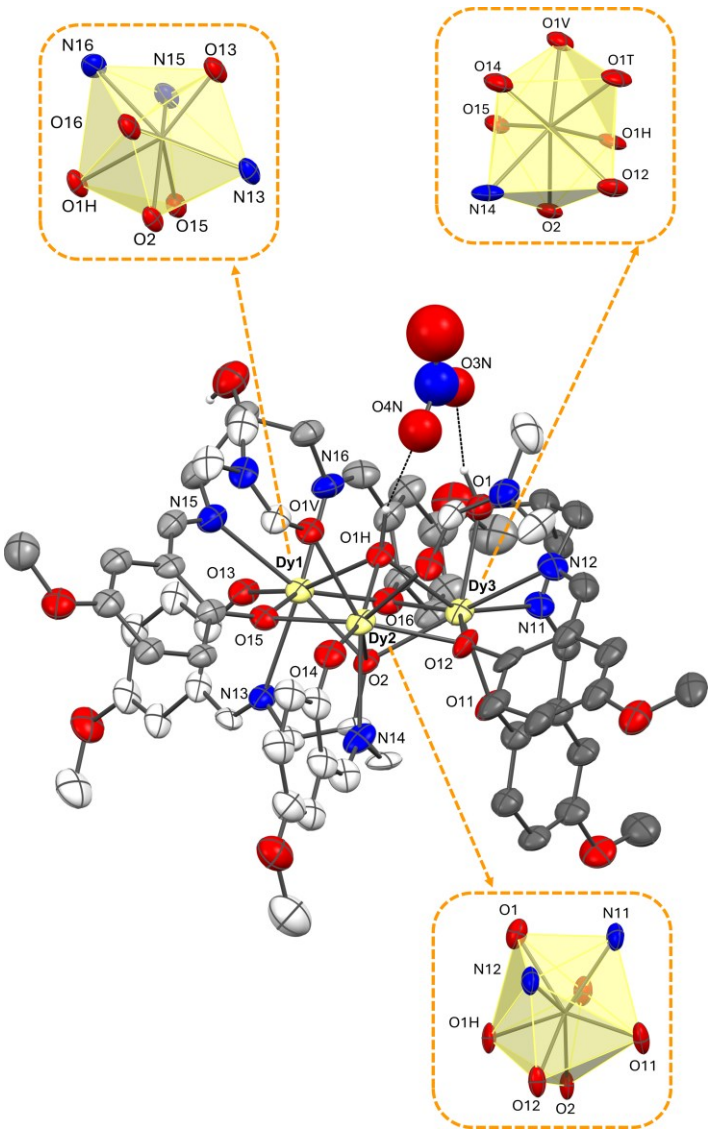

Figure 3.21. Molecular structure of the trimeric complex $[Dy_3(Salpen^{p\text{-}OMe})_3(OH)(DMF)_2(NO_3)]\cdot 2DMF$. Solvent of crystallization and the hydrogen atoms (except for the hydroxyl groups O1H, O1 and O3/O3A) were omitted for clarity. Thermal ellipsoids were depicted at the 30% probability level. The distorted dodecahedral geometries of Dy1 and Dy3 and the distorted antiprismatic geometry of Dy2 are highlighted. Dy (pale-yellow), N (blue), O (red), C (dark grey, grey and light grey), H (white).

The complex $[Dy_4(Salpen)_3(H_2O)_2(OH)_2(HCOO)(DMF)(NO_3)][Dy_4(Salpen)_3(H_2O)(OH)_2(HCOO)(DMF)_2(NO_3)]\cdot(H_2O)_{0.2}\cdot 2.75DMF$ crystalizes in the triclinic crystal system and space group P-1. The asymmetric unit comprises two molecules connected to each other by hydrogen bonds O11W-O112 and O111-O12W as highlighted in **Figure S3.4**. The metals have the same coordination environment except for Dy21 (for the first molecule) and Dy12 (for the second molecule). The first complex molecule (**Figure 3.22**) consists of three independent Salpen ligand molecules, one formate ion, one nitrate ion, one DMF (O11S) and two water molecules (O11W and O21W), while the second molecule differs from the first by having two molecules of DMF (O12S and O22S) and one water molecule (O12W) bound to the metal ions. Since there is a high structural similarity between the two complex entities, they will be described together. All Dy atoms are octa-coordinated and exhibit antiprismatic geometry, except for Dy31, which exhibits a bicapped trigonal prismatic geometry. The three independent ligands are differentially distributed in the metal coordination. Two ligands interact with three metal centers assuming a more elongated conformation, while the more peripheral ligand interacts with two metal centers, and it exhibits a folded conformation. The two imine nitrogen atoms (N151 and N161), the phenolic oxygen atom (O151) and the central hydroxyl oxygen atom (O31) of this ligand interact with the dysprosium atom (Dy41). The other phenolic oxygen atom (O161) is bridged between Dy41 (2.337(6) Å) and Dy31 (2.385(6) Å). The conformationally more elongated ligand (represented by residues X12 and X21) has a central oxygen atom (O11) and phenolic oxygen (O121) bridged between Dy11 (2.308(6) Å) and Dy21 (2.241(7) Å) and Dy41 (2.361(5) Å) and Dy11 (2.331(6) Å) atoms, respectively. The imminic nitrogen atom N121 is coordinated to the dysprosium atom Dy11 (2.492(8) Å) while the other imminic nitrogen atom (N111) and the phenolic oxygen atom (O111) are bound to Dy21, whose distances are 2.487(9) Å and 2.235(6) Å,

respectively. As for the third ligand, the phenolic oxygen (O141) and the imine nitrogen atom (N141) interact with Dy31, while O131 and N131 are bound to Dy11. The central hydroxyl atom is bridged between Dy31, Dy11 and Dy41. The hydroxyl groups O11H and O21H reside on the four independent metal centers with bond distances in the range of 2.355(5)-2.420(5) Å. The coordination environment of Dy21 is completed by two water oxygens (O11W and O21W) and a symmetrical formate ion (O11F and O21F). The coordination of Dy31 (bicapped trigonal prism) is satisfied by a DMF oxygen (O11S) and a bridged formate oxygen (O11F). The nitrate is localized by the central hydroxyl oxygen O31 and the hydroxyl residue O11H, with which it forms hydrogen bonds O11N-O31 and O11H-O31N whose distance is 2,622(1) Å and 2,899(1) Å, respectively. The second entity is described by the same coordination environment, except for the nitrate ion and Dy22, whose coordination is completed by a water oxygen (O12W) and a DMF oxygen (O22S). The nitrate ion is disorder over two positions with occupancy factor of 0.70/0.3 which oxygen atoms O12N and O12NA interact through H-bond with O32. The Dy-N bonding distance varies in the range [2,487(7)-2,513(8) Å]. Oxygen atoms bonded to metal centers (O11H, O21H and O21) have the longest bond length compared to other Dy-O bonds. Similarly, Dy-$O_{phenolate}$ bond distances [2.193(6)- 2.361(5) Å] are the shortest compared to Dy-$O_{central}$ bonds [2.241(7)- 2.414(5)Å]. The exception is the central oxygen atom O31, which interact only with one Dy, and the Dy-O31 distance [2.434(7) Å] is comparable to Dy-$O_{phenolate}$ distances because of the absence of negative charge. The various ligand conformations and their respective dihedral angles are shown in **Figure S3.3**.

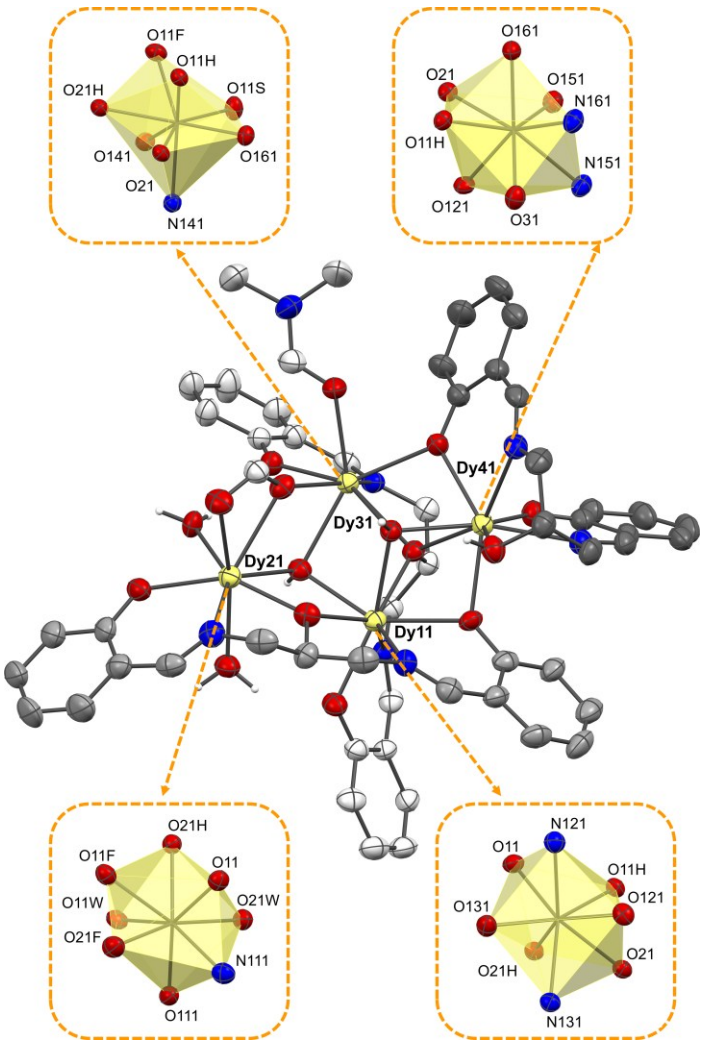

Figure 3.22. Center, molecular structure of the complex $[Dy_4(Salpen)_3(H_2O)_2(OH)_2(HCOO)(DMF)\ (NO_3)]$. Solvent of crystallization and the hydrogen atoms (except for the hydroxyl groups O11H, O21H, the water molecules O11W, O21W and for O31) were removed for clarity. Dy (pale-yellow), N (blue), O (red), C (dark grey, grey and light grey), H (white). Above, representation of the bicapped trigonal prismatic geometry of Dy31 (left) and the antiprismatic geometry of Dy41 (right). Below, representation of the antiprismatic geometries of Dy21 (left) and Dy11 (right). Thermal ellipsoids were depicted at the 30% probability level.

The compound $[Dy_6(Salpen)_4(H_2O)_2(OH)_4(NO_3)_2]\cdot 1.66Acetone$ crystalizes in the orthorhombic crystal system and space group Pbca. The molecular entity comprises six Dy atoms, four Salpen ligands, two nitrate anions, two water molecules and four hydroxyl anions. The molecule lies on an inversion center, with half molecule representing the asymmetric unit, which will be described here. The Dy atoms are octa-coordinated, and in particular, Dy1 shows a distorted dodecahedral geometry, while Dy2 and Dy3 exhibit a distorted antiprismatic geometry (**Figure 3.23**). The two independent ligands behave differently, since the first one (having C1 as the central carbon atom) is binding all three independent metal centers Dy1, Dy2 and Dy3, adopting a semi-bent conformation with the two peripheral phenyl ring that form an angle of approximately 77 deg (**Figure S3.5**). The second ligand (with C2 as the central carbon atom) is bridging between the symmetry related halves of the hexametallic complex, and it adopts a more extended conformation with the dihedral angles between the aromatic rings of approximately 130 deg (**Figure S3.5**). The phenolate oxygen atoms of the folded ligand O12 and O11 interact with Dy1 and Dy3, respectively, whereas the central hydroxyl oxygen atoms are bridging the three metal centers. The Dy1-O11 and Dy3-O12 bond distances are 2.194(4) Å and 2.254(4) Å, respectively, and they are significantly shorter than the M-O1 bond distances of the central hydroxyl moiety [2.384(4)-2.446(4) Å]. As far as the second ligand is concerned, one of the phenolate oxygen atoms (O13) is bridging between Dy1 (2.314(4) Å), and Dy2 (2.410(4) Å), whereas the second phenolate oxygen (O14) is bridging between symmetry generated Dy1' (2.313(4) Å) and Dy4' (2.363(4) Å, symmetry code ' : (1-x;1-y;1-z). The central hydroxyl moiety of the second ligand O2 acts as a bridge between Dy2 (2.265(3) Å) and Dy3' (2.296(4) Å). The hydroxyl group O1H resides over the three independent metal centers with bond distances in the 2.416(4)-2.333(4) Å range. The coordination environment of Dy1 is completed by a bidentate nitrate anion and by an imine nitrogen atom (N11). The coordination for

Dy2 (distorted antiprismatic) is completed by one imine nitrogen atom (N13) and one water oxygen (O1W), whereas an imine nitrogen atom (N14) completes the antiprismatic geometry of Dy3. The Dy-$O_{hydroxyl}$ [2.333(4)-2.443(4) Å] bond distances are longer than the other Dy-$O_{central}$ [(2.265(3)-2.296(4) Å] and Dy-$O_{phenolyc}$ [(2.194(4)-2.410(3) Å] ones due to the fact that hydroxyl oxygen atoms (O1H, O2H and O1) are shared between 3 metal centers, while (O2) and the phenolic oxygen atoms (O12, O13 and O14) are bridging two metal centers. The Dy–N bond distance varies in the range of [2.502(5)–2.518(5) Å].

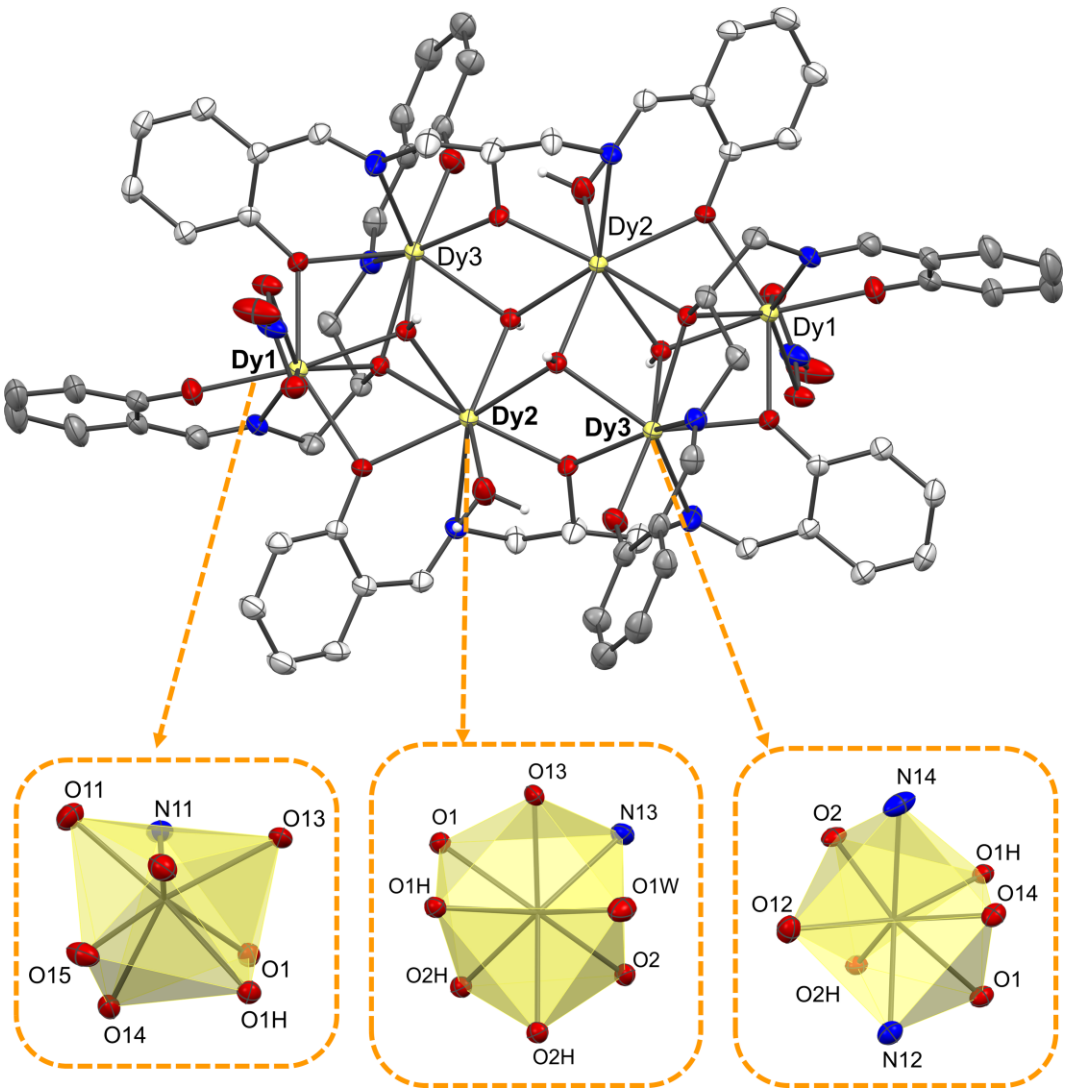

Figure 3.23. Molecular structure of the hexametallic complex $[Dy_6(Salpen)_4(H_2O)_2(OH)_4(NO_3)_2]\cdot 1.66Acetone$. Solvent of crystallization and the hydrogen atoms (except for the hydroxyl groups O1H, O2H and the water molecules O1W) were removed for clarity. Thermal ellipsoids were depicted at the 30% probability level. The distorted dodecahedral geometry of Dy1 and the antiprismatic geometries of Dy2 and Dy3 are highlighted. Dy (pale-yellow), N (blue), O (red), C (grey and light grey), H (white).

The complex $[Y_2(H_2Salpen^{o\text{-}tBut})(EtOH)(NO_3)(Et_3NH)]\cdot EtOH$ crystalizes in the triclinic crystal system and space group P-1. Each of the two symmetry related ligands adopts a semi-bent conformation with the two peripheral phenyl ring that form an angle of approximately 133 deg (**Figure S3.6**). The complex anion exhibits two different metal centers having a distinct coordination geometry. In particular, Y1 is octa-coordinated showing a dodecahedral geometry, whereas Y2 is epta-coordinated having a distorted pentagonal bipyramidal geometry (**Figure 3.24**). The coordination of Y1 is achieved by two phenolate oxygen atoms (O11 and O13), two bridging oxygen atoms (O1 and O2), two amino nitrogen atoms (N13 and N11), and by an almost symmetrically bound bidentate nitrate anion. The $Y–O_{nitrate}$ bond distances [2.533(3) and 2.586(3) Å] are the longest among the Y-O coordination bond distances, but they are comparable to the $Y–N_{amine}$ ones [2.582(3)–2.586(3) Å]. For Y2, the equatorial plane of the pentagonal base is represented by one phenolic oxygen atoms (O12), two bridging oxygen atoms (O1 and O2) of the ligand, and the amine nitrogen atoms (N14 and N12). The other phenolic oxygen atom (O14) and the ethanol oxygen atom (O1S) represent the axial position of the bipyramid. The Y–O bond distances involving the negatively charged oxygen atoms of the ligands [2.172(3)–2.286(3) Å] are shorter than the $Y–O_{ethanol}$ distance [2.391(3) Å]. The $Y–N_{amine}$ bond distances [2.549(3) and 2.568 (3) Å] are shorter than the $Y–O_{ethanol}$ one, but they are longer than the other Y–O bond distances. The ethanol molecule coordinated to the metal is disordered over two sites with 0.45 and 0.55 site occupancy factors, while preserving the same overall complex geometry. The water molecule of crystallization and the triethylammonium cation is located in a pocket formed by two phenyl residues bearing t-Butyl residues, which are arranged in a head to tail fashion. The water molecule acts as hydrogen bond donor towards two phenolate oxygen atoms of the two distinct ligands, hence behaving as a bridge between them [O1W–O14 2.758(4) Å, O1W–O11 2.821(4) Å].

Moreover, the water molecule accepts a hydrogen bond from the triethylammonium cation [N1C–O1W 2.716(6) Å].

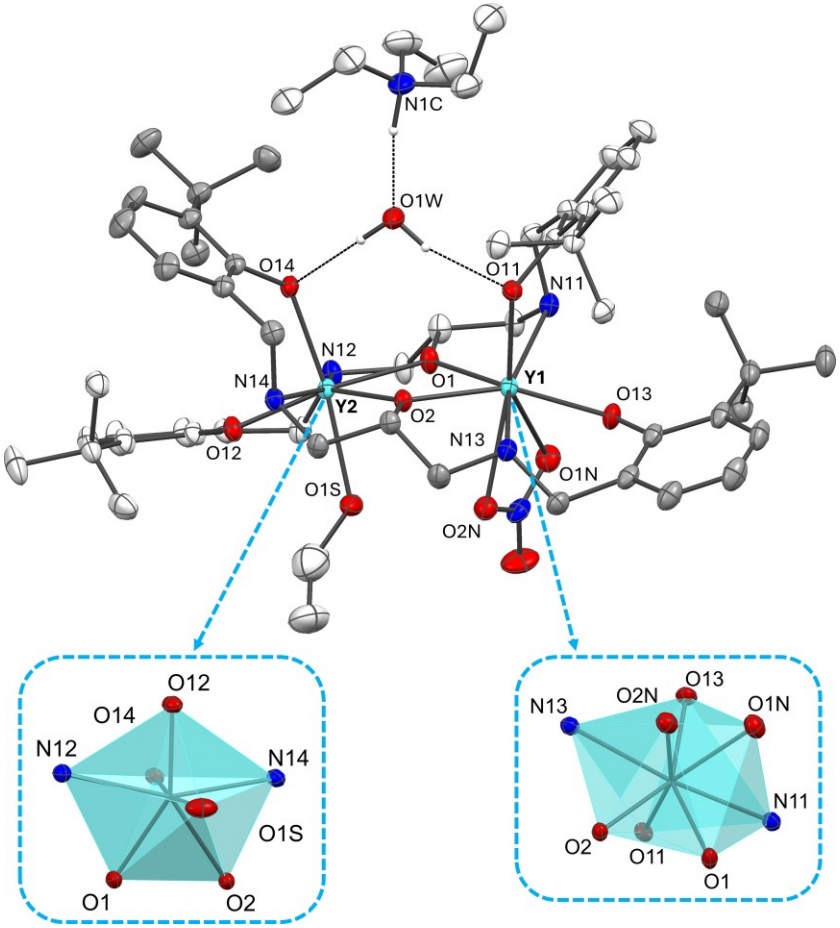

Figure 3.24. Molecular structure of the dimeric complex $[Y_2(H_2Salpen^{o\text{-}^{tBut}})(EtOH)(NO_3)(Et_3NH)]\cdot EtOH$. Solvent of crystallization and the hydrogen atoms (except for the water molecule O1W and the triethylammonium cation N1C) were omitted for clarity. Thermal ellipsoids were depicted at the 30% probability level. The dodecahedral geometry of Y1 and the distorted pentagonal bipyramidal geometry of Y2 are highlighted. Y (light blue), N (blue), O (red), C (grey and light grey), H (white).

3.3.4 Solution studies of Nd/Dy

The formation equilibria of Nd^{III} and Dy^{III} complexes of Salpen (L_1-L_4) and H_2Salpen (L_5-L_8) in EtOH 96% was studied by UV-visible spectrophotometric titration of the ligands with metal solutions, up to a metal/ligand ratio of 3. Titrations were carried out in the presence of 3 eq. of base with respect to the ligand (triethylamine or piperidine). Spectra were acquired in the 225-500 nm (L_1-L_4) or 220-330 nm range (L_5-L_8).

The absorption spectrum of the L_1-L_3 Salpen ligands (black spectra) exhibit three absorption bands at ca. 255, 320 and 410 nm (**Figure 3.25-3.27**). Upon addition of the metal, a decrease of the absorption bands of the ligands was observed, with appearance of a band at ca. 350 nm, which increases in absorbance until metal:ligand equivalence (M/L=1, red spectra). Beyond this value, only a limited red shift of the absorption bands was observed (for -OMe, **Figure 3.26**). Interestingly, the behaviour of L_4 upon addition of up to 3 eq. of metal resulted different from that of the other three ligands of this series (**Figure 3.28**). Actually, the addition of Ln^{III} ions resulted only into a limited decrease and shift of the band related to the ligand at 350 nm, apparently suggesting that with this ligand the complexation equilibria of the metal ions are significantly unfavored compared to L_1, L_2 and L_3.

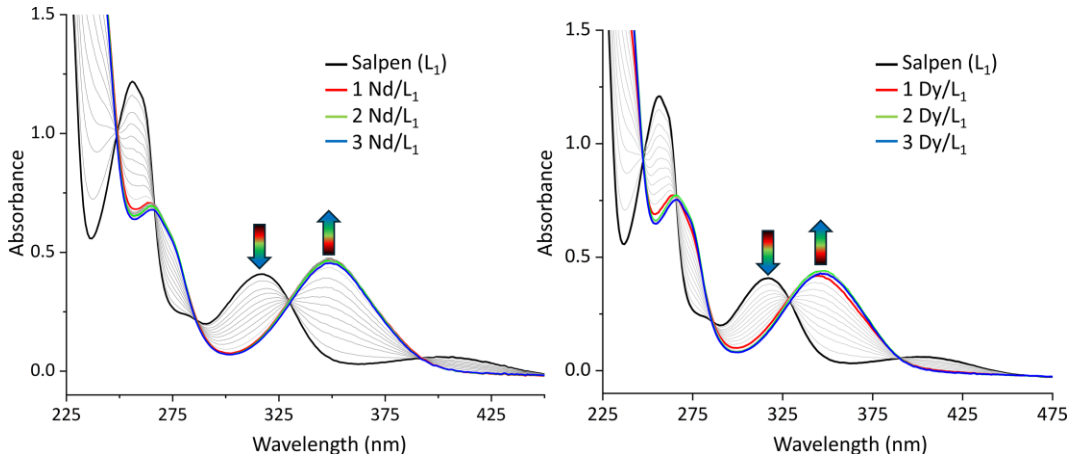

Figure 3.25. Spectra for the titration of Salpen (L_1) with Nd^{III} (left) and Dy^{III} (right) in ethanol (96%). $C_L = 5.07\ 10^{-5}$ M, Ln/L = 0-3, T = 298.2 K. All titrations were performed in the presence of 3 eq. of triethylamine with respect to the ligand.

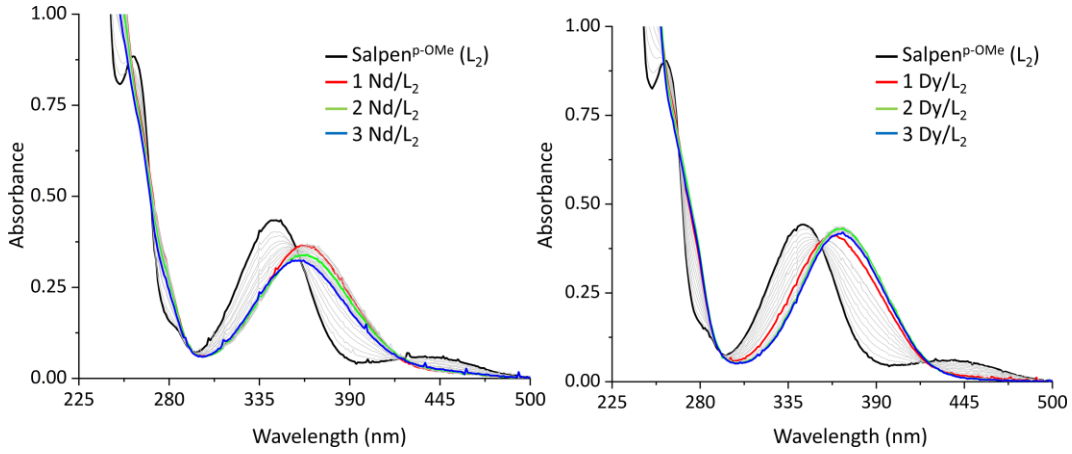

Figure 3.26. Spectra for the titration of $Salpen^{p\text{-}OMe}$ (L_2) with Nd^{III} (left) and Dy^{III} (right) in ethanol (96%). $C_L = 5.36\ 10^{-5}$ M, Ln/L = 0-1, T = 298.2 K. All titrations were performed in the presence of 3 eq. of triethylamine with respect to the ligand.

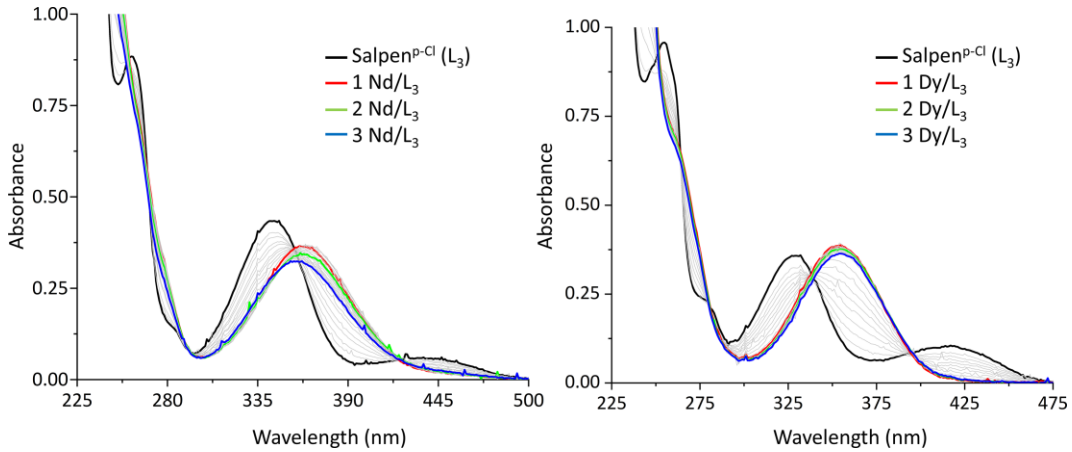

Figure 3.27. Spectra for the titration of Salpen$^{p\text{-}Cl}$ (L_3) with Nd^{III} (left) and Dy^{III} (right) in ethanol (96%). C_L = 5.22 10^{-5} M, Ln/L = 0-1, T = 298.2 K. All titrations were performed in the presence of 3 eq. of triethylamine with respect to the ligand.

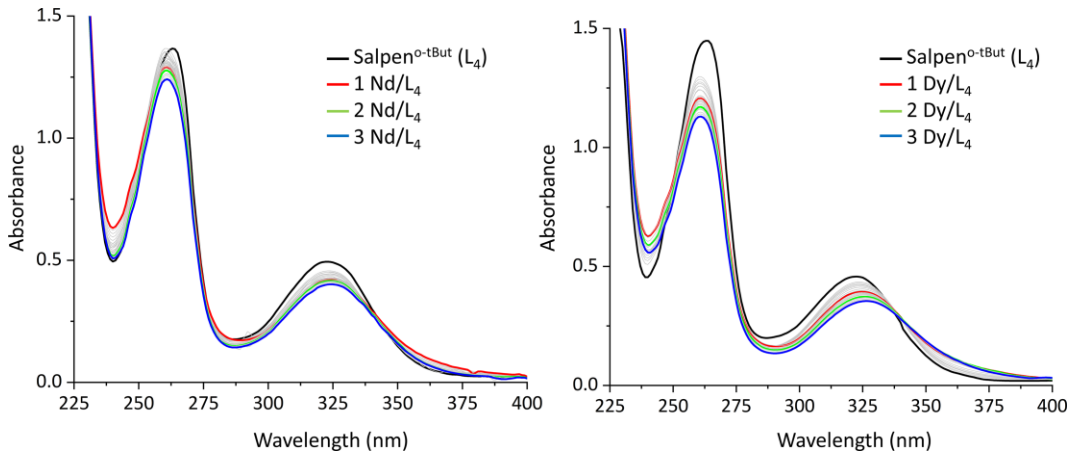

Figure 3.28. Spectra for the titration of Salpen$^{o\text{-}tBut}$ (L_4) with Nd^{III} (left) and Dy^{III} (right) in ethanol (96%). C_L = 4.65 10^{-5} M, Ln/L = 0-1, T = 298.2 K. All titrations were performed in the presence of 3 eq. of triethylamine with respect to the ligand.

Regarding the reduced ligands (L_5-L_8) I will only report the solution study of H_2Salpen (L_5) since it is the only amine ligand that formed complexes with different solubility in ethanol 96 % for the two lanthanides. The titration of H_2Salpen was carried out using the same approach of Salpen^R ligands. The stechiometric ratio ligand:base (piperidine) 1:3 was kept constant while the metal increase from 0 to 3 equivalent with respect to the ligand. The ligand titration is shown in **Figure 3.29**. It exhibits the same trend as Salpen, by increasing the amount of metal, the ligand represented by the black spectrum (275 nm) decreases while a new red band related to the complex (287 nm) increases in intensity. The red band represents the 1:1 metal:ligand stoichiometry ratio, beyond which no more absorption shifts are observed.

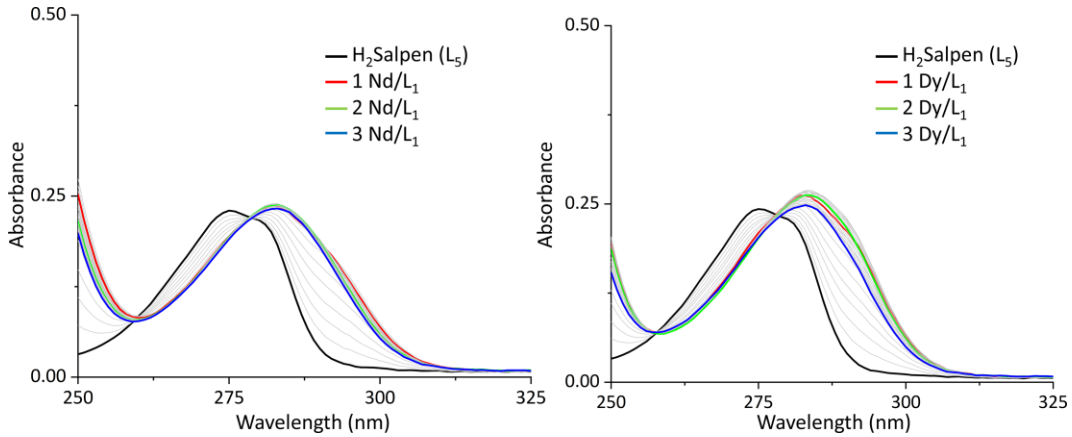

Figure 3.29. Spectra for the titration of H_2Salpen (L_5) with Nd^{III} (left) and Dy^{III} (right) in ethanol (96%). C_L = 5.65 10^{-5} M, Ln/L = 0-1, T = 298.2 K. The titration was performed in the presence of 3 eq. of piperidine with respect to the ligand.

The spectrophotometric titration data were treated with the HypSpec 2014 software, and the speciation models that led to the best fitting of the experimental data are reported in **Table 3.2**.

Table 3.2. Conditional stability constants (log *K*, *K*=([M_nL_m]/([M]^n[L]^m)) of the complexation of Dy^{III} and Nd^{III} with Salpen-type ligands determined by UV-Vis spectrophotometric titration in EtOH 96% at 298 K.

Ligand	Species	Nd^{III}	Dy^{III}
Salpen (L_1)	M_3L_3	32.9(0.6)	30.7(0.2)
	M_6L_4	56.4(0.5)	53.3(0.3)
Salpen$^{p\text{-}OMe}$ (L_2)	M_3L_3	28.1(0.1)	22.9(0.1)
	M_6L_4	48.6(0.7)	40.01(0.1)
Salpen$^{p\text{-}Cl}$ (L_3)	M_3L_3	24.3(0.1)	30.8(0.3)
	M_6L_4	42.3(0.1)	53.6(0.6)
Salpen$^{o\text{-}tBut}$ (L_4)[a]	ML_2	13.3(1)	13.3(1)
	M_2L_2	18(1)	18(1)
H_2Salpen (L_5)	ML_2	14.2(0.1)	10.0(0.2)
	M_3L_3	31.6(0.3)	25.7(0.1)
	M_6L_4	52.37(0.4)	46.1(0.1)

[a]Salpen$^{o\text{-}tBut}$ (L_4) at 328K.

For all imino ligands, with exception of L_4, the first titration endpoint at M/L = 1 was interpreted with the formation of trimeric M_3L_3 species, as suggested by structural data of isolated complex of **(2)**. Spectra collected for the addition of Ln^{III} beyond the

equivalence are not accounted by simple dilution, with a shift of the band at ca. 350 nm rather than a simple decrease in absorbance. Indeed, the best fitting of the spectral dataset for L_1 and L_3 was obtained by introducing a M_6L_4 species, also suggested by analysis of the structure of the isolated complex $Dy_6(Salpen)_4(H_2O)_2(OH)_4(NO_3)_2]\cdot 1.66Acetone$.

Interestingly, the L_4 ligand upon addition of metal ion has shown a very different behavior, in particular related to the absence of a net titration endpoint at M/L = 1. Rather, the change in absorbance at 325 nm for the titration with Nd reveals that a titration endpoint may be identified at M/L = 0.5 (**Figure 3.28**). For this system, the best fitting of the titration data was indeed obtained by a speciation model that includes a ML_2 species rather than a M_6L_4 one, along with M_2L_2. The same speciation model allowed to obtain a fitting of the spectral data for the titration of L_4 with Dy, which is reported in **Figure 3.33** (right). Perhaps most important, it must be noted that the change in absorbance for the titration with Nd is limited, and therefore the data result relatively more affected to experimental errors and instrumental noise. This is reflected into the high standard deviation values of the log *K* for the speciation of the Nd/L_4 system.

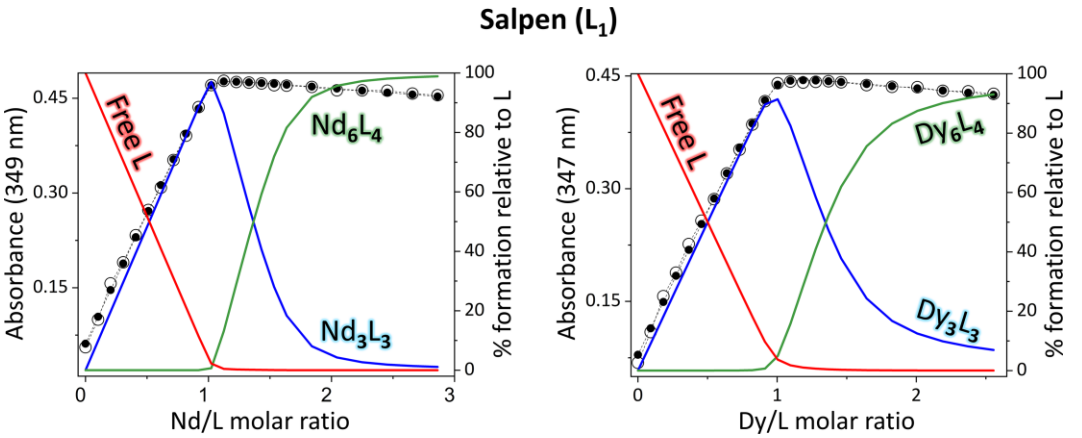

Figure 3.30. Plot of the absorbance values at 349 nm (Nd^{III}) and 347 nm (Dy^{III}) superimposed to the species distribution diagrams. Free ligand (red curve), 3:3 species distribution curve (blue curve), 6:4 species distribution curve (green curve), ● calculated, ○ experimental data.

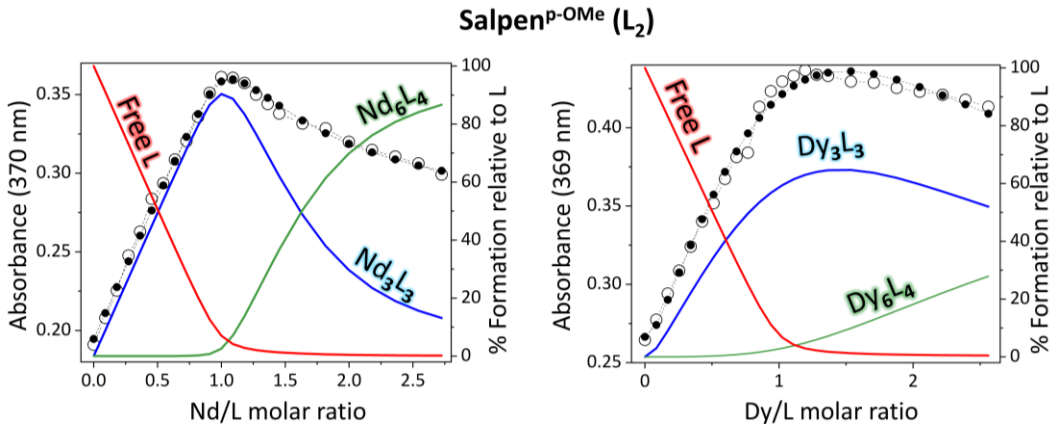

Figure 3.31. Plot of the absorbance values at 370 nm (Nd^{III}) and 369 nm (Dy^{III}) superimposed to the species distribution diagrams. Free ligand (red curve), 3:3 species distribution curve (blue curve), 6:4 species distribution curve (green curve), ● calculated, ○ experimental data.

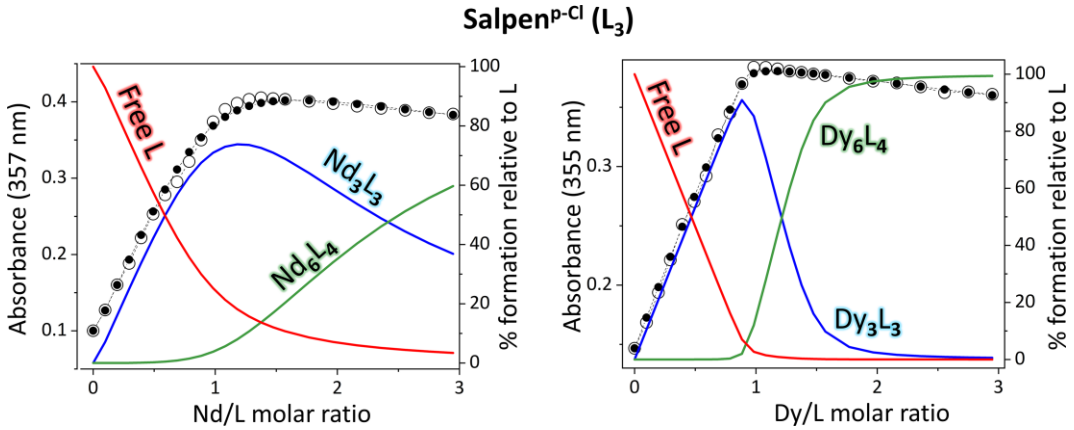

Figure 3.32. Plot of the absorbance values at 357 nm (Nd^{III}) and 355 nm (Dy^{III}) superimposed to the species distribution diagrams. Free ligand (red curve), 3:3 species distribution curve (blue curve), 6:4 species distribution curve (green curve), ● calculated, ○ experimental data.

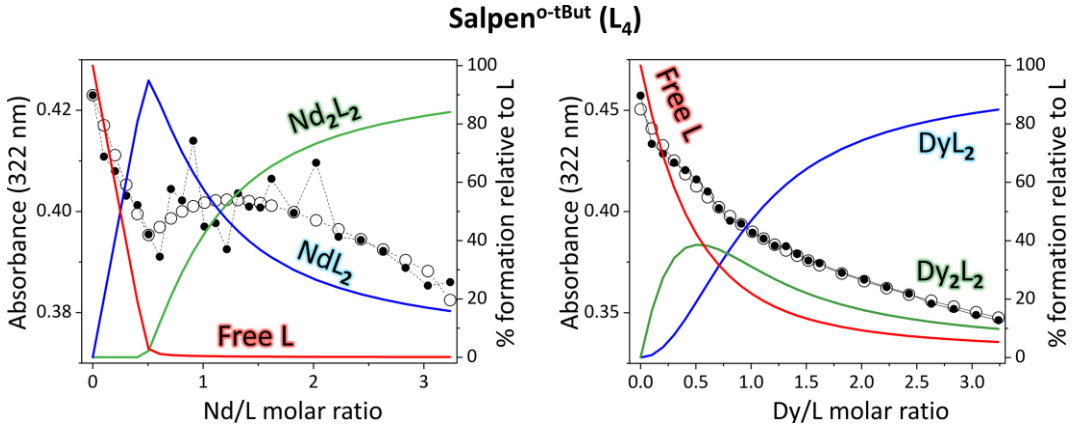

Figure 3.33. Plot of the absorbance values at 322 nm (Nd^{III}) and 322 nm (Dy^{III}) superimposed to the species distribution diagrams. Free ligand (red curve), 1:2 species distribution curve (blue curve), 2:2 species distribution curve (green curve), ● calculated, ○ experimental data.

The free ligand in solution, represented by the red curve, decreases as the metal:ligand ratio increases, while the blue curve corresponding to the 3:3 specie increases up to M/L = 1. By adding more metals, the 3:3 curve decreases and the formation of the 6:4 specie, described by the green curve is observed. As reported in **Table 3.2**, the speciation for Nd and Dy with L_1-L_3 exhibit the same stoichiometry, while L_4 (**Figure 3.33**) shows a M:L 2:1 and 2:2 species. Since there is not significant difference between ligand and the Nd and Dy complexes in term of absorbance, the precise calculation of the log *K* and the deviation standard for Nd-Salpen$^{o\text{-}tBut}$ is difficult although the spectral changes show that complex species are formed in solution. The different species with L_4 could be explained by the steric hindrance of the *t*-butil group in ortho position with respect to the phenolate group that prevent the formation of a specie with more than two metal atoms. This speciations are supported by the crystalline structures obtained for [Dy(Salpen$^{o\text{-}tBut}$)] (**Figure 3.20**), [Dy(Salpen$^{p\text{-}OMe}$)] (**Figure 3.21**) and for [Dy(Salpen)] (**Figure 3.23**) throught X-ray diffraction analysis.

The speciation for Nd and Dy with H_2Salpen (**Figure 3.34**) shows the formation of complexes with the same stoichiometry. The best-fitting model identified the presence of three species, M:L 1:2, 3:3 and 6:4. For Nd, an ML_2 species forms initially, up to the titration point where M/L = 0.5 eq., at which the violet curve corresponding to the first species decreases, and a 3:3 species, represented by the blue curve, begins to form. At the equivalence point (M = 1), the 6:4 species, represented by the green curve, is formed. The only difference observed in the titration with Dy is that all three species coexist from the half-equivalence point (M/L = 0.5 eq.).

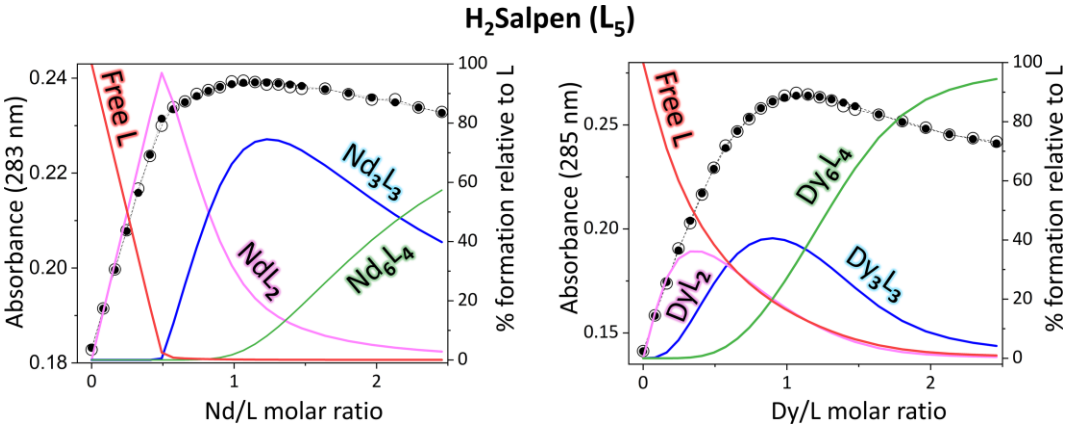

Figure 3.34. Plot of the absorbance values at 283 nm (Nd^{III}) and 285 nm (Dy^{III}) superimposed to the species distribution diagrams. Free ligand (red curve), 1:2 species distribution curve (purple curve), 3:3 species distribution curve (blue curve), 6:4 species distribution curve (green curve), ● calculated, ○ experimental data.

Examining the results described above, we can conclude that Dy and Nd with the same ligand generate the same species in solution. For this reason, the different solubility of the complexes for Nd and Dy in 96% EtOH cannot be attributed to the presence of different species, but rather to the formation of structurally different complexes, possibly due to the presence or absence of a coordinated solvent or the charge of the complex, which drive different interactions in the solid state for the different complexes and which eventually makes the complex of one lanthanide more soluble than that of the other.

3.3.5 Dy and Nd Separation experiments

A systematic series of experiments was conducted to separate neodymium and dysprosium taking advantage of the different solubility of the complexes formed by the two metals, with each experiment performed in duplicate. As stated, this investigation leveraged the solubility differences displayed by the dysprosium and neodymium complexes during the synthesis phase, as illustrated in **Figure 3.18**. Specifically, the [Nd(Salpen)] and [Nd(Salpen$^{p\text{-}OMe}$)] complexes formed precipitates, while a reversal in solubility was observed with ligand L_4, leading to precipitation of the [Dy(Salpen$^{o\text{-}tBu}$)] complex. However, the lanthanide complexes with Salpen$^{p\text{-}Cl}$ (L_3) exhibited no significant solubility difference under similar experimental conditions, so L_3 was excluded from further separation studies. In the separation procedures used, both neodymium and dysprosium nitrates were combined with two of the selected ligands in molar ratios (1.05:0.5:0.5 L:Nd) and subjected to two different reaction times in the presence of three equivalents of TEA (relative to the ligand) in ethanol at 55 °C. The reaction times were tailored for each ligand, taking into account the kinetic aspects of complex precipitation in both single-metal and mixed-metal systems to optimize the maximum separation between the complexes. This procedure led to the formation of a solid precipitate, which was separated from the solution by filtration. Both the solid and liquid phases were then analyzed using Inductively Coupled Plasma-Optical Emission Spectroscopy (ICP-OES) to assess metal distribution. Here I will only report the separation results of Salpen and Salpen$^{o\text{-}tBut}$ because of difficulties in obtaining data Salpen$^{p\text{-}OMe}$ separation with sufficient reproducibility.

For the Salpen (L_1) ligand, separation tests were conducted in 6 mL of 96% ethanol, mixing 1.05 eq. of Salpen (C_L = 22 mM) with 0.5 eq. of each metal (C_{Nd} = C_{Dy} = 11 mM) in the presence of 3 eq. of triethylamine (**Scheme 3.5**).

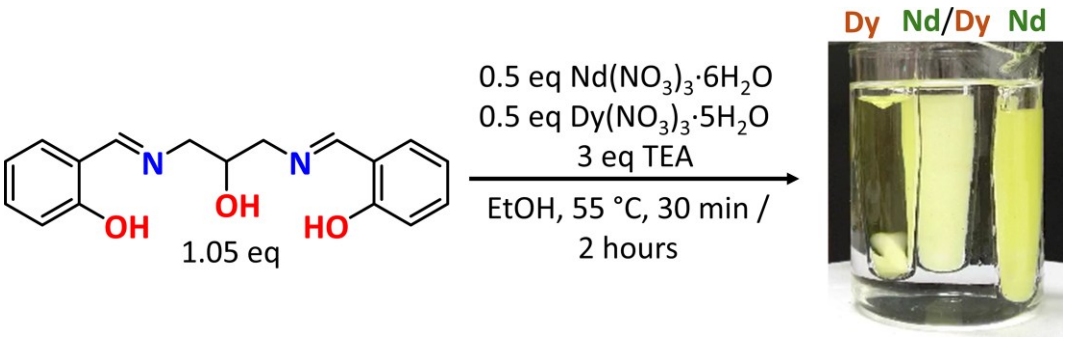

Scheme 3.5. Scheme reaction of the separation tests.

The reactions were stirred at 55 °C for two different reaction times: 30 minutes and 2 hours. The mixtures were filtered, and both the solid phase and the filtrate were analyzed using ICP-OES. As shown in **Figure 3.35**, the separation test with a reaction time of 30 minutes (left) shows an enrichment of Nd in the solid phase, while Dy is enriched in the liquid phase. When the reaction time is 2 hours, both metals show an enrichment in the solid phase, with a higher concentration of Nd. The 2-hour reaction case is of greater interest, as the amount of Nd in solution is very low (4%); further optimization of the separation conditions could maximize Nd precipitation, resulting in pure Dy in solution.

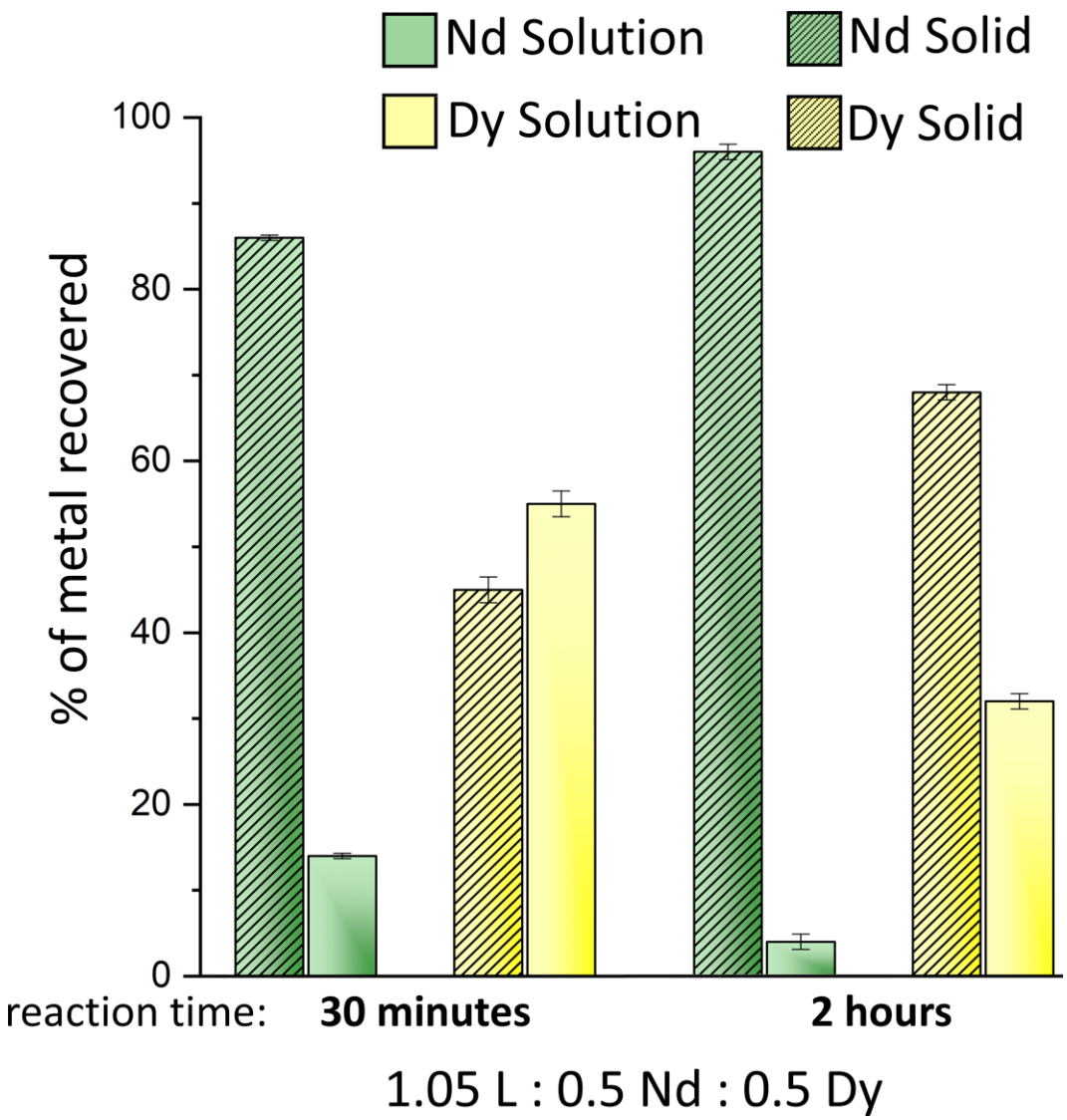

Figure 3.35. The amount of Nd and Dy recovered from the solution and solid phases in EtOH after 30 minutes (left) and 2 hours (right) after mixing Nd^{III}, Dy^{III}, and Salpen (L_1) in the 1.05:0.5:0.5 stoichiometric ratio. The metal cations were added as nitrate salts. Amount of Nd or Dy (reported as % of the initial reactant quantity) determined by ICP-OES analyses.

For the Salpen$^{o\text{-}tBut}$ (L_4) ligand, separation tests were conducted in 6 mL of 96% ethanol, mixing 1.05 eq. of Salpen$^{o\text{-}tBut}$ (C_L = 20 mM) with 0.5 eq. of each metal (C_{Nd} = C_{Dy} = 10 mM) in the presence of 3 eq. of triethylamine (**Scheme 3.6**).

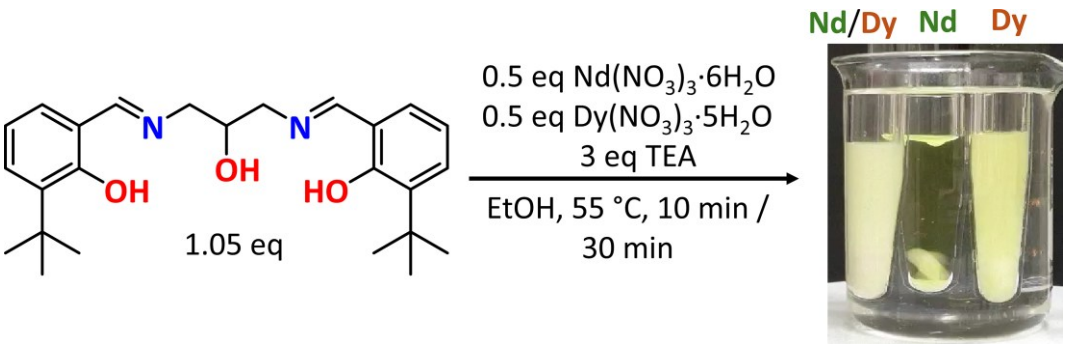

Scheme 3.6. Scheme reaction of the separation tests.

The reactions were stirred at 55 °C for two different reaction times, 10 minutes and 30 minutes. The mixtures were filtered, and both the solid phase and the filtrate were analyzed using ICP-OES. As shown in **Figure 3.36**, the separation test for both reaction times reveals an enrichment of Nd in the liquid phase, while the solid phase becomes enriched with Dy. For this ligand, the soluble complex is that of Nd, and it can be observed that as the reaction time increases, the Nd complex tends to precipitate more, enriching the solid phase almost twice as much compared to the shorter reaction time. For this system, shorter reaction times would optimize the separation between Nd and Dy.

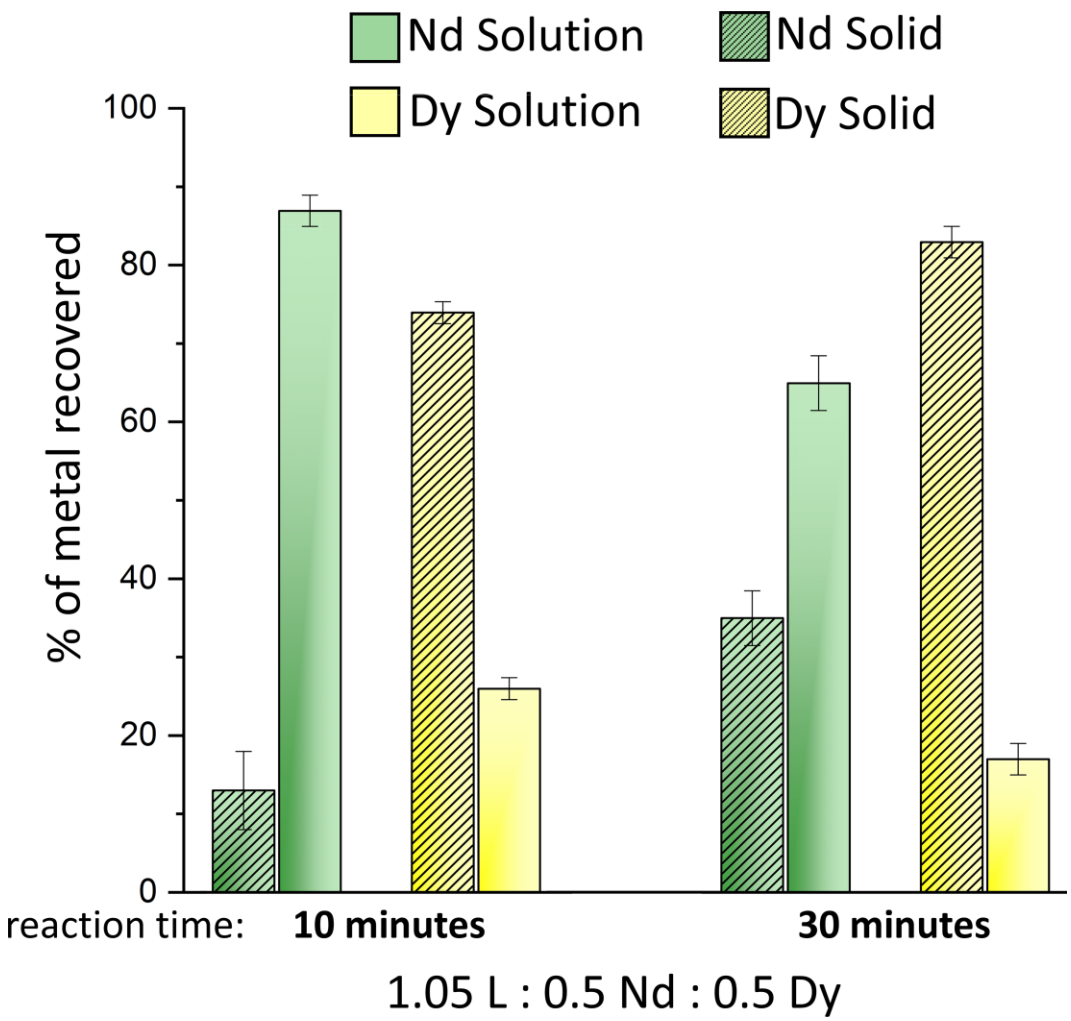

Figure 3.36. The amount of Nd and Dy recovered from the solution and solid phases in EtOH after 10 minutes (left) and 30 minutes (right) after mixing Nd^{III}, Dy^{III}, and $Salpen^{o\text{-}tBut}$ (L_4) in the 1.05:0.5:0.5 stoichiometric ratio. The metal cations were added as nitrate salts. Amount of Nd or Dy (reported as % of the initial reactant quantity) determined by ICP-OES analyses.

The same series of experiments was conducted with the reduced ligand H_2Salpen, the only one in which the Nd and Dy complexes showed different solubility for the

two lanthanides, as shown in **Figure 3.19**. The other ligands were excluded from the study. The separation protocol is identical to the one used previously: neodymium and dysprosium nitrate salts were combined with the ligand in a stoichiometric ratio of L:Nd (1.05:0.5:0.5), in the presence of three equivalents of piperidine relative to the ligand in ethanol at 55 °C for 1 hour. The precipitate formed was separated from the solution by filtration, and both phases were analyzed using Inductively Coupled Plasma-optical Emission Spectroscopy (ICP-OES) to assess the metal distributions.

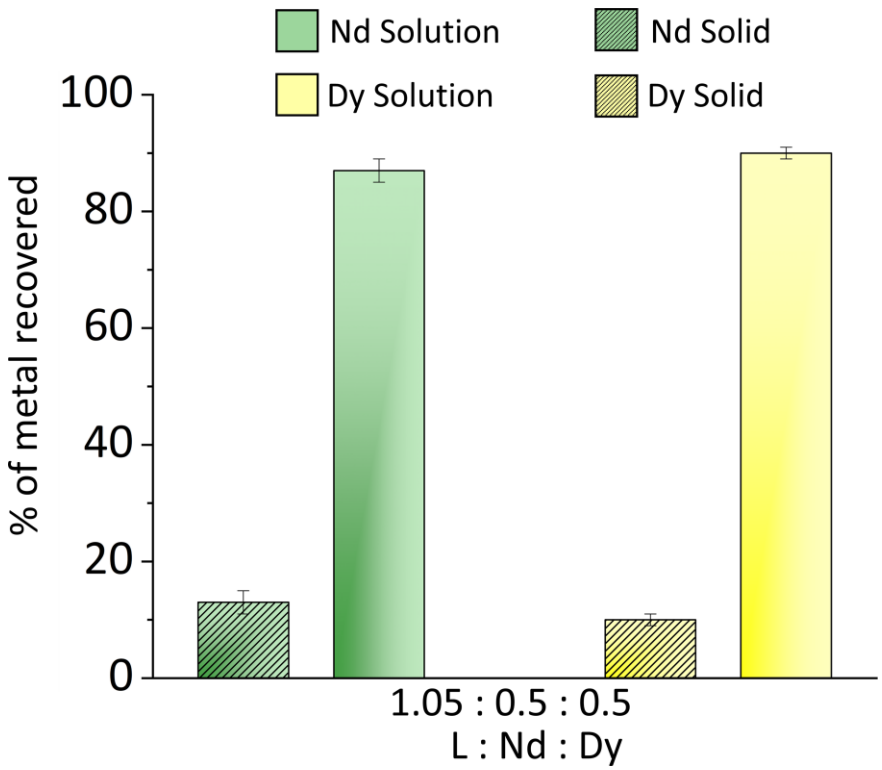

Figure 3.37. The amount of Nd and Dy recovered from the solution and solid phases in EtOH after 1 h after mixing Nd^{III}, Dy^{III}, and H_2Salpen (L_5) in the 1.05:0.5:0.5 stoichiometric ratio. The metal cations were added as nitrate salts. Amount of Nd or Dy (reported as % of the initial reactant quantity) determined by ICP-OES analyses.

Figure 3.37 shows the distribution of the two metals between the solid phase and the solution. The Y-axis represents the percentage of metals recovered relative to the initial weighed amount. Although the presence of a different solubility of the Nd and Dy complexes isolated in ethanol was evident (**Figure 3.19**), the graphs indicate that about 85% of the metals are distributed uniformly in the solid phase, with the remaining 15% in the liquid phase. In perspective, therefore, the use of this ligand eparation of Nd and Dy is not feasible. This can be attributed to possible interaction mechanisms between the complexes, which, when both metals are present simultaneously in the same system, result in the co-precipitation of the soluble complex. Another possible explanation is that these systems tend to form polynuclear species, i.e., mixed Nd-Dy complex, that cause both metals to be present in the same phase. Despite the poor separation properties for Nd and Dy, a distinctive feature of this ligand is its potential for recovery and reuse in further experiments, following a specific protocol that will be described in the next paragraph.

3.3.6 Recovery of the ligand

The recovery of the ligand or materials used in metal extraction processes is a crucial aspect that we have investigated in this project. Recovering the ligand enables in fact the reuse of existing resources, minimizing the need for new ones. The remarkable stability of the ligand in highly acidic and basic environments allows for its near-complete recovery. The recovery process depicted in **Scheme 3.7** an it pivots around the addition of oxalate to obtain the complete precipitation of

oxalate-complexes of the lanthanides and concomitant release of the soluble ligand.

The recovery process was carried out by reacting the ligand with metal nitrate salts in the presence of piperidine in ethanol, yielding Nd and Dy complexes. To the mixture, previously evaporated to dryness, approximately 5 mL of water was added to resuspend the resulting solid. Subsequently, the addition of oxalic acid to the suspension of the complexes in water led to the copious precipitation of a milky white solid, corresponding to the lanthanide oxalates. The mixture was then filtered, and the resulting solution was basified to a pH between 8 and 9, followed by extraction with dichloromethane (DCM) or ethyl acetate (3 x 10 mL). The organic phase was collected, dried over anhydrous sodium sulfate, and analyzed by NMR and IR spectroscopy. The solid obtained from the filtration was washed and analyzed by IR (**Figure 3.39**, red spectrum), resulting in that the phase is pure without any contamination coming from the ligand.

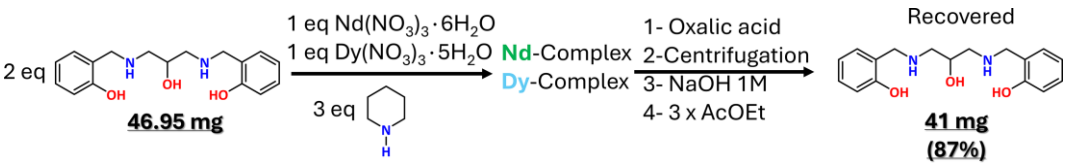

Scheme 3.7. Scheme of the recovery protocol for H_2Salpen.

As shown in the figures below, the NMR spectrum of the pure ligand (**Figure 3.38**) and that of the recovered ligand are identical, and the IR spectrum (**Figure 3.39**) exhibits the same absorption bands. The entire process enabled the recovery of 87% by weight of the initially employed ligand.

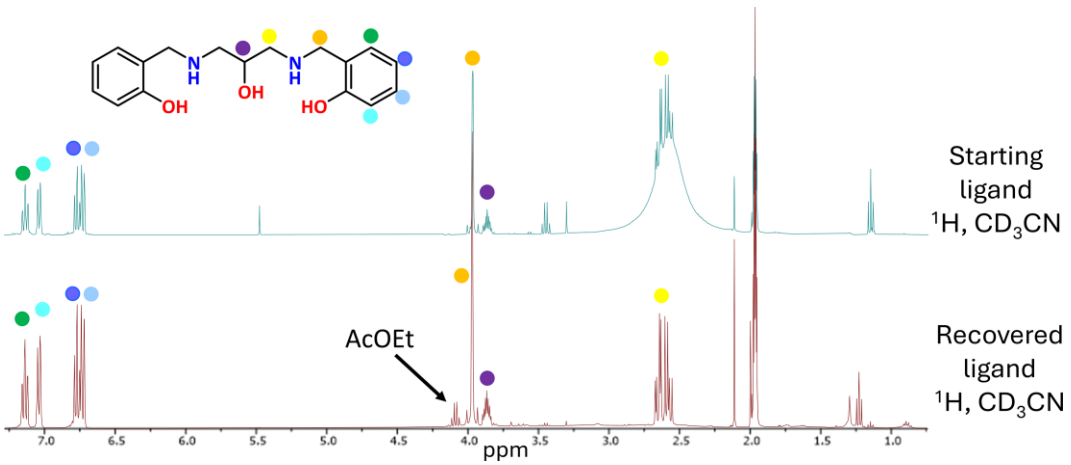

Figure 3.38. ^{1}H NMR (400 MHz, CD_3CN) spectrum of H_2Salpen recovered (bottom) and reference (top).

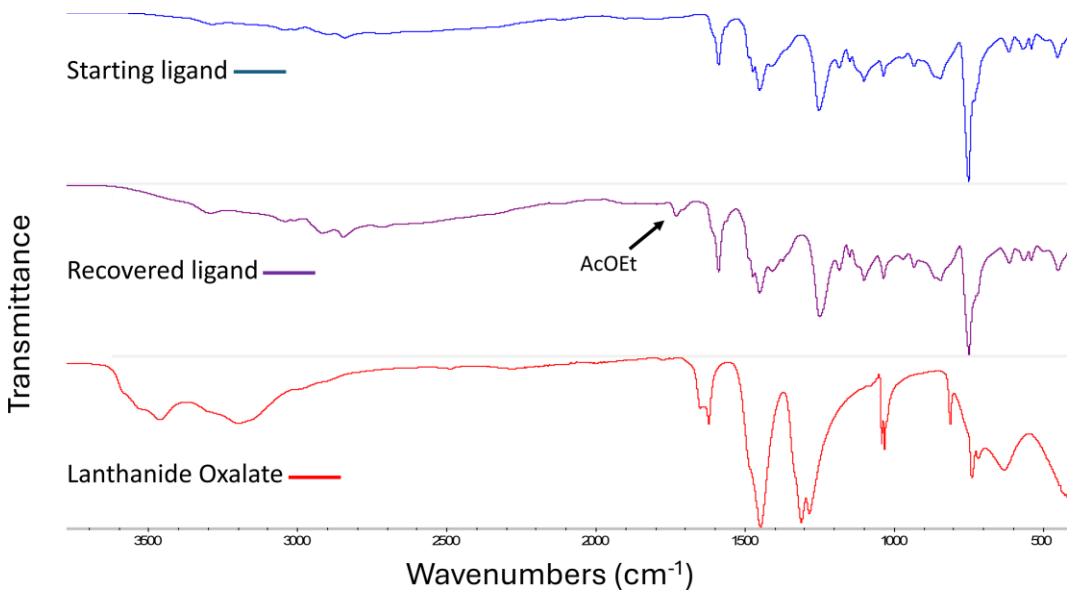

Figure 3.39. FT-IR ATR spectrum of H_2Salpen recovered (blue), reference (purple) and lanthanide oxalate (red).

3.4 Conclusion

Ligands belonging to the Salpen family are characterized by good flexibility and an N_2O_3 donor atom set that makes them suitable for lanthanide complexation. However, unlike the previous case (Trensal ligand, see **Chapter 2**), a single ligand coordinated to the metal is not sufficient to satisfy its coordination needs, as evidenced by observed crystal structures. Despite their tendency to form polynuclear species with very similar structures, confirmed by both X-ray structures and solution speciation, these ligands are capable of forming Nd and Dy complexes with a marked difference in solubility in ethanol. Since the stoichiometry of these species formed by these ligands in solution are nearly identical, we can assume that the different solubility of the Nd and Dy complexes is due to the neutral and/or ionic nature of the complexes formed, or the presence of more solvent molecules coordinated to one or more metal centers in solution. In any case, the complexes of [Dy(Salpen$^{p\text{-}OMe}$)] and [Dy(Salpen)] are soluble in ethanol, while the Salpen$^{o\text{-}tBut}$ ligand forms complexes with an inverse solubility compared to the other two, where the Dy complex is insoluble. The ability to form complexes with such different solubility in a single reaction step under very mild conditions allows these systems to compete with the various existing separation methods, which use large quantities of extractants and solvents. Although separation with these types of ligands is not yet optimized, it represents a promising starting point for the development of new, low-cost, and sustainable specific ligands capable of further separating Dy and Nd.

3.5 Experimental section

3.5.1 Materials and methods

All chemicals were purchased from Merck and Alfa Aesar and were used without further purification. Anhydrous solvents were dried and stored over molecular sieves (3 Å). The UV-Vis spectra were collected on a Photodiode Array Lambda 465 spectrophotometer provided with a Peltier thermostat, using 1 cm path length quartz cuvettes. Spectra of the ligand/metal systems were acquired in the spectral range 200-600 nm. NMR experiments were performed on either a Brüker Avance 400 MHz instrument at 298 K and chemical shifts are reported in ppm relative to tetramethylsilane. Infrared (IR) spectra were obtained with a Thermo Scientific Nicolet 5PCFT-IR-ATR (diamond) spectrometer in the 4000-400 cm^{-1} interval. ESI-MS analyses were carried out by using a Waters Acquity Ultra Performance LC with Waters Acquity SQ Detector and with ESI interface. The mixtures were analyzed in negative ionization mode by direct perfusion in ESI-MS interface; injection flow-rate= 20 ml/min. Elemental analyses (CHN) were performed on Thermo Fischer Scientific FlashSmart CHNS analyzer.

3.5.2 X-ray data collection

Single crystal data were collected with a Bruker D8 PhotonII area detector diffractometer (Mo Kα: λ = 0.71073 Å). Complete datasets were obtained by merging several series of exposure frames collected at 200 K. An absorption correction was applied with the program SADABS.[70] The structures were solved with ShelxT)[71] and refined on F^2 with full-matrix least squares (ShelxL)[72] using the

Olex2 software package.[73] Non hydrogen atoms were refined with anisotropic thermal parameters for all compounds. In **(1)**, both THF molecules of crystallization and coordination were disordered over two sites with site occupancy factors of 0.75/0.25 and 0.5/0.5, respectively. In **(5)**, the ethanol molecule bound to the metal center was disordered over two sites (0.54/0.46 occupancy factors), and one of the ethyl residues of the Et_3NH^+ cation was disordered over two sites (0.74/0.36 occupancy factors. In **(4)**, the acetone molecule of crystallization was disordered in two positions having site occupancy factors of 0.84/0.26. The hydroxyl hydrogen atoms of **(4)** were located from the different Fourier map and refined. The molecular structure of **(3)** contains several DMF molecules of crystallization, some of which were disordered. In particular, O1S is disordered according to a 180 deg. rotation of the molecular plane and both images acts as HB acceptor towards a water molecule (O21W) of coordination. A DMF molecule was refine with 0.25 site occupancy factors (O2S), whereas the remaining DMF molecules (O3S-O5S) were refined with 0.5 s.o.f.

3.5.3 UV-visible titration and stability constant calculations

The UV–vis spectroscopic titration of ligands with $Dy(NO_3)_3{\cdot}5H_2O$ and $Nd(NO_3)_3{\cdot}6H_2O$ was performed on a Photodiode Array Lambda 465 using 1 cm path length quartz cuvettes. The stock solutions of the metals and ligands were prepared in 96% ethanol. The initial volume of the ligand solution ($C_L = 5{\cdot}10^{-5}$ M) in ethanol was 2.73 mL, and aliquots (10 uL to 20 uL) of the metal stock solution (1.5 mM) were added for titration. The stoichiometric ratio of 1:3 ligand:triethylamine was kept constant, while the ratio of ligand:metal ranged from 1:0-3. Spectra were recorded in the range of 200-600 nm. The stability constants of the ligand

complexation with Dy^{III} and Nd^{III} were determined by fitting the titration data using HypSpec2014 software.[76]

3.5.4 ICP-AES analysis

The metal content of the sample was determined via Inductively Coupled Plasma Atomic Emission Spectroscopy (ICP-AES). From 5 to 15 mg of solid sample were suspended in 5 mL of HNO_3 65% and 1 mL of H_2O_2 30%, then digested in a Milestone microwave MLS-1200 MEGA (digestion sequence: 1 min at 250-Watt, 1 min at 0-Watt, 5 min at 250-Watt, 5 min at 400-Watt, 5 min at 650-Watt, 5 min of cooling). The solutions were diluted to 50 mL with bi-distilled water and analyzed using an emission spectrometer JY 2501 with coupled plasma induction in radial configuration HORIBA Jobin Yvon (Kyoto, Japan), ULTIMA2 model. Instrumental features: monochromator Model JY 2501; focal length 1 m; resolution 5 pm; nitrogen flow 2 L/min. ICP source: nebulizer Meinhard, cyclonic spraying chamber; argon flow 12 L/min; wavelengths range 160-785 nm; optical bench temperature 32 °C. The wavelength used for quantitative analysis was chosen by examining the emission line with greater relative intensity, ensuring that there was no spectral interference with the Argon emission lines. Acquisition parameters: wavelength Fe (nm): 238.204, Nd (nm): 410.946 and Dy (nm) 394.469; Voltage (V): 580; gain: 100. The quantitative analysis was performed after the acquisition of a calibration line using standard solutions in HNO_3 10% to simulate the final acidity of the samples; the concentration range of the standards varied from 0.1 mg/L to 50 mg/L of Fe, Dy and Nd. Data acquisitions and processing were performed using the ICP JY v 5.2 software (Jobin Yvon). Measurements were performed in triplicate and the syntheses performed in duplicates.

3.6 Chemistry

3.6.1 Synthesis of the ligands and of the complexes

General procedure for synthesis of ligands L_1-L_4. Salicylaldehydes (2 mmol) was dissolved in absolute ethanol (60 mL). 1,3-Diaminopropan-2-ol (1 mmol) was then added while the mixture was being stirred at 50 °C. The resulting yellow solution was stirred and refluxed for 5 h. The crude product was concentrated under reduced pressure, resulting in a yellow oil, which was subsequently crystallized overnight in ethanol/hexane at -4 °C. The product was then isolated by filtration, washed with cold ethanol, hexane and dried under vacuum, yielding a yellow crystalline solid.

Salpen (L_1). Yellow solid, 85% yield. ^{1}H NMR (400 MHz, DMSO-d6): δ 13.55 (s, 2H, OH), 8.55 (s, 2H, CH-N_{imine}), 7.46 (dd, J = 7.6, 1.7 Hz, 2H, Ar), 7.37 – 7.30 (dt, 2H, Ar), 6.94 – 6.86 (m, 4H, Ar), 5.22 (d, J = 5.3 Hz, 1H, OH), 4.03 (m, 1H, CH), 3.79 (ddd, J = 12.2, 4.4, 1.3 Hz, 2H, CH_2-N), 3.62 (ddd, J = 12.1, 6.6, 1.1 Hz, 2H, CH_2-N). ESI-MS (MeOH): m/z 297 $[L]^-$. Elemental Analysis [Calc. for $C_{17}H_{18}N_2O_3(H_2O)_{0.2}$, %]: C, 67.60; H, 6.14; N, 9.28. [Found %]: C, 67.64; H, 6.03; N, 9.22.

Salpen$^{p\text{-}OMe}$ (L_2). Yellow solid, 87% yield. ^{1}H NMR (400 MHz, DMSO-d6): δ 12.88 (s, 2H, OH), 8.51 (s, 2H, CH-N_{imine}), 7.06 (d, J = 3.1 Hz, 2H, Ar), 6.96 (dd, J = 8.9, 3.1 Hz, 2H, Ar), 6.83 (d, J = 8.9 Hz 2H, Ar), 5.19 (d, J = 5.3 Hz, 1H, OH), 4.02 (m, 1H, CH), 3.78 (ddd, J = 12.0, 4.4, 1.3 Hz, 2H, CH_2-N), 3.72 (s, 6H, O-CH3), 3.60 (ddd, J = 12.1, 6.6, 1.1 Hz, 2H, CH_2-N). ESI-MS (MeOH): m/z 357 $[L]^-$. Elemental Analysis [Calc. for $C_{19}H_{22}N_2O_5$, %] : C, 63.65; H, 6.19; N, 7.81. [Found %]: C, 63.81; H, 6.26; N, 7.85.

Salpen$^{p\text{-}Cl}$ (L_3). Yellow solid, 81% yield. ^{1}H NMR (400 MHz, CD_3CN-d3): δ 13.55 (s, 2H, OH), 8.43 (s, 2H, CH-N_{imine}), 7.42 (d, J = 2.7 Hz, 2H, Ar), 7.33 (dd, J = 8.8, 2.7 Hz, 2H, Ar), 6.92 (d, J = 8.8 Hz 2H, Ar), 4.18 (m, 1H, OH), 3.86 (ddd, J = 12.4, 4.2, 1.3 Hz, 2H, CH_2-N), 3.66 (ddd, J = 12.4, 6.9, 1.2 Hz, 2H, CH_2-N), 3.38 (d, J = 5.4 Hz, 1H, OH). ESI-MS (MeOH): m/z 365 $[L]^-$. Elemental Analysis [Calc. for $C_{17}H_{16}N_2O_3Cl_2$, %]: C, 55.72; H, 4.4; N, 7.65. [Found %]: C, 56.06; H, 4.37; N, 7.61.

Salpen$^{o\text{-}tBut}$ (L_4). Yellow solid, 84% yield. ^{1}H NMR (400 MHz, CD_3CN-d3): δ 14.23 (s, 2H, OH), 8.49 (s, 2H, CH-N_{imine}), 7.38 (dd, J = 7.8, 1.7 Hz, 2H, Ar), 7.25 (dd, J = 7.6, 1.7 Hz, 2H, Ar), 6.87 (t, J = 7.7 Hz, 2H, Ar), 4.19 (m, 1H, CH), 3.86 (ddd, J = 12.4, 4.3, 1.3 Hz, 2H, CH_2-N), 3.68 (ddd, J = 12.5, 6.9, 1.2 Hz, 2H, CH_2-N), 3.43 (d, 1H, J = 5.4 Hz, OH), 1.45 (s, 18H, $C(CH_3)_3$). ESI-MS (MeOH): m/z 409 $[L\text{-}]^-$. Elemental Analysis [Calc. for $C_{25}H_{34}N_2O_3$, %]: C, 73.13; H, 8.34; N, 6.82. [Found %]: C, 72.81; H, 8.37; N, 7.12.

General Procedure for the Synthesis of Ligands H_2L_1–H_2L_4. A yellow solution of L_1-L_4 (1 mmol) in methanol (5 mL) was stirred at room temperature before adding $NaBH_4$ (3 mmol) in small amounts over 15 minutes. Upon the addition of $NaBH_4$, the solution progressively changed from bright yellow to colorless. The reaction mixture was stirred for 1h before quenching it with distilled water (ca. 1 mL). Methanol was removed under reduced pressure and the crude product was extracted with dichloromethane (3x25 mL). The organic layer was dried with Na_2SO_4, filtered, and the solvent was removed by evaporation. The resulting frothy white solid was dried under vacuum.

H_2Salpen (H_2L_1). Frothy white solid, 86% yield. ^{1}H NMR (400 MHz, CD_3CN-d3): δ 7.13 (td, J = 7.7, 1.7 Hz, 2H, Ar), 7.03 (dd, J = 7.5, 1.7 Hz, 2H, Ar), 6.80 – 6.69 (m, 4H, Ar), 3.97 (d, J = 1.8 Hz, 4H, CH_{2bz}-NH), 3.87 (m, 1H, CH), 2.67 – 2.52 (m, 4H, CH_2-NH). ESI-

MS (MeOH): m/z 301 $[L]^-$. Elemental Analysis [Calc. for $C_{17}H_{22}N_2O_3 \cdot (CH_2Cl_2)_{0.2}$, %]: C, 64.71; H, 7.07; N, 8.78. [Found %]: C, 64.88; H, 7.06; N, 9.08.

$H_2Salpen^{p\text{-}OMe}$ (H_2L_2). Frothy white solid, 70% yield. ^1H NMR (400 MHz, CD_3CN-d3): δ 6.71 (dd, J = 8.8, 2.9 Hz, 2H, Ar), 6.68 – 6.61 (m, 4H, Ar), 3.97 (d, J = 1.9 Hz, 4H, CH_{2bz}-NH), 3.84 (m, 1H, CH), 3.71 (s, 6H, O-CH_3), 2.68 – 2.52 (m, 4H, CH_2-N). ESI-MS (MeOH): m/z 361 [L]−. Elemental Analysis [Calc. for $C_{19}H_{26}N_2O_5 \cdot (CH_2Cl_2)_{0.1}$, %]: C, 61.84; H, 7.12; N, 7.55. [Found %]: C, 62.18; H, 7.16; N, 7.68.

$H_2Salpen^{p\text{-}Cl}$ (H_2L_3). Frothy white solid, 85% yield. ^1H NMR (400 MHz, CD_3CN-d3): 7.12 (dd, J = 8.6, 2.7 Hz, 2H, Ar), 7.05 (d, J = 2.6 Hz, 2H, Ar), 6.71 (t, J = 8.6 Hz, 2H, Ar), 3.94 (d, J = 2.5 Hz, 4H, CH_{2bz}-NH), 3.84 (m, 2H, CH), 2.66 – 2.54 (m, 4H, CH_2-N). ESI-MS (MeOH): m/z 369 $[L]^-$. Elemental Analysis [Calc. for $C_{17}H_{20}N_2O_3Cl_2$, %]: C, 55.22; H, 5.44; N, 7.56. [Found %]: C, 55.62; H, 5.22; N, 7.22.

$H_2Salpen^{o\text{-}tBut}$ (H_2L_4). Frothy white solid, 90% yield. ^1H NMR (400 MHz, CD_3CN-d3): δ 7.16 (dd, J = 7.8 1.7 Hz, 2H, Ar), 6.88 (dd, J = 7.5, 1.6 Hz, 2H, Ar), 6.69 (t, J = 7.6 Hz, 2H, Ar), 3.94 (s, J = 1.9 Hz, 4H, CH_{2bz}-N), 3.85 (m, 1H, CH), 2.66 – 2.55 (m, 4H, CH_2-N), 1.40 (s, 18H, $C(CH_3)_3$). ESI-MS (MeOH): m/z 413 $[L\text{-}]^-$. Elemental Analysis [Calc. for $C_{25}H_{38}N_2O_3(CH_2Cl_2)_{0.1}$, %]: C, 71.25; H, 9.1; N, 6.62. [Found %]: C, 71.20; H, 9.0; N, 6.25.

General Procedure for the Synthesis of Complexes. To a yellow solution of $Salpen^R$ (0.105 mmol) and $Ln(NO_3)_3 \cdot XH_2O$ (0.1 mmol) in 96% ethanol (4 mL) was stirred at 55°C for a few minutes before adding triethylamine (0.315 mmol). Upon the addition of the base, a precipitate formed, and the resulting mixture was stirred for 1h. After the reaction, the solid was filtered, washed with ethanol/hexane, and dried under vacuum, obtaining a pale-yellow solid.

[Dy(Salpen)]. Pale-yellow solid, yield XX %. Elemental Analysis [Calc. for $[(Dy_2(C_{17}H_{15}N_2O_3)_2(H_2O)_2))_{0.8}(Dy_6(C_{17}H_{15}N_2O_3)_4(OH)_4(H_2O)_2(NO_3)_2)_{0.2}]$, %]: C, 38.28; H, 3.21; N, 5.58; [Found %] C, 38.24; H, 3.25; N, 5.58.

[Nd(Salpen)]. Pale-yellow solid, yield XX %. Elemental Analysis [Calc. for $[Nd(C_{17}H_{15}N_2O_3)(H_2O)_{0.5}]$, %]: C, 45.74; H, 3.62; N, 6.27; [Found %] C, 45.73; H, 3.51; N, 6.25.

[Dy(Salpen$^{p\text{-}OMe}$)]. Pale-yellow solid, yield XX %. Elemental Analysis [Calc. for $[Dy_2(C_{19}H_{19}N_2O_5)_2(H_2O)]$, %]: C, 43.31; H, 3.82; N, 5.31; [Found %] C, 43.29; H, 3.99; N, 5.6.

[Nd(Salpen$^{p\text{-}OMe}$)]. Pale-yellow solid, yield XX. Elemental Analysis [Calc. for $[Nd_2(C_{19}H_{19}N_2O_5)_2(H_2O)_2]$, %]: C, 44.08; H, 4.08; N, 5.41; [Found %] C, 44.22; H, 3.94; N, 5.71.

[Dy(Salpen$^{p\text{-}Cl}$)]. Pale-yellow solid, yield XX. Elemental Analysis [Calc. for $Dy_3(C_{17}H_{13}N_2O_3Cl_2)_3(OH)(NO_3)(H_2O)$, %]: C, 36.52; H, 2.52; N, 5.84; [Found %] C, 36.6; H, 2.8; N, 5.72.

[Nd(Salpen$^{p\text{-}Cl}$)]. Pale-yellow solid, yield XX. Elemental Analysis [Calc. for $[Nd(C_{17}H_{13}N_2O_3Cl_2)(H_2O)]$, %]: C, 39.45; H, 2.72; N, 5.41; [Found %] C, 39.54; H, 2.77; N, 5.59.

[Dy(Salpen$^{o\text{-}tBut}$)]. Pale-yellow solid, yield 23 mg. Elemental Analysis [Calc. for $[Dy(C_{25}H_{31}N_2O_3)(H_2O)]$, %]: C, 51.26; H, 5.66; N, 4.76; [Found %] C, 51.31; H, 5.83; N, 4.58.

[Nd(Salpen$^{o\text{-}tBut}$)]. Pale-yellow solid, yield 10 mg.

General Procedure for the Synthesis of Complexes. To a white solution of $H_2Salpen^R$ (0.105 mmol) and $Ln(NO_3)_3 \bullet XH_2O$ (0.1 mmol) in 96% ethanol (4 mL) was stirred at 55°C for a few minutes before adding piperidine (0.315 mmol). Upon the addition of the base, a precipitate formed, and the resulting mixture was stirred for 1h. After the reaction, the solid was filtered, washed with ethanol/hexane, and dried under vacuum, obtaining a colorless solid.

[Dy(H_2Salpen)]. Colorless solid, yield 24 mg. Elemental Analysis [Calc. for $[(Dy_2(C_{17}H_{19}N_2O_3)_2(H_2O)_2))_{0.85}(Dy_6(C_{17}H_{19}N_2O_3)_4(OH)_4(H_2O)_2(NO_3)_2)_{0.15}]$, %]: C, 39.74; H, 4.28; N, 4.12; [Found %] C, 39.79; H, 4.12; N, 5.81.

[Nd(H_2Salpen)]. Colorless solid, yield 31 mg. Elemental Analysis [Calc. for $(Nd_2(C_{17}H_{19}N_2O_3)_2(H_2O)_2)_{0.6}(Nd_6(C_{17}H_{19}N_2O_3)_4(OH)_2(H_2O)_8(NO_3)_2)_{0.4}$, %]: C, 38.11; H, 4.22; N, 5.97; [Found %] C, 37.87; H, 4.27; N, 6.24.

Part 2: **Lanthanide^{III}/Gallium^{III} Metallacrowns: highly luminescent complexes for biological imaging**

Chapter 4: **metallacrown, applications and new perspectives**

4.1 Introduction

4.1.1 The history of metallasupramolecular structures

In 1967, Pedersen introduced the synthesis of macrocyclic crown ethers and demonstrated their capacity to selectively interact with alkali and alkaline earth metal ions.[77] This groundbreaking discovery sparked widespread interest among chemists in the field of supramolecular compounds.[78,79] Following Pedersen's pioneering work, a wide range of organic macrocyclic molecules were developed, such as thiacrown ethers[77], azacrown ethers, calixarenes[80], chiral crown ethers[81], cryptands[82].[77,83] These macrocyclic structures have proven useful for binding cations and anions, serving as ion transport agents, stabilizing reactive molecules, and acting as hosts for chemical reactions. Despite these advancements, inorganic chemistry initially lagged in developing metal-containing supramolecular structures. However, there has been a recent surge in both the variety and number of metallasupramolecular complexes synthesized. Beyond their structural beauty, metallamacrocycles are also studied for their potential applications: these compounds have been utilized as agents for cation, anion, and molecular recognition, as catalysts, as building blocks for extended solid materials, and as sensors.

4.1.2. Metallacrowns

Metallacrowns (MC) are the inorganic analogues of crown ethers (**Figure 4.1a and 4.1b**). Traditionally, a metallacrown is described as a cyclic structure composed of repeating units of -[M-N-O]$_n$, where the metal (M) and nitrogen (N) atoms in the ring replace the methylene carbons found in crown ethers. Similar to crown ethers, the naming of metallacrowns is determined by the size of the ring and the number of oxygen donor atoms within it. The nomenclature therefore consists of indicating the size of the organic skeleton by the total number of atoms it contains, followed by the abbreviated name "MC" (metallacrown), and ending with the number of oxygen atoms present. For instance, in 12-MC-4, '12' indicates the total number of atoms in the ring, while '4' represents the number of oxygen atoms. The most studied ring sizes are 9-MC-3 [84], 12-MC-4[85], and 15-MC-5[86].

The first metallacrown structure was reported by Pecoraro and Lah in 1989.[87] Since then, the field has witnessed significant growth, with research expanding globally across laboratories in many countries. A broad spectrum of metallacrown structures has been synthesized since this initial discovery, and they have been employed in various applications, including as antibacterial agents, in constructing two- and three-dimensional solid frameworks, in stabilizing reactive molecules, and as single-molecule magnets.

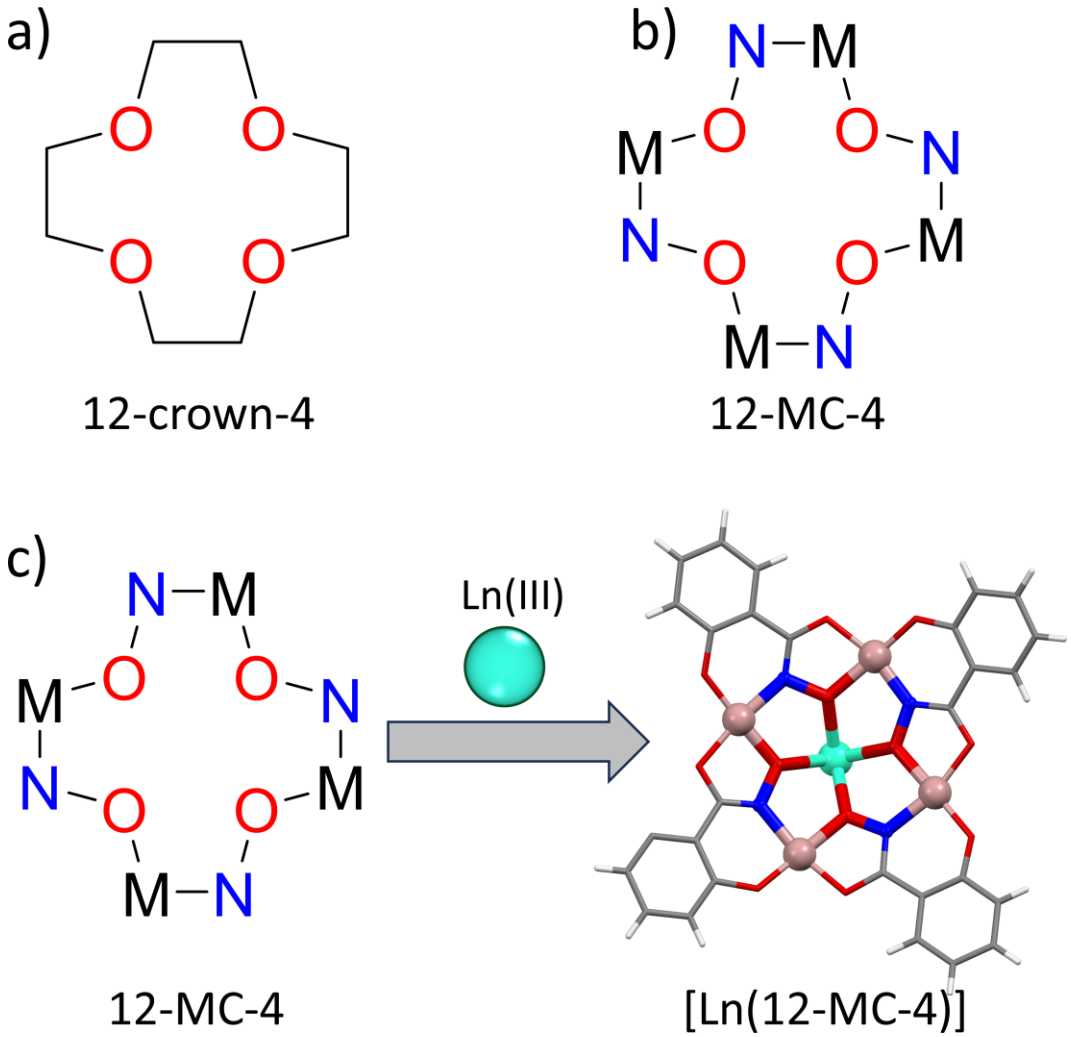

Figure 4.1. Representation of a crown ether (a), the analogy metallacrown (b) and the 12-MC-4 encapsulating a Ln^{III} ion c). M = pink, Ln = green, N = blue, O = red, C = carbon, H = white.

As shown in **Figure 4.1c**, the cavity formed by the inorganic ring of the metallacrown, combined with the Lewis basicity of the oxygen atoms facing inward, makes these entities effective cages for encapsulating cationic species such as transition metals or lanthanides. This unique metallacyclic framework leads to the

formation of supramolecular species with peculiar and in some cases excellent luminescent[88] and magnetic[89] properties.

4.1.3 General features of a metallacrown (MC)

The assembly of these molecules occurs spontaneously in solution: it requires the presence of a central (core) metal ion which templates the metallacrown (MC) formation, and polyfunctional ligands which bridge between the (ring) metal ions (usually d-transition metals) that compose the metallamacrocyclic framework. The most studied metallacrowns have been assembled using hydroxamic acid derivatives and, in particular as shown in **Scheme 4.1**, β-aminohydroxamic acids (or salicylhydroxamic acid).[90–93] The use of β-aminohydroxamic acids and related ligands is very convenient since the completely deprotonated hydroxamite group can act as a (O,O^-) chelating group on one ring metal, and it provides the additional N^- donor atom required to form the (M–N–O)n metallacrown connectivity.[90,94] An additional donor group of the ligand (i.e., NH_2 in β-aminohydroxamates or a deprotonated phenolic OH in salicylhydroxamates) coordinates to a fourth equatorial coordination position of the ring metal.[95] While the equatorial positions on the ring metals saturate upon metallacrown assembly and ring closure, axial coordination positions remain available on the metals on both sides of the metallacycle. These sites are of paramount importance to determine peculiar structural and functional properties of metallacrowns, such as the coordination of anionic ancillary ligands or the formation of helicates in the solid state.

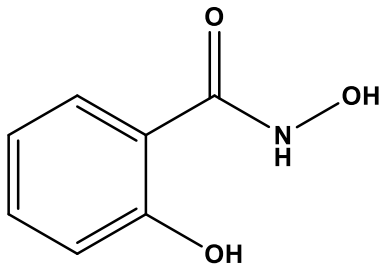

H_3shi

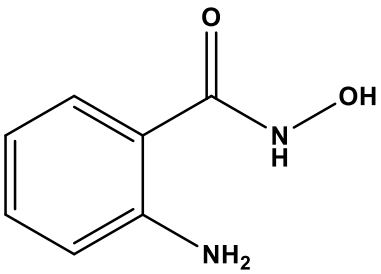

Anha

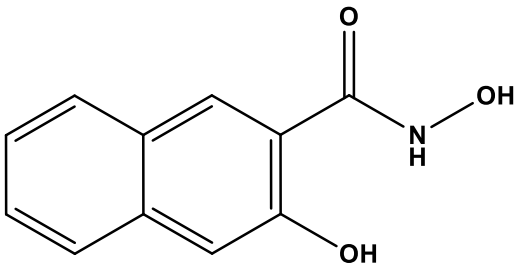

Nha

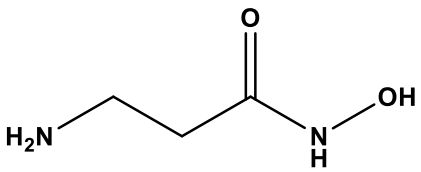

Alaha

Scheme 4.1. Scheme of β-hydroxamic acids. β-Alaha:β-L-alaninehydroxamicacid; H_3shi:salicylhy-droxamicacid; Nha:3-hydroxy-2-naphthylhydroxamicacid; Anha:anilinehydrox-amicacid.

4.1.4 Properties of metallacrown (MC)

Lanthanide metallacrowns have been extensively studied for potential applications as contrast agents in magnetic resonance imaging (MRI), for the selective complexation of lanthanides, and as hosts for the recognition of carboxylates. However, due to the presence of lanthanide ions encapsulated in the cavity, lanthanide-containing metallacrowns exhibit the most interesting properties in their behavior as single-molecule magnets (SMMs) and their distinctive

luminescence. In this thesis, the synthesis of ligands and complexes is presented with the aim of developing new compounds for biological tissue imaging.

4.1.5 The Luminescence Properties of Lanthanides

Lanthanide^{III} ions (Ln^{3+}) possess exceptional luminescence properties due to their unique electronic configurations, making them valuable for diverse applications. Key features of Ln^{3+} ions include sharp emission bands, long luminescence lifetimes, and strong resistance to photobleaching. These properties are advantageous in areas such as bioanalysis, biological imaging, solar energy conversion, diode displays, and telecommunications.[88] The luminescence of Ln^{3+} ions are primarily a result of electronic transitions within their 4f orbitals, which are well-shielded by outer 5s and 5p orbitals. Ln^{3+} ions provide a range of emission bands across the visible and near-infrared (NIR) spectral regions, with emission wavelengths dependent on the specific Ln^{3+} ion. However, the intrinsic f-f transitions of these ions are Laporte-forbidden, resulting in low molar absorption coefficients and, consequently, inefficient direct excitation. This limitation can be overcome using the "antenna effect," where a highly absorbing chromophore, known as an "antenna," is placed close in space to the Ln^{3+} ion. When excited by electromagnetic radiation, the antenna group transfers energy to the Ln^{3+} ion, inducing luminescence as the system returns to its ground state. This process, known as the “antenna effect”, is illustrated in **Figure 4.2**. This strategy allows for the creation of various Ln^{3+}-based luminescent complexes and nanomaterials, where organic ligands are used to tune emission wavelengths within the visible and NIR regions, depending on the selected Ln^{3+} ion.

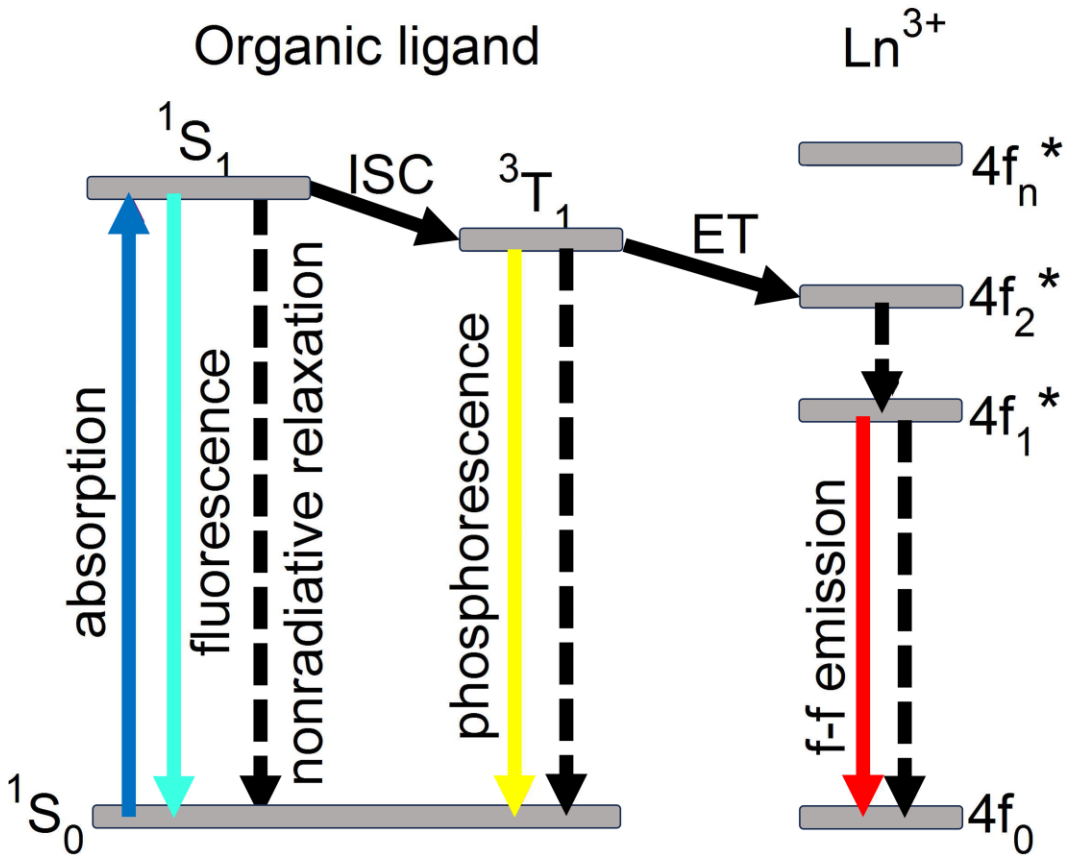

Figure 4.2. Representation of the antenna effect that allows energy transfer to the lanthanide ion from the excited conjugated ligand.

A critical challenge in developing luminescent Ln^{3+}-based coordination compounds is protecting the Ln^{3+} ions from nonradiative deactivation processes. These processes are often caused by vibrational overtones of O-H, N-H, and C-H bonds. The likelihood of nonradiative deactivation is inversely proportional to the energy gap (ΔE) between the emitting level of the Ln^{3+} ion and the highest energy level of the ground multiplet. Effective design strategies must consider this to maximize the luminescence efficiency of Ln^{3+}-based systems.[96]

4.1.6 Metallacrowns as Superior Multifunctional Agents for Tumor Targeting and Optical Imaging

For the reasons described in the previous sections metallacrowns, and particularly those incorporating lanthanide ions (Ln^{3+}), have emerged as highly effective imaging agents for biological tissues, offering distinct advantages over traditional fluorescent probes. Unlike common organic dyes, MCs exhibit superior photophysical properties that include sharp emission bands highly insensitive to the surrounding microenvironment, large Stokes shifts, high quantum yields, and robust resistance to photobleaching. Perhaps importantly, these features enable long-term or repetitive quantitative experiments. Also, sharp emission bands allow selective detection of Ln emission even in the presence of other fluorophores in the medium.

Starting from early 2010s, a series of highly emitting Ln-containing metallacrowns have been developed. The main structural feature in these compounds is the presence of a Ln^{III} ion in the MC cavity that, by virtue of ancillary ligands or by virtue of a complex. Moreover, MCs effectively overcome the fluorescence quenching often caused by the presence of high-energy O-H, N-H, and C-H vibrations in biological environments. This is achieved through strong protection against non-radiative deactivation pathways, which is one of the key reasons for their enhanced performance. Additionally, MCs can be designed to emit in the near-infrared (NIR) region, enhancing the signal-to-noise ratio and minimizing autofluorescence in biological tissues. This property, combined with their ability to selectively target and label specific cell types, such as necrotic cells, without disrupting cellular morphology, positions metallacrowns as promising multifunctional agents for both imaging and therapeutic applications in biological research and medicine.

4.1.7 The Therapeutic Window for Tissue Imaging (UV-Visible and NIR spectroscopy)

Optical imaging of biological tissues encounters significant challenges due to light absorption and scattering, particularly in the ultraviolet (UV) and visible regions of the spectrum.[97,98] In these ranges, chromophores in biomolecules, such as hemoglobin, absorb incident light strongly, limiting the depth of light penetration and reducing the effectiveness of imaging techniques. Additionally, tissue autofluorescence[99], arising from endogenous molecules like riboflavin, flavins, NADH, collagen, and melanin, creates background noise that interferes with accurate signal detection.[100,101] This autofluorescence is especially problematic in the UV and visible ranges, further complicating the imaging process. As shown in **Figure 4.3**, there is a spectral range known as the 'therapeutic window,' defined as the region between 600 nm and 1300 nm, where light absorption and scattering by biological tissues are relatively low. This range is particularly advantageous for optical imaging techniques, as it allows for deeper light penetration into tissues while minimizing unwanted interactions.[102,103]

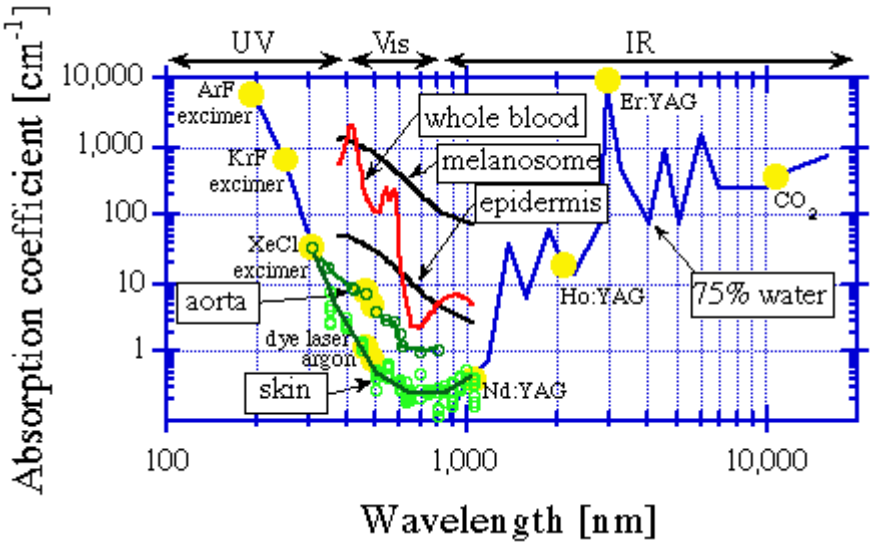

Figure 4.3. Plot of the observed absorption coefficients of biological tissues and fluids at different wavelengths. The main light sources are also indicated on the plot as yellow spots at their respective emission wavelengths. (Reprinted from: S. L. Jacques, K.Lee, and J. C. Ramella-Roman, Proc. SPIE 4001, 14-28, 2000.).

Within this spectral window[104], key tissue components, such as water, blood, and melanosomes, exhibit variable and different absorption features. Although blood and melanosomes[105] are strong absorbers in the red and near-infrared (NIR) regions, their overall impact on absorption is minimal due to their low volume fraction in tissues like the epidermis. Water, on the other hand, shows increased absorption at wavelengths longer than 1300 nm, establishing an upper limit for effective imaging within this window. The reduced absorption in the NIR range of the therapeutic window means that less light energy is required for imaging, which, in turn, minimizes the risk of thermal damage to tissues. Additionally, light scattering is lower in the NIR compared to the visible spectrum, allowing photons to penetrate deeper into tissues and return to the surface with minimal loss.[106] These properties make the NIR range ideal for non-destructive optical measurements, especially in thick or bulky tissues where deep-tissue imaging is needed.[107]

Fluorescence imaging, particularly in the NIR region, benefits significantly from these advantages. When conducted in the NIR range, issues such as high absorption by blood, lipids, and water, as well as tissue autofluorescence, are substantially reduced. Lower photon absorption combined with decreased light scattering results in clearer images with higher sensitivity and reduced background noise. This makes NIR fluorescence imaging especially useful for medical applications, such as

detecting and monitoring tumor cells and assessing therapeutic interventions. By carefully selecting appropriate NIR fluorophores and optimizing imaging conditions, NIR fluorescence imaging can achieve high sensitivity and spatial resolution. This approach enables more accurate, non-invasive, in vivo diagnostics, making it a powerful tool for monitoring treatments and understanding biological processes in real time.

4.1.8 Fluorescent probe for targeting

Fluorescence-based molecular markers have been essential tools in biomolecular imaging since the 1940s, when fluorescein isothiocyanate (FITC)-labeled antibodies were first introduced.[108] Initially used for analyzing fixed biological samples, the field has advanced significantly. Recent developments have enabled the use of fluorescent tags in living organisms, particularly through genetically encoded fluorescent proteins such as GFP.[109,110] Alongside these proteins, small-molecule fluorescent probes are increasingly used to label target cellular proteins directly. The choice of fluorophore[111] depends on both its chemical and photophysical properties, including reactivity, solubility, excitation and emission maxima, molar absorption, quantum yield, and photostability. The product of molar absorption and quantum yield ($\varepsilon \times \Phi$) is a key parameter for evaluating the sensitivity and brightness of a fluorophore, indicating its effectiveness in fluorescence imaging. Far-red and near-infrared (NIR) fluorophores are particularly valuable for imaging applications as they allow deeper penetration into living tissues compared to shorter wavelengths.[112] This deeper penetration is attributed to their ability to excite fluorescence with light that passes through tissues more efficiently. Additionally, these fluorophores are less affected by

background autofluorescence, improving the clarity of biological imaging. However, a significant limitation of many synthetic fluorophores in this range is their low quantum yield in aqueous solutions, which can reduce their effectiveness in fluorescence-based imaging.[113]

4.1.9 Recent Advances in the Synthesis of Multimeric Metallacrown Complexes

The functionalization of organic compounds to obtain ligands with precise geometries is crucial for the construction of 3D assemblies based on coordination systems. Crystal engineering is based on this concept, and examples such as MOFs demonstrate how the combination of precise ligand/linker topologies with the geometries and properties of coordination systems can be exploited to design innovative materials. Many systems have been discovered that exemplify this approach.[90]

The development of oligomeric MC systems has been driven by two main motivations. On the one hand, dimeric systems (**Figure 4.4c**) based on 12-MC-4 have proven to be stable constructs, particularly with respect to the interaction between Ln and solvent molecules, which reduces the decomposition of MCs and the quenching of luminescence.[114] On the other hand, porous MOF-like (**Figure 4.4a** and **Figure 4.4b**)[115] constructs based on MCs have been designed to exploit the magnetic and optical properties of the MCs themselves.

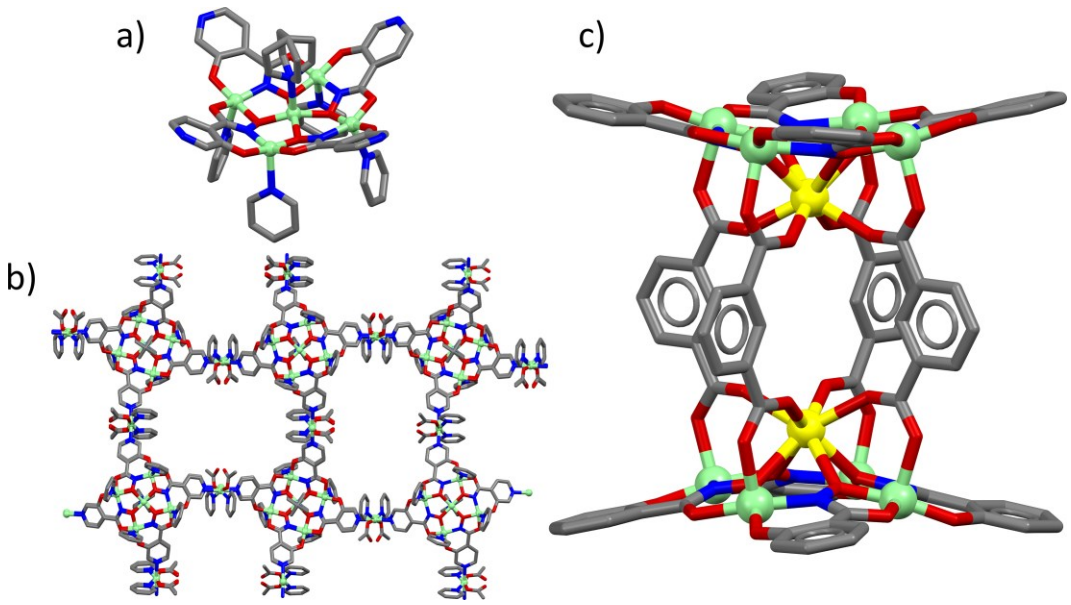

Figure 4.4. a) representation of a {M[12-$MC_{MII,hinHA}$-4]} basic unit of a metallacrown . b) Representation of one layer of the porous network building from {M[12-$_{MCMII,}$ $_{hinHA}$-4]} basic unit. c) representation of a dimeric metallacrown. Transition metal (green), lanthanide (yellow), nitrogen (blue), oxygen (red), carbon (grey). Hydrogen atoms are omitted for clarity.

The aim has been to exploit changes in the magnetic or spectroscopic properties of the porous material in the presence or absence of adsorbed guest molecules to create sensors for these molecules. Although no materials with these specific properties have yet been reported. Our research group has focused on the synthesis and characterization of oligomeric MC compounds. **Figure 4.5** shows the basic unit of a 12-MC-4, composed of 4 hydroxamic acid ligands, 4 Ga atoms, 1 lanthanoid in the center of the cavity, and 4 carboxylate ligands, also known as ancillary ligands, which bridge between the transition metals (Ga) and the lanthanoid in the cavity. Their role is to saturate the metal coordination, along with

any water or solvent molecules, and to impart greater stability to the molecule. However, it has been shown that by replacing these accessory ligands with more complex topologies, such as ditopic dicarboxylate ligands, it is possible to link two or more basic MC units, resulting in dimeric and trimeric entities.[116]

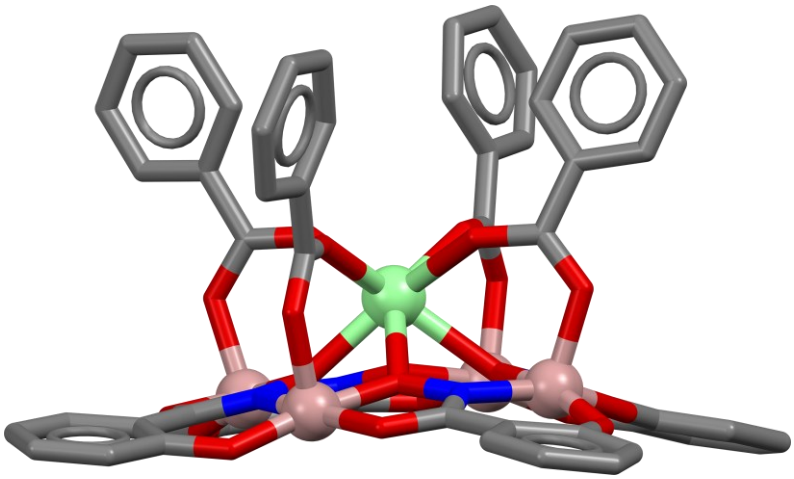

Figure 4.5. Representation of a basic $\{[Ln(12\text{-}MC_{Ga,shi}\text{-}4)(OBz)_4]\}^-$ unit consisting of Ga atoms (pink), oxygen atoms (red), nitrogen atoms (blue), and the lanthanide (green).

The size and structure of the final assembly depend on the topology and the rigidity or flexibility of the dicarboxylate linkers (**Figure 4.6**). The isolation of several dimeric MC assemblies in recent years has led indeed to further investigation into the possibility of generating entities with more than two 12-MC-4 basic units linked together. In 2019, Wang and co-workers successfully created the first trimeric entity using terephthalic acid, which has two carboxylic groups oriented at an angle of 180° to each other.[116] The MC trimer is composed of three 12-MC-4 clusters,

each connected by two dicarboxylates per cluster, resulting in a total of six ligands bridging the MC assemblies. It was discovered that the key factor in determining whether a dimer or trimer is formed is the angle between the dicarboxylic groups. A 120° angle between the carboxylate groups leads to a dimeric entity due to steric constraints, while a linear (180°) angle results in a trimer (see **Figure 4.6**).

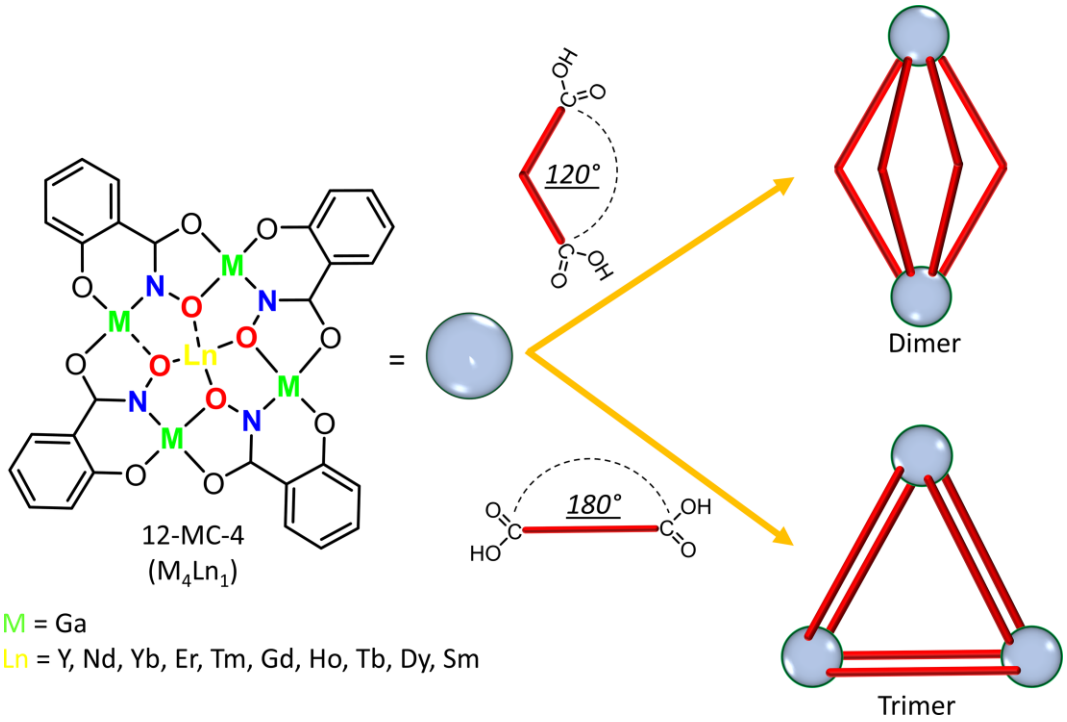

Figure 4.6. Representation of the dimeric and trimeric metallacrown. The pale gray ball represents the base unit of 12-MC-4, while the red line represents the ditopic ligand, showing two different angles between the carboxylic groups.

To date, only the magnetic properties of these trimeric structures have been studied, with no investigations into their luminescence properties. Additionally, no published work has yet explored the type of MC that forms when a carboxylic ligand with an angle between 120° and 180° is used. Finally, it is important to recall that the use of bridging ligands to obtain oligomeric MC systems can be advantageously

used to introduce antenna systems on assembly, either by using intrinsically absorbing ligands in the regions of interest or by functionalizing dicarboxylates with specific groups of interest.

Chapter5: **One-step assembly of Near-Infrared Emitting Lanthanide^{III}/Gallium^{III} Metallacrown Trimers using 2,2'-Bipyridine and Fluorenone Based Linkers**

5.1. Introduction

In this work, commercial dicarboxylic linkers were used to prepare oligomeric metallacrown (MC) systems. Two different linkers were selected for the following reasons. The bipyridyl linker (2,2'-bipyridine-5,5'-dicarboxylic acid, H_2bipy) is linear, and the 180° angle between the two terminal carboxylic acids makes it suitable for the formation of trimeric species, as reported for $[DyMn_4]_3$ MC assemblies.[116] Although the H_2bipy does not radically change the UV-vis absorption of the complex, it could potentially be used for the coordination of *d* metals of interest such as Ru^{III}. The fluorenone ligand (9-fluorenone-2,7-dicarboxylic acid, H_2frn), on the other hand, present a more extended π system than the H_2bipy ligand, resulting in an absorption band close to the visible at λ = 395 nm (**Scheme 5.1**) that could be used for Ln^{III} sensitization. With the two terminal carboxylic acids forming an angle of approximately 167°, the H_2frn linker opens up the possibility of forming oligomeric systems beyond dimeric and trimeric ones.

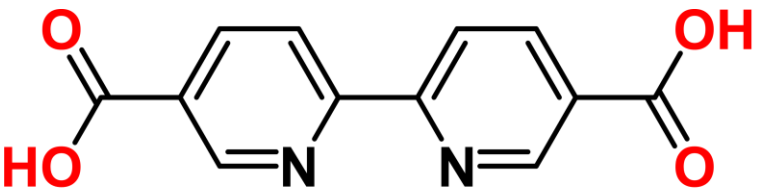

2,2'-bipyridine-5,5'-dicarboxylic acid
H_2bipy

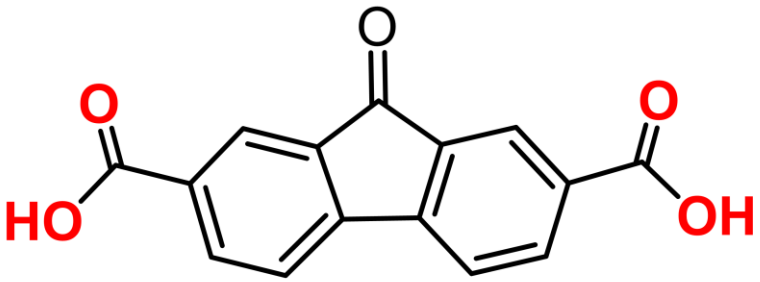

9-fluorenone-2,7-dicarboxylic acid
H_2frn

Scheme 5.1. Left: 2,2'-bipyridine-5,5'-dicarboxylic acid (H_2bipy). Right: 9-fluorenone-2,7-dicaboxylic acid (H_2frn).

5.2. Aim of the project

The aim of this research is the synthesis of novel supramolecular entities based on 12-MC-4 scaffolds that are linked together with dicarboxylic ligands. H_2bipy features a flat angle (180°) between the two carboxylic acids, while H_2frn exhibits an angle of about 167°. These new MCs were characterized both in solution (^{1}H NMR of Y^{III} analogues, UV-vis spectroscopy and ESI-MS) and in the solid state (single crystal and powder X-ray diffraction, ATR FTIR spectroscopy). The spectroscopic properties were recorded both in solution and the solid state.

5.3. Results and discussions

5.3.1 Synthesis and characterization of {[Ln(12-$MC_{Ga,shi}$-4)]$_3$(bipy)$_6$}(HNEt$_3$)$_3$ MCs via ESI-MS and ^{1}H NMR

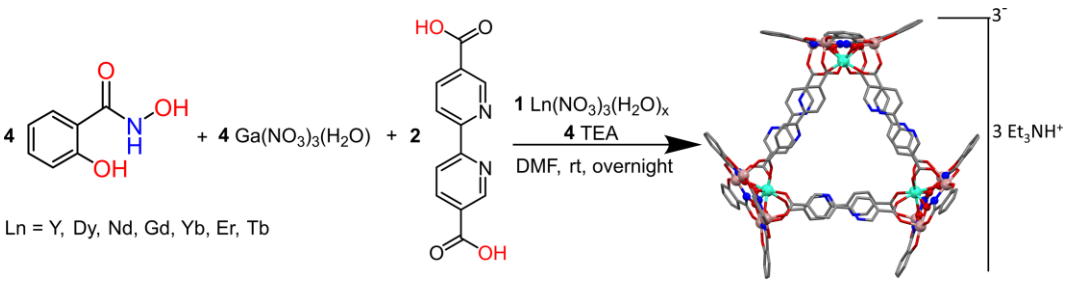

Scheme 5.2. Synthesis of trimeric {[Ln(12-$MC_{Ga,shi}$-4)]$_3$(bipy)$_6$}(HNEt$_3$)$_3$ MCs.

The synthesis of the trimeric {[Ln(12-$MC_{Ga,shi}$-4)]$_3$(bipy)$_6$}(HNEt$_3$)$_3$ metallacrown (**Scheme 5.2**) was carried out using a procedure similar to that reported in the literature for similar systems.[116] All solid reagents were mixed in dimethylformamide (DMF), obtaining a pale gray suspension. Triethylamine was added as the base required to deprotonate both the H_3shi ligands and H_2bipy linkers. Under stirring, ca. 15 minutes after base addition the turbidity of the mixture nearly disappeared, and the color of the solution turned to pale yellow. The stirring was pursued overnight at room temperature. The solution was then filtered and set up for crystallization by slow evaporation. Crystals were obtained after two weeks. The use of inorganic bases such as $NaHCO_3$ or NaOH in place of NEt_3 resulted in the formation of colloidal suspensions that could not be removed by filtration.

The MCs were isolated as microcrystalline powders and were characterized by ESI-MS to confirm the formation of the trimeric species. Indeed, **Figures 5.1-5.6** display the mass spectra of the purified crystalline powders, showing the predominance of a three time negatively charged species as expected, which is confirmed by isotopic peaks being separated by a m/z difference of 0.3.

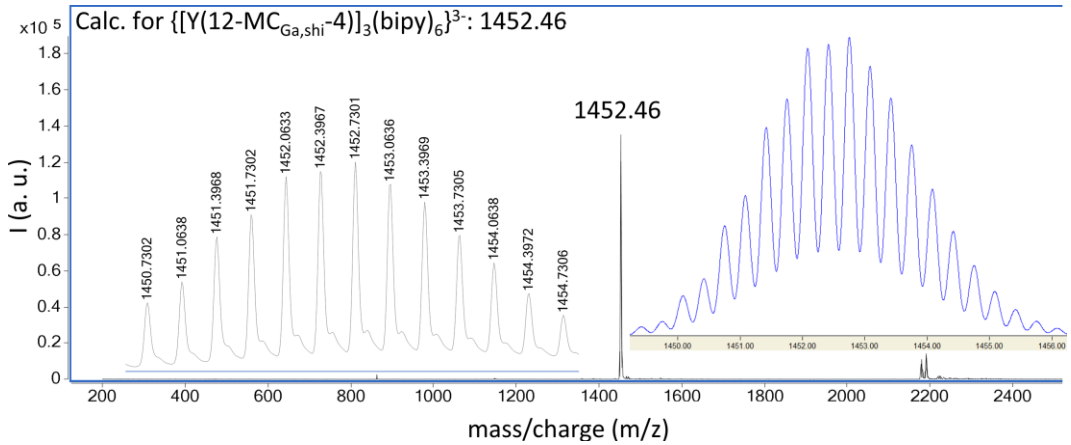

Figure 5.1. ESI-MS spectrum of {[Y(12-MC$_{Ga,shi}$-4)]$_3$(bipy)$_6$}(HNEt$_3$)$_3$ in the negative mode, C = 150 ug/mL (40 µM) in MeOH/DMSO 90:10. Right in blue: simulated spectrum.

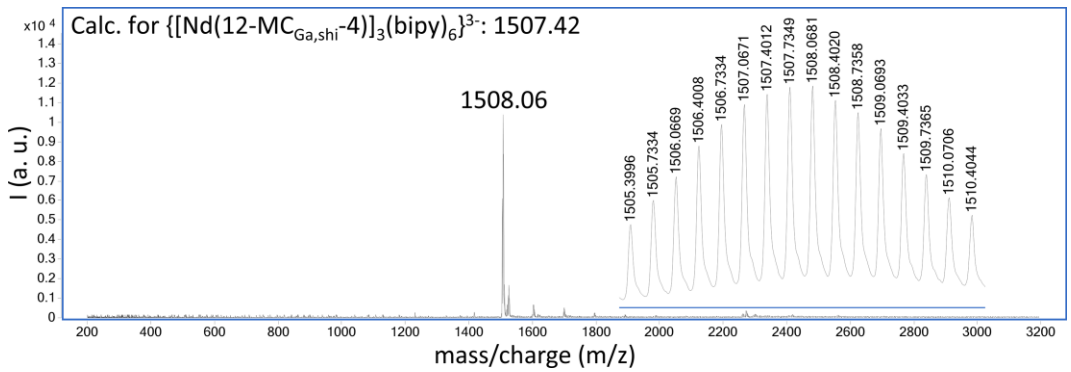

Figure 5.2. ESI-MS spectrum of {[Nd(12-MC$_{Ga,shi}$-4)]$_3$(bipy)$_6$}(HNEt$_3$)$_3$ in the negative mode, C = 150 ug/mL (40 µM) in MeOH/DMSO 90:10.

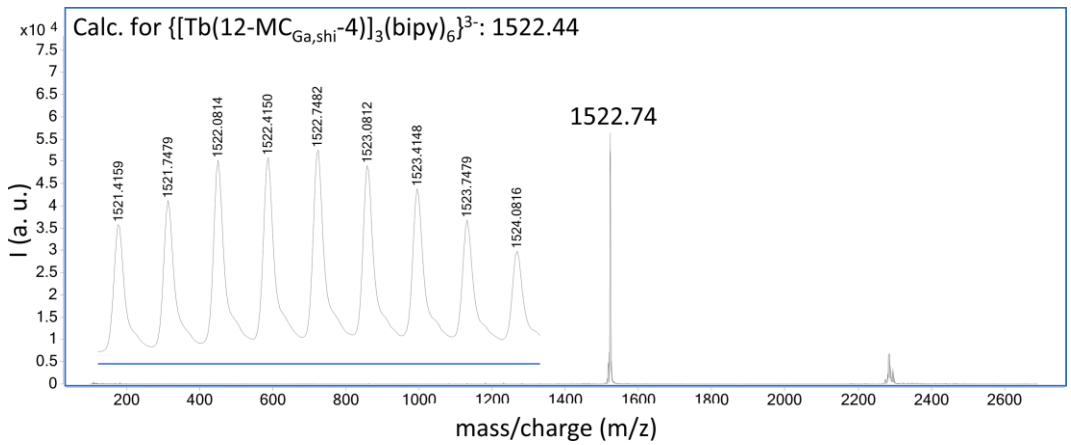

Figure 5.3. ESI-MS spectrum of {[Tb(12-MC$_{Ga,shi}$-4)]$_3$(bipy)$_6$}(HNEt$_3$)$_3$ in the negative mode, C = 150 ug/mL (40 µM) in MeOH/DMSO 90:10.

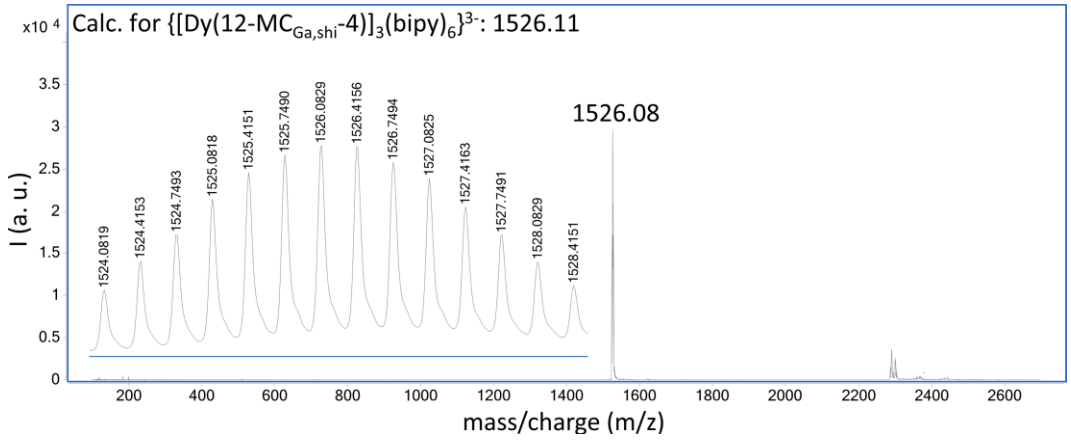

Figure 5.4. ESI-MS spectrum of {[Dy(12-MC$_{Ga,shi}$-4)]$_3$(bipy)$_6$}(HNEt$_3$)$_3$ in the negative mode, C = 150 ug/mL (40 µM) in MeOH/DMSO 90:10.

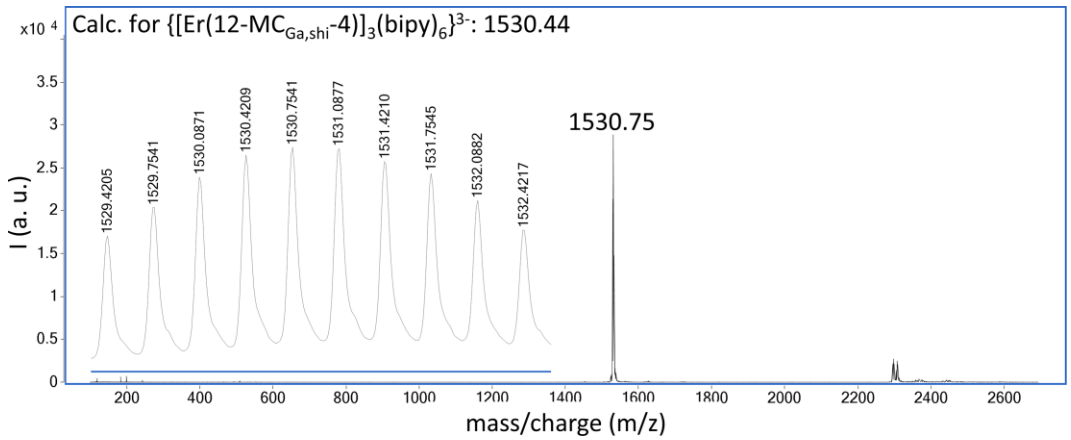

Figure 5.5. ESI-MS spectrum of {[Er(12-MC$_{Ga,shi}$-4)]$_3$(bipy)$_6$}(HNEt$_3$)$_3$ in the negative mode, C = 150 ug/mL (40 µM) in MeOH/DMSO 90:10.

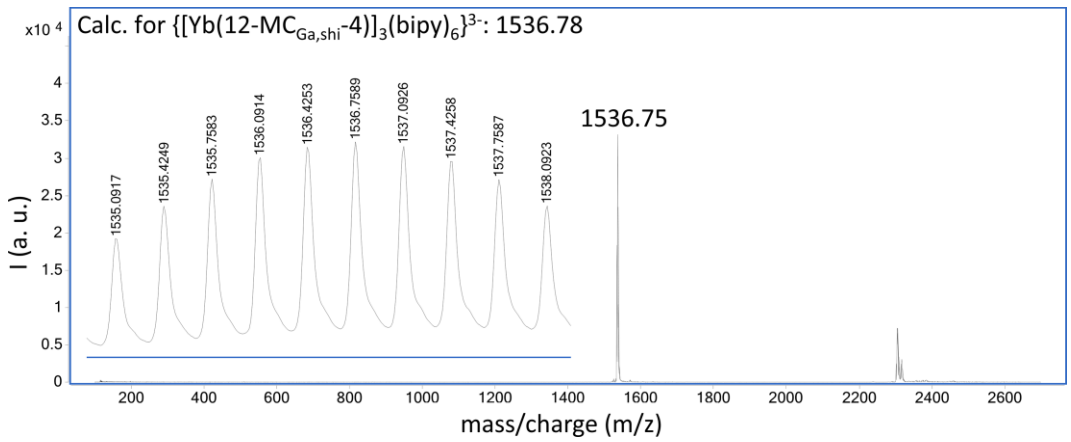

Figure 5.6. ESI-MS spectrum of {[Yb(12-MC$_{Ga,shi}$-4)]$_3$(bipy)$_6$}(HNEt$_3$)$_3$ in the negative mode, C = 150 ug/mL (40 µM) in MeOH/DMSO 90:10.

The diamagnetic {[Y(12-MC$_{Ga,shi}$-4)]$_3$(bipy)$_6$}(HNEt$_3$)$_3$ analogue was used for characterization by ^{1}H NMR spectroscopy (**Figure 5.7**). The multiplets integrating for 12 H each, between 6.69 and 7.95 ppm, are assigned to the aromatic protons of the shi^{3-} ligand forming the 12-MC-4 MC ring (**Figure 5.7**, protons **a** to **d** in blue). It is worth noting here that in trimeric {[Y(12-MC$_{Ga,shi}$-4)]$_3$(bipy)$_6$}$^{3-}$ the protons a to d are detected as wider and more complicated multiplets than in the monomeric {[YGa$_4$(shi)$_4$(bza)$_4$]}$^{-}$[117] and dimeric {[Y$_2$Ga$_8$(shi)$_8$(ip)$_4$]}$^{2-}$ MCs. [117] This is a clear sign that the [LnGa$_4$]$^-$ moieties present distorted geometries in solution[118] and are non-equivalent compared to what can be expected from solid-state X-ray diffraction structures. As usually observed for bidentate ligands containing two nitrogens in the 1,1' positions, the nitrogen atoms likely adopt a *trans* arrangement relative to each other in H$_2$bipy, minimizing the repulsive interactions of the hydrogens in 3,3' positions. The peaks between 8.91 and 9.25 ppm, each integrating for a total of 12 H, are associated to the proton in the ortho position of the nitrogen atoms (g). Conversely, the hydrogens labeled as (e) and (f) are assigned to the series of peaks

between 8.58 and 8.13 ppm. They display an integrated area of a total of 12 H each, as expected. The quadruplet (proton i, integrating for 18 H) at 3.00 ppm and the triplet (proton j, integrating for 27 H) at 1.09 ppm are assigned to the CH_2 and CH_3 groups of the three ethyl substituents of the triethylammonium counter-cations, respectively. Furthermore, the broad singlet at 8.85 ppm, integrating for 3 protons, is attributed to the nitrogen-bound hydrogen of the triethylammoniums. The broadening of this peak is due to two main factors: exchange with water and the intrinsic electric quadrupole moment of nitrogen, which itself causes peak broadening. This effect impacts both the nitrogen peaks (if performing nitrogen NMR) and the ^1H peaks of protons attached to nitrogen Overall, these integrals are consistent with the presence of three $HNEt_3^+$ counter-cations, as expected for a three-time negatively charged $[Ln_3Ga_{12}]$ trimeric MC. In contrast to $[LnGa_4]$ and $[Ln_2Ga_8]$ MCs, where coordination of solvent molecules to Ln^{III} is not possible due to the shielding provided by the ligands, DMF and water can coordinate to Ln^{III} here as the arrangement of bipy linkers leave some room for their coordination to Ln^{III}, as shown by the X-ray diffraction structures (see **Figure 5.8**).

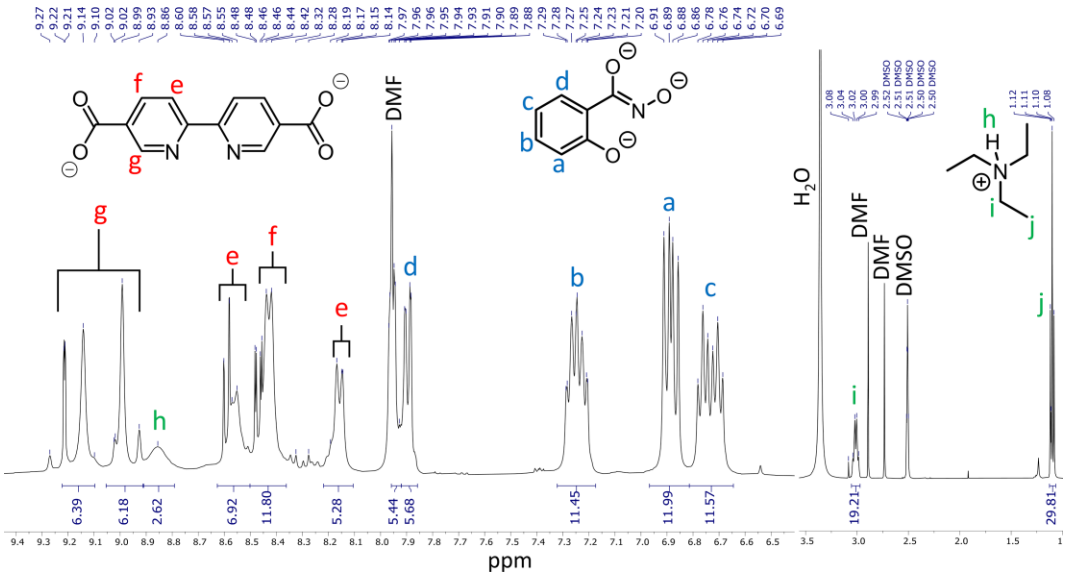

Figure 5.7. ^{1}H NMR spectrum of {[Y(12-MC$_{Ga,shi}$-4)]$_3$(bipy)$_6$}(HNEt$_3$)$_3$ in DMSO-d$_6$, 400 MHz, 298 K. In section **5.3.6**, the DOSY spectrum of {[Y(12−MC$_{Ga,shi}$−4)]$_3$(bipy)$_6$}(HNEt$_3$)$_3$ in DMSO-d$_6$ at 298K will be presented.

5.3.2 Description of the crystal strucures of {[TbNa(12-$MC_{Ga,shi}$-4)]$_3$(bipy)$_6$(DMF)$_2$(H_2O)$_{10}$}(HNEt$_3$)(DMF)$_5$.

The single-crystal X-ray diffraction analysis reveals that the trimeric Tb^{III} 12-MC-4 of shi^{3-} and Ga^{III} crystallizes in a monoclinic crystal system with a C2/c space group and a unit cell volume of 30172.0(12) Å^3. The MC structure of {[TbNa(12-$MC_{Ga,shi}$-4)]$_3$(bipy)$_6$(DMF)$_2$(H_2O)$_{10}$}(HNEt$_3$)(DMF)$_5$ is depicted in **Figure 5.8**. Three [Tb(12-$MC_{Ga,shi}$-4)]$^-$ building blocks are interconnected by six H_2bipy ditopic ligands, adopting a triangular shape with an overall charge of 3$^-$ (**Figure 5.8**, right). Specifically, each [Tb(12-$MC_{Ga,shi}$-4)] block is composed of four Ga^{III} atoms, four shi^{3-} ligands, and one Tb^{III} atom coordinated in the middle of the 12-MC_{Gashi}-4 ring (**Figure 5.8**, at the top left). In 12-MC_{Gashi}-4 MCs, the Ln^{III} are to big to fit in the ring and Tb^{III} is sitting slightly above the MC plane, as expected. Its coordination sphere is completed by the four H_2bipy ligands that are also coordinated the four Ga^{III} cations of the MC ring. The asymmetric unit of the MC contains one complete [Tb(12-$MC_{Ga,shi}$-4)]$^-$ building block and half of another [Tb(12-$MC_{Ga,shi}$-4)]$^-$ block, which includes one lanthanide, two shi^{3-} ligands, two Ga^{III} atoms, one sodium atom (0.5 occupancy), and one triethylammonium ion as counter-cations to balance the charge of the MC; the other half of the molecule is generated by symmetry operations.

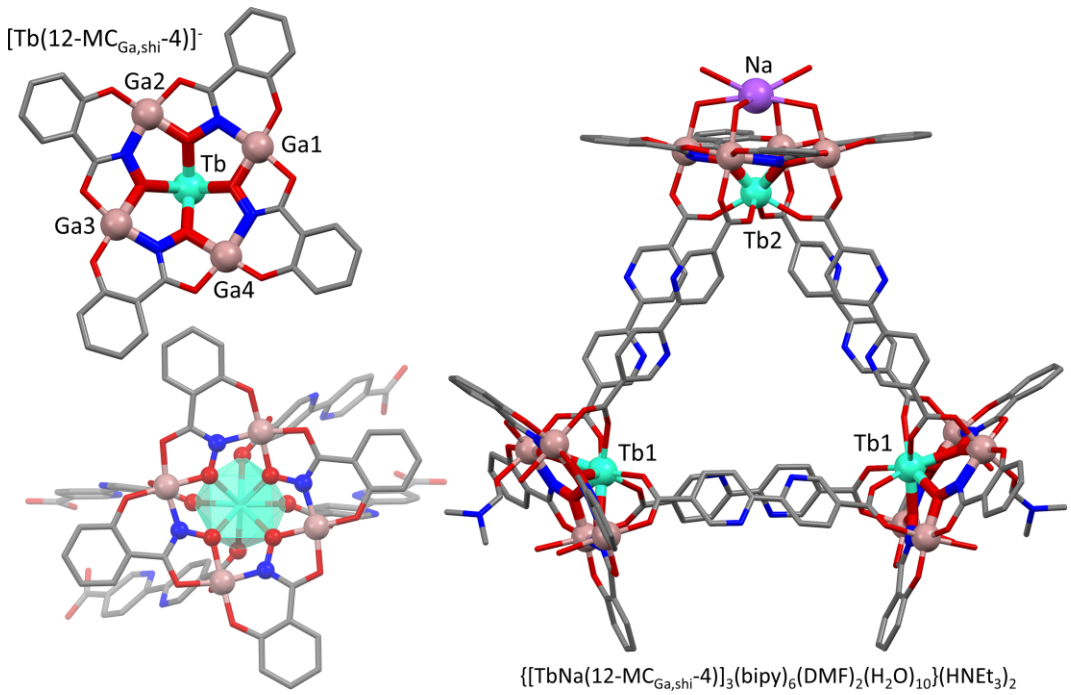

Figure 5.8. X-ray diffraction structure of the $\{[Tb(12\text{-}MC_{Ga,shi}\text{-}4)]_3(bipy)_6\}^{3-}$ MC. Top left: top-down view of the 12-$MC_{Ga,shi}$-4 MC ring; $HNEt_3$ cations are omitted for clarity). Right: Representation of the scaffold of the 12-$MC_{Ga,shi}$-4 MC, with Tb^{III} encapsulated by the 12-$MC_{Ga,shi}$-4 ring and the H_2bipy ditopic ligands. Color code: green-azure (Tb), pink (Ga), Red (oxygen), blue (nitrogen), purple (Na).

In this structure, every MC is interconnected to the two other MCs by four carboxylate groups of four distinct H_2bipy linkers that are each coordinated as to one Ga^{III} and to the the Tb^{III} central ion. As a consequence, the Tb^{III} atom is octacoordinated and exhibits an antiprismatic geometry. The donor atom set comprises four carboxylate oxygen atoms from the ditopic ligands [2.293(5) and 2.396(8) Å] and four hydroxamate oxygen atoms [2.283(9) and 2.393(5) Å] from the 12-MC-4 MC. All Ga^{III} atoms are hexacoordinated, adopting an octahedral geometry (**Figure 5.8**, bottom left). In particular, each Ga^{III} is coordinated on the equatorial

plane (corresponding to the MC mean plane) to one nitrogen and three oxygen atoms belonging to two different shi^{3-} ligands. Additionally, each Ga^{III} is bound in one of the axial positions to a carboxylate oxygen atom, as already described. As for the second axial coordination position, all the Ga atoms are coordinated to a water molecule except for Ga4 (x,y,z: 1-X,+Y,3/2-Z) that are coordinated to a DMF molecule. The average bond distances for $Ga–O_{phenolic}$ [1.790(1) – 1.865(11) Å] are shorter than those for $Ga–O_{carboxyl}$ [1.902(9) – 1.988(2) Å] and $Ga–O_{hydroxamate}$ [1.898(1) – 1.967(7) Å]. This observation is consistent with the presence of a negative charge on the phenolic oxygen atom. The sodium (purple) atom present in the half-basic unit of the 12-MC-4 in the asymmetric unit is coordinated by four oxygen atoms from the water molecules bound to Ga^{III}. Its coordination sphere is completed by two additional water molecules. The hydrogen atom of the triethylammonium ion interacts with the MC through the formation of a hydrogen bond with the oxygen atom of a carboxylate, with a bond distance of 3.692(3) Å. More DMF solvent molecules are present in the crystal structure and have been omitted for clarity. As expected for bipyridyl ligands, the two pyridyl rings adopt a *trans* arrangement with each other due to the proximity of the two nitrogen atoms and the H-H steric hindrance, which by doing so, minimizes the electronic repulsion between them. This observation supports the interpretation of the NMR signals related to the bipyridyl ligand, described in Section 2.1.4. The unit cell volumes determined for the other crystalline compounds (Ln = Nd, Dy, Yb, Er and Y), are exactly the same. The complete diffraction data set was not collected for these compounds, and therefore only the crystallographic tables are given in the Supporting Information.

5.3.3. Synthesis and characterization of $\{[Ln(12\text{-}MC_{Ga,shi}\text{-}4)]_3(frn)_6\}(HNEt_3)_3$ and $\{[Ln(12\text{-}MC_{Ga,shi}\text{-}4)]_4(frn)_8\}(HNEt_3)_4$ metallacrowns

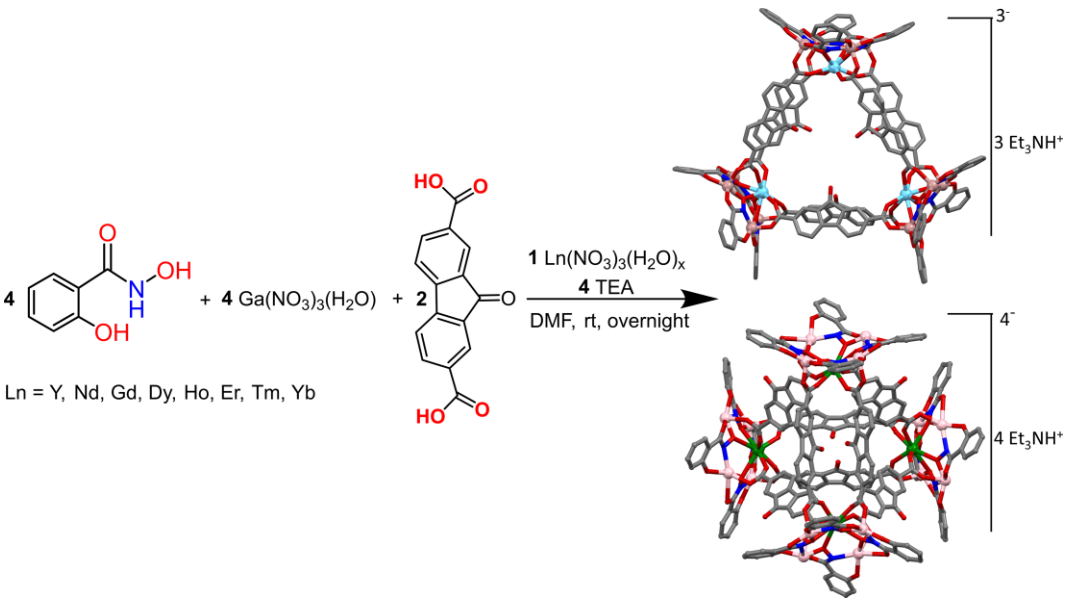

Scheme 5.3. Synthesis of the trimeric $\{[Ln(12\text{-}MC_{Ga,shi}\text{-}4)]_3(frn)_6\}(HNEt_3)_3$ and tetrameric $\{[Ln(12\text{-}MC_{Ga,shi}\text{-}4)]_4(frn)_8\}(HNEt_3)_4$ MCs.

The synthesis of the trimeric $\{[Ln(12\text{-}MC_{Ga,shi}\text{-}4)]_3(frn)_6\}(HNEt_3)_3$ and tetrameric $\{[Ln(12\text{-}MC_{Gashi}\text{-}4)]_4(frn)_8\}(HNEt_3)_4$ MCs (**Scheme 5.3**) was carried out by mixing all the solid reagents in dimethylformamide (DMF), resulting in a pale-yellow solution. Triethylamine was used as the base for the deprotonation of both the H_3shi ligands and the dicarboxylic acids linkers. After its addition, the solution became turbid at first and became clear again after about 15 min. The solution was left stirring overnight, and the precipitate formed was then removed by filtration.

Crystals of the product were obtained after two weeks of slow evaporation of the solvent.

5.3.4 Description of trimer and tetramer metallacrown crystal structures

Single-crystal X-ray diffraction analysis allowed the characterization of the trimeric and tetrameric MCs that can be formed by using H_2frn as a linker. The trimeric{[La(12-$MC_{Ga,shi}$-4)]$_3$(frn)$_6$(H_2O)$_5$(DMF)$_3$}$^{3-}$(DMF) MC crystallizes in a monoclinic crystal system with a P21/n space group and a unit cell volume of 29847(5) Å³. The MC structure consists of {[La(12-$MC_{Ga,shi}$-4)(H_2O)$_4$]$^-$, {[La(12-$MC_{Ga,shi}$-4)(DMF)$_2$(H_2O)]$^-$ and {[La(12-$MC_{Ga,shi}$-4)(DMF)]$^-$ building blocks each carrying one negative charge (**Figure 5.9**, left and right). The blocks are interconnected by H_2frn ligands, which, by bridging these three basic units, generates a triangular supramolecular entity (**Figure 5.9**, middle). Each {[La(12-$MC_{Ga,shi}$-4)]$^-$ unit is itself composed of 4 Ga^{III} atoms, 4 shi^{3-} ligands, water and DMF molecules and 1 La^{III} atom, encapsulated in the cavity formed by the 12-$MC_{Ga,shi}$-4 ring. The La^{III} atoms are all 9-coordinated in a capped antiprismatic geometry, in which the antiprism is formed by four hydroxamate oxygen atoms of the shi^{3-} ligand, four oxygen atoms of the H_2frn ligands, and the capped position is occupied by a water molecule for La1 and La2, and by a DMF molecule for La3. The range bond distances for La-O_{shi} is [2.44(3) – 2.59(2) Å], while for La-$O_{carboxylate}$ is [2.53(2) – 2.57(2)) Å].

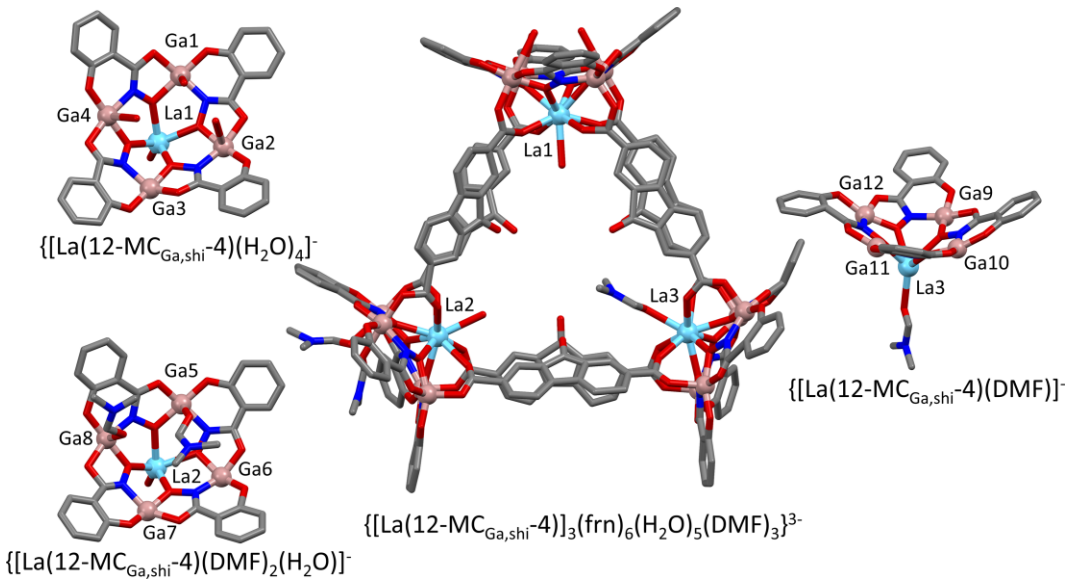

Figure 5.9. Representation of the structure of the {[La(12-MC$_{Ga,shi}$-4)]$_3$(frn)$_6$(H$_2$O)$_5$(DMF)$_3$}$^{3-}$(DMF) complex (middle). Left and right: representation of the framework of the {[La(12-MC$_{Ga,shi}$-4)(H$_2$O)$_4$]$^-$, {[La(12-MC$_{Ga,shi}$-4)(DMF)$_2$(H$_2$O)]$^-$ and {[La(12-MC$_{Ga,shi}$-4)(DMF)]$^-$ MCs, with La^{III} encapsulated. Color code: azure (La), pink (Ga), Red (oxygen), blue (nitrogen). Hydrogens and DMF solvent molecules were omitted for clarity.

The Ga^{III} atoms show different coordination numbers, ranging from five to six, exhibiting square-base pyramid geometry and octahedral geometry, respectively. The set of donor atoms consists of a nitrogen atom and three oxygen atoms belonging to two different shi^{3-} ligands, which forms a quadrangle in equatorial plane that is common to all Ga^{III} atoms. In pentacoordinate Ga^{III}, the axial position is occupied by the oxygen of a carboxylate from the fluorenone ligand that satisfies the entire geometry. In hexacoordinated Ga^{III} atoms, on the other hand, one of the axial positions is occupied by the oxygen atom of a carboxylate of the H$_2$frn, while for pentacoordinated Ga^{III}, a water molecule (Ga1, Ga2 and Ga4) or a DMF molecule

(Ga5 and Ga8) occupy the axial position. The average bond distances for Ga-$O_{phenolic}$ [1.77(2)-1.99(2) Å] are shorter than those for Ga-$O_{carbonyl}$ [1.82(2)-2.04(2) Å] and Ga-$O_{hydroxamate}$ [1.86(2)-1.98(2) Å]. This observation is consistent with the presence of a negative charge on the phenolic oxygen atom. The structure has a consistent cell volume of 29847(5) Å³. 24% of this volume has an unstructured electron density due to the presence of disordered solvent, which renders the modeling of the triethylammonium counter cations complicated. However, its presence is confirmed by ^{1}H NMR and ESI-MS.

The tetrameric $\{[Y(12\text{-}MC_{Ga,shi}\text{-}4)]_4(frn)_8(H_2O)_{16}\}^{3-}$ MC crystallizes in a tetragonal crystal system with a P-4b2 space group and a unit cell volume of 39472(3) Å^3. The MC structure consists of three $\{[Y(12\text{-}MC_{Ga,shi}\text{-}4)(H_2O)_4]^-$ building block each carrying one negative charge (**Figure 5.10**, right). The blocks are interconnected by H_2frn ligands, which, by bridging four basic units, generates a tetragonal supramolecular entity (**Figure 5.10**, left). Each $\{[Y(12\text{-}MC_{Ga,shi}\text{-}4)(H_2O)_4]^-$ unit (**Figure 5.10**, right) is itself composed of 4 Ga^{III} atoms, 4 shi^{3-} ligands, 4 water molecules and 1 Y^{III} atom, encapsulated in the cavity formed by the 12-$MC_{Ga,shi}$-4 ring. The Y^{III} atoms are all octacoordinated in an antiprismatic geometry, in which the antiprism is achieved by four hydroxamate oxygen atoms of the shi^{3-} ligand and four oxygen atoms of the carboxylates of H_2frn ligands. The range bond distances for Y-O_{shi} is [2.270(2) – 2.400(2) Å], while for Y-$O_{carboxylate}$ is [2.301(3) – 2.400(2) Å]. All Ga^{III} atoms are hexacoordinate, adopting an octahedral geometry (**Figure 5.10**, right).

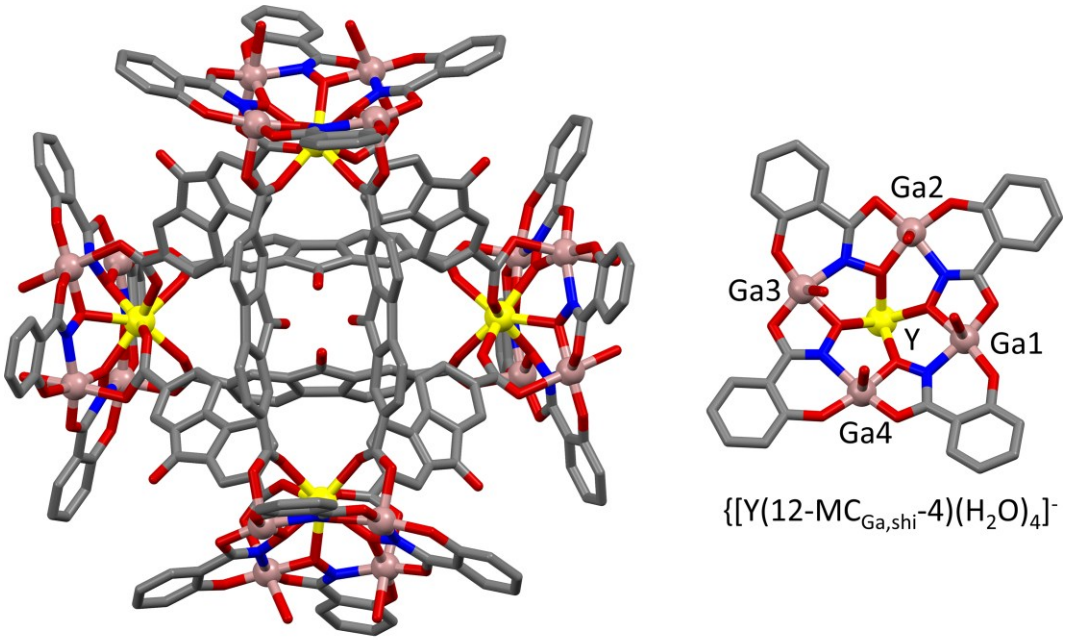

Figure 5.10. Left: representation of the structure of the {[Y(12-MC$_{Ga,shi}$-4)]$_4$(frn)$_8$(H$_2$O)$_{16}$}$^{3-}$complex. Right: Representation of the framework of the {[Y(12-MC$_{Ga,shi}$-4)(H$_2$O)$_4$]$^-$ MC, with Y^{III} encapsulated. Color code: yellow (Y), pink (Ga), Red (oxygen), blue (nitrogen). Hydrogens atoms are omitted for clarity.

Specifically, each Ga^{III} is coordinated in the equatorial plane (corresponding to the MC plane) to a nitrogen atom and three oxygen atoms belonging to two different shi^{3-} ligands. In addition, each Ga^{III} is bound in one of the axial positions to an oxygen atom of the carboxylate of H$_2$frn ligands, and the second axial coordination position is occupied by a water molecule, satisfying the entire geometry. The structure has a consistent cell volume of 39472(3) Å^3. 70% of this volume has an unstructured electron density due to the presence of disordered solvent, which renders the modeling of triethylammonium counter cations complicated. However, its presence is confirmed by ^{1}H NMR and ESI-MS.

We attempt to explain why different oligomers are obtained by using the same H_2frn ligand through the structural analysis of the MC described above. Notably, the formation of trimers or tetramers is governed by the ionic radius of the Ln^{III} used. Trimers are formed with large Ln^{III}, ranging from La^{III} (1.061 Å) to Tb^{III} (0.923 Å), while tetramers are formed with Y^{III}(0.90 Å) and smaller Ln^{III}, ranging from Dy^{III} (0.91 Å) to Lu^{III} (0.848 Å). This can be explained by the Ln–$O_{carboxylate}$ bond distances and O–Ln–O angles between the Ln^{III} and the H_2frn ligands. In both structures, no more than four H_2frn bridges are bonded to each {[Ln(12-$MC_{Ga,shi}$-4)]$^-$ basic unit, but the trimer features longer La–$O_{carboxylate}$ bond distances [2.53(4) to 2.570(5) Å] compared to the shorter Y–$O_{carboxylate}$ distances in the tetramer [2.230(2) to 2.40(2) Å]. These longer distances in the trimer allow the fluorenones to arrange in pairs, forming an O–La–O bond angle of 76° and 80° between fluorenones in the same pair (**Figure 5.11**). In this configuration, all the oxygens of the carbonyl function of the fluorenones point inward, toward the cavity generated by the MC.

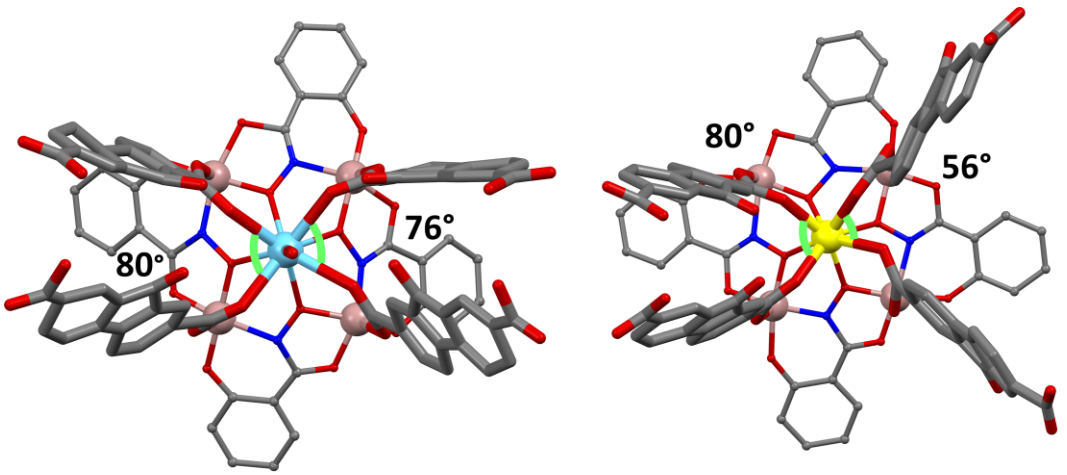

$\{[La(12\text{-}MC_{Ga,shi}\text{-}4)]_3(frn)_6(H_2O)_5(DMF)_3\}^{3-}$ $\{[Y(12\text{-}MC_{Ga,shi}\text{-}4)]_4(frn)_8(H_2O)_{16}\}^{3-}$

Figure 5.11. Representation of the angles between the fluoreone ligands in the trimeric $\{[La(12\text{-}MC_{Ga,shi}\text{-}4)]_3(frn)_6(H_2O)_5(DMF)_3\}^{3-}(DMF)$ MC (left) and in the tetrameric $\{[Y(12\text{-}MC_{Ga,shi}\text{-}4)]_4(frn)_8(H_2O)_{16}\}^{3-}$ MC (right). Color code: azure (La), yellow (Y), pink (Ga), Red (oxygen), blue (nitrogen). Hydrogens and solvent molecules were omitted for clarity.

Additionally, the larger lanthanides in the trimers can accommodate the coordination of an extra solvent molecule, such as water or DMF. In the tetramer, the shorter $Y–O_{carboxylate}$ bond distances still allow the fluorenones to arrange in pairs, but the orientation differs. One pair forms an O–Ln–O bond angle of 80°, with the carbonyl function pointing towards the cavity, while the other pair adopts an O–Ln–O bond angle of 56°, with the carbonyl function oriented away from the cavity. These different arrangements of the ligands lead to optimal geometrical and structural conditions for the formation of an unprecedented self-assembled species. This structural variation can be attributed to two complementary factors: the Ln^{III} ionic radius and the bond angles formed by the carboxylate groups of the ligand. Crystallographic data collected from metallacrowns of Tb support this

conclusion, with detailed crystallographic tables provided in the supporting information.

All MC structures are shown in ellipsoidal-type in the supporting information (**Figures S5.1-S5.3**).

5.3.5 Characterization of $\{[Ln(12\text{-}MC_{Ga,shi}\text{-}4)]_3(frn)_6\}(HNEt_3)_3$ MCs via ESI-Mass Spectrometry

All the solid microcrystalline isolated metallacrowns were characterized by ESI-MS to confirm the formation of the trimeric and tetrameric species in solution (C_{MC} = 150 µg/mL corresponding to ca. 40 µM). Unexpectedly, the tetrameric species of the metallacrown were not observed through the mass analysis in this conditions, possibly indicating that in solution the balance between the stability of these two species is delicate. **Figures 5.12-5.19** display the mass spectra of the purified crystalline powders, showing the predominance of the three-time negatively charged trimeric species, confirmed by isotopic peaks separated by a 0.3 m/z difference.

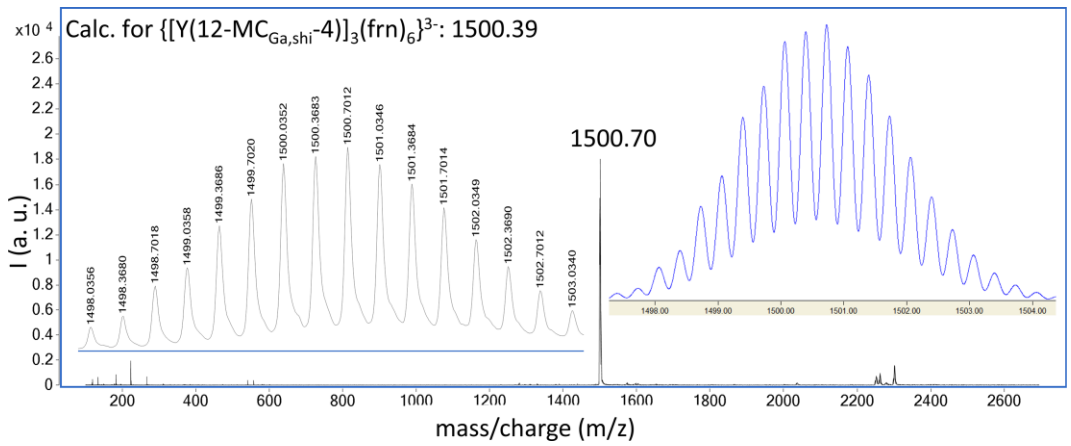

Figure 5.12. ESI-MS spectrum of {[Y(12-MC$_{Ga,shi}$-4)]$_3$(frn)$_6$}(HNEt$_3$)$_3$ in the negative mode, C = 150 ug/mL (40 µM) in MeOH/DMSO 90:10. Right in blue: simulated spectrum.

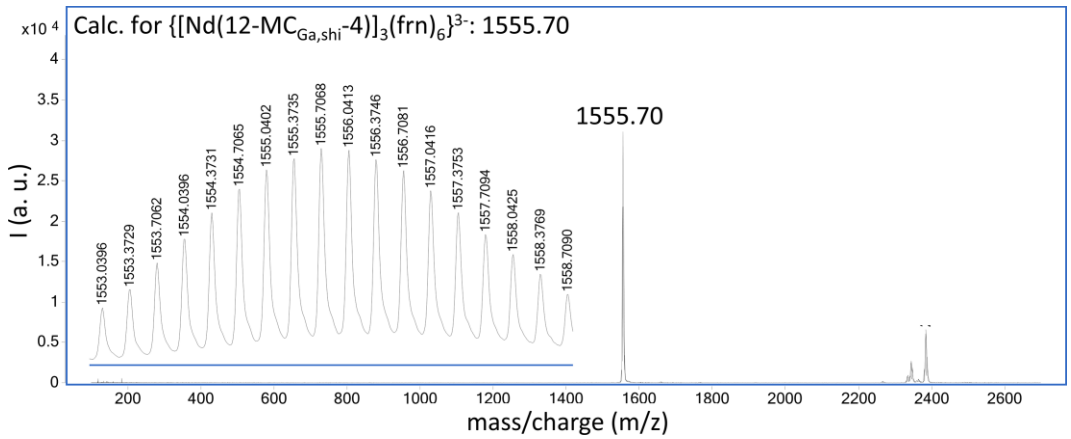

Figure 5.13. ESI-MS spectrum of {[Nd(12-MC$_{Ga,shi}$-4)]$_3$(frn)$_6$}(HNEt$_3$)$_3$ in the negative mode, C = 150 ug/mL (40 µM) in MeOH/DMSO 90:10.

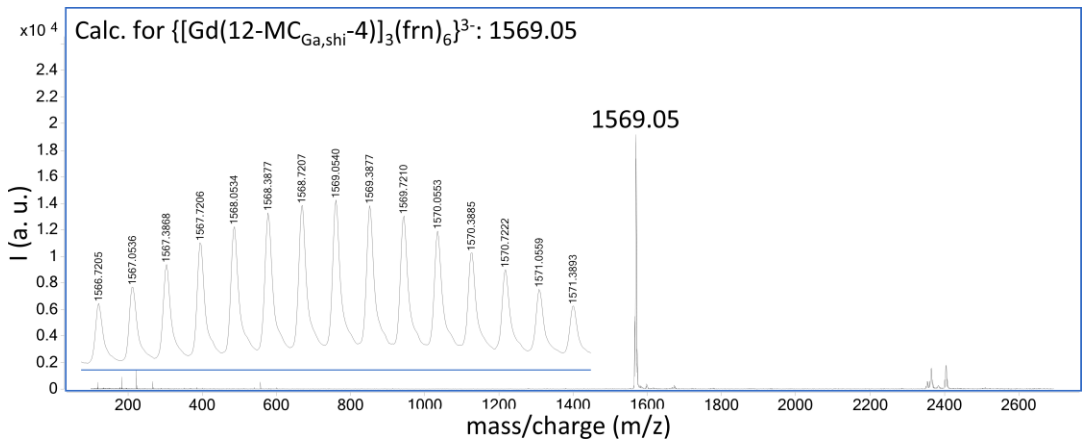

Figure 5.14. ESI-MS spectrum of $\{[Gd(12\text{-}MC_{Ga,shi}\text{-}4)]_3(frn)_6\}(HNEt_3)_3$ in the negative mode, C = 150 ug/mL (40 µM) in MeOH/DMSO 90:10.

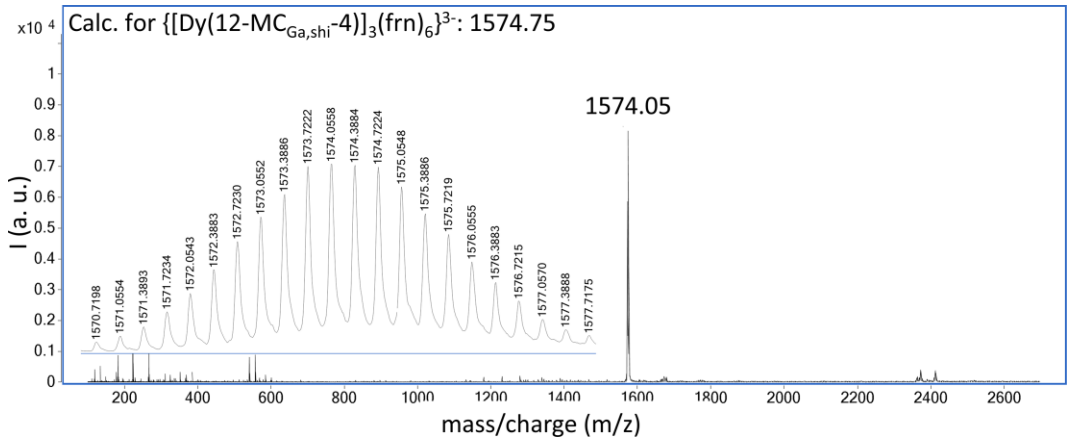

Figure 5.15. ESI-MS spectrum of $\{[Dy(12\text{-}MC_{Ga,shi}\text{-}4)]_3(frn)_6\}(HNEt_3)_3$ in the negative mode, C = 150 ug/mL (40 µM) in MeOH/DMSO 90:10.

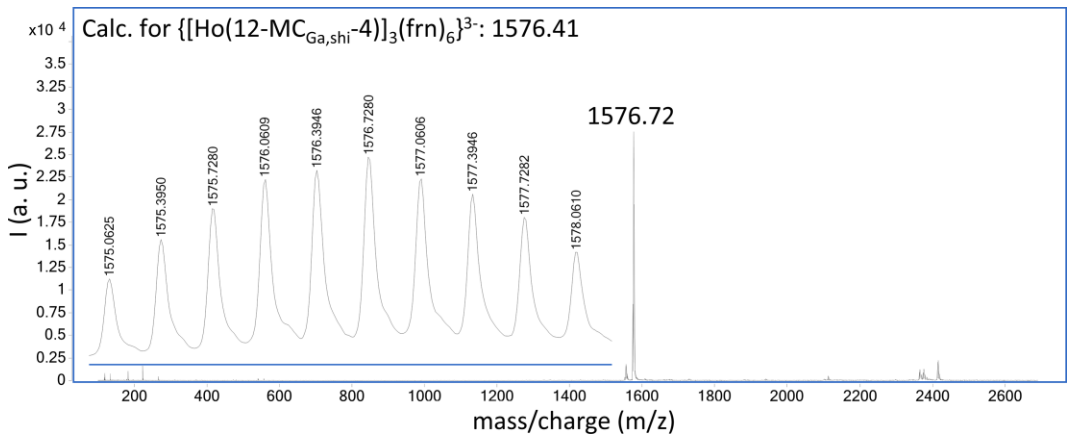

Figure 5.16. ESI-MS spectrum of {[Ho(12-MC$_{Ga,shi}$-4)]$_3$(frn)$_6$}(HNEt$_3$)$_3$ in the negative mode, C = 150 ug/mL (40 µM) in MeOH/DMSO 90:10.

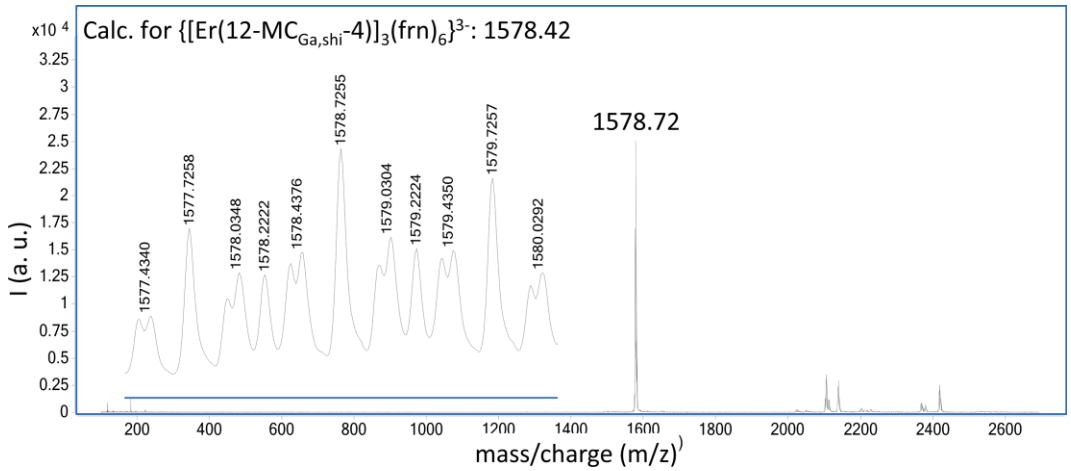

Figure 5.17. ESI-MS spectrum of {[Er(12-MC$_{Ga,shi}$-4)]$_3$(frn)$_6$}(HNEt$_3$)$_3$ in the negative mode, C = 150 ug/mL (40 µM) in MeOH/DMSO 90:10.

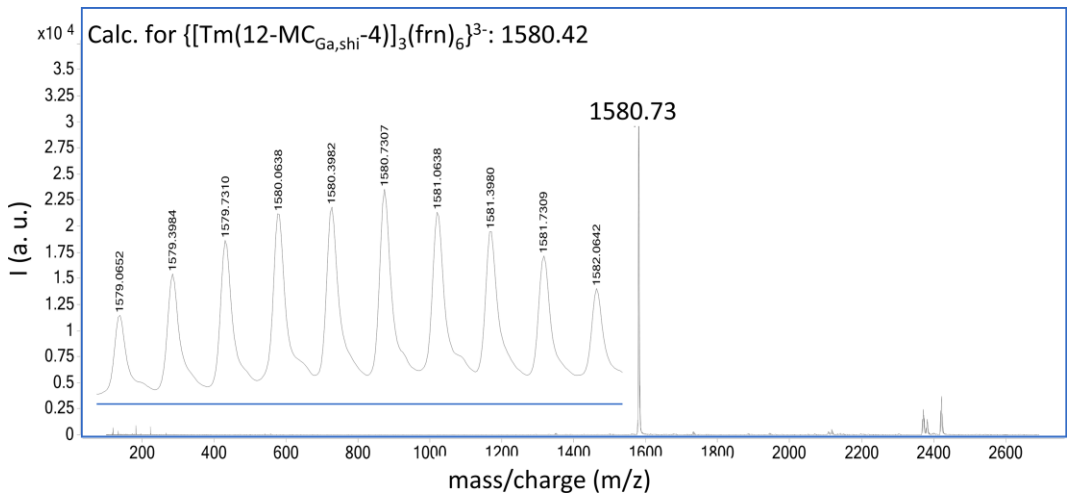

Figure 5.18. ESI-MS spectrum of {[Tm(12-MC$_{Ga,shi}$-4)]$_3$(frn)$_6$}(HNEt$_3$)$_3$ in the negative mode, C = 150 ug/mL (40 µM) in MeOH/DMSO 90:10.

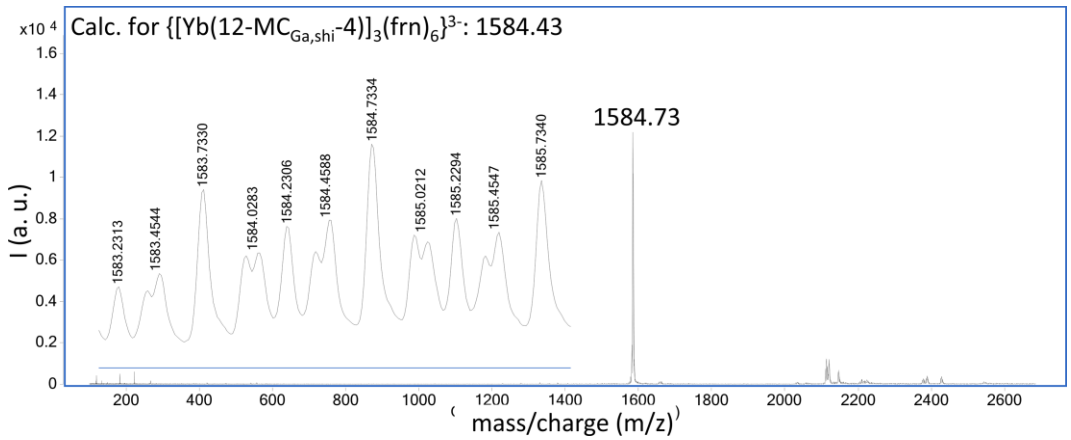

Figure 5.19. ESI-MS spectrum of {[Yb(12-MC$_{Ga,shi}$-4)]$_3$(frn)$_6$}(HNEt$_3$)$_3$ in the negative mode, C = 150 ug/mL (40 µM) in MeOH/DMSO 90:10.

The ESI-MS spectra of the {[Er(12-$MC_{Ga,shi}$-4)]$_3$(frn)$_6$}($HNEt_3$)$_3$ (**Figure 5.17**) and {[Yb(12-$MC_{Ga,shi}$-4)]$_3$(frn)$_6$}($HNEt_3$)$_3$ (**Figure 5.19**) MCs recorded at the University of Michigan display several peaks that seems to be further split in two, suggesting the presence of another species in solution, in addition to the unique trimeric MC detected for Ln^{III} = Y^{III}, Nd^{III}, Gd^{III}, Dy^{III} Ho^{III} and Tm^{III}. For this reason, high-resolution mass spectrometry analyses were performed on the {[Er(12-$MC_{Ga,shi}$-4)]$_3$(frn)$_6$}($HNEt_3$)$_3$ MC by our collaborators at the CBM in Orléans. The sample was injected at two different concentrations: C_{MC} = 0.25 mM and C_{MC} = 0.025 mM (**Figure S5.8**).

While the trimeric MC was detected as the main species for the samples that were run at the University of Michigan, the tetrameric MC is observed as the main species here. Its presence is confirmed by an observed difference of Δm/z = 0.25 between the isotopic peaks, as expected for the four-time negatively charged tetrameric MC. The trimeric MC is also detected as traces (**Figure S5.8**, peaks labelled with *). The two concentrations used suggest a thermodynamic equilibrium between the trimeric and tetrameric forms of the frn MCs in solution. As the sample is diluted, the trimeric form is favored over the tetrameric arrangement.

To confirm the assignment of the peaks to the trimeric and tetrameric MCs, the theoretical isotopic distributions of both trimeric and tetrameric MCs were simulated and superposed with the experimental ESI-MS spectra (**Figure S5.9**). This simulation confirms the assignment of the main peaks (**Figure S5.9**, top, grey traces) to the four-time negatively charged tetrameric MC, with isotopic peaks separated by Δm/z = 0.25 (**Figure S5.9**, middle). The minor species observed can be attributed to the three-time negatively charged trimeric MC (**Figure S5.9**, top and bottom, orange traces), as confirmed by the simulated isotopic distribution with Δm/z = 0.33 (**Figure S5.9**, bottom). Based on these results, it appears that the choice of the MS

spectrometer as well as the ionization and injection/infusion conditions heavily impact the trimeric/tetrameric ratio obtained. This trimeric/tetrameric thermodynamic equilibrium of the frn MCs in solution is still being investigated.

5.3.6 Probing the Speciation of Fluorenone MCs via ^{1}H NMR and DOSY Spectroscopy

To understand the impact of Ln^{III} size and of the 167° angle in H_2frn on the formation of MCs in solution, the diamagnetic rare-earth elements La^{III} (r_i = 1.16 Å for a coordination number = 8), Y^{III} (r_i = 1.019 Å for CN = 8) and Lu^{III} (r_i = 0.977 for CN = 8)[119], of different sizes, were used in their preparation and the ^{1}H NMR spectra of the isolated compounds were recorded in DMSO-d_6 (**Figure 5.20**). However, the obtained spectra are complicated, with peaks spread over the aromatic region and rendering clear peak assignment challenging. We speculate that this complexity results from a thermodynamic equilibrium between the trimeric and tetrameric forms of the MC in solution. For La^{III}, Y^{III} and Lu^{III}, and integration according to 100% of the pure trimer is presented. As both the trimeric and tetrameric MCs share the same frn:shi stoechiometric ratio, the presented integration is representative of the following scenarios: 100% trimer, 100% tetramer, or a mixture of both. An integration for an MC trimer of $\{[Ln(12\text{-}MC_{Ga,shi}\text{-}4)]_3(frn)_6\}(HNEt_3)_3$ molecular formula is presented below for all three lanthanides studied.

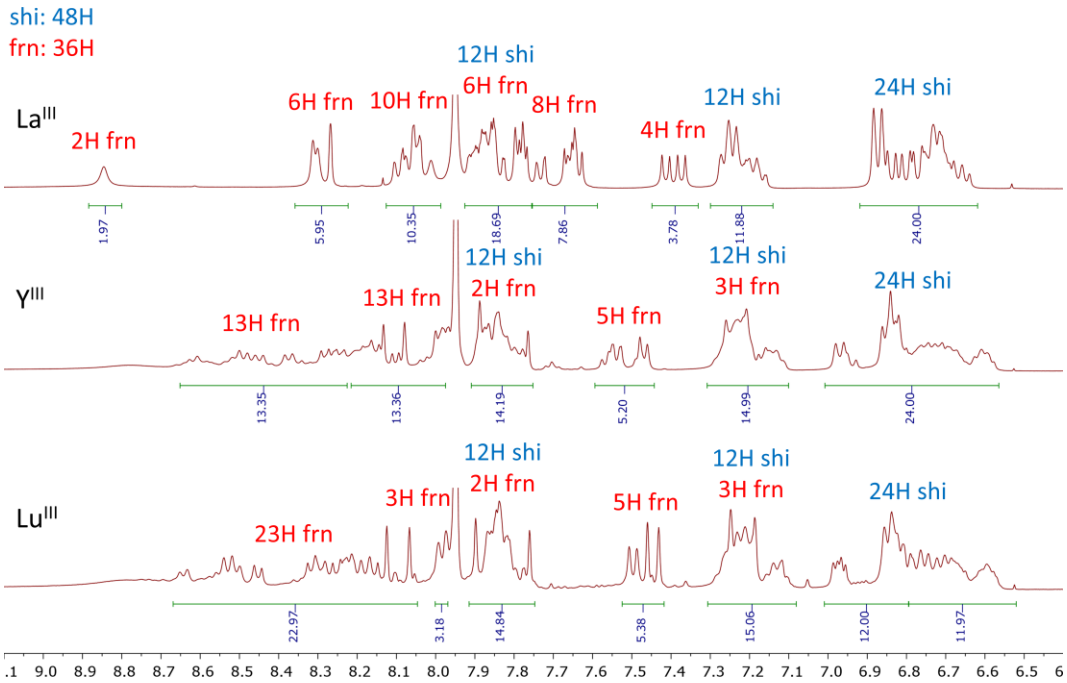

Figure 5.20. ^{1}H NMR spectrum of La^{III}, Y^{III} and Lu^{III} metallacrowns obtained with the H_2frn linker.

The ^{1}H NMR spectrum of the large La^{III} cation shows well resolved peaks while for the smaller Y^{III} and Lu^{III} cations, more peaks are observed. Because larger lanthanides yield X-ray structures of the tetrameric MC with H_2frn, while small one gives the trimeric arrangement, it is tempting to assign the La^{III} spectrum to the presence of a unique tetrameric species in solution. For smaller Lns such as Y^{III} and Lu^{III}, the more complicated spectra would be attributed to the presence of both the trimeric and tetrameric species of the MC with H_2frn, each present as a unique set of peaks due to slow exchange between the two forms at the NMR time scale. In all three cases, the shi protons integrate for the expected number and display the typical chemical shifts expected for [$LnGa_4$] subunits. The rest of the peaks are attributed to the H_2frn linker. A clear attribution of the H_2frn peaks is not possible,

but the overall integration is coherent with the presence of 6 H_2frn linkers for a total of 36H. As for the H_2bipy linker in the trimeric $\{[Ln(12\text{-}MC_{Ga,shi}\text{-}4)]_3(bipy)_6\}^{3-}$ MC, their multiple peaks suggest that they are not equivalent, as depicted by the solid-state X-ray diffraction structure obtained where the H_2frn linkers display several different arrangements.

To address this, Diffusion-Ordered Spectroscopy (DOSY) was performed in hope to discriminate the lighter trimeric species against the heavier tetrameric one. DOSY is an NMR technique that distinguishes different species in solution based on their diffusion coefficients. The diffusion of molecules in solution is governed by their size and shape, and this relationship is quantitatively described by the self-diffusion coefficient, DDD, which is inversely related to molecular size—larger molecules exhibit smaller diffusion coefficients, and vice versa. A series of spin-echo spectra was recorded with varying pulsed field gradient strengths, and the resulting signal decays were analyzed to extract diffusion coefficients. These coefficients were then used to construct the diffusion domain of the DOSY spectrum. For this experiment, NMR tubes were prepared by microfiltering the solutions obtained from the dissolution of 5 mg of compound in 0.7 mL of DMSO-d_6. The experimental parameters were optimized by recording two 1D ^{1}H spectra using identical values for the diffusion delay (Δ) and gradient pulse duration (δ) with different gradient strengths, one at 5% and the other at 95%. Superimposing the two spectra revealed a 5% scaling factor difference, confirming that the chosen Δ = 350 ms and δ = 0.2 ms values were appropriate for the experiment.

Figure 5.21 shows the DOSY spectrum for the compound $\{[La(12\text{-}MC_{Ga,shi}\text{-}4)]_3(frn)_6\}(HNEt_3)_3$ In the spectrum, three distinct signals with different diffusion

coefficients are observed. The topmost signal corresponds to the MC, with a diffusion coefficient (D) ranging from 6.88×10^{-11} to 7.68×10^{-11} m^2/s. The signal at 6.26×10^{-10} m^2/s is attributed to DMF, while the signal at 3.41×10^{-10} m^2/s is associated with triethylammonium.

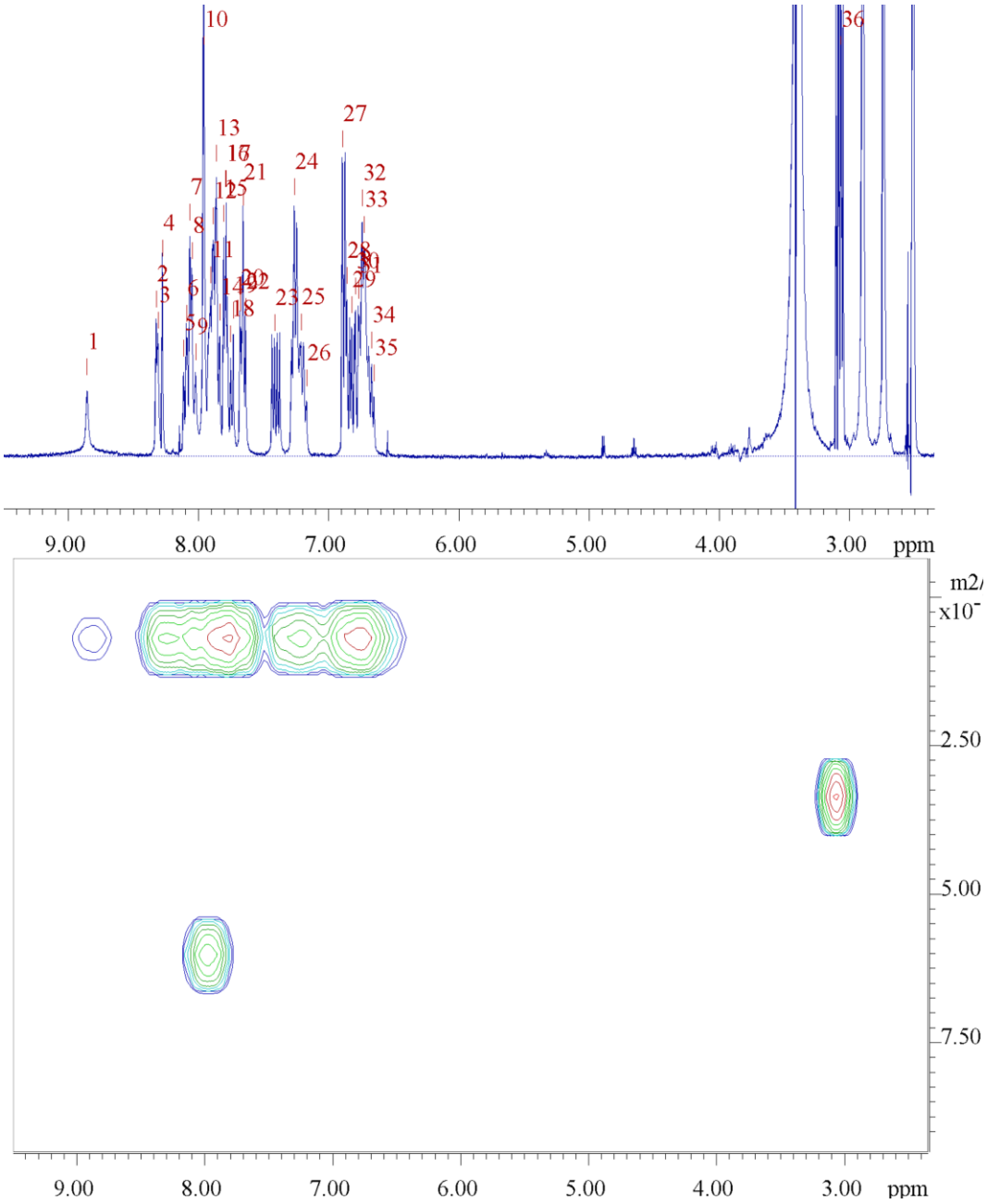

Figure 5.21. 2D DOSY NMR (400 MHz, DMSO, 298 K) spectrum of {[La(12-MC$_{Ga,shi}$-4)]$_3$(frn)$_6$}(HNEt$_3$)$_3$. Big delta (Δ = 350 ms) and little delta (δ = 0.2 ms).

Figure 5.22 presents the DOSY spectra for the compound {[Y(12-$MC_{Ga,shi}$-4)]$_{3/4}$(frn)$_{6/8}$}$(HNEt_3)_{3/4}$. Four main signals can be observed in the spectrum. The topmost signal corresponds to the MC, with a diffusion coefficient (D) ranging between 7.17×10^{-11} and 7.79×10^{-11} m^2/s. The signal at 6.56×10^{-10} m^2/s is attributed to DMF, while the signal at 3.37×10^{-10} m^2/s is associated with triethylammonium. Finally, the signal at 8.13×10^{-10} m^2/s is attributed to the protons of triethylammonium.

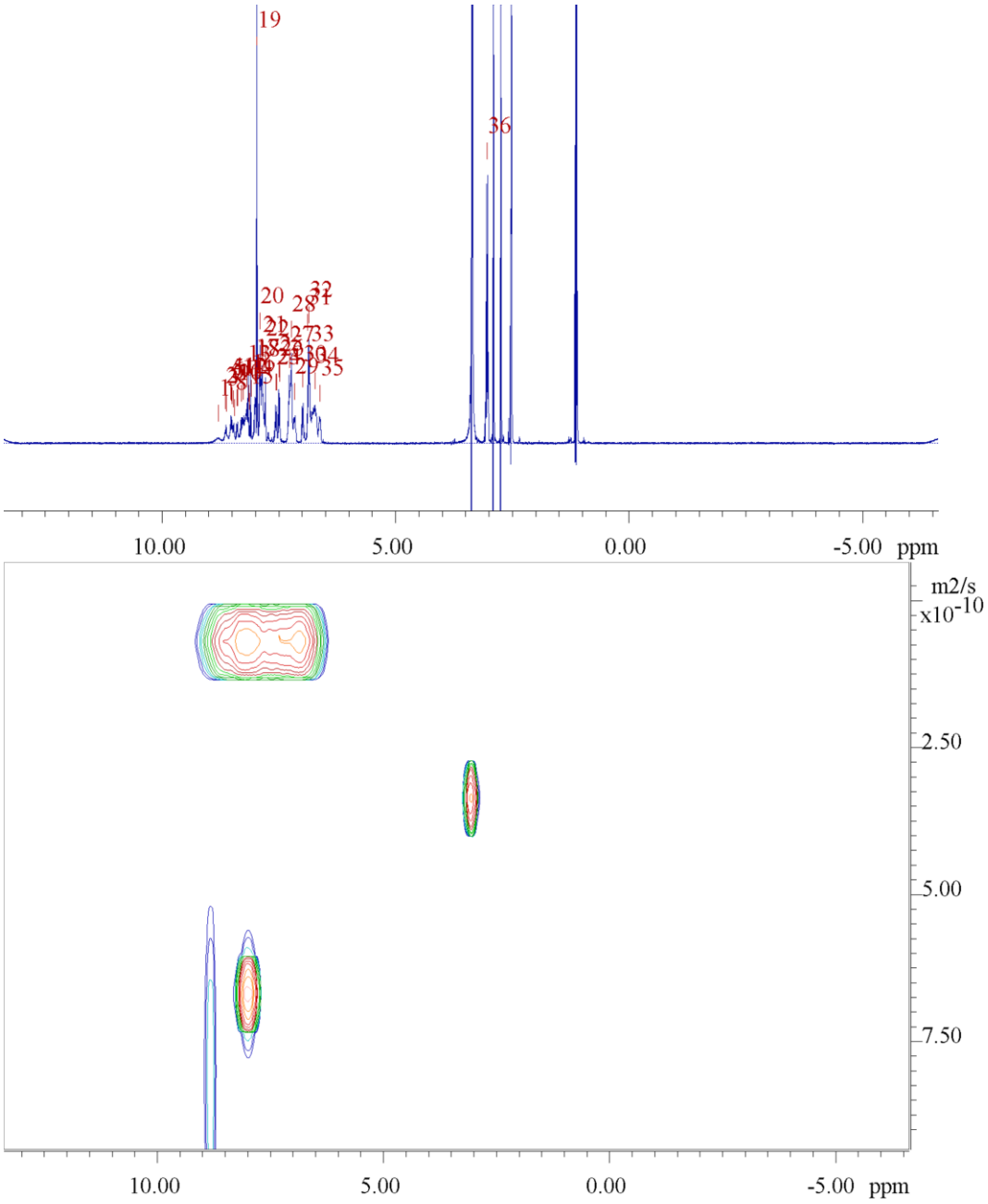

Figure 5.22. 2D DOSY NMR (400 MHz, DMSO, 298 K) spectrum of {[Y(12-MC$_{Ga,shi}$-4)]$_{3/4}$(frn)$_{6/8}$}(HNEt$_3$)$_{3/4}$. Big delta (Δ = 350 ms) and little delta (δ = 0.2 ms).

Figure 5.23 shows the DOSY spectra for the compound {[Lu(12-$MC_{Ga,shi}$-4)]$_{3/4}$(frn)$_{6/8}$}($HNEt_3$)$_{3/4}$. Four main signals are observed. The topmost signal corresponds to the MC, with a diffusion coefficient (D) ranging from 8.09×10^{-11} to 8.71×10^{-11} m^2/s. The other signals, with diffusion coefficients of 3.51×10^{-10} m^2/s, 6.71×10^{-10} m^2/s, and 7.61×10^{-10} m^2/s are attributed to triethylammonium, counter-cation protons, and DMF, respectively.

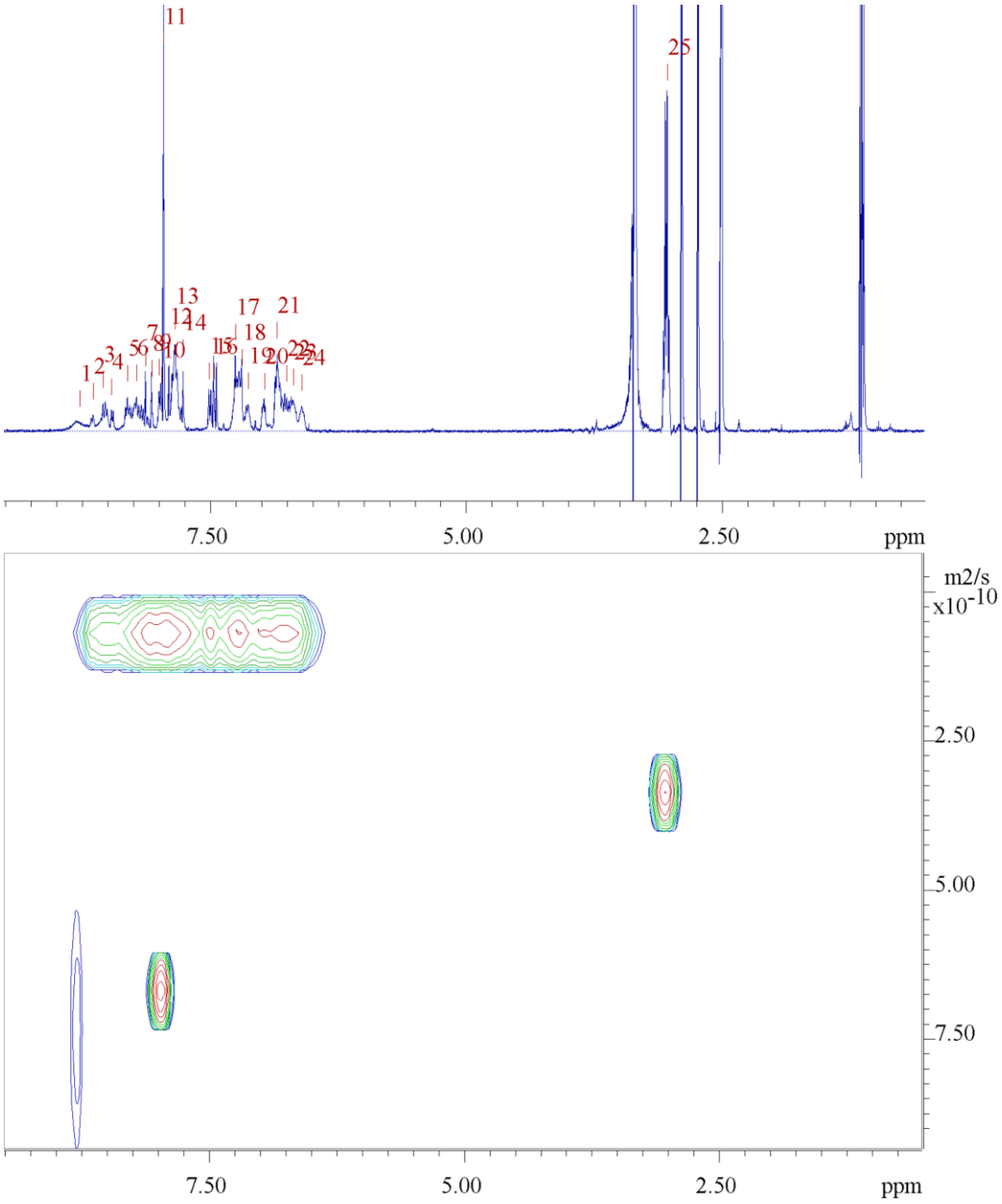

Figure 5.23. 2D DOSY NMR (400 MHz, DMSO, 298 K) spectrum of {[Lu(12-$MC_{Ga,shi}$-4)]$_{3/4}$(frn)$_{6/8}$}$(HNEt_3)_{3/4}$. Big delta (Δ = 350 ms) and little delta (δ = 0.2 ms).

In sections **5.3.1** and **5.3.2** the MC with bipyridyl as a linker was characterized by SC-XRD and in solution by ESI-MS and ^{1}H NMR, confirming the presence of a single trimeric MC species. At this point, a DOSY spectrum of {[Y(12-$MC_{Ga,shi}$-4)]$_3$(bipy)$_6$}(HNEt$_3$)$_3$ was recorded to compare its diffusion coefficient with those observed for the fluorenone MCs of Y^{III}, Lu^{III}, and La^{III} mentioned above. **Figure 5.24** shows the DOSY NMR spectrum of {[Y(12-$MC_{Ga,shi}$-4)]$_3$(bipy)$_6$}(HNEt$_3$)$_3$.

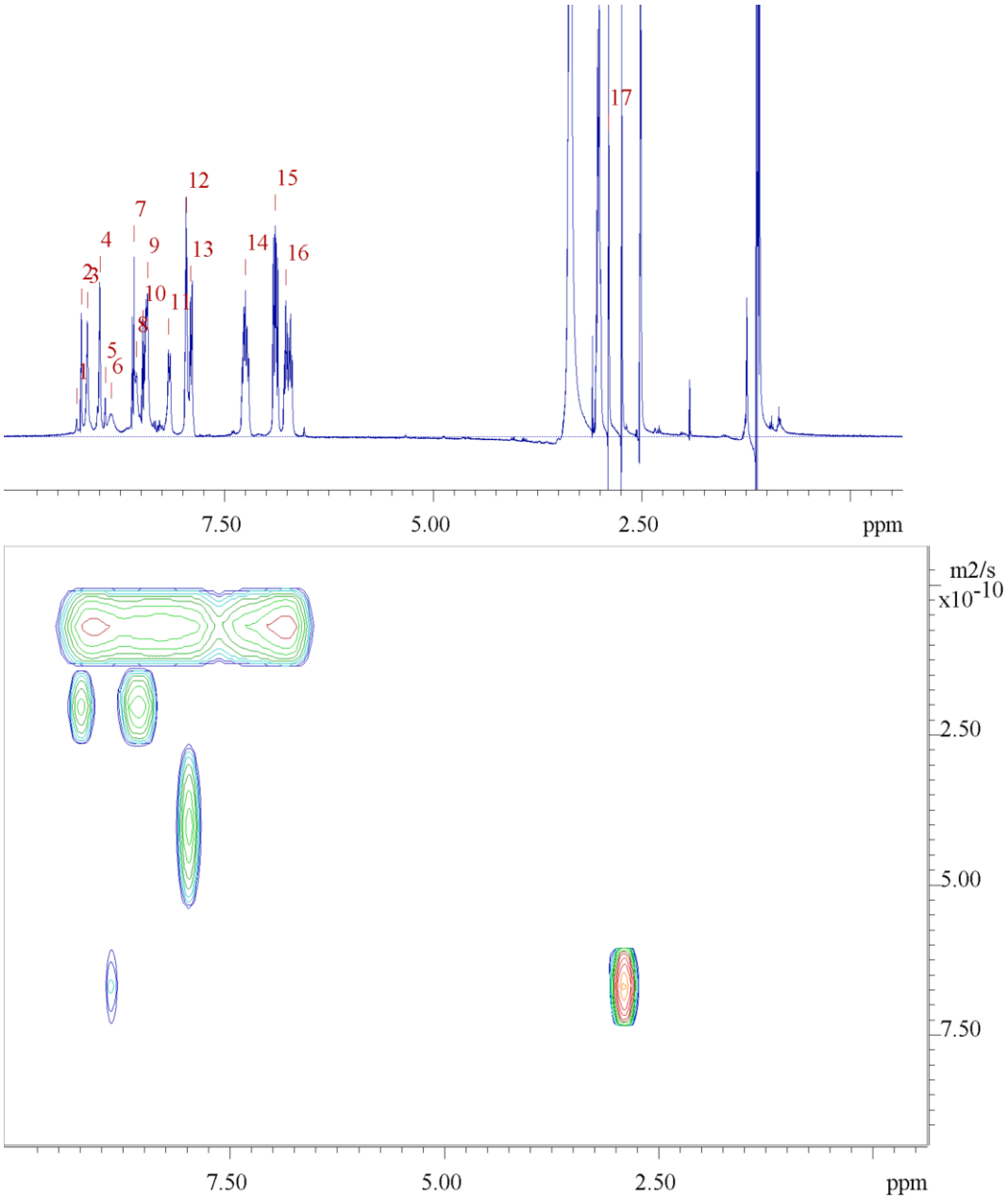

Figure 5.24. 2D DOSY NMR (400 MHz, DMSO, 298 K) spectrum of {[Y(12-$MC_{Ga,shi}$-4)]$_3$(bipy)$_6$}(HNEt$_3$)$_3$. Big delta (Δ = 350 ms) and little delta (δ = 0.2 ms).

Here, the two lowest signals (17 and 6) in the figure above, with diffusion coefficients of 6.60×10^{-10} m²/s and 6.69×10^{-10} m²/s, respectively, can be attributed to the triethylammonium counter-cations. The central signal (12), with a DDD of 3.69×10^{-10} m²/s, is attributed to DMF. The higher signals correspond to the MC molecule, with a diffusion coefficient (D) ranging from 8.37×10^{-11} to 9.63×10^{-11} m²/s. The two signals just below are attributed to the bipyridyl ligands. Their presence may be due to a minor impurity of the ligand in the sample or to the fluxionality of bipyridyl in solution within these complexes, as already described in section **5.3.1**.

The 2D DOSY spectra of fluorenone MC shown in **Figures 5.21**, **5.22**, and **5.23** indicate that, if multiple MC species are present in solution, they share diffusion coefficients of similar values. Since no significant differences are observed, distinguishing one species from another is impossible. There are two hypotheses: the first is that the two species are in fast exchange with each other at the NMR time scale, resulting in an unique diffusion coefficients for both. The second hypothesis is that the trimeric and tetrameric species are in slow exchange with each other at the NMR time scale. In this case, the difference in volume between the two MCs is not sufficient to generate significantly different hydrodynamic radii, resulting in similar diffusion coefficients. In either case, it is not possible to assign the signals observed to either the trimeric or the tetrameric species.

On the other hand, the DOSY spectrum study of the bipyridyl MC reported above (**Figure 5.24**), supported by SC-XRD and ESI-MS characterizations, shows a single signal attributable to a unique trimeric species, whose diffusion coefficient presents the same range of values as the fluorenone MCs.

For Y^{III} and Lu^{III} MCs with the fluorenone, the signal attributed to the hydrogen-bond proton in triethylammonium is confirmed by ^{1}H NMR spectra and further by ^{1}H NMR spectra with water suppression, where the peak in question disappears along with the water peak due to the exchange phenomena. (see Supplementary Information, **Figure S5.5** and **Figure S5.6**). The supporting information includes tables of diffusion coefficients along with ^{1}H NMR spectra with solvent suppression for the metallacrowns described.

5.3.7. UV-Visible Spectroscopic Study of $\{[Ln(12\text{-}MC_{Ga,shi}\text{-}4)]_3(bipy)_6\}(HNEt_3)_3$ and $\{[Ln(12\text{-}MC_{Ga,shi}\text{-}4)]_{3/4}(frn)_{6/8}\}(HNEt_3)_{3/4}$ MCs

All the compounds were characterized by UV-vis spectroscopy. **Figure 5.25** shows the UV-vis spectra of the $\{[Ln(12\text{-}MC_{Ga,shi}\text{-}4)]_3(bipy)_6\}(HNEt_3)_3$ MCs. The solutions of the ligands were obtained by diluting stock solutions at 1 mg/mL in spectral grade DMSO. The spectral range studied is from 280 nm to 370 nm, in which instead of the two distinct peaks displayed in $\{Gd[12\text{-}MC_{Ga,N(shi)}\text{-}4]Na\}_2(miph)_4$ (**Figure S5.7**) MCs at 268 and 320 nm, only one broad peak with the λ_{max} at 300 nm is obtained in the case of $\{[Ln(12\text{-}MC_{Ga,shi}\text{-}4)]_3(bipy)_6\}(HNEt_3)_3$ MCs, due to the presence of additional bipy linkers.

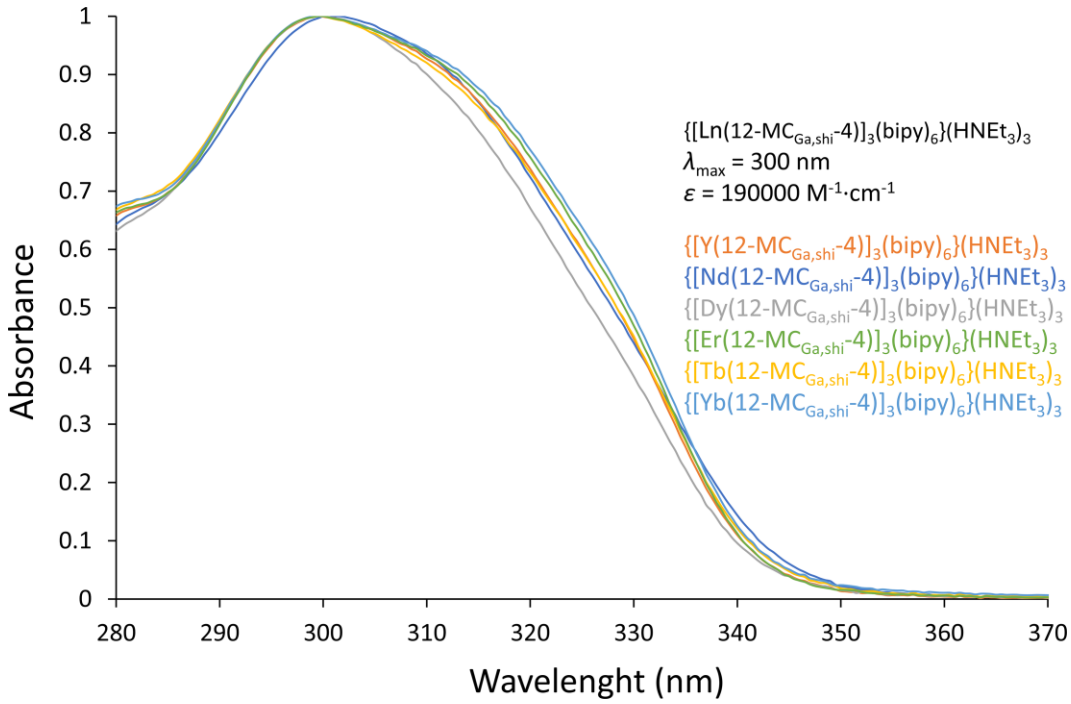

Figure 5.25. UV- visible spectra of {[Ln(12-MC$_{Ga,shi}$-4)]$_3$(bipy)$_6$}(HNEt$_3$)$_3$ MCs, 2-3 µM in spectral grade DMSO, 298 K.

The UV-vis spectra of {[Ln(12-MC$_{Ga,shi}$-4)]$_{3/4}$(frn)$_{6/8}$}(HNEt$_3$)$_{3/4}$ MCs recorded in the same way, as shown in **Figure 5.26**. The systems exhibit three distinct bands with two first bands (λ_{max} = 260 and 320 nm) in the UV that can be attributed to the absorption of the shi ligands of the MC scaffold, and partially of H_2frn for the first band at 260 nm. The third additional band is very broad and spans from 360 to 420 nm. It is attributed to the fluorenone moiety of the H_2frn linkers. The UV-Visible spectrum of H_2frn is reported in **Figure S5.4.**

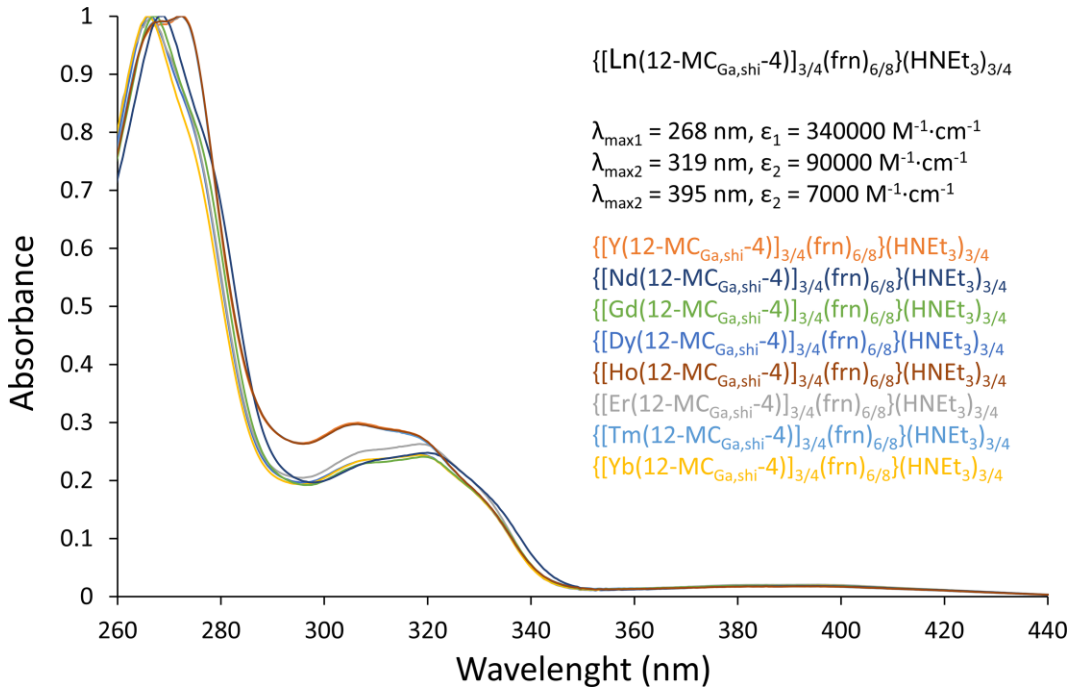

Figure 5.26. UV- visible spectra of {[Ln(12-MC$_{Ga,shi}$-4)]$_{3/4}$(frn)$_{6/8}$}(HNEt$_3$)$_{3/4}$. C_{MC} = 5-8 µM, DMSO (spectrophotometric grade), 298 K.

5.3.8 IR Spectroscopy of {[Ln(12-MC$_{Ga,shi}$-4)]$_3$(bipy)$_6$}(HNEt$_3$)$_3$ and {[Ln(12-MC$_{Ga,shi}$-4)]$_{3/4}$(frn)$_{6/8}$}(HNEt$_3$)$_{3/4}$ MCs

All the isolated MCs with the fluorenone and bypyridine dicarboxylate linkers were characterized by ATR-FTIR spectroscopy. Spectra of samples containing the same linker with different Lns show no significant differences, supporting the hypothesis of a structural similarity of the compounds. **Figure 5.27** and **Figure 5.28** report the IR spectra of {[Ln(12-MC$_{Ga,shi}$-4)]$_3$(bipy)$_6$}(HNEt$_3$)$_3$ and {[Ln(12-MC$_{Ga,shi}$-4)]$_{3/4}$(frn)$_{6/8}$}(HNEt$_3$)$_{3/4}$ metallacrown complexes.

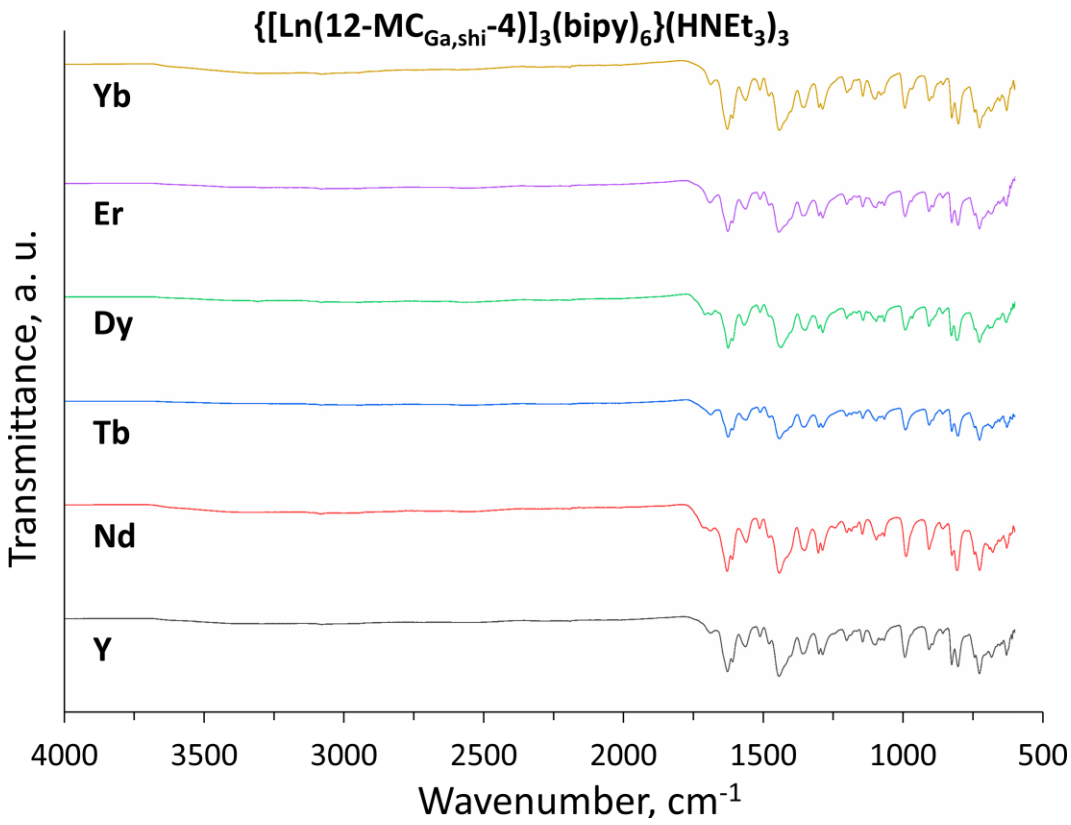

Figure 5.27. FT-ATR-IR spectra of solid {[Ln(12-MC$_{Ga,shi}$-4)]$_3$(bipy)$_6$}(HNEt$_3$)$_3$ metallacrowns (Ln^{III} = Y^{III}, Nd^{III}, Tb^{II}, Dy^{III}, Er^{III}, Yb^{III}).

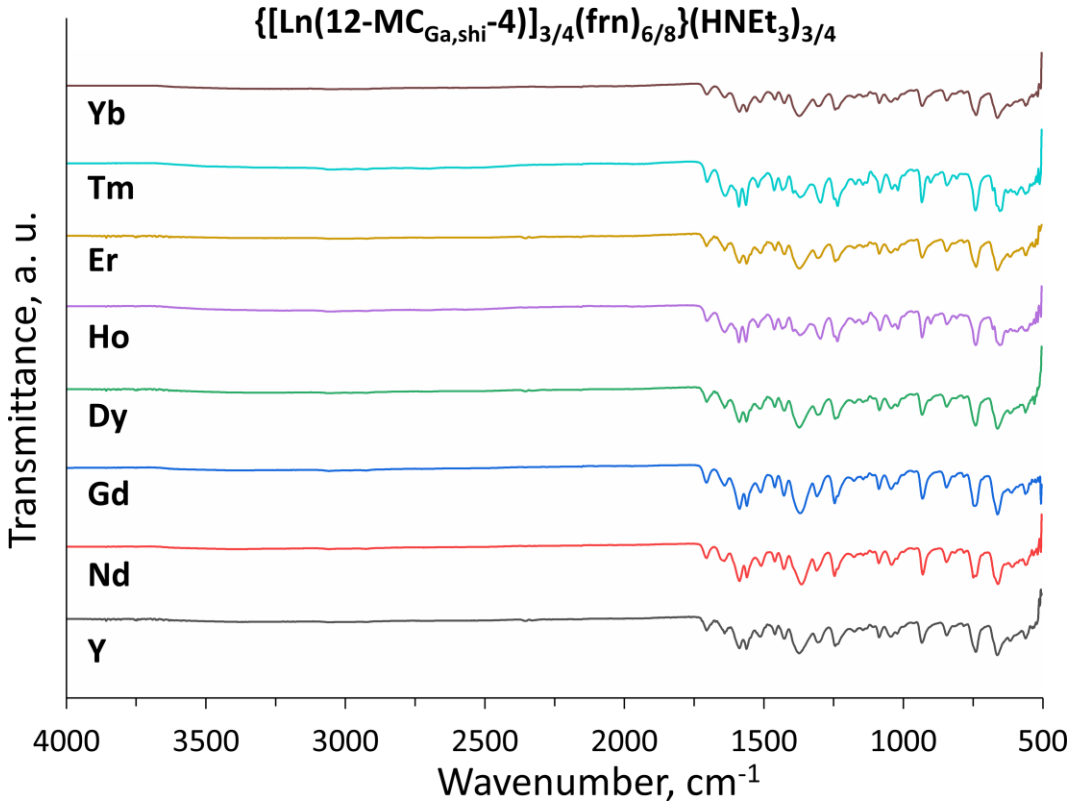

Figure 5.28. FT-ATR-IR spectra of solid $\{[Ln(12\text{-}MC_{Ga,shi}\text{-}4)]_{3/4}(frn)_{6/8}\}(HNEt_3)_{3/4}$ metallacrowns (Ln^{III} = Y^{III}, Gd^{III}, Nd^{III}, Dy^{III}, Ho^{III}, Er^{III}, Tm^{III}, Yb^{III}).

5.3.9 Ln^{III}-centered luminescence: $\{[Ln(12\text{-}MC_{Ga,shi}\text{-}4)]_3(bipy)_6\}^{3-}$ MCs

All photophysical measurements and NIR imaging (capillaries) were done by Dr. Svetlana V. Eliseeva at the Center for Molecular Biophysics (CBM) in Orléans.

The Ln^{III}-centered luminescence properties of $\{[Ln(12\text{-}MC_{Ga,shi}\text{-}4)]_3(bipy)_6\}^{3-}$ MCs were studied both in DMSO solutions and in the solid state (SS). Upon excitation of the MC band in the UV at λ_{exc} = 320 (DMSO) or 340 nm (SS), the characteristic emission signal of the three studied NIR-emitting Lns could be detected (**Figure 5.29**).

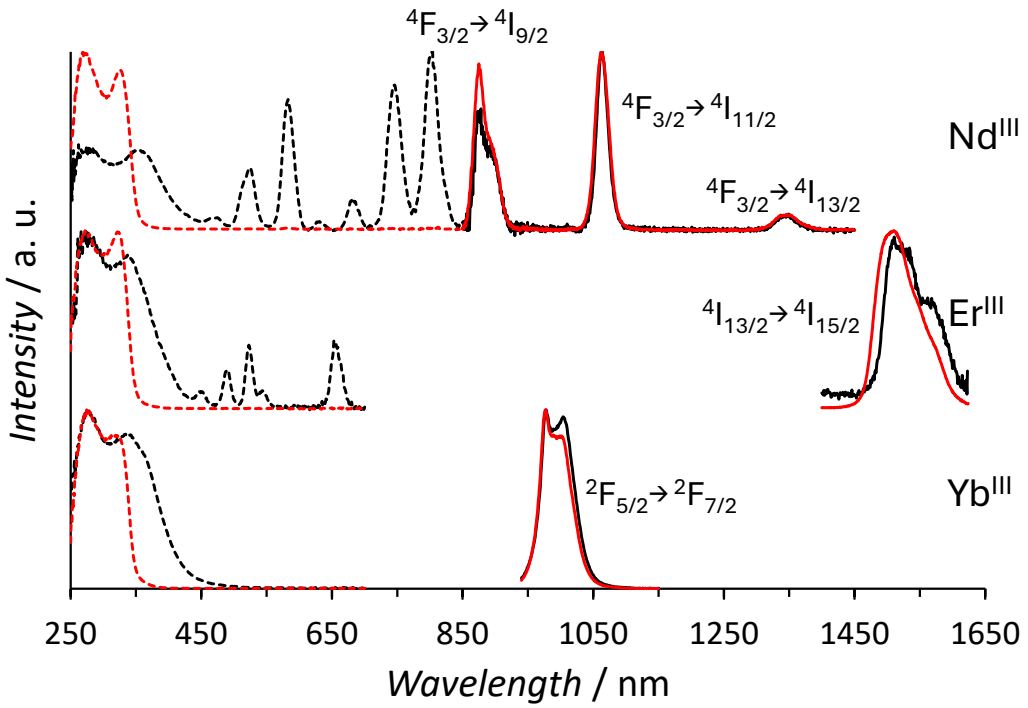

Figure 5.29. Corrected and normalized emission (full lines) and excitation (dotted lines) spectra of $\{[Ln(12\text{-}MC_{Ga,shi}\text{-}4)]_3(bipy)_6\}^{3-}$ MCs in DMSO solutions (red traces, C = 50 µM, λ_{exc} = 320 nm) and in the SS (black traces, λ_{exc} = 340 nm).

Nd^{III} emission is detected as three NIR bands at 886 nm ($^4F_{3/2}\rightarrow{}^4I_{9/2}$), 1062 nm ($^4F_{3/2}\rightarrow{}^4I_{11/2}$) and 1340 nm ($^4F_{3/2}\rightarrow{}^4I_{13/2}$). For Er^{III} and Yb^{III}, only one transition is observed, as expected. It is located at 992 nm for Yb^{III}, arising from the $^2F_{5/2}\rightarrow{}^2F_{7/2}$ transition, and at 1525 nm for Er^{III}, from the $^4I_{13/2}\rightarrow{}^4I_{15/2}$ transition.

Table 5.1. Photophysical properties of MCs, recorded in DMSO (50 µM) and in the SS.

MC / bridge	Conditions	Q_L^{Ln} [a] %	τ_{obs} [b] µs
$[Nd_3Ga_{12}]$ / bipy	DMSO, 50 µM	0.155(1)	2.7(1) [c]
	solid state	0.037(2)	0.90(1) [d]
$[Er_3Ga_{12}]$ / bipy	DMSO, 50 µM	$1.02(3)\cdot10^{-2}$	7.4(2)
	solid state	$8.8(3)\cdot10^{-3}$	2.81(5) [e]
$[Yb_3Ga_{12}]$ / bipy	DMSO, 50 µM	3.69(1)	48.2(2)
	solid state	0.107(9)	12.3(1)

[a] λ_{exc} = 320 nm and 340 nm for DMSO and the solid state, respectively. [b] λ_{exc} = 355 nm. [c] τ_{avg} of τ_1 = 2.8(1) µs (84(3) %) and τ_2 = 1.11(5) µs (16(3) %). [d] τ_{avg} of τ_1 = 0.97(1) µs (72(2) %) and τ_2 = 0.299(7) µs (28(2) %). [e] τ_{avg} of τ_1 = 3.00(5) µs (76.5(2) %) and τ_2 = 1.2(1) µs (23.5(2) %).

The quantum yield in the SS is difficult to interpret due to complicated intermolecular energy transfers and will not be discussed further. In DMSO, quantum yields of 0.155(1) % and 3.69(1) % are obtained for Nd^{III} and Yb^{III}, respectively. Er^{III} sensitization is challenging and a quantum yield of $1.02(3)\cdot10^{-2}$ % is measured. While Nd^{III} cannot be compared to its $\{[Nd(12\text{-}MC_{Ga,shi}\text{-}4)(bza)_4]\}^{1-}$ monomeric equivalent as its isolation is not possible due to the large Nd^{III} cation a

comparison for Er^{III} and Yb^{III} is possible.[116,117] A quantum yield of 3.69(1) % is obtained in DMSO for $\{[Yb(12\text{-}MC_{Ga,shi}\text{-}4)]_3(bipy)_6\}^{3-}$ and that value is comparable to the quantum yield of 4.29(1) % reported for $\{[Yb(12\text{-}MC_{Ga,shi}\text{-}4)(bza)_4]\}^{1-}$ in CD_3OD. The same observation can be made in the case of Er^{III}, with a quantum yield of $1.02(3)\cdot10^{-2}$ % for $\{[Yb\ (12\text{-}MC_{Ga,shi}\text{-}4)]_3(bipy)_6\}^{3-}$ in DMSO and a value of $4.5(3)\cdot10^{-2}$ % for $\{[Yb(12\text{-}MC_{Ga,shi}\text{-}4)(bza)_4]\}^{1-}$ in CD_3OD. Based on this observation and on the solid-state X-ray diffraction structure obtained for $\{[Ln(12\text{-}MC_{Ga,shi}\text{-}4)]_3(bipy)_6\}^{3-}$ where solvent molecules can coordinate to the Ln^{III} emissive centers, it seems that the presence of coordinated solvent does not impact Ln^{III} luminescence too much in these MCs.

5.3.10 NIR-II Luminescence imaging

To probe the amount of light emitted by these NIR-emitting MCs, we monitored their luminescence in capillaries using a macroscopy NIR imaging setup designed for small animal imaging. DMSO solutions of $\{[Ln(12\text{-}MC_{Ga,shi}\text{-}4)]_3(bipy)_6\}^{3-}$ MCs (C_{MC} = 50 µM) were placed in quartz capillaries and the Ln^{III}-centered emission was monitored upon irradiation of the MC scaffold at λ_{exc} = 320 nm.

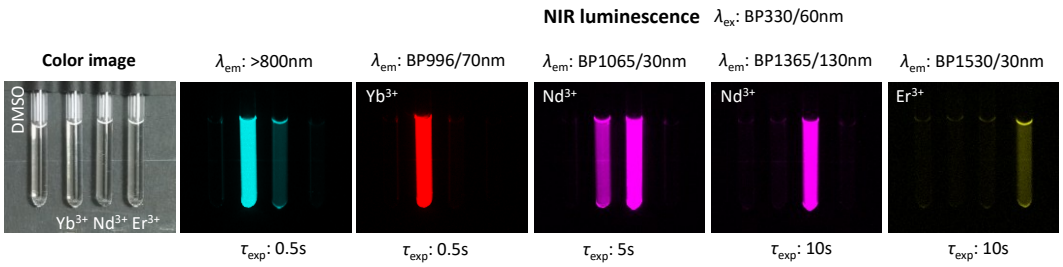

Figure 5.30. Recorded luminescence images of $\{[Ln(12\text{-}MC_{Ga,shi}\text{-}4)]_3(bipy)_6\}^{3-}$ MCs in

DMSO (50 µM) at 298 K in quartz capillaries. λ_{exc} was selected with a BP330/60 nm filter. The NIR emission signal was recorded using a common 800 nm LP filter combined with additional BP filters depending on the nature of the Ln^{III} considered. Yb^{III}: BP996/70 nm; Nd^{III}: BP1065/30 nm and BP1365/130 nm; Er^{III}: BP1530/30 nm. Exposition times: τ_{exp} = 0.5 to 10 s.

As depicted by the recorded images above, the Ln^{III}-centered NIR emission of every Ln^{III} can be detected. The observed intensity is well in line with the measured quantum yields (**Table 5.1**). When only the 800 nm LP is used (**Figure 5.30**, **a**), the strong Yb^{III} emission largely surpass Nd^{III} emission (barely visible), while Er^{III} emission is not detected at all. Every Ln^{III} transition can be selectively isolated using additional bandpass filters (**Figure 5.30**, **c-f**). When the $^4F_{3/2}\rightarrow{}^4I_{11/2}$ transition of Nd^{III} is monitored at 1062 nm (**Figure 5.30**, **d**, BP1065/30 nm), residual Yb^{III} emission from the $^2F_{5/2}\rightarrow{}^2F_{7/2}$ transition at 992 nm is also detected. Nd^{III} can also be monitored further in the NIR due to its $^4F_{3/2}\rightarrow{}^4I_{13/2}$ transition at 1347 nm (**Figure 5.30**, **e**, BP1365/130 nm). The $^4I_{13/2}\rightarrow{}^4I_{15/2}$ transition of Er^{III} at 1510 nm is also detected (**Figure 5.30, f**, BP1530/30 nm), albeit weak due to its lower quantum yield. This simple experiment demonstrates that these NIR-emitting MCs emit enough photons for a sensitive and selective detection of their emission.

5.3.11 Ln^{III}-centered luminescence: frn linker as a Ln^{III} sensitizer in the visible

As described previously, the dicarboxylic acid fluorenone linker H_2frn display an electronic transition in the visible at λ_{abs} = 390 nm, with a molar extinction

coefficient of ε = 7000 $M^{-1}{\cdot}cm^{-1}$. This electronic transition is sufficiently differentiated from the MC scaffold absorption band in the UV at λ_{abs} = 320 nm to investigate its use as an additional antenna absorbing in the visible. While the speciation in solution is still unclear when H_2frn is used in the preparation of MCs as ^{1}H NMR suggest the presence of both the trimeric and tetrameric MCs in solution, it is still of interest to see if the fluorenone linker can be used for Ln^{III} sensitization through its electronic transition in the visible at 390 nm. The photophysical properties of the frn MCs were recorded both in the SS and in DMSO solutions. Characteristic emission bands of Nd^{III}, Er^{III} and Yb^{III} are detected upon irradiation of both the MC scaffold in the UV (**Figure 5.31**) and the frn band (**Figure 5.32**).

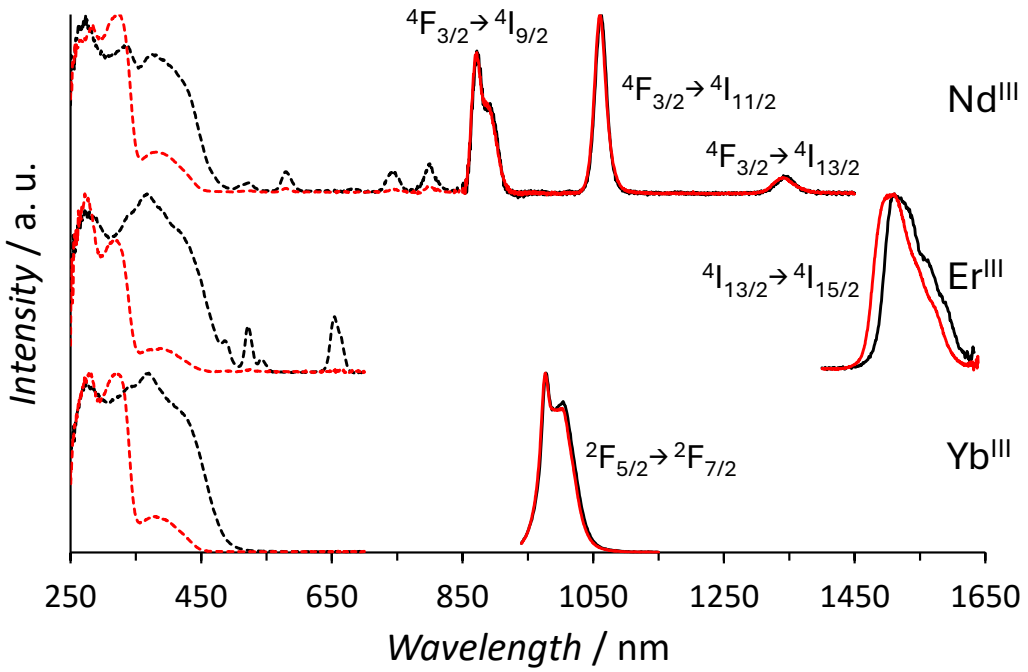

Figure 5.31. Corrected and normalized emission (full lines) and excitation (dotted lines) spectra of frn MCs in DMSO (red traces, C_{MC} = 50 µM, λ_{exc} = 320 nm) and in the SS (black traces, λ_{exc} = 340 nm). Here, Ln^{III} sensitization occurs through the MC scaffold.

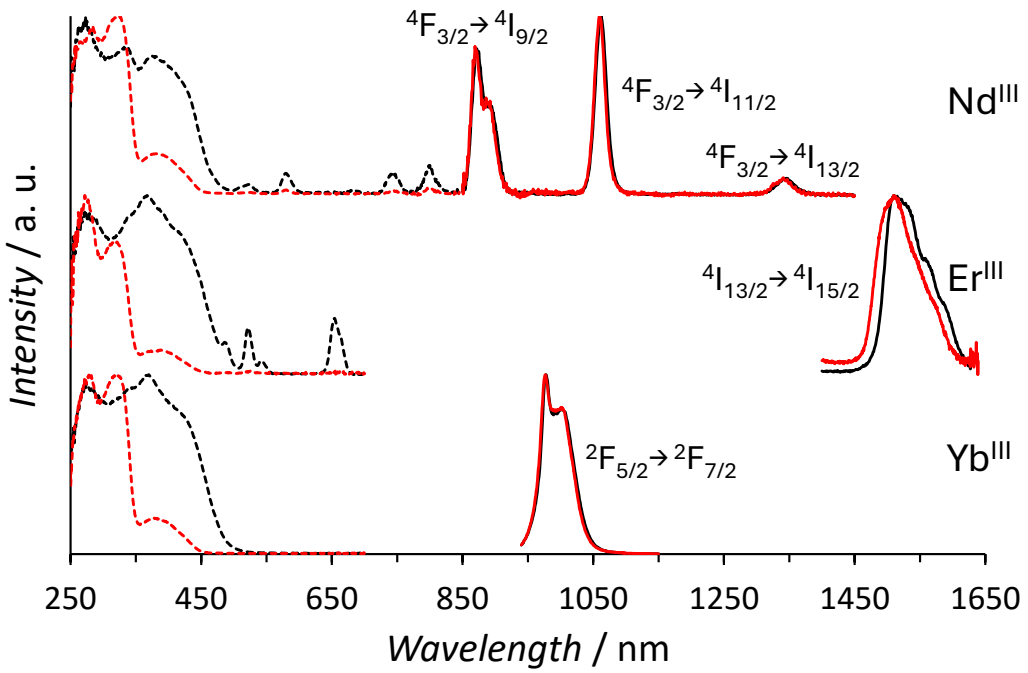

Figure 5.32. Corrected and normalized emission (full lines) and excitation (dotted lines) spectra of frn MCs in DMSO (red traces, C_{MC} = 50 μM, λ_{exc} = 400 nm) and in the SS (black traces, λ_{exc} = 420 nm). Here, Ln^{III} sensitization occurs through the absorption band of the frn linkers in the visible.

The detection of Yb^{III} emission at 994 nm (arising from the $^5F_{5/2}\rightarrow{}^2F_{7/2}$ transition) upon irradiation onto the electronic absorption band of the frn linkers at 400 nm confirms that they can be used as additional antenna for the sensitization of Ln^{III}. Indeed, Yb^{III} does not display any *f-f* transition in the visible range (as opposed to Nd^{III} and Er^{III}) and the only way Yb^{III} emission is detected upon excitation at 400 nm is by an energy transfer from the frn linkers to Yb^{III}. For all three Ln^{III}, the excitation spectra show the presence of the frn band in the visible at 390 nm (**Figure 5.32**, red dotted lines), further confirming the energy transfer from frn to the the three Ln^{III} studied.

Table 5.2. Photophysical properties of frn MCs in DMSO (50 µM) and in the SS with sensitization through the MC scaffold (λ_{exc} = 320 nm and 340 nm in DMSO and SS, respectively) and through the frn absorption band in the visible (λ_{exc} = 400 nm and 420 nm in DMSO and SS, respectively).

MC / bridge	Conditions	λ_{exc}	Q_L^{Ln}	τ_{obs}[a]
		nm	%	µs
[Nd^{III}] / frn	DMSO, 50 µM	320	0.117(2)	3.75(5)
		400	0.088(2)	
	solid state	340	0.200(2)	1.47(1) [b]
		420	0.206(1)	
[Er^{III}] / frn	DMSO, 50 µM	320	$4.50(8)\cdot10^{-3}$	7.6(1)
		400	$3.35(1)\cdot10^{-3}$	
	solid state	340	$1.72(7)\cdot10^{-2}$	3.63(1) [c]
		420	$1.99(3)\cdot10^{-2}$	
[Yb^{III}] / frn	DMSO, 50 µM	320	0.52(1)	52.6(2)
		400	0.357(1)	
	solid state	340	0.44(2)	10.0(1)
		420	0.476(2)	

[a] λ_{exc} = 355 nm. [b] τ_{avg} of τ_1 = 1.51(1) µs (87(1) %) and τ_2 = 0.47(1) µs (13(1) %). [c] τ_{avg} of τ_1 = 3.78(1) µs (84(1) %) and τ_2 = 1.34(3) µs (16(1) %).

As for the MCs with the bipy linker, complicated intramolecular energy transfer occurs in the SS and it will not be discussed in details. By comparison with the bipy MCs (**Table 5.2**), the quantum yields obtained through sensitization using the MC scaffold are slightly lower in the case of frn, probably due to energy transfer from the MC scaffold to the frn linker. Overall, sensitization through the MC scaffold or the frn antenna gives quantum yield values of similar magnitude. This is expected as the frn antenna is directly coordinated to the Ln^{III} emissive centers and the same

transfer mechanisms are involved in both cases. The same trend as in the bipy MCs is obtained, with quantum yields following the series $Yb^{III} > Nd^{III} > Er^{III}$.

5.3.12 NIR-II Luminescence imaging

To probe the amount of light emitted by these NIR-emitting MCs, their luminescence was monitored in capillaries using a macroscopy NIR imaging setup designed for small animal imaging. DMSO solutions of frn MCs (C_{MC} = 50 µM) were placed in quartz capillaries and the Ln^{III}-centered emission was monitored upon irradiation of frn absorption band in the visible at λ_{exc} = 417 nm.

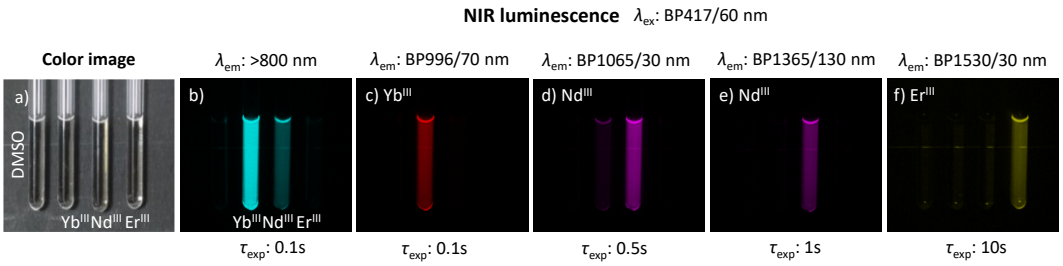

Figure 5.33. Recorded luminescence images of frn MCs NIR emission in DMSO (50 µM, 298 K). λ_{exc} = 417 nm (BP417/60 nm filter). The NIR emission signal was recorded with a 800 nm LP filter combined with additional BP filters depending on the nature of the Ln^{III} considered. Yb^{III}: BP996/70 nm; Nd^{III}: BP1065/30 nm and BP1365/130 nm; Er^{III}: BP1530/30 nm. Exposition times: τ_{exp} = 0.5 to 10 s.

As depicted by the recorded images above, the Ln^{III}-centered NIR emission of every Ln^{III} can be detected upon irradiation in the electronic absorption band of the frn linkers with λ_{exc} = 417 nm. As in the MCs with bipy, when only the 800 nm LP is used (**Figure 33**, **b**), the strong Yb^{III} emission largely surpass Nd^{III} emission (barely visible), while Er^{III} emission is not detected at all. Every Ln^{III} transition can be selectively

isolated using additional bandpass filters (**Figure 33**, **c-f**). When the $^4F_{3/2}\rightarrow{}^4I_{11/2}$ transition of Nd^{III} is monitored at 1062 nm (**Figure 33**, **d**, BP1065/30 nm), residual Yb^{III} emission from the $^2F_{5/2}\rightarrow{}^2F_{7/2}$ transition at 992 nm is also detected. Nd^{III} can also be monitored further in the NIR due to its $^4F_{3/2}\rightarrow{}^4I_{13/2}$ transition at 1347 nm (**Figure 33**, **e**, BP1365/130 nm). The $^4I_{13/2}\rightarrow{}^4I_{15/2}$ transition of Er^{III} at 1510 nm is also detected (**Figure 33**, **f**, BP1530/30 nm), albeit weak due to its lower quantum yield. To obtain images of similar intensity for Yb^{III}, Nd^{III} and Er^{III}, the exposition times were increased in the case of Nd^{III} and Er^{III} to compensate for their lower quantum yields. Overall, the emission intensity is lower than in the bipy MCs, but an excitation of λ_{exc} = 417 nm can be used instead of λ_{exc} = 330 nm. This simple experiment demonstrates that in frn MCs, the absorption band in the visible can still be used for Ln^{III} sensitization and that in all three cases, enough photons are collected for a sensitive and selective detection of their emission. Therefore, the use of dicarboxylic linkers that absorb in the visible is a viable strategy to sensitize NIR-emitting Ln^{III} and produce visible-absorbing MCs that could be used for biological imaging, as excitation wavelength in the UV are detrimental to cells and tissues.

5.4 Conclusion

This work has explored the structural and functional properties of metallacrown (MC) complexes based on bipyridyl and fluorenone dicarboxylic linkers, highlighting the differences in their formation of trimeric and tetrameric oligomeric species. Complexes containing bipyridyl linkers exclusively formed trimeric species, which were observed and characterized in solution by ^1H NMR spectroscopy and ESI-MS, and confirmed in the solid state by X-ray diffraction. The bipyridyl linker was used to achieve luminescent properties in place of the magnetic

properties previously observed with Mn^{II}/Dy^{III}-based trimers.[116] By incorporating Ga^{III} with bipyridyl linkers, we enable lanthanide (Ln) luminescence. In contrast, complexes containing the fluorenone linker demonstrated more complex behavior. X-ray analysis revealed both trimeric and tetrameric species, depending on the size of the lanthanide considered. In solution, ^{1}H NMR spectra of Ln^{III} of different size suggest that the tetrameric and trimeric forms of the MCs are in equilibrium, excepted, maybe, for larger Ln^{III} as depicted by the simplified La^{III} ^{1}H NMR spectrum that is tentatively attributed to a single tetrameric species in solution. The extended π system of the fluorenone linker also showed significant absorption in the visible range and could be used for the sensitization of Ln^{III} in the visible. Both bipyridyl and fluorenone MCs were evaluated as sensitizers of NIR-emitting Ln^{III} and Ln^{III}-centered emission could be detected in both systems. The fluorenone MCs offer the advantage of an excitation in the visible at λ_{exc} = 400 nm, which is advantageous for biological applications as excitation in the UV is harmful to biological samples.

In summary, this study demonstrates how dicarboxylic linkers with distinct characteristics can be used for the preparation of [LnGa4]-based MCs of different topologies and properties. These results open new perspectives for their development and use in photonic and biomedical applications based on their NIR luminescence.

5.5 Experimental section

5.5.1 Materials and methods

All reagents and chemicals were purchased from commercial sources and used without further purification unless otherwise stated. ESI-MS spectra were recorded on an Agilent 6230 TOF HPLC-MS spectrometer in negative or positive modes using the following ionization and cone potentials: 240 V and 65 V for organic molecules, 350 V and 50 V for MCs. Stock solutions of MCs at 1 mg/mL in DMSO were prepared and further diluted to 80-200 µg/µL in MeOH/DMSO 90:10. Recorded data were processed using the Agilent MassHunter software. Elemental analyses were performed by Atlantic Microlab. UV-vis spectra were recorded in DMSO on a Varian Cary 100 Bio UV-visible spectrophotometer using 1 cm Hellma QS or QX quartz glass cuvettes. The IR spectra were collected on a Thermo-Nicolet IS-50 spectrometer in ATR-FTIR configuration. Recorded data were processed using Thermo Scientific OMNIC Specta software.

5.5.2 Photophysical properties

Photophysical measurements were performed on powder samples or freshly prepared solutions of MCs in DMSO placed in 2.4 mm i.d. quartz capillaries or Suprasil® cells. Emission and excitation spectra were measured on a Horiba-Jobin-Yvon Fluorolog 3 spectrofluorimeter equipped with visible and NIR photomultiplier tubes (PMTs: R13456 and H10330-75 from Hamamatsu) upon excitation with a continuous Xenon lamp. Phosphorescence spectra of Gd^{III} MCs were measured at 77 K in time-resolved mode. All spectra were corrected for the

instrumental functions. Luminescence lifetimes were determined under excitation at 355 nm provided by a Nd:YAG laser (YG 980; Quantel), the signals in the NIR range were detected with a H10330-75 PMT connected to an iHR320 monochromator (Horiba Scientific). The output signals from the detectors were fed into a 500 MHz bandpass digital oscilloscope (TDS 754C; Tektronix). Luminescence lifetimes are averages of at least three independent measurements. Quantum yields were determined with a Fluorolog 3 spectrofluorimeter based on the absolute method using an integration sphere (Model G8, GMP SA, Renens, Switzerland). Each sample was measured several times. The experimental error for the determination of quantum yields is estimated as ~10 %. All photophysical measurements were done by Dr. Svetlana V. Eliseeva at the Center for Molecular Biophysics (CBM) in Orléans

5.5.3 NIR luminescence imaging

Images of quartz capillaries containing MCs DMSO solutions (C = 50 µM) were recorded using a custom-designed NIR-II KaerLabs imaging system that includes a ZEPHIR 1.7x camera (Photon etc., Montréal, Quebec, Canada). A 330/60 nm bandpass (BP) filter was used for the selection of the excitation wavelength. Emission signals were recorded using an 800 nm longpass (LP) filter along with additional BP filters depending on the nature of the monitored Ln^{III}.: Yb^{III}-BP996/70 nm; Nd^{III}-BP1065/30 nm and BP1365/130 nm; Er^{III}-BP1530/30 nm. The recorded images were treated using the Fiji distribution of ImageJ/ImageJ2. All NIR imaging (capillaries) where done by Dr. Svetlana V. Eliseeva at the Center for Molecular Biophysics (CBM) in Orléans

5.5.4 X-ray data collection

Single crystal data were collected with a Bruker D8 PhotonII area detector diffractometer MoKα (λ = 0.71073 Å) and CuKα (λ = 1.54184). Complete datasets were obtained by merging several series of exposure frames collected at 200 K. An absorption correction was applied with the program SADABS[70]. The structures were solved with ShelxT[71] and refined on F^2 with full-matrix least squares (ShelxL)[72], using the Olex2 software package[73]. Non hydrogen atoms were refined with anisotropic thermal parameters for all compounds. For $\{[TbNa(12\text{-}MC_{Ga,shi}\text{-}4)]_3(bipy)_6(DMF)_2(H_2O)_{10}\}(HNEt_3)(DMF)_5$, the asymmetric unit is disorder over two site refined with occupancy of 0.75 and 0.25. The triethyl ammonium atom was refined with isotropic thermal parameters. The figures were made with 0.75 occupancy part. For $\{[La(12\text{-}MC_{Ga,shi}\text{-}4)]_3(frn)_6(H_2O)_5(DMF)_3\}^{3-}(DMF)$, three of the shi^{3-} ligand and the DMF coordinated to the lanthanide were disorder over two sites and were refined with free variable. For $\{[Y(12\text{-}MC_{Ga,shi}\text{-}4)]_4(frn)_8(H_2O)_{16}\}^{3-}$, the asymmetric unit is disorder over two sites with 0.5 occupancy.

5.6 Chemistry

5.6.1 Synthetic procedures

Synthesis of $\{[Ln(12\text{-}MC_{Ga,shi}\text{-}4)]_{3/4}(x)_{6/8}\}(HNEt_3)_{3/4}$ metallacrowns (x = bipy, frn). Salicylhydroxamic acid (H_3shi) (50 mg, 326 µmol, 1 eq), 2,2'-bipyridine-5,5'-dicarboxylic acid or 9-fluorenone-2,7-dicarboxylic acid (163µmol, 0.5 eq.), $Ga(NO_3)_3{\cdot}H_2O$ (90 mg, 326 µmol, 1 eq.), and $Ln(NO_3)_3{\cdot}xH_2O$ (Ln = Y, Nd, Gd, Tb, Dy, Er, Yb. 81 µmol, 0.25 eq) were dissolved in 4 mL of DMF. The reaction mixture was

added with triethylamine (181 µL, 1.31 mmol, 4 eq.) and stirred overnight at room temperature. The resulting pale-yellow solution was allowed to stand for 12 hours, and the precipitate was filtered off. The product was obtained by slow evaporation of the solvent in the form of pink crystals after two weeks. The crystals were collected by filtration, washed with cold DMF and *t*-butyl methyl ether, and dried.

{[Y(12-$MC_{Ga,shi}$-4)]$_3$(bipy)$_6$}(HNEt$_3$)$_3$. The synthetic yield was 5.95 % based on $Y(NO_3)_3{\cdot}6H_2O$. ESI-MS (MeOH/DMSO 90:10, negative mode, m/z): {[Y(12-$MC_{Ga,shi}$-4)]$_3$(bipy)$_6$}$^{3-}$: 1452.73 (calc.), 1452.08 (exp.). Elemental analysis for {[Y(12-$MC_{Ga,shi}$-4)]$_3$(bipy)$_6$}(HNEt$_3$)$_3{\cdot}13.1H_2O{\cdot}2.8$DMF: calc.: %C 42.91, %H 3.51, %N 8.18; found: %C 42.92, %H 3.52, %N 8.16.

{[Gd(12-$MC_{Ga,shi}$-4)]$_3$(bipy)$_6$}(HNEt$_3$)$_3$. The synthetic yield was 4.77 % based on $Gd(NO_3)_3{\cdot}6H_2O$. Waiting for the ESI-MS spectra and elemental analysis.

{[Nd(12-$MC_{Ga,shi}$-4)]$_3$(bipy)$_6$}(HNEt$_3$)$_3$. The synthetic yield was 4.92 % based on $Nd(NO_3)_3{\cdot}6H_2O$. ESI-MS (MeOH/DMSO 90:10, negative mode, m/z): {[Nd(12-$MC_{Ga,shi}$-4)]$_3$(bipy)$_6$}$^{3-}$: 1508.09 (calc.), 1508.06 (exp.). Elemental analysis for {[Nd(12-$MC_{Ga,shi}$-4)]$_3$(bipy)$_6$}(HNEt$_3$)$_3{\cdot}6.9H_2O{\cdot}2.3$DMF: calc.: %C 42.41, %H 3.19, %N 8.01; found: %C 42.47, %H 3.36, %N 7.88.

{[Er(12-$MC_{Ga,shi}$-4)]$_3$(bipy)$_6$}(HNEt$_3$)$_3$. The synthetic yield was 2.81 % based on $Er(NO_3)_3{\cdot}5H_2O$. ESI-MS (MeOH/DMSO 90:10, negative mode, m/z): {[Er(12-$MC_{Ga,shi}$-4)]$_3$(bipy)$_6$}$^{3-}$: 1530.78 (calc.), 1530.75 (exp.). Elemental analysis for {[Er(12-$MC_{Ga,shi}$-4)]$_3$(bipy)$_6$}(HNEt$_3$)$_3{\cdot}0.1H_2O{\cdot}6.0$DMF: calc.: %C 43.19, %H 3.29, %N 8.66; found: %C 43.30, %H 3.40, %N 8.54.

{[Yb(12-MC$_{Ga,shi}$-4)]$_3$(bipy)$_6$}(HNEt$_3$)$_3$. The synthetic yield was 4.07 % based on Yb(NO$_3$)$_3$·5H$_2$O. ESI-MS (MeOH/DMSO 90:10, negative mode, m/z): {[Yb(12-MC$_{Ga,shi}$-4)]$_3$(bipy)$_6$}$^{3-}$: 1536.45 (calc.), 1536.75 (exp.). Elemental analysis for {[Yb(12-MC$_{Ga,shi}$-4)]$_3$(bipy)$_6$}(HNEt$_3$)$_3$·10.8H$_2$O: calc.: %C 40.89, %H 3.03, %N 7.40; found: %C 40.57, %H 3.37, %N 7.61.

{[Y(12-MC$_{Ga,shi}$-4)]$_3$(frn)$_6$}(HNEt$_3$)$_3$. The synthetic yield was 2.44 % based on Y(NO$_3$)$_3$·6H$_2$O. ESI-MS (MeOH/DMSO 90:10, negative mode, m/z): {[Y(12-MC$_{Ga,shi}$-4)]$_3$(frn)$_6$}$^{3-}$: 1500.73 (calc.), 1500.70 (exp.). Elemental analysis for {[Y(12-MC$_{Ga,shi}$-4)]$_3$(frn)$_6$}(HNEt$_3$)$_3$·5.0H$_2$O·9.3DMF·3.7tBuOMe: calc.: %C 48.49, %H 4.29, %N 5.76; found: %C 48.50, %H 4.28, %N 5.78.

{[Gd(12-MC$_{Ga,shi}$-4)]$_3$(frn)$_6$}(HNEt$_3$)$_3$. The synthetic yield was 5.58 % based on Gd(NO$_3$)$_3$·6H$_2$O. ESI-MS (MeOH/DMSO 90:10, negative mode, m/z): {[Gd(12-MC$_{Ga,shi}$-4)]$_3$(frn)$_6$}$^{3-}$: 1569.08 (calc.), 1569.05 (exp.). Elemental analysis for {[Gd(12-MC$_{Ga,shi}$-4)]$_3$(frn)$_6$}(HNEt$_3$)$_3$·5.1H$_2$O·3.2DMF: calc.: %C 45.35, %H 3.11, %N 4.77; found: %C 45.53, %H 3.29, %N 4.61.

{[Nd(12-MC$_{Ga,shi}$-4)]$_3$(frn)$_6$}(HNEt$_3$)$_3$. The synthetic yield was 2.11 % based on Nd(NO$_3$)$_3$·6H$_2$O. ESI-MS (MeOH/DMSO 90:10, negative mode, m/z): {[Nd(12-MC$_{Ga,shi}$-4)]$_3$(frn)$_6$}$^{3-}$: 1555.70 (calc.), 1555.70 (exp.). Elemental analysis for {[Nd(12-MC$_{Ga,shi}$-4)]$_3$(frn)$_6$}(HNEt$_3$)$_3$·10.3H$_2$O·5.8DMF: calc.: %C 45.04, %H 3.48, %N 5.21; found: %C 45.08, %H 3.64, %N 5.14.

{[Er(12-MC$_{Ga,shi}$-4)]$_3$(frn)$_6$}(HNEt$_3$)$_3$. The synthetic yield was 3.08 % based on Er(NO$_3$)$_3$·5H$_2$O. ESI-MS (MeOH/DMSO 90:10, negative mode, m/z): {[Er(12-MC$_{Ga,shi}$-4)]$_3$(frn)$_6$}$^{3-}$: 1578.42 (calc.), 1578.72 (exp.). Elemental analysis for {[Er(12-MC$_{Ga,shi}$-4)]$_3$(frn)$_6$}(HNEt$_3$)$_3$·11.3H$_2$O·6.0DMF: calc.: %C 44.36, %H 3.49, %N 5.17; found: %C 44.45, %H 3.58, %N 5.09.

{[Yb(12-$MC_{Ga,shi}$-4)]$_3$(frn)$_6$}(HNEt$_3$)$_3$. The synthetic yield was 4.07 % based on $Yb(NO_3)_3 \cdot 5H_2O$. ESI-MS (MeOH/DMSO 90:10, negative mode, m/z): {[Yb(12-$MC_{Ga,shi}$-4)]$_3$(frn)$_6$}$^{3-}$: 1584.43 (calc.), 1584.73 (exp.). Elemental analysis for {[Yb(12-$MC_{Ga,shi}$-4)]$_3$(frn)$_6$}$(HNEt_3)_3 \cdot 14.9H_2O \cdot 5.0$DMF: calc.: %C 43.66, %H 3.48, %N 4.92; found: %C 43.63, %H 3.45, %N 4.95.

{[La(12-$MC_{Ga,shi}$-4)]$_3$(frn)$_6$}(HNEt$_3$)$_3$. The synthetic yield was 13 % based on $La(NO_3)_3 \cdot 6H_2O$. Waiting for the ESI-MS spectra and elemental analysis.

{[Tb(12-$MC_{Ga,shi}$-4)]$_3$(frn)$_6$}(HNEt$_3$)$_3$. The synthetic yield was 9.4 % based on $Tb(NO_3)_3 \cdot 6H_2O$. Waiting for the ESI-MS spectra and elemental analysis.

{[Lu(12-$MC_{Ga,shi}$-4)]$_3$(frn)$_6$}(HNEt$_3$)$_3$. The synthetic yield was 11.7 % based on $Lu(NO_3)_3 \cdot 5H_2O$. Waiting for the ESI-MS spectra and elemental analysis.

Chapter 6: **Nitro- and amino-benzo-oxadiazole functionalized Ln_2Ga_8 metallacrowns**

6.1 Introduction

The 4-chloro-7-nitro-2,1,3-benzoxadiazole (NBD-Cl) compound (**Scheme 6.1**) is a widely used fluorogenic reagent initially developed for sensing amino acids and other amines. NBD-Cl reacts in fact with amines, allowing the rapid functionalization of these compounds with a luminescent group.[120,121] More specifically, the luminescence of NBD relates to an absorption maximum at 300 nm, with emission of fluorescence at 420 nm. Also, the fluorescence of NBD-based compounds, like NBD-NH-R, typically arises from intramolecular charge transfer (ICT) transitions between the electron-donating amino group and the electron-withdrawing nitro group.

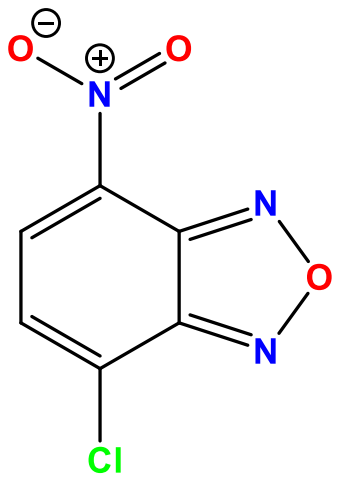

Scheme 6.1. Illustration of NBD-Cl.

NBD derivatives often have low quantum yield in aqueous solutions due to nonradiative deactivation pathways. Despite this, however, the high reactivity of NBD-Cl with biological nucleophiles, such as amines[122] and thiols[123], enables its use in a variety of sensing and labeling applications, particularly in biochemistry and chemical biology. NBD-Cl and its derivatives are therefore widely used, and known for their environmental sensitivity, water solubility, and small size, which facilitate biomolecular interactions and self-assembly in biological systems. These properties make NBD-Cl a versatile tool for developing probes that provide distinct optical signals in complex mixtures, like biological ones, that contain several low-emitting luminescent compounds with emission spread in the entire optical spectrum.

The drawback of the possible applications in vivo of compounds such as NBD is that nitroaromatic compounds, such as nitrobenzene derivatives, have been found to exhibit mutagenic and carcinogenic properties, along with causing allergic reactions, endocrine system impairments, and skin irritation. The toxicity is largely due to the electron-withdrawing nature of the nitro group, which contributes to the stability and resistance of these compounds against degradation.[124] When nitro groups undergo reduction, they can form reactive species such as superoxide anion radicals and hydrogen peroxide, which can generate hydroxyl radicals in the presence of metal ions, leading to significant biomolecular damage. Therefore, caution is necessary when using nitro-containing compounds in biological systems, given their potential harmful effects on cells and living organisms. It was found that the reduction of the nitro group to an amino group in the ligand, operated to reduce its toxic effects, leads to a red shift of 10 nm in the absorption band and in a decreasing of the quantum yield compared to the nitro compound. The presence of the amino group in place of the nitro group opens up however with opportunities for further functionalization of the aromatic fluorophore.

Biotin, also known as vitamin B8, is essential for the human body as it participates in protein metabolism and the synthesis of fatty acids and glucose.[125] Biotin is known for its strong interaction with streptavidin, forming the strongest non-covalent bond known in nature. Biotin has the functional property of retaining the ability to interact strongly with streptavidin even when functionalized on the carboxyl group of the pendant arm.[126] Specifically, amine groups can be made to react with the carboxyl function of Biotin giving rise to an amide. Using this method, Biotin can be linked to amino groups present on other (bio)molecules.[127]

By reacting the amino ligand with Biotin, a new ligand was obtained that shows an absorption band from 400 to up to 600 nm with a maximum at 485 nm. This ligand can be employed to generate dimeric metallacrowns that potentially function as fluorescent probes. When used in synergy with streptavidin, these probes can be applied for targeted tumor imaging and detection.[128] Tumor-targeting applications based on the Biotin-streptavidin system consist of a pretargeting phase in which a monoclonal antibody conjugated with streptavidin or Biotin is first administered to target tumor-associated antigens or receptors, followed by the administration of Biotin or streptavidin conjugated with imaging agents or drugs that target the pretargeted antibody.[129]

6.2 Aim of the project

The aim of this project is to functionalize Ln_2Ga_8 metallacrowns with derivatives of NBD chromophores. We achieved this by coupling the NBD-Cl derivative with dimethyl-5-amino isophthalate via Buchwald-Hartwig amination, forming the NBD-ipa bridge. After reducing it to the amino derivative, ABD-ipa, we observed a decrease in the extinction coefficient due to the loss of charge-transfer transitions. However, the new derivative exhibited a broad absorption band in the visible range, enabling excitation up to 480 nm for Ln^{III} sensitization. We will also show how this amino-functionalized ABD-ipa bridge enabled for the first the functionalization of a metallacrown with four Biotin units.

6.3 Results and discussions

6.3.1 Synthesis and characterization of diMe-NBD-ipa

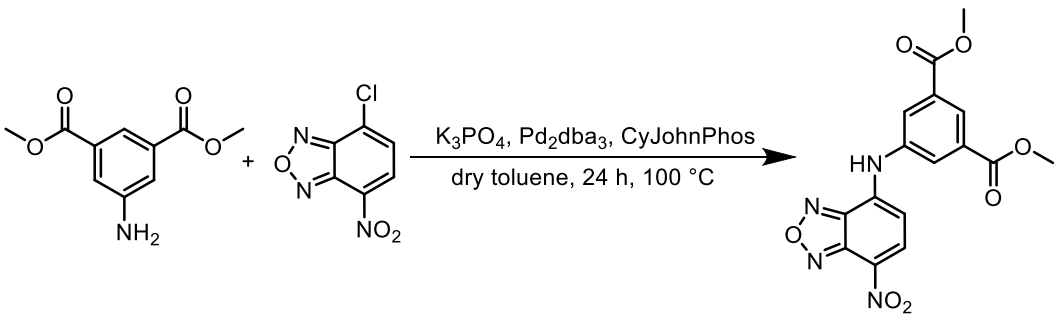

Scheme 6.2. Reaction scheme of DiMe-NBD-ipa synthesis.

The synthesis (**Scheme 6.2**) was carried out by mixing $Pd_2(dba)_3$ (2 mol% Pd), CyJohnPhos (4 mol% ligand), K_3PO_4 as the base (1.4 eq.), dimethyl-5-aminoisophthalic acid (1.2 eq.), and 4-chloro-7-nitro-1,2,3-benzoxadiazole (NBD-Cl, 1.0 eq.) in dry toluene under a nitrogen atmosphere in a reaction vessel. The reaction mixture was stirred at 100°C for 24 hours. The resulting dark red mixture was filtered through a Celite plug. The filtrate was evaporated to dryness, yielding a dark brown solid, which was further purified by flash column chromatography to give diMe-NBD-ipa as a red solid.

The product showed to be sensitive to basic environment and sparingly soluble in organic solvents, therefore posing significant challenges for its purification. Among the stationary phases tested, basic alumina was the only one that provided a satisfactory retention factor (Rf) to effectively separate the product from the starting materials and by-products. The purification was performed using a column with a DCM/MeOH gradient (from 100%/0% to 90%/10%), aiming to elute the product as quickly as possible due to the basicity of the stationary phase, while maintaining high purity within the allowable limits of MeOH concentration. The yields for this product did not exceed 45%.

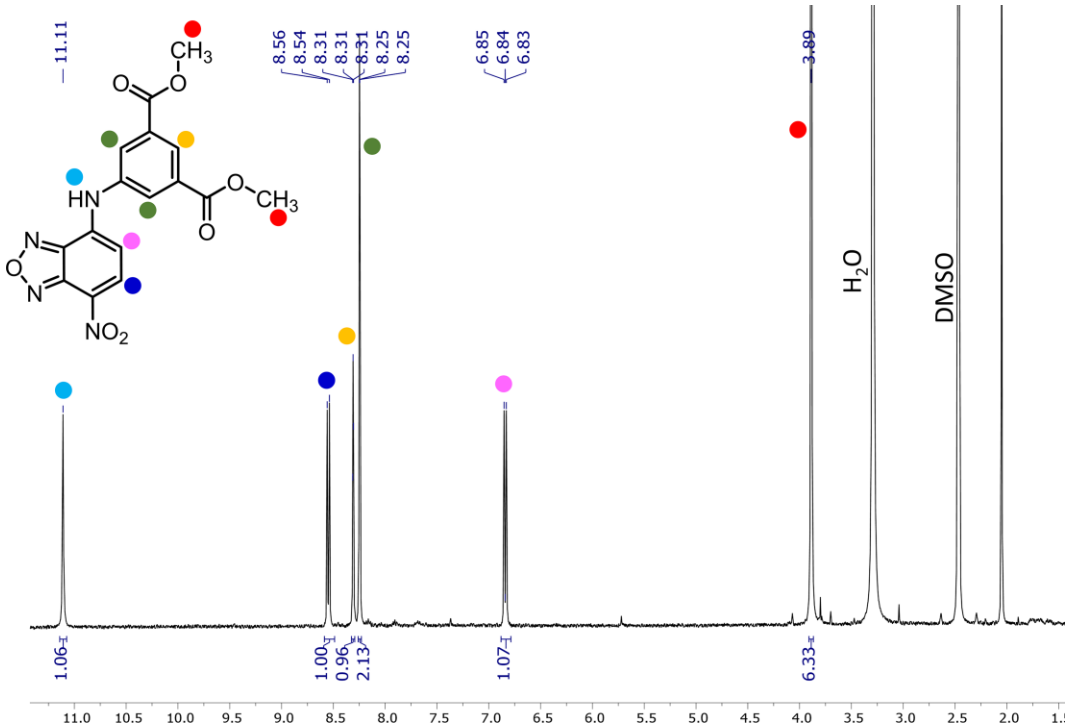

Figure 6.1. ^{1}H NMR spectrum of diMe-NBD-ipa in DMSO-d_6, 400 MHz, 298 K.

Figure 6.1 shows the ^{1}H NMR spectrum in DMSO of the purified product. The singlet at 11.11 ppm corresponds to the proton of the amine (light blue). The peak related to the proton in ortho to the nitro group (1H, blue) falls at higher ppm than that of the proton in the meta position (1H, violet) which is itself in ortho to an amine group. The peaks integrating for two protons (2H, green) and to one proton (1H, yellow) are assigned to the resonances of the aromatic proton of the DiMe-fragment. The singlet a at 3.89 ppm (3H, red) is assigned to the methyl protons of the ester group.

The compound was also characterized by ESI-MC. **Figure 6.2** show the ESI-mass of diMe-NBD-ipa.

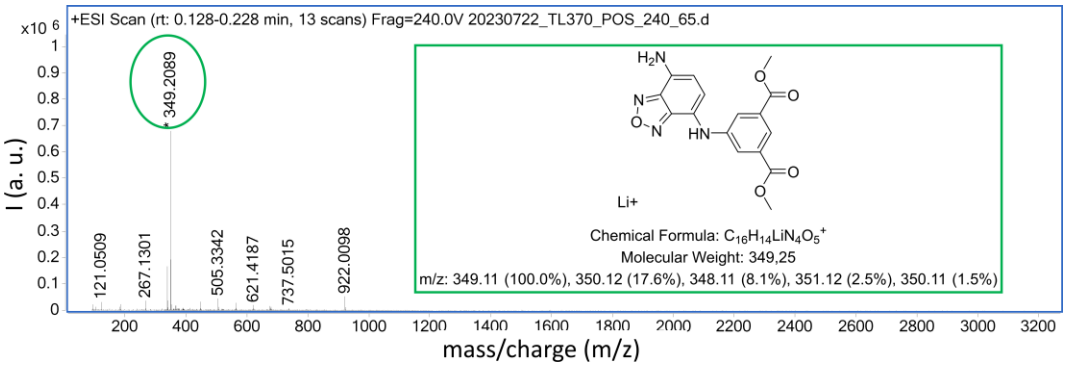

Figure 6.2. ESI-MS spectrum of diMe-NBD-ipa in the negative mode, C = 150 ug/mL (40 µM) in MeOH/DMSO 90:10.

6.3.2 Synthesis and characterization of NBD-ipa

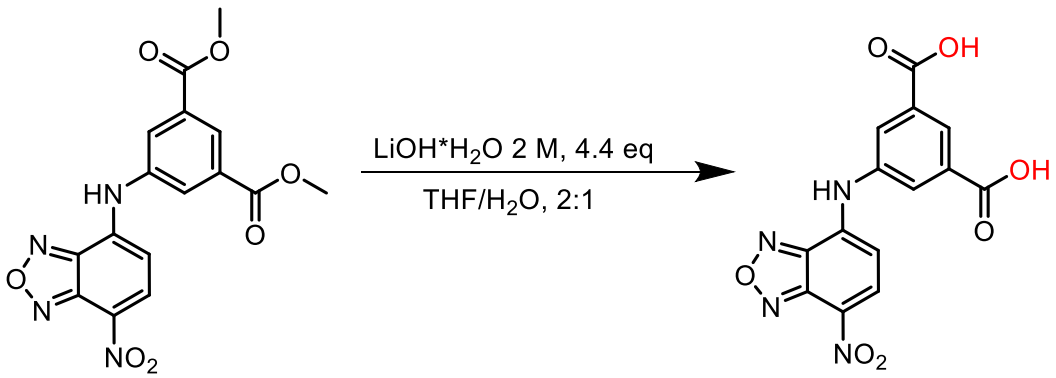

Scheme 6.3. Reaction scheme of NBD-ipa synthesis.

The next step reported in the **Scheme 6.3**, involves deprotection of the ester group to generate the carboxyl group. Given the sensitivity of the reactant to strong bases we chose lithium hydroxide, one of the weakest inorganic bases.

The deprotection was carried out by dissolving diMe-NBD-ipa (1.0 eq.) in a 2:1 THF/water mixture. The addition of 2 M LiOH (4.4 eq.) caused a color change in the solution from red to dark red. The reaction mixture was stirred at room temperature for 20 hours. Afterward, the resulting solution was acidified to pH 2.5, which changed the color from dark red to orange. The solution was then extracted with ethyl acetate, yielding H_2NBD-ipa as a red solid. The amine product was confirmed by NMR in DMSO, as shown in **Figure 6.3**. The yield was > 99%.

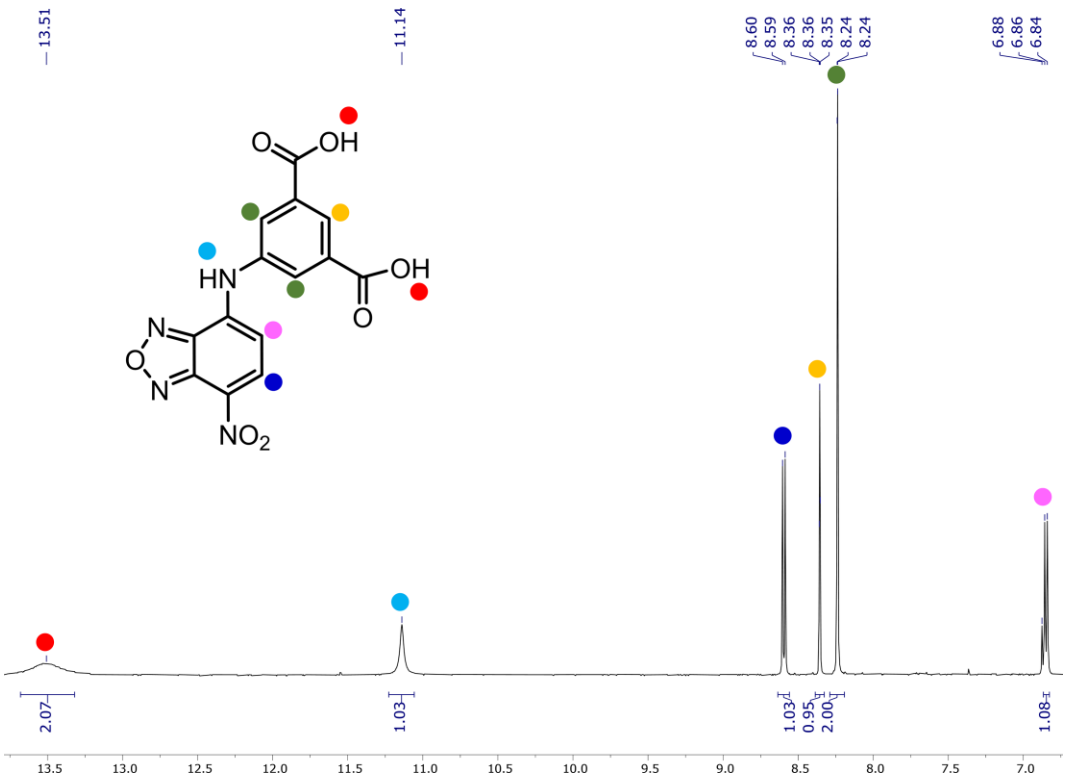

Figure 6.3. ^{1}H NMR spectrum of NBD-ipa in DMSO-d_6, 500 MHz, 298 K.

Figure 6.3 shows the spectrum of the product in DMSO. Compared to the spectrum of the reactant (**Figure 6.1**), the singlet peak corresponding to the methyl protons is absent, while a new signal appeared at 13.51 ppm, integrating for two protons. This indicates the formation of the carboxylic group from the ester function. The positions of the peaks corresponding to the other protons in the molecule did not exhibit significant shifts compared to those of the reactants.

The compound was also characterized by ESI-MC. **Figure 6.4** show the ESI-MS of NBD-ipa.

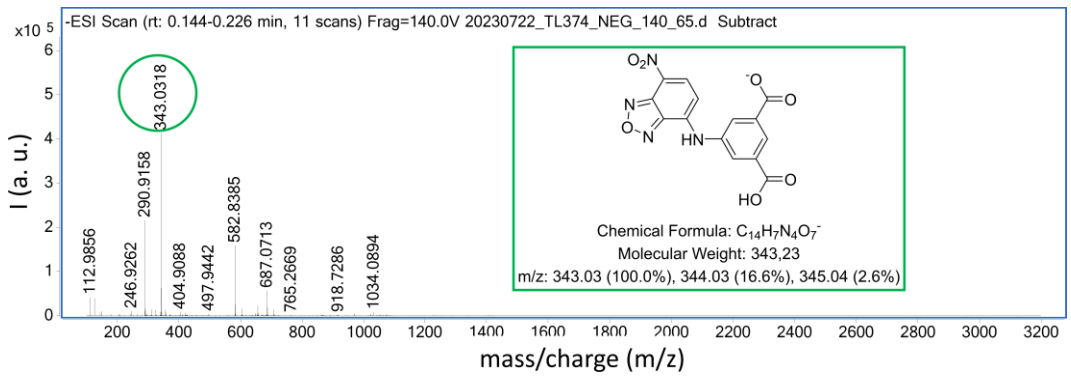

Figure 6.4. ESI-MS spectrum of NBD-ipa in the negative mode, C = 150 ug/mL (40 µM) in MeOH/DMSO 90:10.

6.3.3 Synthesis and characterization of ABD-ipa

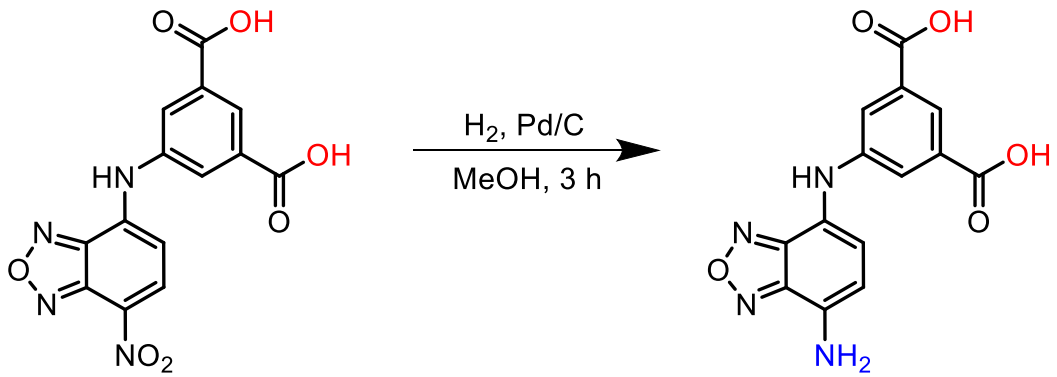

Scheme 6.4. Reaction scheme of ABD-ipa synthesis.

The reaction (**Scheme 6.4**) was conducted by dissolving NBD-ipa (1.0 eq.) in methanol. A catalytic amount of Pd/C (10 wt%) was added to the solution. Hydrogen gas was introduced into the flask at atmospheric pressure using a hydrogen balloon. The mixture was stirred for 3 hours, and then filtered through a plug of Celite. The filtrate was evaporated to dryness, yielding ABD-ipa as a dark brown solid.

The ^{1}H NMR spectrum of the product (**Figure 6.5**) shows the presence of a singlet peak at approximately 6.30 ppm, attributed to the two amine protons (1H, aquamarine). The peaks of the aromatic protons, indicated in violet and blue, are upfield shifted compared to those of the reactant.

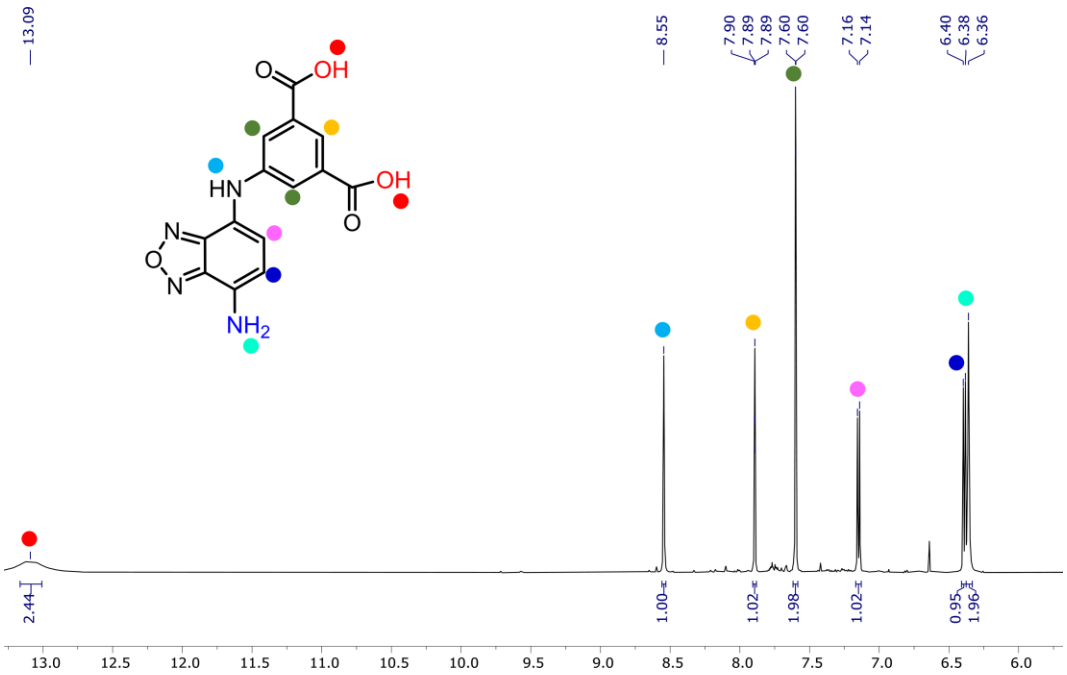

Figure 6.5. ^{1}H NMR spectrum of ABD-ipa in DMSO-d_6, 500 MHz, 298 K.

6.3.4 Synthesis and characterization of Biotin-ABD-ipa

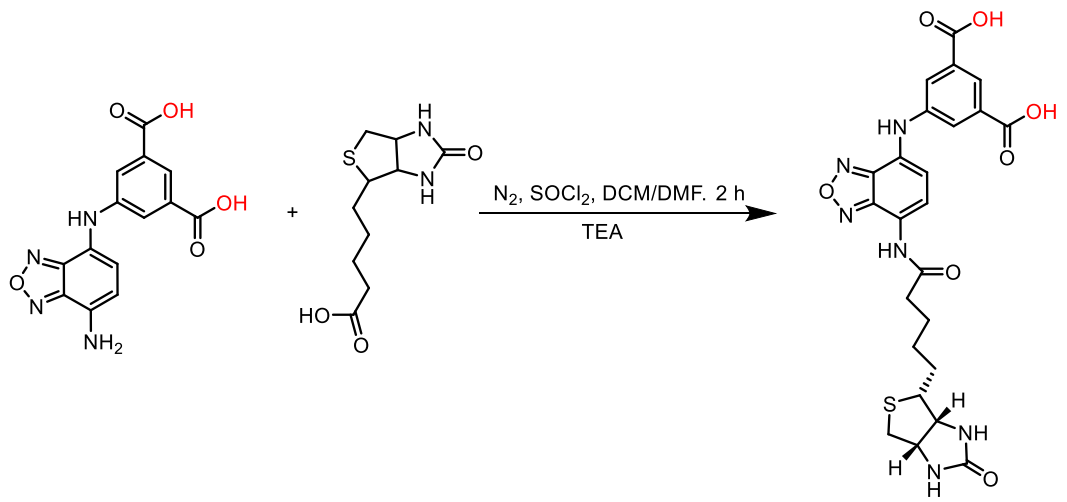

Scheme 6.5. Reaction scheme of the synthesis of Biotin-ABD-ipa.

The synthesis represented in **Scheme 6.5**, was conducted in two steps. The first consisted of the formation of the acylated intermediate by reacting Biotion (1.1 eq.) with thionyl chloride ($SOCl_2$) (10 eq.) in dry DMC under nitrogen atmosphere for 3 h. The resulting colorless solution was evaporated obtaining a pale-yellow oil. In the second step, the acylated intermediate was reacted with ABD-ipa 1(1 eq.) ligand in THF/DCM 1:1 in the presence of triethylamine (0.08 mmol). The mixture was stirred for 3 hours, then the precipitate was filtered off and washed with DCM, yielding a brown solid. The new molecule was characterized by ^1H (**Figure 6.6**) and COSY (**Figure 6.7**) NMR in DMSO. The singlet peak at 10.28 ppm corresponds to the amide proton, confirming the successful outcome of the reaction. At higher fields, the aliphatic protons of the Biotion are present. The protons identified in purple and dark green fall below the DMSO and water peaks, making their integration challenging. At lower fields, the -NH-CO-NH- protons are within the aromatic region and are indicated by yellow and light green dots.

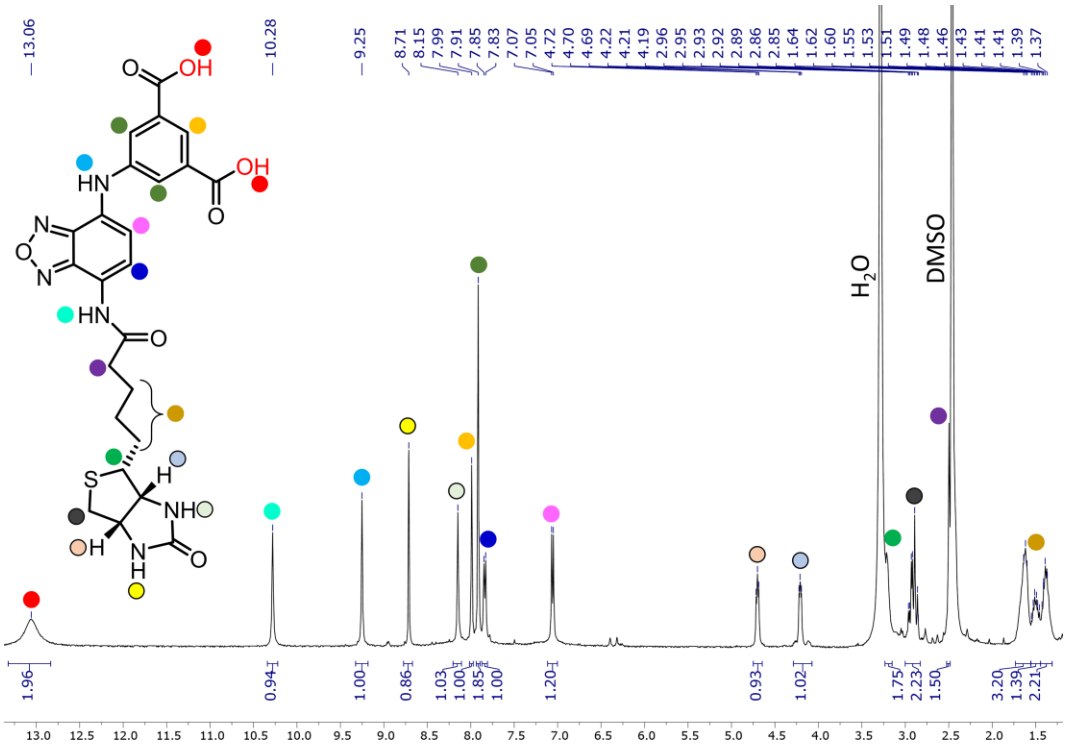

Figure 6.6. ^{1}H NMR spectrum of Biotin-ABD-ipa in DMSO-d_6, 500 MHz, 298 K.

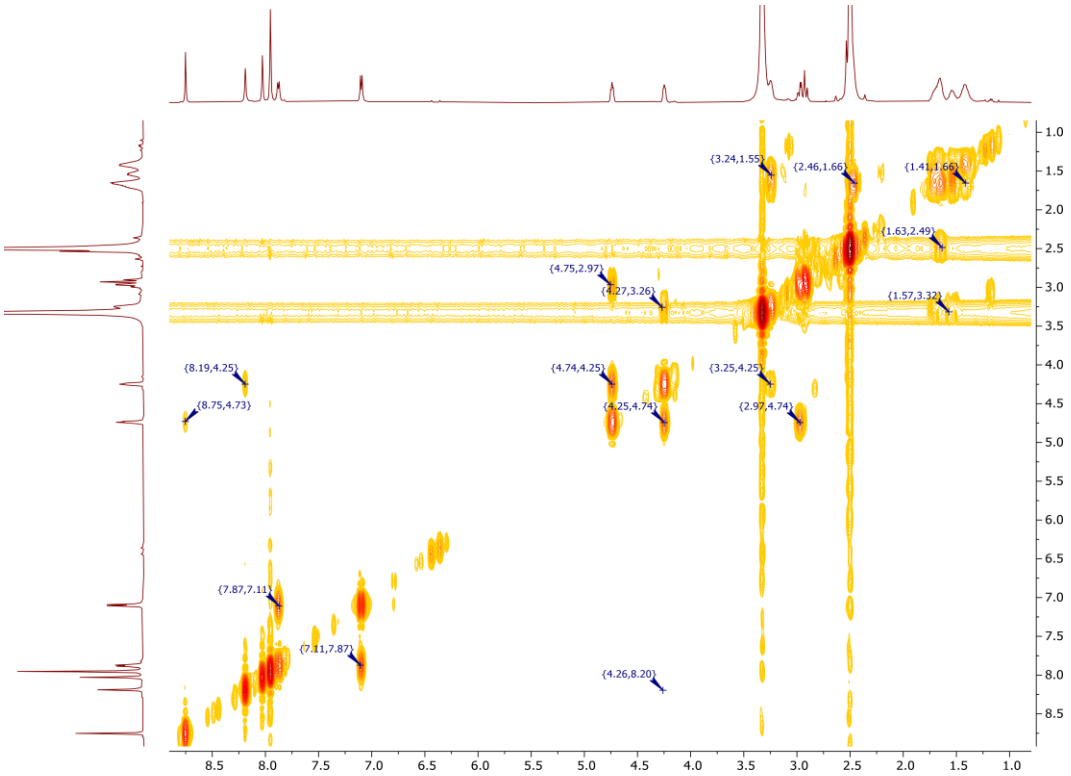

Figure 6.7. COSY NMR spectrum of Biotin-ABD-ipa in DMSO-d_6, 500 MHz, 298 K.

6.3.5 Synthesis and characterization of $\{[Ln(12\text{-}MC_{Ga,shi}\text{-}4)]_2(ABD\text{-}ip)_4\}(HNEt_3)_2$ metallacrowns

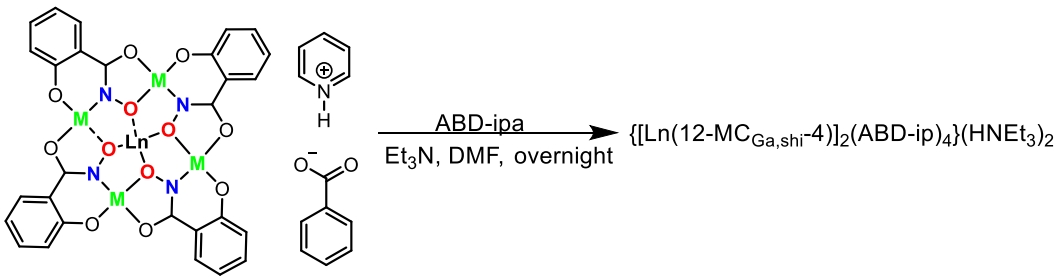

Scheme 6.6. Reaction scheme of $\{[Ln(12\text{-}MC_{Ga,shi}\text{-}4)]_2(ABD\text{-}ip)_4\}(HNEt_3)_2$ synthesis.

Unlike the trimeric and tetrameric metallacrowns described in the previous chapter, these compounds were constructed from the basic unit of pre-synthesized 12-$MC_{Ga,shi}$-4 . In a DMF solution, {[Ln(12-$MC_{Ga,shi}$-4)$(bza)_4$]}pyridinium (1.0 eq.) was dissolved together with ABD-ipa (2.1 eq.), forming a dark red solution. To this, NEt_3 (10.0 eq.) was added, and the mixture was stirred overnight at room temperature. To the solution an antisolvent was added (terz-butil methyl ether) to induce the precipitation, yielding {[Ln(12-$MC_{Ga,shi}$-4)$]_2(ABD\text{-}ip)_4$}$(HNEt_3)_2$ metallacrowns as brown solids (**Scheme 6.6**).

All metallacrowns were characterized by ESI-MS (**Figures 6.9-6.15**), elemental analysis (see **Section 6.6.1**), IR (**Figure S6.1**), and UV-visible spectroscopy (**Figure 6.21**). Additionally, ^{1}H NMR spectrum of {[Y(12-$MC_{Ga,shi}$-4)$]_2(ABD\text{-}ip)_4$}$(HNEt_3)_2$ was recorded (**Figure 6.8**).

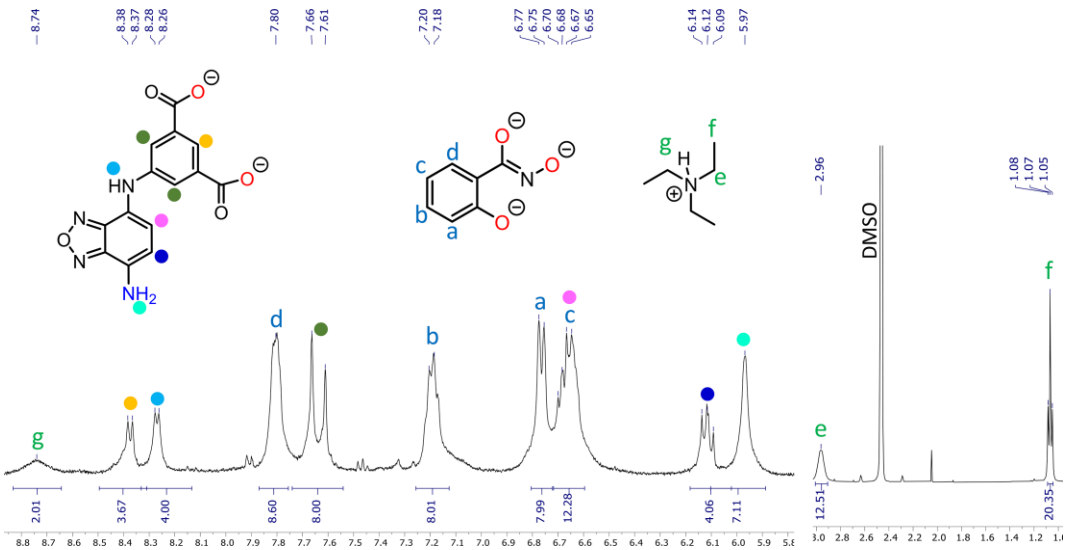

Figure 6.8. ^{1}H NMR spectrum of {[Y(12-$MC_{Ga,shi}$-4)$]_2(ABD\text{-}ip)_4$}$(HNEt_3)_2$ in DMSO-d_6, 500 MHz, 298 K.

The ^{1}H NMR spectrum of the metallacrown (**Figure 6.8**) shows the peaks corresponding to the protons of the shi^{3-} units forming the 12-MC-4 unit, that are indicated by the blue dots in the figure. The spectrum is characterized by the presence of large signals, possibly due to fluxional phenomena that occur close to the NMR time scale. For this reason, the assignment of the peaks corresponding to the protons of the ABD-ip linker is not straightforward, and therefore a tentative assignment is provided in the figure. Importantly, the presence of triethylammonium is confirmed by the peaks of the aliphatic protons at high fields and the broad peak at 8.74 ppm, corresponding to the proton bonded to the amine of the counteraction.

ESI-MS was carried out to verify the presence of the dimeric metallacrown species. To carry out these analyses, stock solutions of the metallacrowns were prepared by dissolving 1 mg of the product in 1 mL of DMSO/methanol 1:9. From these stock solutions, 150 μg/mL solutions of the metallacrowns were prepared. The mass spectra, presented in **Figures 6.9-6.15**, display a molecular peak with the highest intensity corresponding to the metallacrown species, with signals that have an isotopic distribution consistent with the presence of the desired dimeric species. A signal of significant intensity corresponding to a molecular peak is associated to a metallacrown in which the ligands underwent partial degradation during mass analysis. A proposed degradation pathway is shown in **Scheme 6.7**.

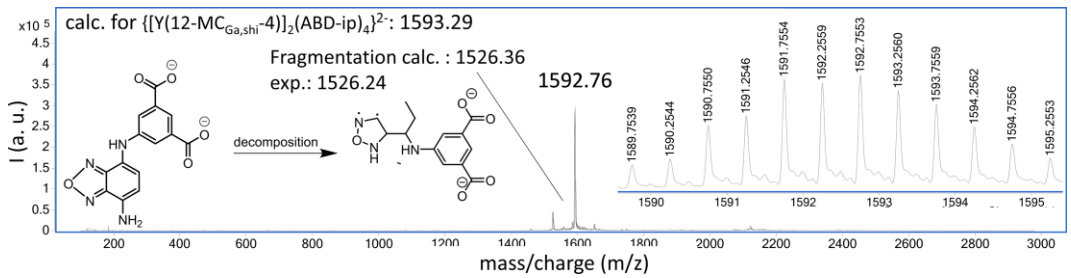

Figure 6.9. ESI-MS spectrum of {[Y(12-MC$_{Ga,shi}$-4)]$_2$(ABD-ip)$_4$}(HNEt$_3$)$_2$ in the negative mode, C = 150 ug/mL (40 µM) in MeOH/DMSO 90:10.

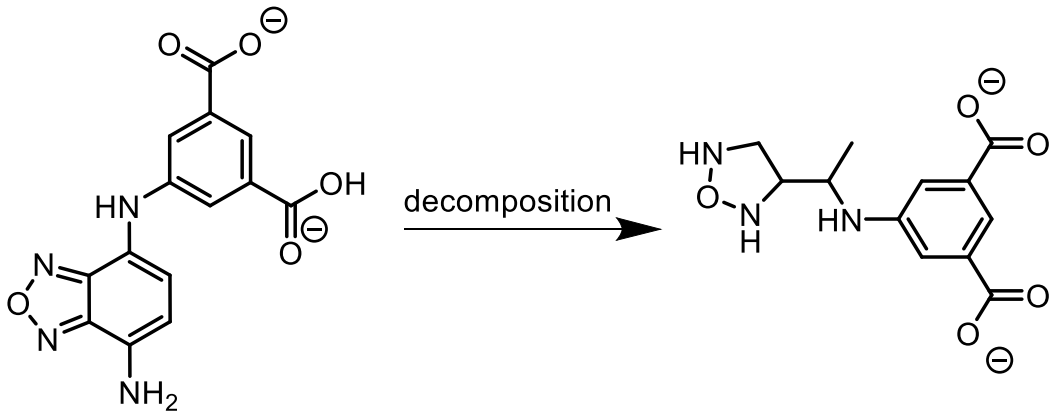

Scheme 6.7. Scheme of proposed degradation pathway of ABD-ip in ESI-MS.

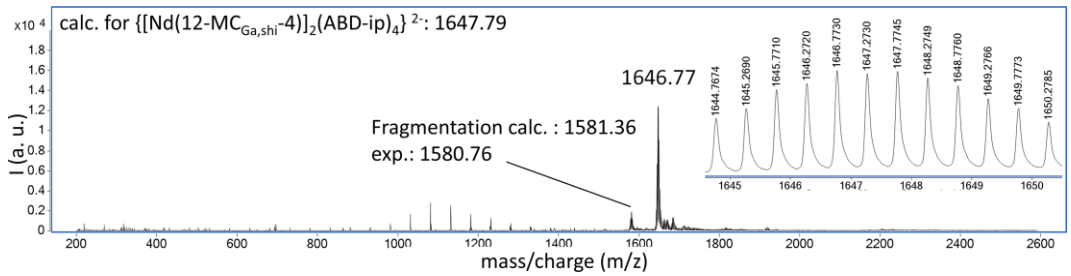

Figure 6.10. ESI-MS spectrum of {[Nd(12-MC$_{Ga,shi}$-4)]$_2$(ABD-ip)$_4$}(HNEt$_3$)$_2$ in the negative mode, C = 150 ug/mL (40 µM) in MeOH/DMSO 90:10.

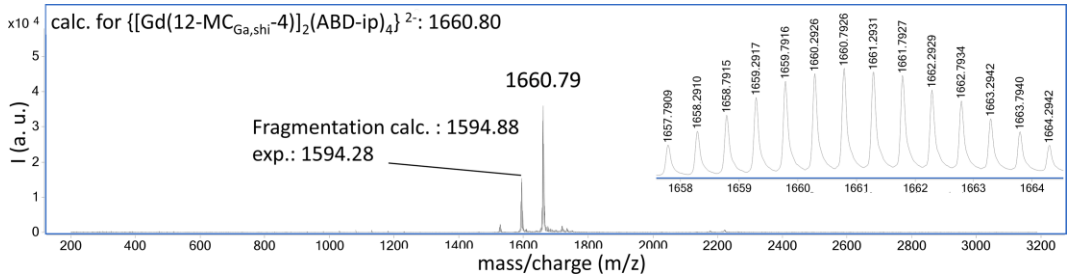

Figure 6.11. ESI-MS spectrum of {[Gd(12-MC$_{Ga,shi}$-4)]$_2$(ABD-ip)$_4$}(HNEt$_3$)$_2$ in the negative mode, C = 150 ug/mL (40 µM) in MeOH/DMSO 90:10.

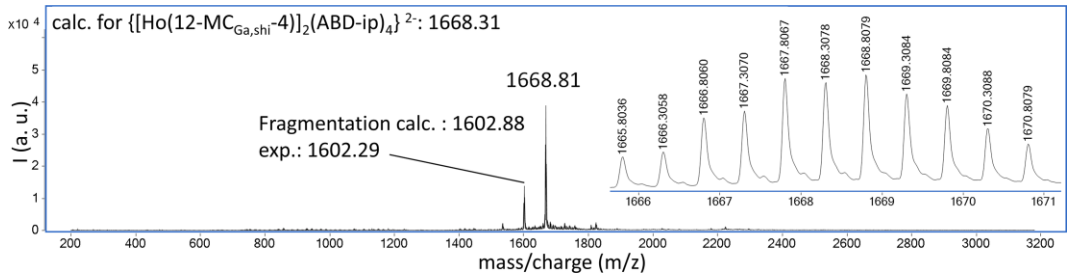

Figure 6.12. ESI-MS spectrum of {[Ho(12-MC$_{Ga,shi}$-4)]$_2$(ABD-ip)$_4$}(HNEt$_3$)$_2$ in the negative mode, C = 150 ug/mL (40 µM) in MeOH/DMSO 90:10.

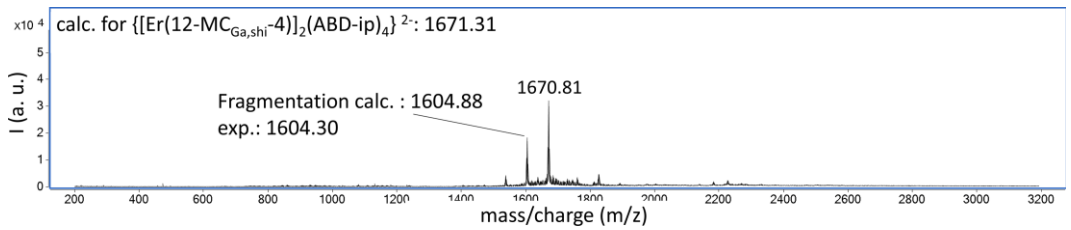

Figure 6.13. ESI-MS spectrum of {[Er(12-MC$_{Ga,shi}$-4)]$_2$(ABD-ip)$_4$}(HNEt$_3$)$_2$ in the negative mode, C = 150 ug/mL (40 µM) in MeOH/DMSO 90:10.

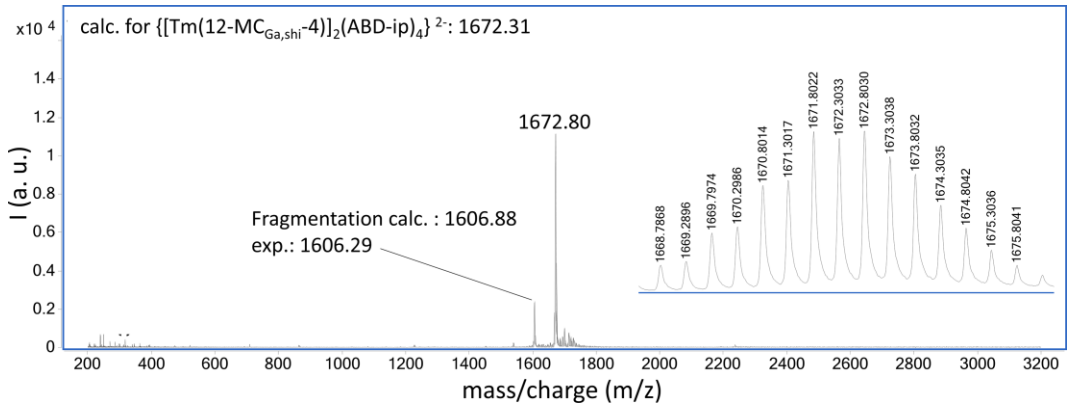

Figure 6.14. ESI-MS spectrum of {[Tm(12-MC$_{Ga,shi}$-4)]$_2$(ABD-ip)$_4$}(HNEt$_3$)$_2$ in the negative mode, C = 150 ug/mL (40 µM) in MeOH/DMSO 90:10.

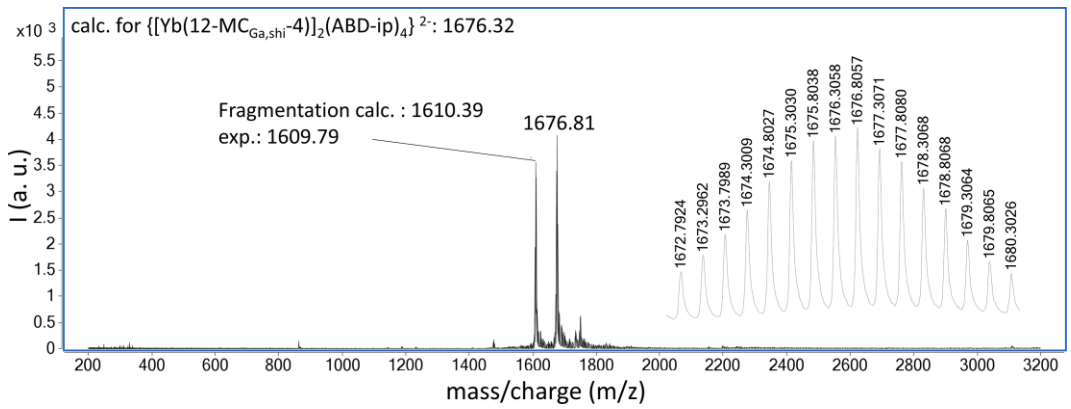

Figure 6.15. ESI-MS spectrum of {[Yb(12-MC$_{Ga,shi}$-4)]$_2$(ABD-ip)$_4$}(HNEt$_3$)$_2$ in the negative mode, C = 150 ug/mL (40 µM) in MeOH/DMSO 90:10.

6.3.6 Synthesis and characterization of {[Ln(12-MC$_{Ga,shi}$-4)]$_2$(Biotin-ABD-ip)$_4$}(HNEt$_3$)$_2$ metallacrowns

Scheme 6.8. Reaction scheme for the synthesis of {[Ln(12-MC$_{Ga,shi}$-4)]$_2$(Biotin-ABD-ip)$_4$}(HNEt$_3$)$_2$.

Only the yttrium (Y) and Yb metallacrown of this series was synthesized for characterization by NMR, along with the ytterbium (Yb) metallacrown, as a proof-of-knowledge of the synthetic procedure.

The procedure to obtain these metallacrowns (MCs) is identical to the one described in the previous section. {[Ln(12-$MC_{Ga,shi}$-4)$(bza)_4$]}pyridinium (1.0 eq.) was dissolved in DMF, followed by the addition of Biotin-ABD-ip (2.2 eq.) and NEt_3 (10.0 eq.) to form a dark red solution. The mixture was stirred overnight at room temperature. To the solution was added an antisolvent (terz-butil methyl ether) to induce the precipitation to yield {[Ln(12-$MC_{Ga,shi}$-4)$]_2$(Biotin-ABD-ip)$_4$}$(HNEt_3)_2$ metallacrowns as brown solids (**Scheme 6.8**).

The ^{1}H NMR spectrum and COSY NMR spectrum of the Y metallacrown is shown in Figure **Figure 6.16** and in **Figure 6.17** respectively. The coupling with ABD-ip did not result in significant shifts for the peaks corresponding to the aliphatic protons of Biotin. The aromatic protons of the shi^{3-} ligand are labeled with blue letters, while the protons of triethylammonium are labeled in green.

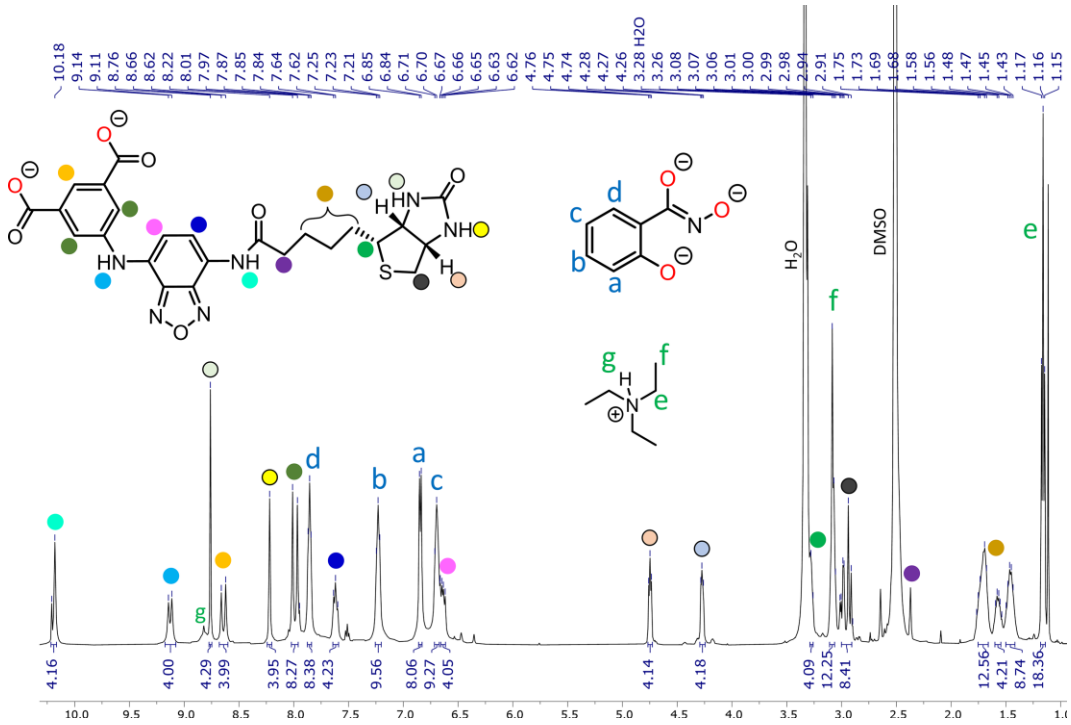

Figure 6.16. ^{1}H NMR spectrum of {[Y(12-MC$_{Ga,shi}$-4)]$_2$(Biotin-ABD-ip)$_4$}(HNEt$_3$)$_2$ in DMSO-d$_6$, 500 MHz, 298 K.

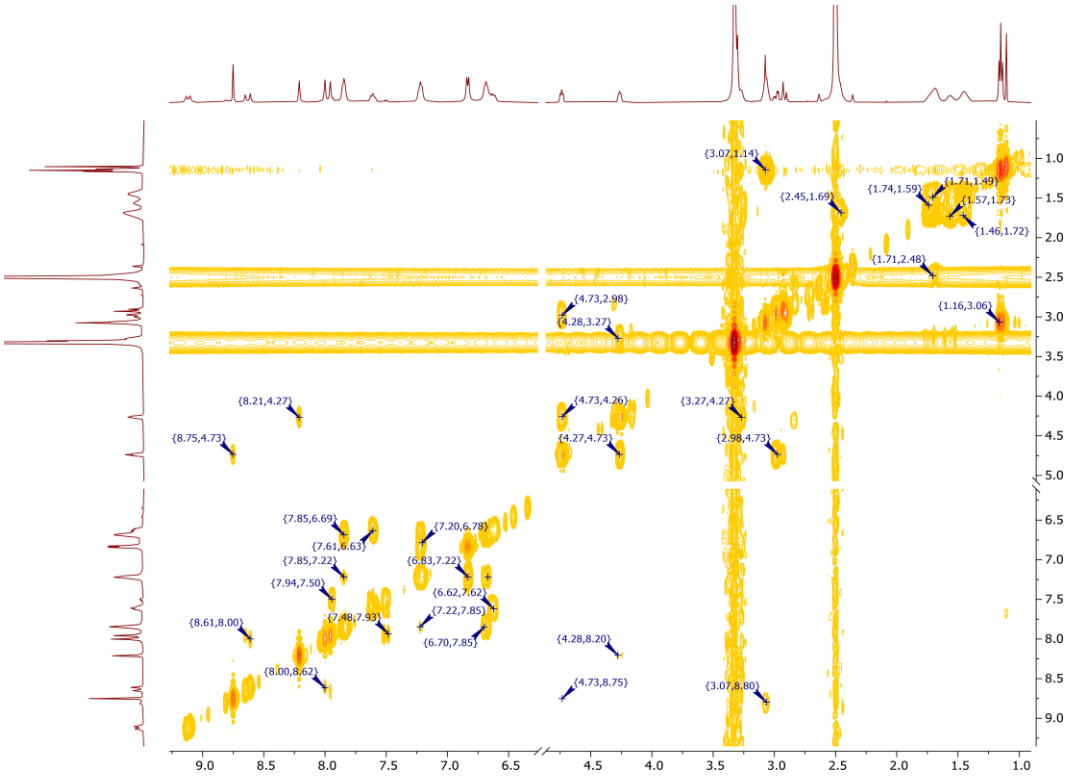

Figure 6.17. COSY NMR spectrum of {[Y(12-MC$_{Ga,shi}$-4)]$_2$(Biotin-ABD-ip)$_4$}(HNEt$_3$)$_2$ in DMSO-d$_6$, 500 MHz, 298 K.

ESI-MS was carried out to verify the presence of the dimeric metallacrown species. To carry out these analyses, stock solutions of the metallacrowns were prepared by dissolving 1 mg of the product in 1 mL of DMSO/methanol 1:9. From these stock solutions, 150 µg/mL solutions of the metallacrowns were prepared. The mass spectra, presented in **Figures 6.18-6.19**, display a molecular peak with the highest intensity corresponding to the metallacrown species, with signals that have an isotopic distribution consistent with the presence of the desired dimeric speciesThe peaks corresponding to 2044.41 m/z and 2057.91 m/z are related to two different potential partial degradation pathways of the ligand in ESI-mass. **Scheme 6.9** illustrates these two possible degradation routes.

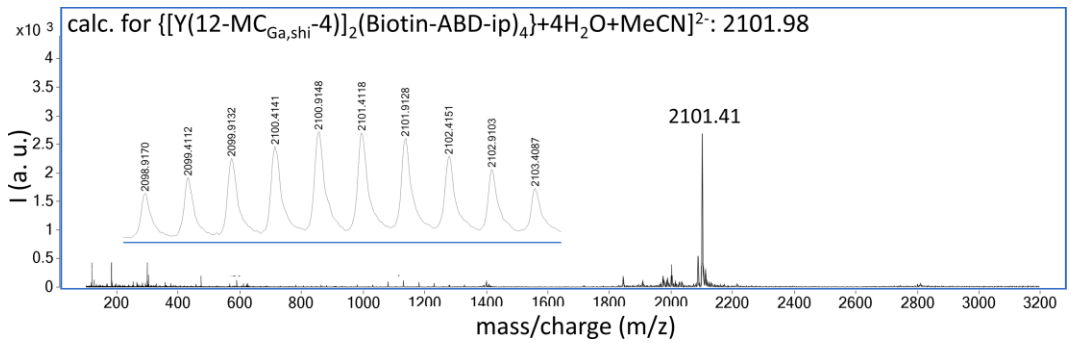

Figure 6.18. ESI-MS spectrum of {[Y(12-MC$_{Ga,shi}$-4)]$_2$(Biotin-ABD-ip)$_4$}(HNEt$_3$)$_2$ in the negative mode, C = 150 ug/mL (40 µM) in MeOH/DMSO 90:10.

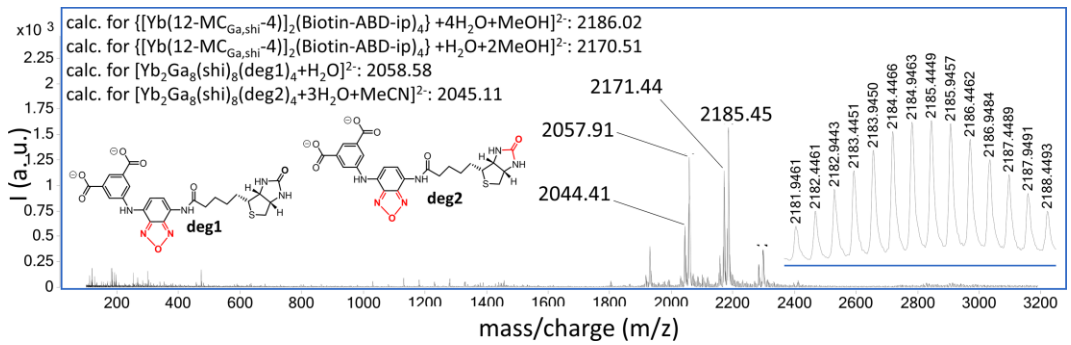

Figure 6.19. ESI-MS spectrum of {[Yb(12-MC$_{Ga,shi}$-4)]$_2$(Biotin-ABD-ip)$_4$}(HNEt$_3$)$_2$ in the negative mode, C = 150 ug/mL (40 µM) in MeOH/DMSO 90:10.

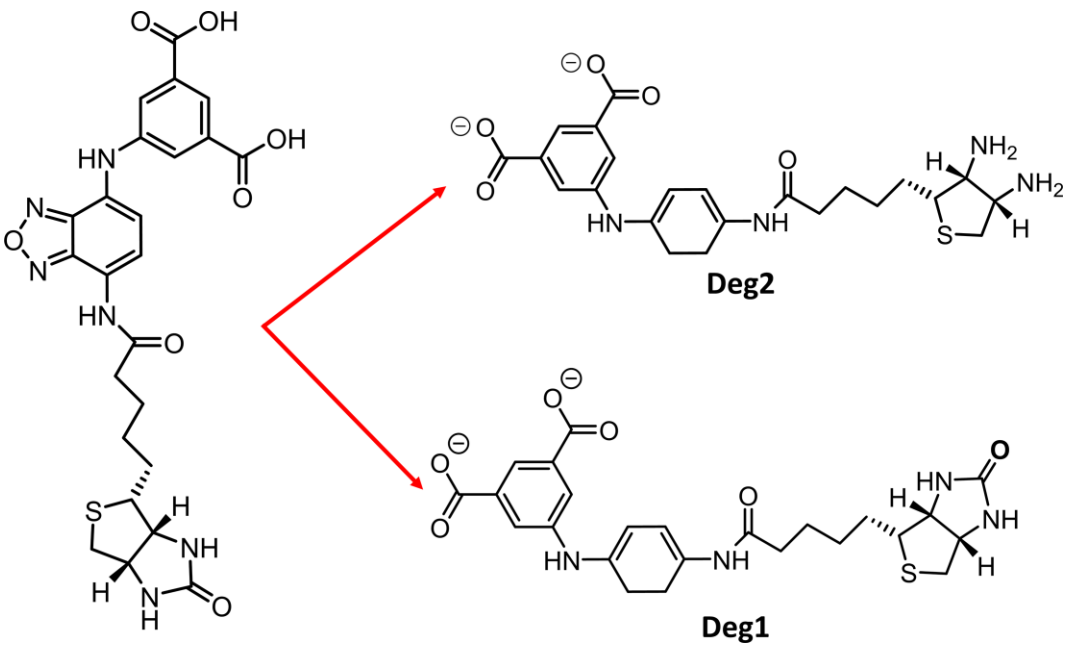

Scheme 6.9. Scheme of proposed degradation pathway of ABD-ipa in ESI-MS.

6.3.7 Characterization of ABD and ABD-Biotin Metallacrown Complexes through UV-Visible Spectroscopy

Characterization of the ligands by uv-visible is critical for our purposes because it allows us to see in which spectral region the ligands absorb. **Figure 6.20** shows the spectra of the three synthesized ligands NBD-ipa, ABD-ipa and Biotin-ABD-ipa. The solutions of the ligands were obtained by diluting stock solutions prepared by dissolving 1 mg/mL of analyte in DMSO (spectrophotometric grade). The concentrations of the analyzed solutions are 4.0×10^{-5} M, 9.5×10^{-5} M and 7.4×10^{-5} M, respectively. All ligands show a broad absorption band from 400 to 600 nm with the maximum at 485.5 ($\varepsilon = 20187\ M^{-1} \cdot cm^{-1}$), 479 ($\varepsilon = 2958.3\ M^{-1} \cdot cm^{-1}$) and 460

(ε = 5961.3 $M^{-1}{\cdot}cm^{-1}$) nm. These bands can be attributed mainly to the π/π* and n/π* transitions based on their extinction coefficients.

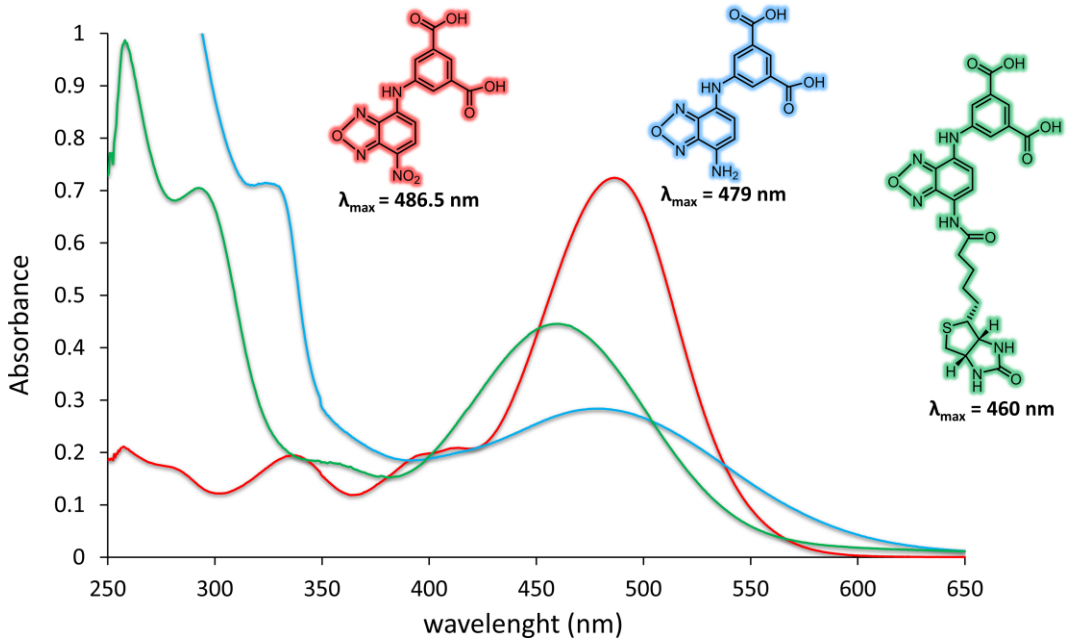

Figure 6.20. UV- visible spectra of NBD-ipa (red), ABD-ipa (blue) and Biotin-ipa (green) in DMSO at room temperature.

The NBD-ipa ligand has been studied in depth in another article, and I will only discuss the other two ligands. All ABD-ipa complexes were studied in UV-visible. Solutions of the complexes were prepared by the same procedure as before, obtaining solutions with concentrations between 5 and 7 uM in DMSO (spectrophotometric grade). The absorption spectrum of the complexes in this case consists of 3 bands. The first, in the UV region, is attributable to the basic metallacrown unit, which generally does not absorb in the visible region. In contrast,

the band at about 350 nm and the broad band from 400 to 650 nm with a maximum at 480 nm are attributable to the ligand (**Figure 6.21**).

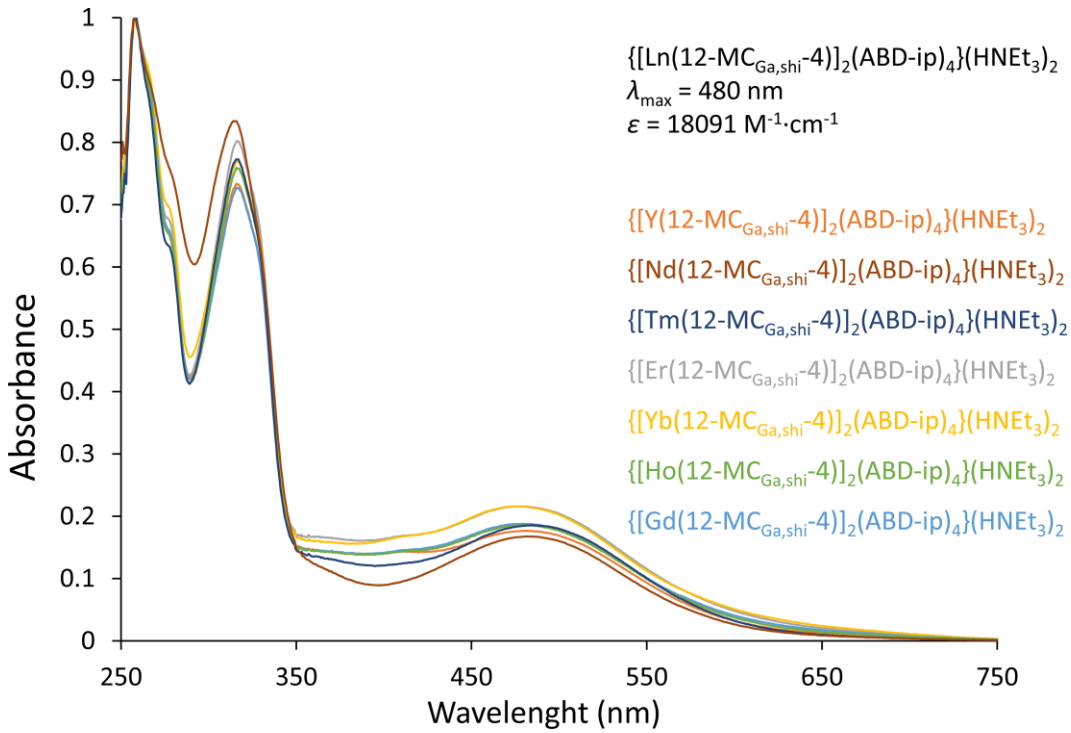

Figure 6.21. UV- visible spectra of {[Ln(12-MC$_{Ga,shi}$-4)]$_2$(ABD-ip)$_4$}(HNEt$_3$)$_2$ in DMSO at room temperature. Ln = Y^{III}, Nd^{III}, Tm^{III}, Er^{III}, Yb^{III}, Ho^{III}, Gd^{III}.

The last complexes studied were those in which the ABD-ipa ligand was functionalized with Biotin. Solutions for analysis were prepared using the same procedure as obtained previously. The solution concentration of Y is 5.8 uM and that of Yb is 7.8 uM. In this case, for timing issues, only the complexes of Y^{III} and Yb^{III} were synthesized. As can be seen from **Figure 6.22**, the same pattern of complexes assembled with the precursor ligand is observed. The differences are a slight blue-

shift effect due to the lower conjugation of the ligand (from 480 nm to 464 nm) and a narrowing of the absorption band.

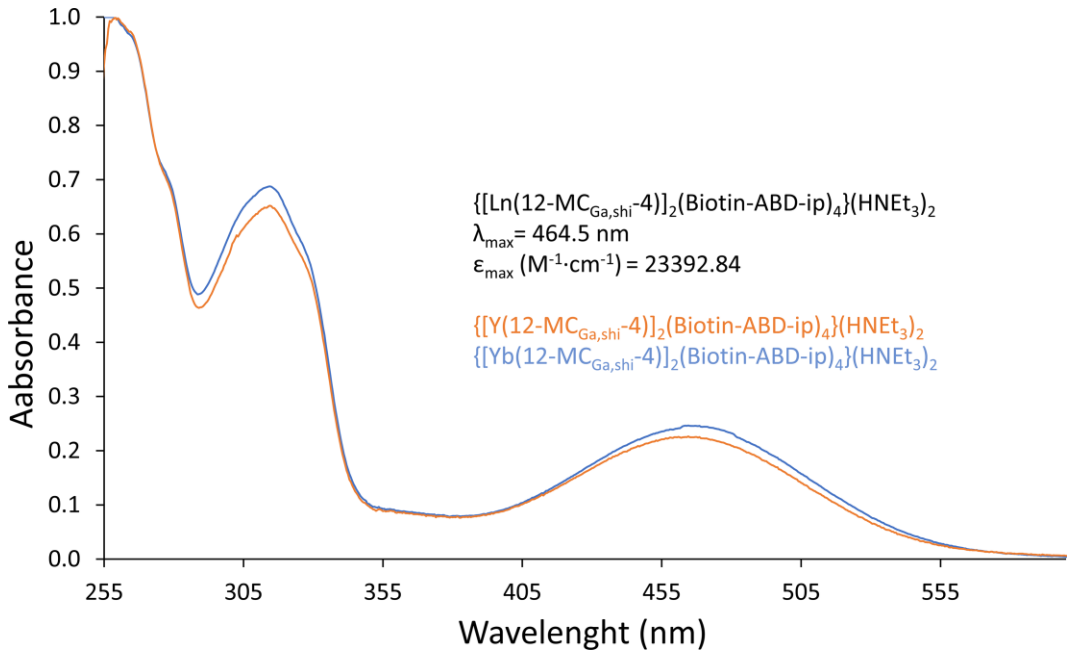

Figure 6.22. UV- visible spectra of {[Ln(12-MC$_{Ga,shi}$-4)]$_2$(Biotin-ABD-ip)$_4$}(HNEt$_3$)$_2$ in DMSO at room temperature. Ln = Y^{III} and Yb^{III}.

6.3.8 Exploring Luminescence in ABD-Functionalized and Biotinylated Metallacrowns

All photophysical measurements were carried out by Dr. Svetlana V. Eliseeva at the Center for Molecular Biophysics (CBM) in Orléans.

Based on the Uv-Visible graphs described above, the absorption maxima of metallacrown complexes with the two different ligands were identified. These were subsequently used to study the luminescent properties of the metallacrowns. The figures below show the excitation and emission bands for metallocrowns assembled with the ABD-ipa (**Figure 6.23**) and Biotin-ABD-ipa (**Figure 6.24**) ligand. The excitation and emission bands are represented by dashed and solid lines, respectively, while the colors refer to measurements of the compounds in solution (red) and solid state (black). The ^{1}H NMR spectrum (see **Figure 6.8**) of {[Y(12-MC$_{Ga,shi}$-4)]$_2$(ABD-ip)$_4$}(HNEt$_3$)$_2$ supports the formation of the expected complex with four ABD-ip antennas. It further confirms the complete replacement of the pyridinium counter-cations of the {[Ln(12-MC$_{Ga,shi}$-4)(bza)$_4$]}pym (see **Scheme 6.6**) precursors by the HNEt$_3^+$, as expected. Upon irradiation of the ABD-ip antenna at λ_{exc} = 480 in 50 µM DMSO solution, both the $^4I_{13/2}\rightarrow{}^4I_{15/2}$ (Er^{III}) and $^2F_{5/2}\rightarrow{}^2F_{7/2}$ (Yb^{III}) transition bands are observed, showing energy transfer from ABD-ip to the Ln^{III} emissive centers, as confirmed by the excitation spectra. The quantum yields decrease by a factor ≈ 2.4 for Er^{III} and by about an order of magnitude in the case of Yb^{III} when the ABD-ip band is used (λ_{exc} = 480) instead of the MC scaffold (λ_{exc} = 320).

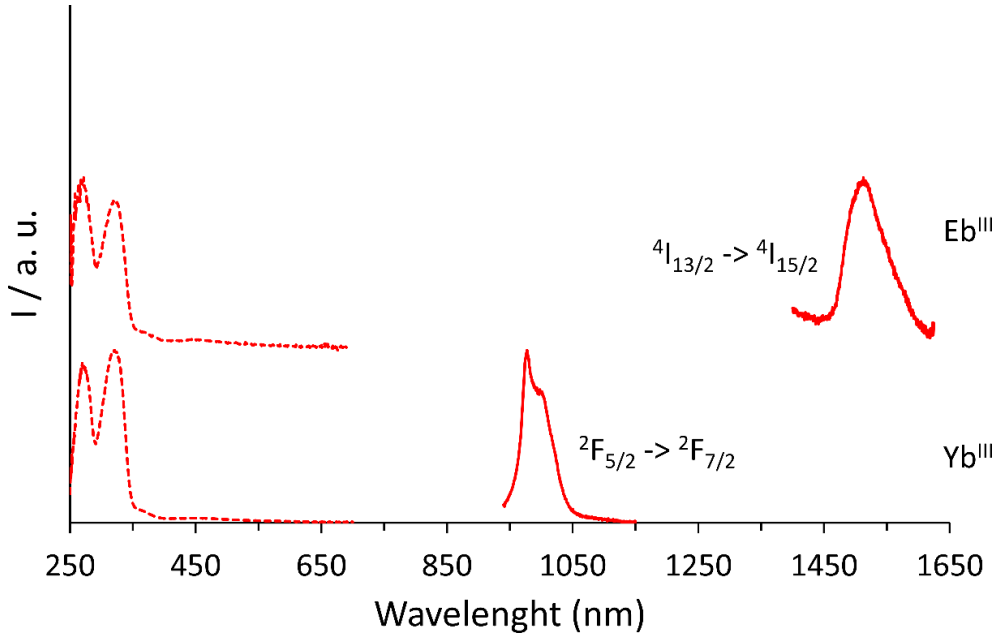

Figure 6.23. Corrected and normalized emission (full lines) and excitation (dotted lines) spectra for $\{[Ln(12\text{-}MC_{Ga,shi}\text{-}4)]_2(ABD\text{-}ip)_4\}^{2-}$ MCs at 298 K, 50 µM in DMSO (red lines). Emission: λ_{exc} = 480 nm. Excitation: λ_{em} = 1525, and 980 nm for Er^{III} and Yb^{III}, respectively.

At the same time, the ^1H NMR shows broader peaks, which could be associated with exchanges in solution and a decreased stability of the ABD-ip MC. That observation is further reinforced by the absence of light detected in the solid state for the corresponding Er^{III} and Yb^{III} complexes and the black color of the samples, casting reasonable doubts about their long-term stability. In solution, weak luminescence is detected and the quantum yields decrease. Due to the lower extinction coefficient of ABD-ip, the associated brightness drops further. The ^1H NMR spectrum of $\{[Y(12\text{-}MC_{Ga,shi}\text{-}4)]_2(Biotin\text{-}ABD\text{-}ip)_4\}(HNEt_3)_2$ again show the formation of the expected MC and a complete replacement of the pyridinium

counter-cations. The peaks are sharp and well resolved, coherent with a stable MC in DMSO solution. In the corresponding Yb^{III} complex, the quantum yield increase by factors ≈ 9.3 with respect to ABD-ip MCs, and the best brightness is obtained at λ_{exc} = 480 nm, with a value of B = 113(20) $M^{-1}{\cdot}cm^{-1}$.

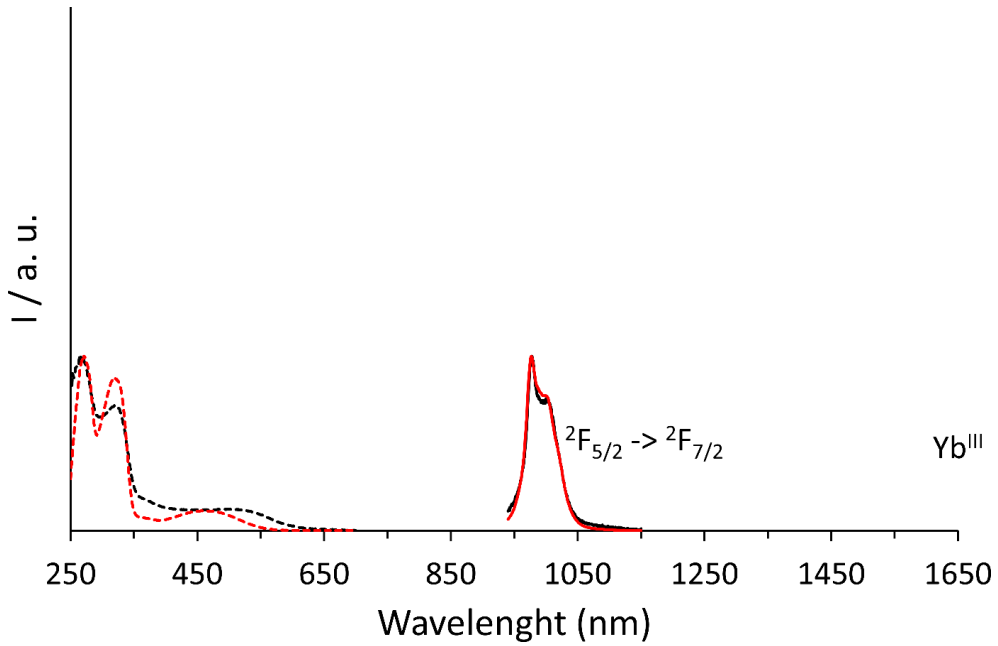

Figure 6.24. Corrected and normalized emission (full lines) and excitation (dotted lines) spectra for $\{[Yb(12\text{-}MC_{Ga,shi}\text{-}4)]_2(Biotin\text{-}ABD\text{-}ip)_4\}^{2-}$ MCs at 298, 50 µM in DMSO (red lines) and in the solid state (black lines). Emission: λ_{exc} = 480 nm (DMSO) and 475 nm (solid state). Excitation: λ_{em} = 980 nm for Yb^{III}.

The following Table shows the ignition lambda, molar extinction coefficient, quantum yield and radiation duration of the data observed in the graphs described.

Table 6.1. Photophysical properties of MCs, 50 µM in DMSO.

Metallacrown	λ_{exc} nm	Q_L^{Ln} %	ε_{max}[a] $M^{-1}\cdot cm^{-1}$	B_{max}[b] $M^{-1}\cdot cm^{-1}$	τ_{obs}[c] µs
{[Er(12-$MC_{Ga,shi}$-4)]$_2$(ABD-ip)$_4$}$^{2-}$	320	$6.0(3)\cdot10^{-3}$	$7.1(4)\cdot10^{4}$	4.3(3)	6.44(1)
	480	$8.41(4)\cdot10^{-4}$	$1.8(2)\cdot10^{4}$	0.15(1)	
{[Yb(12-$MC_{Ga,shi}$-4)]$_2$(ABD-ip)$_4$}$^{2-}$	320	0.769(2)	$7.1(4)\cdot10^{4}$	550(32)	44.8(8)
	480	$5.8(1)\cdot10^{-2}$	$1.8(2)\cdot10^{4}$	10(1)	
{[Yb(12-$MC_{Ga,shi}$-4)]$_2$(Biotin-ABD-ip)$_4$}$^{2-}$	320	2.7(2)	$5.9(9)\cdot10^{4}$	1592(268)	54.4(3)
	480	0.542(7)	$2.1(4)\cdot10^{4}$	113(20)	

[a]ABD-ip: average of recorded values for Ln^{III} = Y^{III}, Gd^{III}, Er^{III} and Yb^{III}. B-ABD-ip: average of recorded values for Ln^{III} = Y^{III} and Yb^{III}. b $B_{max} = Q_L^{Ln}\cdot\varepsilon_{max}$. c λ_{exc} = 355 nm.

6.4. Conclusion

In conclusion, this study investigated the synthesis, functionalization, and photophysical properties of Ln_2Ga_8 dimeric metallacrowns (MCs) modified with NBD-based chromophores. The NBD-ip bridge was obtained by a Buchwald-Hartwig amination between NBD-Cl and 5-amino-isophthalate. This bridge was used in the preparation of {[Ln(12-$MC_{Ga,shi}$-4)]$_2$(NBD-ip)$_4$}$^{2-}$ MCs. The nitro group of the NBD-ip bridge was further reduced to an amino group, yield the ABD-ip bridge that was used in the preparation of the corresponding [Ln_2Ga_8] MCs. Both NBD-ip and ABD-ip MCs displayed broad absorption bands in the visible range that could be used for the sensitization of NIR-emitting Ln^{III}.. While the reduction of the nitro group resulted in limited stability of the ABD-ip MCs solution, the amino group in the ABD-ip bridge could be further used to form an amide bond with a Biotin moiety,

restoring MCs stability of $\{[Ln(12\text{-}MC_{Ga,shi}\text{-}4)]_2(Biotin\text{-}ABD\text{-}ip)_4\}^{2-}$.The presence of four Biotin groups creates the opportunity for specific targeting applications through the strong Biotin-streptavidin interaction. The two-step functionalization of an isophthalic acid bridging ligand with a NBD-based chromophore and a Biotin lead to a new bridging ligand with distinct optical properties, including an absorption band in the visible. Detailed spectroscopic analyses, including UV-vis, ESI-MS and ^1H NMR, provided insights into the structural and luminescent properties of the synthesized MCs. The UV-vis spectra confirmed the presence of an additional absorption band in the visible, attributed to the NBD/ABD chromophores in the corresponding bridging ligands. Photophysical studies further revealed that the Biotin-ABD-ip functionalized MCs exhibited enhanced luminescent properties compared to their ABD-ip equivalents. The Biotinylated complexes with Yb^{3+} exhibited a 9.3-fold increase in quantum yield relative to the ABD-ipa metal complexes (MCs) upon visible excitation, resulting in an improved brightness value. This enhancement in brightness and stability in the $\{[Ln(12\text{-}MC_{Ga,shi}\text{-}4)]_2(Biotin\text{-}ABD\text{-}ip)_4\}^{2-}$ MCs makes them attractive compounds for targeted probes in biological imaging applications.

In summary, this study has laid foundational insights into the impact of the bridging ligand on the stability and optical performance of the corresponding Ln_2Ga_8 MCs, identifying that Biotin-functionalized MCs are promising candidates for targeted imaging in complex biological environments. These results provide strong bases for future development aimed at refining the photophysical properties of these MCs for their use in specific bio-nanotechnological applications, while addressing the stability challenges associated with chemical functions present on the bridging ligand.

6.5 Experimental section

6.5.1 Materials and methods

All reagents and chemicals were purchased from commercial sources and used without further purification unless otherwise stated. SiO_2 (215-400 mesh) and Al_2O_3 (activated, basic, Brockmann I) were used for flash column chromatography. ESI-MS spectra were recorded on an Agilent 6230 TOF HPLC-MS spectrometer in negative or positive modes using the following ionization and cone potentials: 240 V and 65 V for organic molecules, 350 V and 50 V for MCs. Stock solutions of MCs at 1 mg/mL in DMSO were prepared and further diluted to 80-200 µg/µL in MeOH/DMSO 90:10. Recorded data were processed using the Agilent MassHunter software. Elemental analyses were performed by Atlantic Microlab. UV-vis spectra were recorded in DMSO on a Varian Cary 100 Bio UV-visible spectrophotometer using 1 cm Hellma QS or QX quartz glass cuvettes. The IR spectra were collected on a Thermo-Nicolet IS-50 spectrometer in ATR-FTIR configuration. Recorded data were processed using Thermo Scientific OMNIC Specta software.

6.5.2 Photophysical properties

Photophysical measurements were performed on powder samples or freshly prepared solutions of MCs in DMSO placed in 2.4 mm i.d. quartz capillaries or Suprasil® cells. Emission and excitation spectra were measured on a Horiba-Jobin-Yvon Fluorolog 3 spectrofluorimeter equipped with visible and NIR photomultiplier tubes (PMTs: R13456 and H10330-75 from Hamamatsu) upon excitation with a continuous Xenon lamp. Phosphorescence spectra of Gd^{III} MCs were measured at 77 K in time-resolved mode. All spectra were corrected for the

instrumental functions. Luminescence lifetimes were determined under excitation at 355 nm provided by a Nd:YAG laser (YG 980; Quantel), the signals in the NIR range were detected with a H10330-75 PMT connected to an iHR320 monochromator (Horiba Scientific). The output signals from the detectors were fed into a 500 MHz bandpass digital oscilloscope (TDS 754C; Tektronix). Luminescence lifetimes are averages of at least three independent measurements. Quantum yields were determined with a Fluorolog 3 spectrofluorimeter based on the absolute method using an integration sphere (Model G8, GMP SA, Renens, Switzerland). Each sample was measured several times. The experimental error for the determination of quantum yields is estimated as ~10 %. All photophysical measurements and NIR imaging (capillaries) were done by Dr. Svetlana V. Eliseeva at the Center for Molecular Biophysics (CBM) in Orléans

6.6. Chemistry

6.6.1. Synthetic procedures

Synthesis of diMe-NBD-ipa. Pd_2dba_3 (27.5 mg, $3.00 \cdot 10^{-2}$ mmol, 2% mol. Pd), (2-biphenyl)dicyclohexylphosphine (CyJohnPhos, 42.1 mg, $1.20 \cdot 10^{-1}$ mmol, 4% mol. ligand), K_3PO_4 (892 mg, 4.2 mmol, 1.4 eq.), dimethyl-5-amino-isophthalic acid (753 mg, 3.6 mmol, 1.2 eq.) and 4-chloro-7-nitro-1,2-3-benzoxadiazole (NBD-Cl, 599 mg, 3.0 mmol, 1.0 eq.) were placed in a 10 mL vial. The reagents were placed under a nitrogen atmosphere and 6 mL of dry toluene were added to the reaction vessel. The reaction was then stirred at 100 °C for 24 h. During that time, the solution became dark red. The reaction mixture was cooled down to room temperature and diluted with DCM (100 mL). The solution was filtered over a plug of celite, and the

celite was washed with DCM (ca. 200 mL). The filtrate solutions were combined, and the solvent removed in vacuo. The obtained crude brown solid was further purified by flash column chromatography (aluminium oxide activated, basic, Brockmann I, DCM:MeOH 100:0 to 90:10). The pure product was obtained as 498 mg of diMe-NBD-ipa as a red solid (1.34 mmol, 45 %). ^{1}H NMR (DMSO-d_6, 400 MHz) δ, ppm: 11.11 (1H, s), 8.54 (1H, d, *J* = 8.4 Hz), 8.31 (1H, t, *J* = 1.7 Hz), 8.25 (2H, d, *J* = 1.7 Hz), 6.84 (1H, bs), 6.81 (1H, d, *J* = 8.4 Hz), 3.89 (6H, s). ESI-MS: (positive mode, m/z): $[C_{16}H_{14}N_4O_5Li]^+$: 349.2 (exp.), 349.25 (calc.).

Synthesis of the NBD-ipa. diMe-NBD-ipa (90.5 mg, 0.24 mmol, 1.0 eq.) were solubilized in 18.9 mL of THF and 9.45 mL of water. LiOH 2 M (534 µL, 1.07 mmol, 4.4 eq.) was added and the solution turned from red to dark red. The solution was stirred at room temperature for 20 h. The resulting solution was acidified pH 2.5 with HCl 6 M, turning to orange color. The solution was extracted with ethyl acetate (2x 120 mL). The organic phase was washed with NH_4Cl (100 mL), dried over Na_2SO_4, and then evaporated to dryness. The product was collected as a red solid (84 mg, 0.24 mmol, 100 %). ^{1}H NMR (DMSO-d_6, 500 MHz) δ, ppm: 13.51 (2H, bs), 11.14 (1H, bs), 8.59 (1H, d, *J* = 9.0 Hz), 8.35 (1H, t, *J* = 1.7 Hz), 8.24 (2H, d, *J* = 1.5 Hz), 6.84 (1H, d, *J* = 8.5 Hz). ESI-MS (negative mode, m/z): $[C_{14}H_7N_4O_7]^-$: 343.03 (exp.), 343.23 (calc.).

Synthesis of the ABD-ipa. NBD-ipa (161 mg, 0.47 mmol, 1.0 eq.) were solubilized in 50 mL of MeOH. Pd/C (3.2 mg, 10 wt %) were added to the solution and the flask was filled with H_2 (1 atm, balloon). The mixture was stirred at room temperature for 3 h, filtered over a plug of celite, and celite washed with 30 mL of MeOH. The filtrate was evaporated to dryness to yield ABD-ipa as a dark brown solid. (144 mg, 0.46 mmol, 98 %). ^{1}H NMR (DMSO-d_6, 500 MHz) δ, ppm: 13.09 (2H, bs), 8.55 (1H,

s), 7.90 (1H, s), 7.60 (2H, d, *J* = 1.0 Hz), 7.14 (1H, d, *J* = 8.0 Hz), 6.40 (1H, d, *J* = 8.0 Hz), 6.36 (2H, bs). ESI-MS: no molecular adduct detected (fragmentation).

Synthesis of {[Ln(12-MC$_{Ga,shi}$-4)]$_2$(ABD-ip)$_4$}(HNEt$_3$)$_2$ metallacrowns (Ln = Y, Gd, Ho, Er, Tm, Yb). {[Ln(12-MC$_{Ga,shi}$-4)(bza)$_4$]}pyridinium ($2.00\cdot10^{-2}$ mmol, 1.0 eq.) were dissolved in 400 µL of DMF and ABD-ip (12.9 mg, $4.2\cdot10^{-2}$ mmmol, 2.1 eq.) were added to form a dark red solution. NEt$_3$ (27.9 µL, $2.00\cdot10^{-1}$ mmol, 10.0 eq.) were added to the solution and the solution stirred overnight at room temperature. The solvent was evaporated to dryness and the solid was suspended in 3 mL of MeOH. The solid was filtered, washed with MeOH (1 mL), water (10 mL), MeOH (5 mL), tBuOMe (10 mL) and dried under vacuum for 24 h to yield {[Ln(12-MC$_{Ga,shi}$-4)]$_2$(ABD-ip)$_4$}(HNEt$_3$)$_2$ metallacrowns as brown solids.

{[Y(12-MC$_{Ga,shi}$-4)]$_2$(ABD-ip)$_4$}(HNEt$_3$)$_2$. The yield was 26 % based on {[Y(12-MC$_{Ga,shi}$-4)(bza)$_4$]}pyridinium. ESI-MS (MeOH/DMSO 90:10, negative mode, m/z): {[Y(12-MC$_{Ga,shi}$-4)]$_2$(ABD-ip)$_4$}$^{2-}$: 1593.29 (calc.), 1592.76 (exp.). Elemental analysis for {[Y(12-MC$_{Ga,shi}$-4)]$_2$(ABD-ip)$_4$}(HNEt$_3$)$_2\cdot$8.9H$_2$O: calc.: %C 41.95, %H 3.23, %N 10.26; found: %C 41.77, %H 3.03, %N 10.26.

{[Gd(12-MC$_{Ga,shi}$-4)]$_2$(ABD-ip)$_4$}(HNEt$_3$)$_2$. The yield was 32 % based on {[Gd(12-MC$_{Ga,shi}$-4)(bza)$_4$]}pyridinium. ESI-MS (MeOH/DMSO 90:10, negative mode, m/z): {[Gd(12-MC$_{Ga,shi}$-4)]$_2$(ABD-ip)$_4$}$^{2-}$: 1660.80 (calc.), 1660.79 (exp.). Elemental analysis for {[Gd(12-MC$_{Ga,shi}$-4)]$_2$(ABD-ip)$_4$}(HNEt$_3$)$_2\cdot$9.8H$_2$O$\cdot$0.3tBuOMe: calc.: %C 40.42, %H 3.22, %N 9.76; found: %C 40.52, %H 3.06, %N 9.60.

{[Ho(12-MC$_{Ga,shi}$-4)]$_2$(ABD-ip)$_4$}(HNEt$_3$)$_2$. The yield was 26 % based on {[Ho(12-MC$_{Ga,shi}$-4)(bza)$_4$]}pyridinium. ESI-MS (MeOH/DMSO 90:10, negative mode, m/z): {[Ho(12-MC$_{Ga,shi}$-4)]$_2$(ABD-ip)$_4$}$^{2-}$: 1668.31 (calc.), 1668.81 (exp.). Elemental analysis

for {[Ho(12-$MC_{Ga,shi}$-4)]$_2$(ABD-ip)$_4$}($HNEt_3$)$_2$·10.8H_2O·0.6tBuOMe: calc.: %C 40.25, %H 3.32, %N 9.61; found: %C 40.38, %H 3.18, %N 9.47.

{[Er(12-$MC_{Ga,shi}$-4)]$_2$(ABD-ip)$_4$}($HNEt_3$)$_2$. The yield was 29 % based on {[Er(12-$MC_{Ga,shi}$-4)(bza)$_4$]}pyridinium. ESI-MS (MeOH/DMSO 90:10, negative mode, m/z): {[Er(12-$MC_{Ga,shi}$-4)]$_2$(ABD-ip)$_4$}($HNEt_3$)$_2^{2-}$: 1671.31 (calc.), 1670.81 (exp.). Elemental analysis for {[Er(12-$MC_{Ga,shi}$-4)]$_2$(ABD-ip)$_4$}($HNEt_3$)$_2$·12.3H_2O·0.3tBuOMe: calc.: %C 39.72, %H 3.30, %N 9.60; found: %C 39.92, %H 3.06, %N 9.36.

{[Tm(12-$MC_{Ga,shi}$-4)]$_2$(ABD-ip)$_4$}($HNEt_3$)$_2$. The yield was 20 % based on {[Tm(12-$MC_{Ga,shi}$-4)(bza)$_4$]}pyridinium. ESI-MS (MeOH/DMSO 90:10, negative mode, m/z): {[Tm(12-$MC_{Ga,shi}$-4)]$_2$(ABD-ip)$_4$}$^{2-}$: 1671.31 (calc.), 1672.80 (exp.). Elemental analysis for {[Tm(12-$MC_{Ga,shi}$-4)]$_2$(ABD-ip)$_4$}($HNEt_3$)$_2$·12.3H_2O·0.2tBuOMe: calc.: %C 39.62, %H 3.27, %N 9.61; found: %C 39.75, %H 3.05, %N 9.39.

{[Yb(12-$MC_{Ga,shi}$-4)]$_2$(ABD-ip)$_4$}($HNEt_3$)$_2$. The yield was 31 % based on {[Yb(12-$MC_{Ga,shi}$-4)(bza)$_4$]}pyridinium. ESI-MS (MeOH/DMSO 90:10, negative mode, m/z): {[Yb(12-$MC_{Ga,shi}$-4)]$_2$(ABD-ip)$_4$}$^{2-}$: 1676.32 (calc.), 1676.81 (exp.). Elemental analysis for {[Yb(12-$MC_{Ga,shi}$-4)]$_2$(ABD-ip)$_4$}($HNEt_3$)$_2$·9.0H_2O: calc.: %C 40.03, %H 3.09, %N 9.79; found: %C 40.19, %H 3.03, %N 9.63.

One-pot synthesis of {[Nd(12-$MC_{Ga,shi}$-4)]$_2$(ABD-ip)$_4$}($HNEt_3$)$_2$ metallacrown. salicylhydroxamic acid (25.0 mg, $1.63\cdot10^{-1}$ mmol, 8.0 eq.), ABD-ipa (25.5 mg, $8.10\cdot10^{-2}$ mmol, 4.0 eq.), $Ga(NO_3)_3$ hydrate (41.7 mg, $1.63\cdot10^{-1}$ mmol, 8.0 eq.) and $Nd(NO_3)_3\cdot6H_2O$ (17.5 mg, $4.00\cdot10^{-2}$ mmol, 2.0 eq.) were dissolved in 2 mL of DMF. $N(Et_3)$ (90.77 µL, 0.816 mmol, 40 eq.) were added to the solution and the solution stirred overnight at room temperature. The solvent was evaporated to dryness and the solid was suspended in 2 mL of MeOH. The solid was filtered, washed with MeOH (2 mL), water (10 mL), MeOH (5 mL), tBuOMe (10 mL) and dried under

vacuum for 24 h to yield 12.2 mg of {[Nd(12-$MC_{Ga,shi}$-4)]$_2$(ABD-ip)$_4$} metallacrown as a brown solid ($1.09 \cdot 10^{-1}$ mmol, 17 % based on $Nd(NO_3)_3 \cdot 6H_2O$). ESI-MS (MeOH/DMSO 90:10, negative mode, m/z): {[Nd(12-$MC_{Ga,shi}$-4)]$_2$(ABD-ip)$_4$}$^{2-}$: 1647.79 (calc.), 1646.77 (exp.).

Synthesis of ABD-Biotin-ipa. Biotin (19.41mg, 0.08 mmol, 1.1 eq.) was suspended in DCM dry (10 mL) under inert atmosphere, and three drops of DMF were added. Thionyl Chloride ($SOCl_2$) (0.05 mL, 0.72 mmol, 10 eq.) was added dropwise and the solution stirred for 2 h at 50 °C. The resulting colorless solution was evaporated to dryness to give a pale-yellow oil. The oil was re-dissolved in DCM (10 mL), added with a 1 mL solution of ABD-ipa (22.7 mg, 0.072 mmol, 1 eq.) in THF, and with triethylamine (0.08 mmol, 11 µL). The mixture was stirred for 3 h, the precipitate filtered off and washed with DCM to yield 26 mg of brown solid (67%). ^{1}H NMR (DMSO-d_6, 500 MHz) δ, ppm: 13.06 (2H, bs), 10.28 (1H, s), 9.25 (1H, s), 8.71 (1H, s), 8.15 (1H, s), 7.99 (1H, s) 7.95 (2H, s), 7.88 (1H, d), 7.05 (1H, d, *J* = 8.0 Hz), 4.70 (1H, t, *J* = 7.2 Hz), 4.22 (1H, t), 3.25 (1H, m), 3.0 – 2.90 (2H, m), 2.54 (2H, s), 1.75 – 1.64 (3H, m), 1.58 – 1.51 (1H, m), 1.47 – 1.37 (2H, m).

Synthesis of {[Ln(12-$MC_{Ga,shi}$-4)]$_2$(Biotin-ABD-ip)$_4$}$(HNEt_3)_2$ metallacrowns (Ln = Y, Yb). {[Ln(12-$MC_{Ga,shi}$-4)(bza)$_4$]}pyridinium ($9.00 \cdot 10^{-3}$ mmol, 1.0 eq.) were dissolved in 500 µL of DMF, Biotin-ABD (10.3 mg, $1.9 \cdot 10^{-2}$ mmol, 2.2 eq.) added to yield a dark red solution. NEt_3 (12.3 µL, $8.6 \cdot 10^{-2}$ mmol, 10.0 eq.) were added to the solution and the solution stirred overnight at room temperature. The solution was evaporated to dryness and the solid suspended in 3 mL of MeOH. The solid was filtered, washed with MeOH (1 mL), water (10 mL), MeOH (5 mL), tBuOMe (10 mL) and dried under vacuum for 24 h to yield {[Ln(12-$MC_{Ga,shi}$-4)]$_2$(Biotin-ABD-ip)$_4$}$(HNEt_3)_2$ metallacrowns as brown solids.

{[Yb(12-MC$_{Ga,shi}$-4)]$_2$(Biotin-ABD-ip)$_4$}(HNEt$_3$)$_2$. The yield was 21 % based on {[Yb(12-MC$_{Ga,shi}$-4)(bza)$_4$]}pyridinium. ESI-MS (MeOH/DMSO 90:10, negative mode, m/z): {{[Yb(12-MC$_{Ga,shi}$-4)]$_2$(Biotin-ABD-ip)$_4$}+H$_2$O+3MeOH]}$^{2-}$: 2186.02 (calc.), 2185.44 (exp.). {{[Yb(12-MC$_{Ga,shi}$-4)]$_2$(Biotin-ABD-ip)$_4$}+H$_2$O+2MeOH]}$^{2-}$: 2170.51 (calc.), 2171.44 (exp.). [Yb$_2$Ga$_8$(shi)$_8$(deg2)$_4$+H$_2$O]$^{2-}$: 2058.54 (calc.), 2058.54 (exp.). [Yb$_2$Ga$_8$(shi)$_8$(deg1)$_4$+3H$_2$O+MeCN]$^{2-}$: 2045.11 (calc.), 2044.41 (exp.).

{[Y(12-MC$_{Ga,shi}$-4)]$_2$(Biotin-ABD-ip)$_4$}(HNEt$_3$)$_2$. The yield was 18 % based on {[Y(12-MC$_{Ga,shi}$-4)(bza)$_4$]}pyridinium. ESI-MS (MeOH/DMSO 90:10, negative mode, m/z): {[Y(12-MC$_{Ga,shi}$-4)]$_2$(Biotin-ABD-ip)$_4$}+4H$_2$O+MeCN]$^{2-}$: 2101.98 (calc.), 2101.41 (exp.).

Bibliography

(1) Gross, M. Nature's Building Blocks. *Chem Ind* **2014**, *78* (12), 18–21. https://doi.org/10.1002/cind.7812_4.x.

(2) *NOMENCLATURE OF INORGANIC CHEMISTRY IUPAC Recommendations 2005 IUPAC Periodic Table of the Elements Fm No*; 2005.

(3) Sagawa, M.; Hirosawa, S.; Yamamoto, H.; Fujimura, S.; Matsuura, Y. Nd砷fe砷b Permanent Magnet Materials. *Jpn J Appl Phys* **1987**, *26* (6R), 785–800. https://doi.org/10.1143/JJAP.26.785.

(4) Coey, J. M. D. Permanent Magnet Applications. *J Magn Magn Mater* **2002**, *248* (3), 441–456. https://doi.org/10.1016/S0304-8853(02)00335-9.

(5) Yin, M.; Li, G.; Zhou, M.; Zhao, C. Modeling of the Wind Turbine with a Permanent Magnet Synchronous Generator for Integration. *2007 IEEE Power Engineering Society General Meeting, PES* **2007**. https://doi.org/10.1109/PES.2007.385982.

(6) Prashanth, N. A. Flux Maximization in Wind Turbine Permanent Magnet Synchronous Generator Made of NdFeB Permanent Magnets. *Mater Today Proc* **2022**, *49*, 731–737. https://doi.org/10.1016/J.MATPR.2021.05.224.

(7) Wang, H.; Lamichhane, T. N.; Paranthaman, M. P. Review of Additive Manufacturing of Permanent Magnets for Electrical Machines: A Prospective on Wind Turbine. *Materials Today Physics* **2022**, *24*, 100675. https://doi.org/10.1016/J.MTPHYS.2022.100675.

(8) Yang, Y.; Walton, A.; Sheridan, R.; Güth, K.; Gauß, R.; Gutfleisch, O.; Buchert, M.; Steenari, B. M.; Van Gerven, T.; Jones, P. T.; Binnemans, K. REE Recovery from End-of-Life NdFeB Permanent Magnet Scrap: A Critical Review. *Journal of Sustainable Metallurgy*. Springer Science and Business Media Deutschland GmbH March 1, 2017, pp 122–149. https://doi.org/10.1007/s40831-016-0090-4.

(9) Binnemans, K.; Jones, P. T.; Blanpain, B.; Van Gerven, T.; Yang, Y.; Walton, A.; Buchert, M. Recycling of Rare Earths: A Critical Review. *J Clean Prod* **2013**, *51*, 1–22. https://doi.org/10.1016/j.jclepro.2012.12.037.

(10) Orefice, M.; Binnemans, K. Solvometallurgical Process for the Recovery of Rare-Earth Elements from Nd–Fe–B Magnets. *Sep Purif Technol* **2021**, *258*. https://doi.org/10.1016/j.seppur.2020.117800.

(11) Binnemans, K.; Jones, P. T. Solvometallurgy: An Emerging Branch of Extractive Metallurgy. *Journal of Sustainable Metallurgy*. Springer Science and Business

Media Deutschland GmbH September 1, 2017, pp 570–600. https://doi.org/10.1007/s40831-017-0128-2.

(12) Balaram, V. Rare Earth Elements: A Review of Applications, Occurrence, Exploration, Analysis, Recycling, and Environmental Impact. *Geoscience Frontiers* **2019**, *10* (4), 1285–1303. https://doi.org/10.1016/J.GSF.2018.12.005.

(13) Schulze, R.; Buchert, M. Estimates of Global REE Recycling Potentials from NdFeB Magnet Material. *Resour Conserv Recycl* **2016**, *113*, 12–27. https://doi.org/10.1016/J.RESCONREC.2016.05.004.

(14) Klinger, J. M. A Historical Geography of Rare Earth Elements: From Discovery to the Atomic Age. *Extr Ind Soc* **2015**, *2* (3), 572–580. https://doi.org/10.1016/J.EXIS.2015.05.006.

(15) Dushyantha, N.; Batapola, N.; Ilankoon, I. M. S. K.; Rohitha, S.; Premasiri, R.; Abeysinghe, B.; Ratnayake, N.; Dissanayake, K. The Story of Rare Earth Elements (REEs): Occurrences, Global Distribution, Genesis, Geology, Mineralogy and Global Production. *Ore Geol Rev* **2020**, *122*, 103521. https://doi.org/10.1016/J.OREGEOREV.2020.103521.

(16) Cotton, Simon. Lanthanides and Actinides. London Macmillan Education Ltd, 1991..Pdf.

(17) Elkina, V.; Kurushkin, M. Promethium: To Strive, to Seek, to Find and Not to Yield. *Front Chem* **2020**, *8* (July), 1–8. https://doi.org/10.3389/fchem.2020.00588.

(18) Lu, J. B.; Jiang, X. L.; Hu, H. S.; Li, J. Norm-Conserving 4f-in-Core Pseudopotentials and Basis Sets Optimized for Trivalent Lanthanides (Ln = Ce-Lu). *J Chem Theory Comput* **2023**, *19* (1), 82–96. https://doi.org/10.1021/ACS.JCTC.2C00922/ASSET/IMAGES/LARGE/CT2C00922_0010.JPEG.

(19) Seitz, M.; Oliver, A. G.; Raymond, K. N. The Lanthanide Contraction Revisited. *J Am Chem Soc* **2007**, *129* (36), 11153–11160. https://doi.org/10.1021/JA072750F/SUPPL_FILE/JA072750FSI20070419_060034.CIF.

(20) Peters, J. A.; Djanashvili, K.; Geraldes, C. F. G. C.; Platas-Iglesias, C. The Chemical Consequences of the Gradual Decrease of the Ionic Radius along the Ln-Series. *Coord Chem Rev* **2020**, *406*, 213146. https://doi.org/10.1016/j.ccr.2019.213146.

(21) Nkiawete, M. M.; Vander Wal, R. L. Rare Earth Elements: Sector Allocations and Supply Chain Considerations. *Journal of Rare Earths* **2024**. https://doi.org/10.1016/j.jre.2024.01.020.

(22) Massari, S.; Ruberti, M. Rare Earth Elements as Critical Raw Materials: Focus on International Markets and Future Strategies. *Resources Policy* **2013**, *38* (1), 36–43. https://doi.org/10.1016/j.resourpol.2012.07.001.

(23) *Study on the Critical Raw Materials for the EU 2023 – Final Report*.

(24) Geological Survey, U. *MINERAL COMMODITY SUMMARIES 2024*; 2024.

(25) Binnemans, K.; Jones, P. T.; Van Acker, K.; Blanpain, B.; Mishra, B.; Apelian, D. Rare-Earth Economics: The Balance Problem. *Jom* **2013**, *65* (7), 846–848. https://doi.org/10.1007/s11837-013-0639-7.

(26) Gutfleisch, O.; Willard, M. A.; Brück, E.; Chen, C. H.; Sankar, S. G.; Liu, J. P. Magnetic Materials and Devices for the 21st Century: Stronger, Lighter, and More Energy Efficient. *Advanced Materials* **2011**, *23* (7), 821–842. https://doi.org/10.1002/adma.201002180.

(27) Eu, E. *European Raw Materials Alliance (ERMA) @EU_ERMA #EUerma Rare Earth Magnets and Motors: A European Call for Action*.

(28) Chau, K. T.; Chan, C. C.; Liu, C. Overview of Permanent-Magnet Brushless Drives for Electric and Hybrid Electric Vehicles. *IEEE Transactions on Industrial Electronics* **2008**, *55* (6), 2246–2257. https://doi.org/10.1109/TIE.2008.918403.

(29) München, D. D.; Veit, H. M. Neodymium as the Main Feature of Permanent Magnets from Hard Disk Drives (HDDs). *Waste Management* **2017**, *61*, 372–376. https://doi.org/10.1016/J.WASMAN.2017.01.032.

(30) Hirosawa, S.; Nishino, M.; Miyashita, S. Perspectives for High-Performance Permanent Magnets: Applications, Coercivity, and New Materials. *Advances in Natural Sciences: Nanoscience and Nanotechnology* **2017**, *8* (1), 13002. https://doi.org/10.1088/2043-6254/aa597c.

(31) Reimer, M. V.; Schenk-Mathes, H. Y.; Hoffmann, M. F.; Elwert, T. Recycling Decisions in 2020, 2030, and 2040—When Can Substantial NdFeB Extraction Be Expected in the EU? *Metals (Basel)* **2018**, *8* (11). https://doi.org/10.3390/met8110867.

(32) Xiao, F.; Hu, W.; Zhao, J.; Zhu, H. Technologies of Recycling REEs and Iron from NdFeB Scrap. *Metals*. MDPI April 1, 2023. https://doi.org/10.3390/met13040779.

(33) Akcil, A.; Ibrahim, Y. A.; Meshram, P.; Panda, S.; Abhilash. Hydrometallurgical Recycling Strategies for Recovery of Rare Earth Elements from Consumer Electronic Scraps: A Review. *Journal of Chemical Technology and Biotechnology* **2021**, *96* (7), 1785–1797. https://doi.org/10.1002/jctb.6739.

(34) Lee, C. H.; Chen, Y. J.; Liao, C. H.; Popuri, S. R.; Tsai, S. L.; Hung, C. E. Selective Leaching Process for Neodymium Recovery from Scrap Nd-Fe-B Magnet. *Metall Mater Trans A Phys Metall Mater Sci* **2013**, *44* (13), 5825–5833. https://doi.org/10.1007/s11661-013-1924-3.

(35) Önal, M. A. R.; Aktan, E.; Borra, C. R.; Blanpain, B.; Van Gerven, T.; Guo, M. Recycling of NdFeB Magnets Using Nitration, Calcination and Water Leaching for REE Recovery. *Hydrometallurgy* **2017**, *167*, 115–123. https://doi.org/10.1016/j.hydromet.2016.11.006.

(36) Belfqueh, S.; Seron, A.; Chapron, S.; Arrachart, G.; Menad, N. Evaluating Organic Acids as Alternative Leaching Reagents for Rare Earth Elements Recovery from NdFeB Magnets. *Journal of Rare Earths* **2023**, *41* (4), 621–631. https://doi.org/10.1016/j.jre.2022.04.027.

(37) Blenau, L. W.; Vogt, D.; Lonski, O.; Abrar, A.; Fabrichnaya, O.; Charitos, A. Development of a Process to Recycle NdFeB Permanent Magnets Based on the CaO-Al2O3-Nd2O3 Slag System. *Processes* **2023**, *11* (6). https://doi.org/10.3390/pr11061783.

(38) Firdaus, M.; Rhamdhani, M. A.; Durandet, Y.; Rankin, W. J.; McGregor, K. Review of High-Temperature Recovery of Rare Earth (Nd/Dy) from Magnet Waste. *Journal of Sustainable Metallurgy* **2016**, *2* (4), 276–295. https://doi.org/10.1007/s40831-016-0045-9.

(39) Orefice, M.; Binnemans, K. Solvometallurgical Process for the Recovery of Rare-Earth Elements from Nd–Fe–B Magnets. *Sep Purif Technol* **2021**, *258*, 117800. https://doi.org/https://doi.org/10.1016/j.seppur.2020.117800.

(40) Cheisson, T.; Schelter, E. J. *Rare Earth Elements: Mendeleev's Bane, Modern Marvels*. https://www.science.org.

(41) Pereira Neves, H.; Max Dias Ferreira, G.; Max Dias Ferreira, G.; Rodrigues de Lemos, L.; Dias Rodrigues, G.; Albis Leão, V.; Barbosa Mageste, A. Liquid-Liquid Extraction of Rare Earth Elements Using Systems That Are More Environmentally Friendly: Advances, Challenges and Perspectives. *Sep Purif Technol* **2022**, *282* (August 2021). https://doi.org/10.1016/j.seppur.2021.120064.

(42) Hu, Y.; Florek, J.; Larivière, D.; Fontaine, F. G.; Kleitz, F. Recent Advances in the Separation of Rare Earth Elements Using Mesoporous Hybrid Materials. *Chemical Record* **2018**, *18* (7–8), 1261–1276. https://doi.org/10.1002/tcr.201800012.

(43) Vander Hoogerstraete, T.; Blanpain, B.; Van Gerven, T.; Binnemans, K. From NdFeB Magnets towards the Rare-Earth Oxides: A Recycling Process Consuming Only

Oxalic Acid. *RSC Adv* **2014**, *4* (109), 64099–64111. https://doi.org/10.1039/c4ra13787f.

(44) Tasaki-Handa, Y.; Abe, Y.; Ooi, K.; Narita, H.; Tanaka, M.; Wakisaka, A. Environmentally Friendly Separation of Dysprosium and Neodymium by Fractional Precipitation of Coordination Polymers. *RSC Adv* **2014**, *4* (39), 20496–20498. https://doi.org/10.1039/c4ra00257a.

(45) Carron, M. K.; Naeser, C. R.; Rose, H. J.; Hildebrand, F. a. Fractional Precipitation of Rare Earths with Phosphoric Acid. *U.S. Geol. Surv. Bull* **1958**, *1036-N*, 253–275.

(46) Belfqueh, S.; Chapron, S.; Giusti, F.; Pellet-Rostaing, S.; Seron, A.; Menad, N.; Arrachart, G. Selective Recovery of Rare Earth Elements from Acetic Leachate of NdFeB Magnet by Solvent Extraction. *Sep Purif Technol* **2024**, *339*, 126701. https://doi.org/10.1016/j.seppur.2024.126701ï.

(47) R. G. M., . (1985). S. R. Taylor & S. M. McLennan 1985. The Continental Crust Its Composition and Evolution. Xvi + 312 Pp. Oxford, London, Edinburgh, Boston, Palo Alto, .Pdf.

(48) Roa, A.; López, J.; Cortina, J. L. Recovery of Rare Earth Elements from Acidic Mine Waters: A Circular Treatment Scheme Utilizing Selective Precipitation and Ion Exchange. *Sep Purif Technol* **2024**, *338*. https://doi.org/10.1016/j.seppur.2024.126525.

(49) Belfqueh, S.; Chapron, S.; Giusti, F.; Pellet-Rostaing, S.; Seron, A.; Menad, N.; Arrachart, G. Selective Recovery of Rare Earth Elements from Acetic Leachate of NdFeB Magnet by Solvent Extraction. *Sep Purif Technol* **2024**, *339*, 126701. https://doi.org/10.1016/j.seppur.2024.126701.

(50) Riaño, S.; Petranikova, M.; Onghena, B.; Vander Hoogerstraete, T.; Banerjee, D.; Foreman, M. R. S.; Ekberg, C.; Binnemans, K. Separation of Rare Earths and Other Valuable Metals from Deep-Eutectic Solvents: A New Alternative for the Recycling of Used NdFeB Magnets. *RSC Adv* **2017**, *7* (51), 32100–32113. https://doi.org/10.1039/c7ra06540j.

(51) Angew Chem Int Ed - 2015 - Bogart - An Operationally Simple Method for Separating the Rare-Earth Elements Neodymium and.Pdf.

(52) Falco, A.; Neri, M.; Melegari, M.; Baraldi, L.; Bonfant, G.; Tegoni, M.; Serpe, A.; Marchiò, L. Semirigid Ligands Enhance Different Coordination Behavior of Nd and Dy Relevant to Their Separation and Recovery in a Non-Aqueous Environment. *Inorg Chem* **2022**, *61* (40), 16110–16121. https://doi.org/10.1021/acs.inorgchem.2c02619.

(53) Melegari, M.; Neri, M.; Falco, A.; Tegoni, M.; Maffini, M.; Fornari, F.; Mucchino, C.; Artizzu, F.; Serpe, A.; Marchiò, L. Tailoring the Use of 8-Hydroxyquinolines for the Facile Separation of Iron, Dysprosium and Neodymium. *ChemSusChem* **2024**. https://doi.org/10.1002/cssc.202400286.

(54) O'Connell-Danes, J. G.; Ngwenya, B. T.; Morrison, C. A.; Love, J. B. Selective Separation of Light Rare-Earth Elements by Supramolecular Encapsulation and Precipitation. *Nat Commun* **2022**, *13* (1). https://doi.org/10.1038/s41467-022-32178-3.

(55) Gao, H. Y.; Peng, W. L.; Meng, P. P.; Feng, X. F.; Li, J. Q.; Wu, H. Q.; Yan, C. S.; Xiong, Y. Y.; Luo, F. Lanthanide Separation Using Size-Selective Crystallization of Ln-MOFs. *Chemical Communications* **2017**, *53* (42), 5737–5739. https://doi.org/10.1039/c7cc01898c.

(56) Yin, X.; Wang, Y.; Bai, X.; Wang, Y.; Chen, L.; Xiao, C.; Diwu, J.; Du, S.; Chai, Z.; Albrecht-Schmitt, T. E.; Wang, S. Rare Earth Separations by Selective Borate Crystallization. *Nat Commun* **2017**, *8*. https://doi.org/10.1038/ncomms14438.

(57) Di Bernardo, P.; Melchior, A.; Tolazzi, M.; Zanonato, P. L. Thermodynamics of Lanthanide(III) Complexation in Non-Aqueous Solvents. *Coordination Chemistry Reviews*. January 2012, pp 328–351. https://doi.org/10.1016/j.ccr.2011.07.010.

(58) Polinski, M. J.; Grant, D. J.; Wang, S.; Alekseev, E. V.; Cross, J. N.; Villa, E. M.; Depmeier, W.; Gagliardi, L.; Albrecht-Schmitt, T. E. Differentiating between Trivalent Lanthanides and Actinides. *J Am Chem Soc* **2012**, *134* (25), 10682–10692. https://doi.org/10.1021/ja303804r.

(59) Dam, H. H.; Reinhoudt, D. N.; Verboom, W. Multicoordinate Ligands for Actinide/Lanthanide Separations. *Chem Soc Rev* **2007**, *36* (2), 367–377. https://doi.org/10.1039/B603847F.

(60) Tyumentsev, M. S.; Foreman, M. R. St. J.; Slawin, A. M. Z.; Cordes, D. B.; Savolainen, O.; Ylmén, R.; Steenari, B.-M.; Ekberg, C. Coordination of Trivalent Lanthanides with Bismalonamide Ligands: Implications for Liquid–Liquid Extraction. *Eur J Inorg Chem* **2017**, *2017* (37), 4285–4298. https://doi.org/https://doi.org/10.1002/ejic.201700801.

(61) Rosario-Amorin, D.; Ouizem, S.; Dickie, D. A.; Wen, Y.; Paine, R. T.; Gao, J.; Grey, J. K.; de Bettencourt-Dias, A.; Hay, B. P.; Delmau, L. H. Synthesis, Lanthanide Coordination Chemistry, and Liquid–Liquid Extraction Performance of CMPO-Decorated Pyridine and Pyridine N-Oxide Platforms. *Inorg Chem* **2013**, *52* (6), 3063–3083. https://doi.org/10.1021/ic3025342.

(62) Liu, Y.; Wang, C. Z.; Wu, Q. Y.; Lan, J. H.; Chai, Z. F.; Liu, Q.; Shi, W. Q. Theoretical Prediction of the Potential Applications of Phenanthroline Derivatives in Separation of Transplutonium Elements. *Inorg Chem* **2020**, *59* (16), 11469–11480. https://doi.org/10.1021/ACS.INORGCHEM.0C01271.

(63) Liu, Y.; Wang, C. Z.; Wu, Q. Y.; Lan, J. H.; Chai, Z. F.; Liu, Q.; Shi, W. Q. Theoretical Insights into Transplutonium Element Separation with Electronically Modulated Phenanthroline-Derived Bis-Triazine Ligands. *Inorg Chem* **2021**, *60* (14), 10267–10279. https://doi.org/10.1021/ACS.INORGCHEM.1C00668/ASSET/IMAGES/MEDIUM/IC1C00668_M006.GIF.

(64) Cole, B. E.; Cheisson, T.; Nelson, J. J. M.; Higgins, R. F.; Gau, M. R.; Carroll, P. J.; Schelter, E. J. Understanding Molecular Factors That Determine Performance in the Rare Earth (TriNOx) Separations System. *ACS Sustain Chem Eng* **2020**, *8* (39), 14786–14794. https://doi.org/10.1021/acssuschemeng.0c03974.

(65) Craze, A. R.; Huang, X. Da; Etchells, I.; Zheng, L. M.; Bhadbhade, M. M.; Marjo, C. E.; Clegg, J. K.; Moore, E. G.; Avdeev, M.; Lindoy, L. F.; Li, F. Synthesis and Characterisation of New Tripodal Lanthanide Complexes and Investigation of Their Optical and Magnetic Properties. *Dalton Transactions* **2017**, *46* (36), 12177–12184. https://doi.org/10.1039/c7dt02556d.

(66) Shannon, R. D. Revised Effective Ionic Radii and Systematic Studies of Interatomic Distances in Halides and Chalcogenides. *Acta Crystallographica Section A* **1976**, *32* (5), 751–767. https://doi.org/10.1107/S0567739476001551.

(67) Sun, Y.; Hou, T.; He, X.; Man, V. H.; Wang, J. Development And Test of Highly Accurate Endpoint Free Energy Methods. 2: Prediction of Logarithm of n-Octanol-Water Partition Coefficient (LogP) for Druglike Molecules Using MM-PBSA Method. *J Comput Chem* **2023**, *44* (13), 1300. https://doi.org/10.1002/JCC.27086.

(68) Masuya-Suzuki, A.; Hosobori, K.; Sawamura, R.; Abe, Y.; Karashimada, R.; Iki, N. Selective Crystallization of Dysprosium Complex from Neodymium/Dysprosium Mixture Enabled by Cooperation of Coordination and Crystallization. *Chem Commun (Camb)* **2022**, *58* (14), 2283–2286. https://doi.org/10.1039/D1CC06174G.

(69) Binnemans, K.; McGuiness, P.; Jones, P. T. Rare-Earth Recycling Needs Market Intervention. *Nature Reviews Materials 2021 6:6* **2021**, *6* (6), 459–461. https://doi.org/10.1038/s41578-021-00308-w.

(70) Krause, L.; Herbst-Irmer, R.; Sheldrick, G. M.; Stalke, D. Comparison of Silver and Molybdenum Microfocus X-Ray Sources for Single-Crystal Structure Determination. *J Appl Crystallogr* **2015**, *48* (1), 3–10. https://doi.org/10.1107/S1600576714022985.

(71) Sheldrick, G. M. SHELXT - Integrated Space-Group and Crystal-Structure Determination. *Acta Crystallogr A* **2015**, *71* (1), 3–8. https://doi.org/10.1107/S2053273314026370.

(72) Sheldrick, G. M. Crystal Structure Refinement with SHELXL. *Acta Crystallogr C Struct Chem* **2015**, *71*, 3–8. https://doi.org/10.1107/S2053229614024218.

(73) Dolomanov, O. V.; Bourhis, L. J.; Gildea, R. J.; Howard, J. A. K.; Puschmann, H. OLEX2: A Complete Structure Solution, Refinement and Analysis Program. *J Appl Crystallogr* **2009**, *42* (2), 339–341. https://doi.org/10.1107/S0021889808042726.

(74) Kanesato, M.; Yokoyama, T. Crystal Structures of Dysprosium(III) and Holmium(III) Complexes of Tripodal Tris[2-(Salicylideneamino)Ethyl]Amine. *Analytical Sciences* **2000**, *16* (3), 335–336. https://doi.org/10.2116/analsci.16.335.

(75) Kanesato, M.; Yokoyama, T.; Itabashi, O.; Suzuki, T. M.; Shiro, M. Synthesis and Structural Characterization of Praseodymium(III) and Neodymium(III) Complexes of Tripodal Tris[2-(Salicylideneamino)Ethyl]Amine. *Bull Chem Soc Jpn* **1996**, *69* (5), 1297–1302. https://doi.org/10.1246/bcsj.69.1297.

(76) Gans, P.; Sabatini, A.; Vacca, A. Investigation of Equilibria in Solution. Determination of Equilibrium Constants with the HYPERQUAD Suite of Programs. *Talanta* **1996**, *43* (10), 1739–1753. https://doi.org/10.1016/0039-9140(96)01958-3.

(77) Cotton, F. A.; Wilkinson, G.; Pedersen, C. J.; Stengle,) T R; Baldeschwieler, J. D. *The Principles of Nuclear Magnetism*; The Clarendon Press, 1966; Vol. 55.

(78) Perspectives in Supramolecular Chemistry—From Molecular Recognition towards Molecular Information Processing and Self-Organization.

(79) Philp, D.; Fraser Stoddart, J. Self-Assembly in Natural and Unnatural Systems. *Angewandte Chemie (International Edition in English)*. 1996, pp 1154–1196. https://doi.org/10.1002/anie.199611541.

(80) Calixarenes, Macrocycles with (Almost) Unlimited Possibilities.

(81) Shinkai, S.; Ogawa, T.; Nakaji, T.; Kusano, Y.; Nanabe, O. Photocontrolled Extraction Ability of Azobenzene-Bridged Azacrown Ether. *Tetrahedron Letters*. 1979, pp 4569–4572. https://doi.org/10.1016/S0040-4039(01)86651-X.

(82) ALKALI METAL SOLUTIONS. EFFECT OF CRYPTANDS ON.

(83) Chiral Crown Ethers Derived from (+)-(IS,2S)-Trans-Cyclohexane-l,2-.

(84) Pecoraro, V. L. Structural Characterization of [VO(Salicylhydroximate)(CH3OH)]3: Applications to the Biological Chemistry of Vanadium(V). *Inorganica Chim Acta* **1989**, *155* (2), 171–173. https://doi.org/10.1016/S0020-1693(00)90405-5.

(85) Lou, T.; Yang, H.; Zeng, S.; Li, D.; Dou, J. A New Family of Heterometallic LnIII[12-MCFeIIIN(Shi)-4] Complexes: Syntheses, Structures and Magnetic Properties. *Crystals 2018, Vol. 8, Page 229* **2018**, *8* (5), 229. https://doi.org/10.3390/CRYST8050229.

(86) Stemmler, A. J.; Kampf, J. W.; Pecoraro, V. L. A Planar [15]Metallacrown-5 That Selectively Binds the Uranyl Cation. *Angewandte Chemie International Edition in English*. 1996, pp 2841–2843. https://doi.org/10.1002/anie.199628411.

(87) Soo Lah, M.; Pecoraro, V. L.; Chem Soc, M. J.; Trans, D. *Coordination Chemistry of Macrocyclic Complexes·*; Plenum Press, 1989; Vol. 11. https://pubs.acs.org/sharingguidelines.

(88) Chow, C. Y.; Eliseeva, S. V; Trivedi, E. R.; Nguyen, T. N.; Kampf, J. W.; Petoud, S.; Pecoraro, V. L. Ga3+/Ln3+ Metallacrowns: A Promising Family of Highly Luminescent Lanthanide Complexes That Covers Visible and Near-Infrared Domains. *J Am Chem Soc* **2016**, *138* (15), 5100–5109. https://doi.org/10.1021/jacs.6b00984.

(89) Zaleski, C. M.; Depperman, E. C.; Kampf, J. W.; Kirk, M. L.; Pecoraro, V. L. Synthesis, Structure, and Magnetic Properties of a Large Lanthanide–Transition-Metal Single-Molecule Magnet. *Angewandte Chemie International Edition* **2004**, *43* (30), 3912–3914. https://doi.org/10.1002/ANIE.200454013.

(90) Mezei, G.; Zaleski, C. M.; Pecoraro, V. L. Structural and Functional Evolution of Metallacrowns. *Chemical Reviews*. November 2007, pp 4933–5003. https://doi.org/10.1021/cr078200h.

(91) Ostrowska, M.; Fritsky, I. O.; Gumienna-Kontecka, E.; Pavlishchuk, A. V. Metallacrown-Based Compounds: Applications in Catalysis, Luminescence, Molecular Magnetism, and Adsorption. *Coordination Chemistry Reviews*. Elsevier B.V. November 15, 2016, pp 304–332. https://doi.org/10.1016/j.ccr.2016.04.017.

(92) Idroxamic Acid.

(93) Alam, M. A. Methods for Hydroxamic Acid Synthesis. *Curr Org Chem* **2019**, *23* (9), 978–993. https://doi.org/10.2174/1385272823666190424142821.

(94) Tegoni, M.; Remelli, M. Metallacrowns of Copper(II) and Aminohydroxamates: Thermodynamics of Self Assembly and Host-Guest Equilibria. *Coord Chem Rev* **2012**, *256* (1–2), 289–315. https://doi.org/10.1016/j.ccr.2011.06.007.

(95) Zaleski, C. M. *Advances in Metallacrown Chemistry*; 2022. https://doi.org/10.1007/978-3-031-08576-5.

(96) Salerno, E. V; Eliseeva, S. V; Schneider, B. L.; Kampf, J. W.; Petoud, S.; Pecoraro, V. L. Visible, Near-Infrared, and Dual-Range Luminescence Spanning the 4f Series Sensitized by a Gallium(III)/Lanthanide(III) Metallacrown Structure. *J Phys Chem A* **2020**, *124* (50), 10550–10564. https://doi.org/10.1021/acs.jpca.0c08819.

(97) Dhawan, A. P.; D'Alessandro, B.; Fu, X. Optical Imaging Modalities for Biomedical Applications. *IEEE Rev Biomed Eng* **2010**, *3*, 69–92. https://doi.org/10.1109/RBME.2010.2081975.

(98) Bouza Dominguez, J.; Dominguez, B.; Jorge. Optical Imaging of Biological Tissues. *PhDT* **2012**.

(99) Monici, M. Cell and Tissue Autofluorescence Research and Diagnostic Applications. *Biotechnol Annu Rev* **2005**, *11* (SUPPL.), 227–256. https://doi.org/10.1016/S1387-2656(05)11007-2.

(100) Kumamoto, Y.; Taguchi, A.; Kawata, S. Deep-Ultraviolet Biomolecular Imaging and Analysis. *Adv Opt Mater* **2019**, *7* (5), 1801099. https://doi.org/10.1002/ADOM.201801099.

(101) Young, A. R. Chromophores in Human Skin. *Phys Med Biol* **1997**, *42* (5), 789. https://doi.org/10.1088/0031-9155/42/5/004.

(102) Jacques, S. L. Optical Properties of Biological Tissues: A Review. *Phys Med Biol* **2013**, *58* (11). https://doi.org/10.1088/0031-9155/58/11/R37.

(103) Keiser, G.; Kao, F.-J. Biophotonic Applications of Optical Communication Devices. *Biophotonics: Photonic Solutions for Better Health Care* **2008**, *6991* (August), 69911E. https://doi.org/10.1117/12.779945.

(104) Alabugin, A. Near-IR Photochemistry for Biology: Exploiting the Optical Window of Tissue. *Photochem Photobiol* **2019**, *95* (3), 722–732. https://doi.org/10.1111/PHP.13068.

(105) Glickman, R. D.; Jacques, S. L.; Hall, R. M.; Kumar, N. Revisiting the Internal Absorption Coefficient of the Retinal Pigment Epithelium Melanosome. *https://doi.org/10.1117/12.434697* **2001**, *4257*, 134–141. https://doi.org/10.1117/12.434697.

(106) Tuchin, V. V. Light Scattering Study of Tissues. *Physics-Uspekhi* **1997**, *40* (5), 495–515. https://doi.org/10.1070/PU1997V040N05ABEH000236/XML.

(107) Aswathy, R. G.; Yoshida, Y.; Maekawa, T.; Kumar, D. S. Near-Infrared Quantum Dots for Deep Tissue Imaging. *Analytical and Bioanalytical Chemistry*. June 2010, pp 1417–1435. https://doi.org/10.1007/s00216-010-3643-6.

(108) COONS, A. H.; KAPLAN, M. H. Localization of Antigen in Tissue Cells; Improvements in a Method for the Detection of Antigen by Means of Fluorescent Antibody. *J Exp Med* **1950**, *91* (1), 1–13. https://doi.org/10.1084/jem.91.1.1.

(109) Shimomura, O. Discovery of Green Fluorescent Protein (GFP) (Nobel Lecture). *Angew Chem Int Ed Engl* **2009**, *48* (31), 5590–5602. https://doi.org/10.1002/anie.200902240.

(110) Zimmer, M. Green Fluorescent Protein (GFP): Applications, Structure, and Related Photophysical Behavior. *Chem Rev* **2002**, *102* (3), 759–781. https://doi.org/10.1021/CR010142R/ASSET/IMAGES/LARGE/CR010142RF00016.JPEG.

(111) Ptaszek, M. Rational Design of Fluorophores for In Vivo Applications. *Prog Mol Biol Transl Sci* **2013**, *113*, 59–108. https://doi.org/10.1016/B978-0-12-386932-6.00003-X.

(112) Yuan, L.; Lin, W.; Zheng, K.; He, L.; Huang, W. Far-Red to near Infrared Analyte-Responsive Fluorescent Probes Based on Organic Fluorophore Platforms for Fluorescence Imaging. *Chem Soc Rev* **2013**, *42* (2), 622–661. https://doi.org/10.1039/c2cs35313j.

(113) Martynov, V. I.; Pakhomov, A. A.; Popova, N. V.; Deyev, I. E.; Petrenko, A. G. Synthetic Fluorophores for Visualizing Biomolecules in Living Systems. *Acta Naturae* **2016**, *8* (4), 33–46. https://doi.org/10.32607/20758251-2016-8-4-33-46.

(114) Salerno, E. V.; Foley, C. M.; Marzaroli, V.; Schneider, B. L.; Sharin, M. D.; Kampf, J. W.; Marchiò, L.; Zeller, M.; Guillot, R.; Mallah, T.; Tegoni, M.; Pecoraro, V. L.; Zaleski, C. M. Unique Dimerization Topology and Countercation Binding Modes in 12-Metallacrown-4 Compounds. *Eur J Inorg Chem* **2022**, *2022* (32). https://doi.org/10.1002/ejic.202200439.

(115) Atzeri, C.; Marchiò, L.; Chow, C. Y.; Kampf, J. W.; Pecoraro, V. L.; Tegoni, M. Design of 2D Porous Coordination Polymers Based on Metallacrown Units. *Chemistry - A European Journal* **2016**, *22* (19), 6482–6486. https://doi.org/10.1002/chem.201600562.

(116) Wang, J.; Lu, G.; Liu, Y.; Wu, S. G.; Huang, G. Z.; Liu, J. L.; Tong, M. L. Building Block and Directional Bonding Approaches for the Synthesis of {DyMn 4 } n (n = 2, 3) Metallacrown Assemblies. *Cryst Growth Des* **2019**, *19* (3), 1896–1902. https://doi.org/10.1021/acs.cgd.8b01879.

(117) Chow, C. Y.; Eliseeva, S. V.; Trivedi, E. R.; Nguyen, T. N.; Kampf, J. W.; Petoud, S.; Pecoraro, V. L. Ga3+/Ln3+ Metallacrowns: A Promising Family of Highly Luminescent Lanthanide Complexes That Covers Visible and Near-Infrared Domains. *J Am Chem Soc* **2016**, *138* (15), 5100–5109. https://doi.org/10.1021/JACS.6B00984/SUPPL_FILE/JA6B00984_SI_001.CIF.

(118) Melegari, M.; Marzaroli, V.; Polisicchio, R.; Seletti, D.; Marchiò, L.; Pecoraro, V. L.; Tegoni, M. Insights on the Structure in Solution of Paramagnetic LnIII/GaIII 12-Metallacrown-4 Complexes Using 1D 1H NMR and Model Structures. *Inorg Chem* **2023**, *62* (27), 10645–10654. https://doi.org/10.1021/ACS.INORGCHEM.3C00983/ASSET/IMAGES/LARGE/IC3C00983_0007.JPEG.

(119) Shannon, R. D. Revised Effective Ionic Radii and Systematic Studies of Interatomic Distances in Halides and Chalcogenides. *Acta Crystallographica Section A* **1976**, *32* (5), 751–767. https://doi.org/10.1107/S0567739476001551.

(120) Aly, H.; El-Shafie, A. S.; El-Azazy, M. Utilization of 7-Chloro-4-Nitrobenzo-2-Oxa-1,3-Diazole (NBD-Cl) for Spectrochemical Determination of L-Ornithine: A Multivariate Optimization-Assisted Approach. *RSC Adv* **2019**, *9* (38), 22106–22115. https://doi.org/10.1039/c9ra03311d.

(121) Jiang, C.; Huang, H.; Kang, X.; Yang, L.; Xi, Z.; Sun, H.; Pluth, M. D.; Yi, L. NBD-Based Synthetic Probes for Sensing Small Molecules and Proteins: Design, Sensing Mechanisms and Biological Applications. *Chemical Society Reviews*. 2021, pp 7436–7495. https://doi.org/10.1039/d0cs01096k.

(122) Elbashir, A. A.; Suliman, F. E. O.; Aboul-Enein, H. Y. The Application of 7-Chloro-4-Nitrobenzoxadiazole (NBD-Cl) for the Analysis of Pharmaceutical-Bearing Amine Group Using Spectrophotometry and Spectrofluorimetry Techniques. *Appl Spectrosc Rev* **2011**, *46* (3), 222–241. https://doi.org/10.1080/05704928.2011.557121.

(123) Wang, J.; Liao, Y.; Shao, S. An NBD-Based Fluorescent Probe with High Selectivity to Cysteine over Homocysteine under Neutral Physiological Conditions. *Chem Lett* **2015**, *44* (10), 1437–1439. https://doi.org/10.1246/CL.150544.

(124) Enviro Toxic and Chemistry - 2017 - Gooch - In Vivo Toxicity of Nitroaromatics A Comprehensive Quantitative Structure.Pdf.

(125) Dakshinamurti, K. Biotin - A Regulator of Gene Expression. In *Journal of Nutritional Biochemistry*; 2005; Vol. 16, pp 419–423. https://doi.org/10.1016/j.jnutbio.2005.03.015.

(126) Wilchek, M.; Bayer, E. A.; Livnah, O. Essentials of Biorecognition: The (Strept)Avidin–Biotin System as a Model for Protein–Protein and Protein–Ligand Interaction. *Immunol Lett* **2006**, *103* (1), 27–32. https://doi.org/10.1016/J.IMLET.2005.10.022.

(127) Dundas, C. M.; Demonte, D.; Park, S. Streptavidin-Biotin Technology: Improvements and Innovations in Chemical and Biological Applications. *Appl Microbiol Biotechnol* **2013**, *97* (21), 9343–9353. https://doi.org/10.1007/s00253-013-5232-z.

(128) Diamantis, D. A.; Agalou, A.; Chatziathanasiadou, M. V.; Markopoulos, G. S.; Bellou, S.; Kanaki, Z.; Crook, T.; Syed, N.; Rampias, T.; Klinakis, A.; Kolettas, E.; Beis, D.; Tzakos, A. G. Biotin-Yellow a Biotin Guided NIR Turn-on Fluorescent Probe for Cancer Targeted Diagnosis. *Sens Actuators B Chem* **2021**, *337*. https://doi.org/10.1016/j.snb.2021.129807.

(129) Liu, T.; Nedrow-Byers, J. R.; Hopkins, M. R.; Wu, L. Y.; Lee, J.; Reilly, P. T. A.; Berkman, C. E. Targeting Prostate Cancer Cells with a Multivalent PSMA Inhibitor-Guided Streptavidin Conjugate. *Bioorg Med Chem Lett* **2012**, *22* (12), 3931–3934. https://doi.org/10.1016/j.bmcl.2012.04.110.

2.7 Supporting information: Chapter 2

2.7.1 Single Crystal X-ray Structures

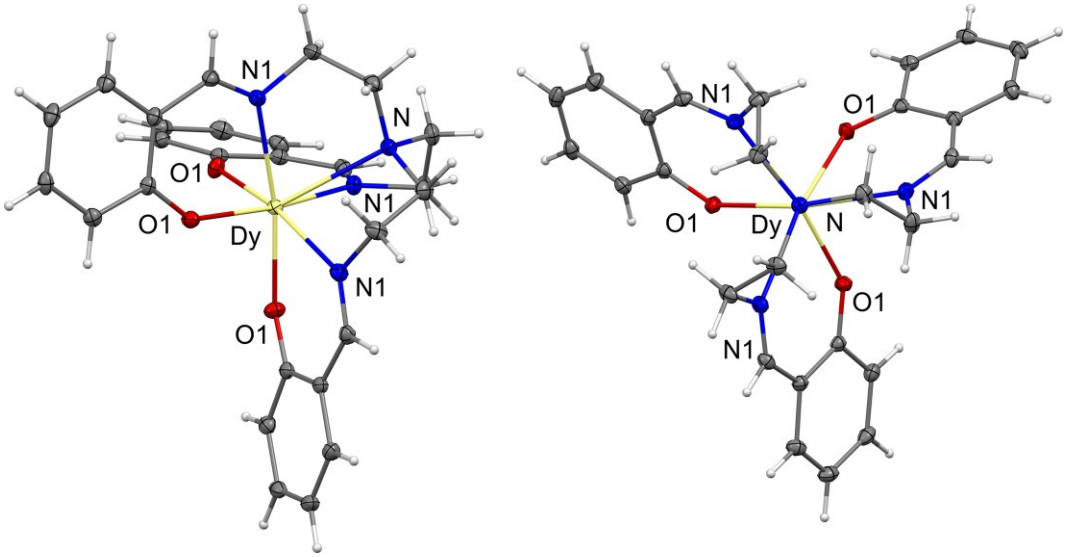

Figure S2.1. Representation of the structure of **1**. Thermal ellipsoids were depicted at the 30% probability level. Left: view of the structure of the complex highlighting the capped octahedron molecular geometry. Right: view along the central axis N-Dy. Dy (pale-yellow), N (blue), O (red), C (gray) and H (light gray). Image reprinted from https://pubs.acs.org/doi/full/10.1021/acs.inorgchem.2c02619.

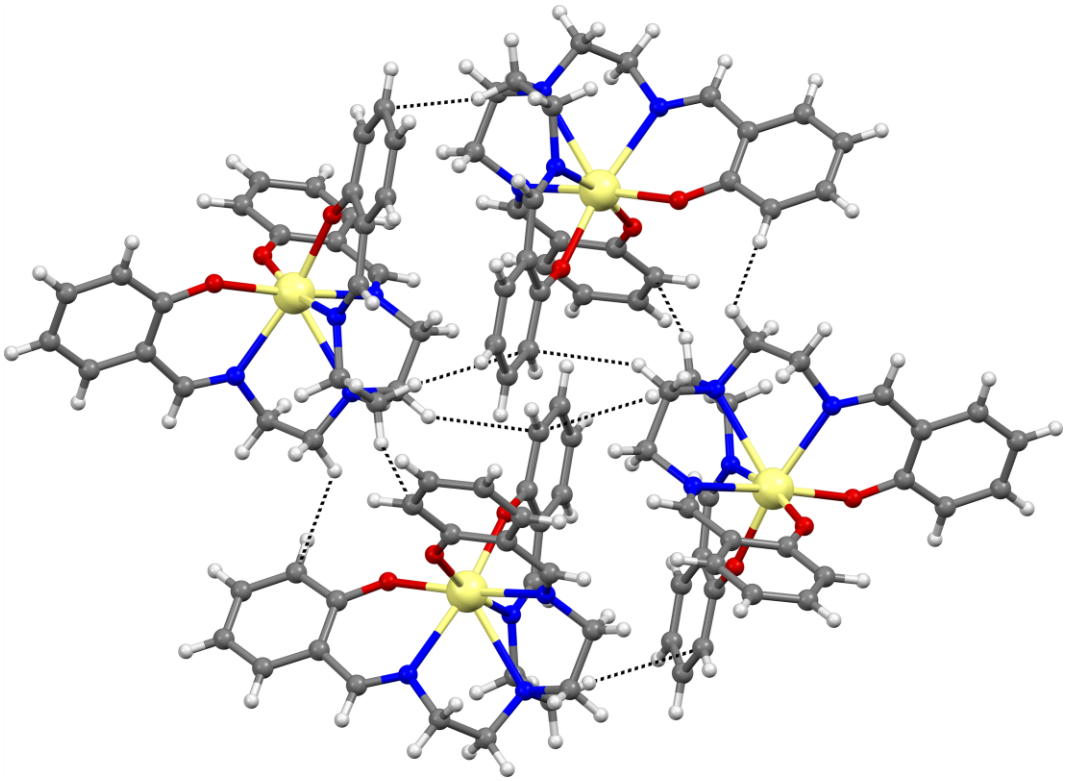

Figure S2.2. Representation of a portion of the crystal packing of **1**. Dashed bonds represent the main C-H···π interactions. Dy (pale-yellow), N (blue), O (red), C (gray) and H (light gray). Image reprinted from https://pubs.acs.org/doi/full/10.1021/acs.inorgchem.2c02619.

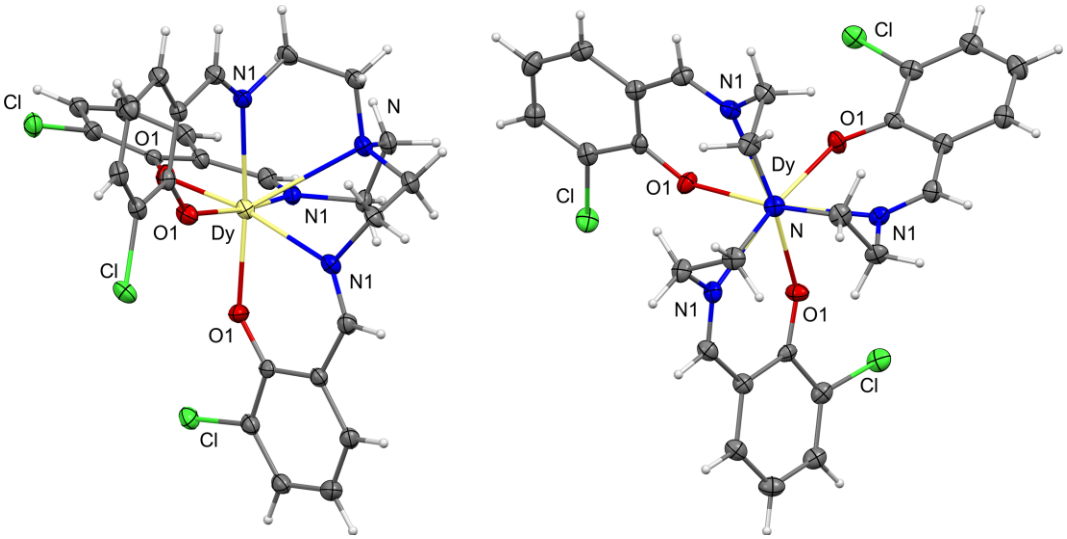

Figure S2.3. Representation of the structure of **2**. Thermal ellipsoids were depicted at the 30% probability level Left: view of the structure of the complex highlighting the capped octahedron molecular geometry. Right: view along the central axis N-Dy. Dy (pale-yellow), N (blue) O (red), Cl (green), C (gray) and H (light gray). Image reprinted from https://pubs.acs.org/doi/full/10.1021/acs.inorgchem.2c02619.

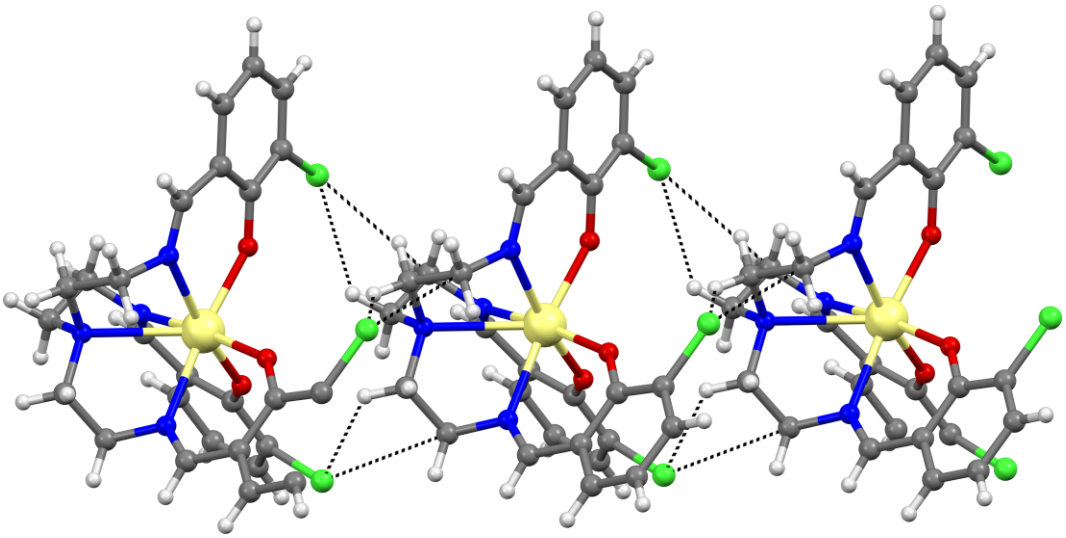

Figure S2.4. Representation of a portion of the crystal packing of **2**. Dashed bonds represent the main C-H···Cl interactions. Dy (pale-yellow), N (blue), O (red), Cl (green), C (gray) and H (light gray). Image reprinted from https://pubs.acs.org/doi/full/10.1021/acs.inorgchem.2c02619.

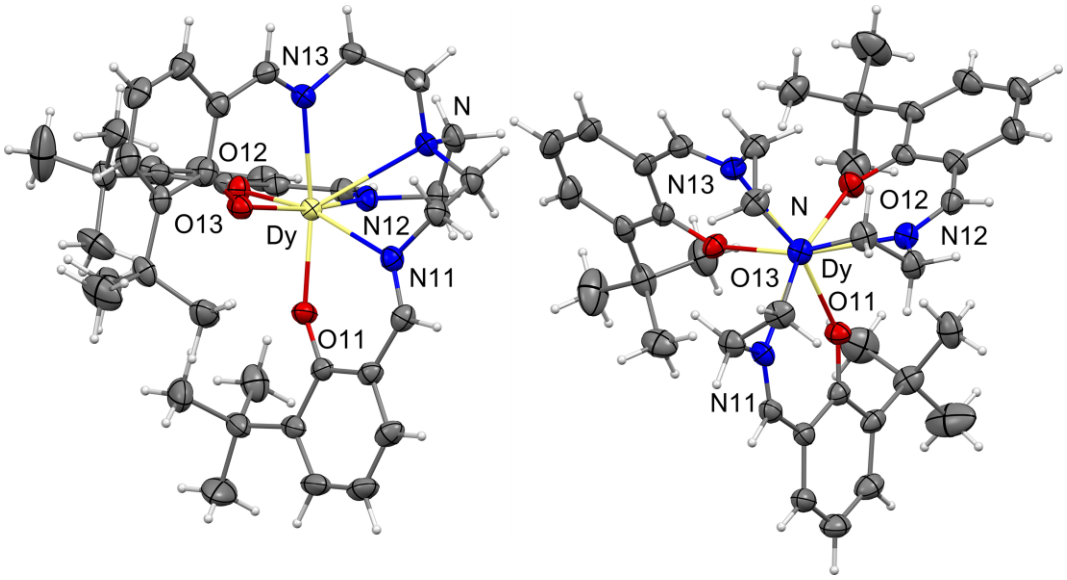

Figure S2.5. Representation of the structure of **3**. Thermal ellipsoids were depicted at the 30% probability level. Left: view of the structure of the complex highlighting the capped octahedron molecular geometry. Right: view along the central axis N-Dy. Dy (yellow), N (blue) and O (red), C (gray) and H (light gray). Crystallization solvent acetone was omitted for clarity. Image reprinted from https://pubs.acs.org/doi/full/10.1021/acs.inorgchem.2c02619.

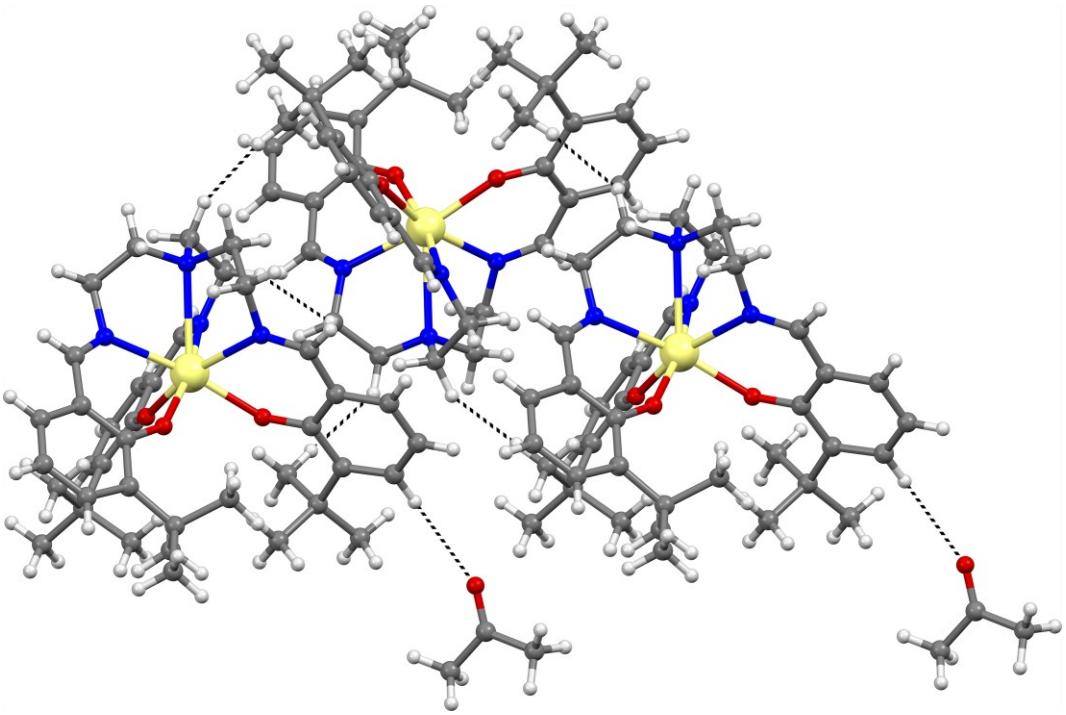

Figure S2.6. Representation of a portion of the crystal packing of **3**·Acetone. Dashed bonds represent the Interactions between the complex and acetone. Dy (pale-yellow), N (blue), O (red), C (gray) and H (light gray). Image reprinted from https://pubs.acs.org/doi/full/10.1021/acs.inorgchem.2c02619.

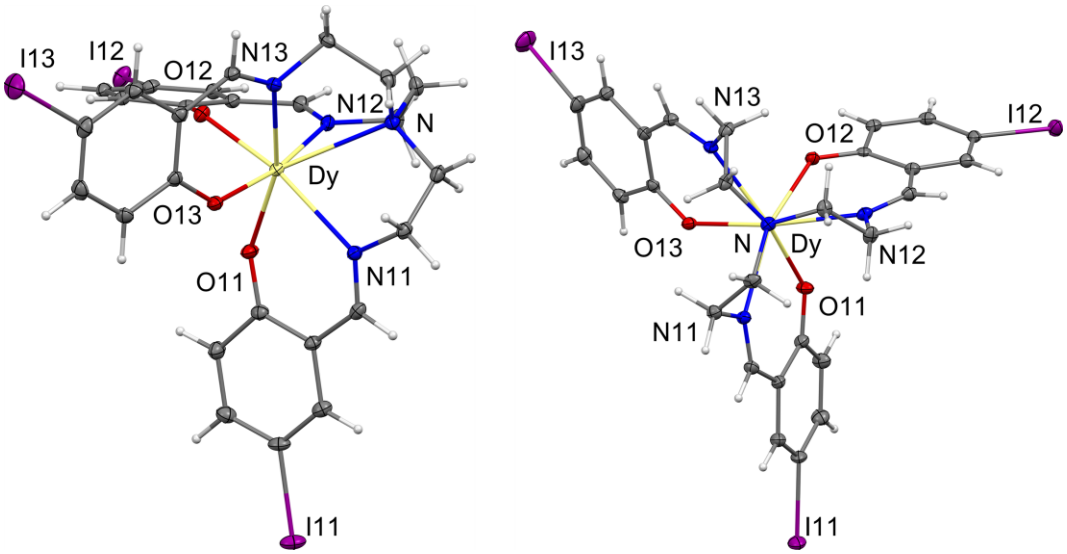

Figure S2.7. Representation of the structure of **4**. Thermal ellipsoids were depicted at the 30% probability level. Left: view of the structure of the complex highlighting the capped octahedron molecular geometry. Right: view along the central axis N-Dy. Dy (yellow), N (blue) and O (red), I (purple), C (gray) and H (light gray). Crystallization solvent DMF was omitted for clarity. Image reprinted from https://pubs.acs.org/doi/full/10.1021/acs.inorgchem.2c02619.

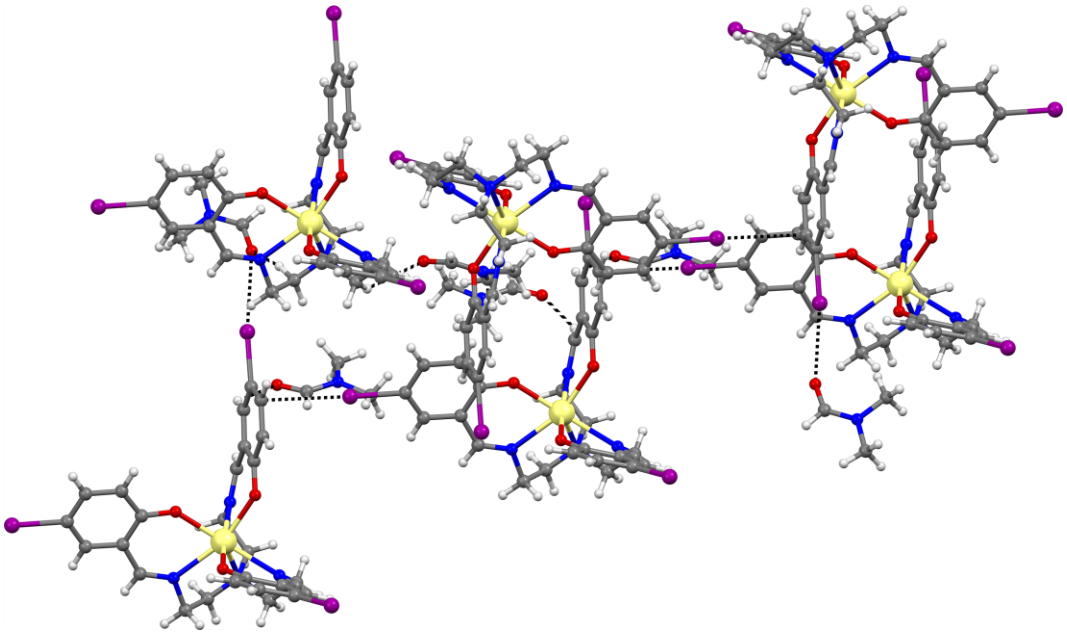

Figure S2.8. Representation of a portion of the crystal packing of **4**·3DMF. Dashed bonds represent the main C-H···O interactions and the halogen bonds with the DMF molecules of crystallization. Dy (pale-yellow), N (blue), O (red), I (purple), C (gray) and H (light gray). Image reprinted from https://pubs.acs.org/doi/full/10.1021/acs.inorgchem.2c02619.

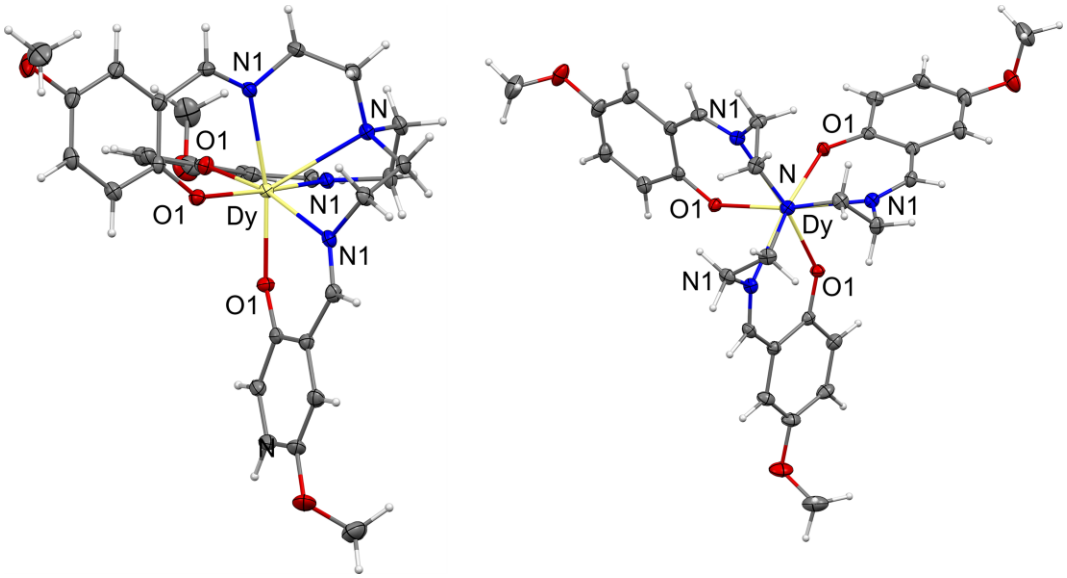

Figure S2.9. Representation of the structure of **5**. Thermal ellipsoids were depicted at the 30% probability level. Left: view of the structure of the complex highlighting the capped octahedron molecular geometry. Right: view along the central axis N-Dy. Dy (yellow), N (blue) and O (red), C (gray) and H (light gray). Image reprinted from https://pubs.acs.org/doi/full/10.1021/acs.inorgchem.2c02619.

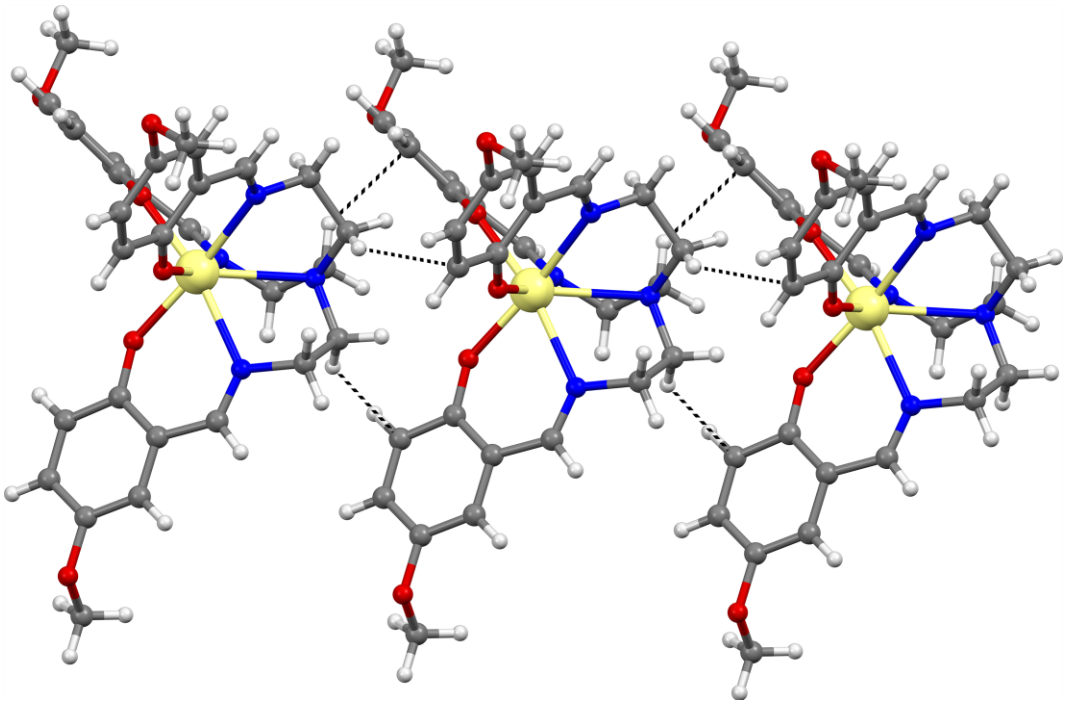

Figure S2.10. Representation of a portion of the crystal packing of **5**. Dashed bonds highlight the main C-H···π interactions. Dy (pale-yellow), N (blue), O (red), C (gray) and H (light gray). Image reprinted from https://pubs.acs.org/doi/full/10.1021/acs.inorgchem.2c02619.

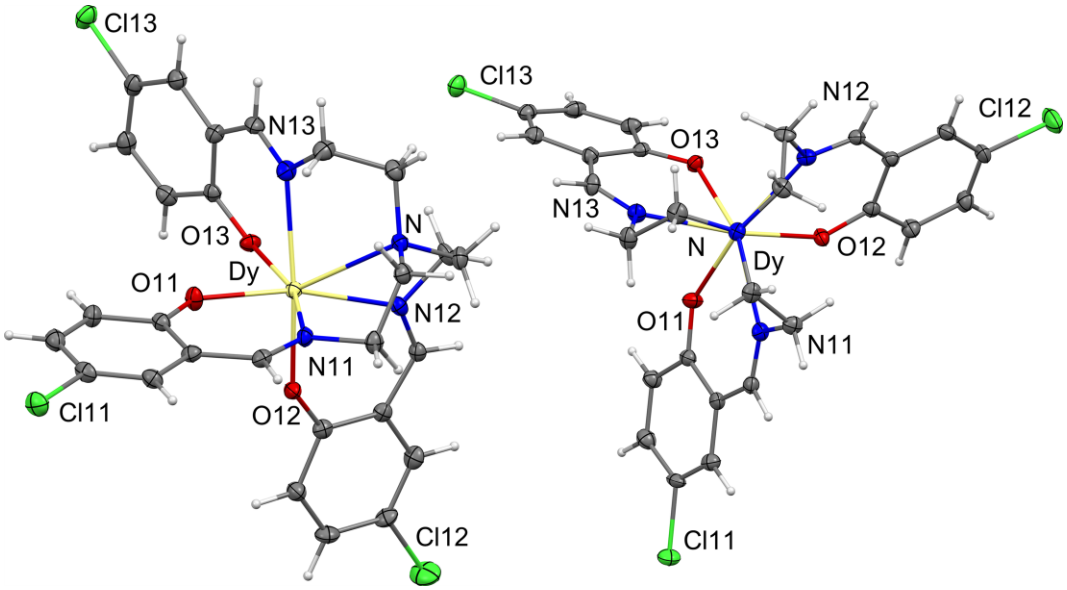

Figure S2.11. Representation of the structure of **6**. Thermal ellipsoids were depicted at the 30% probability level. Left: view of the structure of the complex highlighting the capped octahedron molecular geometry. Right: view along the central axis N-Dy. Dy (yellow), N (blue) and O (red), Cl (green), C (gray) and H (light gray). Image reprinted from https://pubs.acs.org/doi/full/10.1021/acs.inorgchem.2c02619.

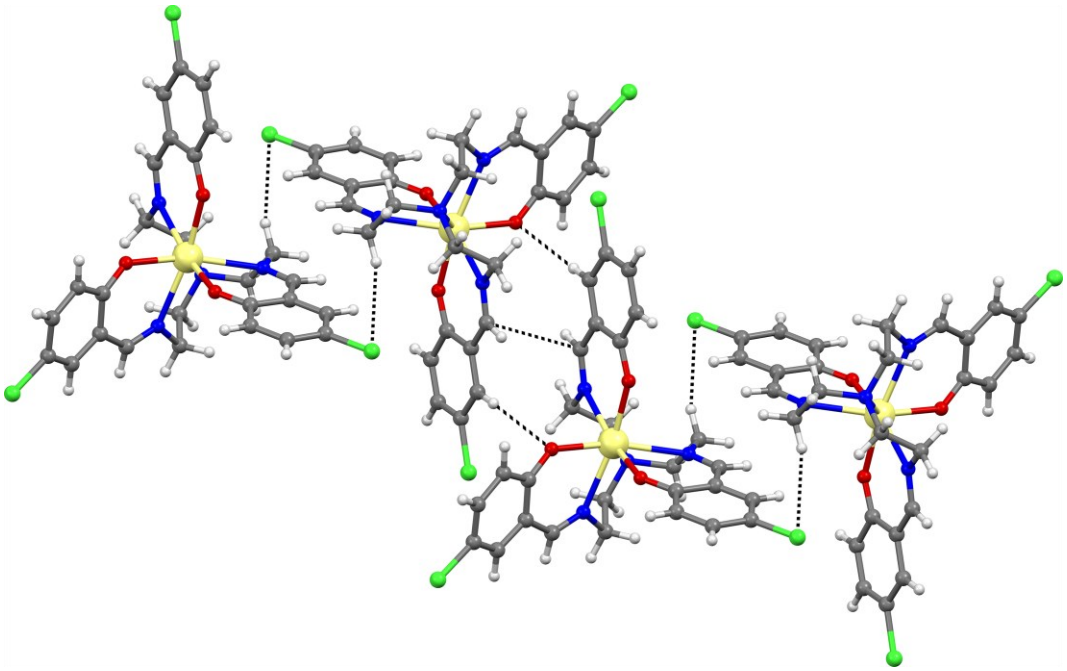

Figure S2.12. Representation of a portion of the crystal packing of **6**. Dashed bonds highlight the main C-H···O and C-H···Cl interactions. Dy (pale-yellow), N (blue), O (red), Cl (green), C (gray) and H (light gray). Image reprinted from https://pubs.acs.org/doi/full/10.1021/acs.inorgchem.2c02619.

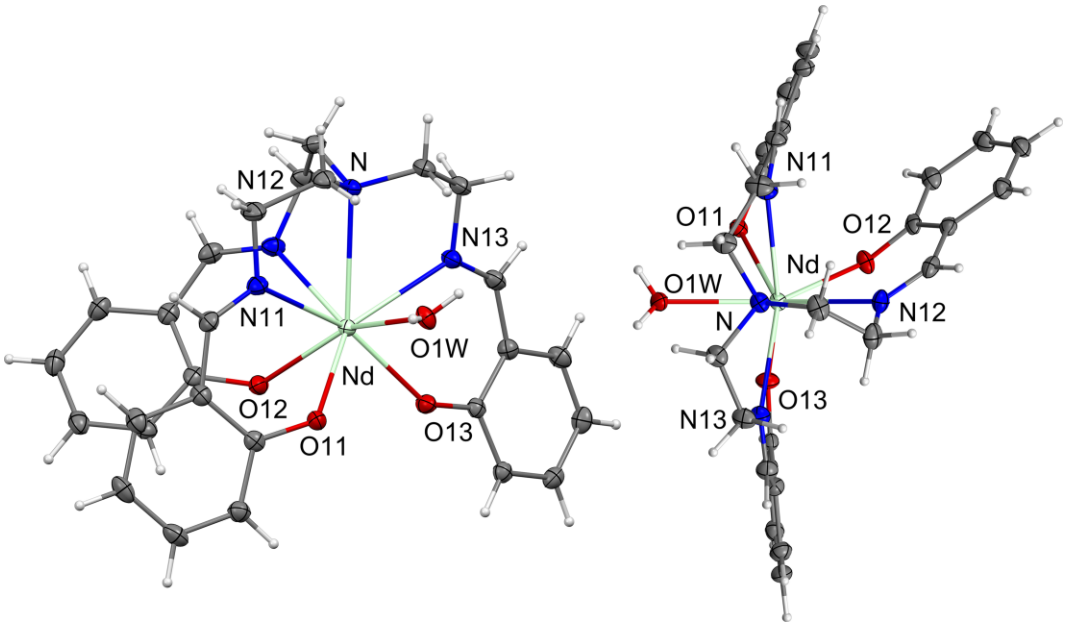

Figure S2.13. Representation of the structure of **7**. Thermal ellipsoids were depicted at the 30% probability level. Left: view of the structure of the complex highlighting the antiprismatic molecular geometry (left). Right: view along the central axis N-Nd. Nd (light green), N (blue) and O (red), C (gray) and H (light gray). Image reprinted from https://pubs.acs.org/doi/full/10.1021/acs.inorgchem.2c02619.

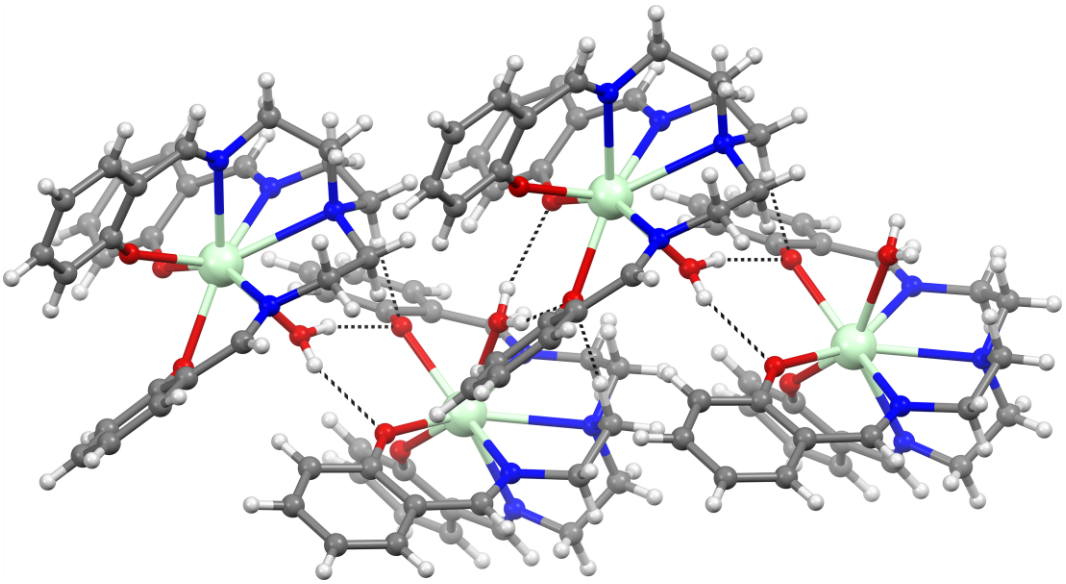

Figure S2.14. Representation of a portion of the crystal packing of **7**. The main interactions are represented by hydrogen bonds between coordinated water and the oxygen atoms of symmetry related molecules. Nd (pale-green), N (blue), O (red), C (gray) and H (light gray). Image reprinted from https://pubs.acs.org/doi/full/10.1021/acs.inorgchem.2c02619.

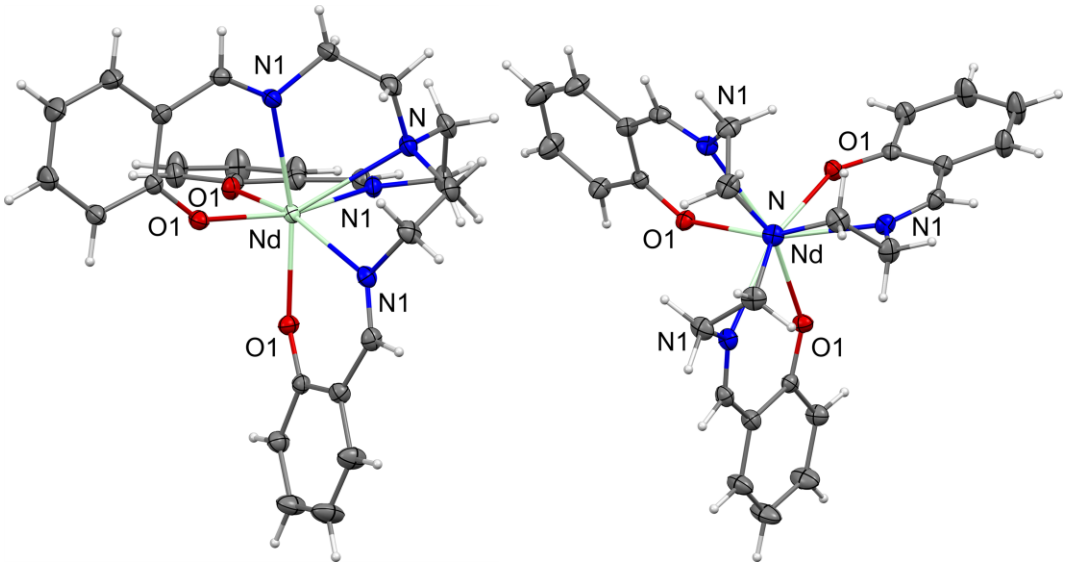

Figure S2.15. Representation of the structure of **8**. Thermal ellipsoids were depicted at the 30% probability level. Left: view of the structure of the complex highlighting the capped octahedron molecular geometry. Right: view along the central axis N-Nd. Nd (light green), N (blue) and O (red), C (gray) and H (light gray). Crystallization solvent ACN was omitted for clarity. Image reprinted from https://pubs.acs.org/doi/full/10.1021/acs.inorgchem.2c02619.

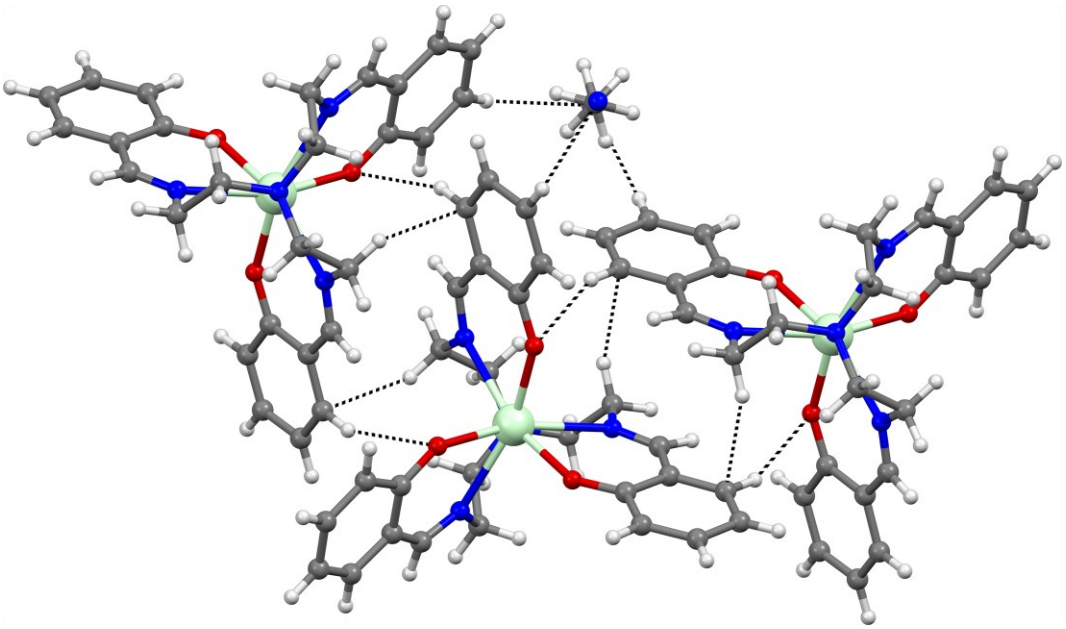

Figure S2.16. Representation of a portion of the crystal packing of **8**·ACN. The dashed bonds represent the main C-H···O and C-H···π interactions. Nd (pale-green), N (blue), O (red), C (gray) and H (light gray). Image reprinted from https://pubs.acs.org/doi/full/10.1021/acs.inorgchem.2c02619.

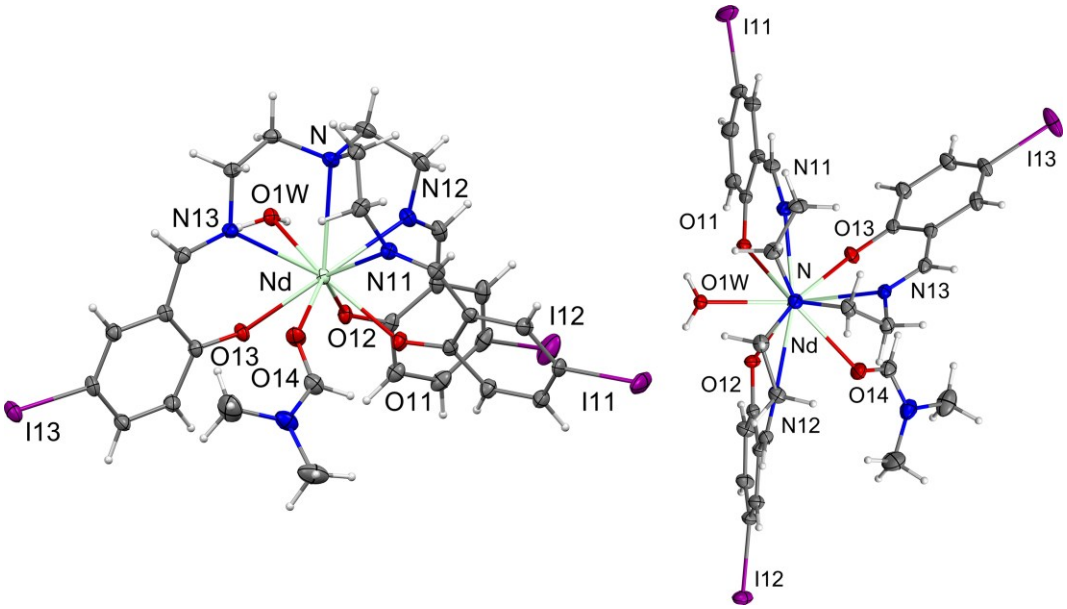

Figure S2.17. Representation of the structure of **9**·DMF. Thermal ellipsoids were depicted at the 30% probability level. Left: view of the structure of the complex highlighting the capped octahedron molecular geometry. Right: view along the central axis N-Nd. Nd (light green), N (blue) and O (red), I (purple), C (gray) and H (light gray). Crystallization solvent DMF was omitted for clarity. Image reprinted from https://pubs.acs.org/doi/full/10.1021/acs.inorgchem.2c02619.

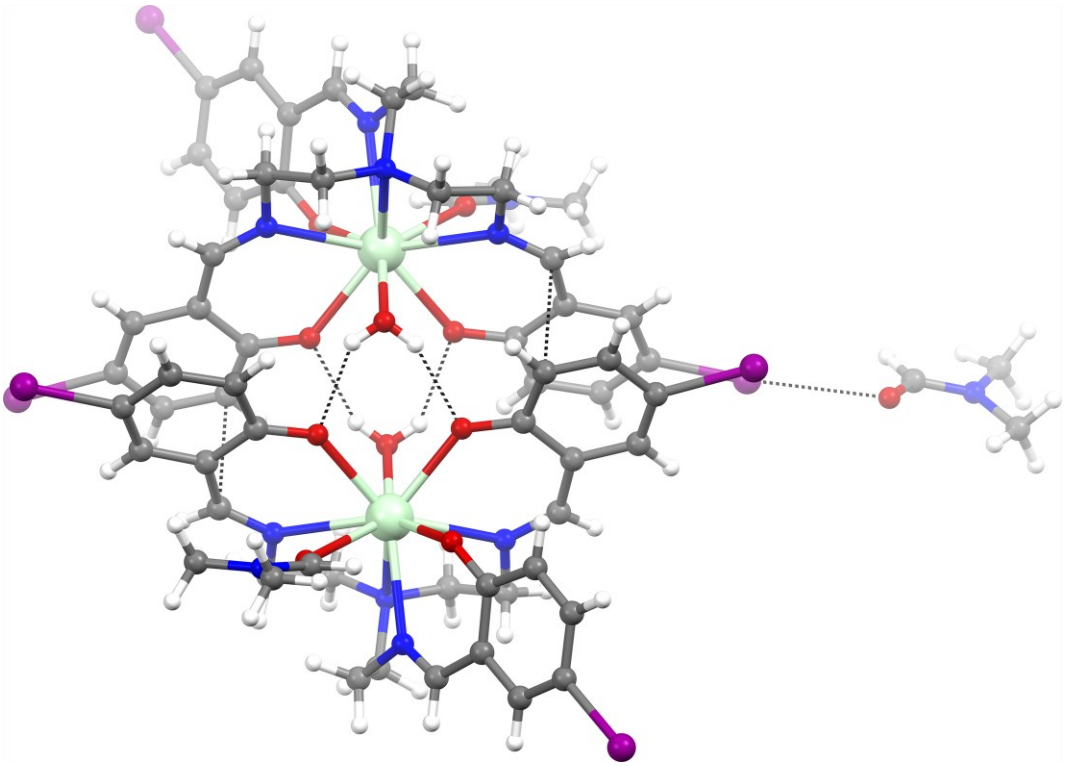

Figure S2.18. Representation of a portion of the crystal packing of **9**·DMF. The dashed line represent the hydrogen bonds exchanged by coordinated water, and halogen bonds with DMF molecules of crystallization. Nd (pale-green), N (blue), O (red), I (purple), C (gray) and H (light gray). Image reprinted from https://pubs.acs.org/doi/full/10.1021/acs.inorgchem.2c02619.

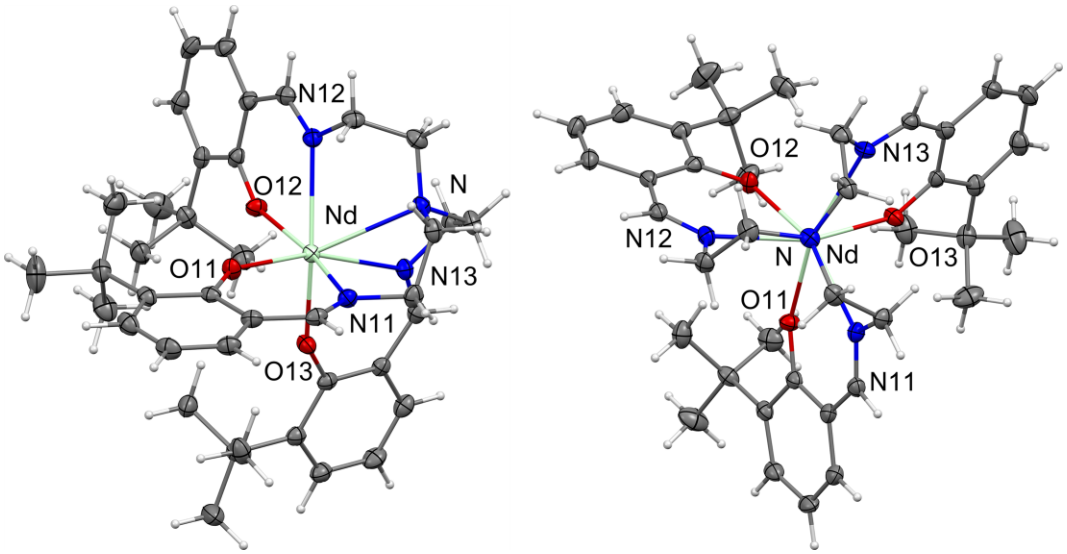

Figure S2.19. Representation of the structure of **10**. Thermal ellipsoids were depicted at the 30% probability level. Left: view of the structure of the complex highlighting the capped octahedron molecular geometry. Right: view along the central axis N-Nd. Nd (light green), N (blue) and O (red), C (gray) and H (light gray). Crystallization solvent DMF was omitted for clarity. Image reprinted from https://pubs.acs.org/doi/full/10.1021/acs.inorgchem.2c02619.

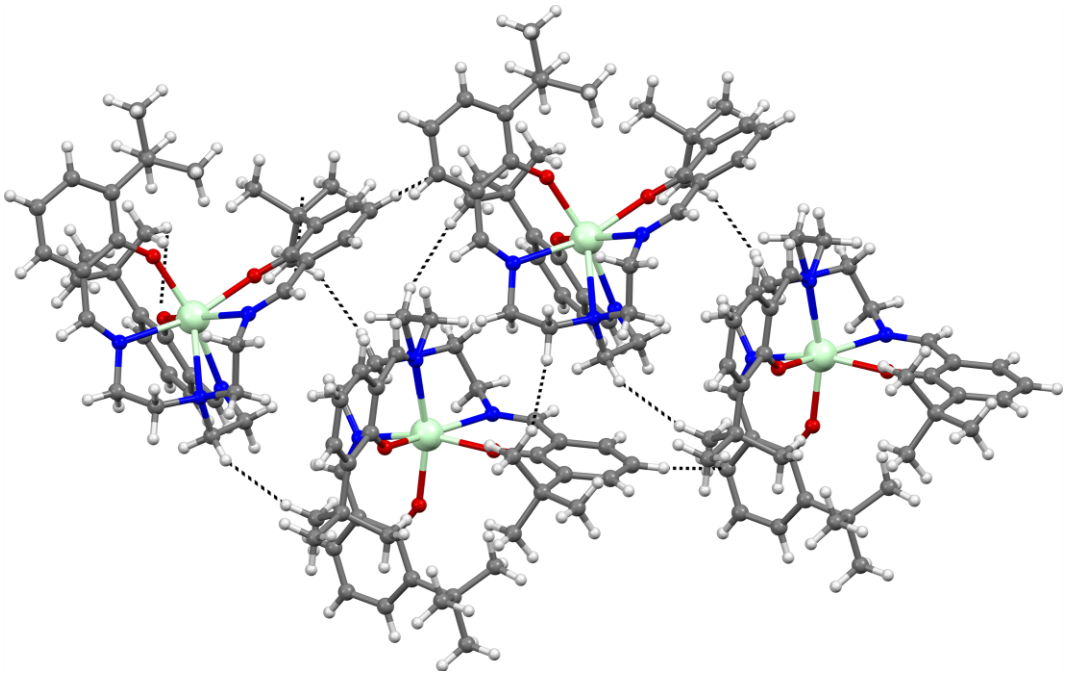

Figure S2.20. Representation of a portion of the crystal packing of **10**. Dashed bond represent the weak interactions that involve C-H groups. Nd (pale-green), N (blue), O (red), C (gray) and H (light gray). Image reprinted from https://pubs.acs.org/doi/full/10.1021/acs.inorgchem.2c02619.

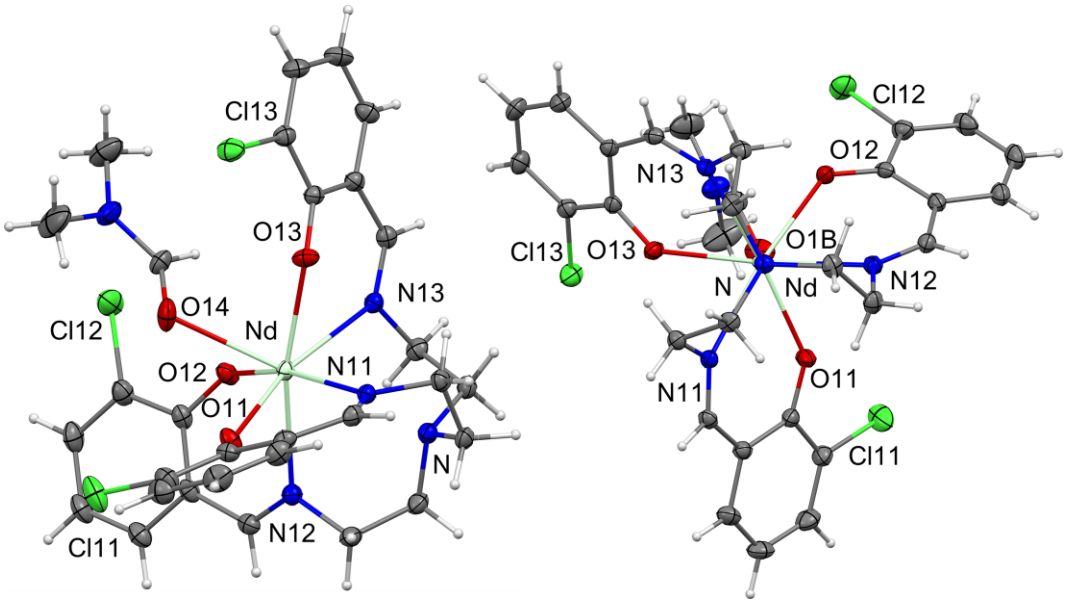

Figure S2.21. Representation of the structure of **11**. Thermal ellipsoids were depicted at the 30% probability level. Left: view of the structure of the complex highlighting the capped octahedron molecular geometry. Right: view along the central axis N-Nd. Nd (light green), N (blue) and O (red), Cl (green), C (gray) and H (light gray). Crystallization solvent DMF was omitted for clarity. Image reprinted from https://pubs.acs.org/doi/full/10.1021/acs.inorgchem.2c02619.

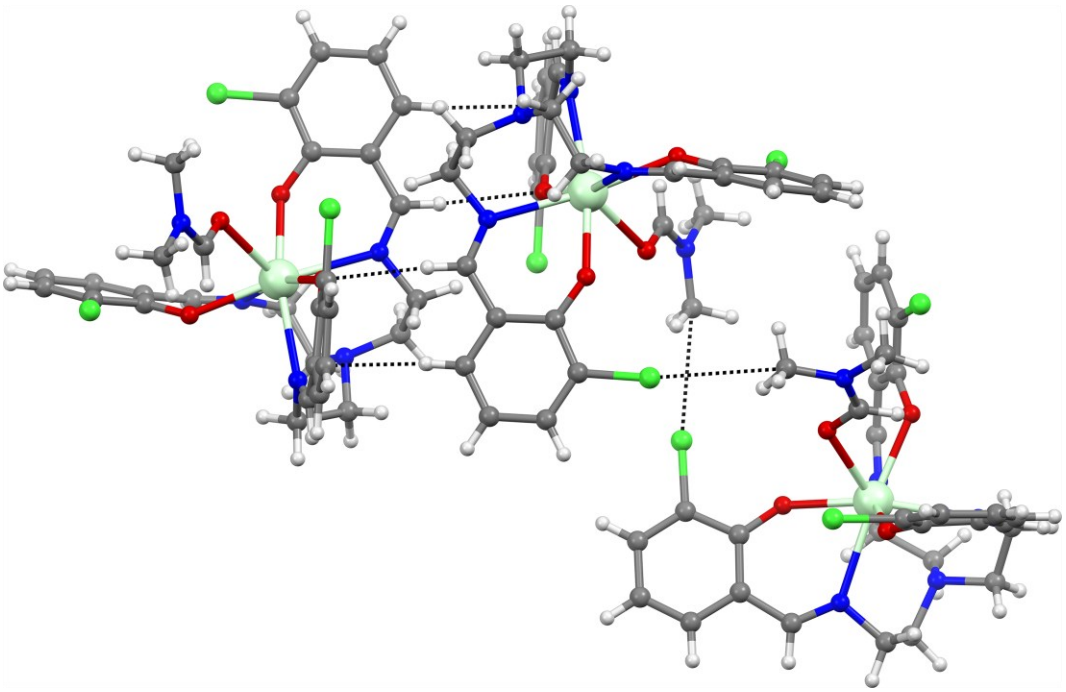

Figure S2.22. Representation of a portion of the crystal packing of **11**. Dashed bonds highlight C-H···O interactions and the halogen Cl···CH_3 bonds. Nd (pale-green), N (blue), O (red), Cl (green), C (gray) and H (light gray). Image reprinted from https://pubs.acs.org/doi/full/10.1021/acs.inorgchem.2c02619.

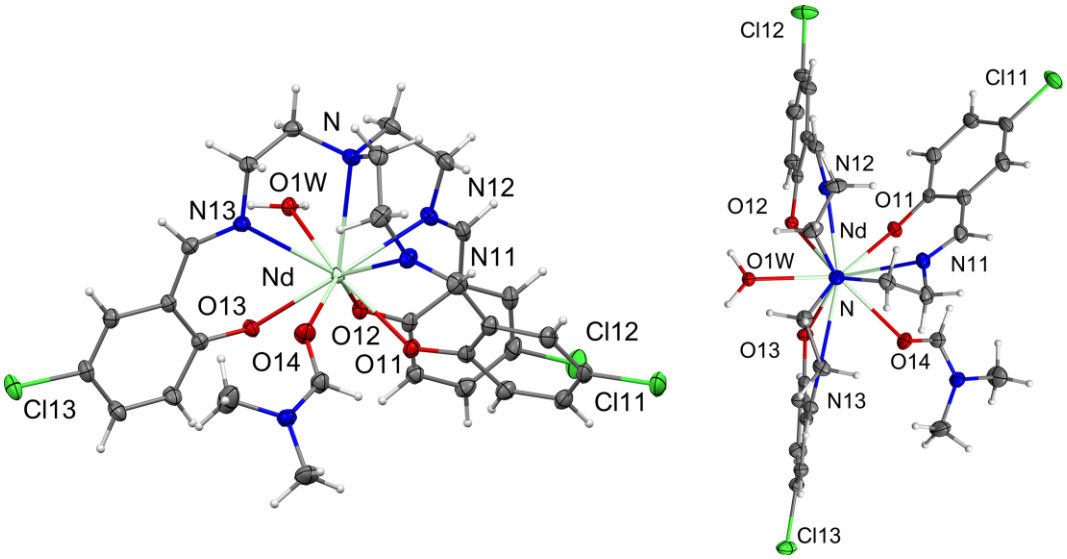

Figure S2.23. Representation of the structure of **12**. Thermal ellipsoids were depicted at the 30% probability level. Left: view of the structure of the complex highlighting the capped octahedron molecular geometry. Right: view along the central axis N-Nd. Nd (light green), N (blue) and O (red), Cl (green), C (gray) and H (light gray). Image reprinted from https://pubs.acs.org/doi/full/10.1021/acs.inorgchem.2c02619.

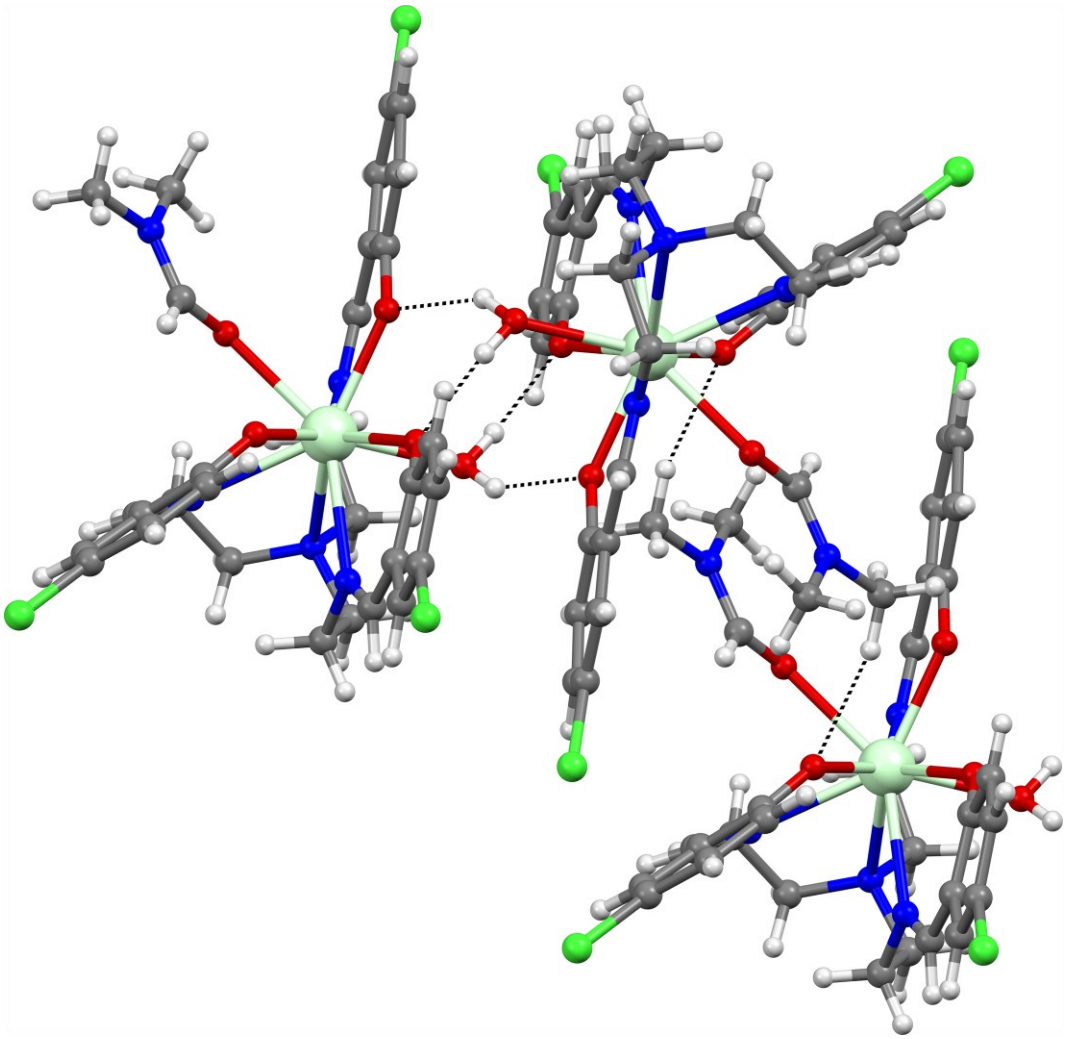

Figure S2.24. Representation of a portion of the crystal packing of **12**. Hydrogen bonds exchanged by coordinated water, and CH···O interactions are reported as dashed bonds. Nd (pale-green), N (blue), O (red), Cl (green), C (gray) and H (light gray). Image reprinted from https://pubs.acs.org/doi/full/10.1021/acs.inorgchem.2c02619.

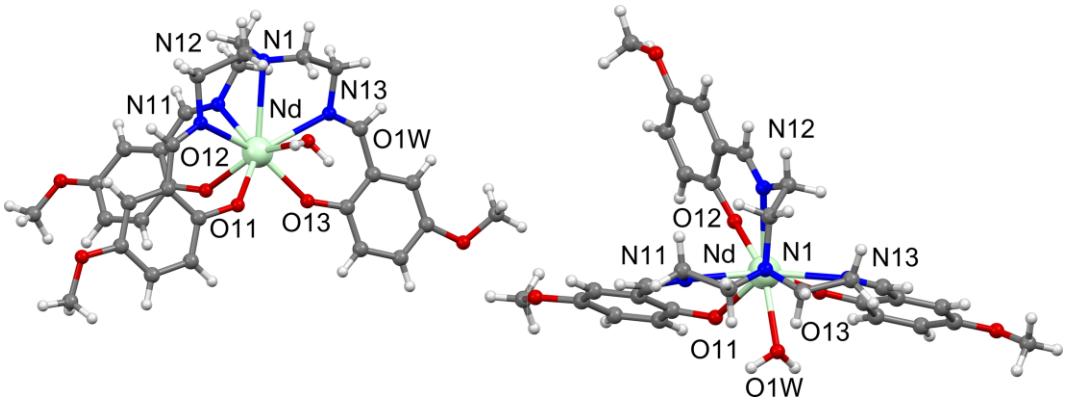

Figure S2.25. Ball and stick representation of the structure of **13**. Left: view of the structure of the complex highlighting the antiprismatic molecular geometry. Right: view along the central axis N-Nd. Nd (light green), N (blue) and O (red), C (gray) and H (light gray). Image reprinted from https://pubs.acs.org/doi/full/10.1021/acs.inorgchem.2c02619.

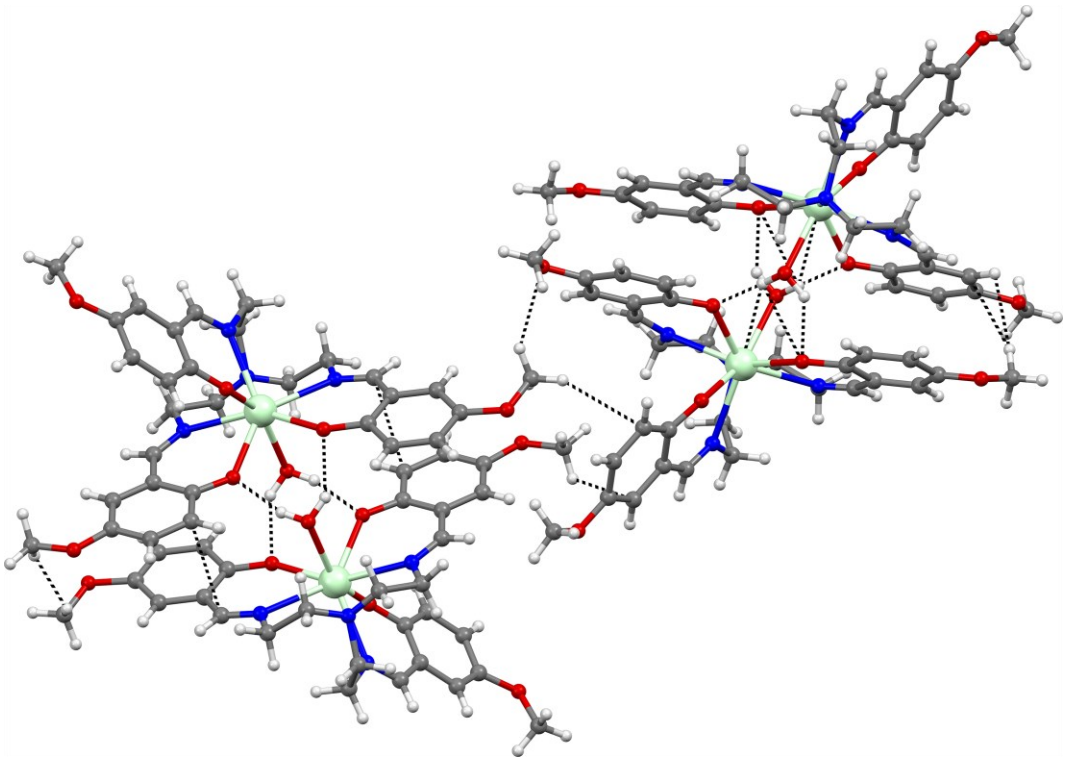

Figure S2.26. Representation of a portion of the crystal packing of **13**. Dashed bonds represent the main CH···O interactions. Nd (pale-green), N (blue), O (red), C (gray) and H (light gray). Image reprinted from https://pubs.acs.org/doi/full/10.1021/acs.inorgchem.2c02619.

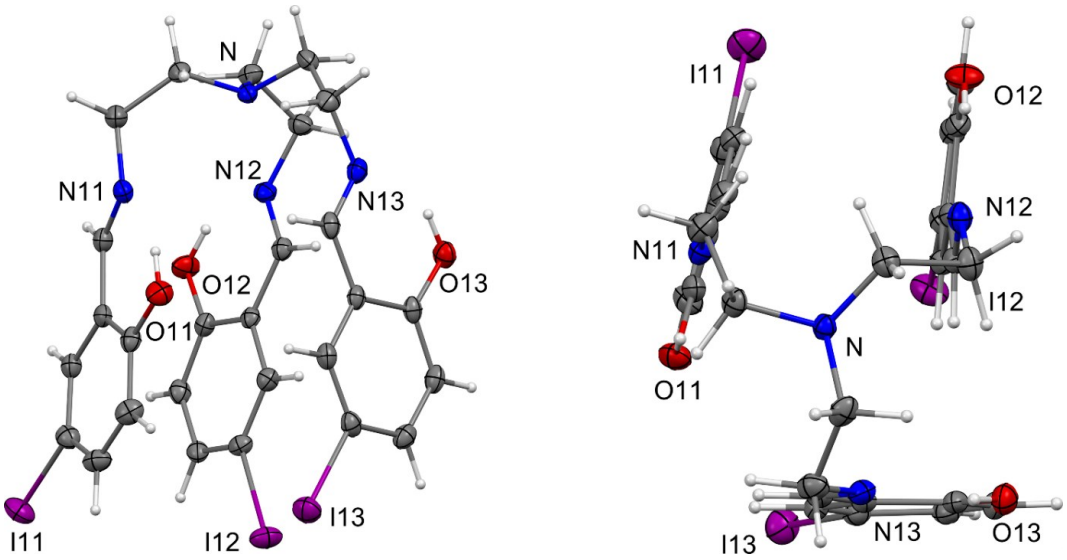

Figure S2.27. Representation of the structure of $\mathbf{L_5}$. Thermal ellipsoids were depicted at the 30% probability level. N (blue) and O (red), I (purple), C (gray) and H (light gray). Image reprinted from https://pubs.acs.org/doi/full/10.1021/acs.inorgchem.2c02619.

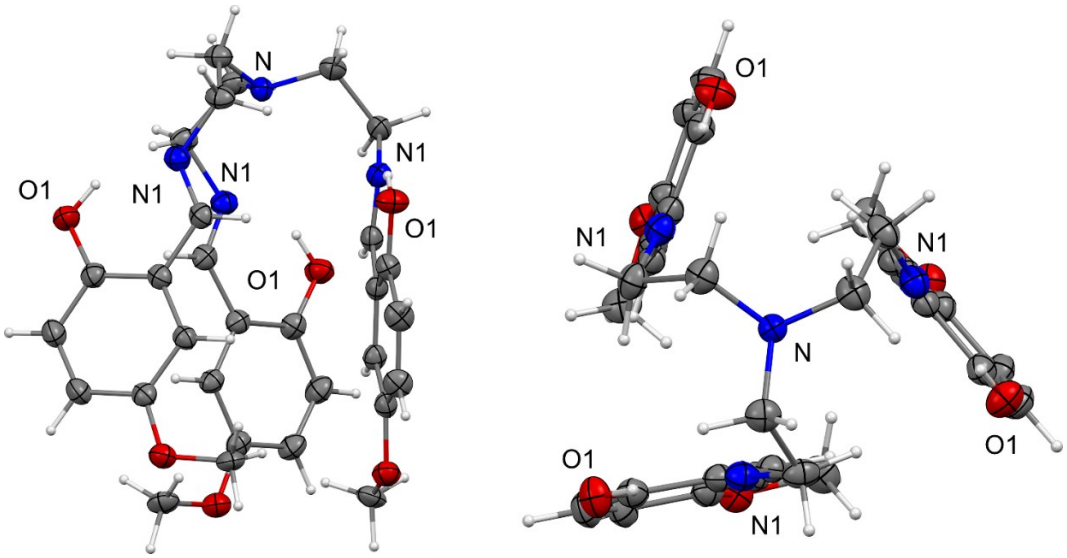

Figure S2.28. Representation of the structure of $\mathbf{L_2}$. Thermal ellipsoids were depicted at the 30% probability level. N (blue) and O (red), C (gray) and H (light gray). Image reprinted from https://pubs.acs.org/doi/full/10.1021/acs.inorgchem.2c02619.

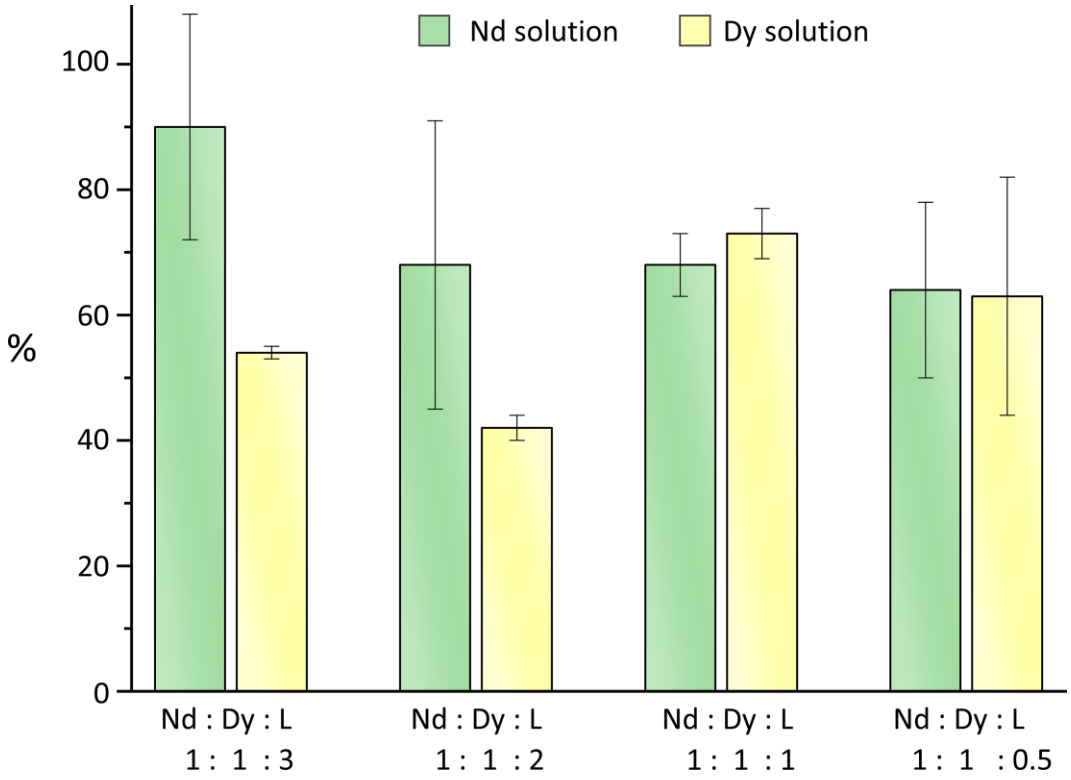

Figure S2.29. Amount of Nd and Dy in solution (ICP-AES analysis) at different Trensal$^{p\text{-}OMe}$:Ln stochiometric ratios. Percentage values refer to total Ln in the system. Image reprinted from https://pubs.acs.org/doi/full/10.1021/acs.inorgchem.2c02619.

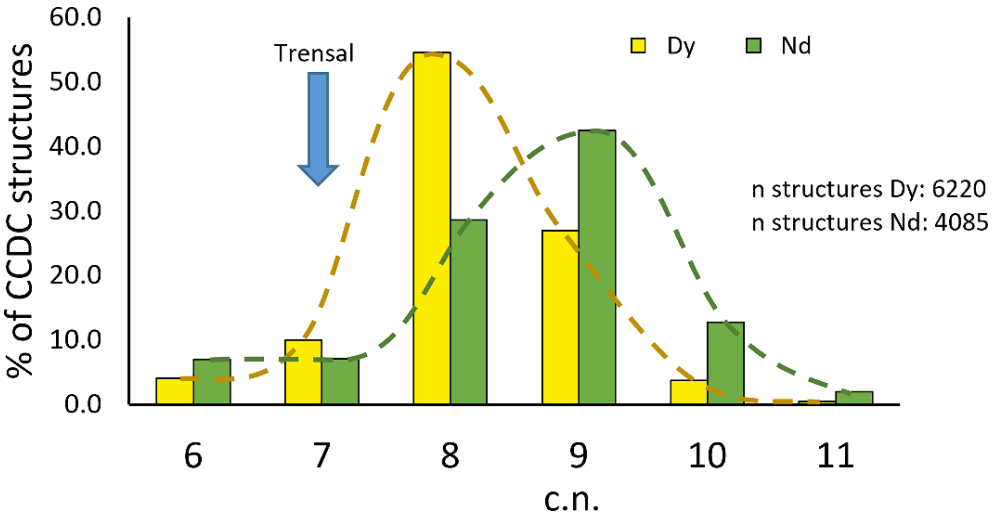

Figure S2.30. Percentage of Nd and Dy-containing structures deposited in the CCDC *vs* coordination number of the metal (c.n.). Image reprinted from https://pubs.acs.org/doi/full/10.1021/acs.inorgchem.2c02619.

2.7.2 Crystal data and structural geometric parameters

Table S2.1. Summary of X-ray crystallographic data for **1**, **2** and **3**·Acetone.

Identification code	[Dy(Trensal)][a]	[Dy(Trensal$^{o\text{-}Cl}$)]	[Dy(Trensal$^{o\text{-}tBu}$)]·Acetone
Empirical formula	$C_{27}H_{27}DyN_4O_3$	$C_{27}H_{24}Cl_3DyN_4O_3$	$C_{42}H_{57}DyN_4O_4$
Formula weight	618.02	721.36	844.41
Temperature/K	200.0	200.0	200
Crystal system	trigonal	trigonal	monoclinic
Space group	P-3c1	P-3	C2/c
a/Å	13.0116(4)	13.9712(6)	21.5004(8)
b/Å	13.0116(4)	13.9712(6)	12.1501(4)
c/Å	16.3938(5)	7.8155(5)	31.5994(10)
α/°	90	90	90
β/°	90	90	95.7190(10)
γ/°	120	120	90
Volume/Å^3	2403.65(16)	1321.16(14)	8213.7(5)
Z	4	2	8
ρ_{calc}g/cm^3	1.708	1.813	1.366
μ/mm^{-1}	3.146	18.237	1.863
F(000)	1228.0	710.0	3480.0
Crystal size/mm^3	0.18 × 0.11 × 0.08	0.19 × 0.04 × 0.04	0.21 × 0.15 × 0.13
Radiation	MoKα (λ = 0.71073)	CuKα (λ = 1.54178)	MoKα (λ = 0.71073)
2Θ range for data	6.146 to 51.388	7.306 to 139.936	3.856 to 52.104
Index ranges	-15 ≤ h ≤ 15, -15 ≤ k ≤	-16 ≤ h ≤ 16, -17 ≤ k	-26 ≤ h ≤ 26, -14 ≤ k ≤
Reflections	52201	10103	40218
Independent	1523 [R_{int} = 0.0430,	1666 [R_{int} = 0.1465,	8089 [R_{int} = 0.0351,
Data/restraints/p	1523/0/106	1666/0/115	8089/0/471
Goodness-of-fit	1.049	1.003	1.003
Final R indexes	R_1 = 0.0177, wR_2 =	R_1 = 0.0423, wR_2 =	R_1 = 0.0369, wR_2 =
Final R indexes	R_1 = 0.0197, wR_2 =	R_1 = 0.0666, wR_2 =	R_1 = 0.0429, wR_2 =
Largest diff.	0.33/-1.38	1.55/-0.88	1.30/-2.37

[a] Structure already present in the database as CCDC 618519.

Table S2.2. Summary of X-ray crystallographic data for **4**·3DMF, **5** and **6**.

Identification code	[Dy(Trensal$^{p\text{-}I}$)]·3DMF	[Dy(Trensal$^{p\text{-}OMe}$)]	[Dy(Trensal$^{p\text{-}Cl}$)]
Empirical formula	$C_{36}H_{45}DyI_3N_7O_6$	$C_{30}H_{33}DyN_4O_6$	$C_{27}H_{24}Cl_3DyN_4O_3$
Formula weight	1214.99	708.11	721.35
Temperature/K	150.0	200.0	200.0
Crystal system	triclinic	trigonal	monoclinic
Space group	P-1	P-3	$P2_1/n$
a/Å	13.0475(5)	14.7962(8)	12.6245(7)
b/Å	13.4115(5)	14.7962(8)	15.2077(7)
c/Å	15.1120(6)	7.6514(8)	15.0627(9)
α/°	73.4640(10)	90	90
β/°	65.4600(10)	90	110.359(2)
γ/°	62.1540(10)	120	90
Volume/Å^3	2113.45(14)	1450.7(2)	2711.2(3)
Z	2	2	4
ρ_{calc}g/cm^3	1.909	1.621	1.767
μ/mm^{-1}	4.009	2.625	3.089
F(000)	1166.0	710.0	1420.0
Crystal size/mm^3	0.4 × 0.05 × 0.04	0.22 × 0.19 × 0.15	0.21 × 0.2 × 0.15
Radiation	MoKα (λ = 0.71073)	MoKα (λ = 0.71073)	MoKα (λ = 0.71073)
2Θ range for data collection/°	3.934 to 52.84	5.324 to 51.502	3.936 to 51.5
Index ranges	-16 ≤ h ≤ 16, -16 ≤ k ≤ 16, -18 ≤ l ≤ 18	-18 ≤ h ≤ 18, -18 ≤ k ≤ 16, -9 ≤ l ≤ 9	-15 ≤ h ≤ 15, -18 ≤ k ≤ 17, -18 ≤ l ≤ 18
Reflections collected	34347	11634	26851
Independent reflections	8659 [R_{int}= 0.0415, R_{sigma}= 0.0345]	1854 [R_{int} = 0.0501, R_{sigma} = 0.0284]	5166 [R_{int}= 0.0635, R_{sigma}= 0.0502]
Data/restraints/parameters	8659/56/532	1854/0/125	5166/0/343
Goodness-of-fit on F^2	1.017	1.073	1.056
Final R indexes [I>=2σ (I)]	R_1= 0.0245, wR_2= 0.0471	R_1 = 0.0195, wR_2 = 0.0421	R_1= 0.0350, wR_2= 0.0740
Final R indexes [all data]	R_1= 0.0310, wR_2= 0.0493	R_1 = 0.0226, wR_2 = 0.0434	R_1= 0.0492, wR_2= 0.0810
Largest diff. peak/hole / e Å^{-3}	1.33/-1.05	0.51/-0.57	1.66/-0.86

Table S2.3. Summary of X-ray crystallographic data for **7**, **8**·ACN and **9**·DMF.

Identification code	[Nd(Trensal)(H_2O)]	[Nd(Trensal)]·ACN[a]	[Nd(Trensal$^{p\text{-}I}$)DMF(H_2O)]·DMF
Empirical formula	$C_{27}H_{29}N_4NdO_4$	$C_{28}H_{28}N_{4.5}NdO_3$	$C_{33}H_{40}I_3N_6NdO_6$
Formula weight	617.78	619.79	1141.65
Temperature/K	220	160.0	200.0
Crystal system	monoclinic	trigonal	triclinic
Space group	$P2_1/n$	P-3	P-1
a/Å	11.3824(2)	13.5381(7)	12.7307(19)
b/Å	8.55910(10)	13.5381(7)	13.1608(12)
c/Å	24.9240(4)	8.1270(4)	13.8742(15)
α/°	90	90	98.604(4)
β/°	93.551(2)	90	106.887(4)
γ/°	90	120	112.474(4)
Volume/Å^3	2423.51(6)	1289.96(15)	1964.1(4)
Z	4	2	2
ρ_{calc}g/cm^3	1.693	1.597	1.930
μ/mm^{-1}	2.185	2.051	3.728
F(000)	1244.0	624.0	1094.0
Crystal size/mm^3	0.3 × 0.03 × 0.03	0.21 × 0.19 × 0.12	0.12 × 0.03 × 0.018
Radiation	MoKα (λ = 0.71073)	MoKα (λ = 0.71073)	MoKα (λ = 0.71073)
2Θ range for data collection/°	3.848 to 51.362	6.1 to 51.48	3.806 to 51.356
Index ranges	-13 ≤ h ≤ 13, -10 ≤ k ≤ 9, -30 ≤ l ≤ 30	-16 ≤ h ≤ 16, -14 ≤ k ≤ 16, -9 ≤ l ≤ 9	-15 ≤ h ≤ 15, -15 ≤ k ≤ 16, -16 ≤ l ≤ 16
Reflections collected	28747	10121	30719
Independent reflections	4598 [R_{int}= 0.0338, R_{sigma}= 0.0226]	1641 [R_{int}= 0.0247, R_{sigma}= 0.0159]	7422 [R_{int}= 0.0282, R_{sigma}= 0.0236]
Data/restraints/parameters	4598/2/331	1641/0/115	7422/2/454
Goodness-of-fit on F^2	1.038	1.023	1.016
Final R indexes [I>=2σ (I)]	R_1= 0.0217, wR_2 = 0.0560	R_1= 0.0136, wR_2 = 0.0368	R_1= 0.0276, wR_2 = 0.0613
Final R indexes [all data]	R_1= 0.0258, wR_2 = 0.0581	R_1= 0.0136, wR_2 = 0.0368	R_1= 0.0305, wR_2 = 0.0629
Largest diff. peak/hole / e Å^{-3}	0.37/-0.49	0.26/-0.60	3.17/-2.50

[a] Structure already present in the database as CCDC 1272122.

Table S2.4. Summary of X-ray crystallographic data for **10**·DMF, **11**·DMF and **12**

Identification code	[Nd(Trensal$^{o\text{-}tBut}$)]DMF	[Nd(Trensal$^{o\text{-}Cl}$)(DMF)]·DMF	[Nd(Trensal$^{p\text{-}Cl}$)(DMF)(H_2O)]
Empirical formula	$C_{42}H_{58}N_5NdO_4$	$C_{33}H_{38}Cl_3N_6NdO_5$	$C_{30}H_{33}Cl_3N_5NdO_5$
Formula weight	841.17	849.28	794.20
Temperature/K	200.0	200.0	200.0
Crystal system	monoclinic	monoclinic	triclinic
Space group	C2/c	C2/c	P-1
a/Å	21.5929(14)	26.3461(7)	11.5773(5)
b/Å	11.9510(9)	13.1816(3)	11.9645(5)
c/Å	31.788(2)	22.3923(6)	13.0394(6)
α/°	90	90	77.635(2)
β/°	93.616(2)	111.1890(10)	81.139(2)
γ/°	90	90	67.3280(10)
Volume/Å^3	8186.9(10)	7250.7(3)	1622.81(12)
Z	8	8	2
ρ_{calc}g/cm^3	1.365	1.556	1.625
μ/mm^{-1}	1.314	1.701	1.893
F(000)	3496.0	3432.0	798.0
Crystal size/mm^3	0.17 × 0.13 × 0.12	0.25 × 0.19 × 0.11	0.19 × 0.16 × 0.16
Radiation	MoKα (λ = 0.71073)	MoKα (λ = 0.71073)	MoKα (λ = 0.71073)
2Θ range for data collection/°	3.898 to 51.462	3.71 to 51.426	3.824 to 51.576
Index ranges	-26 ≤ h ≤ 26, -14 ≤ k ≤ 14, -31 ≤ l ≤ 38	-32 ≤ h ≤ 32, -16 ≤ k ≤ 16, -27 ≤ l ≤ 27	-14 ≤ h ≤ 14, -14 ≤ k ≤ 14, -15 ≤ l ≤ 15
Reflections collected	29087	56760	47397
Independent reflections	7635 [R_{int} = 0.0497, R_{sigma} = 0.0475]	6889 [R_{int} = 0.0339, R_{sigma} = 0.0184]	6203 [R_{int} = 0.0629, R_{sigma} = 0.0323]
Data/restraints/parameters	7635/0/480	6889/18/476	6203/0/400
Goodness-of-fit on F^2	1.060	1.043	1.052
Final R indexes [I>=2σ (I)]	R_1 = 0.0430, wR_2 = 0.1097	R_1 = 0.0199, wR_2 = 0.0452	R_1 = 0.0189, wR_2 = 0.0455
Final R indexes [all data]	R_1 = 0.0524, wR_2 = 0.1143	R_1 = 0.0255, wR_2 = 0.0485	R_1 = 0.0213, wR_2 = 0.0464
Largest diff. peak/hole / e Å^{-3}	1.42/-1.48	0.48/-0.49	0.56/-0.54

Table S2.5. Summary of X-ray crystallographic data for **13.**

Identification code	[Nd(Trensal$^{p\text{-}OMe}$)(H_2O)]
Empirical formula	$C_{30}H_{35}N_4NdO_7$
Formula weight	707.86
Temperature/K	200.00(10)
Crystal system	monoclinic
Space group	$P2_1/c$
a/Å	31.292(5)
b/Å	8.7088(19)
c/Å	22.605(4)
α/°	90
β/°	110.27(2)
γ/°	90
Volume/Å^3	5779(2)
Z	8
ρ_{calc}g/cm^3	1.627
μ/mm^{-1}	14.168
F(000)	2872.0
Crystal size/mm^3	0.1 × 0.1 × 0.02
Radiation	CuKα (λ = 1.54184)
2Θ range for data collection/°	6.022 to 108.474
Index ranges	-32 ≤ h ≤ 32, -9 ≤ k ≤ 9, -23 ≤ l ≤ 23
Reflections collected	35749
Independent reflections	6870 [R_{int} = 0.4169, R_{sigma} = 0.2214]
Data/restraints/parameters	3852/570/648
Goodness-of-fit on F^2	1.069
Final R indexes [I>=2σ (I)]	R_1 = 0.1598, wR_2 = 0.3796
Final R indexes [all data]	R_1 = 0.2301, wR_2 = 0.4331
Largest diff. peak/hole / e Å^{-3}	1.79/-1.12

Table S2.6. Selected geometric parameters (Å) for **1**, **2**, **3**·Acetone, **4**·3DMF, **5**, **6**.

1		**2**	
Dy-N	2.728(3)	Dy-N	2.766(7)
Dy-N(1)	2.486(2)	Dy-N(1)	2.462(5)
Dy-O(1)	2.206(1)	Dy-O(1)	2.213(4)
3·Acetone		**4**·3DMF	
Dy-N	2.764(4)	Dy-N	2.674(3)
Dy-N(11)	2.495(4)	Dy-N(11)	2.460(2)
Dy-N(12)	2.499(4)	Dy-N(12)	2.469(2)
Dy-N(13)	2.503(4)	Dy-N(13)	2.490(3)
Dy-O(11)	2.189(3)	Dy-O(11)	2.199(2)
Dy-O(12)	2.188(3)	Dy-O(12)	2.222(2)
Dy-O(13)	2.187(3)	Dy-O(13)	2.223(2)
5		**6**	
Dy-N	2.691(3)	Dy-N	2.724(4)
Dy-N(1)	2.470(2)	Dy-N(11)	2.474(4)
Dy-O(1)	2.205(2)	Dy-N(12)	2.490(4)
		Dy-N(13)	2.496(4)
		Dy-O(11)	2.203(3)
		Dy-O(12)	2.212(3)
		Dy-O(13)	2.199(3)

Table S2.7. Selected geometric parameters (Å) for **7**, **8**·ACN, **9**·DMF and **10**·DMF.

7		**8**·ACN	
Nd-N	2.776(2)	Nd-N	2.798(2)
Nd-N(11)	2.583(2)	Nd-N(1)	2.596(1)
Nd-N(12)	2.652(2)	Nd-O(1)	2.273(1)
Nd-N(13)	2.677(2)		
Nd-O(11)	2.410(2)		
Nd-O(12)	2.299(2)		
Nd-O(13)	2.360(2)		
Nd-O(1W)	2.523(2)		
9·DMF		**10**·DMF	
Nd-N	2.841(3)	Nd-N	2.821(4)
Nd-N(11)	2.647(3)	Nd-N(11)	2.573(5)
Nd-N(12)	2.664(3)	Nd-N(12)	2.590(4)
Nd-N(13)	2.708(3)	Nd-N(13)	2.601(4)
Nd-O(11)	2.352(3)	Nd-O(11)	2.261(3)
Nd-O(12)	2.397(2)	Nd-O(12)	2.248(4)
Nd-O(13)	2.361(2)	Nd-O(13)	2.259(4)
Nd-O(1W)	2.531(3)		
Nd-O(14)	2.588(3)		

Table S2.8. Selected geometric parameters (Å) for **11**·DMF and **12**.

11·DMF		**12**	
Nd-N	3.012(2)	Nd-N	2.846(2)
Nd-N(11)	2.595(2)	Nd-N(11)	2.626(2)
Nd-N(12)	2.603(2)	Nd-N(12)	2.649(2)
Nd-N(13)	2.622(2)	Nd-N(13)	2.733(2)
Nd-O(11)	2.303(1)	Nd-O(11)	2.349(1)
Nd-O(12)	2.337(1)	Nd-O(12)	2.410(1)
Nd-O(13)	2.320(1)	Nd-O(13)	2.365(1)
Nd-O(14)	2.522(4)	Nd-O(1W)	2.525(1)
Nd-O(14A)	2.460(6)	Nd-O(14)	2.535(1)

Table S2.9. Selected geometric parameters (Å) for **13**.

13			
Nd1-N(1)	2.82(3)	Nd2-N(2)	2.82(2)
Nd1-N(11)	2.58(3)	Nd2-N(14)	2.64(2)
Nd1-N(12)	2.59(3)	Nd2-N(15)	2.61(2)
Nd1-N(13)	2.69(2)	Nd2-N(16)	2.72(2)
Nd1-O(11)	2.38(2)	Nd2-O(14)	2.34(2)
Nd1-O(12)	2.33(3)	Nd2-O(15)	2.24(2)
Nd1-O(13)	2.34(3)	Nd2-O(16)	2.31(2)
Nd1-O(1W)	2.49(2)	Nd2-O(2W)	2.53(2)

3.7 Supporting information: Chapter 3

3.7.1 Single Crystal X-ray Structures

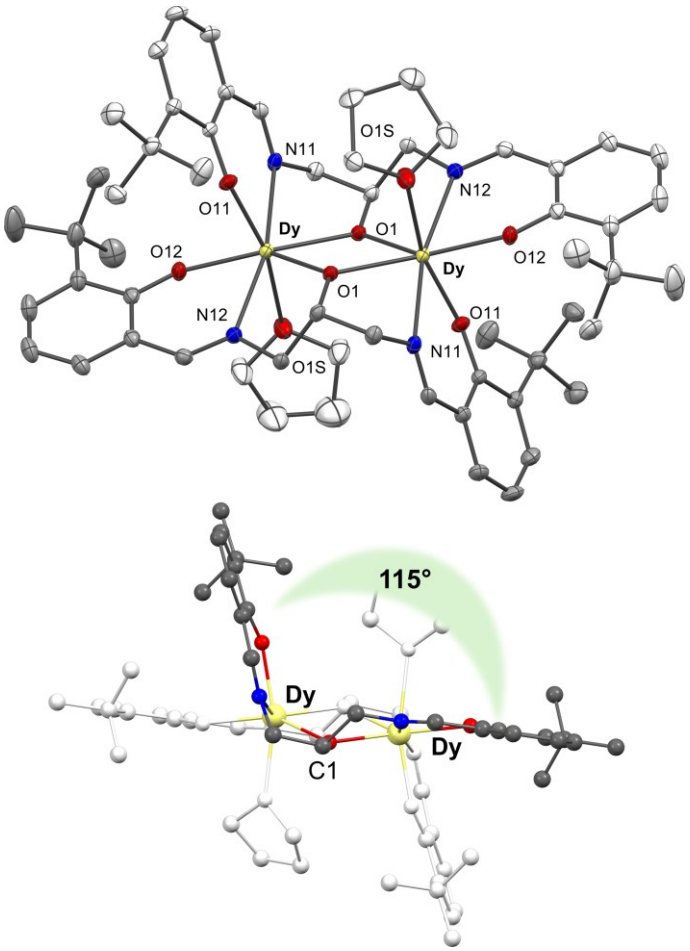

Figure S3.1. Above, representation of the structure of the dimeric complex [Dy(Salpen$^{o\text{-}tBut}$)THF]$_2$·THF. Solvent of crystallization and the hydrogen atoms were removed for clarity. Thermal ellipsoids were depicted at the 30% probability level. Dy (yellow), N (blue) and O (red) and C (grey, light grey).

Below, depiction of the semi-bent conformation adopted by the Salpen$^{o\text{-}tBut}$ ligand in the complex. The dihedral angle of 115 deg. is calculated from the mean planes passing through the two aromatic rings.

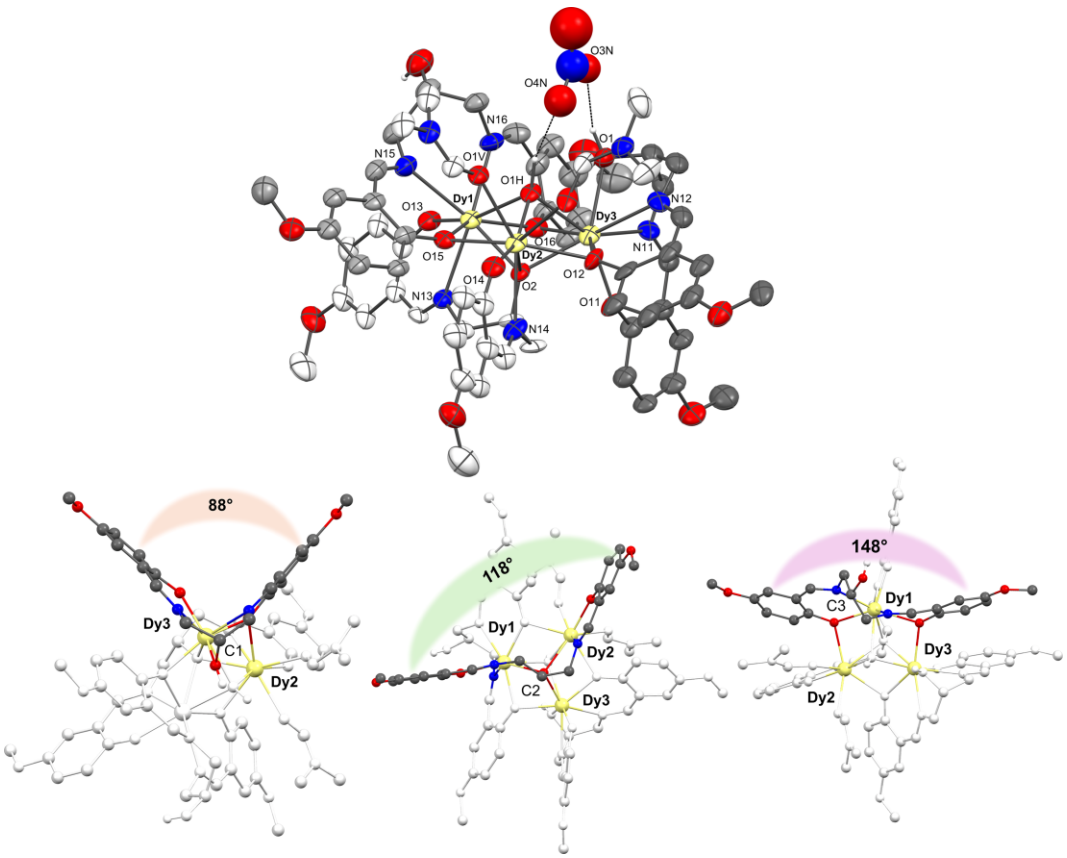

Figure S3.2. Above, representation of the structure of the trimeric complex $[Dy_3(Salpen^{p\text{-}OMe})_3(OH)(DMF)_2(NO_3)]\cdot 2DMF$. Solvent of crystallization and the hydrogen atoms (except for the hydroxyl groups O1H, O1 and O3/O3A) were removed for clarity. Thermal ellipsoids were depicted at the 30% probability level. Dy (yellow), N (blue), O (red), C (dark grey, grey and light grey), H (white). Hydrogen bonds are represented with black dashed lines.

Below, depiction of the conformations adopted by the Salpen$^{p\text{-}OMe}$ ligands. The ligand containing C1 adopts a bent conformation, the ligand containing C2 adopts a semi-bent conformation whereas the ligand containing C3 adopts an extended conformation. The dihedral angles are calculated from the mean planes passing through the two aromatic rings for each ligand.

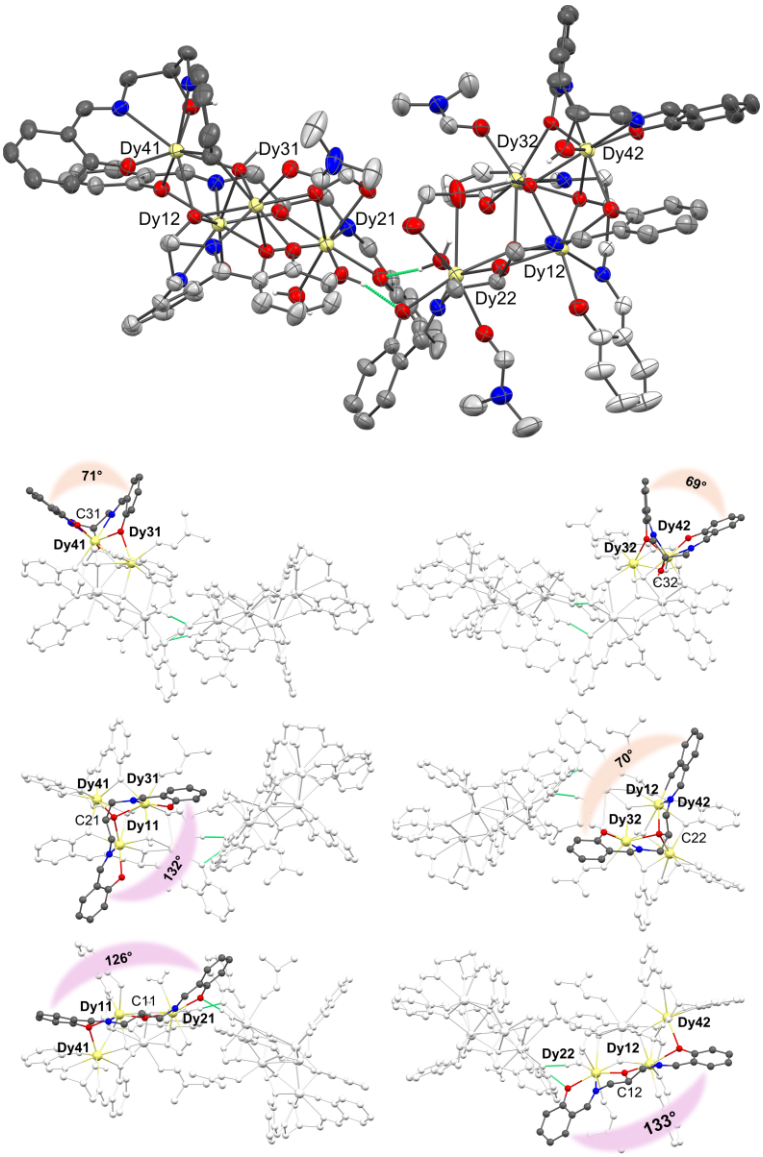

Figure S3.3. Above, representation of the structure of the complex $[Dy_4(Salpen)_3(H_2O)_2(OH)_2(HCOO)(DMF)(NO_3)]$ $[Dy_4(Salpen)_3(H_2O)(OH)_2(HCOO)(DMF)_2(NO_3)](H_2O)_{0.2}\cdot 2.75DMF$. Solvent of crystallization and the hydrogen atoms were removed for clarity. Hydrogen bonds are represented with green dashed lines. Thermal ellipsoids were depicted at the 30% probability level. Dy (yellow), N (blue) and O (red) and C (dark grey, grey and light grey), H (white). Below, depiction of the conformations adopted by the Salpen ligands. The ligands containing C31 and C32 adopt a bent conformation, the ligands containing C21 and C22 adopt a semi bent conformation, whereas the ligands containing C11 and C12 adopt an extended conformation. The dihedral angles are calculated from the mean planes passing through the two aromatic rings for each ligand.

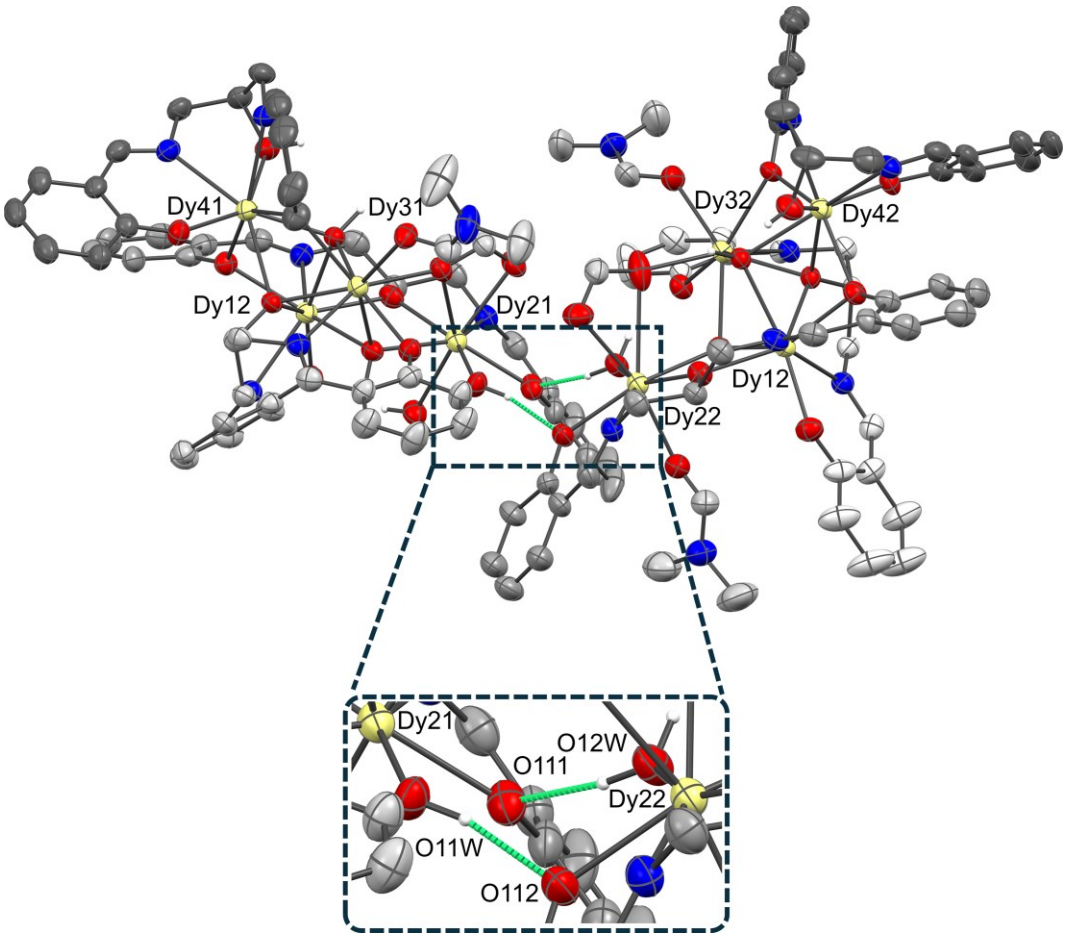

Figure S3.4. Representation of the complex $[Dy_4(Salpen)_3(H_2O)_2(OH)_2(HCOO)(DMF)]$ $[Dy_4(Salpen)_3(H_2O)(OH)_2(HCOO)(DMF)_2](NO_3)_2(H_2O)_{0.2}\cdot 2.75DMF$ highlighting the hydrogen bonding between the two distinct molecular entities (represented with green dashed bonds). Solvent of crystallization and the hydrogen atoms were removed for clarity (except for the water molecules O11W, O12W). Thermal ellipsoids were depicted at the 30% probability level. Dy (yellow), N (blue) and O (red) and C (dark grey, grey and light grey), H (white).

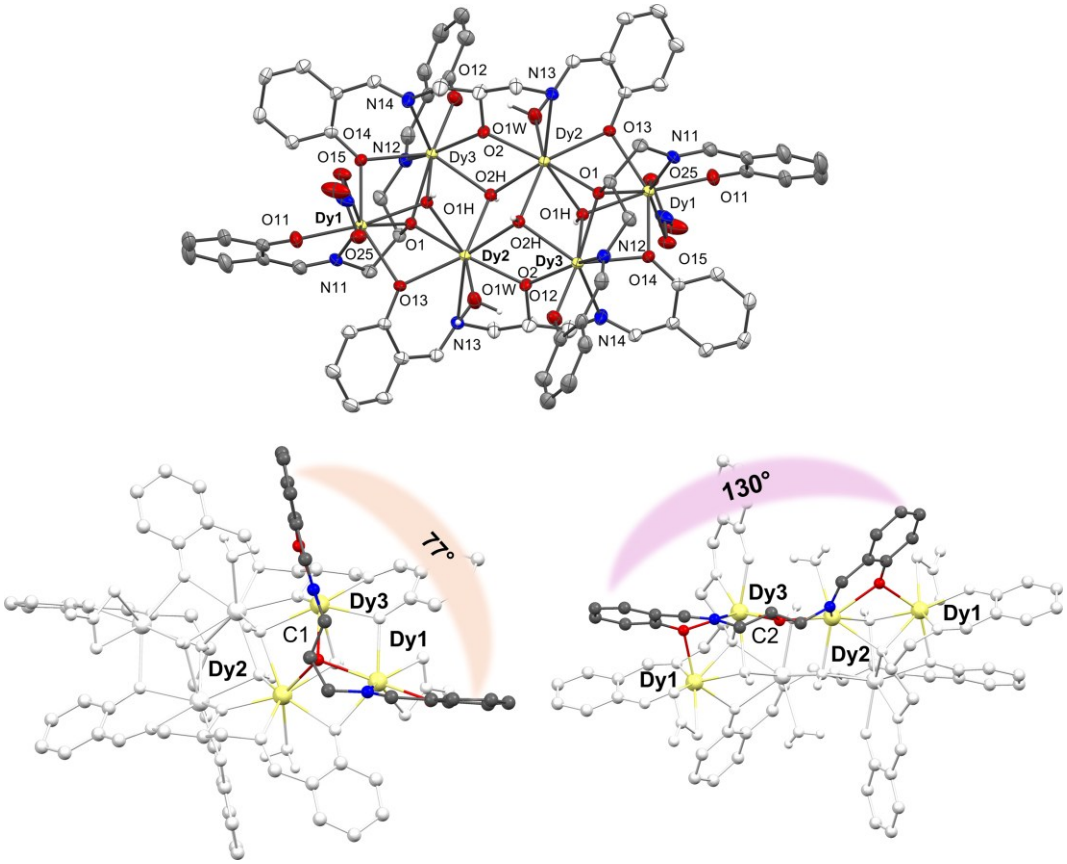

Figure S3.5. Above, representation of the structure of the hexametallic complex $[Dy_6(Salpen)_4(H_2O)_2(OH)_4(NO_3)_2]\cdot 1.66$ Acetone. Solvent of crystallization and hydrogen atoms (except for the hydroxyl groups O1H, O2H and the water molecules O1W) were removed for clarity. Dy (yellow), N (blue), O (red) and C (grey and light grey), H (white). Thermal ellipsoids were depicted at the 30% probability level. Below, depiction of the conformations adopted by the Salpen ligands. The ligand containing C1 adopts a semi bent conformation whereas the ligand containing C2 adopts an extended conformation. The dihedral angles are calculated from the mean planes passing through the two aromatic rings for each ligand.

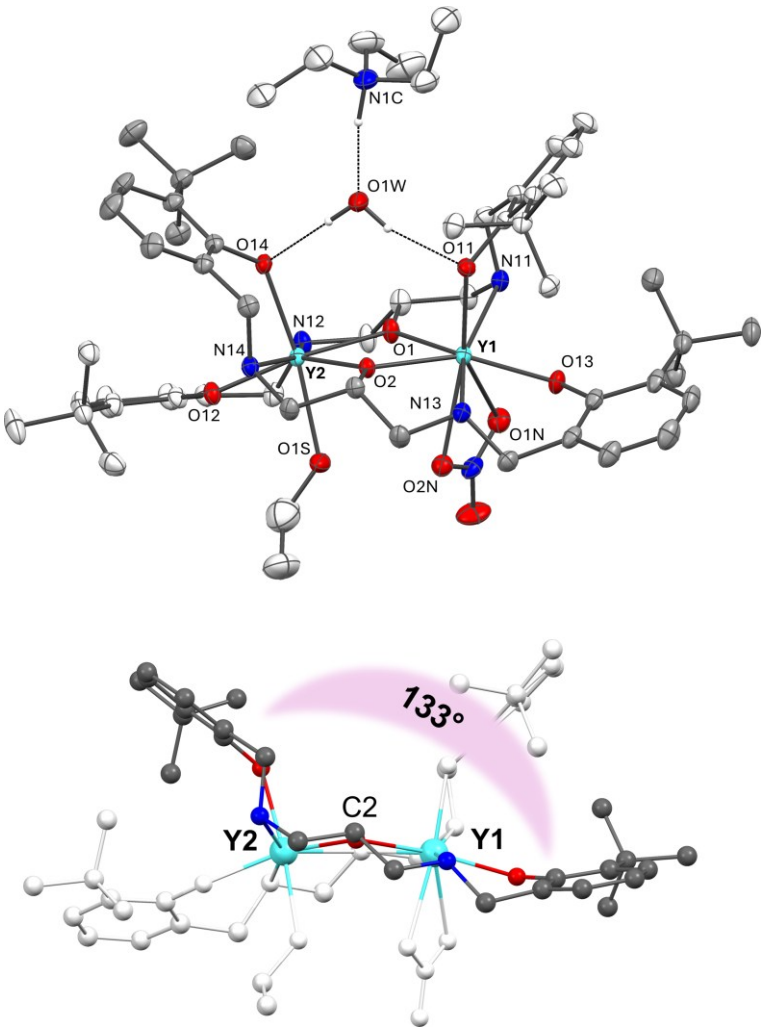

Figure S3.6. Above, representation of the structure of the dimeric complex $Et_3NH[Y_2(H_2Salpen^{o\text{-}tBut})_2(EtOH)(NO_3)]\cdot EtOH$. Solvent of crystallization and the hydrogen atoms (except for the water molecule O1W and the triethylammonium cation N1C) were removed for clarity. Thermal ellipsoids were depicted at the 30% probability level. Hydrogen bonds are represented with black dashed lines. Y (light blue), N (blue) and O (red) and C (grey, light grey), H (white). Below, depiction of the extended conformation adopted by the $H_2Salpen^{o\text{-}tBu}$ ligand in the complex. The dihedral angle of 133 deg. is calculated from the mean planes passing through the two aromatic rings.

3.7.2 Crystal data and structural geometric parameters

Table S3.1. Summary of X-ray crystallographic data for (**1**)

Identification code	$[Dy(Salpen^{o\text{-}tBut})THF]_2 \cdot THF$
Empirical formula	$C_{27}H_{27}DyN_4O_3$
Formula weight	618.02
Temperature/K	200.0
Crystal system	trigonal
Space group	P-3c1
a/Å	13.0116(4)
b/Å	13.0116(4)
c/Å	16.3938(5)
α/°	90
β/°	90
γ/°	120
Volume/$Å^3$	2403.65(16)
Z	4
ρcalcg/cm^3	1.708
μ/mm^{-1}	3.146
F(000)	1228.0
Crystal size/mm^3	0.18 × 0.11 × 0.08
Radiation	MoKα (λ = 0.71073)
2Θ range for data collection/°	6.146 to 51.388
Index ranges	-15 ≤ h ≤ 15, -15 ≤ k ≤ 15, -19 ≤ l ≤ 19
Reflections collected	52201
Independent reflections	1523 [Rint = 0.0430, Rsigma = 0.0117]
Data/restraints/parameters	1523/0/106
Goodness-of-fit on F^2	1.049
Final R indexes [I>=2σ (I)]	R1 = 0.0177, wR2 = 0.0498
Final R indexes [all data]	R1 = 0.0197, wR2 = 0.0527
Largest diff. peak/hole / e $Å^{-3}$	0.33/-1.38

Table S3.2. Summary of X-ray crystallographic data for (**2**)

Identification code	$[Dy_3(Salpen^{p\text{-}OMe})_3(OH)(DMF)_2(NO_3)]\cdot 2DMF$
Empirical formula	$C_{69}H_{88}Dy_3N_{11}O_{23}$
Formula weight	1927.00
Temperature/K	100.00
Crystal system	monoclinic
Space group	P21/c
a/Å	20.565(4)
b/Å	17.805(4)
c/Å	23.359(5)
α/°	90
β/°	105.29(3)
γ/°	90
Volume/$Å^3$	8250(3)
Z	4
ρcalcg/cm^3	1.551
μ/mm^{-1}	1.938
F(000)	3844.0
Crystal size/mm^3	0.1 × 0.05 × 0.02
Radiation	Synchrotron (λ = 0.620)
2Θ range for data collection/°	1.79 to 43.312
Index ranges	$-24 \le h \le 24$, $-21 \le k \le 21$, $-27 \le l \le 27$
Reflections collected	33103
Independent reflections	14251 [Rint = 0.1671, Rsigma = 0.1932]
Data/restraints/parameters	14251/481/938
Goodness-of-fit on F^2	1.025
Final R indexes [I>=2σ (I)]	R1 = 0.0883, wR2 = 0.2168
Final R indexes [all data]	R1 = 0.1937, wR2 = 0.2688
Largest diff. peak/hole / e $Å^{-3}$	1.90/-1.44

Table S3.3. Summary of X-ray crystallographic data for (**3**)

Identification code	$[Dy_4(Salpen)_3(H_2O)_2(OH)_2(HCOO)(DMF)]$ $[Dy_4(Salpen)_3(H_2O)(OH)_2(HCOO)(DMF)_2](NO_3)_2(H_2O)_{0.2}\cdot 2.75DMF$
Empirical formula	$C_{60.62}H_{69.83}Dy_4N_{9.88}O_{20.48}$
Formula weight	1914.43
Temperature/K	200.00
Crystal system	triclinic
Space group	P-1
a/Å	17.0290(5)
b/Å	19.0630(6)
c/Å	27.0387(7)
α/°	107.216(2)
β/°	97.737(2)
γ/°	108.659(2)
Volume/$Å^3$	7684.2(4)
Z	4
ρcalcg/cm^3	1.655
μ/mm^{-1}	21.042
F(000)	3722.0
Crystal size/mm^3	0.13 × 0.09 × 0.07
Radiation	CuKα (λ = 1.54178)
2Θ range for data collection/°	3.536 to 145.194
Index ranges	? ≤ h ≤ ?, ? ≤ k ≤ ?, ? ≤ l ≤ ?
Reflections collected	30283
Independent reflections	30283 [Rint = ?, Rsigma = 0.0554]
Data/restraints/parameters	30283/194/1692
Goodness-of-fit on F^2	0.995
Final R indexes [I>=2σ (I)]	R1 = 0.0658, wR2 = 0.1841
Final R indexes [all data]	R1 = 0.0821, wR2 = 0.1974
Largest diff. peak/hole / e $Å^{-3}$	1.25/-1.54

Table S3.4. Summary of X-ray crystallographic data for (**4**)

Identification code	$[Dy_6(Salpen)_4(H_2O)_2(OH)_4(NO_3)_2]\cdot 1.66Acetone$
Empirical formula	$C_{77.99}H_{87.98}Dy_6N_{10}O_{27.33}$
Formula weight	2577.72
Temperature/K	200.00
Crystal system	orthorhombic
Space group	Pbca
a/Å	21.466(4)
b/Å	19.837(4)
c/Å	21.147(4)
α/°	90
β/°	90
γ/°	90
Volume/$Å^3$	9005(3)
Z	4
ρcalcg/cm^3	1.901
μ/mm^{-1}	4.994
F(000)	4962.0
Crystal size/mm^3	0.1 × 0.07 × 0.04
Radiation	MoKα (λ = 0.71073)
2Θ range for data collection/°	4.106 to 51.36
Index ranges	-26 ≤ h ≤ 25, -24 ≤ k ≤ 23, -25 ≤ l ≤ 25
Reflections collected	91585
Independent reflections	8509 [Rint = 0.0758, Rsigma = 0.0308]
Data/restraints/parameters	8509/85/594
Goodness-of-fit on F^2	1.060
Final R indexes [I>=2σ (I)]	R1 = 0.0304, wR2 = 0.0736
Final R indexes [all data]	R1 = 0.0410, wR2 = 0.0803
Largest diff. peak/hole / e $Å^{-3}$	1.69/-0.55

Table S3.5. Summary of X-ray crystallographic data for (**5**)

Identification code	$[Y_2(H_2Salpen^{o\text{-}tBut})(EtOH)(NO_3)(Et_3NH)]\cdot EtOH$ **(5)**
Empirical formula	$C_{60}H_{100}N_6O_{12}Y_2$
Formula weight	1275.27
Temperature/K	200.00
Crystal system	triclinic
Space group	P-1
a/Å	12.8725(8)
b/Å	16.3901(10)
c/Å	17.6416(9)
α/°	80.535(2)
β/°	74.351(2)
γ/°	75.811(2)
Volume/Å^3	3455.4(4)
Z	2
ρ_{calc}g/cm^3	1.226
μ/mm^{-1}	1.728
F(000)	1352.0
Crystal size/mm^3	0.18 × 0.09 × 0.05
Radiation	MoKα (λ = 0.71073)
2Θ range for data collection/°	3.71 to 51.472
Index ranges	-15 ≤ h ≤ 15, -20 ≤ k ≤ 19, -21 ≤ l ≤ 21
Reflections collected	161024
Independent reflections	13171 [R_{int} = 0.1281, R_{sigma} = 0.0616]
Data/restraints/parameters	13171/110/812
Goodness-of-fit on F^2	1.028
Final R indexes [I>=2σ (I)]	R_1 = 0.0498, wR_2 = 0.1271
Final R indexes [all data]	R_1 = 0.0817, wR_2 = 0.1455
Largest diff. peak/hole / e Å^{-3}	0.98/-0.57

Table S3.6. Selected geometric parameters (Å) for **(1)**.

(1)	
Dy-Dy1	3.750(1)
Dy-O11	2.191 (2)
Dy-O1	2.263(2)
Dy-O1[1]	2.321(2)
Dy-O12[1]	2.197(2)
Dy-N11	2.474(2)
Dy-N12[1]	2.457(2)
Dy-O13	2.488(2)

[1]1-X,1-Y,1-Z

Table S3.7. Selected geometric parameters (Å) for **(2)**.

(2)			
Dy1-Dy2	3.568 (1)	Dy2-O1T	2.416(10)
Dy1-Dy3	3.553 (1)	Dy2-O1V	2.395(10)
Dy1-O15	2.336(12)	Dy2-O12	2.411(10)
Dy1-O1H	2.449(9)	Dy2-O14	2.190(16)
Dy1-O2	2.345(11)	Dy2-N14	2.540(18)
Dy1-O13	2.220(10)	Dy3-O1H	2.393(9)
Dy1-O16	2.321(13)	Dy3-O2	2.376(11)
Dy1-N13	2.499(14)	Dy3-O12	2.302(13)
Dy1-N15	2.540(14)	Dy3-O16	2.324(11)
Dy1-N16	2.523(18)	Dy3-O1	2.433(14)
Dy2-Dy3	3.554(2)	Dy3-O11	2.204(11)
Dy2-O15	2.391(10)	Dy3-N12	2.481(15)
Dy2-O1H	2.318(14)	Dy3-N11	2.483(16)
Dy2-O2	2.411(9)		

Table S3.8. Selected geometric parameters (Å) for **(3)**.

(3)			
Dy12-Dy32	3.575(7)	Dy11-O131	2.266(6)
Dy12-Dy42	3.521(6)	Dy11-N131	2.487(7)
Dy12-Dy22	3.833(7)	Dy11-N121	2.492(8)
Dy12-O22H	2.402(6)	Dy41-O21	2.388(5)
Dy12-O122	2.360(5)	Dy41-O11H	2.355(5)
Dy12-O12H	2.423(5)	Dy41-O161	2.337(6)
Dy12-O22	2.404(5)	Dy41-O151	2.193(6)
Dy12-O12	2.294(6)	Dy41-O121	2.361(5)
Dy12-O132	2.222(7)	Dy41-O31	2.434(7)
Dy12-N132	2.488(7)	Dy41-N151	2.513(8)
Dy12-N122	2.522(7)	Dy41-N161	2.492(7)
Dy32-Dy42	3.566(6)	Dy42-O122	2.351(6)
Dy32-O22H	2.415(6)	Dy42-O12H	2.329(5)
Dy32-O12H	2.380(5)	Dy42-O22	2.425(5)
Dy32-O22	2.361(5)	Dy42-O152	2.193(6)
Dy32-O142	2.265(5)	Dy42-O162	2.333(6)
Dy32-N142	2.500(7)	Dy42-O32	2.444(7)
Dy32-O162	2.394(5)	Dy42-N152	2.515(8)
Dy32-O12S	2.360(7)	Dy42-N162	2.482(8)
Dy32-O12F	2.327(7)	Dy21-O21H	2.381(6)
Dy31-Dy11	3.529(6)	Dy21-O11W	2.338(6)
Dy31-Dy41	3.573(7)	Dy21-O11F	2.540(7)
Dy31-O21	2.373(5)	Dy21-O11	2.241(7)
Dy31-O21H	2.420(5)	Dy21-O21W	2.381(6)
Dy31-O11H	2.360(5)	Dy21-O111	2.235(6)
Dy31-O141	2.254(6)	Dy21-O21F	2.435(6)
Dy31-O161	2.385(6)	Dy21-N111	2.487(9)
Dy31-O11F	2.392(6)	Dy22-O12F	2.810(11)
Dy31-O11S	2.362(6)	Dy22-O22H	2.386(6)
Dy31-N141	2.509(7)	Dy22-O12W	2.340(6)
Dy11-Dy41	3.515(7)	Dy22-O22S	2.319(7)
Dy11-Dy21	3.767(7)	Dy22-O112	2.267(6)
Dy11-O21	2.414(5)	Dy22-O12	2.246(6)
Dy11-O21H	2.360(6)	Dy22-O22F	2.381(8)
Dy11-O11H	2.378(5)	Dy22-N112	2.469(8)
Dy11-O11	2.308(6)		
Dy11-O121	2.331(6)		

Table S3.9. Selected geometric parameters (Å) for **(4)**.

(4)			
Dy2-Dy21	3.980(7)	Dy1-O11	2.194(4)
Dy2-Dy1	3.585(8)	Dy1-O13	2.314(4)
Dy2-Dy31	3.792(8)	Dy1-O25	2.480(4)
Dy2-Dy3	3.541(5)	Dy1-O15	2.500(4)
Dy2-O1H	2.333(4)	Dy1-N15	2.896(5)
Dy2-O1W	2.364(4)	Dy1-N11	2.490(5)
Dy2-O2	2.265(3)	Dy3-Dy21	3.792(7)
Dy2-O1	2.446(4)	Dy3-O1H	2.416(4)
Dy2-N13	2.518(5)	Dy3-O141	2.363(4)
Dy2-O13	2.410(4)	Dy3-O21	2.296(4)
Dy2-O2H1	2.389(4)	Dy3-O1	2.384(4)
Dy2-O2H	2.443(4)	Dy3-O12	2.254(4)
Dy1-Dy3	3.523(5)	Dy3-O2H	2.368(4)
Dy1-O1H	2.350(4)	Dy3-N12	2.502(5)
Dy1-O141	2.313(4)	Dy3-N141	2.503(5)
Dy1-O1	2.413(4)		

Table S3.10. Selected geometric parameters (Å) for **(5)**.

(5)			
Y1-Y2	3.7632(5)	Y1-N12	2.582(3)
Y1-O22	2.286(3)	Y2-O31	2.208(3)
Y1-O12	2.227(3)	Y2-O22	2.246(2)
Y1-O21	2.283(2)	Y2-O21	2.279(2)
Y1-O11	2.183(3)	Y2-O32	2.172(3)
Y1-O14	2.533(3)	Y2-O1T	2.391(3)
Y1-O24	2.586(3)	Y2-N21	2.549(3)
Y1-N11	2.586(3)	Y2-N22	2.568(3)

5.7. Supporting information: Chapter 5

5.7.1 Single Crystal X-ray Structures

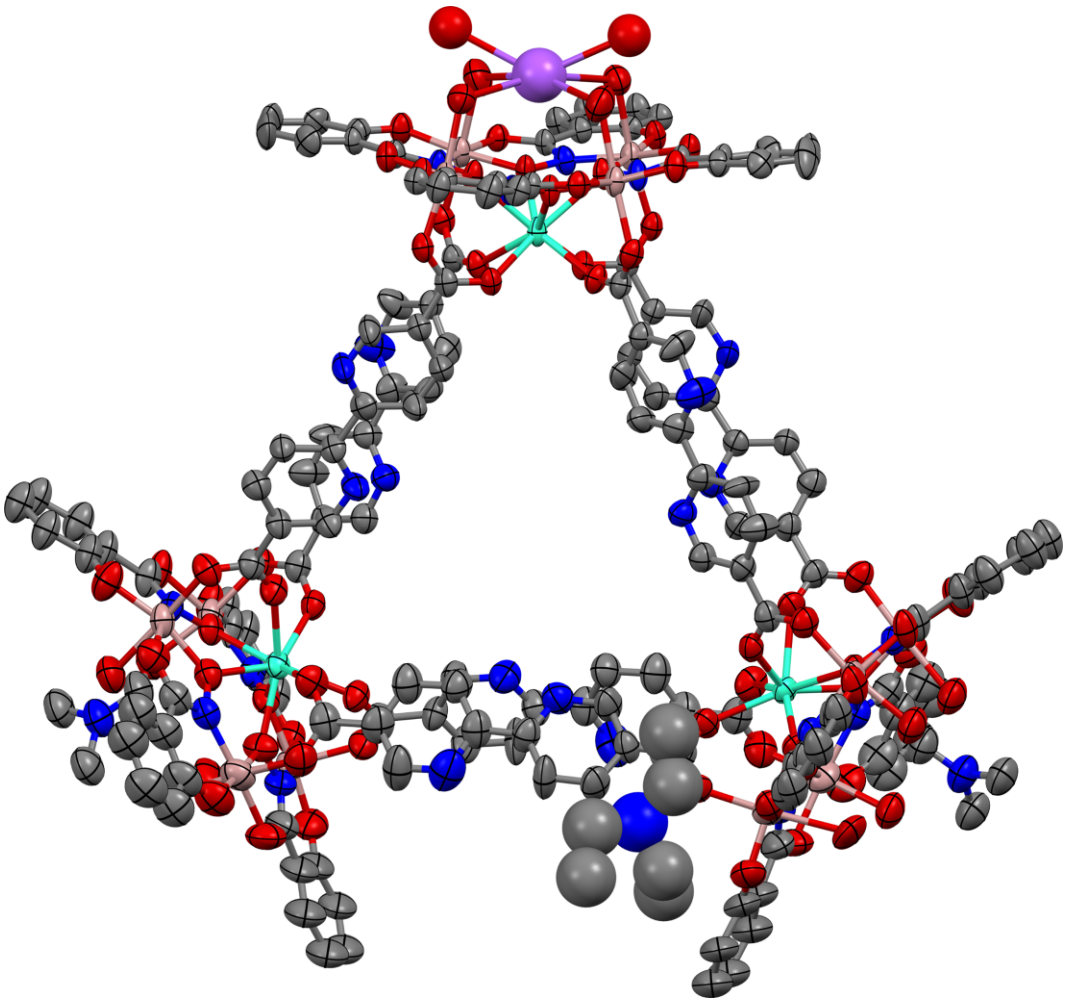

Figure S5.1. Representation of the structure of the {[TbNa(12-$MC_{Ga,shi}$-4)]$_3$(bipy)$_6$(DMF)$_2$(H_2O)$_{10}$}(HNEt_3)(DMF)$_5$ complex. Green-azure (Tb), pink (Ga), Red (oxygen), blue (nitrogen), grey (carbon), white (hydrogen), purple (Na). The hydrogens and crystallization solvent (DMF) were removed for clarity. Thermal ellipsoids were depicted at the 30% probability level.

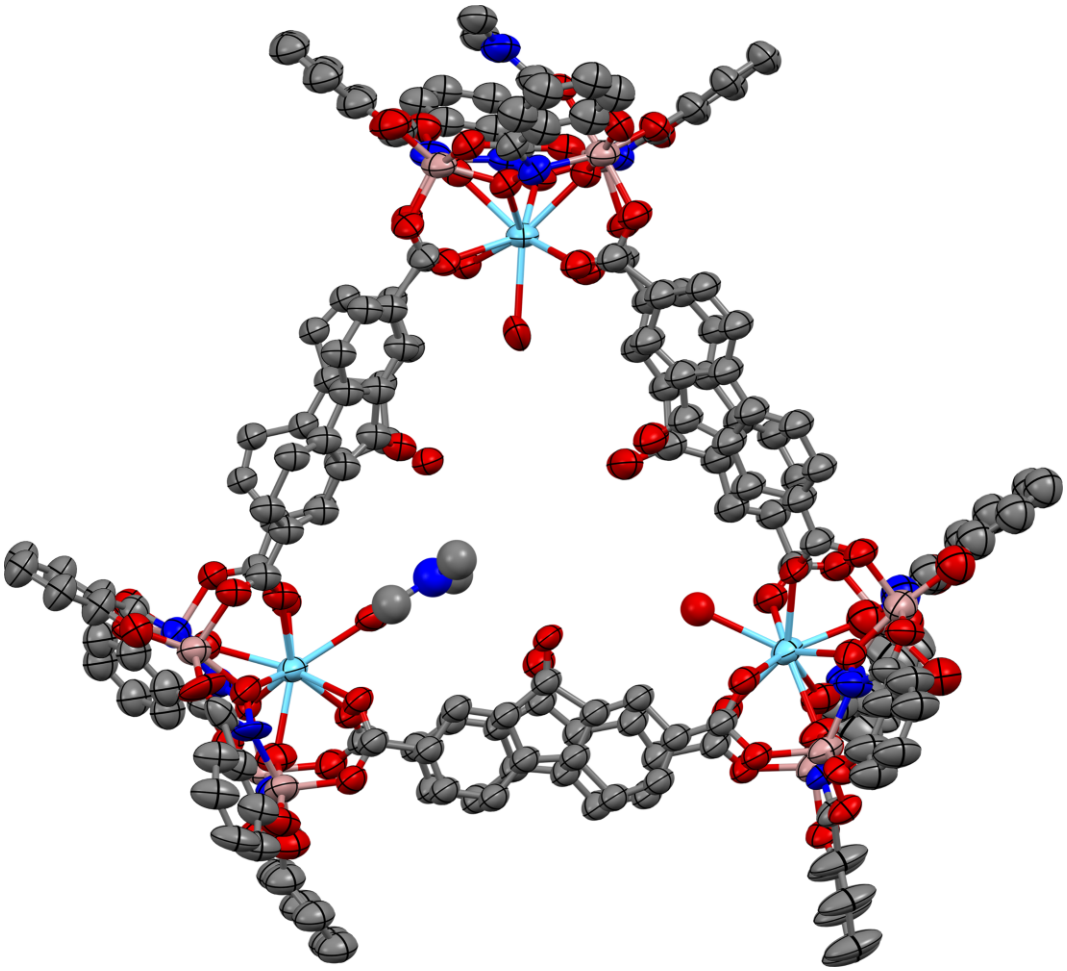

Figure S5.2. Representation of the structure of the {[La(12-$MC_{Ga,shi}$-4)]$_3$(frn)$_6$(H_2O)$_5$(DMF)$_3$}$^{3-}$(DMF) complex. Azure (La), pink (Ga), Red (oxygen), blue (nitrogen), grey (carbon). Hydrogens and crystallization solvent (DMF) were removed for clarity. Thermal ellipsoids were depicted at the 30% probability level.

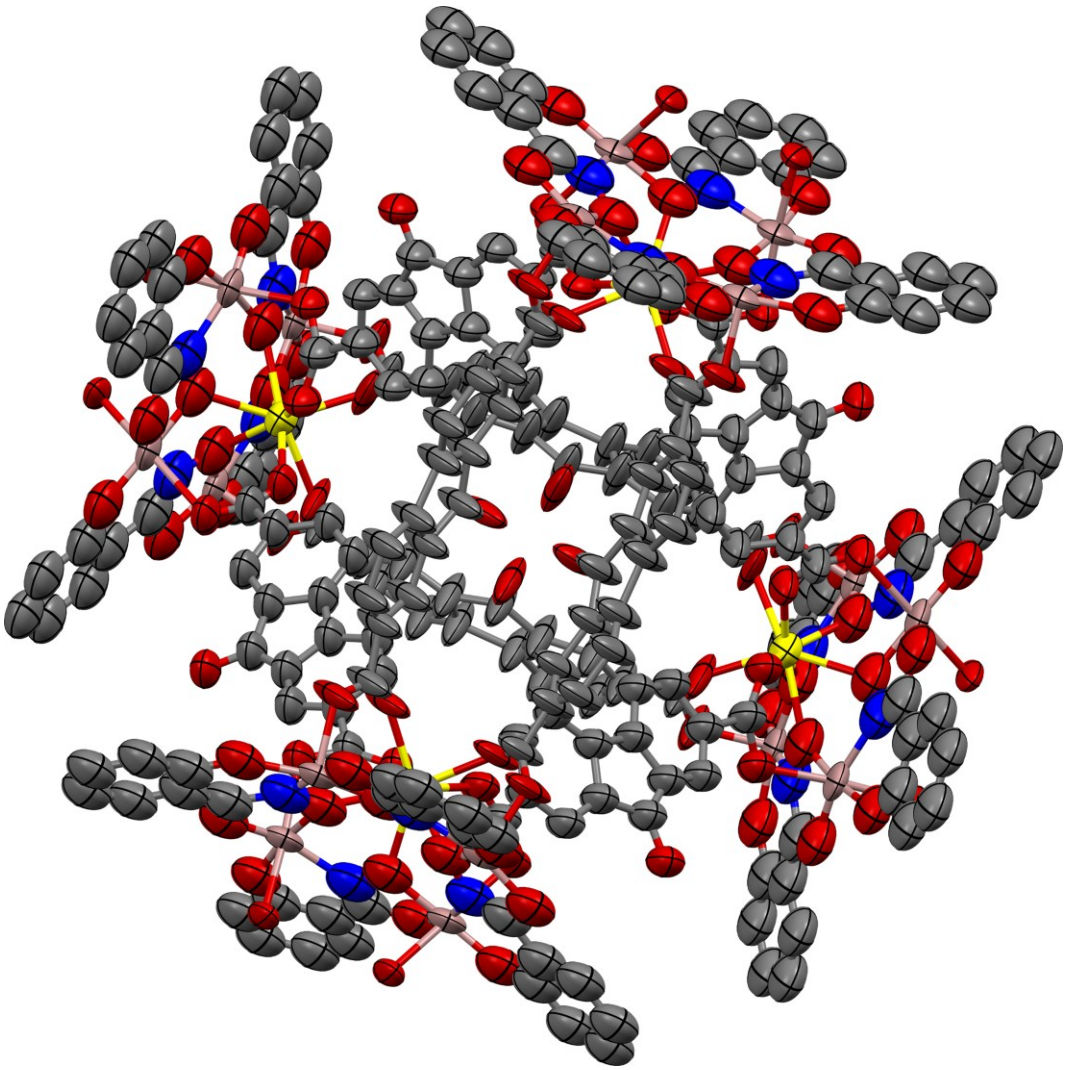

Figure S5.3. Representation of the structure of the {[Y(12-$MC_{Ga,shi}$-4)]$_4$(frn)$_8$(H_2O)$_{16}$}$^{3-}$complex. Yellow (Y), pink (Ga), Red (oxygen), blue (nitrogen), grey (carbon). Hydrogens were removed for clarity. Thermal ellipsoids were depicted at the 30% probability level.

5.7.2. UV-Visible, NMR and ESI-MS characterization

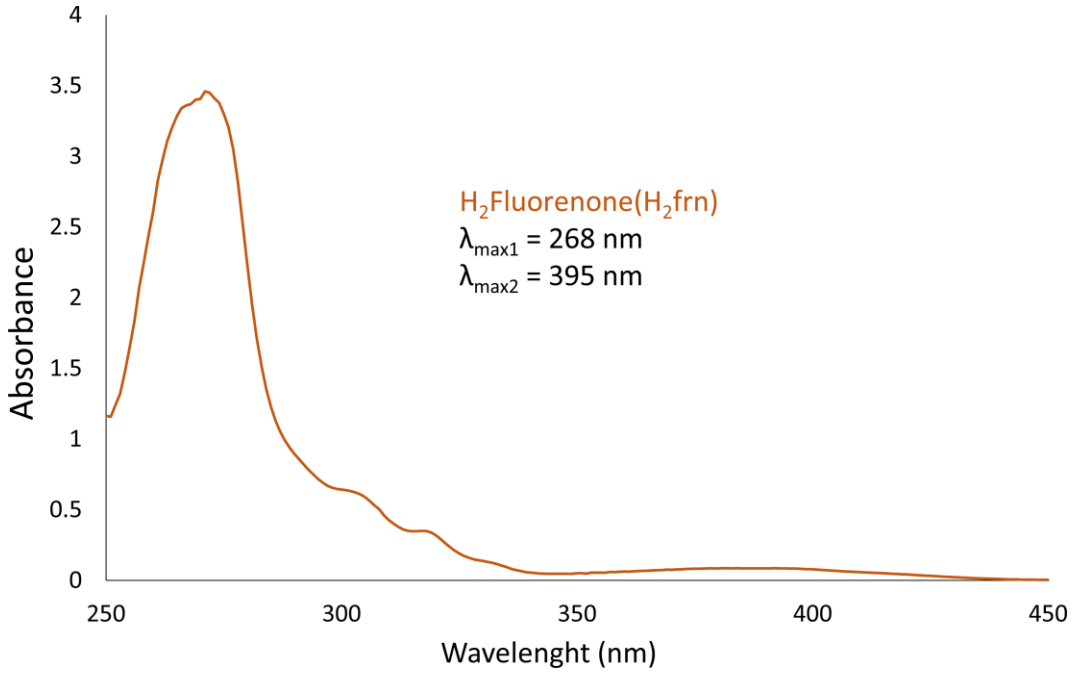

Figure S5.4. Uv-visible spectra of fluorenone ligand in DMSO (spectrophotometric grade), recorded at room temperature. C_{ligand} = 1x10^{-4} M.

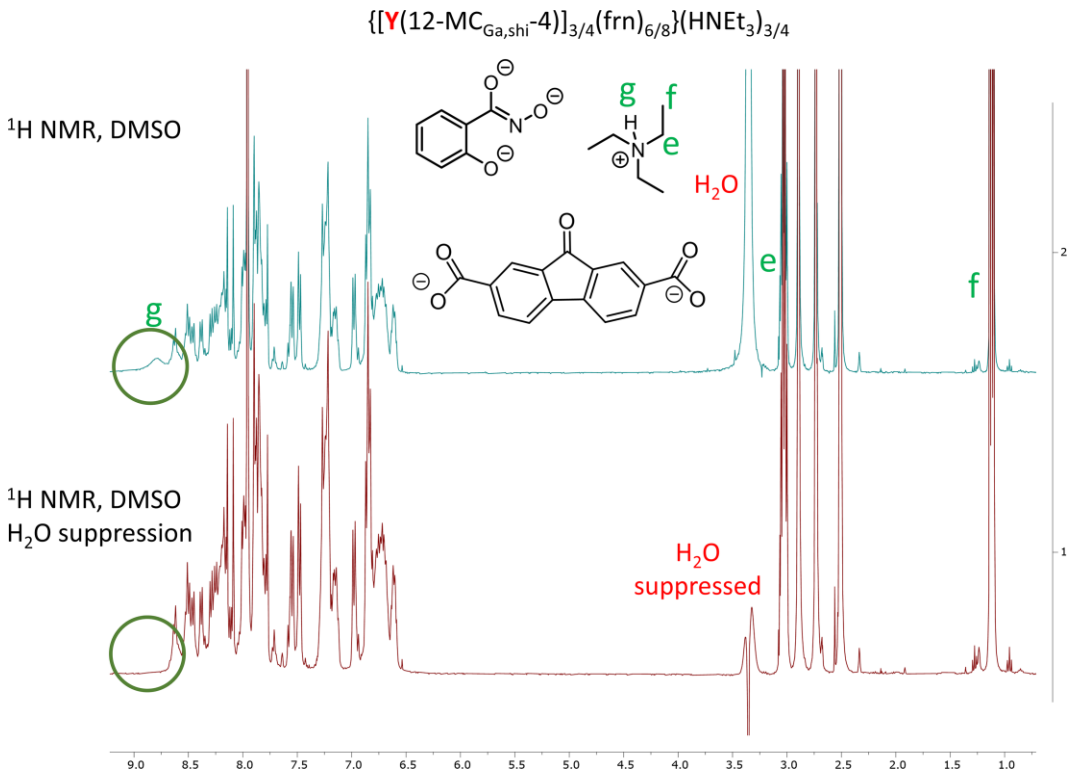

Figure S5.5. Top: ^{1}H NMR spectra of {[Y(12-MC$_{Ga,shi}$-4)]$_{3/4}$(frn)$_{6}$/$_{8}$}(HNEt$_3$)$_{3/4}$. Bottom: ^{1}H NMR spectra of {[Y(12-MC$_{Ga,shi}$-4)]$_{3/4}$(frn)$_{6}$/$_{8}$}(HNEt$_3$)$_{3/4}$ with water suppression in DMSO at 298 K.

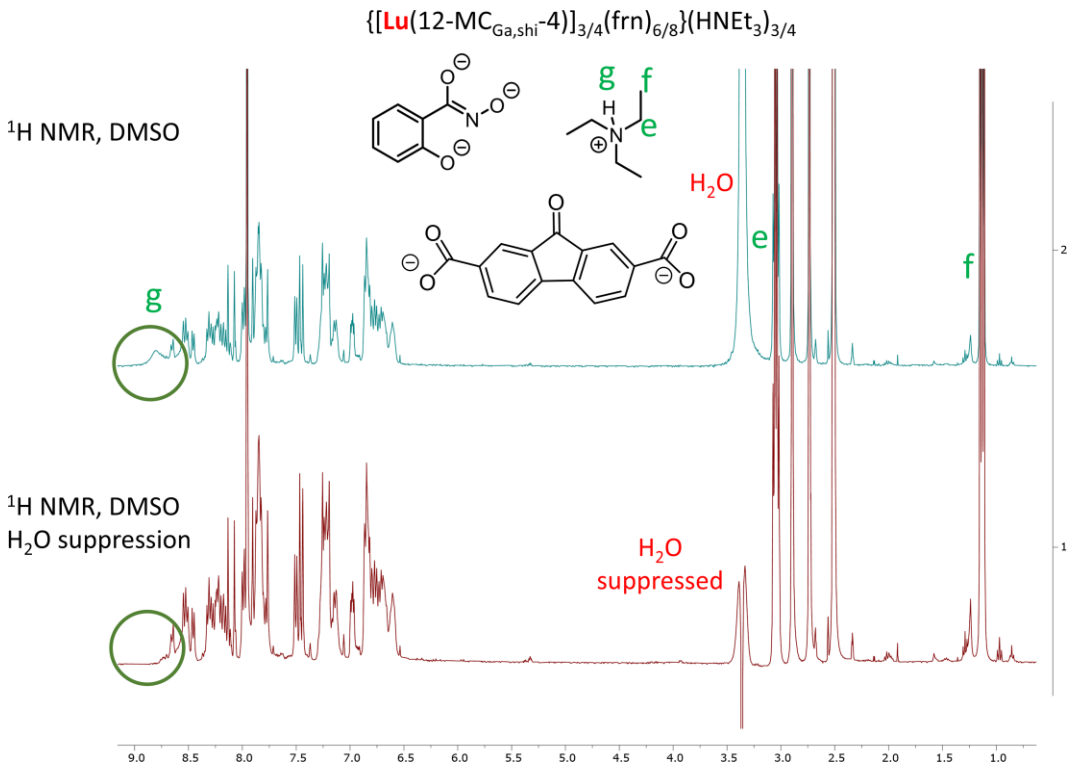

Figure S5.6. Top: ^{1}H NMR spectra of {[Lu(12-MC$_{Ga,shi}$-4)]$_{3/4}$(frn)$_{6}$/$_{8}$}(HNEt$_{3}$)$_{3/4}$. Bottom: ^{1}H NMR spectra of {[Lu(12-MC$_{Ga,shi}$-4)]$_{3/4}$(frn)$_{6}$/$_{8}$}(HNEt$_{3}$)$_{3/4}$ with water suppression in DMSO at 298 K.

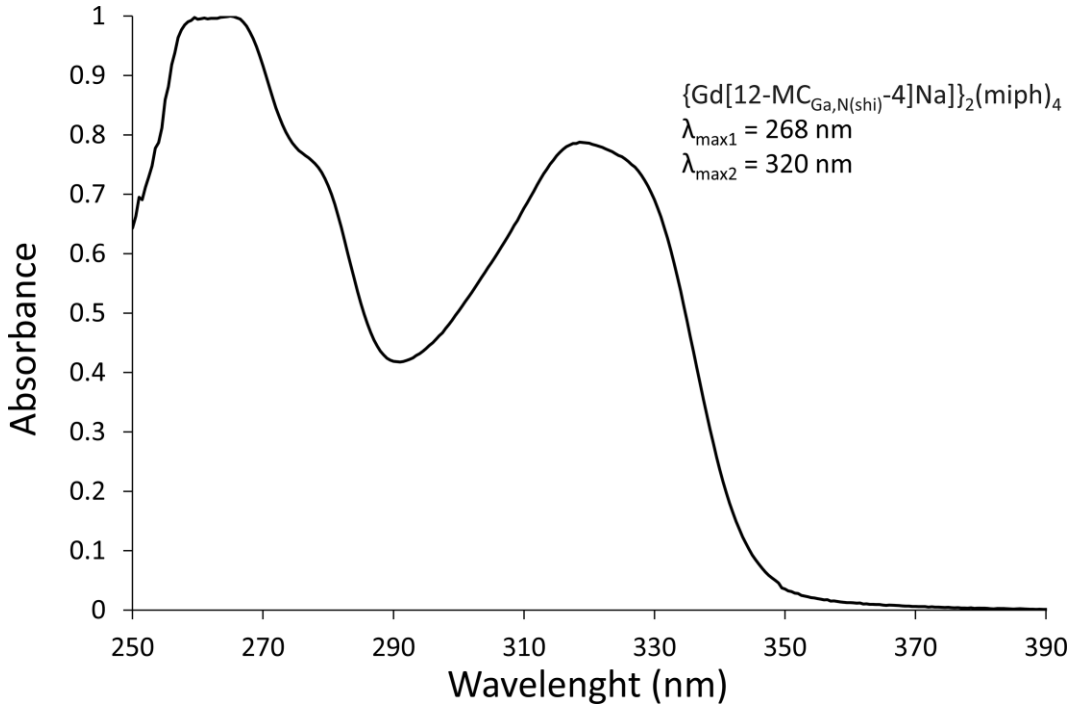

Figure S5.7. Uv-Visible spectrum of {Gd[12-MC$_{Ga,N(shi)}$-4]Na]}$_2$(miph)$_4$ in MeOH, recorded at room temperature. C_{MC} = 3 µM.

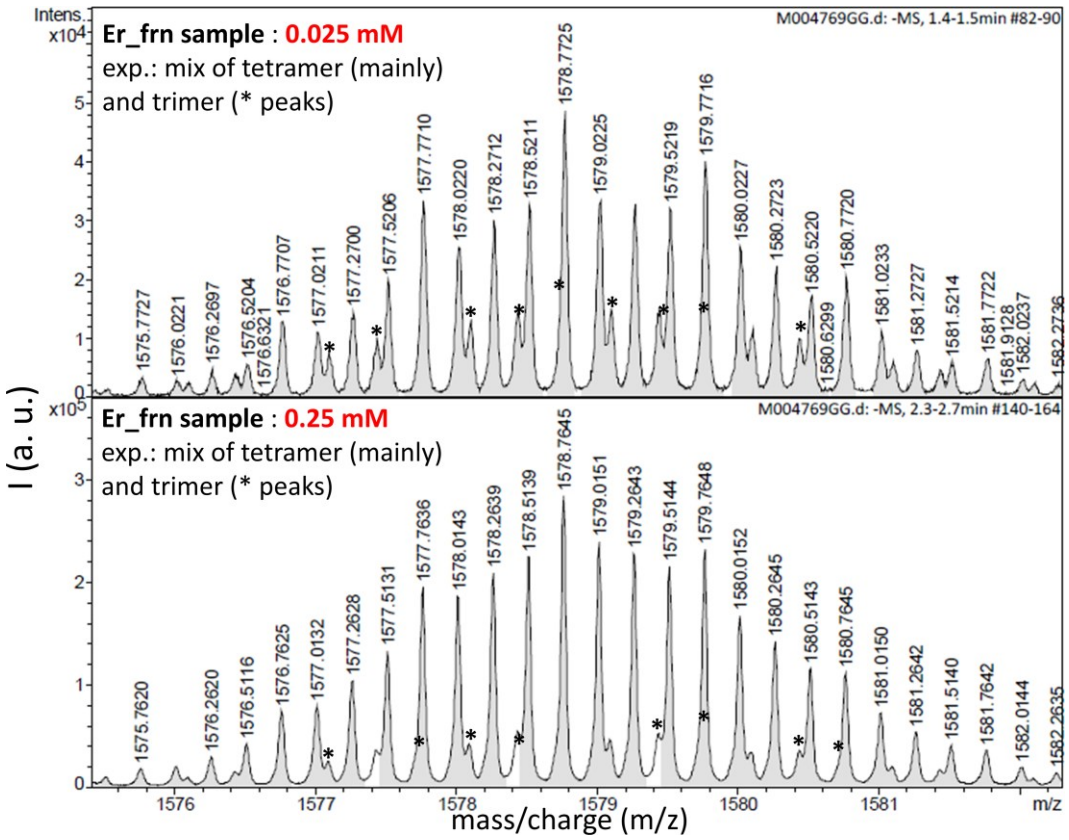

Figure S5.8. Experimental ESI-MS spectra of $\{[Er(12\text{-}MC_{Ga,shi}\text{-}4)]_3(frn)_6\}(HNEt_3)_3$ MC in the negative mode; C_{MC} = 0.025 mM (top) and C_{MC} = 0.25 mM (bottom), MeOH/DMSO 90:10.

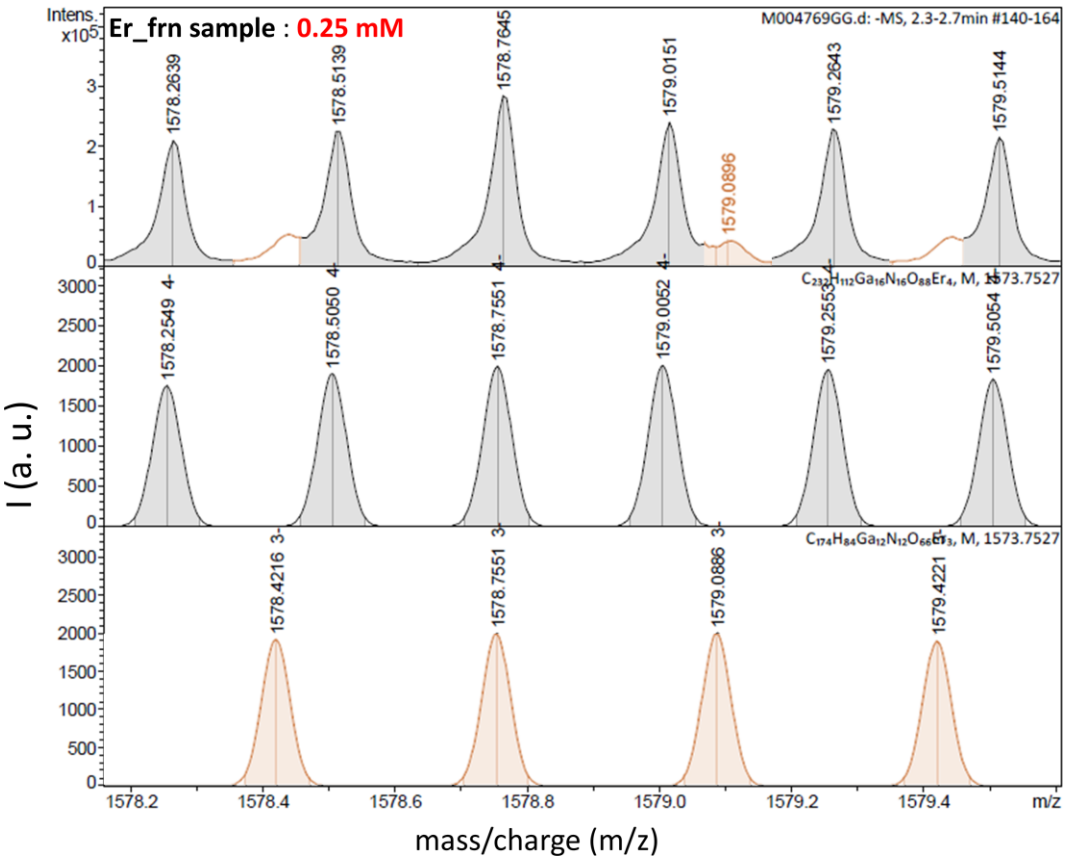

Figure S5.9. Top: experimental ESI-MS spectra of $\{[Er(12\text{-}MC_{Ga,shi}\text{-}4)]_3(frn)_6\}(HNEt_3)_3$ in the negative mode at C_{MC} = 0.25 mM in MeOH/DMSO 90:10. Middle: simulated isotopic distribution for the tetrameric MC. Bottom: simulated isotopic distribution for the trimeric MC.

5.7.3 Crystal data, structural geometric parameters and DOSY tables

Table S5.1. Summary of X-ray crystallographic data for {[TbNa(12-$MC_{Ga,shi}$-4)]$_3$(bipy)$_6$(DMF)$_2$(H_2O)$_{10}$}($HNEt_3$)(DMF)$_5$

Identification code	{[TbNa(12-$MC_{Ga,shi}$-4)]$_3$(bipy)$_6$(DMF)$_2$(H_2O)$_{10}$}($HNEt_3$)(DMF)$_5$
Empirical formula	$C_{218.7}H_{257.3}Ga_{12}N_{42.78}NaO_{88.4}Tb_3$
Formula weight	6236.10
Temperature/K	200.15
Crystal system	monoclinic
Space group	C2/c
a/Å	43.5579(8)
b/Å	26.2034(6)
c/Å	27.5083(6)
α/°	90
β/°	106.057(2)
γ/°	90
Volume/Å^3	30172.0(12)
Z	4
ρ_{calc}g/cm^3	1.373
μ/mm^{-1}	5.245
F(000)	12617.0
Crystal size/mm^3	0.25 × 0.15 × 0.07
Radiation	CuKα (λ = 1.54184)
2Θ range for data collection/°	3.978 to 140.15
Index ranges	-53 ≤ h ≤ 53, -31 ≤ k ≤ 29, -33 ≤ l ≤ 31
Reflections collected	111735
Independent reflections	28179 [R_{int} = 0.0582, R_{sigma} = 0.0413]
Data/restraints/parameters	28179/1176/2312
Goodness-of-fit on F^2	1.084
Final R indexes [I>=2σ (I)]	R_1 = 0.0931, wR_2 = 0.2747
Final R indexes [all data]	R_1 = 0.1160, wR_2 = 0.3067
Largest diff. peak/hole / e Å^{-3}	0.83/-1.43

Table S5.2. Unit cell data for {[Ln(12-$MC_{Ga,shi}$-4)]$_3$(bipy)}($HNEt_3$) complexes.

Identification code	Yb	Er	Dy	Y
Space group	C2/c	C2/c	C2/c	C2/c
a/Å	43.436(4)	43.444(3)	43.549(4)	43.5154(19)
b/Å	26.059(2)	26.1631(17)	26.2566(17)	26.2037(11)
c/Å	27.463(3)	27.4581(17)	27.489(2)	27.4235(11)
α/°	90.0	90	90	90
β/°	105.819(11)	105.605(6)	105.860(8)	105.615(4)
γ/°	90.0	90	90	90
Volume/$Å^3$	29908(5)	30059(3)	30236(4)	30116(2)

Table S5.3. Summary of X-ray crystallographic data for {[La(12-$MC_{Ga,shi}$-4)]$_3$(frn)$_6$(H_2O)$_5$(DMF)$_3$}$^{3-}$(DMF)

Identification code	{[La(12-$MC_{Ga,shi}$-4)]$_3$(frn)$_6$(H_2O)$_5$(DMF)$_3$}$^{3-}$(DMF)
Empirical formula	$C_{185.5}H_{105.5}Ga_{12}La_3N_{16}O_{75}$
Formula weight	5011.72
Temperature/K	200.00
Crystal system	monoclinic
Space group	P21/n
a/Å	14.3223(13)
b/Å	29.221(3)
c/Å	71.462(5)
α/°	90
β/°	93.663(5)
γ/°	90
Volume/Å^3	29846(4)
Z	4
ρcalcg/cm^3	1.115
μ/mm^{-1}	4.952
F(000)	9894.0
Crystal size/mm^3	0.075 × 0.05 × 0.04
Radiation	CuKα (λ = 1.54178)
2Θ range for data collection/°	3.91 to 84.184
Index ranges	-12 ≤ h ≤ 12, -25 ≤ k ≤ 24, -62 ≤ l ≤ 62
Reflections collected	112640
Independent reflections	20342 [Rint = 0.1288, Rsigma = 0.0798]
Data/restraints/parameters	20342/1993/2494
Goodness-of-fit on F^2	1.068
Final R indexes [I>=2σ (I)]	R1 = 0.1254, wR2 = 0.3335
Final R indexes [all data]	R1 = 0.1570, wR2 = 0.3593
Largest diff. peak/hole / e Å^{-3}	0.77/-0.66

Table S5.4. Summary of X-ray crystallographic data for $\{[Tb(12\text{-}MC_{Ga,shi}\text{-}4)]_3(frn)_6(Na)_{0.25}(DMF)_3\}^{3-}$

Identification code	$\{[Tb(12\text{-}MC_{Ga,shi}\text{-}4)]_3(frn)_6(Na)_{0.25}(DMF)_3\}^{3-}$
Empirical formula	$C_{174}H_{80.5}Ga_{12}N_{12}O_{69}Tb_3Na_{0.25}$
Formula weight	4762.15
Temperature/K	200.00
Crystal system	monoclinic
Space group	$P2_1/c$
a/Å	14.161(2)
b/Å	40.246(4)
c/Å	47.443(5)
α/°	90
β/°	93.133(8)
γ/°	90
Volume/Å^3	26998(5)
Z	4
ρcalcg/cm^3	1.172
μ/mm^{-1}	5.621
F(000)	9321.0
Crystal size/mm^3	0.075 × 0.05 × 0.04
Radiation	CuKα (λ = 1.54178)
2Θ range for data collection/°	4.328 to 79.938
Index ranges	-11 ≤ h ≤ 11, -33 ≤ k ≤ 31, -39 ≤ l ≤ 36
Reflections collected	105224
Independent reflections	16214 [R_{int} = 0.2487, R_{sigma} = 0.0906]
Data/restraints/parameters	16214/2135/1604
Goodness-of-fit on F^2	2.277
Final R indexes [I>=2σ (I)]	R_1 = 0.2641, wR_2 = 0.5900
Final R indexes [all data]	R_1 = 0.3410, wR_2 = 0.6274
Largest diff. peak/hole / e Å^{-3}	2.55/-1.51

Table S5.5. Summary of X-ray crystallographic data for $\{[Y(12\text{-}MC_{Ga,shi}\text{-}4)]_4(frn)_8(H_2O)_{16}\}^{3-}$.

Identification code	$\{[Y(12\text{-}MC_{Ga,shi}\text{-}4)]_4(frn)_8(H_2O)_{16}\}^{3-}$
Empirical formula	$C_{232}H_{144}Ga_{16}N_{16}O_{104}Y_4$
Formula weight	6290.78
Temperature/K	200.00(10)
Crystal system	tetragonal
Space group	P-4b2
a/Å	27.6767(9)
b/Å	27.6767(9)
c/Å	51.530(3)
α/°	90
β/°	90
γ/°	90
Volume/Å^3	39472(3)
Z	2
ρcalcg/cm^3	0.529
μ/mm^{-1}	1.234
F(000)	6264.0
Crystal size/mm^3	0.35 × 0.2 × 0.08
Radiation	Cu Kα (λ = 1.54184)
2Θ range for data collection/°	5.67 to 89.018
Index ranges	-24 ≤ h ≤ 14, -25 ≤ k ≤ 23, -46 ≤ l ≤ 46
Reflections collected	75226
Independent reflections	15122 [Rint = 0.1125, Rsigma = 0.0599]
Data/restraints/parameters	15122/2195/888
Goodness-of-fit on F^2	0.984
Final R indexes [I>=2σ (I)]	R1 = 0.0551, wR2 = 0.1518
Final R indexes [all data]	R1 = 0.0787, wR2 = 0.1724
Largest diff. peak/hole / e Å^{-3}	0.36/-0.21
Flack parameter	0.5

Table 5.6. Diffusion analysis data for {[La(12-$MC_{Ga,shi}$-4)]$_{3/4}$(frn)$_6$/$_8$}$(HNEt_3)_{3/4}$.

peak name	F2[ppm]	Io	error	D [m^2/s]	error
1	8.856	1.50E+05	3373	7.68E-11	4.31E-12
2	8.323	3.34E+05	1663	7.04E-11	9.01E-13
3	8.308	2.73E+05	1661	7.03E-11	1.10E-12
4	8.276	4.95E+05	2956	7.17E-11	1.09E-12
5	8.113	2.03E+05	2635	7.01E-11	2.35E-12
6	8.09	2.61E+05	2447	6.95E-11	1.69E-12
7	8.065	5.35E+05	2119	6.92E-11	7.10E-13
8	8.047	4.43E+05	1785	6.97E-11	7.26E-13
9	8.02	2.00E+05	2589	7.17E-11	2.37E-12
10	7.959	1.56E+06	3.12E+04	6.26E-10	2.71E-11
11	7.907	3.71E+05	3230	7.11E-11	1.59E-12
12	7.888	5.11E+05	2440	6.99E-11	8.60E-13
13	7.862	6.86E+05	1938	6.92E-11	5.06E-13
14	7.836	2.83E+05	1565	7.00E-11	9.98E-13
15	7.805	5.25E+05	2472	7.00E-11	8.50E-13
16	7.793	3.79E+05	1987	6.88E-11	9.35E-13
17	7.785	6.05E+05	1844	6.98E-11	5.49E-13
18	7.752	2.36E+05	1633	7.00E-11	1.25E-12
19	7.73	2.88E+05	2131	7.07E-11	1.35E-12
20	7.68	3.23E+05	2370	6.99E-11	1.32E-12
21	7.653	4.96E+05	2524	6.95E-11	9.14E-13
22	7.636	3.08E+05	1780	7.10E-11	1.05E-12
23	7.413	2.70E+05	2481	6.94E-11	1.65E-12
24	7.262	6.12E+05	2416	6.96E-11	7.10E-13
25	7.211	2.82E+05	1706	6.99E-11	1.09E-12
26	7.168	1.35E+05	1837	7.08E-11	2.47E-12
27	6.892	6.96E+05	2578	6.93E-11	6.64E-13
28	6.859	3.85E+05	2245	6.89E-11	1.04E-12
29	6.822	3.21E+05	2189	6.96E-11	1.22E-12
30	6.792	3.60E+05	1539	6.97E-11	7.69E-13
31	6.769	3.46E+05	2114	6.98E-11	1.10E-12
32	6.74	5.73E+05	1572	6.98E-11	4.94E-13
33	6.725	5.03E+05	2119	6.89E-11	7.52E-13
34	6.669	2.26E+05	1430	7.03E-11	1.15E-12
35	6.65	1.45E+05	1934	6.96E-11	2.39E-12
36	3.064	4.19E+06	1.01E+04	3.41E-10	1.81E-12

Table 5.7. Diffusion analysis data for $\{[Y(12\text{-}MC_{Ga,shi}\text{-}4)]_{3/4}(frn)_{6/8}\}(HNEt_3)_{3/4}$.

peak name	F2[ppm]	Io	error	D [m^2/s]	error
1	8.788	7.22E+04	1.08E+04	8.13E-10	2.59E-10
2	8.638	1.67E+05	3363	7.79E-11	3.90E-12
3	8.617	2.29E+05	5246	7.70E-11	4.41E-12
4	8.525	1.84E+05	4309	7.36E-11	4.37E-12
5	8.511	3.67E+05	3886	7.45E-11	1.99E-12
6	8.489	2.96E+05	4786	7.36E-11	3.02E-12
7	8.47	2.40E+05	4993	7.17E-11	3.81E-12
8	8.448	2.71E+05	4546	7.71E-11	3.24E-12
9	8.394	2.67E+05	5363	7.31E-11	3.73E-12
10	8.374	2.91E+05	3.89E+03	7.54E-11	2.53E-12
11	8.301	2.57E+05	3368	7.43E-11	2.46E-12
12	8.26	3.29E+05	5097	7.64E-11	2.97E-12
13	8.174	5.37E+05	4454	7.64E-11	1.59E-12
14	8.143	9.17E+05	6000	7.52E-11	1.24E-12
15	8.121	2.32E+05	4623	7.74E-11	3.85E-12
16	8.09	9.44E+05	6528	7.43E-11	1.30E-12
17	8.01	5.13E+05	3037	7.36E-11	1.11E-12
18	7.989	5.86E+05	6690	7.61E-11	2.18E-12
19	7.959	8.26E+06	1.76E+05	6.56E-10	3.01E-11
20	7.897	1.31E+06	5995	7.45E-11	8.60E-13
21	7.849	1.02E+06	4376	7.40E-11	8.02E-13
22	7.775	8.86E+05	5430	7.43E-11	1.15E-12
23	7.557	5.09E+05	4405	7.35E-11	1.61E-12
24	7.538	4.91E+05	2876	7.43E-11	1.10E-12
25	7.488	6.78E+05	5945	7.27E-11	1.62E-12
26	7.47	6.08E+05	5548	7.21E-11	1.68E-12
27	7.269	8.98E+05	5964	7.41E-11	1.25E-12
28	7.217	1.20E+06	5274	7.47E-11	8.29E-13
29	7.159	3.49E+05	6351	7.58E-11	3.47E-12
30	6.99	5.02E+05	5151	7.28E-11	1.90E-12
31	6.872	7.33E+05	5463	7.38E-11	1.39E-12
32	6.851	1.40E+06	6751	7.40E-11	9.05E-13
33	6.827	9.54E+05	9121	7.41E-11	1.79E-12
34	6.721	5.09E+05	6015	7.48E-11	2.23E-12
35	6.618	3.65E+05	6019	7.52E-11	3.12E-12
36	3.037	3.42E+06	1.79E+04	3.37E-10	3.88E-12

Table 5.8. Diffusion analysis data for $\{[Lu(12\text{-}MC_{Ga,shi}\text{-}4)]_{3/4}(frn)_6/_8\}(HNEt_3)_{3/4}$.

peak name	F2[ppm]	Io	error	D [m^2/s]	error
1	8.777	4.45E+04	6.59E+03	7.61E-10	2.41E-10
2	8.644	9.19E+04	2865	8.59E-11	6.50E-12
3	8.548	1.54E+05	3721	8.33E-11	4.94E-12
4	8.465	9.63E+04	2405	8.23E-11	5.05E-12
5	8.312	1.97E+05	2715	8.36E-11	2.82E-12
6	8.22	1.93E+05	3163	8.31E-11	3.33E-12
7	8.135	3.45E+05	3910	8.18E-11	2.28E-12
8	8.075	3.28E+05	3151	8.20E-11	1.93E-12
9	7.999	2.04E+05	4182	8.54E-11	4.25E-12
10	7.98	2.47E+05	6.26E+03	8.69E-11	5.32E-12
11	7.957	2.64E+06	5.21E+04	6.71E-10	2.85E-11
12	7.905	3.72E+05	3277	8.21E-11	1.77E-12
13	7.846	4.91E+05	4272	8.18E-11	1.75E-12
14	7.767	3.47E+05	2326	8.43E-11	1.38E-12
15	7.515	2.47E+05	2831	8.15E-11	2.30E-12
16	7.467	3.94E+05	3962	8.09E-11	2.01E-12
17	7.257	4.40E+05	2986	8.33E-11	1.38E-12
18	7.192	3.23E+05	3411	8.35E-11	2.16E-12
19	7.13	1.48E+05	3.64E+03	8.40E-11	5.04E-12
20	6.973	1.38E+05	4051	8.25E-11	5.95E-12
21	6.85	4.39E+05	3957	8.35E-11	1.84E-12
22	6.754	2.00E+05	3165	8.12E-11	3.17E-12
23	6.692	1.73E+05	4171	8.31E-11	4.90E-12
24	6.606	1.37E+05	3053	8.14E-11	4.48E-12
25	3.037	1.98E+06	1.07E+04	3.51E-10	4.15E-12

Table 5.9. Diffusion analysis data for {[Y(12-$MC_{Ga,shi}$-4)]$_3$(bipy)$_6$}(HNEt$_3$)$_3$.

Peak name	F2 [ppm]	Io	error	D [m^2/s]	error
1	9.27	9.64E+05	2.29E+04	8.92E-11	5.10E-12
2	9.213	6.98E+06	6.14E+04	2.13E-10	4.17E-12
3	9.142	6.48E+06	3.98E+04	8.44E-11	1.26E-12
4	8.993	8.67E+06	4.31E+04	8.46E-11	1.03E-12
5	8.928	2.08E+06	6.09E+04	9.63E-11	6.68E-12
6	8.857	1.30E+06	5.71E+04	6.69E-10	6.32E-11
7	8.583	9.35E+06	1.94E+05	1.91E-10	8.80E-12
8	8.552	3.57E+06	2.37E+04	8.37E-11	1.36E-12
9	8.422	7.98E+06	3.91E+04	8.38E-11	1.00E-12
10	8.479	5.91E+06	1.14E+05	1.89E-10	8.11E-12
11	8.169	4.90E+06	2.57E+04	8.57E-11	1.09E-12
12	7.956	1.13E+07	1.06E+06	3.69E-10	7.59E-11
13	7.905	7.86E+06	3.95E+04	8.37E-11	1.03E-12
14	7.247	8.22E+06	4.47E+04	8.49E-11	1.12E-12
15	6.893	1.19E+07	5.70E+04	8.40E-11	9.83E-13
16	6.763	7.49E+06	4.10E+04	8.45E-11	1.13E-12
17	2.893	1.00E+08	8.50E+05	6.60E-10	1.20E-11

Table S5.10. Selected geometric parameters (Å) for {[TbNa(12-$MC_{Ga,shi}$-4)]$_3$(bipy)$_6$(DMF)$_2$(H_2O)$_{10}$}($HNEt_3$)(DMF)$_5$

{[TbNa(12-$MC_{Ga,shi}$-4)]$_3$(bipy)$_6$(DMF)$_2$(H_2O)$_{10}$}($HNEt_3$)(DMF)$_5$			
Tb2-O251	2.293(5)	Ga32-O192	2.06(2)
Tb2-O2511	2.293(5)	Ga32-O2W	2.106(9)
Tb2-O1311	2.392(6)	Ga32-O92	1.83(2)
Tb2-O131	2.392(6)	Ga32-O42	1.90(3)
Tb2-O1611	2.366(6)	Ga32-O52	1.94(3)
Tb2-O161	2.366(6)	Na-O6W1	2.882(10)
Tb2-O2911	2.326(6)	Na-O5W1	2.863(14)
Tb2-O291	2.326(6)	Na-O5WA1	2.76(3)
Tb2-O1321	2.243(14)	Na-O6WA1	2.79(4)
Tb2-O132	2.243(14)	Na-O1WN1	2.79(3)
Tb2-O162	2.280(16)	Na-O1WN	2.79(3)
Tb2-O1621	2.280(16)	O211-Ga411	2.012(13)
Tb1-O71	2.355(8)	O5WA-Na	2.76(3)
Tb1-O271	2.346(8)	O222-Ga221	1.992(19)
Tb1-O41	2.361(7)	O212-Tb11	2.385(15)
Tb1-O201	2.348(9)	O6WA-Na	2.79(4)
Tb1-O2211	2.283(9)	O162-Ga621	1.933(16)
Tb1-O101	2.284(9)	Ga22-O62	1.89(3)
Tb1-O11	2.290(9)	Ga22-O58	2.01(3)
Tb1-O82	2.288(17)	Ga42-N42	1.720(8)
Tb1-O232	2.299(18)	Ga42-O82	1.994(19)
Tb1-O202	2.278(16)	Ga42-O242	2.084(19)
Tb1-O42	2.37(2)	Ga42-O72	2.10(2)
Tb1-O12	2.375(16)	Ga42-O1W1	2.15(4)
Ga51-O141	1.942(8)	Ga42-O15	1.84(2)
Ga51-N521	1.935(6)	Ga52-N52	1.758(6)
Ga51-O131	1.944(6)	Ga52-O262	2.008(18)
Ga51-O301	2.034(7)	Ga52-O5WA	2.27(3)
Ga51-O1811	1.845(7)	Ga52-O132	1.938(16)
Ga51-O6W	2.176(9)	Ga52-O142	1.86(2)
Ga61-O171	1.939(8)	Ga52-O1	1.891(18)
Ga61-O151	1.839(7)	Ga12-N12	1.772(11)
Ga61-O161	1.933(6)	Ga12-O282	2.053(19)
Ga61-O261	2.030(7)	Ga12-O102	1.97(2)
Ga61-O5W	2.159(14)	Ga12-O112	2.01(3)

Ga21-N32	1.939(7)	Ga12-O32	1.85(2)
Ga21-O81	1.931(10)	Ga12-O4W2	2.014(17)
Ga21-O71	1.968(8)	Ga62-N62	1.824(6)
Ga21-O61	1.873(10)	Ga62-O302	2.027(17)
Ga21-O241	1.997(9)	Ga62-O6WA	2.13(4)
Ga21-O1D1	2.090(12)	Ga62-O1721	1.945(17)
Ga31-N42	1.848(8)	Ga62-O152	1.84(2)
Ga31-O281	2.003(8)	Ga62-O1621	1.933(16)
Ga31-O101	1.941(10)	N52-Ga511	1.935(6)
Ga31-O91	1.865(11)	O181-Ga511	1.845(7)
Ga31-O111	1.899(14)	O6W-Na	2.883(10)
Ga31-O4W	2.253(11)	O5W-Na	2.863(14)
Ga11-N22	1.987(9)	O221-Tb11	2.283(9)
Ga11-O41	1.937(8)	Ga41-O11	1.906(11)
Ga11-O51	1.901(12)	Ga41-O2111	2.012(13)
Ga11-O191	2.026(10)	Ga41-O21	1.998(15)
Ga11-O31	1.780(11)	Ga41-O3W	2.227(13)
Ga11-O2W	2.315(9)	Ga22-N22	1.944(10)
Ga41-N12	1.939(10)	Ga22-O2221	1.992(19)
Ga41-O121	1.794(12)	Ga22-O22	1.70(3)
Ga22-O12	2.00(2)		

[1]1-X,+Y,3/2-Z

Table S5.11. Selected geometric parameters (Å) for {[La(12-$MC_{Ga,shi}$-4)]$_3$(frn)$_6$(H_2O)$_5$(DMF)$_3$}$^{3-}$(DMF)

{[La(12-$MC_{Ga,shi}$-4)]$_3$(frn)$_6$(H_2O)$_5$(DMF)$_3$}$^{3-}$(DMF)			
La2-O36	2.587(18)	Ga8-O18	1.860(18)
La2-O17L	2.584(19)	Ga8-O37	1.97(2)
La2-O5L	2.519(19)	Ga8-O1S	2.362(19)
La2-O10L	2.49(2)	Ga8-N18	1.90(3)
La2-O5W	2.73(2)	Ga11-O14L	2.021(18)
La2-O38	2.495(18)	Ga11-O312	1.96(2)
La2-O35	2.547(18)	Ga11-O111	1.86(2)
La2-O12L	2.617(19)	Ga11-O212	1.91(3)
La2-O37	2.480(19)	Ga11-N111	2.00(2)
La1-O30L	2.489(19)	Ga11-C112	2.51(4)
La1-O31	2.544(17)	Ga3-O32	1.95(2)
La1-O34	2.54(2)	Ga3-O6L	1.913(18)
La1-O32	2.52(2)	Ga3-O22	2.04(2)
La1-O2L	2.48(2)	Ga3-O13	1.90(3)
La1-O25L	2.53(2)	Ga3-N13	2.05(4)
La1-O7L	2.506(18)	Ga12-O39	1.97(2)
La1-O1W	2.74(2)	Ga12-O21L	1.96(2)
La1-O33	2.49(3)	Ga12-O112	1.87(2)
La3-O20L	2.538(18)	Ga12-N112	2.07(3)
La3-O3S	2.60(2)	Ga12-O29	1.92(2)
La3-O39	2.50(2)	Ga4-O1L	1.979(19)
La3-O312	2.44(3)	Ga4-N14	1.91(3)
La3-O311	2.483(17)	Ga4-O14	1.95(2)
La3-O27L	2.53(2)	Ga4-O3W	2.33(3)
La3-O310	2.507(17)	Ga4-O33	2.07(3)
La3-O15L	2.537(18)	Ga4-O23	1.99(3)
La3-O22L	2.573(17)	Ga9-O210	2.007(19)
Ga2-O12	1.88(2)	Ga9-O310	1.960(15)
Ga2-O31	1.87(2)	Ga9-O26L	1.95(2)
Ga2-O21	1.94(5)	Ga9-O19	1.93(2)
Ga2-O24L	1.918(19)	Ga9-N19	1.84(3)
Ga2-N12	2.00(2)	Ga5-O28	1.835(19)
Ga2-C11	2.49(4)	Ga5-O38	1.95(2)
Ga2-O21A	1.91(4)	Ga5-N15	2.08(2)
Ga10-O19L	1.926(18)	Ga5-O9L	1.960(18)

Ga10-O211	1.927(18)	Ga1-O29L	1.893(19)
Ga10-O110	1.897(19)	Ga1-O34	1.92(2)
Ga10-O311	1.950(18)	Ga1-N11	1.97(2)
Ga10-N110	2.00(3)	Ga1-O24	1.99(2)
Ga6-O25	1.88(2)	Ga1-O11	1.910(15)
Ga6-O11L	1.942(18)	Ga1-O2W	2.50(2)
Ga6-N16	1.87(3)	Ga8-O27	2.04(2)
Ga6-O35	1.983(18)	Ga8-O4L	1.990(17)
Ga6-O16	1.82(2)	Ga7-N17	1.99(3)
Ga7-O36	1.864(19)	Ga7-O17	1.77(2)
Ga7-O16L	1.872(17)	Ga5-O2S	2.213(19)
Ga7-O26	2.03(2)	Ga5-O15	1.91(2)

Table S5.12. Selected geometric parameters (Å) for $\{[Y(12\text{-}MC_{Ga,shi}\text{-}4)]_4(frn)_8(H_2O)_{16}\}^{3-}$

$\{[Y(12\text{-}MC_{Ga,shi}\text{-}4)]_4(frn)_8(H_2O)_{16}\}^{3-}$			
O26A-Y	2.396(13)	Ga1A-N11A	1.91(2)
O25A-Y	2.382(15)	Ga1A-O11A	1.768(17)
Y-O26	2.301(3)	Ga1A-O34A	1.98(3)
Y-O25	2.301(3)	Ga1A-O24A	1.89(2)
Y-O553	2.10(2)	Ga1A-O1WA	2.279(14)
O55A-Y2	2.60(2)	Ga1A-O15A	2.008(19)
O46A-Y1	2.42(3)	O56A-Ga4A1	1.96(2)
O33-Y	2.392(16)	O45A-Ga2A2	2.314(18)
Y-O32	2.288(9)	O16A-Ga3A	1.840(19)
Y-O31	2.302(15)	Ga1-O34	1.959(14)
Y-O33A	2.330(16)	Ga1-O24	1.798(3)
Y-O32A	2.267(19)	Ga1-N11	1.995(18)
Y-O31A	2.359(11)	Ga1-O11	1.705(13)
Y-O34A	2.27(2)	Ga1-O1W	2.305(14)
Y-O461	2.39(3)	Ga1-O15	2.251(16)
O34-Y	2.383(10)	Ga3-N13	1.860(12)
Ga4-N14	1.957(11)	Ga3-O13	1.882(16)
Ga4-O14	1.789(13)	Ga3-O32	1.984(7)
Ga4-O33	1.942(17)	Ga3-O22	2.022(13)
Ga4-O23	1.848(15)	Ga3-O3W	2.359(16)
Ga4-O4W	2.035(16)	Ga3-O16	2.13(2)
Ga4-O453	1.95(3)	Ga2-N12	1.840(5)
Ga2A-N12A	1.916(15)	Ga2-O12	1.840(13)
Ga2A-O12A	1.877(16)	Ga2-O31	1.942(17)
Ga2A-O31A	1.902(3)	Ga2-O21	1.951(19)
Ga2A-O21A	1.899(3)	Ga2-O2W	2.14(2)
Ga2A-O2WA	2.279(17)	Ga2-O561	2.38(2)
Ga3A-N13A	1.951(17)	Ga4A-O33A	1.923(18)
Ga3A-O13A	1.893(18)	Ga4A-O23A	1.85(2)
Ga3A-O32A	1.980(19)	Ga4A-C13A	2.49(3)
Ga3A-O22A	1.91(2)	Ga4A-N14A	1.96(2)
Ga3A-O3WA	2.304(14)	Ga4A-O14A	1.960(18)
Ga4A-O4WA	2.52(2)		

[1]1-X,-Y,+Z; 2+Y,-X,1-Z; 3-Y,+X,1-Z

6.7 Supporting information: Chapter 6

6.7.1 IR spectrum

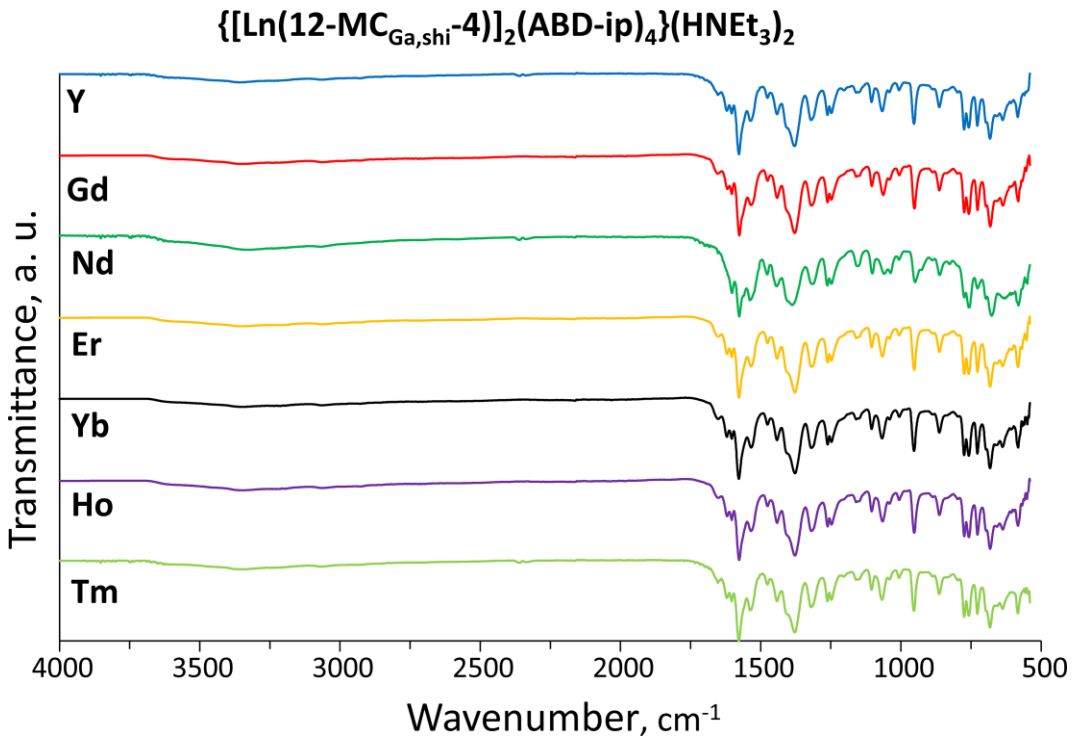

Figure S6.1. FT-ATR-IR spectra of {[Ln(12-MC$_{Ga,shi}$-4)]$_2$(ABD-ip)$_4$}(HNEt$_3$)$_2$ metallacrowns in the solid state (Ln^{III} = Y^{III}, Gd^{III}, Nd^{III}, Ho^{III}, Er^{III}, Tm^{III}, Yb^{III}).

Acknowledgments

First and foremost, I would like to thank my mom, Gabriella, my grandfather, Nando, and my grandmother, Iole, for constantly supporting me throughout these three years, filled with ups and downs. Thank you for never abandoning me and for always believing in me.

I would also like to thank my partner, Marta, and my friends, Davide M., Lorenzo M., Lorenzo F., Mirko S., and Cristiano M., for their constant support.

I would like to express my heartfelt thanks to my supervisor, Professor Matteo Tegoni. His patience, support, and deep expertise have been invaluable throughout this journey. He has guided me through challenges, encouraged me to grow, and given me the space to explore. I am truly grateful for the trust he has placed in me and the countless opportunities he has provided to help me reach this point.

In particular, I am deeply grateful to Professor Luciano Marchiò, who has supported me both professionally and personally. I also want to thank my lab colleague Dr. Matteo Melegari for his invaluable help and partnership in our research endeavors. A special thanks goes to Dr. Davide Balestri, whose support has been with me since the very first day of my Ph.D. I am also grateful to all the colleagues who shared this path with me: Dr. Giulia Bonfant, my first co-tutor, Dr. Martina Neri, Dr. Fabio Fornari and Alessia Panizzi. Additionally, I extend my thanks to Dr. Monica Maffini from the University of Parma for their professional support.

I am also incredibly grateful for the time spent at the University of Michigan, particularly in Professor Vincent L. Pecoraro's lab. I sincerely thank Professor Pecoraro for hosting me in his laboratory and for guiding me throughout my time there. This experience was deeply enriching, both scientifically and culturally, thanks also to the welcoming environment created by my colleagues.

I would like to express my sincere thanks to Dr. Timothee Lathion for his support, both scientifically and personally, during my time abroad in Professor Pecoraro’s lab, as well as for his continued collaboration on our shared projects even after my return. My gratitude also extends to Dr. Svetlana V. Eliseeva for her invaluable scientific guidance on the work I conducted in Michigan, and to Dr. Stephane Petoud from the Center for Molecular Biophysics (CBM) in Orléans for their support and contributions.

Lastly, I would like to express my appreciation to my external collaborators, Angela Serpe from the University of Cagliari and Flavia Artizzu from the University of Piemonte Orientale, for their contributions.